Universidade de Aveiro Departamento de Engenharia Cerâmica e do Vidro
2011

Kiryl Yasakau

Protecção activa de corrosão na liga AA2024 por revestimentos sol-gel com inibidores de corrosão

Active corrosion protection of AA2024 by sol-gel coatings with corrosion inhibitors

Kiryl Yasakau

Protecção activa de corrosão na liga AA2024 por revestimentos sol-gel com inibidores de corrosão

Active corrosion protection of AA2024 by sol-gel coatings with corrosion inhibitors

Dissertação apresentada à Universidade de Aveiro para cumprimento dos requisitos necessários à obtenção do grau de Doutor em Ciência e Engenharia de Materiais, realizada sob a orientação científica do Doutor Mário Guerreiro Silva Ferreira, Professor Catedrático do Departamento de Engenharia Cerâmica e do Vidro da Universidade de Aveiro, e do Doutor Mikhail Zheludkevich, Investigador Auxiliar da Universidade de Aveiro.

Dedicated to my mother Elena and to the memory of my grandmother Liliana
for their immense love and care

o júri

presidente

Prof. Doutor Domingos Moreira Cardoso
professor catedrático do Departamento de Matemática da Universidade de Aveiro

Prof. Doutor Mário Guerreiro Silva Ferreira
professor catedrático do Departamento de Engenharia Cerâmica e do Vidro da Universidade de Aveiro

Doutor Mikhail Zheludkevich
investigador auxiliar do Departamento de Engenharia Cerâmica e do Vidro da Universidade de Aveiro

Prof. Doutor Christopher Michael Ashton Bret
professor catedrático do Departamento de Engenharia Química da Faculdade de Ciências e Tecnologia da Universidade de Coimbra

Prof. Doutor Fernando Manuel Bico Marques
professor catedrático do Departamento de Engenharia Cerâmica e do Vidro da Universidade de Aveiro

Doutora Maria de Fátima Grilo da Costa Montemor
investigadora auxiliar do Departamento de Engenharia Química e Biológica do Instituto Superior Técnico da Universidade Técnica de Lisboa

Prof. Doutor Herman Terryn
professor catedrático da Universidade Livre de Bruxelas

palavras-chave

AA2024, pré-tratamento, sol-gel, corrosão, protecção activa, auto-reparação, inibidor, EIS, SKPFM, SVET

resumo

A indústria aeronáutica utiliza ligas de alumínio de alta resistência para o fabrico dos elementos estruturais dos aviões. As ligas usadas possuem excelentes propriedades mecânicas mas apresentam simultaneamente uma grande tendência para a corrosão. Por esta razão essas ligas necessitam de protecção anticorrosiva eficaz para poderem ser utilizadas com segurança. Até à data, os sistemas anticorrosivos mais eficazes para ligas de alumínio contêm crómio hexavalente na sua composição, sejam pré-tratamentos, camadas de conversão ou pigmentos anticorrosivos. O reconhecimento dos efeitos carcinogénicos do crómio hexavalente levou ao aparecimento de legislação banindo o uso desta forma de crómio pela indústria. Esta decisão trouxe a necessidade de encontrar alternativas ambientalmente inócuas mas igualmente eficazes.

O principal objectivo do presente trabalho é o desenvolvimento de pré-tratamentos anticorrosivos activos para a liga de alumínio 2024, baseados em revestimentos híbridos produzidos pelo método sol-gel. Estes revestimentos deverão possuir boa aderência ao substrato metálico, boas propriedades barreira e capacidade anticorrosiva activa. A protecção activa pode ser alcançada através da incorporação de inibidores anticorrosivos no pré-tratamento.

O objectivo foi atingido através de uma sucessão de etapas. Primeiro investigou-se em detalhe a corrosão localizada (por picada) da liga de alumínio 2024. Os resultados obtidos permitiram uma melhor compreensão da susceptibilidade desta liga a processos de corrosão localizada. Estudaram-se também vários possíveis inibidores de corrosão usando técnicas electroquímicas e microestruturais.

Numa segunda etapa desenvolveram-se revestimentos anticorrosivos híbridos orgânico-inorgânico baseados no método sol-gel. Compostos derivados de titania e zirconia foram combinados com siloxanos organofuncionais a fim de obter-se boa aderência entre o revestimento e o substrato metálico assim como boas propriedades barreira. Testes industriais mostraram que estes novos revestimentos são compatíveis com os esquemas de pintura convencionais actualmente em uso. A estabilidade e o prazo de validade das formulações foram optimizados modificando a temperatura de armazenamento e a quantidade de água usada durante a síntese.

As formulações sol-gel foram dopadas com os inibidores seleccionados durante a primeira etapa e as propriedades anticorrosivas passivas e activas dos revestimentos obtidos foram estudadas numa terceira etapa do trabalho. Os resultados comprovam a influência dos inibidores nas propriedades anticorrosivas dos revestimentos sol-gel. Em alguns casos a acção activa dos inibidores combinou-se com a protecção passiva dada pelo revestimento mas noutros casos terá ocorrido interacção química entre o inibidor e a matriz de sol-gel, de onde resultou a perda de propriedades protectoras do sistema combinado.

Atendendo aos problemas provocados pela adição directa dos inibidores na formulação sol-gel procurou-se, numa quarta etapa, formas alternativas de incorporação. Na primeira, produziu-se uma camada de titania nanoporosa na superfície da liga metálica que serviu de reservatório para os inibidores. O revestimento sol-gel foi aplicado por cima da camada nanoporosa. Os inibidores armazenados nos poros actuam quando o substrato fica exposto ao ambiente agressivo. Numa segunda, os inibidores foram armazenados em nano-reservatórios de sílica ou em nanoargilas (halloysite), os quais foram revestidos por polielectrólitos montados camada a camada. A terceira alternativa consistiu no uso de nano-fios de molibdato de cério amorfo como inibidores anticorrosivos nanoparticulados. Os nano-reservatórios foram incorporados durante a síntese do sol-gel. Qualquer das abordagens permitiu eliminar o efeito negativo do inibidor sobre a estabilidade da matriz do sol-gel.

Os revestimentos sol-gel desenvolvidos neste trabalho apresentaram protecção anticorrosiva activa e capacidade de auto-reparação. Os resultados obtidos mostraram o elevado potencial destes revestimentos para a protecção anticorrosiva da liga de alumínio 2024.

abstract

The aerospace industry employs high strength aluminum alloys as a constructional material for aircrafts. Aluminum alloys possess advanced mechanical requirements, though suffer from corrosion. Therefore, corrosion protection is always used for aluminum alloys. Up to now the most effective corrosion protection systems include chromium (VI) as the main constituent of pretreatments and corrosion inhibitive pigments. However, the chromates are strongly carcinogenic and the present health regulations banned the use of Cr (VI) containing materials in industry. Consequently, there is a need for environmentally safe corrosion protection systems.

The main objective of the present work is the development of active anti-corrosion pre-treatments for 2024 aluminum alloy on the basis of hybrid sol-gel layers. The effective corrosion pre-treatment should confer adequate adhesion together with good barrier properties and active corrosion protection ability. The active corrosion protection can be achieved by introducing the corrosion inhibitors in the pre-treatment.

Successful fulfilment of the main objective required accomplishing of different stages of the work. At first the localized corrosion of AA2024 was investigated in detail. The obtained results provide better understanding of the intimate aspects of the corrosion susceptibility of AA2024. Different prospective corrosion inhibitors were investigated using electrochemical and microstructural methods.

At the second stage the development of hybrid sol-gel coatings was performed. Titania and zirconia based derivatives were combined with organofunctional silanes in order to provide the enhanced adhesion between the metal and the coating and to confer good barrier properties. Industrial tests show that the developed sol-gel coatings are compatible with common organic protection systems. The stability and life time of the sol-gel formulations were also optimized by changing the storage temperature and the amount of water during the synthesis.

Sol-gel systems were doped with the selected corrosion inhibitors and studied from the point of view of passive and active corrosion protective properties at the third stage of the work. The results demonstrate the influence of the inhibitive additives on the corrosion performance of the sol-gel coatings. Some inhibitors can provide active corrosion protection in combination with the sol-gel coating, but some chemically interact with the sol-gel matrix resulting in failure of the protective properties of coatings.

New approaches of inhibitor incorporation and delivery were used in the fourth stage of the work due to problems associated with the direct introduction of inhibitors in the sol-gels. A nanoporous titania-based pre-layer applied directly to the alloy was employed for storage and release of inhibitors. Nanocontainers of corrosion inhibitors based on silica and halloysite nanoclay with Layer-by-Layer assembled polyelectrolyte shells were used in the second approach. Amorphous cerium molybdate nanowires have been used as corrosion inhibitor nanoparticles in the third approach. During the sol-gel synthesis these nanocontainers were added to impart active corrosion protective properties of the sol-gel coatings. Using these approaches the negative effect of inhibitor on the sol-gel matrix stability was eliminated. The developed sol-gel pretreatments demonstrate important active corrosion protection and self-healing ability.

The obtained results show high potential of the developed hybrid sol-gel pre-treatment doped with corrosion inhibitors for the corrosion protection of AA2024.

Contents

List of abbreviations and symbols

General symbols and abbreviation

A	Surface area
BSA	Boric sulfuric anodizing
C	Capacitor in equivalent circuits
C_{coat}	Coating capacitance
C_{dl}	Double layer capacitance
C_{inh}	Capacitance of inhibitive layer
C_{ox}	Oxide capacitance
C, C_{ox}, C_{red}	Concentration, Concentration of oxidative and reductive species
C_0	Coating capacitance at the beginning of exposure to electrolyte
C_x	Coating capacitance at the end of exposure to electrolyte
CCC	Chemical conversion coating
CE	Counter electrode
CPE	Constant phase element
d	Distance
D_{ox}, D_{red}	Diffusion coefficient of oxidative and reductive species
E	Electrode potential
E_{corr}	Corrosion potential
ECP	Electroactive conducting polymers
E_{eq}	Equilibrium potential
E_{pit}	Pitting potential
i_{corr}	Corrosion current density
i_L	Limiting current density
i_0	Exchange current density
I_0	Current amplitude
E_F	Fermi level
F	Faraday constant
f	Frequency
IGC	Intergranular corrosion
K_f, K_b	Reaction rate constants for the forward and backward reaction
L	Inductor in equivalent circuits
NBB	Nanobuilding blocks
n	Number of electrons involved in electrochemical process
nm	Nanometer
ORR	Oxygen reduction reaction
Q	Fitting parameter of equivalent circuit with capacitor
r_f, r_b	Rates of forward and backward reaction
r	Water to alkoxide ratio
R	Resistor in equivalent circuits
R	Universal gas constant
R, Y, A	Organic functional groups in chemical formulas
R_{coat}	Coating resistance
RE	Reference electrode
R_{inh}	Resistance of inhibitive layer
R_{ox}	Oxide resistance
R_{polar}	Polarization resistance
R_{sol}	Solution resistance
SAA	Sulfuric acid anodizing
SCC	Stress corrosion cracking
SCE	Saturated calomel electrode
SHE	Standard Hydrogen Electrode
t	Time
T	Temperature
TSA	Tartaric sulfuric anodizing
V_0	Voltage amplitude

V_{AC}	Externally applied alternating voltage
V_{CPD}	Contact potential difference
V_{DC}	Externally applied constant voltage
V_{VPD}, VPD	Volta potential difference
W, Z_w	Warburg impedance
WE	Working electrode
Wm, Wp	Work function of metal and probe
wt.%	Weight percentage
Y_0	Admittance
Z, Z_0, $Z(\omega)$	Impedance
Z', Z''	Real and imaginary part of impedance
α	Fraction of polarization
βa , βc	Cathodic and anodic Tafel constant
ΔG_f^* , ΔG_b^*	activation energy of forward and backward reaction
ΔV	Potential difference
δ	Diffusion layer thickness
ϵ	Dielectric permittivity
ϵ_0	Dielectric permittivity of vacuum
ϵ_w	Dielectric permittivity of water
η	Polarization
η_a	Cathodic polarization
η_c	Anodic polarization
η_{act} , η_{conc}	Activation and concentration polarization
μm	Micrometer
ρ	Specific resistance
σ	Warburg coefficient
τ	Time constant
φ	Phase shift
ω	Angular frequency

Experimental techniques

AES	Auger Electron Spectroscopy
AFM	Atomic Force Microscopy
DC-polarization	Direct current polarization
DTA	Differential thermal analysis
EDS	Energy Dispersive Spectroscopy
EIS	Electrochemical impedance spectroscopy
FTIR	Fourier Transformed Infrared Spectroscopy
SEM	Scanning Electron Microscopy
SIET	Scanning Ion-Selective Electrode Technique
SKPFM	Scanning Kelvin Probe Microscopy
SRET	Scanning Reference Electrode Technique
SVET	Scanning Vibrating Electrode Technique
TEM	Transmission Electron Microscopy
TOF-SIMS	Time of flight Secondary Ions Mass Spectroscopy
TGA	Thermogravimetric analysis
XPS	X-ray Photoelectron Spectroscopy

Inhibitors and reagents

8HQ	8-Hydroxyquinoline
AcAc	Acetylacetone
BTA	Benzotriazole
EtAcAc	Ethylacetoacetate
GPTMS	3-glycidoxypropyltrimethoxysilane

MBT	2-mercaptobenzothiazole
MPS	3-methacryloxypropyltrimethoxysilane
PAH	Polyallylhydrochloride
PEI	Polyethyleneimine
PSS	Polystyrenesulfonate
QA	Quinaldic acid
SAL	Salycilaldoxime
TEOS	Tetraetylorthosilicate
TPOT	Titanium (IV) propoxide
TPOZ	Zirconium (IV) propoxide

List of Figures

12

13

List of Tables

Preface

Corrosion can be generally characterized as a chemical degradation of materials under the action of external factors. Corrosion of metallic structures is associated with the loss of material under the action of environment and is a huge problem for many activities. It links a lot of fields like aerospace, naval, automotive, constructional and others. Material degradation due to corrosion calls for the replacement of damaged metallic parts, failure of equipment and engineering systems and can lead to fatal catastrophes. Corrosion of pipelines or tanks can lead even to ecological disasters. Therefore problems associated with corrosion cause significant economic impact and can lead to irretrievable human loses.

In order to fight problems associated with corrosion significant funds have been invested in the area of corrosion protection. Defense strategies against corrosion were created based on the knowledge of the corrosion susceptibility and corrosion activity of different materials. The first strategy is to determine the parameters that influence corrosion of metals. These parameters can be different such as atmosphere aggressiveness, temperature, type of water and solution. Successful control of such parameters can decrease corrosion, but it is possible only in some particular cases. In the majority of the circumstances it is not possible to avoid factors responsible for corrosion. In such way a second strategy can be applied, which is based on creating a protection system e.g. coating. Most of the protection using coatings is called "passive" corrosion protection and usually is only a temporal measure. Because of damaging, defects or ageing the coating "barrier" can fail, which results in appearance of corrosion. The second type of protection has chemical nature and is called "active" corrosion protection. In order to provide active protection, barrier coatings often are combined with inhibitive compounds which can significantly reduce the rate of corrosion of the materials. Cathodic protection is another kind of protection of metal structures such as buried pipelines and naval structures. However, this sort of protection can be applied only in some special cases.

The aerospace industry employs barrier coatings for corrosion protection of main structural alloys. The barrier coatings usually consist of an organic polymeric matrix with different fillers and pigments used to increase the lifetime of metallic materials and enhance physical properties like mechanical resistance to scratches and provide long term corrosion protection. Corrosion protection properties of coatings also depend on adhesion between metal and organic coatings. Even a good coating can not protect metal when adhesion is poor between them. In many cases a proper pre-treatment of metal surface is required before application of organic coatings because there is a lack of adhesion between organic coating and the substrate. Different sort of pre-treatments could be used like conversion coatings, anodized layers, sol-gel derived coatings and others.

Chromate based compounds were mostly used for making pretreatments for aerospace aluminum alloys and for active corrosion protection of metallic structures [1-3]. The combination of its high inhibiting efficiency and easy integration in conversion coatings or anodized layers made it a good inhibitor for decades. However, in spite of valuable properties, the use of chromates is dangerous for the ecology, environment and human health [4]. The exposure to chromates can cause cancer and genetic mutations, which make them significantly harmful for living organisms. Therefore recent environmental regulations almost banned completely the use of Cr (VI) in industry, thus opening a big discussion for the replacement of chromate base compounds and finding new methods of pretreatments and corrosion protection of metals. Hence, one of the challenges nowadays is to find effective pretreatments for aluminum alloys and environmentally safe inorganic or organic inhibitors to substitute the use of chromates in industry.

The main objective of the thesis is the development of active anti-corrosion pre-treatments for 2024 aluminum alloy on the basis of hybrid sol-gel layers. Successful fulfillment of the main objective required accomplishing of different particular objectives of the work presented below:

- Investigation of the localized corrosion activity of AA2024. The obtained results provide better understanding of the intimate aspects of the corrosion susceptibility of AA2024.

- Study of different potential corrosion inhibitors based on the corrosion investigation of the alloy using electrochemical and microstructural methods.

- Development of hybrid sol-gel pre-treatments for AA2024 and study the corrosion protective properties and mechanism of corrosion of the sol-gel coated alloy.

- Study the stability of the sol-gel systems and influence of the alloy surface preparation on the corrosion protective properties of the sol-gel coated alloy.

- Study passive and active corrosion protective properties of the sol-gel systems with the selected corrosion inhibitors and influence of inhibitor addition on the corrosion protective properties of different coatings.

- Investigation into new approaches of inhibitor incorporation and delivery that include a combination of the sol-gel and nanocontainers of inhibitors such as nanoporous titania-based pre-layer, nanocontainers of corrosion inhibitors with Layer-by-Layer assembled polyelectrolyte shells and nanostructured compound based on cerium and molybdate ions.

18

The thesis is constructed of four main parts: introduction, experimental, results and discussion and conclusions. The objective of the introduction is to give an insight on the issues related to corrosion and corrosion protection of aluminum alloys. The first chapter will be addressed looking at the nature of the corrosion activity of aluminum alloys and different examples of localized corrosion attack occurring on alloy surface. Subsequent topics include information available in literature on the corrosion protection of aluminum alloys using different inhibitors. Two major strategies, namely active and passive corrosion protection used for aluminum alloys, will be reviewed. In the second chapter of the introduction different alternative pretreatments are presented as examples of environmentally acceptable substitutions to toxic chromate based pretreatments used in industry. The details of the sol-gel processing, advantages of the sol-gel coatings over other pretreatments and their application are described in more details, as the main topic of the thesis is the use of the sol-gel coatings as pretreatments for 2024 aluminum alloy. The third chapter is devoted to the short description of the theoretical background of main testing methods used in studying the corrosion of 2024 aluminum alloy. The instrumentation, application and theoretical background of the techniques such as atomic force microscopy, DC polarization, electrochemical impedance spectroscopy and localized potentiometry are discussed.

The experimental part presented in the fourth chapter is an overview of the materials used in the study, sample preparation methods, preparation of the sol-gel formulation and application of the sol-gel films, experimental conditions of the main testing methods, corrosion tests and methods of surface and chemical analysis.

The results and discussion part is constituted of three chapters and presents the core of the thesis. The chapters are separated into three main topics accessing the corrosion susceptibility and corrosion protection of the bare alloy by different inhibitors, investigating the sol-gel systems as pretreatments for the alloy, and investigating the pretreatments with active corrosion protective properties. A study of the localized corrosion activity of the alloy was performed in the fifth chapter to more clearly understand the corrosion mechanism of the alloy. The knowledge of the localized corrosion activity has been used to select different inorganic (salts of rare earth elements and complex inorganic compounds such as Cerium molybdate) and organic (triazole and thiazole derivatives, effective complexants and chelates compounds) corrosion inhibitors for effective protection of the alloy.

The sixth chapter provides a detailed study of the sol-gel systems based on Zr and Ti alkoxides and organomodified silane as pretreatments for AA2024. The study includes the characterization of the sol-gel formulations with different compositions, detailed corrosion and microstructural investigation of the obtained sol-gel pretreatments. A study of different factors such as ageing of the sol-gel formulation and influence of AA2024 substrate preparation on the effectiveness of the corrosion protection conferred by the sol-gel coatings has been additionally performed. Mechanism of corrosion of the sol-gel coated alloy has been suggested basing on the study of the sol-gel pretreatments. Since sol-

gel coatings provide only passive corrosion protection different strategies have been developed to impart active corrosion protection properties to the sol-gel coatings. Although the monitoring of active corrosion protection and self-healing abilities of the coatings might be complicated by different factors, several model experiments have been performed using EIS and SVET techniques to prove the ability to monitor the inhibition of the corrosion process on the sol-gel coated alloy.

The seventh chapter presents studies of the sol-gel systems with direct inhibitor addition and incorporation of inhibitor in nanocontainers to impart active corrosion protection to the coatings. Corrosion protective properties of the sol-gel coatings with inorganic and organic inhibitors have been evaluated using different methods. The results showed that direct inhibitor addition in the sol-gel systems can not always be beneficial for the corrosion protection. Therefore the selected inhibitors were included in nanocontainers and combined with the sol-gel formulations to avoid disadvantages of direct inhibitor addition into the sol-gel coatings. The nanoporous titania-based networks with benzotriazole, silica-core based nanocontainers with polyelectrolyte multilayers containing benzotriazole, halloysites nanoclays with incorporated mercaptobenzothiazole and coated with polyelectrolyte multilayers, nanowires of cerium molybdate have been used as nanocontainers with inhibitors. The obtained sol-gel coatings were studied using electrochemical impedance and localized techniques to reveal active corrosion protection.

The last part of the thesis summarizes particular conclusions of the work and presents the recommendations for future work.

INTRODUCTION

1   Corrosion and corrosion protection of aluminum alloys

1.1   Corrosion susceptibility of aluminum alloys

Aluminum alloys have been the primary material of choice for different structural components of aircrafts due to the combination of valuable mechanical properties, known fabrication cost and low density [5,6]. Aerospace industry is one of the branches of engineering that uses high strength aluminum alloys for skinning and structural applications. However, due to the presence of additional alloying metals the corrosion susceptibility of alloys increases, especially in chloride solutions. Typical alloying elements are copper, silicon, iron, manganese, magnesium, zinc and others. The segregation of alloying elements during the solidification from the melt results in formation of different phases which are noble with respect to aluminum solid solution, thus making alloys susceptible to various forms of corrosion, especially in chloride containing solutions. Such inhomogeneity of the alloys results in appearance of localized corrosion activity which was a subject of research in many works [7-17]. One of the most commonly used aluminum alloys for skinning applications in aerospace industry is AA2024. It may contain up to 5 wt. % of copper, which is the main alloying element. There are two main intermetallic phases formed during the heat treatment of the alloy. One of the most abundant phases that occupy around 3% of surface area of alloy is Al-Cu-Mg phase with Al_2MgCu nominal composition which is called S-phase. Among other intermetallics S-phase may occupy up to 60% of space. The other phase is Al-Cu-Fe-Mn, which is mainly presented by Al_6(Cu-Mn-Fe) and Al_2Cu_2Fe intermetallic phases. Generally more noble elements like Cu and Fe are contained in such phases making them more noble compared to aluminum. However, the behavior of the S-phase can be different. Electrochemical measurements made on S-phase showed that corrosion potential in NaCl solution is more active compared to Al-4Cu solid solution [18]. Based on these measurements one can conclude that during the corrosion exposure of AA2024 the S-phase will be anodically polarized, which will cause its dealloying. Dealloying is the process when more active elements "run away" or dissolve from metallic phase leaving more noble elements inside [15]. As a result of such process Mg dissolves and copper is left inside the phase changing the electrochemical behavior of S-phase in AA2024 from anodic to cathodic and promotes a localized pitting activity.

The nature of the corrosion activity of aluminum alloys becomes clear when making analysis of the composition and electrochemical behavior of the main constituents. Aluminum by itself is a very reactive metal that has a low standard reduction potential -1.66V [17], though under normal conditions it is covered by a thin amorphous oxide film which protects it against corrosion in neutral environment. However, the presence of acids or alkalis can change its corrosion behavior. In water solutions the thermodynamics of

aluminum was summarized by Pourbaix *et al.* and presented as a diagram of potential versus pH (Figure 1.1.1.) [19]. It reflects theoretical conditions at which aluminum becomes active or passive. From the diagram it can be seen that aluminum is stable in the pH range from 4 to approximately 9 due to the presence of aluminum oxide film, which makes possible to use it for many applications where corrosion resistance is required [20]. However, in acidic and alkali environments aluminum corrodes with the formation of Al^{3+} and AlO_2^- ionic species respectively. It should also be noted that passivity of aluminum in neutral solutions can be overruled, if in the solution there are species like chlorides that can cause breakdown of the oxide film and assist the corrosion of metal.
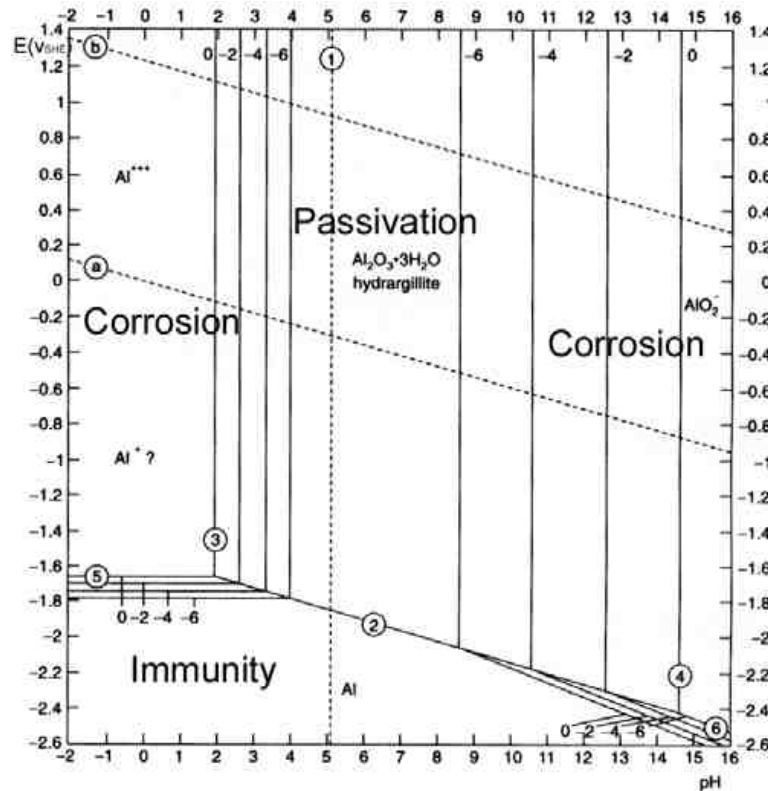
Figure 1.1.1. Potential - pH equilibrium diagram for the system aluminium – water at 25ºC [19].

When aluminum is combined with another metal which is electrochemically nobler a galvanic element is formed in humid or water environment. The galvanic cell consisting of two electrochemically different phases supports anodic and cathodic partial reactions that are responsible for corrosion activity. Aluminum alloys have heterogeneous composition. For instance, AA2024 has various copper containing intermetallic inclusions. Such inclusions form a micro galvanic cell that leads to the localized corrosion. The most common types of corrosion of aluminum alloys are pitting corrosion, crevice corrosion and filiform corrosion. Other types of corrosion that can also be found are intergranular

corrosion associated with temperature variation and stress corrosion cracking. A more detailed description of different corrosion cases will be discussed in the following paragraphs.

1.1.1 Pitting corrosion

A localized corrosion attack in metallic surface with the formation of shallow holes, deep penetrations or undercuts is called pitting corrosion. Pits have different shapes and propagate inside the metal. Pitting formation is very common for different passive materials like stainless steels and nickel alloys with chromium, aluminum alloys in the presence of chlorides. It occurs when there is a breakdown of passive oxide film due to external factors. Pitting initiation can be characterized by pitting potential Epit. At that potential current rapidly increases during the anodic polarization of metals due to the initiation of pitting. Pitting potential can be schematically shown in Figure 1.1.2. The resistance to pitting formation can be characterized by Epit that is higher for pitting-resistant alloys. In the presence of chlorides Epit decreases.

Pitting activity can be divided into three stages of pitting initiation, metastable pitting formation and pitting growth [21]. Developing of pitting occurs in the place of defects or breakdown in natural oxide film on alloy surface, which stimulates further anodic and cathodic activities. There are different models that consider adsorption on passive film, ion penetration and migration. Possible mechanisms of pitting initiation due to the adsorption of aggressive ions from the solution and their movement across the film can be found in ref. [22-24]. Metastable pitting formation occurs at the potential lower than Epit and the lifetime of such pitting is very short. Within a short period of time metastable pit activates and repassivates. Those pits that can survive the intermediate stage continue to grow forming stable pitting.
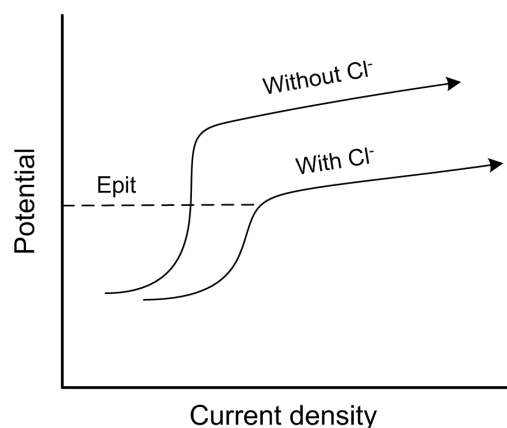
Figure 1.1.2. Schematic representation of pitting potential Epit on the anodic polarisation curve for aluminium alloy.
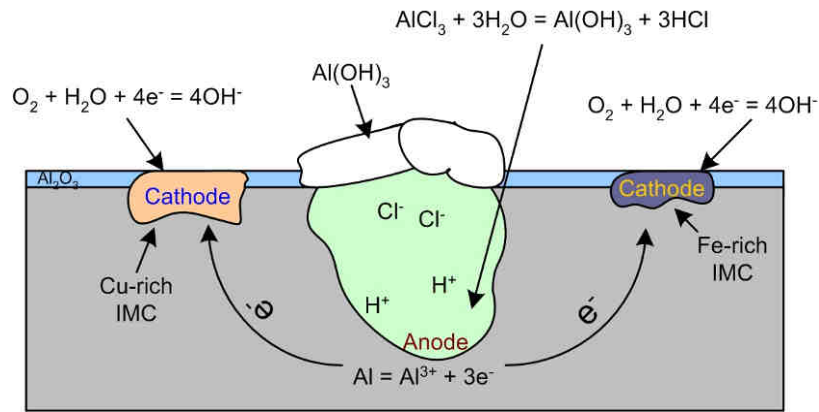
Figure 1.1.3. Schematic representation of pitting activity of aluminium alloy in chloride containing solution. Adapted from ref. [6]

As was mentioned before pitting corrosion is a localized electrochemical process which is separated into anodic and cathodic parts. The schematic picture of the mechanism of pitting propagation for aluminum alloys is shown in Figure 1.1.3.

In anodic part of the pit (Figure 1.1.3) the oxidation reaction occurs and electrochemically active metal (aluminum) is removed from the alloy as aluminum ions and electrons are injected in the metal:

$$Al \rightarrow Al^{3+} + 3e^- \tag{1.1.1}$$

at the same time the cathodic process occurs at noble electrochemical places like copper or iron containing intermetallics and involves the reduction process of dissolved oxygen in water and hydroxyl ions formation:

$$2H_2O + O_{2(aq)} + 4e^- \rightarrow 4OH^- \tag{1.1.2}$$

though the reaction of hydrogen evolution is possible in acidic environment as well:

$$2H^+ + 2e^- \rightarrow H_2 \tag{1.1.3}$$

Electron transfer between cathodic and anodic parts is provided by bulk alloy. In case of localized corrosion if cathodic area is much bigger than the anodic one, then the anodic current density is significantly higher than the cathodic one and dissolution of metal from the anodic part becomes very rapid. Aluminum in a cationic form attracts chloride ions from the solution and hydrochloric acid is produced as a consequence of water hydrolysis of aluminum cations leading to significant acidification of the solution near the anode according to following equation [25]:

$$Al^{3+} + 3Cl^- + 3H_2O \rightarrow Al(OH)_3 + 3HCl \tag{1.1.4}$$

Such decrease of pH promotes further dissolution of aluminum and the total process becomes autocatalytic. An insoluble cap of aluminum hydroxide is formed in

24

contact with neutral bulk solution at the pit mouth (Figure 1.1.3). The cap is porous enough for the transport of chloride ions to the pit.

Propagation of pitting further into the metal surface may result in mechanical failure of a constructional part during the service application, which can be a serious problem causing significant damage. Hence, the protection of alloys against corrosion is a matter of prime importance in engineering. It should be noted, that the presented mechanism of pitting is simplified. The proposed model describes a stable pitting growth. However, the mechanisms of pitting initiation, development and the role of intermetallic particle in pitting activity are not fully clear and must be a subject of further investigations. Understanding of the mechanism of pitting corrosion can help to prevent appearance of pits and even create the methods to "cure" them.

1.1.2 Crevice corrosion

Another type of a localized attack which is very similar to pitting corrosion is crevice corrosion. It occurs when there is a crevice that is created when two materials are in contact. The chemistry of crevice corrosion is very similar to pitting corrosion. Diffusion limitation of oxygen in a crevice can cause differential aeration that creates favorable conditions for metal dissolution and eventually a localized corrosion. Accumulation of chlorides in a crevice can accelerate the development of corrosion. If a crevice is initiated, it continues to propagate according to the reactions (1.1.1-1.1.4) where the anodic process of aluminum dissolution and hydrolysis is coupled with a large surrounding cathode where oxygen reduction takes place.

1.1.3 Filiform corrosion

Appearance of a narrow from 0.05 to 3 mm wide network of tunnels or filaments either under the thin film, thick coating or native oxide film of alloy on the surface is called the filiform corrosion. An example of the filiform corrosion on the coated steel substrate is presented in Figure 1.1.4a. The protection against the filiform corrosion is very important since it is a starting point of coating undermining. Without the proper control it can significantly deteriorate the bonding between the coating and the metal and result in the significant damage in that area. Usually such type of corrosion starts in flaws, micro defects or scratches present in organic coatings. However, poor adhesion of paint and coatings to aluminum substrate can also be a reason for the appearance of such corrosion activity. The factors that accelerate filiform corrosion are the increase of relative humidity and temperature. It was shown that the most rapid growth of filaments occurs at the relative humidity about 80 % and the temperature around 40ºC. Penetration of water inside the defects forms differential aeration cells with localized anodic and cathodic activity. Schematically the mechanism of the filiform corrosion is presented in Figure 1.1.4.

a)

b)
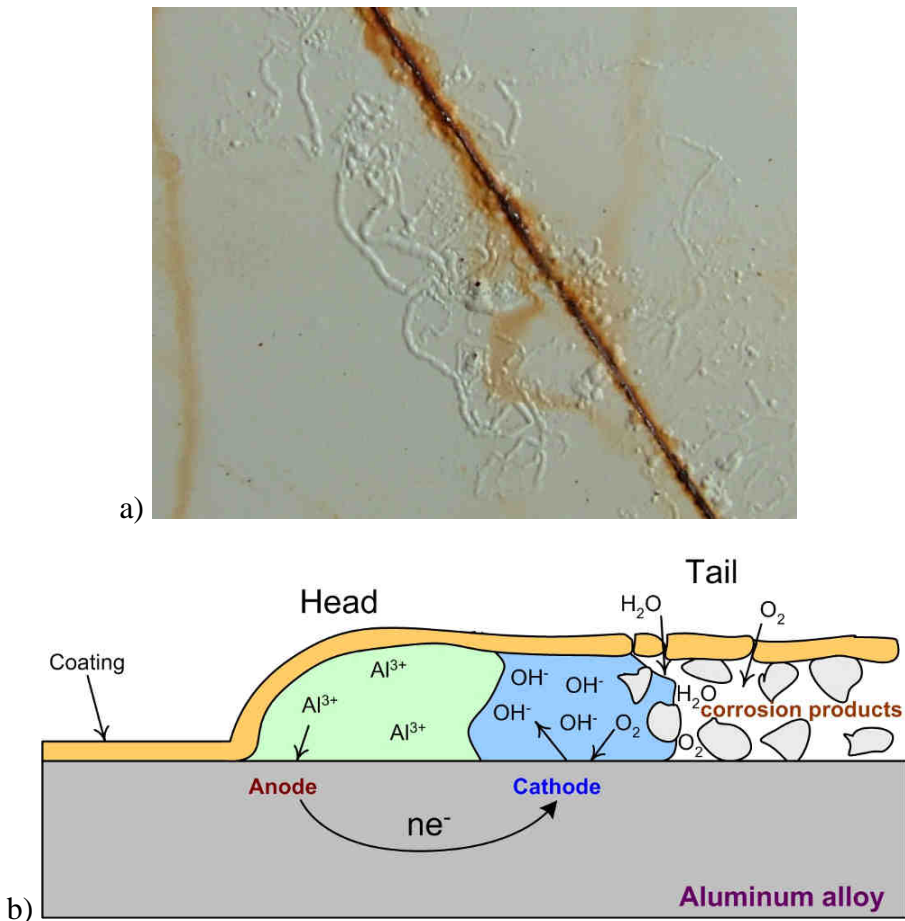
Figure 1.1.4. Example of the filiform corrosion on a coated steel substrate a) and schematic representation of the filiform corrosion mechanism b). Figure b is adapted from ref. [26].

The filament is separated into head and tail corrosion parts. At the head there is an anodic reaction of aluminum dissolution (1.1.1) with the formation of aluminum cations. The reaction of hydrolysis of aluminum species (1.1.4) in chloride containing solution decreases pH that assists further propagation of corrosion. Atmospheric constituents like sulfates, sulfides and carbon dioxide also assist acidification. During the corrosion process the head of filament is moving forward while the tail stays behind. Corrosion products of aluminum stay in the tail of the filament and assists migration of soluble species, oxygen and water. The cathodic process of oxygen reduction (1.1.2) takes place in the tail of the filament, which makes localized alkali environment nearby.

In order to deactivate filiform corrosion the cathodic process must be stopped by eliminating transport of oxygen to the metal surface. Development of filiform corrosion can be also stopped when the relative humidity is decreased below 60%, therefore dehydrating the galvanic cell. However, such countermeasure is often an impossible task

for real industrial applications like in airplanes or naval constructions where there is an unavoidable contact with humid and corrosive environment.

1.1.4 Intergranular corrosion and stress corrosion cracking

Heterogeneous nature of aluminum alloys and heat treatment conditions result in precipitation of different metallic phases. Aluminum containing intermetallic compounds are usually precipitated along the grain boundaries. Such phases can be very active in galvanic coupling with the interior of the grains, which is the reason of intergranular corrosion (IGC) attack. Figure 1.1.5 shows schematically the propagation of IGC in alloy. During such corrosion metallic material is dissolved from the grain boundaries more actively which results in propagation of cracks along the grains as shown in the Figure.

In Al-Mg and Al-Mg-Zn alloys the corrosion goes preferably along the grain boundary because of precipitation of active phases. The precipitation of β-phase (Mg_2Al_3) that has low corrosion potential about -1.3V vs. SCE, commonly occurs in Al-Mg alloys [27]. Al-Mg-Zn alloys contain $MgZn_2$ and AlZnMg phases that are active with respect to the surrounding solid solution. Al-Cu or Al-Mg-Zn-Cu alloys such as AA2024 and AA7075 have cathodic copper containing intermetallics like Al_2Cu or $Al_xCu_yMg_z$. During the thermal treatment and ageing of alloys copper depleted zones are formed at the grain boundary of copper containing intermetallics with aluminum matrix. Such zones corrode anodically, which causes strong intergranular corrosion attack [26]. Sensitization to IGC is well known problem when using welding or any other heat treatment of aluminum alloys. The formation of active phases occurs more rapidly at the grain boundaries, which significantly affects the resistance of alloys to IGC. Galvele *et al.* investigated the relation between the pitting and IGC and factors that influence the appearance of IGC on specially prepared Al-Cu alloys [28]. The results showed that IGC occurs in the presence of certain ions and in the narrow range of Al-Cu alloy electrode potentials. Therefore a combination of different factors like temperature, environment, and electrode potential can significantly affect the corrosion resistivity of alloys.

One of the forms of corrosion attack related to mechanical failure of an alloy exposed to a corrosive environment is Stress corrosion cracking (SCC). The main factors associated with SCC are tensile stress, susceptible material, and corrosive environment. These factors can be found in the service conditions of materials and may not be present together to cause SCC. There are two types of SCC attack, namely transgranular and intergranular. The first case happens when crack propagated directly through the grains and in the second case crack follows the path in between the grains. Intergranular failures are more commonly occur rather than transgranular.

Stress corrosion cracking of aluminum alloys is a combination of intergranular corrosion susceptibility, static tensile and mechanical stresses and environmental conditions. Aged alloys have higher susceptibility to stress-corrosion cracking. The

precipitation of active phases because of the temper or ageing conditions significantly affects IGC and consequently SCC resistance [6]. Control of the amount of stress or mechanical load on alloy parts can prevent failure due to SCC. Environmental conditions such as humid air, seawater, water solutions provoke corrosion, though it can be controlled by restricting the presence of aggressive species. Susceptibility to stress corrosion cracking of AA2024 has been investigated in [29]. The results of corrosion investigation in NaCl solution show that the alloy has two pitting potentials corresponding to pitting at the grain boundaries and within the grains. The susceptibility of the alloy to SCC occurred at potentials above the pitting potential of the grain boundaries and was caused by the dissolution of the solute-denuded zones along the grain boundaries [29]. Cathodic protection in most of the cases eliminates SCC. However, high cathodic polarization can cause hydrogen induced embrittlement which is dangerous for high strength alloys [26].
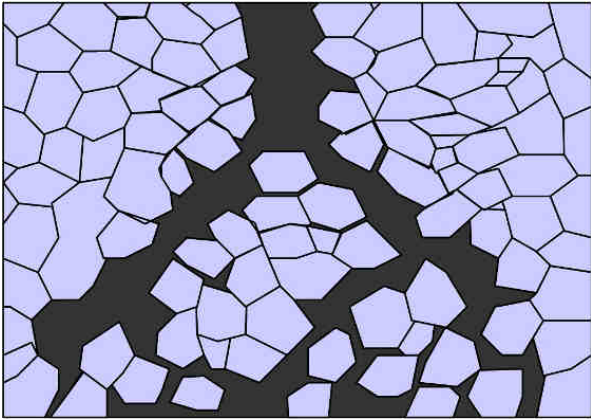
Figure 1.1.5. Schematic representation of Intergranular corrosion.

1.2   Corrosion protection of aluminum alloys.

1.2.1 Corrosion inhibition and the use of chromates

The corrosion rate of metals can be reduced when a proper chemical is added to a solution in contact with metal. Chemical compounds which effectively decrease the corrosion rate of metals when added in small amounts to the corrosive environment of a corroding metal are called inhibitors [6]. The process of corrosion has electrochemical nature and is associated with transfer of electrons between anodes and cathodes. If inhibitor decreases the rate of the anodic process, it is called anodic inhibitor. In other way, when inhibitor decreases the rate of the cathodic process, it is called cathodic inhibitor. The action of such inhibitors on kinetics of anodic and cathodic processes can be illustrated in Figure 1.2.1. Solid lines show possible cathodic and anodic current-voltage lines in the absence of inhibitor. The corrosion current density current (i_{corr}) and the corrosion potential (E_{corr}) are indicated in the Figure 1.2.1. Dotted lines represent the case when inhibitors are added. In the case of cathodic inhibitor cathodic polarization is increased, which results in decrease of cathodic current. As can be seen from the Figure 1.2.1, intersection of dashed line of cathodic process with solid line of anodic process makes shift in corrosion potential in negative direction and decreases corrosion current density until (i_{corr}''). The same discussion, but with the anodic polarization, is valid for anodic inhibitors. The corrosion current density becomes in this case i_{corr}'. If inhibitor diminishes the anodic activity, the cathodic one will also decrease.

Inhibiting compounds can be different inorganic and organic substances that affect either cathodic or anodic processes or both of them. For example, phosphates, silicates, carbonates can decrease corrosion rate of metals in aqueous solution and serve as anodic inhibitors. These substances form a protective film on the metal surface, thus increasing the anodic polarization. The addition of metal salts like magnesium, zinc, and cerium can form precipitates in cathodic places, where oxygen reduction reaction takes place, thus reducing the corrosion rate of metal. However, inhibitors work for chosen metallic substrates with some exceptions and efficiency of inhibitors is affected by the corrosion environment.
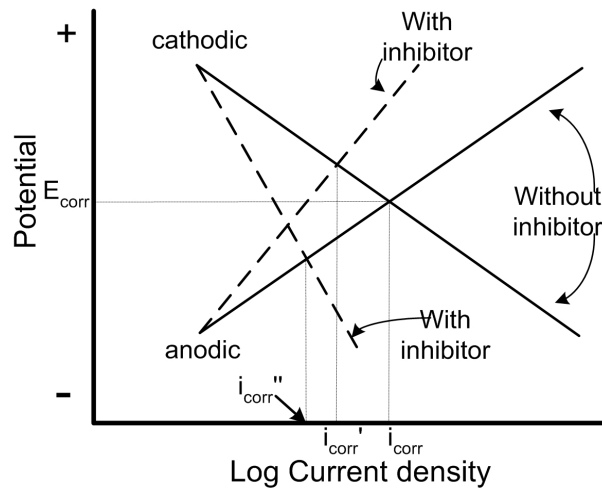
Figure 1.2.1. Potential vs. log i curves showing two half-cell reactions involving metal and environment (solid lines); the influence of inhibitors on the anodic and the cathodic currents is shown by dashed lines. Corrosion currents due to action of anodic and cathodic inhibition are i_{corr}' and i_{corr}'' respectively.

Up to the present days the most efficient inhibitors for aluminum alloys are based on Cr (VI) compounds. Pretreatments that include Cr (VI) or additives of chromates as pigments into organic coating layers were actively used for protection of aluminum alloys in aerospace industry. The chromate pigments are slightly soluble in water, and the released chromate ions can diffuse to active corrosion sites. Efficient inhibition properties of chromates are based on high oxidative ability. Less than few millimoles of chromates in solution already provide corrosion inhibition. The corrosion can start in the case of a defect or scratch formation on the coated metal surface when it is exposed to corrosion environment. However, in water solutions chromates can be leached out from the conversion coating or from the paint providing significant decrease of the corrosion rate, thus making "healing" of the defected area and providing long term corrosion protection [30-32]. The formation of a chromate protective film on the surface of aluminum can be described in the following way [33]:

$$Cr_2O_7^{2-} + 2Al + 2H^+ \rightarrow 2CrOOH \downarrow + 2AlOOH \downarrow \qquad (1.2.1)$$
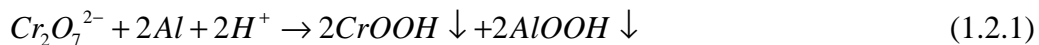
Chromates form a mixed layer of Cr (III) oxyhydroxides and aluminum hydroxides that protects metal against further reactivity. Studies of the corrosion activity of AA2024 in NaCl containing electrolyte show inhibitive action of chromates that act as cathodic inhibitor [34]. The localized corrosion of copper rich intermetallics of AA2024 is inhibited by chromates even if the surface of intermetallics is scratched (by AFM probe), thus demonstrating very fast formation of inhibiting film [35]. Strong inhibition action of chromates on aluminum alloys is associated with the suppression of the localized cathodic process that occurs on copper and iron containing intermetallics [35-37]. Localized

methods of chemical analysis (XPS and AES) confirm that a mixed layer of Cr III and Cr VI oxyhydroxides is formed on the surface of intermetallics that reduces dealloying and ORR [36]. Electrochemical investigations of galvanic pairs made of copper and aluminum show a spike of current reduction when chromate was added to the corrosive solution that indicates the reduction of Cr (VI) to Cr (III) forming a monolayer of oxyhydroxides on the copper surface. The mechanism of inhibition seems to be irreversible. Such mechanism is supported by the fact that after removing the chromates from the corroding solution the samples were still under protection. Studies of the adsorption of chromates on the aluminum surface showed that the presence of chromates hampers adsorption of chloride ions because of lowering the zeta potential of aluminum oxide surface, thus preventing the corrosion [38,39]. Owing to the extraordinary corrosion inhibition properties chromates became very popular, however, the toxicity of Cr (VI) compounds overweighs the usability in industry. The present health regulations ban the use of chromates in industry, thus making a challenge among the scientists to find efficient inhibitors which can substitute the use of chromates for pre-treatments and as pigments in paints.

Alternative to chromates inhibitors for corrosion protection of aluminum alloys are needed in order to substitute environmentally unfriendly chromates. Investigation of potential replacement for chromate pigments replacements in protection systems for AA2024 was done by Cook *et al.* [40]. Using the EIS technique a number of compounds was tested in NaCl solutions to access the inhibiting properties and rank the compounds compared to chromates. Several candidates appeared promising inhibitors such as barium metaborate, cerium chloride, cerium oxalate, lanthanum chloride, and sodium metavanadate. From another source, the most promising candidates being investigated as active inhibitors were cerium compounds, molybdates, vanadates and phosphates [41].

The tested compounds show different inhibiting action and therefore can be organized in different groups. One of the possible classifications of inhibiting compounds is by their chemical functionality. However, inorganic and organic compounds show different mechanisms of corrosion inhibition action on metallic substrates. Therefore, the most appropriate organization scheme applied to inhibitors consists of regrouping them in a functionality scheme [42]. This scheme includes four groups: cathodic, passivating (anodic), precipitation and organic inhibitors. In the following part different corrosion inhibitors and their functionality will be discussed.

Cathodic inhibitors. Inhibitors that affect the rate of cathodic reaction or selectively precipitate on cathodic areas providing a diffusion barrier to the reducible species are called cathodic inhibitors. The corrosion potential shifts to more negative values (Figure 1.2.1) when using cathodic inhibitors, which in the case of aluminum alloys protects metal from pitting corrosion. Salts of cerium were found to be the most promising substitution for chromate as corrosion inhibitors [41]. Cerium salts are typical cathodic inhibitors which inhibition effectiveness is believed to be because of the precipitation of insoluble Ce

oxyhydroxides in the region of high pH [43-45]. Aldykewicz *et al.* studied the inhibiting effects of Ce (III) salts on aluminum copper galvanic couples and found that the formation of the precipitates of insoluble cerium hydroxides occurs on copper cathode, thus reducing the rate of the oxygen reduction reaction [44]. The precipitation mechanism is believed to be a chemical reaction between cerium cations and hydroxyl anions produced at the cathode surface, although there are evidences that the formation of peroxide can influence the precipitation mechanism and increase the efficiency of cerium salts [45]. Inhibition of corrosion by lanthanides was also studied for other aluminum based alloy like AA5083 with Mg as a main alloying element [46]. Molybdates have been tested as inhibitors due to their oxidizing properties and stability of the oxidized products that form a passive layer on the metal surface. Electrochemical measurements showed that molybdate and cobalt ions added to the corrosion solution provide inhibition of ORR on AA2024 [47] However, in case of molybdate the inhibition is not observed when molybdates are removed from the corrosion solution. This suggests the influence of adsorption on the mechanism of inhibition of molybdate anions. Rare earth diphenilphosfates show mixing inhibiting effect reducing the rate of cathodic and anodic processes [48]. Detailed study of the action of vanadates on the corrosion inhibition of AA2024 has been done by Iannuzzi [49,50]. It was established that metavanadates species are effective inhibitors of ORR on copper in AA20224. The suggested mechanism of inhibition includes the formation of passive layer of inhibitor on the cathodic surface, which blocks reactive sites on the s-phase intermetallics. The NMR spectra recorded in vanadate solutions with different pH showed that metavanadate (V1,V2,V4) species are present in slightly alkali solutions, whereas acidic solution contains mostly decavanadate (V10) species. The inhibition by V10 species was found to be not as effective as for metavanadates.

Passivating (anodic) inhibitors. Inhibiting mechanism of passivating inhibitors is related to a large increase of the corrosion potential (Figure 1.2.1) forcing the metal into the passivation range. Typically oxidizing ions such as chromates, vanadates, nitrates work as passivating inhibitors for steels. Recent studies have shown the influence of metavanadate species in tetrahedral configuration on the positive shift of anodic pitting potential of AA2024 [51]. Studies made by Breslin *et al.* showed the increase of the pitting potential of aluminum in neutral and alkali media, showing anodic inhibition of molybdates [52]. The passive film was formed by molybdate species with different oxidation states (presumably IV and IV). More complicated molybdate oxo-species exist with decrease of pH. The complexity of the molybdate species results in different inhibition efficiency [53,54]. However, the effect on the positive E_{pit} potential shift in case of molybdate was more dependent on the concentration of the NaCl solution used for the polarization study rather than on the change of molybdates concentration [53]. The proposed mechanism of passivation was based on the competitive adsorption between chlorides and molybdates followed by the oxidation-reduction process with the formation

of Mo (IV) oxides. The inhibiting process of molybdates on copper is efficient only in short range of pH (8-9) [55].

Precipitation inhibitors. Such inhibitive compounds chemically interact with the metal surface or with the products of the corrosion process on metal, thus forming a protective insoluble film that reduces the corrosion rate. The precipitation reduces cathodic and anodic activity indirectly. Phosphates, silicates, carbonates show such inhibiting behavior [22]. A number of conditions influence the inhibiting efficiency such as temperature, concentration of inhibitor, pH and others. Zinc phosphates are non toxic comparing to chromates. They provide inhibition of AA2024 corrosion by forming a protective film consisting of $Zn_3(PO_4)_2 \times 4 H_2O$ [56]. A search of other effective inhibitors was conducted by MacQueen *et al.* using the EIS technique among several phosphate containing pigments embedded in protective coatings. Calcium strontium zinc phosphosilicates provide the most effective inhibition among other ten tested compounds [57].

Organic inhibitors. A lot of studies of inhibition action of different classes of organic compounds have been performed. Organic molecules with specific functionality can form a hydrophobic layer on the metal surface because of adsorption effects. This film protects the metal from further dissolution. Usually, compounds with organic groups containing oxygen, nitrogen and sulfur like carbonyl-, carboxyl-, amino-, tio-, demonstrate enhanced adsorption properties. The effectiveness of the inhibition depends on the chemical composition and affinity to the metal surface. Chelates forming compounds that form complexes with low solubility are effective inhibitors [58]. Chelating compounds can be adsorbed on copper rich intermetallics in AA2024 and form insoluble complexes, therefore providing inhibition. Organic compounds that actively suppress the cathodic process were studied in many works. Tetrazole derivatives [59], organics with oxime group, such as (salycilaldoxime and benzoinoxime) [60], 8-hydroxyquinoline [61], morpholine-methylene-phosphonic acid [62] and others provide corrosion protection. Tetrazoles derivatives with mercapto radicals are effective as mixed corrosion inhibitors for copper corrosion in NaCl and NaF containing solutions [59,63]. The inhibitive effect could depend on the immersion time indicating slow kinetics of adsorption process for corrosion inhibition of aluminum by 8-hydroxyquinoline [61]. Longer immersion time gives thicker inhibitive film, which imparts higher protection. The formation of insoluble complexes on the surface and in turn prevention of the adsorption of chlorides could explain the action of these type of inhibitors [61,64]. Finding appropriate inhibitors for corrosion suppression of different types of alloys and metals is important when fighting against corrosion.

1.2.2 "Passive" corrosion protection

In most industrial applications aluminum alloys have been exposed to open air where humidity often changes from low to high values, so does the temperature. Such cycling combined with corrosive environment coming along with atmosphere conditions that contains sulfurous gases, nitric gases, carbon dioxide or saline solutions coming from sea cause significant corrosion impact on many kind of metallic structures. To fight this problem engineers had to create a protection system. One approach includes corrosion protective coatings that are intended to form a barrier to restrict ingress of corrosion species to the metal surface and to provide long term corrosion protection.

The main function of a "passive" corrosion protection system is to make a physical barrier against the aggressive environment, thus significantly decreasing corrosion rate of alloys and increasing the lifetime of service parts. It is not a mystery that up to the present days the most popular systems providing barrier corrosion protection are based on organic coatings and their combinations. There are some criteria [65] which are important when making choice of barrier protective systems:

- Adhesion to the metallic substrate

- Good barrier properties that include low diffusion of corrosive species and low coating conductivity

- Chemical stability to weather conditions and environment

- Compatibility with pigments

These factors must be taken in consideration when developing organically-based protective systems. It is impossible to create an ideal protection system with no defects and no permeation of electrolyte. In any protective systems there are inhomogeneities and defects. The defects present in the coating can cause localized corrosion of the substrate when immersed in a corrosive electrolyte. Therefore, in order to fight such problem multilayered coating systems are applied, because it is highly improbable that two defects in different layers will coincide.

A typical scheme of corrosion protection that is used in aerospace industry [41] is presented in Figure 1.2.2. The protection system includes three components, namely, pretreatment, primer coating and top coating that have different functions.

The surface of metals is usually is not clean; it has a scale, stains of grease, oil, dirt that have an adverse effect on coating adherence. Even if the coating is good, but the surface is not well prepared, the system will not provide adequate corrosion protection. The most important part of the coating process is the surface preparation and pretreatment. Both of them play an important role to enhance adhesion between the metal and the organic coating. Surface preparation includes mechanical cleaning, degreasing, removing the scales by acid pickling, etching that is used to increase the surface area of the substrate by increasing roughness. Application of surface pretreatments for aluminum alloys has

been critically reviewed in works of Critchlow *et al.* [66,67]. Different mechanical, chemical, electrochemical pretreatments were described in these works. A diverse range of surface examination techniques were described, that provide information on adhesion, surface chemistry and topography studies. The influence of different surface cleaning procedures for aluminum alloys is presented in ref. [68]. The studies demonstrate that noble inclusions present on the alloy surface make an adverse effect on effective size of the cathodic area and, therefore, an appropriate pretreatment must be used in order to remove the inclusions from the surface of alloy.

Figure 1.2.2. Schematic representation of industrial coating system for aluminium alloys. Adapted from ref. [41].

Pretreatments have several important functions. First, they provide additional corrosion protection of the alloy since it is an additional barrier on the way of corrosion species ingress to the metal surface. The most significant function of a pretreatment is the increase of adhesion between the metal and the following organic coatings, which is very important to prevent delamination of the coatings. The formation of chemical bonds between the metal and the pretreatment and the coating provides better adhesion than mechanical interlocking. The increase of wettability after pretreatment also facilitates application of the coating.

In order to provide integrity and avoid defects two coatings, namely primer and top-coat, are usually applied. The primer coating provides optimal adhesion properties for the following top-coating and has supplementary additives like pigments that impart different valuable properties such as corrosion protection, additional mechanical resistance. Top-coat provides appearance of the entire protection system, mechanical resistance, and protects the entire system from the influence of environmental factors. Fillers used in top-coat additionally decrease permeability of the coating and provide shading from the high energy solar radiation. Very often organic protective coatings are applied from a liquid phase by different methods like spraying, rolling, brushing. The liquid phase usually consists of solvent which carries blended or dissolved mixture of resin and pigment. Due to

strict environmental regulation water is mostly used as the solvent. Upon application the solvent must be evaporated out of the film thus creating the protective layer on the metal surface. As a last step coating often needs to be cured at elevated temperatures to provide additional crosslinking and remove an excess of solvent.

1.2.3 "Active" corrosion protection.

When the coating system is damaged and the metal becomes exposed to aggressive environment, corrosive species easily come in contact with the metal surface and initiate corrosion process. Coating systems providing "passive" protection are unable to stop developing corrosion activity of metal in the damaged zone because of leakage of active protection. The aim of "active" corrosion protection is to slow down or stop the electrochemical reactions that occur on metal in contact with the corrosive environment. The example of an industrially applied coating scheme for "active" corrosion protection of aluminum alloys is presented in Figure 1.2.3.
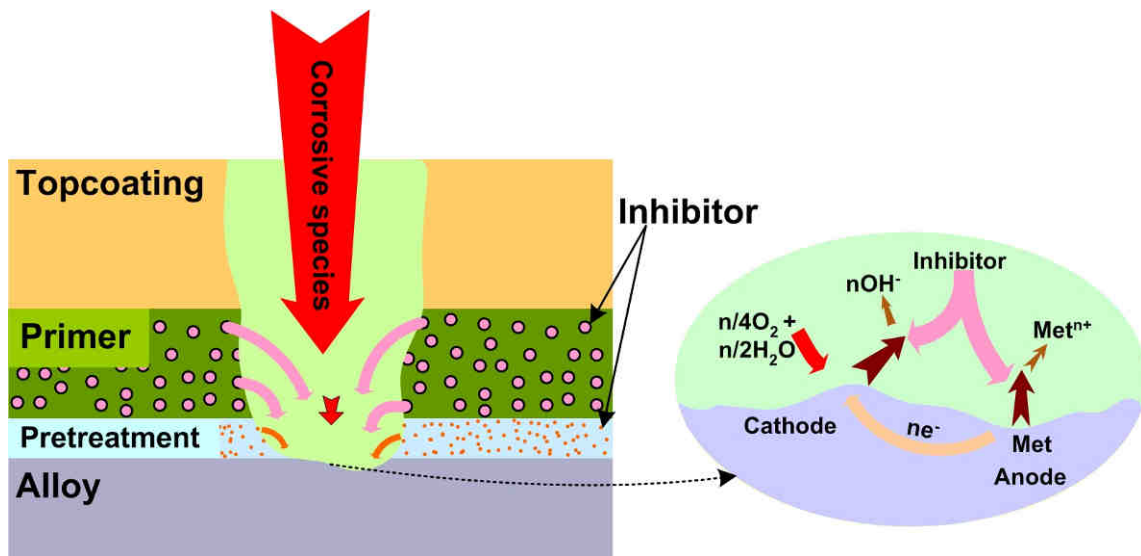
Figure 1.2.3. Schematic representation of active corrosion protection system for aluminium alloys.

The presented picture shows an active corrosion protection scheme of a coating system on aluminum alloys. Active corrosion protection is provided by the incorporated corrosion inhibitors in pretreatment and primer coating. When a coating system is damaged the corrosion starts upon contact with the corrosion environment (Figure 1.2.3). In contact with the electrolyte inhibitor leaches out and diffuses to the defect area. As a consequence,

the inhibitor heals the developed corrosion when it comes to the place of the corrosion activity as shown in the right part of Figure (1.2.3). The leaching of the incorporated inhibitor depends on the interactions between the inhibitor and paint, inhibitor concentration, distribution in the coating and solubility in the solvents.

Pretreatments usually applied in industry contain Cr (IV) that provides inhibitive properties. However, the concentration of inhibitors is not sufficient to provide effective inhibition of corrosion in large defects. Therefore primer coatings with inhibitors mainly provide corrosion protection in significantly damaged areas. The primer coating can be loaded with the corrosion protection pigment up to 20% of its dry weight. Salts of chromates were the most used pigment for corrosion protection of aluminum alloys. Pigments such as $SrCrO_4$ and $BaCrO_4$ are suited because of their low solubility and compatibility with the coating systems.

Chromate conversion coatings and Chromic acid anodizing coatings (CAA) have been used as pretreatments for aluminum alloys in aerospace industry. The process of conversional layer formation goes through three steps of metal surface activation, initiation of film formation and oxide growth [69].The formation of the conversion layer on aluminum alloys surface can be significantly affected by the intermetallic inclusions [70]. The reduction of Cr (VI) to Cr (III) and formation of an oxyhydroxide layer chemically bonded to the metal surface occurs during the CCC process. The formed layer provides increased adhesion to the followed organic coatings. In addition, the chromate conversion layer has Cr (VI) species left inside during the process. The presence of such species was confirmed by XANES spectroscopy [71]. Thus, when defect appears, chromate ions can diffuse to a defect place where corrosion started conferring inhibition and providing active corrosion protection properties [71,72]. The CAA process results in formation of amorphous aluminum oxide layer on the surface of alloy. Such protective layer is thick enough to provide good barrier protection and typically is less than 5 µm. The presence of nanoporosity and nano-rough structure combined with good wettability is of great importance for the paint adhesion and formation of good mechanical interlocking between the CAA layer and following organic coatings. Moreover, the adhesion to the metal is very good because of metal and oxide connection making CAA favorable, yet toxic pretreatment.

Application of metallic coatings or cladding can be used for some high and middle strength aluminum alloys to impart active corrosion protection and to provide additional barrier against environment. Typically, a layer of aluminum or aluminum alloy that is electrochemically more active than the metal underneath is applied on top of the substrate by hot rolling or coextrusion process that forms a continuous pressure-welded layer. Such layer acts as a sacrificial anode and can provide galvanic protection by supplying negative current to the substrate. However, metallic coatings have some disadvantages, such as susceptibility to filiform corrosion.

Electro active conducting polymers (ECP) were explored as non toxic potential substitutes of chromates for the active corrosion protection of metallic substrates. The ECP are electroactive conjugated polymers. Polymers display some level of conductivity because they are partially oxidized (p-doped) and contain counter anions for overall charge neutrality [73]. ECP can be different polyanilines, polyheterocycles and poly(phenylene vinylens) synthesized using electrochemical or chemical reactions directly on the metal surface. Such polymers may exist as primer coatings, as pretreatments or as additives to usual protection coatings. The mechanism of corrosion protection of conducting polymers is based on their Red/Ox properties and electric conduction and may be illustrated using the following reaction:

$$\left[(PANI)_n^+ A^-\right]_m \xleftrightarrow{\quad me^- \quad} \left[(PANI)_n\right]_m + mA^- \qquad\qquad (1.2.2)$$
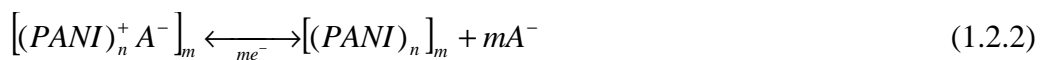
where the left part is presented by emeraldine salt of PANI with specific counter anion (A^-). When electron transfer occurs, salt is reduced to form Leuco base with subsequent anion release. The Red/Ox potential of ECP lies near the potential of chromates. Such noble potential creates anodic polarization of underlying metal that can shift its potential to the passive region. ECP anodically protect metals that form passive films under anodic polarization. The results of the corrosion protection of different metals like iron, steels, copper are presented in many works [74-80].

Other metals, such as aluminum and its alloys can not be protected by this way, because they do not achieve anodic passive state. An alternative way to protect metals from corrosion involves the use of a released counter anion. When appropriate inhibitive anion is incorporated in the ECP coating, it can provide corrosion inhibition of iron substrate when released [81]. Kendig *et al.* developed corrosion protection using ECP coatings with incorporated corrosion inhibitors for AA2024 [82]. When a scratch is formed on coated aluminum alloy, the polarization from metal causes release of the inhibitive anion from polymer coating that decreases corrosion in the place of defect. Therefore the ECP system with incorporated corrosion inhibitor may serve as a "smart" reservoir of inhibitors. Corrosion protection of aluminum alloys using ECP are described in different articles and books [83-91].

In spite of enhanced corrosion protection, ECP coatings did not find actual application in industry. This can be because there are a number of standard tests for coating systems that conducting polymers have not yet passed. The leak of chemical stability, compatibility with organic paint systems, adhesion to the metal substrate or to organic coatings and high electroactivity can also be a reason for such problem.

2   Pretreatments for corrosion protection of aluminium alloys

Up to date pretreatments based on hexavalent chromium compounds have been used in industrial applications before applying organic coatings. However, nontoxic and environmentally friendly pretreatments are needed. As a substitute to chromate based treatments some other processes have been developed. One of the substitutes can be inorganic coatings that are formed of a tightly adherent layer of oxides or other inorganic compounds on the surface of alloy. The coatings have has higher thickness, corrosion resistance and adhesion to organic paints than the natural aluminum oxide layer. The inorganic coatings include anodized layers, chemical conversion coatings, silane based coatings and others. Anodized coatings can be produced by oxide film growth at anodic potential in electrolyte. Chemical conversion coatings can be produced by precipitation of insoluble inorganic compounds from an inorganic solution. Coatings based on different derivatives of silanes became attractive because of good corrosion protection and adhesion properties to organic paints. The silane coatings are produced by direct application from the silane containing solution. More detailed information on the different pretreatments and their corrosion protection properties are presented in the following paragraphs.

2.1   Anodic films

Electrolytic oxidation of aluminum forms a layer of aluminum oxide on the surface which can be used either as a complete anticorrosive coating or as a pretreatment for application of organic primer and topcoatings. Electrochemical process involves passage of electric current through aluminum that works as anode in different kind of electrolytes like phosphoric [92,93], sulfuric [94], oxalic or chromic acids electrolytes and mixtures boric-sulfuric electrolytes [67]. The mutual migration of aluminum cations outwards and oxygen ions inwards creates a layer of aluminum oxide often with hexagonal porous structure. Such structure of anodic oxide is formed due to the action of electrolyte that assists the dissolution of oxide during anodization. The aluminum oxide coatings have thicknesses up to some micrometers depending on the anodization procedure. However, film thickness more than 5 µm has high fatigue sensitivity, thus making them unfavorable to be used in many applications. Anodized layer consists of two parts: an inner layer that is compact and an external layer that is porous. The external layer improves the adhesion of organic paints that mechanically interlock with the oxide. Moreover, the anodic layers are very resistant to delamination because the metal is continuously transformed to oxide during the anodization process.

The schematic view of the porous anodic oxide is shown in Figure 2.1.1. There can be seen a porous outer part of the oxide and a dense part (barrier layer) that is in direct

contact with the metal. Sealing or clogging the pores is often used to decrease porosity and increase dielectric properties of the oxide layer Figure 2.1.1b.

Anodization of aluminum alloys produces layers with limited corrosion protective properties because of heterogeneous structure of alloy containing different intermetallics. Thus, the anodized layer becomes very deformed, porous and has spongy like structure which requires additional protection using sealing, paint application etc. The EIS technique can be successfully applied for studying the sealing process of anodic coatings on aluminum alloys [95]. The application of different electrochemical models for EIS spectra permitted to evaluate corrosion protective properties of oxide films and corrosion process on alloys. The effect of intermetallics on the properties of the anodized coatings has been studied in several works [96-99]. In AA2024 alloy the presence of voids after anodization is associated with the production of large bubbles of oxygen during water oxidation on copper rich intermetallics. Migration of Cu^{2+} during anodization creates mechanical defects responsible for film cracking. Such disadvantages of anodization of aluminum alloys require a search for other methods of surface pretreatment.
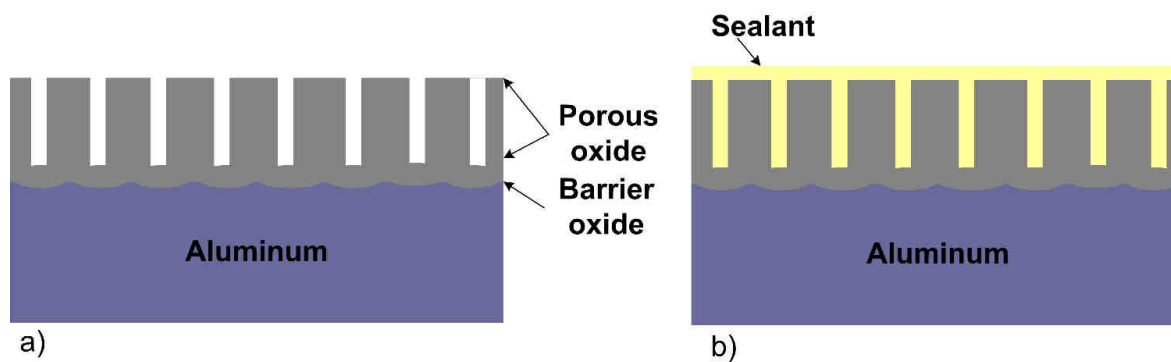
Figure 2.1.1. Schematic representation of porous anodized layer formed on aluminium a), pores are closed using sealant b).

2.2   Chemical conversion coatings

Application of chemical conversion coatings (CCC) does not require the use of high power supply used for anodizing. The process of conversion occurs in solution through chemical reaction between the solution components and alloy. The formation of the conversion layer can be accelerated under mild heating or with the presence of oxidizing additives. Conversion coatings made of non-chromate reagents have adequate strength and mechanical properties compared to chromate based [100]. Many environmentally acceptable chemical compounds such as phosphates, permanganates, fluorozirconates and their combinations and cerate have been studied as possible substitutes for eco-unfriendly chromate conversion coatings.

Phosphate conversion coating is an alternative approach to substitute chromate based pretreatments. The phosphate solution usually consists of zinc dihydrogen phosphates $Zn(H_2PO_4)_2x2H_2O$, manganese phosphates with phosphoric acid added to lower the pH. The speed of the process is increased when oxidizers are added in the bath. The process results in formation of aluminum and zinc phosphate layer $Zn_xAl_y(PO_4)_z$ on the metal surface. The phosphotization treatment can be done by spraying or prolonged immersion in the solution. Different methods of application of phosphate treatment for aluminum alloys have been studied in [101,102]. Although the phosphate layer facilitated adhesion to organic paints, the results of corrosion testing showed that the phosphate layer can not provide adequate protection because of its discontinuity.

There are similarities between the elements going from left to right in the fourth row of transition elements in periodic table such as V, Cr, Mn in terms of their chemical nature and physical properties. Therefore one can expect that the conversion coatings produced by Cr (VI) compounds will be similar to the ones produced by the Mn (VII) compounds. Some methods of conversion coating formation using permanganates as promising candidates for chromium (VI) substitution have been reported in works [103,104]. In order to pass corrosion tests the procedure includes different steps of pretreatment including boiling water immersion, treatment by aluminum salts followed by permanganate conversion bath immersion. Conversion coatings deposited from acidic solutions with permanganates have two layers structure that includes MnO_2 outer layer and an internal layer with mixed MnO_2 and aluminum oxide [105]. AES profiles indicate that Mn oxide has thickness about 60 nm. The increase of immersion time did not result in further coating growth. Permanganate conversion coatings on AA2024 using supporting electrolytes were reported in [106]. Complete coverage of intermetallic zones by manganese dioxide was observed because of the oxidative power of permanganate that is transformed to dioxide on cathodic places. The rest of the aluminum matrix was covered by a nonuniform porous layer of manganese dioxide. Mixed phosphate-permanganate treatment for different magnesium alloys has also been studied in [107,108] where relatively uniform coatings were obtained. Nevertheless, the barrier properties of such

coatings are not comparable to those of chromate pretreatment and further research is necessary.

Corrosion protective properties and composition of fluozirconate or fluotitanate pretreatments were studied for aluminum [109], different aluminum alloys [110,111] and others alloys [112,113]. The application of a pre-etching step, composition of bath, temperature and pH influence the properties of the final coatings that contain titanium, fluoride and aluminum oxide at the metal interface. The mechanism of the titania- or zirconia- conversion layer formation on aluminum alloys has localized nature [114,115]. The partial oxygen reduction causes increase of pH locally on the cathodic intermetallics and favors precipitation of the conversion layer in the vicinity of cathodes. Such layer consists of small round shaped particles of titanium and zirconium oxides. The parameters like temperature, concentration of reagent, the presence of oxidants during the pretreatment process influence the deposition speed. The use of such pretreatments as adhesion promoters might have a positive outcome, though they did not find application in the aerospace industry due to the low barrier properties.

Cerium salts are the known cathodic inhibitors that form insoluble precipitates over the cathodic active zones because of the reaction with hydroxyl ions. The use of cerate conversion coatings for the protection of aluminum alloys have been reported in a number of papers [116-122]. The formed cerate conversion layer usually covers active cathodic sites when deposited on the aluminum alloy substrates. However, it often happens that other parts of metal are not covered by this layer. Such surface heterogeneities cause a poor corrosion protection of the conversion layer. Therefore different additives are used in order to facilitate deposition of cerium oxide on the surface of the alloy. Cerate conversion coatings can be applied at different conditions such as boiling solution of cerium salts [116,117], solution of Ce^{3+} chlorides or nitrides with hydrogen peroxide to accelerate deposition [118-120,122]. Cerium conversion coatings deposited from the solution with oxidizer have Ce^{4+} as a main form in its composition. However, the corrosion protection efficiency does not depend on the ratio between Ce^{3+} and Ce^{4+} in the coating [118]. In addition the use of Ce^{3+} nitrates in the conversion coating process provides more homogeneous coatings compared with Ce^{3+} chloride salt [119]. Apart from composition of the electrolyte there are a lot of evidences that the treatment of aluminum alloys before the conversion coating application plays an important role to obtain more homogeneous layer. For example, treatment of the alloy in boiling solution with Ce salts followed by molybdate bath immersion during polarization increases the resistance to corrosion [116]. However, such procedure is long and power consuming. Copper smut formation after acid pickling increases coverage by cerium conversion coating [121]. Nevertheless, upon defect or crack formation the corrosion can be accelerated [122] because of the higher effective area of a copper cathode that was formed prior to the conversion layer. The problem of inhomogeneous coverage by a CeO_2 conversion layer still persists.

2.3 Anodized and chemical conversion coatings for active corrosion protection

The chromate-based treatment confers good paint adhesion, efficient corrosion protection and additional active corrosion protection for aluminum alloys. However, because of the environmental issues it needs to be substituted by environmental friendly pretreatments that can offer active corrosion protection. One of the approaches to impart active corrosion protection is based on the modification of the standard CAA pretreatment procedures. In this approach less toxic or environmentally friendly compounds are used to substitute chromates in pretreatment processes. In the case when active corrosion protection is needed, inhibitors can be incorporated into the protective system. The pretreatment in this case will act as a reservoir of inhibitor and provide its release when contacting water.

As a substitute for CAA different electrolytes can be used like phosphoric acid, sulfuric acid and others [42,67,123]. Sulfuric acid anodizing (SAA) has some limitations because of poor fatigue and adhesion properties. Nevertheless, the combination of organic and inorganic electrolytes like boric/sulfuric acids (BSA) or tartaric/sulfuric (TSA) acids can solve the problem of the SAA process [124]. Active corrosion protection of anodic coatings can be achieved by sealing the porous oxide structure with different inhibitors [124]. Corrosion protective properties of BSA anodized coatings sealed with rare earth salts were similar to those obtained after chromate sealing [124]. Incorporation of molybdates or permanganates during SAA process of AA2024 also imparts additional corrosion protection [125]. Sealing of the anodic layer using cerate solution increased corrosion protection performance of the 2024 aluminum alloy [126].

Molybdates, vanadates were considered as possible substitutes to chromates because they have lower toxicity. Since Mo and V elements are near Cr in the periodic table, they show some similarities, like relatively high Red/Ox potentials of the species in high oxidized states that can be used for a conversion coating process. The use of molybdates as corrosion inhibitors has been studied for different metals like aluminum [52-54], copper [55], zinc [127] and magnesium [128]. Inhibition of corrosion was attributed to the formation of a molybdenum-containing layer that decreases the adsorption of corrosion species on the surface. The reduction of molybdates leads to the formation of oxide film that also acts as a barrier to the metal dissolution. The formation of conversion coatings on metals using molybdates can be done either via immersion in a chemical conversion bath or by means of electrodeposition at cathodic potential. The comparison of different procedures for conversion coatings formation on galvanized steel substrates has been performed in [129]. Bath composition can vary and usually includes additives of inorganic acids. The factors like the composition of a bath and pH can significantly influence the quality of the coating on the substrates. The evaluation of the corrosion performance of different coatings using the EIS technique showed that the coatings produced by immersion in molybdate bath with phosphoric acid demonstrate better protection among others. The increase of impedance during immersion was attributed to active corrosion

protection provided by conversion coatings. However, effect didn't last for a long time. A study of conversion coating formation on galvanized steel substrates using XPS showed that initially molybdenum was present in the coating in (V) or (VI) valence state [130] which has also been confirmed by Wharton *et al.* using EXAFS [131]. After the corrosion exposure the valence state was changed to (III) or (IV) states. However, the Mo signal strength was found to be lower after the corrosion exposure, which is associated with the partial solubility of the oxides in chloride environment. In general, the corrosion protective properties of molybdate based conversion coatings on zinc are not exciting compared with chromates. Increased corrosion protection was found for conversion coatings deposited from a molybdate/phosphate bath on magnesium alloys [128]. Little information concerning the use of molybdate conversion coatings on aluminum and its alloys can be found in literature.

Vanadates, owing to their corrosion protection properties, were also considered as alternative pretreatment candidates for active corrosion protection. Conversion coatings for corrosion protection of AA2024 have been studied by Guan *et al.* [132]. The produced mixed vanadium oxide layer is about 500 nm thick which provides additional corrosion protection. The formed layer can confer self-healing protective properties based on the release of vanadium (V) inhibitive species from the layer during the exposure to corrosive electrolyte. Good corrosion protective properties of vanadium-based conversion coatings applied on magnesium alloy were obtained [133] unlike for galvanized steel [127].

Rare earth salts are almost non-toxic and can be used in many industrial applications as corrosion inhibitors. Therefore, different cerium salts have been used for the formation of conversion coatings [116,119,134-136]. When deposited on aluminum alloys cerium-based conversion coatings can have active corrosion protective properties because of entrapment in the layer of cerium (III) salts that diffuse to the defect area and provide corrosion inhibition. Such corrosion inhibition can be interpreted as self-healing. Corrosion protection performance of cerate conversion coatings evaluated using the EIS technique demonstrates the increase of impedance during 3 days of immersion of AA2024 [137]. In order to assist the deposition of a cerate layer a copper smut was deposited on the alloy surface prior to conversion coating formation [137]. Measurements show that the corrosion process does not accelerate on the alloy because of copper smut that is in contradiction with the other reported results [122]. The mechanism of corrosion protection of zinc substrate with cerium based conversion coatings [138,139] is similar to the one described for aluminum alloy [135,136]. The cerate protection layer was formed on the surface of zinc in a solution of cerium salt. The corrosion study revealed the retention of corrosion protection after scratching the surface. The presence of cerium hydroxides was found in the scratch, which is associated with the migration of cerium cations from the conversion coating and precipitation on the bare zinc surface hindering the corrosion activity [138,139].

2.4   Organosilane pretreatments

Pretreatments based on organosilanes and their derivatives attracted scientists by their simple application and valuable adhesion properties. A number of studies have been performed during the past decades on the applicability of silanes for replacement of chromate pretreatments for aluminum [140-142], aluminum alloys [143-149], magnesium alloys [150,151] and steel substrates [152,153]. A number of reviews and thesis have been published concerning the use of silanes for protection of metals [154-156].

The organosilanes have general formula $(RO)_3Si(CH_2)_mY$ and are called mono-silanes. In formula RO- represents an alkoxide which can be transformed as a result of a hydrolysis reaction to a silanol group (Si-OH); Y represents an organofunctional group such as chlorine, primary or secondary amines, vinyl, epoxy and others. Typically, the value of n is 3, but individual moieties can vary. Both the type of Y group and the value of m have a strong influence whether a particular organosilane monomer is water-soluble or not. However, in general most of them are water soluble at some extent.

The modifications of silanes called bis-silanes are used for additional crosslinking in combination with mono-silanes [157] or as adhesion promoters to organic layers [158,159]. A general formula of bis-silanes is $(RO)_3Si(CH_2)_mR1(CH_2)_lSi(OR)_3$ with 6 hydrolysable "RO-" groups and specific functionality "R1" in-between the two silane ends. The presence of organic chains between Si provides additional hydrophobic properties to the silane layer on the metal surface. The thickness of the obtained silane films is usually around several hundreds of nanometers and almost linearly depends on the concentration of silanes in alcohol based solutions [156].

The study of deposition of silanes on the surface of aluminum demonstrates the influence of functional groups in the silane molecules on the corrosion resistance. For example, the formation of a positively charged layer originated from amine groups assist the dissolution of aluminum, whereas the formation of a negatively charged layer composed by carboxyl groups inhibits dissolution. These effects can be related with the action of the charged layer that increases or decreases the adsorption of aggressive ions from electrolyte (Cl^- or others) [160]. Studies of the aluminum silane interface by FTIR spectroscopy show that the formation of covalent bonds between aluminum and siloxane groups is assisted by adsorbed water [160]. The formation of Al-O-Si covalent bonds between the alumina and silane was proven by Tof-SIMS analysis [161]. A combination of alloy pretreatment using boiling or hot water and silane coating showed increased adhesion between metal and coatings [146,147]. Electrodeposition of silanes on aluminum substrate has increased performance over the standard dip coating method facilitating the bonding strength between the metal and silanes [148,162].

Silane based coatings demonstrate good adhesion to metal and organic coatings. However, there are several drawbacks that limit their applicability in industry. Silane films are relatively thin, about 100-300 nm, and they do not provide long term barrier protection of metallic substrate. In addition films are not resistive to mechanical damage. The major

drawback is the absence of active corrosion protection of silane coatings. Therefore, additional modifications are needed in order to improve the corrosion behavior and mechanical properties of silane coatings.

2.4.1 Organosilane pretreatments with active protection

Corrosion protective properties of silane pretreatments can be improved if corrosion inhibitors are added into the protective system. Such inhibitors can leach out from the film and reduce corrosion activity in defects. The efficiency of inhibitors depends on a number of factors such as the solubility, leachability, the permeability of the silane coating and the compatibility of inhibitors with the silane. The influence of different additives on the corrosion protective properties of silane coatings is presented below.

The incorporation of small amount of Ce salts in silane coatings cause significant increase of barrier properties of the coatings deposited on AA2024 compared to inhibitor free coating [163,164]. DC polarization measurements on scratched coated substrates demonstrate increase of protection (current decrease) after longer immersion time that is associated with active corrosion protection by cerium (III) leaching from the coating. Incorporation of organic inhibitors such as tolyltriazole and benzotriazole also shows positive action on the corrosion protection properties of the silane films [163]. However, the tolyltriazole inhibitor provides much better corrosion protection, i.e. lower cathodic current on polarization scans compared to benzotriazole [163]. This can be associated with chemical interaction of benzotriazole with silane and reduction of its inhibitive ability. Coatings formed on galvanized steel using bis-[triethoxysilylpropyl] tetrasulfide silane doped with Ce or La salts show good anti corrosion performance as well [165-167]. Corrosion activity of zinc substrate can be reduced using silane protection coatings. Moreover, when sodium silicate and cerium (III) nitrate were used as inhibitive additives for the silane coatings a self-healing effect can be achieved [168].

Mechanical properties and corrosion protection of an aluminum substrate with a deposited silane film can be improved by the addition of silica nanoparticles [169]. The study showed that the amount of nanoparticles added to the silane can significantly affect corrosion protection. The corrosion performance of silane films doped with 15 ppm and less of silica nanoparticles is better than the films with 50 ppm of nanoparticles, although the thickness of both coatings is very similar for both amounts of nanoparticles. The corrosion inhibition effect is attributed to the formation of silicates due to the dissolution of silica nanoparticles in alkali environment near the cathodic zone. Such silicates can form insoluble compounds on the surface of alloy, therefore reducing the corrosion activity [169]. Silane films have been found useful for the corrosion protection of galvanized steel substrates [170]. The incorporation of silica or CeO_2 nanoparticles increases corrosion protection of the metallic substrate. In case of silica doped silane films the protection mechanism is claimed to be similar to the one described in ref. [169]. However, doping of

silane films with CeO_2 nanoparticles increases their protection efficiency compared to silica nanoparticles. There are also evidences of synergetic effect between the incorporated nanoparticles and cerium (III) salts. In case of silica or CeO_2 nanoparticles the activation of the nanoparticles with cerium ions enhanced the corrosion protective behavior [170].

2.5 Sol-gel pretreatments

2.5.1 Chemistry of the sol-gel synthesis

Sol-gel processes have been used in different applications to prepare homogeneous powders [171], bulk glasses materials [172], xerogels, membranes [173], coatings [174], ceramic composites, fibers [175] and others. A lot of reviews and books contain wide information on synthesis, processing and applications of sol-gel derived materials [176-183]. The sol-gel method allows combing silicon and/or metal containing precursors to produce inorganic or organically-modified oxide materials with tailored properties. The sol-gel method implies the evolution of precursors solution through the colloidal system (sol) followed by a highly branched system called (gel). Sols are dispersions of colloidal particles with diameters of 1-100 nm [178] or 1-1000 nm [176] in a liquid. Gel is an interconnected rigid network with pores of submicrometer dimensions and polymeric chains whose average length is greater than a micrometer [178]. The precursors for the sol-gel process can be different metals and silicon (Ti, Zr, Ce, Al, Si etc.) alkoxides with general formula $(A(OR)_4)$, where A is a metal or Si atom, OR is an alkoxy group and R is typically an alkyl ligand. The common reaction of alkoxides upon contact with water is hydrolysis [176]:

$$A(OR)_4 + H_2O \rightarrow HO-A(OR)_3 + ROH \qquad (2.5.1)$$

The hydroxyl ion attaches to the A atom producing alcohol and partially hydrolyzed precursor. Subsequently, two partially hydrolyzed precursors can link together in condensation reactions:

$$(RO)_3A-OH + HO-A(OR)_3 \rightarrow (RO)_3A-O-A(OR)_3 + H_2O \qquad (2.5.2)$$

$$(RO)_3A-OR + HO-A(OR)_3 \rightarrow (RO)_3A-O-A(OR)_3 + ROH \qquad (2.5.3)$$
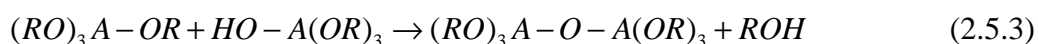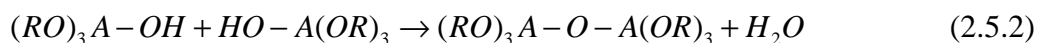
The reactions (2.5.2) and (2.5.3) can continue building branched network with -O-A-O- bridges by the process of polymerization until the gel point where continuous solid network is formed including liquid phase in pores.

The rate of hydrolysis reaction is commonly higher than the rate of condensation process [184,185]. Reactivity of silicon and metal alkoxides is different and increases in the order: $Si(OR)_4 << Ti(OR)_4 < Zr(OR)_4 < Ce(OR)_4$. Since the silicon alkoxides react very slowly with water, additional catalysis is normally used to accelerate the process. Acetic acid, different mineral acids, amines, alkali metal hydroxides, Lewis bases can be used as catalysts [186-188]. As can be seen from the Figure 2.5.1, both acidic and basic catalysts increase the rate of hydrolysis reaction of silanes in aqueous solution. However, the nature of catalyst can affect the microstructure of the condensed products. For instance, compact and highly branched networks are formed from alkoxy silanes when using basic catalyst. On the contrary, acidic catalyzed hydrolysis results in the formation of linear randomly branched networks.
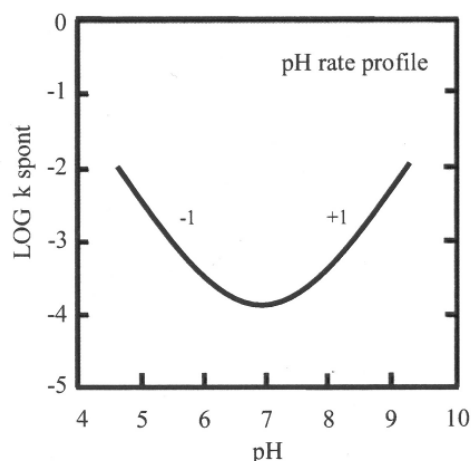
Figure 2.5.1. Dependence of γ-glycidoxypropyltrialkoxysilane hydrolysis rate in water on pH taken from [176].

For the purpose of coating formation it is highly desirable to make a dense sol-gel film that can be obtained using acid-catalysed hydrolysis and condensation. One of the possible (S_N2) mechanisms in acidic media for silicon alkoxides hydrolysis and condensation reactions is presented below. Initial protonation of alkoxy group makes silicon more electrophilic, thus more susceptible to attack by water. Alcohol leaves the intermediate complex that turns into hydroxo substituted Si alkoxide:

$$(2.5.4)$$
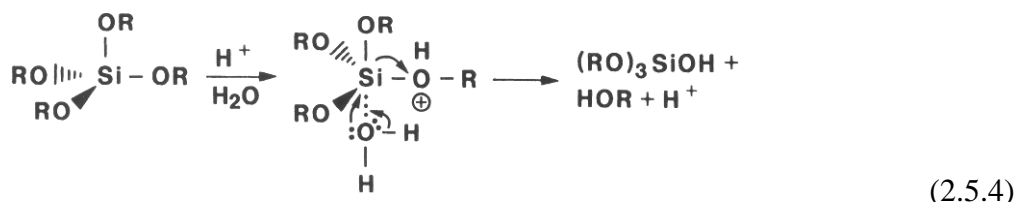
In the case of transition metal alkoxides with general formula $M(OR)_4$, where M is a metal (Ti, Zr, Ce, Al), the hydrolysis process can readily go through simple reaction with water via (S_N) mechanism due to low electronegativity and unsaturated coordination:

$$(2.5.5)$$
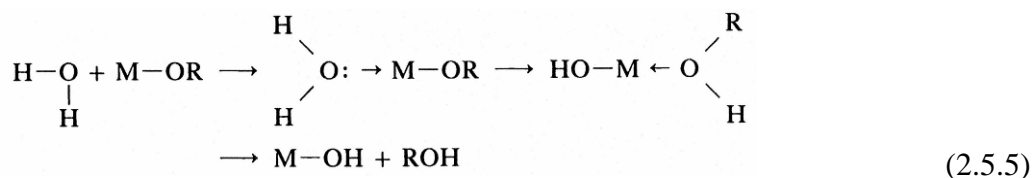
Instead of catalysts different inhibitors should be used to control the kinetics of hydrolysis and condensation reactions of $M(OR)_4$ [189-191]. Complexing agents such as different β-diketones, carboxylic acids, glycols and others can act as inhibitors [192-195]. Many aspects of hydrolysis and condensation processes and the use of inhibitors for metal alkoxide hydrolysis are discussed in [182,183]. Nucleophylic agents (inhibitors) in most cases react with initial Me-alkoxides via S_N mechanism presented above. However, when

alkoxides are coordinatively unsaturated, the reaction of inhibitor (XOH) and metal alkoxide can proceed via A_N mechanism as well:

$$XOH + M(OR)_4 \rightarrow M(OR)_4(XOH) \tag{2.5.6}$$

In any case the resulting product of metal alkoxide with the complexing agent is more stable toward hydrolysis or condensation reactions. In excess of water the (Me-O-R) bonds are slowly broken thus allowing more controlled hydrolysis conditions [182,189]. The reactivity of metal alkoxides depends also on electrophylic properties of metal, metal coordination number and nucleophile strength [183]. The higher the electrophylity and coordination unsaturation, the more reactive metal alkoxides are.

The most important parameters that influence the hydrolysis and condensation reaction are the water to alkoxide ratio r, pH, temperature, concentration of reagents, and nature of the alkoxide groups. The variation of such parameters can influence not only kinetics of the sol-gel process but the micro- and nanostructure of the final product [196]. Ultrasonic energy applied during the sol-gel synthesis could provide an additional catalytic activity during the synthesis and can influence the uniformity of liquid-solid systems [197,198]. The application of ultrasonic energy for synthesis of nanoparticles and sol-gel solutions has been studied in different works [194,199-203]. Using the ultrasonic energy a fine distribution of nanoparticles can be obtained which might be successfully used for the creation of different hybrid and nano- composite materials with tailored properties.

2.5.2 Inorganic and hybrid sol-gel materials

Historically, the first classes of sol-gel materials were inorganic oxide powders, bulk composites, glasses, mixed ceramics, inorganic coatings [178,181,201]. The protective coatings composed by different oxides were suggested for different metals [204-208]. The disadvantage of purely inorganic sol-gel derived materials is the formation of cracks upon drying or curing. It takes a very long time to form a glass like material from silicon based alkoxides at room temperature [178]. Crack-free inorganic sol-gel coatings can be obtained with only very low thickness about 100 nm. On the other hand different hybrid materials are obtained when mixing organic and inorganic components. Coatings produced in such way are crack free and thicker compared to pure inorganic coatings because the addition of organic part increases the elasticity of the composite. The variation of inorganic part can be used to improve toughness and scratch resistance [209,210]. It is important to take into account the interaction between the components of the sol-gel that can modify properties of the final material. For instance, the addition of TEOS to the mixture of epoxy resin and hardener can actually reduce the glass transition temperature because of a side reaction between the product of TEOS hydrolysis and hardener [211].

The sol-gel hybrid materials can be classified in two major classes according to Judeinstein *et al.* [183]. Class I of hybrid materials is based on physical mixing of organic

and inorganic phases without covalent bonds between inorganic and organic components (Figure 2.5.2). Van der Waals, ionic and hydrogen bonding interactions are the only forces that arise between the components. The synthesis of such hybrid materials can be performed by simple mixing of inorganic sol with organic matrix [212-214]. The produced composites have different valuable mechanical properties, in particular increased hardness when the organic polymer matrix is impregnated with inorganic oxides. However, such materials can not provide adequate barrier protection because of porosity and loss of chemical bonds.

In Class II hybrid materials chemical bonds are formed between the inorganic and organic parts by means of functional groups or organo-modified precursors (mostly by organo-modified silanes). The structure of the Class II hybrid materials is shown in Figure 2.5.3. It presents three principal approaches for preparation of organic-inorganic networks from organofunctional alkoxide precursors [182]. The first type of class II hybrid materials is shown in Figure 2.5.3 A. In this example the organo-modified alkoxides $((RO)_n$-E-Y and $E(OR`)_m)$ are linked via oxygen bridges. The specific functionality group (Y) does not react and is retained inside the hybrid material. In this example alkoxides are optionally added for the purpose of inorganic network formation.

Figure 2.5.3 B presents the second type of class II hybrid materials. In this case chemical binding occurs in two different ways. The hydrolysis of alkoxy groups and condensation reaction forms an inorganic network. The reaction between organic functional groups (A) of organo-modified precursors $(RO)_n$-E-A forms organic network (curved lines). An additional cross linking between the organic functional groups can be used to achieve higher density and better mechanical properties of the composites. In the third type (Figure 2.5.3 C) the hybrid network is formed by functionalized building blocks of oxide clusters or colloidal particles. The inorganic clusters are linked by the organic functional groups. Using different combinations of these methods and types of precursors, there are many possibilities to chemically modify organic-inorganic hybrid polymers and thus to tailor their functionality and macroscopic properties [215].
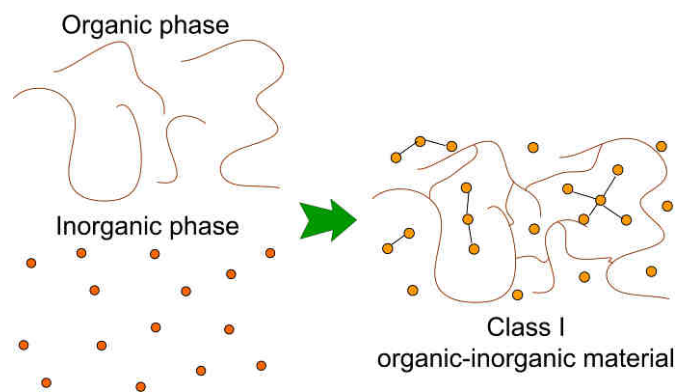
Figure 2.5.2. Class I hybrid material (no covalent bonds are formed between inorganic and organic phases). Adapted from ref. [183].
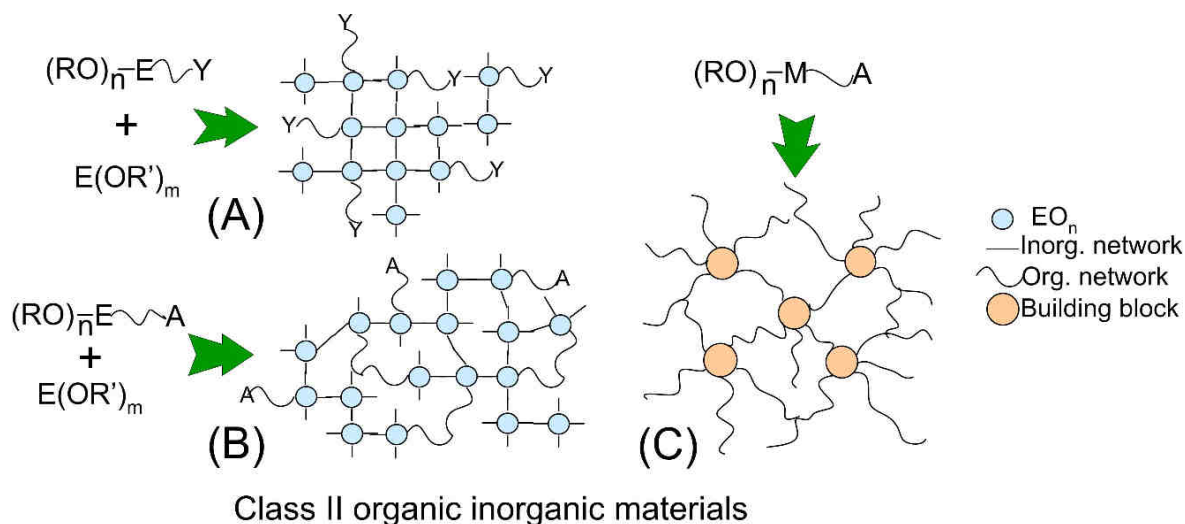
Figure 2.5.3. Class II hybrid materials; (A) hybrid network with added functionality (Y) linked by inorganic bonds; (B) hybrid network linked by inorganic and organic bonds; (C) organic-inorganic network made of nano-building blocks linked through organic bonds. Adapted from ref. [183].

Typical nonfunctional organic groups used to build hybrid networks (Figure 2.5.3 A) are different alkyl groups [162,216-220]. Commonly used organofunctional groups for building hybrid materials (Figure 2.5.3 B,C) are epoxy [185,217,221-224] and methacrylic [187,199,225,226]. Such groups are used for synthesis of hybrid organo-inorganic materials since they can provide additional polymerization and cross-linking of hybrid sol-

52

gel matrix using appropriate initiators or cross-linking agents. Functional groups that have also been used in organofunctional precursors are phenyl [162,227], amino [228,229], alkyd [210,230]. Additional hydrophobic properties can be provided by alkyd and phenyl groups [162,213]. Amino groups can also be used to facilitate adhesion to epoxy containing top coating [229].

In situ synthesis of nanoparticles via the controlled hydrolysis of different alkoxides in hybrid organic inorganic matrix is an alternative way to create nanostructured materials. In comparison to the conventional sol-gel route the controlled hydrolysis of hybrid silanes or metal alkoxides can be used to create modified nanoparticles or molecular clusters. Control of local structures and degree of organization is important for tailoring properties of such inorganic compounds. A better definition of the hybrid matrix can be done using calibrated objects like clusters, nanoparticles or nanolayered compounds. These nanoobjects or nanobuilding blocks (NBB) are usually capped with polymerizable ligands, organic spacers or functional groups. The use of such nanoobjects is preferable because of several advantages like higher stability towards hydrolysis. Nanoobjects can have controllable shape and composition which can be done employing different chemical synthesis routes. Employing different NBB as structural material in combination with different assembling strategies allows building a variety of architectures and hybrid interfaces [189]. The NBB approach is developed for various systems such as oligosilsesquioxanes, organotin-oxo clusters, organically functionalized heteropolyoxo-tungstates, transition metal-oxo clusters and others. The nature of the interface between the inorganic and organic components and their connectivity is important for the controlling properties of the final material. For silicon oxo-clusters coupling with the organic matrix can be done via Si-R bond using different functionality and organic radicals. Polyoxometalates can not form metal carbon (M-R) bond because it is easily hydrolysable except for Sn-C bond that is very stable [231]. Therefore polyoxometalates can be functionalized by the M-O-Si-R bond and the obtained NBB are linked through the (R) functional group. Organic modification of metal-oxo clusters can also be performed using the complexing ligands. The example of such organically modified clusters can be zirconium-oxo-poly acetoacetoxyethylmethacrylate that was synthesized and studied by In *et al.* [232]. The strategies offered by the sol-gel chemistry and the NBB approach allow assembling of a large variety of structurally well-defined clusters or nanoparticles into complex architectures that can be used for designing new advanced materials.

2.5.3 Hybrid sol-gel pretreatments for passive and active corrosion protection

Sol-gel systems as pretreatments must fulfill several important requirements. An important property of the pretreatment is a good adhesion between the metal/sol-gel and sol-gel/paint interfaces. Adhesion to the metal substrate is greatly facilitated because of chemical interactions between the metal and siloxane molecules. In humid environment a cleaned surface of metal contains many hydroxyl groups. Upon contact with sol-gel

solution hydrolyzed siloxane molecules are attracted to the metal surface by van der Waals and electrostatic forces. During curing of the sol-gel film stable covalent bonds are formed between the metal surface and silane molecules during the water condensation reaction according to the following reaction [233]:

$$Al-OH+HO-Si(R)_n \rightarrow Al-O-Si(R)_n+H_2O, \quad \Delta H=\text{-462 kJ mol}^{-1} \quad (2.5.7)$$

$$Al-OH+HO-Al \rightarrow Al-O-Al+H_2O, \quad \quad \Delta H=\text{-48 kJ mol}^{-1} \quad (2.5.8)$$
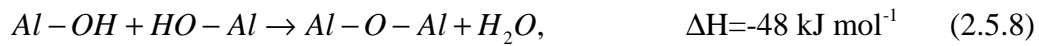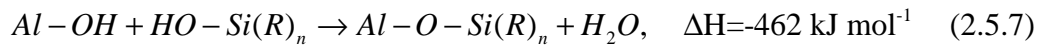
Thermodynamic calculations made by Schmidt *et al.* show that the Gibbs energy of the formation of bonds between alumina and silica for reaction (2.5.7) is lower compared to boehmite that is produced during the oxidation of aluminum by water (reaction 2.5.8) [233]. Therefore the interface between the sol-gel and metal becomes very stable.

Another important issue of the sol-gel pretreatments is the adhesion to the paints that are used in corrosion protection systems. Good adhesion between the sol-gel and paint ensures high barrier properties and corrosion protection of the entire system. Usually in aeronautical industry paints consist of epoxy- functionalized components cross-linked by amine containing agents. To ensure good adhesion the sol-gel coating must be chemically bonded to the paint, which can be done using the approaches presented in Figure 2.5.3. Epoxy functionalized silanes can be incorporated in the sol-gel formulation forming Class II hybrid material with specific organic functionality. Epoxy groups of the sol-gel coating can react with amine groups or epoxy groups of paints therefore making a good binding between sol-gel and paint system as can be seen in Figure 2.5.4.

Hybrid sol-gel process allows developing protective coatings with tailored mechanical properties that is also an important parameter for the quality of pretreatment. Too rigid coatings might be easily broken during tension and too soft coatings might not tolerate mechanical impacts. The necessary level of flexibility can be adjusted by using organic substituted silanes in order to withstand the excess of stress. A lot of information on characterization of mechanical properties and relation between nanostructure and mechanical properties of hybrid organic inorganic materials can be found in ref. [234]. The mechanical properties of the sol-gel coatings can be altered using appropriate organo-silane compounds. In this way thicker coatings with higher barrier properties are obtained. However, introducing organic groups often influences wear resistance and other mechanical properties.
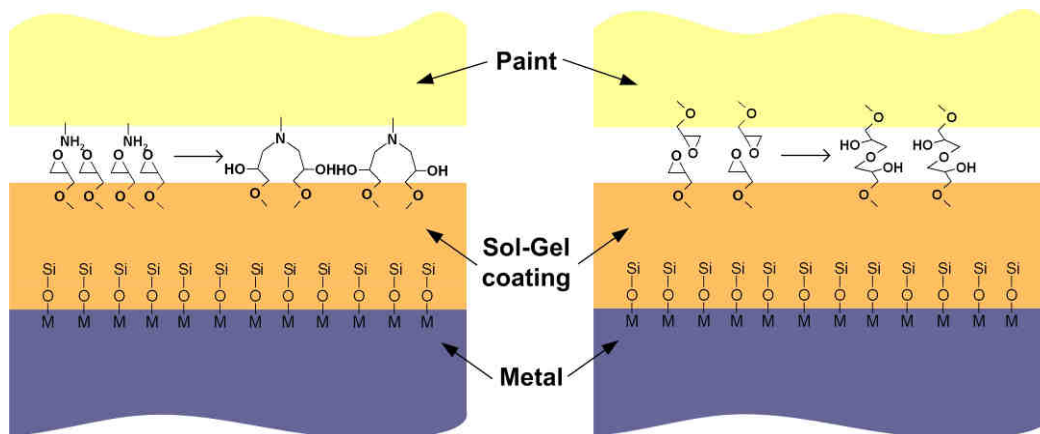
Figure 2.5.4. Scheme of chemical bond formation between metal, sol-gel and paint [188].

One of the possible ways to improve the mechanical properties is to impregnate a sol-gel with different kind of oxide nanoparticles thus reinforcing the sol-gel matrix which lowers crack formation tendency [235-237]. Although the addition of nanoparticles does not always improve mechanical properties, the interfacial binding between the nanoparticles and components of the sol-gel is also important and must be taken into account. Usually the barrier properties of the nanoparticles-reinforced sol-gel coatings are higher compared to standard coatings. However, when exciding a critical concentration of silica nanoparticles a more porous coating is formed [238]. A remarkable increase of barrier properties of sol-gel coatings with addition of fused silica nanoparticles substrates was also observed by Conde *et al.* on aluminum alloys [217]. Addition of particles leads to the decrease of porosity of the coating, which increases the pathway for corrosive electrolyte to the metal surface. On the other hand crack-free and relatively thick sol-gel coatings can be obtained by spinning the organomodified sol-gel system with nanoparticles of Al_2O_3, ZrO_2 and SiC that were Si-OH modified prior to addition [239]. Good mechanical properties and corrosion protection were found in this case. A modification of hybrid sol-gel films with microparticles of glass about 3 µm diameter increases mechanical properties in particular wear resistance [240]. However, stress occurs in the "neck" between the microparticles and the sol-gel coating resulting in cracks formation. In spite of hopeful results, the nanoparticles addition is associated with some negative effects like agglomeration during the processing that could create highly defected structure and poor connection between the particles and matrix [237].

The disadvantages of nanoparticles doped sol-gel coatings can be avoided if the nanoparticles are synthesized in situ during the sol-gel process. The formation of self assembled nanophase particles (SNAP) of silica during the sol-gel synthesis is presented by Vreugdenhil *et al.* [241]. The approach was used to create sol-gel protective coatings

based on combination of GPTMS and TEOS in order to substitute the chromate pretreatments for metals. Different methods were used for the characterization of the obtained sol-gel coatings. The combination of analytical and chemical methods and surface analysis techniques like XRD, XPS, NMR, IR, TOF-SIMS, light scattering and AFM was used for the characterization of the nanostructured properties of the obtained sol-gel coatings [242,243]. However, the presented experimental evidences are insufficient to claim the presence of self-organization in the prepared sol-gel coatings. Therefore, more studies on the self-organization in the sol gel systems are needed in order to characterize and develop new nanostructured materials.

Sol-gel pretreatments for passive corrosion protection

Among the variety of applications of the sol-gel process considerable interest has been found in developing novel corrosion protection systems for metals. Many sol-gel coatings were prepared on steel substrates using various silica based precursors and their mixtures [199,207,225,244]. It has been found that the parameters like sol-gel ageing time and temperature of curing have an important influence on the properties of final coatings. Effect of the sol-gel ageing time on the corrosion performance of the applied coatings has been studied for a hybrid sol-gel system based on (tetraetylorthosilicate) TEOS and (3-methacryloxypropyl-trimethoxysilane) MPS applied on steel substrates and cured at 300ºC [225,244]. The results clearly demonstrate the decrease of corrosion protection of the applied coatings for longer ageing times. The influence of the time and curing temperature of sol-gel coatings based on zirconia propoxide mixed with polymethylmethacrylate or silica based precursors was studied in [199,207]. Generally, when increasing the curing temperature the corrosion protection of the coatings increases. However, too high temperature can deteriorate the sol-gel coating and decrease the protection efficiency. The protection of magnesium alloys using sol-gel coatings has also been studied in the past years [245-247]. Sol-gel coatings can also be applied for sealing the porous anodizing layer providing additional protection [245]. Effect of pickling of magnesium has strong effect on the protection efficiency of the sol-gel coating [246]. In spite of the integrity of sol-gel coatings on magnesium alloys, the reactivity of the latter is very high and the protection does not last for a long time. Novel sol-gel coatings with TEOS and diethylphosphonatoethyltriethoxysilane show increased corrosion performance compared to other sol-gel systems because of chemical reaction between phosphonate groups and the magnesium alloy surface [247].

One of the applications of sol-gel coatings is found in corrosion protection of different kinds of aluminum alloys in order to substitute chromate based corrosion pretreatments used in industry. A vast number of works deal with pretreatments of 2024 aluminum alloy substrates by different sol-gel systems and investigations of their corrosion protection efficiency [208,216,221,222,248-251]. Comparative evaluation of sixteen different full protection coating systems based on different pretreatments like Alodine

56

1200, Chromate Conversion Coating (CCC) and sol-gel for AA2024 has been performed by Khobaib *et al.* [208]. The obtained results demonstrate adequate barrier protective properties of the systems based on sol-gel pretreatments. However, scribe tests show lack of corrosion protection. Alodine and CCC pretreatment processes have active corrosion protection of the alloy due to incorporated inhibitive species in comparison to sol-gel films. In contrast to that, the corrosion studies performed in [222] and [249] demonstrate the increased protection of the sol-gel coated aluminum alloy compared to the Alodine 1200 pretreated [222] and CCC pretreated alloy [249]. However, such difference is attributed to increased barrier protection properties of thick sol-gel coatings compared to the thin films obtained by Alodine and CCC surface treatments. The thickness of the sol-gel coatings depends on the silicon based precursors and nature of the organic radicals. The influence of nature of the alkyl radical in organically modified silane based coatings on the corrosion behavior was investigated by Metroke *et al.* [216]. The results show that the increase of the alkyl chain size allows depositing thicker films with higher barrier protection. Corrosion protection properties of the sol-gel coatings deposited on AA2024 substrates were investigated in [252]. The precursors such as TEOS and GPTMS were used for the sol-gel synthesis. In order to provide better barrier properties and increase the crosslinking degree the sol-gels were additionally impregnated by different amines. The corrosion studies showed that the amino silanes increase the barrier properties of the sol-gel coatings compared to diethylenetriamine. Amino silanes used as cross linking agents form a denser sol-gel matrix because of increased crosslinking degree between the components of the system. The cross linking occurs between the epoxy groups of the GPTMS and amines and between the hydrolyzed silanol groups of GPTMS and amines. Investigations of the corrosion protection properties of the sol-gel coatings with a complete protection system including a chromate loaded primer and a top coat show good performance of the sol-gel system compared to the chromate based pretreatments in scratch tests [253]. However, the corrosion protection was not satisfactory when performing tests without a chromate based primer demonstrating leak of active corrosion protection properties of the sol-gel pretreatments.

The approaches presented above allow creating coatings with tunable properties needed for corrosion protection systems. Mechanical properties of the sol-gel coatings can be adjusted by the different organo silane compounds and by impregnating the sol-gel coatings with nanoparticles. The use of cross linkers and different functionalized organo silanes can increase the crosslinking degree of the sol-gel matrix which increases the barrier properties of the coatings. In addition proper functionalization of the sol-gel can be used to enhance the adhesion between the sol-gel coating and organic paint. Nevertheless, none of the sol-gel pretreatments can achieve the "self-healing" ability of chromates. Therefore, in order to achieve "active" corrosion protection sol-gel pretreatments have to be used in combination with different methods that impart active corrosion protection properties

Sol-gel pretreatments for active corrosion protection

In spite of many advantages of the sol-gel pretreatments some problems are found in corrosion protection tests. The indicated drawback is the absence of active corrosion protection and corrosion inhibition of the underlying metallic substrate. Therefore the incorporation of corrosion inhibitors inside the sol-gel coatings might partially enhance the active corrosion protection properties of the sol-gel. The corrosion inhibitors can be introduced in different components of the coating system: pre-treatment, primer and top-coat. The inhibiting agents are effective only if their solubility in the corrosive environment is in the right range. Very low solubility of inhibitor leads to the lack of enough active agent at the metal interface and consequently to weak inhibition. If the solubility is too high, the substrate will be protected, but for only a relatively short time since the inhibitor will be rapidly leached out from the coating. Another drawback, which can appear due to high solubility, is the osmotic pressure that leads to blistering and delamination of protective coatings. The osmotic pressure can facilitate the water ingress through the coating, which acts as a semipermeable membrane causing a fast destruction of the barrier layer.

Inorganic chemicals like phosphates, vanadates, molybdates, cerium salts and others are the known inhibitors of corrosion for different kind of aluminum alloys. Numerous reports show positive effect of the incorporation of cerium salts inside the sol-gel coatings as substitute for chromate pretreatments for different aluminum alloys and zinc substrates [254-257]. Different Ce (III) and Ce (IV) salts incorporated into the sol-gel coatings do not alter their oxidation state in the coatings [254]. This demonstrates the stability of the inhibitor in the sol-gel matrix. The inhibiting efficiency of the sol-gel coatings with incorporated Ce (IV) nitrates is higher compared to Ce (III) for corrosion protection of 3005 aluminum alloy [257]. Nevertheless, high concentration of inhibitors can deteriorate the barrier properties of the sol-gel coatings. For example, sol-gel coatings doped with Ce (III) salt and deposited on zinc substrates provide inhibition only below some critical concentration of inhibitor being in the range of 0.2-0.6 wt.%. Higher concentration of inhibitor yields network defects in the sol-gel and decreases the corrosion protection [256].

Voevodin *et al.* investigated the corrosion protection properties of sol-gel coatings with 4 or 5 wt.% of incorporated inorganic inhibitors such as $Ce(NO_3)_3$, Na_2MoO_4, $NaVO_3$ and $Na_2Cr_2O_7$ by means of the potentiodynamic polarization method [255]. Sol-gel coatings doped with cerium salt on AA2024 substrates showed as good behavior as sol-gel coatings without inhibitors. On the other hand, sol-gel coatings doped with molybdate or vanadate salts didn't show adequate corrosion protection of the aluminum alloy because of the decreased sol-gel matrix stability. However, the results are questionable, since only anodic potentiodinamic scans were made on the sol-gel coatings with inhibitors. As well known, such inhibitors show cathodic inhibiting properties on aluminum alloys [44,47,49]. Therefore measurements using another electrochemical method or making cathodic potentiodynamic scans could show an increase in corrosion protection. Besides, the

inhibitors concentration (4-5 wt.%) used in this study [255] is relatively high and could cause significant destruction of the sol-gel coatings as was studied in [256] using the EIS technique. The positive effect of the addition of molybdate compounds as corrosion inhibition to the sol-gel coatings can be achieved when molybdate is added in the "bound" form after reaction with cycloaliphatic amine in contrast to the "free" ionic form (MoO_4^{2-}). The bound form of the inhibitor prevents its undesirable interaction with the sol-gel matrix and increases the matrix stability [258].

Organic inhibitors have been also incorporated in the sol-gel matrix in order to improve the corrosion protection of aluminum alloy substrates [227,259-262]. The addition of organic inhibitors such as aminopiperazine, aminopiperidine and combinations of tetraethyl dimethylenediphosphonate and mercaptobenzotriazole at concentration 0.5 wt.% into the previously prepared sol-gel increases the corrosion protection properties of the sol-gel coatings [259]. Sol-gel coatings with aminopiperazine show the most efficient corrosion protection compared to other additives. Nevertheless, organic inhibitors can negatively affect the sol-gel matrix stability when added at high concentration. The addition of high content of chloranil ($12*10^{-4}$ M) did not provide adequate corrosion protection due to the disorganization of the sol–gel matrix. Such disorganization could occur because of low solubility of the organic compound in the sol-gel. Thus the crystallized compound can create defects and voids in the sol-gel matrix which negatively influences the barrier properties of the sol-gel coating. On the other hand, lower concentration of chloranil provided homogeneous structure of the coating and increased the corrosion protection properties of the sol–gel coatings based on TPOZ and organomodified silanes [260].

The incorporation of organic compounds in the sol-gel systems does not always provide additional corrosion inhibition compared to undoped sol-gel coatings. Such effect can be related to a low release of organic compounds from the sol-gel system due to the electrostatic interactions between the organic compounds and the sol-gel components. In some cases the release of ionizable organic compounds from the sol-gel matrix can be triggered by the pH changes of the electrolyte. The pH can influence the zeta potential of the sol-gel matrix and the charge of the organic compounds. Therefore, when pH is adjusted, the organic molecules can loose the charge and electrostatic interactions with the sol-gel matrix become weak providing the release of the organics [263]. However, ionizable inhibitors show a far weaker release than that of non ionizable ones since the first are too strongly attached to the sol-gel matrix and, thus, cannot be released during the corrosion exposure [262]. A controlled release of inhibitor can be also achieved when there are interactions between the functional groups of sol-gel matrix and the inhibitor. Sheffer *et al.* studied corrosion protective properties of the sol-gel coatings based on phenyltrimethoxysilane with and without phenylphosphonic acid inhibitor. The inhibitor becomes entrapped inside the sol-gel matrix due to specific π-π interactions between the phenyl rings. Sol-gel coatings with phenylphosphonic acid deposited on aluminum

substrates demonstrate the enhanced corrosion protection attributed to the prolonged release of phosphonate ions [227].

Low efficiency of the coatings containing the inhibitor in their internal structure calls for the development of new approaches that isolate the inhibitor from the coating materials confining them in nano- and microreservoirs. The shell of these reservoirs can prevent direct interaction of the inhibitor with the sol-gel matrix avoiding the negative effect of inhibiting species on the stability of the anticorrosion coating. The possibility of using nano reservoirs for inhibitor incorporation based on β-cyclodextrin has been presented in [261]. Complexes of β-cyclodextrin with mercaptobenzothiazole and mercaptobenzimidazole inhibitors were created and incorporated in the sol-gel coatings in order to control the release of inhibitors and provide the prolonged protection. The corrosion investigation performed using Scanning Vibrating Electrode Technique showed that the encapsulation of inhibitors inside β-cyclodextrin improves the corrosion protection properties of the sol-gel coating applied on AA2024 in comparison to the coatings with directly incorporated inhibitors. The design and creation of new generation of protection systems based on nanoreservoirs of inhibitor with intelligent release and active corrosion protection is a topic for the present and future works in the field of corrosion protection of metals.

3   Theoretical background of the main experimental techniques

The purpose of this section is to give a short overview of the main techniques used to evaluate the corrosion protection efficiency of the developed coatings as well as to study the corrosion and protection mechanisms. Atomic Force Microscopy (AFM) and Scanning Kelvin Probe Force Microscopy (SKPFM) were shown to be useful for the investigation of the electrochemical nature of local zones on the metallic and alloy surfaces contributing to the deeper understanding of mechanisms of localized corrosion processes. DC-polarization technique was applied to analyze the inhibiting performance of different corrosion inhibitors under study. Moreover a cathodic or anodic inhibiting action of the inhibitors can be confirmed by means of this method. Electrochemical Impedance Spectroscopy (EIS) was successfully used to study the corrosion protection of AA2024 substrates and the self-healing abilities conferred by different sol-gel coatings. The localized corrosion activity in micro-confined defects was accessed by means of Scanning Vibrating Electrode technique (SVET) that was successfully employed in this study for investigation of the self-healing effect on the sol-gel coated substrates.

3.1   AFM / SKPFM

AFM belongs to a family of Scanning Probe Microscopy (SPM). The technique has a unique ability to measure surface topography of different materials with sub-nanometer resolution. The main working principle of AFM is to scan a sharp tip along the surface while probe-sample interactions are monitored. Historically a first type of SPM was developed in 1982 by Gerd Binning, Heinrich Rohrer, Gerber and Weibel at IBM in Zurich, Switzerland. Later Binning and Rohrer won the Nobel Prize in Physics for this invention in 1986. AFM was developed in 1986 by Binning, Quate, and Gerber in collaboration between IBM and Stanford University.

3.1.1 Instrumentation

The basic AFM components are presented in Figure 3.1.1. It includes a cantilever with a sharp tip which is used to scan along a sample surface. When the tip is brought close to a sample surface, forces between the tip and sample lead to a deflection of the cantilever. Depending on the situation there are different forces that are measured in AFM such as mechanical contact force, van der Waals forces, capillary forces, chemical bonding, electrostatic forces, magnetic forces etc. Typically the deflection of the cantilever is measured using a laser beam that is reflected from the cantilever surface to an array of

photodiodes. When the tip is scanned along the surface it can be crashed into it because of inhomogeneity of the surface topography. A feedback mechanism is employed in order to maintain tip at the same height to the surface with a constant tip-sample interaction forces. Such feedback is provided by a piezoelectric scanner that can move the sample in 3d directions. Moving the tube along x and y allows scanning the sample surface, while moving in z direction controls the force between the tip and the sample. The resulting map (x,y,z) presents the topography of the sample surface.
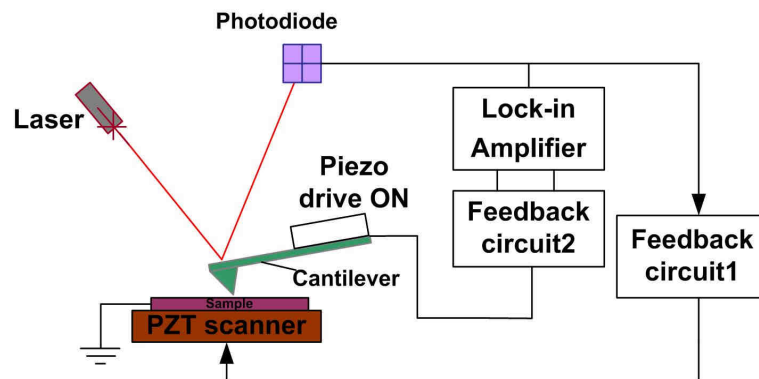
Figure 3.1.1. Schematic diagram of AFM microscope

There are three primary modes of AFM operation namely: Contact Mode AFM, Tapping Mode™ AFM and Non-contact Mode AFM.

In the contact mode tip-sample interactions are monitored through the cantilever deflections. The tip is simply dragged along the surface and electronics maintains the constant force between the tip and the sample using information on deflection. The disadvantage of such mode is possible destruction of the sample surface during the scan.

In Tapping Mode™ the cantilever is externally oscillated close to its fundamental resonance frequency using a piezo actuator. The amplitude of this oscillation is typically around 100 to 200 nm. The oscillation amplitude, phase and resonance frequency are modified by tip-sample interaction forces as tip comes closer to the sample surface; these changes in oscillation with respect to the external reference oscillation provide information about the sample's characteristics. A tapping AFM image is therefore produced by imaging the force of the oscillating contacts of the tip with the sample surface. It is much more gentle compared to the contact mode for imaging a soft substrate such as single polymeric chains, DNA molecules etc.

In the Non-contact mode the tip does not contact the surface of a sample. The cantilever is oscillated above the fundamental resonance frequency with amplitude of some nanometers. When the tip comes closer to the surface, any long range force or van der Waals forces cause shift in the resonance frequency of the cantilever. Therefore the

changes of a vibration frequency reflect changes of tip-sample distance. The feedback system monitors the vibration frequency of the cantilever and keeps it constant. Scanning the tip along the surface gives a topography map.

Several modifications of a standard AFM were made in order to extend its operational capabilities. New techniques such as Magnetic Force Microscopy (MFM) Electrostatic Force Microscopy (EFM) were developed to extend the capability of a standard AFM.

3.1.2 Theoretical background

The Scanning Kelvin Probe Force Microscopy (SKPFM) is a technique related to Electrical Force Measurements. Nonetheless, it operates with a different principle [264,265]. It allows mapping of the Volta potential difference along the surface. This approach is very attractive for corrosion science since it provides the possibility to distinguish zones with different electrochemical nature on the metallic surfaces.

The main aspects of the working principle can be illustrated using an energy diagram of the AFM probe and the metal under study as presented in Figure 3.1.2. The materials of the probe and the metal are characterized by different work functions (W energy required to remove an electron from the material surface to outside in vacuum with no net charge) (Figure 3.1.2a). According to Kelvin theory, when two different metals are in electrical contact, electrons are going from the metal with lower work function (W_m) to the metal (probe) with higher work function (W_p) as shown in Figure 3.1.2b. The electrons flow is finished when the Fermi levels (E_F) of both metals become equal Figure 3.1.2b. The potential difference called Contact potential difference (V_{CPD}) or Volta potential difference (V_{VPD}) builds up between the metal and the probe as a consequence of the net charge transfer (Figure 3.1.2b). If an external voltage (V_{DC}) is applied between the metal and the probe the charge disappears when the applied voltage (V_{DC}) equals to V_{CPD} (Figure 3.1.2c). This fact is successfully used in SKPFM technique.
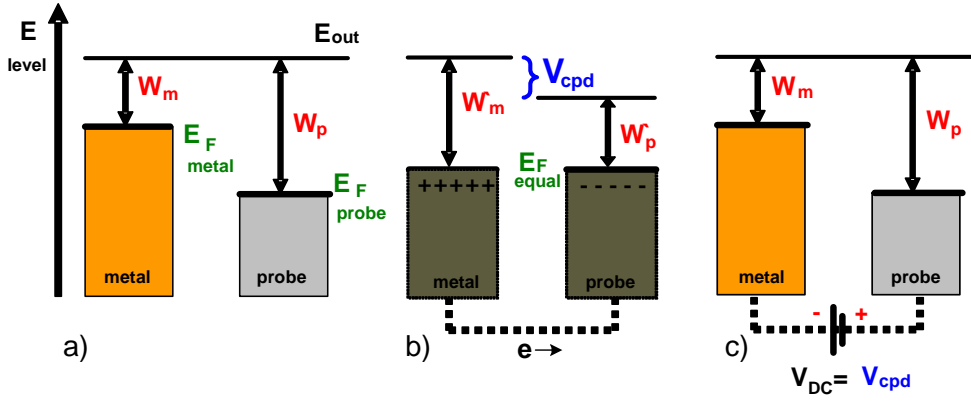
Figure 3.1.2. Energy diagram of metal and material of the AFM probe without electrical contact a); when there is an electrical contact b); when voltage is applied externally c). Adapted from ref. [264].

A schematic diagram of a SKPFM setup is presented in Figure 3.1.3. It includes the same elements as for conventional AFM (Figure 3.1.1) with additional electronic circuits. The main differences of operation mode in the SKPFM are the following. During the SKPFM mode the piezo drive is turned off and $V_{DC} + V_{AC}$ signals are applied to the cantilever, the frequency of V_{AC} signal is the same as the cantilever resonance frequency. As a result of these biasing conditions, an oscillating electrostatic force appears, inducing an oscillation of the cantilever. The general expression of this electrostatic force is the following:

$$F = -\frac{1}{2}\frac{dC}{dz}V^2 \tag{3.1.1}$$

The first harmonic of this force that is used to measure VPD can be described as:

$$F_\omega \sim \frac{dC}{dz}V_{AC}(V_{DC} - V_{VPD})\sin(\omega t) \tag{3.1.2}$$

The lock-in amplifier is used to detect the cantilever oscillation at frequency ω. During the scan V_{DC} is adjusted in such way that the cantilever oscillations become 0 and consequently V_{DC} equals to V_{VPD}. Scanning the sample along the x and y directions the Volta potential difference (VPD) map of the surface is obtained.
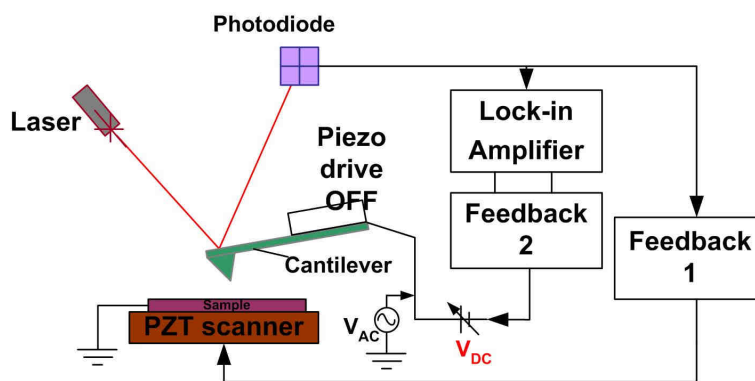
Figure 3.1.3. Schematic diagram of SKPFM microscope

SKPFM is a powerful non-destructive method that can be used to analyze the electrochemical character of the metal surface. Schmutz and Frankel were the first who correlated VPD measured in air with the corrosion potential of the metal in water solution [266]. The graph of VPD vs. OCP is presented in Figure 3.1.4. The results clearly demonstrate that the VPD measured by SKPFM can be linearly correlated to the electrochemical activity of metals. Although there are some limitations of this method, this correlation can be used for analysis of the corrosion susceptibility and localized corrosion behavior of metals and alloys. The main limitations of this method are the sensitivity to the surface oxide films, to the presence of adsorbed layers of water and oxygen molecules and to films of reaction products. These factors can change the measured VPD. Since the surface of a probe can be modified during the measurement the use of a reference sample is required as well.
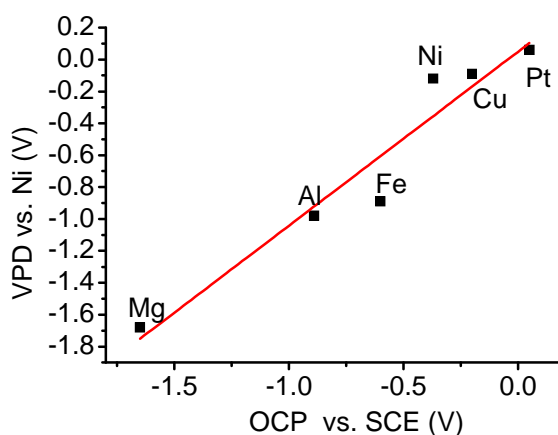
Figure 3.1.4. Plot of VPD measured in air vs. OCP measured in water solution for different pure metals. Graph is adapted from ref. [266].

3.2 DC polarization

DC polarization is a relatively robust method that employs measurement of cathodic or anodic currents with respect to applied overpotential. The obtained current-voltage response is presented as a polarization curve. The analysis of a curve shape can be used qualitatively to see passive regions, diffusion limitations etc. Using this method it is possible to determine the polarization resistance and then calculate the corrosion current that is related to the kinetics of an electrochemical process at a metal interface. Polarization resistance can be determined making a polarization curve on metal with a small perturbation (around +/- 10 mV vs. OCP). Corrosion current can be estimated by extrapolation of linear Tafel region to corrosion potential of metal (with some limitations).

3.2.1 Instrumentation and electrochemical cell

Nowadays a potentiostat is normally used for polarization measurements. It automatically controls the potential applied to the working electrode and permits the measurements of the current flowing. A scheme of an electrochemical setup for polarization measurements is presented in Figure 3.2.1. A three electrode cell arrangement is usually employed for polarization measurements. The cell consists of a counter electrode (CE), working electrode (WE) and reference electrode (RE) Figure 3.2.1. A potentiostat controls the potential applied to the WE and measures the current passing between the WE and CE.

The polarization method can be successively applied to study the corrosion rate of metallic substrates with some limitations such as concentration polarization. However, the application of the polarization method for coated substrates is doubtful. First of all it is not clear what potential is being measured on highly resistive coatings where a significant potential drop can occur due to the Ohmic losses. Furthermore, dc currents resulting from a polarization test may degrade the properties of the coating [267], produce undesired reactions on the substrate (e.g. oxygen reduction), or initiate electro-osmosis. This can result in changes of coating properties and false interpretations of the experimental results. Therefore the link between the polarization resistance and the protective capacity of the coating might not be quantitative. Nevertheless, anodic polarization sometimes is used to evaluate protective efficiency of organic coatings [268]. Though, in some circumstances cathodic polarization measurements might be more helpful for the investigation of the protective coatings with incorporated inhibitors. In summary, polarization method has been quite often used for different substrates. However, the given limitations must be considered when investigating coated metallic substrates.
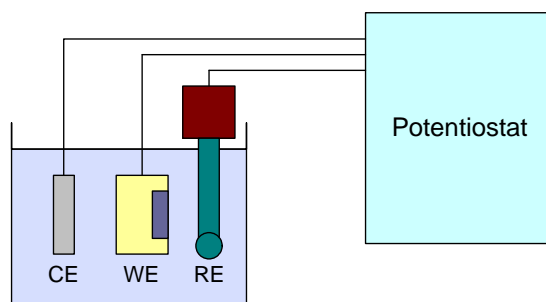
Figure 3.2.1. Schematic setup for potentiostatic polarization measurements.

3.2.2 Theoretical background

The application of DC polarization is directly related to the electrochemical processes that occur at the interfacial region between an electrode and solution. The thermodynamical possibility of an electrode reaction is described by the standard electrode potential. Thermodynamics tells us the possibility that a reaction may or may not occur at given conditions, but it does not give information on how fast the reaction occurs. Kinetics studies the rate of reactions and their mechanisms. In this paragraph a short introduction to the kinetics of corrosion is presented.

Corrosion rate

Corrosion in aqueous environment is related to the electrochemical reactions taking place at an electrode surface. Such reactions involve transfer of electrons. For example a half-cell reaction of metal oxidation can be written in the following way:

$$Met = Met^{n+} + ne^{-} \tag{3.2.1}$$

The rate of electron flow can be a measure of the electrochemical reaction rate. Faraday's law describes the relation between the electron flow and the mass of reactant involved in an electrochemical reaction by the following equation:

$$m = \frac{ItM}{nF}, \tag{3.2.2}$$

where I is the current (A), t - time (s), M - molar mass (g/mole), n - number of electrons involved in reaction, F is Faraday's constant (Coulomb/mole). The corrosion rate r can be expressed as the mass of reacted metal (m) divided by the surface area A (cm^2) and the time t (s). After substituting the mass using equation (2.1.4) we obtain:

$$r = \frac{m}{At} = \frac{iM}{nF} \tag{3.2.3}$$

where i is the current density (A/cm^2). The corrosion rate is proportional to the loss of metal and the current density.

Exchange current density

Considering the reaction of reduction of hydrogen:

$$2H^+ + 2e^- \xrightleftharpoons[r_b]{r_f} H_2 \qquad (3.2.4)$$

At equilibrium the rate of the forward reaction hydrogen reduction (r_f) equals to the rate of the backward reaction hydrogen oxidation (r_b) i.e.:

$$r_f = r_b = \frac{i_0 M}{nF} \qquad (3.2.5)$$

where, i_0 is exchange current density. The exchange current density is affected by the electrode surface and depends on the material and the preparation of the electrode. For instance the exchange current density of reaction 3.2.4 hydrogen reduction and oxidation on mercury electrode is about 10^{-12} A/cm^2 and on platinum is significantly higher 10^{-3} A/cm^2.

Electrochemical polarization

When the potential (E) of an electrode is changed from the equilibrium potential (E_{eq}) the electrode becomes polarized. The difference $E - E_{eq}$ is called overpotential η. If the electrons are supplied to an electrode the polarization is negative and is called cathodic polarization η_c. On the contrary, if electrons are removed from an electrode the polarization is positive and is called anodic polarization η_a. The polarization is related to the occurrence of an electrochemical process at the metal surface. There are two main types of polarization, namely activation polarization and concentration polarization. When the rate of an electrochemical reaction is limited by an electron transfer it is said that the reaction is under activation control. This suggests the presence of activation barriers i.e. energy that is required to overcome in order to achieve the intermediate activated state before the reaction occurs. When the rate of an electrochemical reaction is very high the concentration of a reagent becomes limited by diffusion and we have concentration polarization.

Activation polarization

Let's consider reaction 3.2.4 of hydrogen reduction/oxidation. The energy profile of this reaction is presented in Figure 3.2.2. The activation energy of forward and backward reactions are respectively ΔG_f^* and ΔG_b^*. At equilibrium the difference between the activation energy of forward and backward reactions is related with the standard potential (E_{eq}) via:

$$\Delta G_f^* - \Delta G_b^* = -nFE_{eq} \tag{3.2.6}$$

The relationship between the rate of forward (r_f) or backward reaction (r_b) and temperature obeys the Arrhenius equation:

$$r_f = K_f \exp\left[-\frac{\Delta G_f^*}{RT}\right] \tag{3.2.7}$$

$$r_b = K_b \exp\left[-\frac{\Delta G_b^*}{RT}\right] \tag{3.2.8}$$

where K_f and K_b are reaction rate constants for the forward and backward reaction respectively, R is the molar gas constant and T - the temperature. At equilibrium conditions the rates of both reactions are equal and according to equation (3.2.5):

$$i_0 = K\grave{}_f \exp\left[-\frac{\Delta G_f^*}{RT}\right] = K\grave{}_b \exp\left[-\frac{\Delta G_b^*}{RT}\right] \tag{3.2.9}$$

The last equation shows that exchange current density depends on the activation energy.
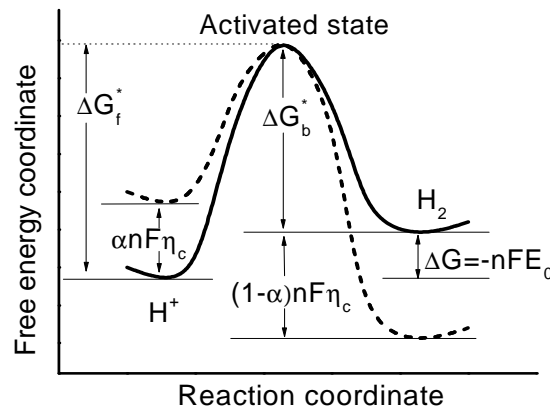
Figure 3.2.2. Energy profile of half cell reaction; solid line presents equilibrium state and dashed line presents polarized state. Graph is adapted from ref. [26].

Polarization of an electrode shifts the energy profiles. For cathodic polarization the activation energy of forward reaction of hydrogen reduction is decreased by $\alpha nF\eta_c$ and activation energy of backward reaction is increased by $(1-\alpha)nF\eta_c$ as shown on energy profile that describes the polarized state (dashed line) (Figure 3.2.2). Factor α shows the

fraction of polarization η_c taken by forward reaction. By analogy with equation (3.2.9) the cathodic current density of forward reaction is:

$$i_c = K`_f \exp\left[-\frac{\Delta G_f^* - \alpha nF\eta_c}{RT}\right] \qquad (3.2.10)$$

and the anodic current density of the backward reaction is:

$$i_a = K`_b \exp\left[-\frac{\Delta G_b^* + (1-\alpha)nF\eta_c}{RT}\right] \qquad (3.2.11)$$

The net current that flows becomes:

$$i = i_c - i_a = i_0 \exp\left[\frac{\alpha nF\eta_c}{RT}\right] - i_0 \exp\left[\frac{-(1-\alpha)nF\eta_c}{RT}\right] \qquad (3.2.12)$$

This equation represents the Butler-Volmer equation and shows the dependence of the rate of the electrochemical process on the applied cathodic electrical potential. At high polarization the rate of backward reaction (oxidation) is very low and the right term of equation 3.2.12 can be neglected, thus:

$$i_c = i_0 \exp\left[\frac{\alpha nF\eta_c}{RT}\right]$$

or

$$\eta_c = \frac{2.3RT}{\alpha nF} \log\left(\frac{i_c}{i_0}\right) \qquad (3.2.13)$$

and

$$\beta_c = \frac{2.3RT}{\alpha nF} \qquad (3.2.14)$$

Equation 3.2.13 is called the Tafel equation and β_c is called Tafel constant. The same discussion can be applied to anodic polarization:

$$\eta_a = \frac{2.3RT}{(1-\alpha)nF} \log\left(\frac{i_a}{i_0}\right) \qquad (3.2.15)$$

$$\beta_a = \frac{2.3RT}{(1-\alpha)nF} \qquad (3.2.16)$$

where β_a is the Tafel constant for the anodic reaction.

The plot of potential E or overpotential η versus $\log i$ gives straight lines with slope equal to the Tafel constants when the electrochemical reaction is under activation control,

which can be seen in Figure 3.2.3. The intersection of the two straight lines gives the equilibrium potential E_{eq} and the exchange current density i_0.
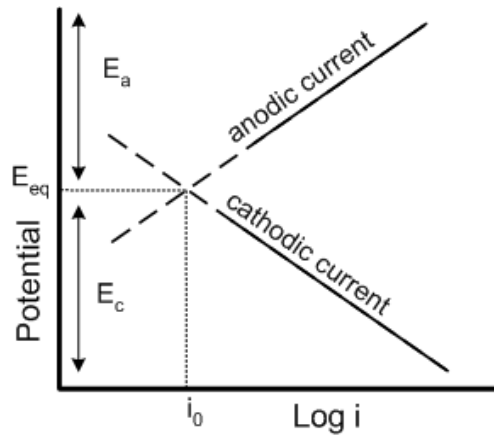
Figure 3.2.3. Potential vs. log i showing linear Tafel behaviour (straight lines).

Concentration polarization

If the rate of an electrochemical reaction is high the concentration of electroactive species at the electrode surface decreases. Figure 3.2.4a shows the decrease of a concentration of electroactive species at the electrode surface due to high rate of the electrochemical process. The distance (d) is a thickness of a solution layer with gradient of concentration, C_{bulk} and $C_{electrode}$ are the concentrations of electroactive species in the bulk solution and at the electrode surface respectively. Eventually, when there is no more reagent at the electrode surface, the flowing current becomes limited by the transport of the reagent to the electrode surface. The value of maximal current when $C_{electrode}$ will be 0 or (much less than the C_{bulk}) is called limiting current i_L Figure (3.2.4b). The limiting current can be found using the following equation:

$$i_L = \frac{DnFC_{bulk}}{d} \tag{3.2.17}$$

where n is the number of electrons in the electrochemical process, F is Faraday constant, D is the diffusion coefficient of the electroactive species. At limiting current density the electrode process occurs at the maximum rate as can be seen in Figure 3.2.4b. Since the concentration of electroactive species at the electrode is decreasing, thus according to Nernst equation the half cell electrode potential will be changed thus more polarization is needed in order to maintain the current flow. This excess polarization is called concentration polarization (η_{conc}):

$$\eta_{conc} = \frac{2.3RT}{\alpha nF} \log\left(1 - \frac{i}{i_L}\right) \tag{3.2.18}$$

When the corrosion current i_0 is much lower than the limiting current density then the overpotential near the E_{eq} is due to the activation of charge transfer. Figure 3.2.5 shows the combined activation polarization and concentration polarization. Near the E_{eq} the electrochemical process is under activation control and η_{act} is dominating. However, when the current density approaches i_L, concentration polarization takes over from activation polarization process and the current density becomes limited by the diffusion (Figure 3.2.5). The equation that combines both activation and concentration polarization is the following:

$$\eta = \frac{2.3RT}{\alpha nF}\log\left(\frac{i_c}{i_0}\right) + \frac{2.3RT}{\alpha nF}\log\left(1 - \frac{i_c}{i_L}\right) \qquad (3.2.19)$$

This equation can be used for calculation of kinetic parameters when normal Tafel plots are complicated by mass transfer processes.
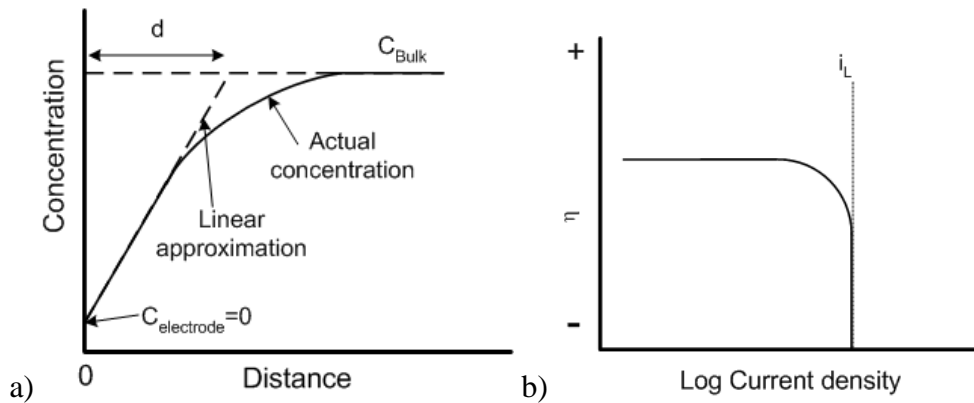
Figure 3.2.4. Concentration profile of electroactive species near the electrode surface a); overpotential (η) vs. current density at mass transfer conditions b) Adapted from ref. [26].
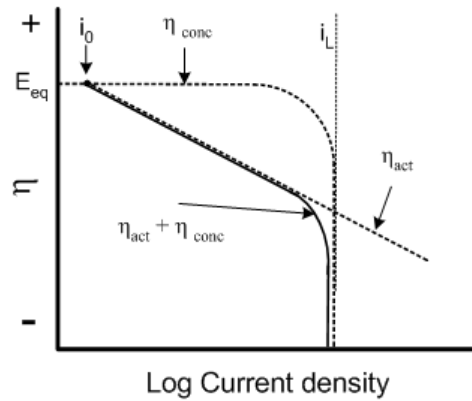
Figure 3.2.5. Overpotential η vs. log*i* showing activation polarization (η_{act}), concentration polarization (η_{conc}) and combined polarization ($\eta_{act}+\eta_{conc}$). Adapted from ref. [26].

Mixed potential theory

When a couple of half cell reactions occur on the metal surface the total rate of oxidation must be equal to the total rate of reduction according to the charge conservation principle. Consequently the sum of anodic currents equals to the sum of cathodic currents. Let's consider two half cell reactions occurring on zinc in acid solution, namely, hydrogen reduction and zinc oxidation (Figure 3.2.6).
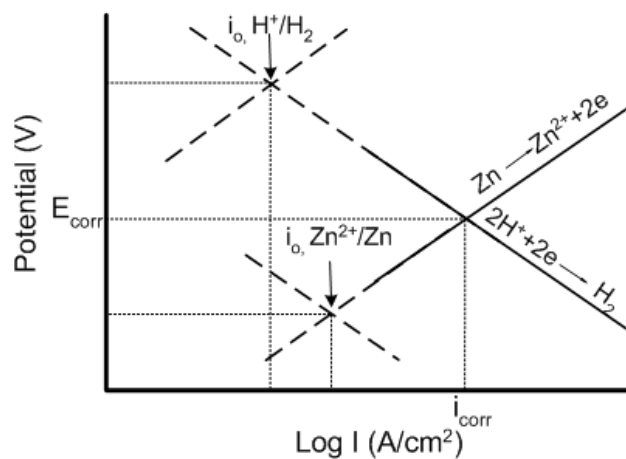
Figure 3.2.6. E vs. log I plot showing two half cell reactions on zinc surface. Adapted from ref. [26].

Each half cell reaction has its exchange current and equilibrium potential. As the half cells are in contact, since they occur on the same surface, the equilibrium potentials of

the half cell reactions change until they become equal to E_{corr}. At this potential the anodic current equals the cathodic current ($I_a=I_c$) and if the areas where both reactions take place are the same:

$$i_a = i_c = i_{corr}$$

where i_{corr} is called corrosion current and is proportional to corrosion rate of metal.

3.3 Electrochemical Impedance Spectroscopy

EIS or AC impedance spectroscopy is a valuable method for analysis of many electrochemical systems. This technique can be applied in many areas of materials characterization including semiconductors, batteries, electrodeposition, corrosion and characterization of organic coatings. Unlike DC-polarization the EIS is a non destructive technique that normally uses only a small potential perturbation near the corrosion potential of the analyzed electrochemical system thus eliminating polarization effect. The impedance method can resolve numerous parameters of the electrochemical processes at a metal interface and electrical properties of oxide films and coatings by modeling the interface through the combination of electrical circuits. This provides means for determination of the kinetics of the reactions occurring at an interface and properties of coatings and passive layers.

The concept of electrical impedance was first introduced by Oliver Heaviside in the 1880s and further developed in terms of vector diagrams and complex representation by A. E. Kennelly and especially C. P. Steinmetz [269]. A recall of papers dealing with the mathematical procedures for impedance treatment was presented in ref. [270]. In the 20th it is worth to mention works of Grahame [271], Randles [272], Erschler [273] and Epelboin. [274] Applications of EIS for investigation of corrosion protection by organic coatings have been reported by Potente and Braches [275], Scantlebury *et al.* [276], Beaunier *et al.* [277], Mansfeld *et al.* [278]. Abundance of information on application of EIS in many fields ranging from metal or semiconductor electrode-electrolyte interface, electrode/layer/electrolyte system, porous electrodes, solid electrolytes exists in many books and chapters [269,279-282].

3.3.1 Instrumentation

Traditionally impedance measurements were performed using AC-bridge and oscilloscope. With the appearance of frequency response analyzers (FRA) it became possible to perform impedance measurements easier. FRA is used to generate the excitation signal and analyze the response. Small amplitude sine wave signal is applied to the electrochemical cell and the response is measured at the same time. Usually the measurements are done in the range of frequencies from highest to lowest values in order to get information from different processes occurring in the system. A FRA correlates the response of the system in terms of current to an applied voltage and determines the impedance. Comparison with other systems and positive and negative characteristics of FRA can be found in ref. [283].

The FRA system normally includes a waveform generator to produce the sine waves and a potentiostat to control the potential (Figure 3.3.1). It must control both the DC potential as well as the AC excitation voltage. The instrumentation must also contain an

analyzer that accurately measures the AC components of both the voltage and the current and the phase relation between them. These data are used to calculate the impedance of the system. Because of the complexity to optimize and coordinate these AC measurements, a computer is generally used to run the experiment and to display the results in real time.
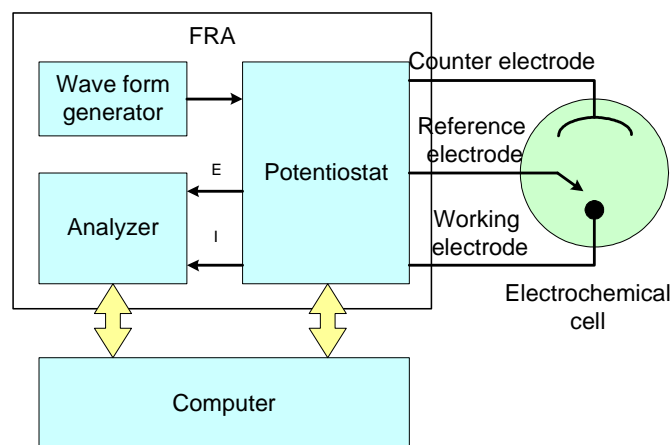
Figure 3.3.1. A block diagram of the instrumentation used for EIS. Adapted from ref. [284].

3.3.2 Theoretical background

For a linear response system a small applied AC voltage as a function of time is expressed as:

$$V(\omega) = V_o \sin(\omega t) \tag{3.3.1}$$

where V_0 is the voltage amplitude, ω is the angular frequency ($\omega=2\pi f$, f – frequency in Hz) and t is the time. The response to the voltage perturbation is an AC current that has the same frequency but different amplitude I_0 and an additional phase shift φ (deg):

$$I(\omega) = I_o \sin(\omega t + \varphi) \tag{3.3.2}$$

Schematically the wave forms of the two signals are presented in Figure 3.3.2.

An expression analogous to the Ohm's law can be written based on the voltage and current functions:

$$Z(\omega) = \frac{V_o \sin(\omega t)}{I_o \sin(\omega t + \varphi)} = Z_o \frac{\sin(\omega t)}{\sin(\omega t + \varphi)} \tag{3.3.3}$$

The Z(ω) function is defined as the impedance of the system. When plotting the applied sinusoidal voltage signal against the measured current signal on the x, y graph a

Lissajous Figure is obtained (Figure 3.3.3). From this plot it is possible to calculate the impedance |Z| graphically [282].
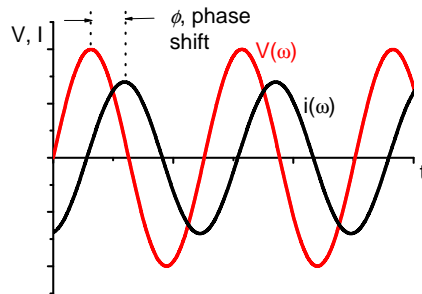
Figure 3.3.2. Sinusoidal signals of the applied voltage and current response with phase shift.
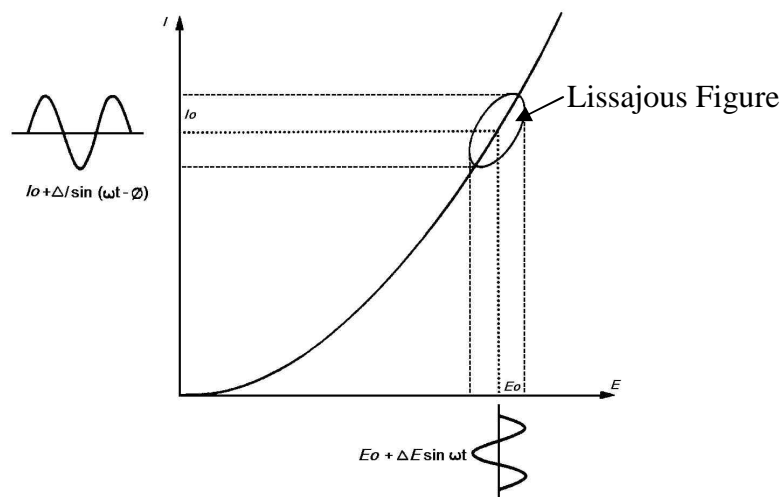
Figure 3.3.3. Lissajous Figure (an oval) formed by applied voltage signal on the X axis and current response signal on the Y axis. Adapted from [282].

Using the Euler relation:

$$e^{j\omega t} = \cos \omega t + j \sin \omega t \qquad (3.3.4)$$

where j=√-1, equation 3.3.3 can be rewritten as:

$$Z(\omega) = |Z| e^{j\varphi} = |Z| \cos \varphi + j |Z| \sin \varphi \qquad (3.3.5)$$

In such a way the impedance is presented as a complex number with real and imaginary parts:

$$Z(\omega) = Z'_{(real)}(\omega) + jZ''_{(imaginary)}(\omega) \tag{3.3.6}$$

The introduction of complex numbers allows presenting the impedance in an Argand diagram or Complex plane plot in both Cartesian and polar coordinates (Figure 3.3.4a). Impedance spectra can be also presented in the Complex plane plots when plotting its real part on the X axis and its imaginary part on the Y axis (Figure 3.3.4b). In the Complex plane plots the low frequency data are presented on the right part of the diagram and the high frequency data are presented on the left part. The modulus of impedance |Z| is shown as a vector and corresponds to a single frequency at each point:

$$|Z| = \sqrt{Z'(\omega)^2 + Z''(\omega)^2} \tag{3.3.7}$$

The phase angle φ can be given as:

$$\varphi = \arctan \frac{Z''(\omega)}{Z'(\omega)} \tag{3.3.8}$$

Another way of impedance representation is a Bode plot where the *log* modulus of impedance and the phase angle are plotted as a function of *log* frequency (Figure 3.3.5). The use of Bode representation has many advantages compared to Complex plane plots particularly if impedance is measured over a wide range of frequency or need to be presented in the same graph. The first one is the homogeneous distribution of the points of the graph unlike for Complex plane plots where the majority of the points are presented on the left or right side of the Figure 3.3.4b. The frequency information is available on the graph. The phase angle showed in Bode plot is a sensitive indicator of small changes in the spectra [285].
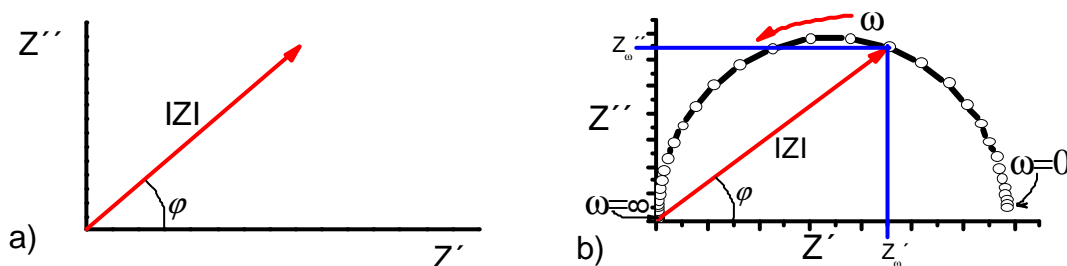
Figure 3.3.4. Argand diagram showing impedance vectors a), Complex plane plots representation of real and imaginary parts of impedance spectra at different frequencies on real axis (Z`) and imaginary axis (Z``) b).
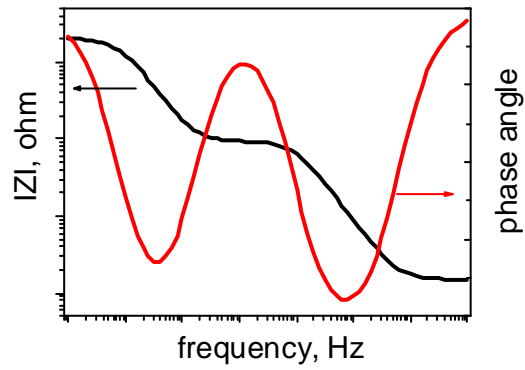
Figure 3.3.5. Bode plots representation of modulus of impedance and phase angle vs. frequency.

The interpretation of impedance data usually is associated with the use of equivalent circuits that are used as analogy to the physico-chemical processes occurring in the electrochemical system. Such circuits can be modeled by elements used in passive electrical circuits such as resistor, capacitor and inductor presented in Table 3.3.1. For a resistor the impedance does not depend on frequency and does not have an imaginary part. The current passing through the resistor is proportional to the applied voltage and is in phase with it. For a capacitor the impedance has only imaginary component that decreases when increasing the frequency. The phase shift between current and voltage is -90° for an ideal capacitor. In contrast to capacitance the impedance of inductor element increases with frequency and the phase angle shift between current and voltage is 90°. Figures 3.3.6, 3.3.7 and 3.3.8 present the Complex plane and Bode plots corresponded to frequency dependent impedance of resistor, capacitor and inductor elements.
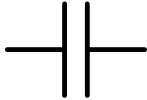
More complex equivalent circuits contain two or more elements which are combined either in series or in parallel. The impedance of the circuits follows Kirchhoff's laws. The total impedance Z of combination of elements with impedance Z_1 and Z_2 is expressed as:

$$Z = Z_1 + Z_2 \quad \text{For series circuit} \tag{3.3.9}$$

$$\frac{1}{Z} = \frac{1}{Z_2} + \frac{1}{Z_2} \quad \text{For parallel circuit} \tag{3.3.10}$$

Examples of the Complex plane and Bode plots for RC elements connected in series or in parallel are presented in Figures 3.3.9 and 3.1.10. Figure 3.3.11 presents the impedance of circuit R1(R2C) that has an additional resistance (R1) combined in series with R2C parallel element.

Table 3.3.1. Common electrical elements used in circuits

Element	symbol	Impedance expression
Resistor (R)	—\/\/\/—	R
Capacitor (C)	—||—	$\dfrac{1}{j\omega C}$
Inductor (L)	—mmm—	$j\omega L$

Many electrochemical processes can not be modeled employing only the simple electrical elements discussed above. In various electrochemical systems an additional element called Warburg impedance (W) which is related to a mass transfer processes may be needed. The equation for Warburg impedance is the following [269]:

$$Z_w = \sigma\omega^{-1/2} + j\sigma\omega^{-1/2} \tag{3.3.11}$$

The coefficient σ is:

$$\sigma = \frac{RT}{n^2 F^2 A \sqrt{2}} \left[\frac{1}{C_{ox} D_{ox}^{1/2}} + \frac{1}{C_{red} D_{red}^{1/2}} \right] \tag{3.3.12}$$

where C_{ox}, C_{red} and D_{ox}, D_{red} are the concentrations and diffusion coefficients of the oxidative and reductive species, n is the number of electrons involved in electrochemical reaction, A surface area of an electrode, F - Faraday constant, R - universal gas constant and T - temperature. Warburg impedance appears normally at low frequencies as a straight line with the slope of 45º on Complex plane plots. This form of impedance is valid when the diffusion layer thickness is infinite. However in corrosion related systems the diffusion layer has a finite thickness which results in another equation applied for bounded conditions:

$$Z_o = \sigma\omega^{-1/2}(1-j)\tanh\left(\delta\left(\frac{j\omega}{D}\right)^{-1/2} \right) \tag{3.3.12}$$

where δ is the diffusion layer thickness and D is some average diffusion coefficient of the species involved in the process.
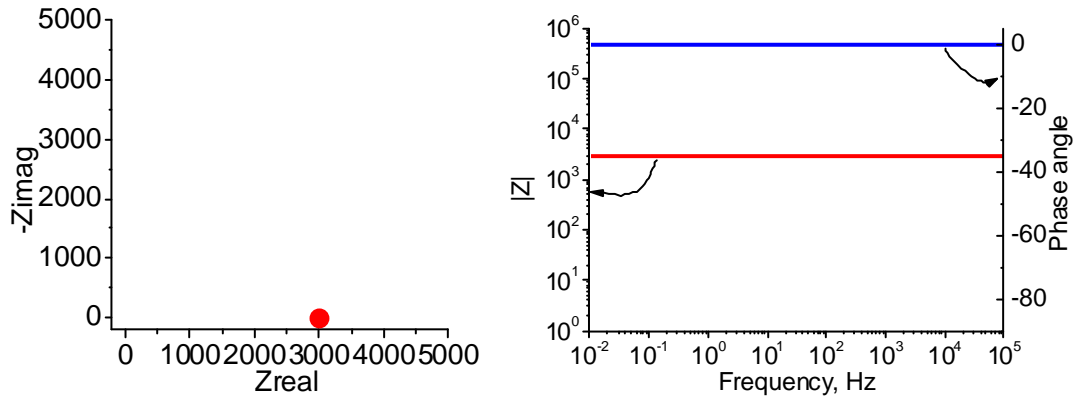
Figure 3.3.6. Complex plane and Bode plots representing the impedance of 3000 Ohm resistor.
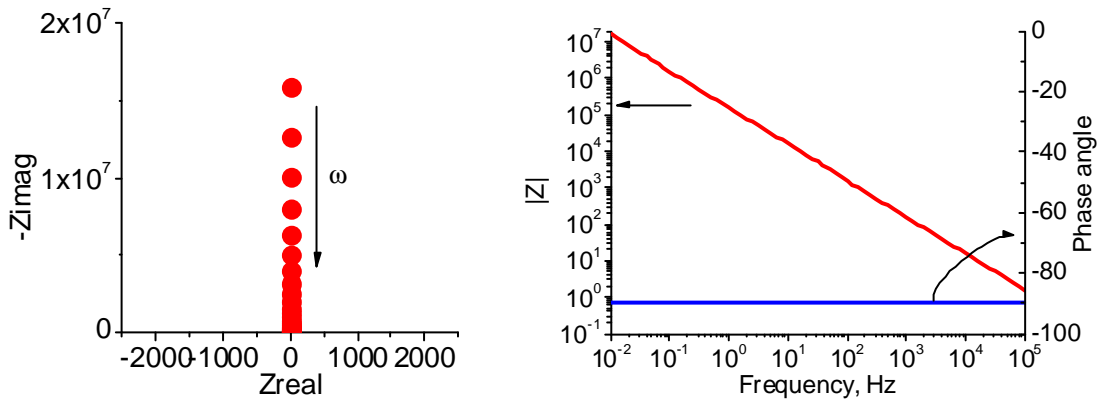
Figure 3.3.7. Complex plane and Bode plots representing the impedance of $1*10^{-6}$ F capacitor.
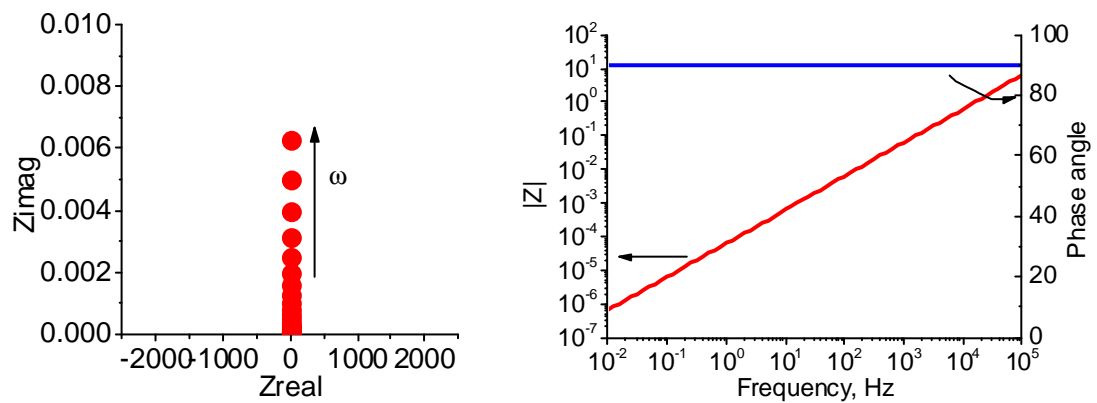
Figure 3.3.8. Complex plane and Bode plots representing the impedance of $1*10^{-5}$H inductor.

$$Z = R - \frac{j}{\omega C}$$ Impedance of RC circuit in series (3.3.14)
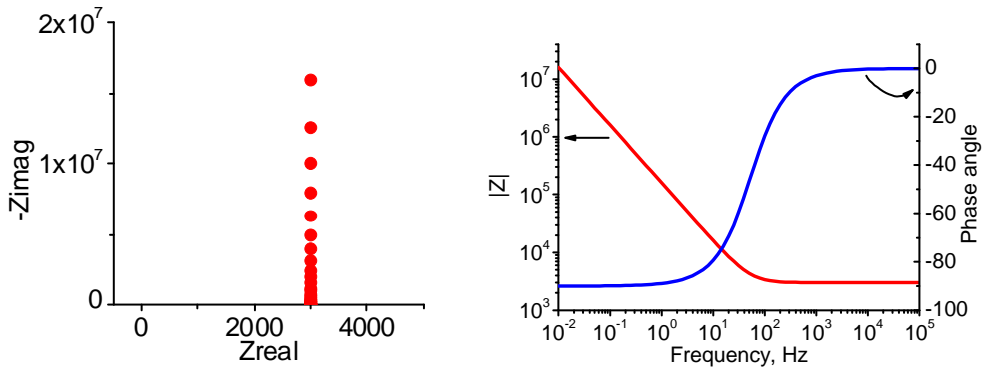
Figure 3.3.9. Complex plane and Bode plots representing the impedance of R-C element combined in series. R=3000 Ohm, C=1*10^{-6} F.

$$Z = \frac{1}{1 + j\omega RC}$$ Impedance of RC circuit in parallel (3.3.15)
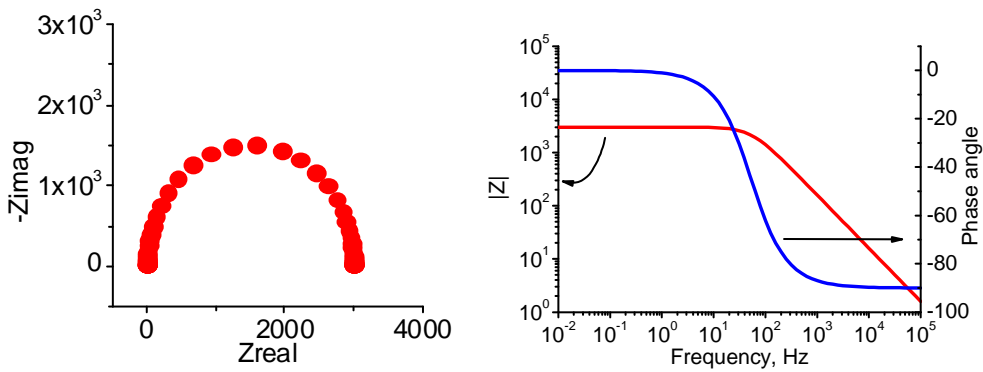
Figure 3.3.10. Complex plane and Bode plots representing the impedance of R-C element combined in parallel. R=3000 Ohm, C = 1*10^{-6} F.

$$Z = R_1 + \frac{R_2}{1 + j\omega R_2 C} \qquad \text{Impedance of R1(R2C) (Randles) circuit} \qquad (3.3.16)$$
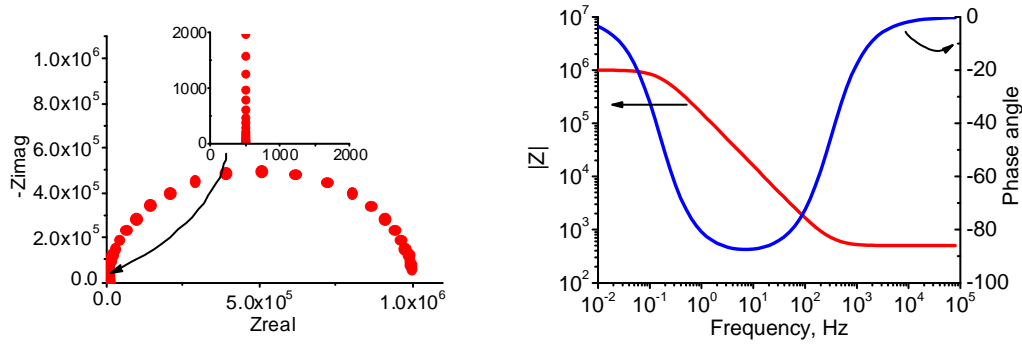
Figure 3.3.11. Complex plane and Bode plots representing the impedance of R1R2C circuit. R1 = 500 Ohm, R2 = $1*10^6$ Ohm, C=$1*10^{-6}$ F.

In the equivalent circuit models presented above a capacitor element was used. However, in real electrochemical systems different anomalies are present and the impedance spectra do not follow a true capacitive behavior. The deviation of the capacitative behavior from ideal can be originated from inhomogeneities of the electrode–material system and it can be described in terms of a nonnormalizable distribution of relaxation times [286]. The deviation can also originate from non uniform diffusion whose electrical analog is an inhomogeneously distributed RC transmission line [287]. For instance in the Complex plane plots a semicircle associated with a RC circuit in parallel is often depressed. The phase angle of such system does not present pure capacitative behavior and deviates from -90°. Various mathematical approaches have been used to model such deviation and one of them is to present a capacitor as the so called constant phase element (CPE). The expression for impedance of such element is the following:

$$Z_{CPE} = \frac{1}{Y_0 (j\omega)^n} \qquad (3.3.17)$$

where Y_0 is admittance independent on frequency and the exponent n is usually $0 \leq n \leq 1$. Given that the CPE is a general element it can describe different elements: resistor (n = 0), Warburg (n = 0.5) or capacitor (n = 1).

CPE is often used for studying the corrosion systems in order to describe their non ideal behavior. The parameter Y_0 which is obtained after the fitting procedure has dimensions s^n/Ω that is different from that of a capacitance (s/Ω or F) [307]. Thus, there is a difference between the Y_0 and a capacitance and the use of Y_0 for calculations of a thickness or a dielectric constant can result in errors. Therefore in this work the

capacitance was calculated from the fitting parameters using the relation presented by Hsu and Mansfeld [307]:

$$C_{real} = Q(\omega_{max})^{n-1} \tag{3.3.18}$$

where ω_{max} is the angular frequency at which the imaginary impedance reaches a maximum for the respective time constant, Q ($S*s^n/cm^2$) and n are the fitting parameters of the CPE element.

A parameter known as time constant (τ) is used to describe a relaxation process that occurs when a perturbation is applied to a steady state system:

$$\tau = RC \tag{3.3.19}$$

where R and C are the resistance and capacitance. It can be described as a relaxation time of the process i.e. characteristic time response to the applied perturbation. Each time constant has its characteristic frequency f that can be ascertained by:

$$f = \frac{1}{2\pi\tau} \tag{3.3.20}$$

The equation shows that fast processes occur at high frequency and slow processes occur at low frequency.

3.3.3 Validation of impedance data

The impedance spectroscopy method is based on certain assumptions that must be fulfilled in order to get valid data. These assumptions are [283]:

- Causality. The response of the system is only due to the perturbation applied and does not contain significant components from spurious sources.

- Linearity. The perturbation/response of the system is described by a set of differential laws. This condition requires that the impedance is independent on the magnitude of the perturbation. However, in practice this is hardly achieved since the current exponentially depends on the applied potential. Nevertheless, when the applied perturbation is small enough typically around 1-10 mV a system is pseudo linear.

- Stability. The system must be stable in the sense that it returns to its original state after the perturbation is removed. This requirement is hardly obtainable for corroding systems because by the end of the measurement the system might be changed to another state. Therefore it is suggested to perform the measurement as fast as possible before the change of the system.

- Finity. The transfer function must be finite valued at $\omega \rightarrow 0$ and $\omega \rightarrow \infty$ and must be continuous and finite-valued function at all intermediate frequencies.

84

Under the above mentioned assumptions a set of transforms between the real an imaginary parts were shown to hold by Kramers and Kronig. In order to validate an impedance data Macdonald *et al.* suggested the use of Kramers-Kronig (KK) transforms [288,289]. These transforms are mathematical relations which convert the real component into the imaginary component and vice versa. When the experimentally observed real component is transformed by K-K transforms, it should yield the experimentally observed imaginary component. If it is not the case, then the obtained experimental results are not valid and can not be interpreted as impedance. However, the applicability of KK transforms sometimes is questioned because the conditions of finity can not be satisfied in many experimental cases [290,291]. In real systems it is not possible to go until very low frequencies in order to meet the requirements needed for KK transforms to agree with experimental data.

3.3.4 Interpretation and application of impedance data

For analysis of impedance data the main problem is to choose the model that is applicable for a particular case. If the spectrum presents one time constant element only the equivalent circuit is simple. However, for more complicated impedance spectra a combination of electrical elements can be used either in series or in parallel. It should be noted that an equivalent circuit consisting of more than 3 elements can be rearranged in different ways yet giving the same impedance at all frequencies. Therefore the physical meaning of impedance spectra is essential for creating an appropriate equivalent circuit model for the electrochemical system.

The electrical equivalent circuit of a simplified electrochemical interface also known as Randles circuit (without Warburg impedance) is described in Figure 3.3.11. This circuit is completed by the addition of the R1 resistance, in series with parallel capacitance C and R2 resistance elements. The determination of the components of this circuit [272] provides important information about the reactions and structure of the metal/solution interface. In a typical case R1 is the solution resistance, R2 is the polarization resistance (R_{polar}) and C is the double layer capacitance (C_{dl}). In addition to its usefulness the Randles model usually is a starting point for more complex models. In certain circumstances Warburg impedance is introduced in series with polarization resistance to characterize mass transfer limitations [271]. When organic coatings or oxide layers are present on the metal surface additional elements have to be introduced in the equivalent circuit model.

A number of reviews have been published describing the experimental methods, conditions, models, approaches for evaluation of the impedance data and applicability of EIS for studying corrosion protection of coated metallic substrates [292-296]. Typical behavior of a coated metal system in electrolyte solution during different stages of corrosion is presented in Figure 3.3.12. Initially the intact coating can be characterized by the equivalent circuit presented in Figure 3.3.12a. Uncompensated solution resistance (R_{sol})

is in series with the capacitative response (C_{coat}) of the coating. In the plot $\log|Z|$ vs. $\log f$ a straight line appears due to pure capacitative behavior of the coating and in the plot φ vs. $\log f$ the phase angle becomes -90º. However at high frequency a resistive plateau related to the solution resistance is visible (Figure 3.3.12 plot a). When electrolyte solution penetrates the coating through the defects or pores it forms conductive pathways down to the metal substrate. Another component (R_{coat}) appears in the equivalent circuit that describes the resistance of the coating. A resistive response can be seen on impedance spectra at low frequencies (Figure 3.3.12 plot b). When the aggressive species achieve the metal substrate a corrosion process starts and two additional elements namely polarization resistance and double layer capacitance should be added to the equivalent circuit (Figure 3.3.12c). Short explanations concerning the principals and properties of each element are given below.
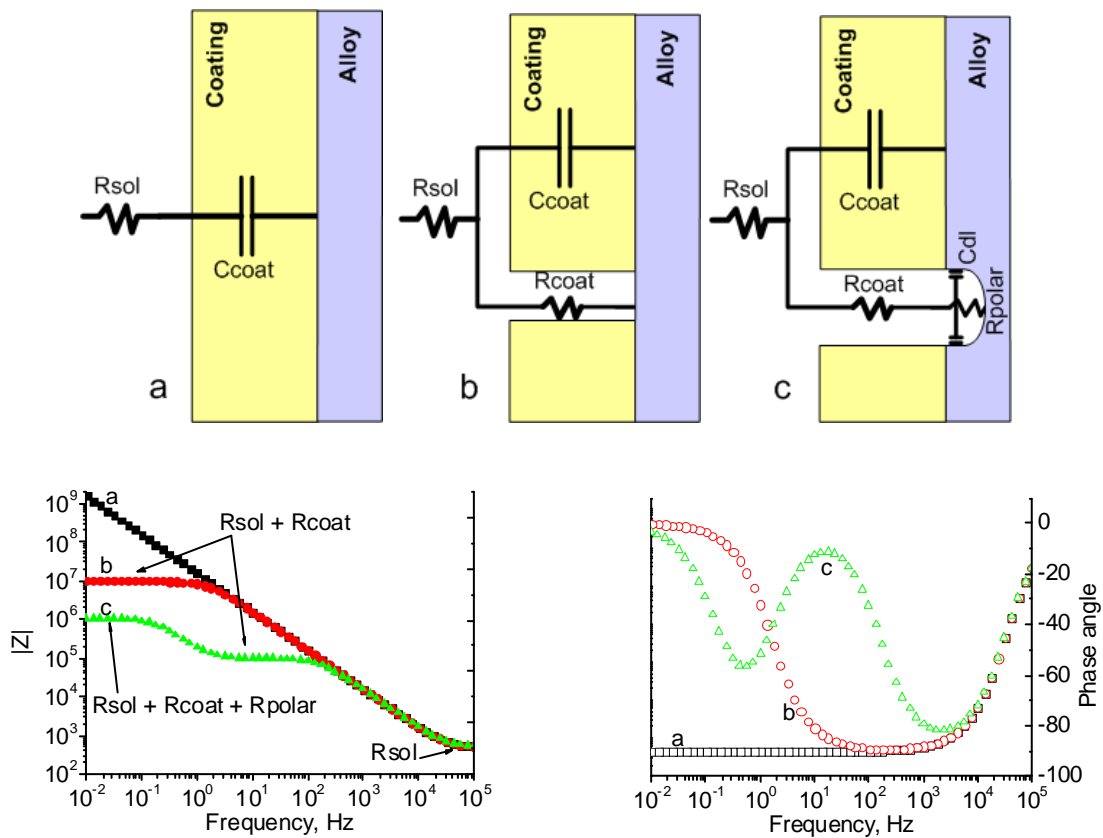
Figure 3.3.12. Equivalent circuits and corresponding Bode plots representing different stages of metal-coating degradation; a) the intact coating, b) the porous coating, c) the porous coating and the started corrosion activity.

Solution resistance

Solution resistance R_{sol} arises between the reference and the working electrodes and often is considered in the equivalent circuit models. Solution resistance depends on the distance between the electrodes and on the conductivity of the electrolyte used during the spectra acquisition. It can be a significant factor for electrochemical measurements. When R_{sol} is higher than the resistance of other elements in the electrochemical circuit the response of such elements in impedance spectra can be barely distinguishable. For instance the impedance spectra taken in concrete may be influenced by R_{sol} because of high impedance between the reference and the working electrodes. When making impedance measurements on the metal substrates with thin coatings or inhibitive layers, R_{sol} must be low enough to be able to distinguish a low resistance response from the coatings or layers.

Coating capacitance

When the metal is separated from the electrolyte by a dielectric coating a capacitor can be considered to be formed with the conductive plates being at the metal, coating and coating-solution interfaces. The capacitance of the coating C_{coat} can be expressed as:

$$C_{coat} = \frac{\varepsilon \varepsilon_0 A}{d} \qquad (3.3.21)$$

where ε is the relative dielectric permittivity of the coating, ε_0 is the permittivity of vacuum (F/cm), A – surface area (cm^2) and d – coating thickness (cm). Changes of the coating capacitance normally can be associated with changes of the dielectric permittivity due to water uptake. Since the relative dielectric constant of organic coatings is small, typically around 3-4, unlike of water that is around 80 at 25ºC, the ingress of water in the coating significantly increases the capacitance. The coating capacitance can also be influenced by the increase of the coating thickness caused by the swelling processes.

The empirical relationship derived by Brasher-Kingsbury [297] is the most used for calculation of the amount of water absorbed by the coating:

$$W\% = 100 * \frac{Lg\left(\frac{C_0}{C_t}\right)}{Lg\left(\varepsilon_w\right)} \qquad (3.3.22)$$

where, W% is the volume percentage of the absorbed water by the coating, C_0 (F/cm^2) is the capacitance of the coating at the beginning of exposure; C_t (F/cm^2) is the capacitance of the coating at the time t of exposure, ε_w – is the dielectric constant of water equal to 80. However, Brasher and Kingsbury observed that the calculated values of water uptake are often higher than the values measured using gravimetry. More recently, Bellucci and Nicodemo [298] developed two models, the discrete model (DM) and the continuous model (CM), for the determination of the ratio W/Ws between the adsorbed water (W) and adsorbed water at saturation (Ws). In the DM, the film is considered homogeneous and

described by a simple RC circuit. The CM model considers the film as a set of individual layers of thickness δd, each of them being homogeneous and described by a RC circuit. Apart from these models there are also other works that describe the theory of permittivity of heterogeneous materials presented by Rayleigh, Boettcher, and others [299]. More recently another model for estimation of water uptake in polymeric coatings was presented by Castela *et al.* [300,301]. The model considers that the film consists of three phases such as water, air and solid (coating). The electrical properties of this system can be described by series of RC elements through the film thickness. A new model to estimate water uptake inside non-conductive films was established taking into consideration the film tortuosity [302]. Although there are numerous different approaches for the water permeation calculation, in the present work a simplified equation derived by Brasher-Kingsbury was used.

Coating resistance

Coatings provide a barrier against corrosive species. However, no ideal coatings can be made and there are always defects and nano-/micro-pores in the coating which favor electrolyte penetration. The electrolyte in the defects and pores forms conductive pathways down to the metallic substrate. Thus the magnitude of R_{coat}, at a given time is an indication of the barrier properties and of the state of degradation of the coating caused by solution ingress via pathways through the film. In general R_{coat} is electrolyte sensitive and decreases when the concentration of the electrolyte increases [303].

Double layer capacitance

When a metal is immersed in an electrolyte a potential drop arises across the interface metal/electrolyte. The appearance of such potential drop is associated with the formation of charged layers at the interface. A charge separation arises between the charges in the metal and ions in the solution. This separation is often very small in the order of angstroms. As well known charge separation across the interface forms a capacitor that is called electrochemical double layer (C_{dl}). In corrosion studies C_{dl} is correlated with the corrosion process and also can be related to the degree of delamination of coatings [304,305].

The value of the double layer capacitance depends on different factors like electrode potential, temperature, ionic concentration, ions type, electrode roughness, specific adsorption, presence of oxide films etc. The typical values can be in the range of 10-50 $\mu F/cm^2$.

Polarization resistance

The polarization resistance (R_{polar}) is related to the kinetics of the electrochemical reaction (corrosion current density) via Stern-Geary equation [306]. Therefore the polarization resistance can be the measure of the corrosion rate of the metallic substrate.

3.3.5 Equivalent circuits used for fitting of impedance spectra

Quantitative analysis of impedance data was based on physical modeling of the processes occurring at the interfaces. The equivalent circuit models presented in Figure 3.3.13 were used for fitting of impedance spectra of bare alloy samples immersed in a corrosive electrolyte. The immersion of a bare metal in a corrosive electrolyte results in appearance of a charged layer and occurrence of electrochemical processes on the metal. EIS makes possible to detect the charged layer that corresponds to double layer capacitance (C_{dl}) and electrochemical processes that are related to polarization resistance (R_{polar}). The equivalent circuit model presented in Figure 3.3.13a was used to fit impedance spectra of the corroding metal at initial immersion time. At longer immersion a diffusion of electroactive species to the metal surface can be significant due to the formation of a corrosion products film that impedes the transport of electroactive species. The diffusion limitations results in appearance of a new element, namely Warburg impedance. Equivalent circuit presented in Figure 3.3.13b corresponds to the case when diffusion element is introduced into the model.

When the metal has a dense oxide film covering its surface the impedance spectra at initial immersion time in corrosive electrolyte can be described by the model presented in Figure 3.3.13c. During the initial time the corrosion process has not yet started and impedance spectra can be fitted by a circuit describing the properties of the passive oxide film (C_{ox} and R_{ox}). The corrosion progress eventually starts when corrosive species come into the contact with the metal surface through the defects or pores in the oxide film. The transport limitations of electroactive species may result in the appearance of an additional time constant element associates with the diffusion process (Warburg W). The equivalent circuit models presented in Figure 3.3.13d,e were used to describe the corrosion progress on the metal with the passive film. In the case when inhibitive species are present in the corrosion electrolyte a new time constant element can appear on the impedance spectra. This element is associated with the presence of an inhibitive film on the surface of metal (C_{inh} and R_{inh}). The film can be an adsorption layer of inhibitive species on the metal surface or layer of insoluble corrosion products of metal and inhibitor. The equivalent circuit that accounts for the inhibiting film is presented in Figure 3.3.13f.
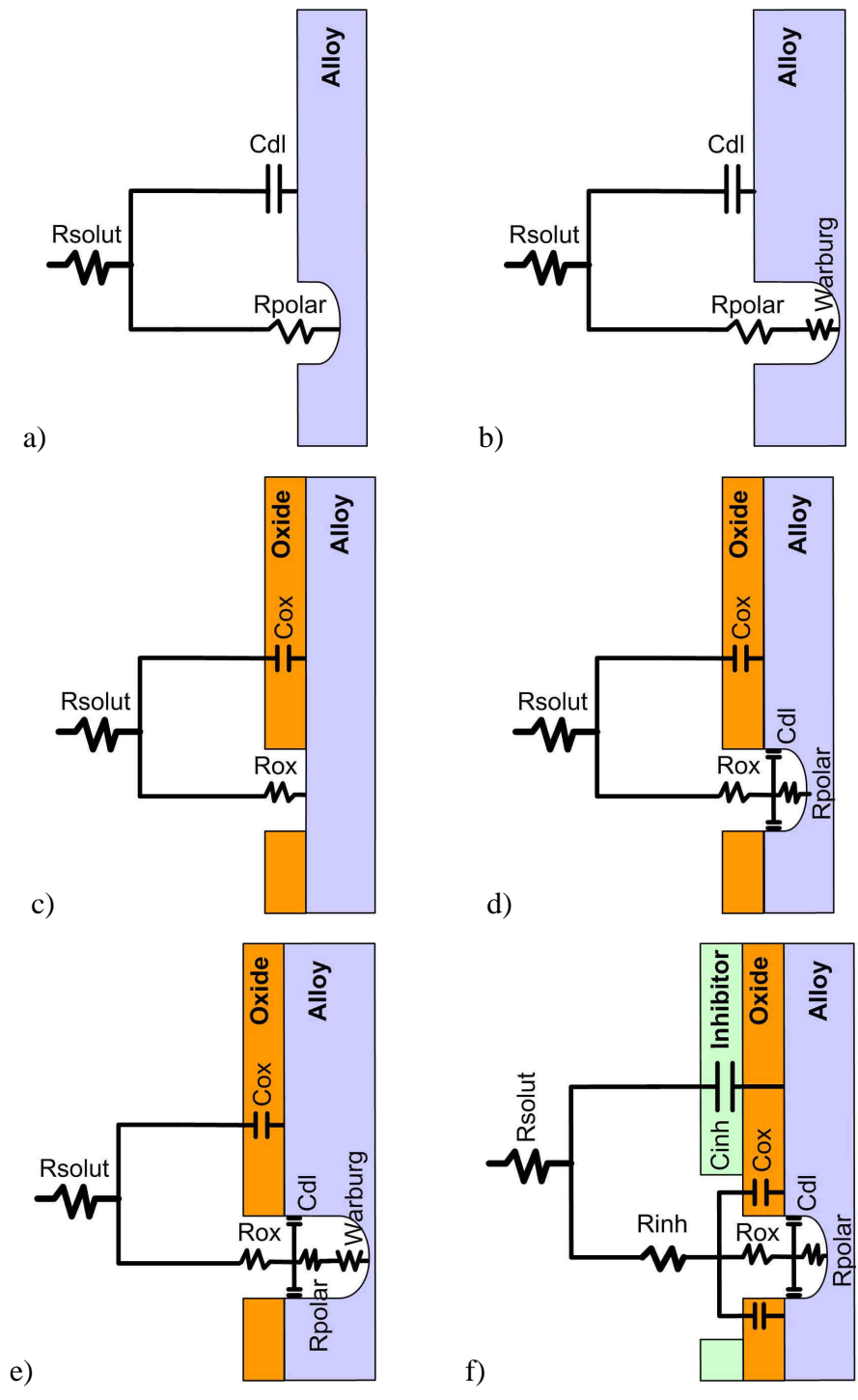
Figure 3.3.13. Equivalent circuits used for fitting of impedance spectra of the alloy samples during immersion in corrosive electrolytes.

Figure 3.3.14 presents equivalent circuit models used for fitting impedance spectra of the sol-gel coated substrates during immersion in a corrosive electrolyte. Bode plots of the sol-gel coated alloy substrate has two time constants that are attributed to the barrier oxide film formed during the etching of alloy and sol-gel coating. At the beginning of immersion corrosion species slowly penetrate the sol-gel coating. The equivalent circuit presented in Figure 3.3.14a was used to fit the impedance spectra at the beginning of immersion. The circuit has following elements C_{coat} and R_{coat} that correspond to the properties of the sol-gel coating. Penetration of the barrier film usually takes longer time thus only dielectric properties of the barrier film can be detected and therefore circuit includes only capacitance of the barrier oxide film (C_{ox}). During the development of corrosion aggressive electrolyte penetrates the barrier oxide. As a consequence, a new element (R_{ox}) associated with the resistance of the barrier layer is added in the equivalent circuit (Figure 3.3.14b). Corrosion process appears after the contact of an aggressive electrolyte with the metallic surface. Two elements related to the corrosion activity are added to the circuit (C_{dl} and R_{polar}) which can be seen in Figure 3.3.14c. In some cases the impedance spectra may contain an additional time constant element associated with the diffusion process (Warburg W) which can be added to the circuit in order to increase the quality of fitting of impedance spectra (Figure 3.3.14d).
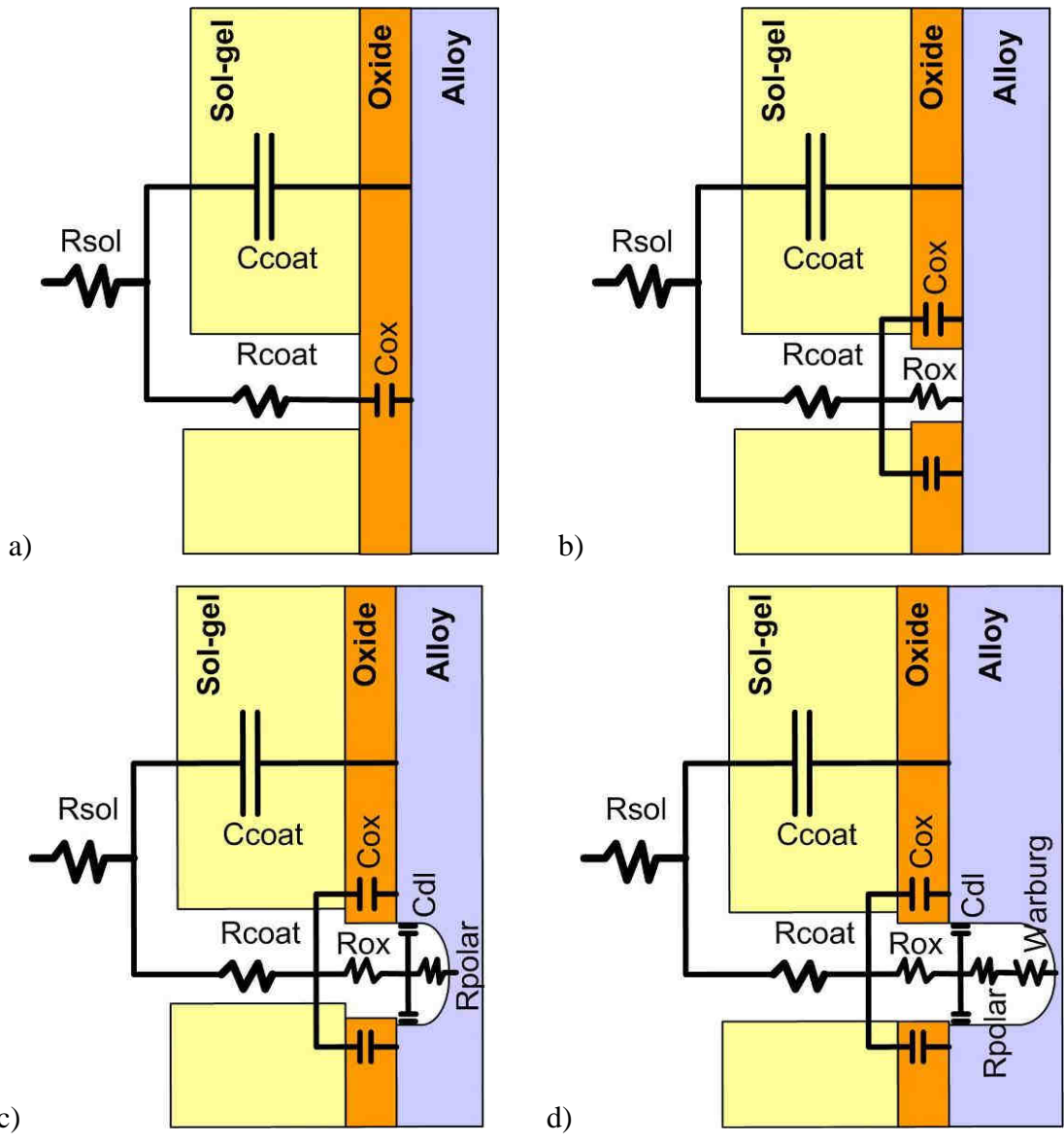
Figure 3.3.14. Equivalent circuits used for fitting of impedance spectra of the sol-gel coated alloy samples during immersion in corrosive electrolytes.

3.4 Scanning microelectrode techniques

Extensive development of scanning microelectrode techniques has been done in life sciences [308,309]. Nevertheless scanning microelectrode techniques has found a useful application in the investigation of the localized corrosion processes occurring on the metal and alloy surfaces. Common examples of the localized corrosion activity are pitting, intergranular, crevice and galvanic corrosion. Even the general corrosion normally occurs via development of localized anodic and cathodic zones. The measurements of the localized currents in different systems can be performed by Scanning Reference Electrode Technique (SRET) or Current density probe also known as Scanning Vibrating Electrode Technique (SVET) that have been initially applied in biological science [310-312]. Isaacs demonstrated application of such techniques in localized corrosion studies [313,314]. SVET technique has been used to study various localized corrosion processes, including stress corrosion cracking of stainless steel [315] and corrosion inhibition by cerium salts [316]. More recently, other workers have successfully applied the SVET to the study of corrosion on coil-coated steel [317] and in cut-edge zones [318].

3.4.1 Basic principles of SVET and SRET

SVET and SRET techniques are based on the detection of the difference in electric potentials in the electrolyte due to existing ionic current flows close to metallic substrates. In the case of corrosion processes such current gradients come from the localized anodic and cathodic corrosion activity. The local flows of anodic and cathodic currents can be interpreted in terms of half-reactions that occur at different zones of metal surface. The cathodic current flow (flow of anions) usually is produced by the reaction of oxygen reduction with the formation of hydroxyl ions or hydrogen reduction:

$$n/4O_2 + n/2H_2O + ne^- \rightarrow nOH^- \qquad (3.4.1)$$

$$nH^+ + ne^- \rightarrow n/2H_2 \qquad (3.4.2)$$
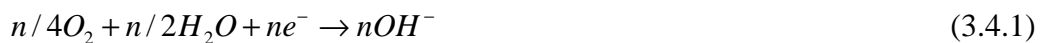
The respective anodic current (flow of cations) is caused by the dissolution of metal according to the following reaction:

$$Me \rightarrow Me^{n+} + ne^- \qquad (3.4.3)$$
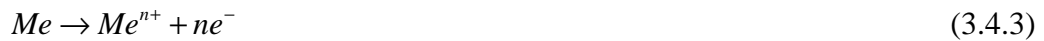
Figure 3.4.1 shows a schematic view of the potential and current distribution above the surface of a local anode. Close to the metal surface current lines go almost radial to the metal surface and intersect the potential lines perpendicularly (Figure 3.4.1). For a solution with a specific resistance ρ the potential difference (ΔV) measured between the two points with distance d indicated in the Figure 3.4.1 is related to the local current passing between these two points via equation [313,314]:

$$i_{local} = \frac{\Delta V}{\rho d}$$
(3.4.4)

The difference can be measured using two microelectrodes. In SRET two microelectrodes are separated with a fixed distance between them. The potential gradients are measured while moving the electrode setup above the surface. However the signal-to-noise ratio is relatively low in the case of such arrangement. On the other hand, the potential difference can be measured by only one electrode vibrating between the two positions (d) in the electrolyte. This approach with a vibrating electrode is used in SVET. The potential gradient is measured in the direction of electrode vibration as shown in Figure 3.4.2b. Both techniques use a precise X-Y – scanning system that controls the movement of the electrodes in the plane of the sample surface. A map of localized currents is obtained when scanning the surface in (x,y) plane.

SVET has many advantages compared to SRET such as higher resolution and sensitivity for small currents. This is achieved by using lock-in amplifiers. The vibrating probe transforms the measuring signal into AC signal with the same frequency as the vibration. A lock-in is used to receive the component related only to the vibration frequency and filters any other interference increasing the signal to noise ratio. In order to use values of the measured potential difference a calibration procedure is usually performed by placing the microelectrode at known distance from another microelectrode that is a source of ions. This calibration is valid for the electrolyte solution used and for the particular vibration frequency and amplitude of the probe [319].
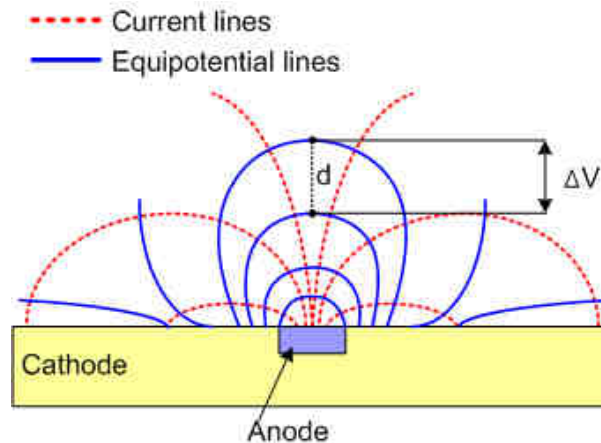
Figure 3.4.1. Schematic sketch of current and potential distribution above a local anodic zone. Adapted from ref. [320].
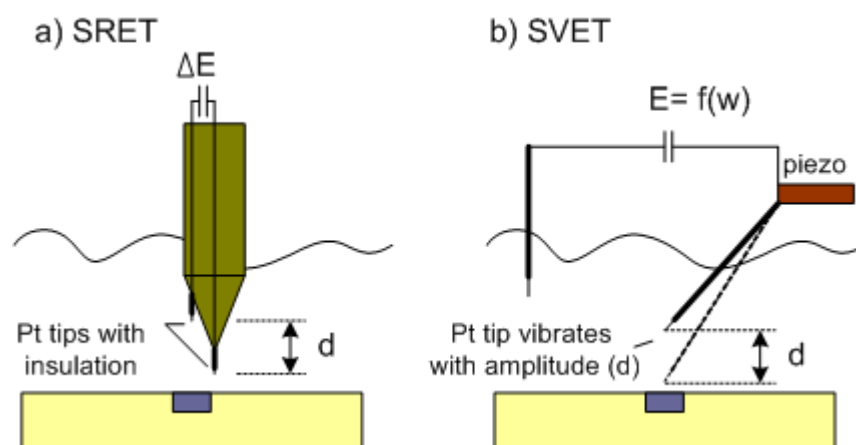
Figure 3.4.2. Scheme of SRET a) where two Pt tips are separated on distance "*d*" and SVET b) where a single tip vibrates with amplitude "*d*". Adapted from ref. [320]

3.4.2 Micro-amperometry and micro-potentiometry

There are other techniques which use scanning microelectrodes for localized investigation. Scanning micro-amperometry and micro-potentiometry methods belong to family of (SMET) scanning microelectrode techniques and are based on the measurements of current and potential difference at micro-scale. Local amperometry has been found usable in various applications for medicine, biochemistry and analytical chemistry [321-323]. In experimental work platinum microdiscs are mostly used as microelectrodes because the mathematical relation between the current and concentration of electroactive species is simplest and well known.

Micropotentiometry has been extensively developed in life sciences [324]. Local potentiometry in corrosion has been used more often for determination of pH [325] and pH and concentration of chloride ions [326] using Ion-selective micro-electrodes. Nevertheless it can be successfully used for measurements of concentration of various cations [327,328]. For corrosion studies Ogle has demonstrated the applicability of both SVET and micropotetentiometric detection of pH on the cut-edge corrosion [318]. A study of distribution of pH over galvanic couple between Zn and steel was reported in [329]. Experimental procedure is simple and uses the same approach as conventional ion-selective electrodes. A system includes an indicator electrode sensitive to a particular ion and a reference electrode connected to the electrometer. Normally a calibration curve is made for each system before measurement in order to get a relation between the potential difference and concentration (activity) of ions.

EXPERIMENTAL

4   Materials, sample preparation, synthesis and experimental techniques

4.1   Materials

4.1.1 Aluminium alloy

An aluminum alloy 2024-T3 was used as a primary substrate. The nominal composition of the alloy is given in Table 4.1.1.

Table 4.1.1. Composition of aluminum alloy 2024-T3, wt. %.

Element	Cu	Cr	Fe	Mg	Mn	Si	Ti	Zn	Other	Al
Conc.	3.8-4.9	0.1	0.5	1.2-1.8	0.3-0.9	0.5	0.15	0.25	0.15	Bal.

4.1.2 Chemicals
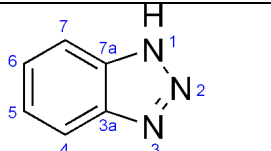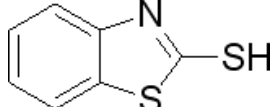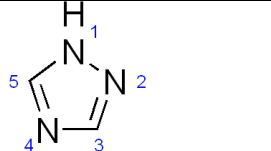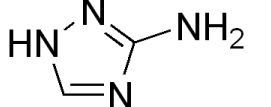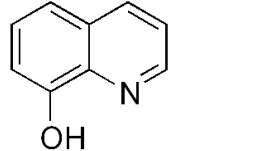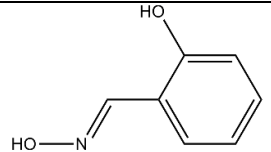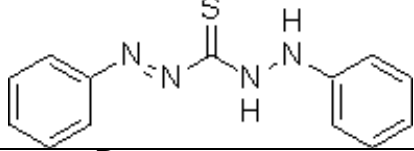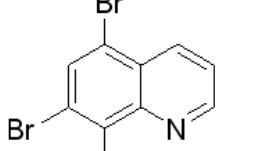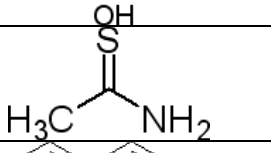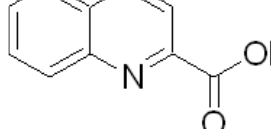
A list of reagents that were used for synthesis is presented in Table 4.1.2.
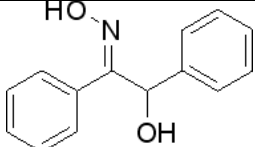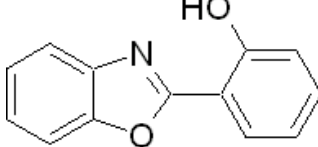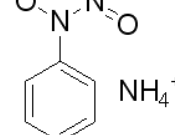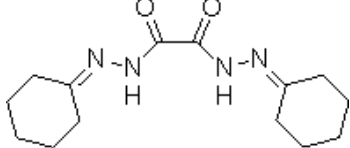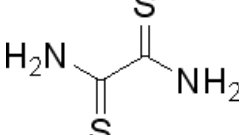
Table 4.1.2. List of reagents used for synthesis.

Reagent name	Abbreviation	Producer
3-glycidoxypropyltrimethoxysilane	GPTMS	Sigma-Aldrich
Zirconium (IV) propoxide	TPOZ	Sigma-Aldrich
Ethylacetoacetate	EtAcAc	Fluka
2-propanol	2-propanol	Sigma-Aldrich
Acetylacetone	AcAc	Fluka
Titanium (IV) propoxide	TPOT	Sigma-Aldrich
Pluronic® F-127	Pluronic	Sigma-Aldrich

The inhibitors used for testing the corrosion protection of the alloy are presented in Table 4.1.3.

Table 4.1.3. List of compounds used for testing their corrosion inhibition properties for 2024 aluminum alloy.

Reagent name	Formula	Molar mass	Producer
Cerium nitrate hexahydrate	$Ce(NO_3)_3*6H_2O$	434.22	Sigma-Aldrich
Lanthanum nitrate hexahydrate	$La(NO_3)_3*6H_2O$	433.22	Fluka
Cerium molybdate	$Ce_2(MoO_4)_3$ (amorphous)	~760.04	INM GmbH
Benzotriazole		119.12	Sigma-Aldrich
2-Mercaptobenzothiazole		167.25	Sigma-Aldrich
1,2,4-triazole		69.07	Sigma-Aldrich
3-amino-1,2,4-triazole		84.08	Sigma-Aldrich
8-hydroxyquinoline		145.16	Fluka
Salicylaldoxime		137.14	Alfa Aesar
Dithizone		256.33	Alfa Aesar
5,7-Dibromo-8-hydroxyquinoline		302.95	Alfa Aesar
Thioacetamide		75.13	Sigma-Aldrich
Quinaldic acid		173.17	Sigma-Aldrich

α-Benzoin oxime		227.26	Alfa Aesar
2-(2-Hydroxyphenyl) benzoxazole		211.22	Sigma-Aldrich
Cupferron		155.15	Sigma-Aldrich
Cuprizone		278.35	Alfa Aesar
Dithiooxamide		120.20	Sigma-Aldrich

4.2 Sample preparation

4.2.1 Polishing 1

For localized analysis using AFM/SKPFM techniques aluminum samples were gradually polished by SiC paper and finished by diamond paste grade 3 and finally grade 1. The polished samples were ultrasonically cleaned in 2-propanol during 5 min and stored in a desiccator prior to analysis.

4.2.2 Polishing 2

For corrosion study of bare aluminum substrates aluminum plates 3x4 cm were mechanically polished using SiC paper until 1200 grit grain size in 2-propanol followed by ultrasonic cleaning in 2-propanol and drying in a flow of air.

Chemical pretreatment

Two methods of chemical pretreatment of AA2024 were tested. Before any treatment the alloy plates were degreased in acetone.

4.2.3 Alkaline cleaning

The first method includes immersion in water solution of the alkaline cleaner TURCO™ 4215 - 50 g/l during 25-35 min at 60-70ºC followed by rinsing with distillated water then immersion in 20% solution of nitric acid during 10 min at 20-30ºC followed by rinsing with distillated water and drying.

4.2.4 Chemical etching

In the second method the alloy samples were etched using an industrial 3-step cleaning procedure. Aluminum plates were alkaline cleaned in Metaclean T2001 at 60-70 ^{o}C for 15-25 min followed by alkaline etching in Turco Liquid Aluminetch N2 at 60±5 ^{o}C for 30-60 s and etched in Turco Liquid Smutgo NC at 25±7 ^{o}C for 5-10 min. Washing with distillated water was done after each step of cleaning. At the end the metallic panels were dried in a flow of air.

4.3 Synthesis and application of the sol-gel films

The main purpose of the films applied on the alloy is to increase the adhesion between the metal and the organic paints. In addition the films must provide some degree of barrier protection. Therefore the approach of the sol-gel synthesis is based on the combination of different functionalized reagents used to build a system with tailored properties. In the present work epoxy-functionalized silane (GPTMS) and metalorganic compounds (Zr or Ti alkoxides) were used as main components of the sol-gel systems. GPTMS has epoxy groups that are compatible with the paint formulations used in industry. The epoxy groups can easily react with the functional groups of paints and provide necessary adhesion. In addition the silicon alkoxy group can be hydrolyzed and chemically bonded to the metal surface thus providing adhesion to the metal. Metalorganic compounds play a role of inorganic network formers. Oxide nanoparticles can be formed after partial hydrolysis of metalorganic precursors. These nanoparticles reinforce the coating matrix making it harder and denser. The detailed description of the synthesis procedure of different sol-gel formulations is the following.

4.3.1 Synthesis of Zr based sol-gel formulations (SgZr1,2)

Zirconia based hybrid sol-gel formulations were synthesized using a controllable sol-gel route mixing two different sols. The first sol (sol 1) containing a zirconium precursor was combined with the second sol (sol 2), which is organosilane based. The first sol was prepared from 70% zirconium (IV) propoxide (TPOZ) solution in 2-propanol mixed with a complexing agent at 1:4 molar ratio (Table 4.3.1). After 20 min which were necessary to obtain complexation of the precursor, synchronous ultrasonic agitation was started and 0.5 ml of water with pH 0.5 was added (Table 4.3.1) to TPOZ for hydrolysis and condensation, which continued for 90 min. Ethylacetoacetate or Acetylacetone were used as complexing agents in this synthesis to reduce the reactivity of metallic alkoxides. The molar ratio of TPOZ/Complexing agent/Water was 1:3.5:5.5 (Table 4.3.1). The second organosilane sol was prepared by hydrolyzing GPTMS in 2-propanol using acidified water (HNO$_3$ was used for acidification; pH ~ 0.5) in 4.5:13:7.2 molar ratios of GPTMS/2-propanol/water for 1 h under rigorous stirring. The third sol was obtained by mixing the zirconium-based sol with the organosilane-based one at a 1:2 volume ratio. The final sol-gel solution was stirred under ultrasonic agitation for 1 h and then aged for 1 h. During the synthesis the sol-gel solutions were cooled down using a circulating water thermostat system working at 22 ±1 °C.

4.3.2 Synthesis of Ti based sol-gel formulation (SgTi1,2)

Titanium based sol-gel systems were synthesized according to controllable sol-gel route mixing two different sols. The procedure is similar to zirconium based sol-gel. The

first sol (sol 1) was obtained by controlled hydrolysis of 70% titanium (IV) propoxide (TPOT) solution in 2-propanol mixed with a complexing agent at 1:4 molar ratio (Table 4.3.1). After 20 min which were necessary to obtain complexation of the metalorganic precursor, synchronous ultrasonic agitation was started and 0.5ml of water with pH 0.5 (HNO_3 was used for acidification; pH ~ 0.5) was added for hydrolysis and condensation, which continued for 60 min. Ethylacetoacetate or Acetylacetone were used as complexing agents in this synthesis to reduce the reactivity of metallic alkoxides. The molar ratio of TPOT/Complexing agent/Water was 1:3.7:5.5 (Table 4.3.1). The second sol (sol 2) was prepared by hydrolysis of GPTMS in 2-propanol solution in the presence of a small amount of acidified water with molar ratios 4.5:13:7.2 of GPTMS:2-propanol:water (Table 4.3.1). The hydrolysis was performed under stirring by a magnetic stirrer for 1 h. The third hybrid solution was obtained by mixing the titanium-based sol with the organosilane-based one at a 1:2 volume ratio. The final sol-gel solution was stirred under ultrasonic agitation for 1 h and then aged for 1 h. During the ultrasonic agitation the sol-gel solutions were cooled down using a circulating water thermostat system working at 22 ±1 ^{o}C.

4.3.3 Synthesis of Ti-based nanostructured network layers with corrosion inhibitor (TiOxSgZr1/ TiOxBTASgZr1)

TiO$_x$ based sol was prepared at room temperature by hydrolysis of TPOT as follows. At first ethanol solution of the nonionic block-copolymer Pluronic F 127 was prepared in 1:30 weight ratio of Pluronic to ethanol. TPOT was added to the ethanol solution with the concentration $7*10^{-3}$ mol/L. After stirring for 1 hour the solution was hydrolyzed by addition of acidified water (pH ~ 1) in molar ratio 1:100 of TPOT precursor to water. In 30 min the alloy substrates were dip-coated in the obtained sol and dried. The time of deposition in the prepared sol was 3 minutes followed by controlled withdrawal with speed 18 cm/min. The deposited titanium based organic-inorganic films were then dried at 250 ^{o}C. Inhibitor loading was performed on AA2024 samples with TiOx layer in a solution of BTA in ethanol (0.05g/l). The AA2024 panels with TiOx layer were immersed in the BTA solution and drawn out with a speed of 18 cm/min and then dried at 80 ^{o}C.

4.3.4 Preparation of SiO$_2$-based nanocontainers with corrosion inhibitor (SgZr1NCBT/ SgZr1NCBTx2)

To produce inhibitor-loaded nanocontainers having silica nanoparticles as core the layer-by-layer deposition procedure was performed involving both large polyelectrolyte molecules and small benzotriazole inhibitor ones. The initial SiO$_2$ nanoparticles are negatively charged and the deposition of the positive poly(ethylene imine) (PEI, MW ~ 2000) was performed on the first stage mixing 20 ml of SiO$_2$ (15% wt.) colloidal solution with 3 ml of 2 mg/ml PEI solution for 15 min. Then, the SiO2/PEI sample was washed

three times by centrifugation in distilled water. This washing procedure was performed after each deposition step. Deposition of the negative poly(styrene sulfonate) (PSS, MW ~ 70000) layer was carried out from 2 mg/ml PSS solution in 0.5 M NaCl. Deposition of the third inhibitor layer was accomplished in acidic media (pH=3) from 10 mg/ml solution of benzotriazole. The last two deposition steps (PSS and benzotriazole) were repeated once to ensure higher inhibitor loading in the final LbL structure. The resulting nanocontainers have SiO_2/PEI/PSS/benzotriazole/PSS/benzotriazole layer structure. The benzotriazole content in nanocontainers is equal to 95 mg per 1 g of the initial SiO_2 particles. The incorporation of nanocontainers in the sol-gel was performed during the preparation of the first sol containing TPOZ (Table 4.3.1).

4.3.5 Preparation of Halloysite nanocontainers with corrosion inhibitor (SgZrHSMBT SgZrHS)

The preparation of halloysites loaded with inhibitor is the following. Dispersed halloysite powder was mixed with 10 mg/ml solution of MBT in ethanol. A vial containing the mixture was transferred to a vacuum jar and then evacuated using a vacuum pump. Slight fizzing of the suspension indicates the air being removed from the halloysite interior. After the fizzing was stopped, the vial was sealed for 30 min to reach equilibrium in MBT distribution. The halloysite suspension was centrifuged to remove excess of the dissolved MBT, cleaned in water three times, and dried. This process was repeated four times to ensure the saturation of the inner halloysite cavity with precipitated MBT. After that the obtained halloysites with inhibitor were coated by polyelectrolyte layers made of Pollyallylhydrochloride (PAH) and poly(styrene sulfonate) PSS employing the procedure similar to described in the previous paragraph. The final nanocontainers have inhibitor/halloysite/PAH/PSS/PAH/PSS layer structure. The maximum MBT quantity loaded into halloysite tubes is 5 % wt.

4.3.6 Incorporation of inhibitive additives in the sol-gel system SgZr1

Inhibiting compounds such as BTA, 8HQ and $Ce(NO_3)_3$ were dissolved in one of the components of the sol-gel and then incorporated in the sol-gel systems at the respective hydrolysis steps indicated in Table 4.3.1. The molar ratio of TPOZ and inhibitors was 1:0.0536 (Table 4.3.1). Slurry of cerium molybdate compound was added to one of the sols during the sol-gel synthesis. The concentration of inhibitor in the final sol-gel solution was 0.0132 mol and 0.0263 mol or 0.3 wt.% and 0.6 wt.% respectively (Table 4.3.1).

Table 4.3.1. Sol-gel formulations.

Sample name	TPOZ, (sol1) mol	TPOT, (sol1) mol	Ethacac, (sol1), mol	AcAc, (sol1) mol	Water (sol1), mol	GPTMS, (sol2), mol	2-propanol, (sol2) mol	Water (sol2), mol
SgZr1,2	1		3.5	4	5.5	4.5	13	7.2
SgTi1,2		1	3.7	4	5.5	4.5	13	7.2

Sample name	TPOZ, (sol1) mol	Ethacac, (sol1), mol	Water (sol1), mol	GPTMS, (sol2), mol	2-propanol, (sol2) mol	Water (sol2), mol	Step of inhibitor addition, mol Sol 1	Sol 2	Sol 3	Inhibitor
SgZr1BT1	1	3.5	5.5	4.5	13	7.2	0.0536			BTA
SgZr1BT2	1	3.5	5.5	4.5	13	7.2		0.0536		
SgZr1BT3	1	3.5	5.5	4.5	13	7.2			0.0536	
SgZr1HQ1	1	3.5	5.5	4.5	13	7.2	0.0536			8HQ
SgZr1HQ2	1	3.5	5.5	4.5	13	7.2		0.0536		
SgZr1HQ3	1	3.5	5.5	4.5	13	7.2			0.0536	
SgZr1Ce1	1	3.5	5.5	4.5	13	7.2	0.0536			$Ce(NO_3)_3$
SgZr1Ce2	1	3.5	5.5	4.5	13	7.2		0.0536		
SgZr1Ce3	1	3.5	5.5	4.5	13	7.2			0.0536	

Sol-gel formulation

Intermediate network TiOx

Sample name	TPOZ, (sol1) mol	Ethacac, (sol1), mol	Water (sol1), mol	GPTMS, (sol2), mol	2-propanol, (sol2) mol	Water (sol2), mol	TPOT, mol	Pluronic F127, wt	Water (TPOT), mol	BTA in EtOH
TiOxSgZr1	1	3.5	5.5	4.5	13	7.2	1	30%	100	-
TiOxBTSgZr1	1	3.5	5.5	4.5	13	7.2	1	30%	100	+

NanoContainers SiO2

Sample name	TPOZ, (sol1) mol	Ethacac, (sol1), mol	Water (sol1), mol	GPTMS, (sol2), mol	2-propanol, (sol2) mol	Water (sol2), mol	NanoContainers SiO2 Sol 1	Sol 2	Sol 3
SgZr1NCBT	1	3.5	5.5	4.5	13	7.2	+ SiO2+BTA		
SgZr1NCBTx2	1	3.5	5.5	4.5	13	7.2	+ x2 SiO2+BTA		

NanoContainers Halloysites

SgZrHSMBT	1	3.5	5.5	4.5	13	7.2	+ HS/MBT
SgZrHS	1	3.5	5.5	4.5	13	7.2	+HS empty

NanoContainers (Cerium molybdate CeMoOx)

SgZrMo1	1	3.5	5.5	4.5	13	7.2	+ 0.3wt% CeMoOx
SgZrSiMo3	1	3.5	5.5	4.5	13	7.2	+ 0.3wt% CeMoOx
SgZrSiMo3x2	1	3.5	5.5	4.5	13	7.2	+ 0.6wt% CeMoOx

4.3.7 Dipcoating

A home made dip-coating system with vibration isolation and possibility to control the withdrawal speed was used. The sol-gel films were produced by dip-coating of chemically cleaned aluminum substrates with immersion time in the sol-gel solution of 100 seconds followed by withdrawal at 18 cm/min. Cross-linking, gelation and solvent evaporation of the produced sol-gel coatings was carried out in an oven afterwards.

4.3.8 Curing

The sol-gel coated alloy samples were dried in open air after dipcoating and then put in an oven at 120 or 130 ^{o}C during 80 or 60 min respectively. When ready the samples were taken out from the oven and cooled down at ambient atmosphere.

4.4 Experimental conditions of the main techniques used in the study

4.4.1 AFM and SKPFM

A commercial AFM Digital Instruments NanoScope III system with Extender[tm] Electronic Module was used for studying in situ the kinetics of formation of precipitates on the surface of AA2024. The evolution of the Volta potential difference (VPD) on the alloy surface was studied ex situ before and after corrosion exposure.

The AFM was operated in contact mode for studying in situ the kinetics of the corrosion process. The topographical measurements were performed using a liquid cell compatible with the AFM and silicon nitride probes with tip radii less than 10nm that were purchased from Veeco instruments. Preliminary a topography map with a visible intermetallic inclusion was obtained in air in order to check the stability of a scanning tip. Then the tip was withdrawn from the surface on a small distance and a corrosive solution was introduced in the liquid cell. After engagement of the tip on the surface of the alloy, the topography was continuously mapped during the corrosion exposure.

The procedure for VPD measurements is different. The AFM was operated in Tapping mode using interleave mode with two pass scans. The first scan acquired topography of the surface using a Tapping mode to avoid contamination and deterioration of the tip. During the second scan the tip is lifted up from the surface to the distance of 100nm, the piezoelectric actuator was switched off and an AC voltage of 1000 mV amplitude with the frequency of the cantilever resonance is applied between the tip and the sample to induce oscillations of the cantilever. Using a nulling technique the VPD between the sample and the tip was measured over the whole surface to obtain the VPD map. The values of the measured VPD were referenced versus the AFM probe or versus the VPD measured on Ni surface that was used as a reference due to stable properties of its native oxide [266]. For all SKPFM measurements, silicon probes (Budget Sensors) covered with Cr-Pt layers were used.

4.4.2 DC polarization

In the present study the polarization curves were taken on the bare alloy in 0.05 M NaCl solution or in the same solution doped with the most effective inhibitors in order to understand their inhibition mechanism and to estimate the inhibition efficiency. Polarization was performed with a scanning rate of 1 mV/sec using a VoltaLab PGZ 100 potentiostat. A current-voltage curve was obtained by scanning the potential separately in the positive and negative direction starting from the open circuit potential of the alloy or only in the positive direction starting from the cathodic potential. The working electrode was partially coated by Lacomit varnish in such a way to form a square opening to the bare metal with approximate surface area of 1 cm^2. Platinum foil was used as counter electrode and saturated calomel electrode (SCE) was used as reference Figure 4.4.1.
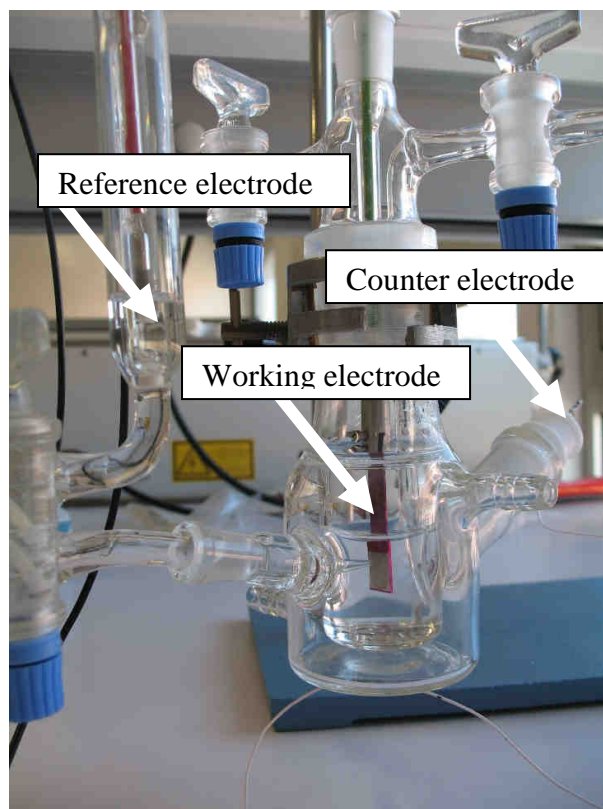
Figure 4.4.1. Cell for polarization measurements.

4.4.3 EIS

The EIS technique was used to estimate the evolution of the corrosion protection performance of bare and coated alloy substrates during immersion in NaCl solutions with different concentrations 0.005M, 0.05M and 0.5M. For each condition at least two samples were tested in order to ensure reproducibility of the results. The EIS measurements were carried out at room temperature in a Faraday cage. Prior to measurement the open circuit potential (OCP) was let to stabilize during 2-5 min. A frequency range between 100 kHz and 2 mHz with 7 or 10 points per decade and 10 mV AC perturbation amplitude vs. OCP were used. The measurements were performed using a Gamry FAS2 Femtostat with a PCI4 Controller or a Gamry potentiostat PCI4. Three-electrode cell arrangement was used in the study (Figure 4.4.2 b). The working electrode comprises alloy plate with tightly glued PMMA cylinder with a surface area around 3.35 cm^2 (Figure 4.4.2a). The electrochemical cell consists of a SCE reference electrode, platinum foil counter electrode and alloy substrate as a working electrode (Figure 4.4.2b). The EIS spectra were fitted and analyzed using Echem Analyst software provided by Gamry.
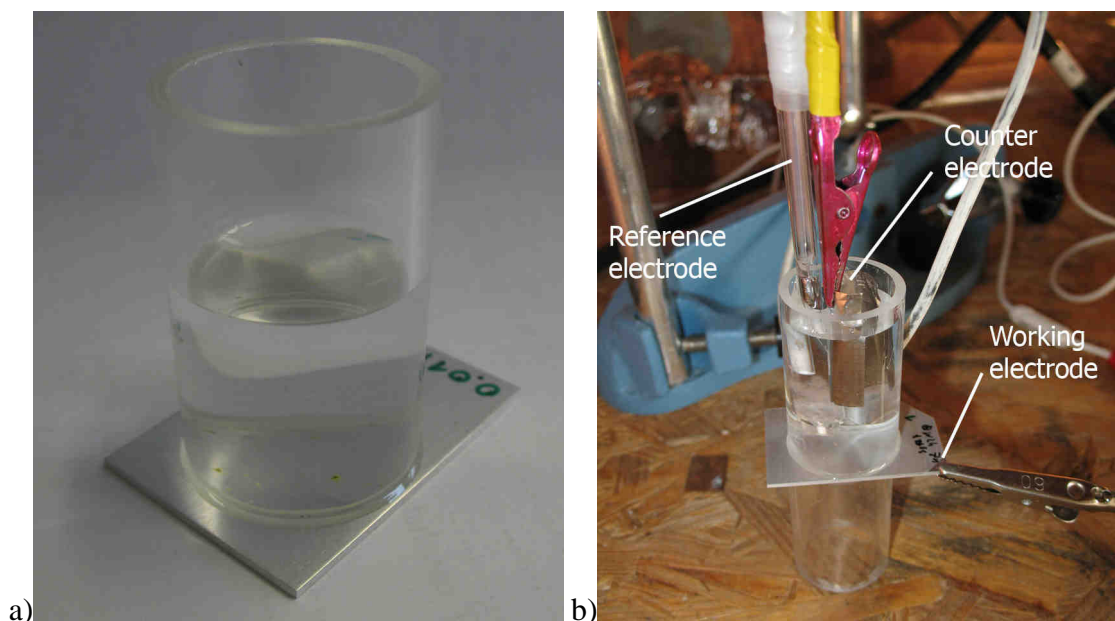
Figure 4.4.2. Cell for impedance measurements a); the electrode arrangement b).

4.4.4 SVET and microelectrode techniques

SVET

SVET equipment manufactured by Applicable Electronics Inc. (USA) was used in the present work. The equipment was controlled by the ASET 2.0 program developed by Sciencewares (USA). The electrochemical setup is presented in Figure 4.4.3a and includes a Pt microelectrode, two pseudo-reference electrodes and a sample. The microelectrodes were prepared from polymer insulated Pt-Ir wires produced by Microprobes Inc. (USA) (Figure 4.4.3b). A 10-20 µm diameter platinum black sphere was electrodeposited on the tip as can be seen in the Figure 4.4.3b. The microelectrode vibrates in two directions, one parallel (X axis) and another perpendicular (Z axis) to the sample surface at different frequencies. The amplitudes of vibration are twice the tip diameter (Figure 4.4.3b). Signals are processed by two lock-in amplifiers. Only signals from the field normal to the surface (Z axis) were considered in the present study. The measured voltage differences are converted to ionic currents by a prior calibration routine performed with a point current source (microelectrode with a tip of ~3µm) driving a current of 60 nA at 150 µm from the vibrating probe [330,331].
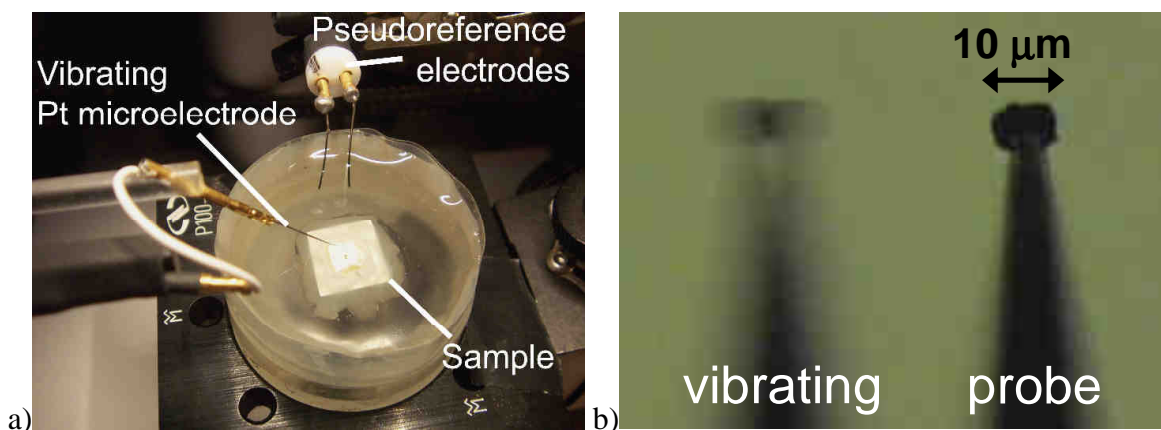
Figure 4.4.3. Electrochemical setup for SVET measurements, vibrating Pt probe b).

Micropotentiometry

For the micropotentiometry measurements two electrode arrangement was used (Figure 4.4.4a). Home made pH micro-potentiometric electrodes were used as ion selective electrodes. The electrode comprised silanized glass capillaries with a tip of 2 µm in diameter on one end (Figure 4.4.4b). The capillaries were back filled with 0.1M KCl + KH_2PO_4 0.01M – (internal solution) and front filled with a 20-30 µm column of hydrogen I cocktail B ionophore (Fluka, Ref. 95293) as shown in Figure 4.4.4b. Silver wire coated with silver chloride served as internal reference electrode and was inserted in the internal solution. The microelectrode was mounted in the same 3D positioning system used for SVET. Home made Ag/AgCl electrode was used as a reference electrode (Figure 4.4.4a). An IPA2 amplifier (input resistance $> 10^{13}$ Ω) manufactured by Applicable Electronics Inc. was controlled by the ASET program to measure and record the data. The microelectrodes were calibrated before and after measurements with commercial pH buffers (Riedel-de Haen), giving a linear response in the 5 to 13 pH range (Figure 4.4.5).
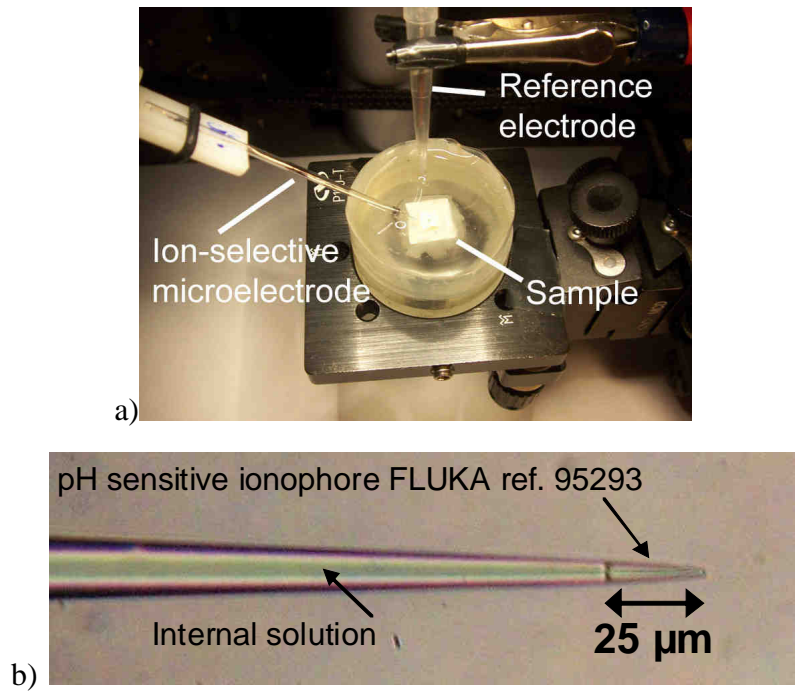
Figure 4.4.4. Electrochemical setup for SIET measurements a), top end of the ion selective electrode b).
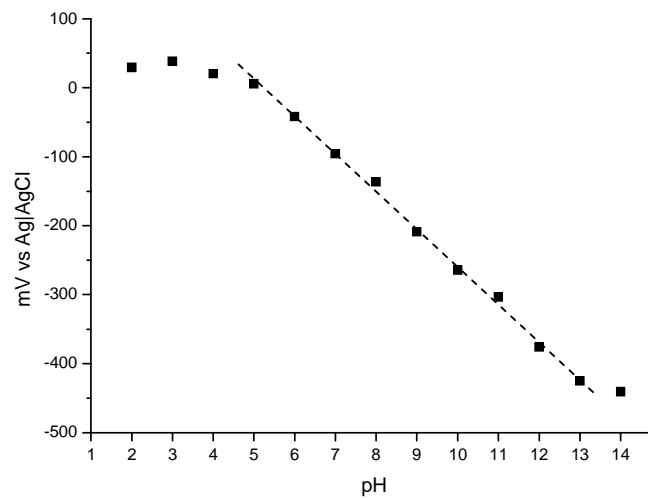
Figure 4.4.5. Calibration curve between the pH of the buffer solutions and response of the micro potentiometric probe for pH detection.

Microamperometry

The micro-amperometric detection of dissolved oxygen was made using the IPA2 amplifier in the amperometric mode. A two electrode cell was used Figure 4.4.6a. The working microelectrode was a 10 µm diameter platinum microdisc (Figure 4.4.6b) (CH Instruments, USA, Ref. CHI100) and a homemade Ag|AgCl electrode worked as both counter and reference electrode (Figure 4.4.6a). Given the small measured currents in the range of pico to nano amperes, the reference electrode can maintain its integrity and a fairly stable potential, especially if the measurements are not too long. The measured current magnitude is proportional to the rate of an electrochemical reaction at the Pt microelectrode surface. The tip potential was set at -0.7V vs. Ag|AgCl, well inside the region were oxygen reduction current was diffusion controlled (Figure 4.4.7). The electrode and the pre-amplifier were mounted in the same 3D positioning system used for SVET and the ASET program controlled the measurements.

a)   b)
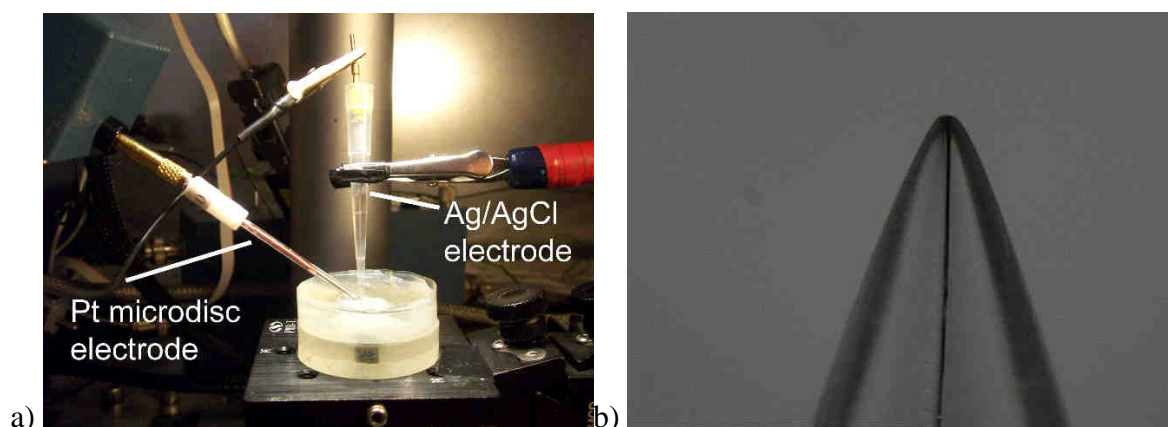
Figure 4.4.6. Electrochemical setup for microamperometric measurements a), a tip of Pt microdisc electrode b).
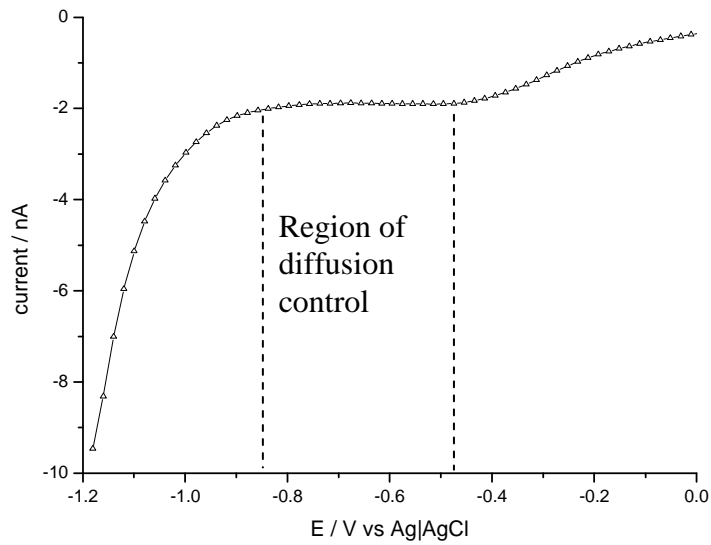
Figure 4.4.7. Polarization curve obtained in cathodic direction made on Pt electrode showing the diffusion limited plateau of oxygen reduction reaction.

Test cell

Figure 4.4.8 shows schematically the sketch of a test cell consisting of a holder, metallic substrate and wax coating. A test cell was prepared in the following way. A metallic substrate is glued to an epoxy holder (Figure 4.4.8). The holder was wrapped with a scotch tape in such a way to form a reservoir for corrosion solution. A mixture of beeswax and colophony masked the sample surface except a small opening at about 2x2 mm as schematically shown in Figure 4.4.8. The test solution was 0.05M NaCl solution.
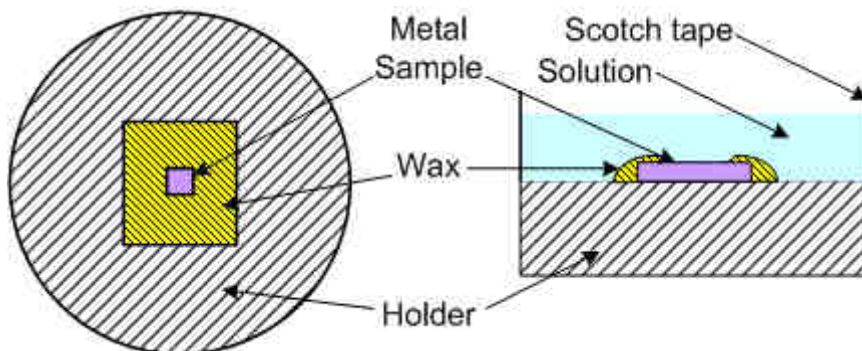
Figure 4.4.8. Schematic sketch of a cell for SVET, SIET and Microamperometric measurements.

4.5   Experimental conditions of supplementary experimental methods

4.5.1 Salt spray test for sol-gel coated AA2024 substrates

Salt spray test was performed according to ISO 9227. The samples were scratched according to the following dimensions: 1000 µm (width) x 200 µm (depth) then supported in holders at an angle of 6 deg from the vertical and placed in the salt spray chamber. The salt spray chamber run continuously at the following conditions: temperature was 35 ±1.7 °C, electrolyte was NaCl 5±1 wt. %, salt fallout 1-2 ml/h of NaCl solution. For inspection, the samples were washed with deionized water, dried with nitrogen and examined within 30min after removal from the chamber.

4.5.2 Cross-cut test

This test was applied in order to determine the paint adhesion to the substrate with cross cut testing at the initial stage and after 14 days water storage. The test was performed according to ISO 2409. After the cuts were made the cross was brushed with a soft scrubber. Afterwards, adhesive tape was pressed parallel to one of the cut directions on the cross. The tape was removed from the cross within 1 second at an angle of 60 deg. The cross test was performed after 30 min of removal samples from water storage. Deionized water was used in the water storage.

4.5.3 SEM coupled with EDS

A Scanning Electron Microscopy/Energy Dispersion Spectroscopy (SEM/EDS) was employed to reveal the evolution of the microstructure and composition of the surface of the specimens and changes of the chemical composition. SEM images were taken with a Hitachi S-4100 system at 25.0 keV beam energy. EDS spectra were taken from point analysis or averaging on the surface area of 100x100 µm.

4.5.4 Ultramicrotomy and TEM observations

In order to allow observation by TEM, electron transparent cross sections of samples must be prepared. Sectioning was performed with a Leica Ultracut UCT ultramicrotome. The sol-gel coated samples were previously embedded in a hard epoxy based resin and then cured for 2 days. After curing a truncated pyramid was prepared in such a way that the sample cross section appeared at the edge of the pyramid. The edge of the specimen was precut with a glass knife to remove residual surface roughness. Final sections were cut using a diamond knife (Microstar) approximately normal to the sample.

A nominal thickness of sections was set to 15 nm. A TEM Hitachi H-9000 with electron beam energy 300 kV was used for examination of the cross sections.

4.5.5 Optical microscopy

High resolution optical photographs of the alloy samples after corrosion were taken by a digital camera with 10 mega pixels resolution with or without inverted optical microscope JENAPHOT 2000 (ZEISS). Low resolution photographs of the alloy samples were taken by a digital camera in macro mode

4.5.6 XPS

The X-Ray photoelectron spectroscopy measurements were performed using a Microlab 310 F (from Thermo Electron - former Vg Scientific). The spectra were taken in CAE mode (20 eV), using an Al (non-monochromatic) anode. The accelerating voltage was 15 kV. The quantitative XPS analysis was performed using the Avantage software. The relative atomic concentration (Ax) was calculated using the following relation:

$$Ax = Normalised\ peak\ area\ 100\ /\ (\textstyle\sum_i Normalised\ peak\ areas) \tag{2.2.1}$$

where, the subscript (x) refers to the quantified species and the subscript (i) refers to the other species detected in the XPS spectra. The normalised peak area was obtained by dividing the intensity of the XPS peak of the species (after background subtraction) by the sensitivity factor of the corresponding species.

The background subtraction was performed using the Shirley algorithm, which gives a curve S shaped and assumes that the intensity of the background is proportional to the peak area on the higher kinetic energy side of the spectrum.

The quantification was performed after peak fit. The peak fit function used was a Gaussian-Lorentzian product function and the algorithm was based on the Simplex optimisation as used in the Avantage software.

4.5.7 FTIR

A Bruker Equinox IFS 55 infrared spectrophotometer was used to collect the Fourier transform infrared (FTIR) spectra.

4.5.8 TGA/DTA

Differential thermal analysis (DTA) and thermogravimetric analysis (TGA) of powder samples were performed using a Setaram SetSys 16/18 instrument under air atmosphere. The heating rate was 5 ^{o}C/min. Prior to TGA analysis the sol-gel samples were heated at 50 ^{o}C during 5 days.

4.5.9 Particle size and zeta-potential analysis

The size and electrophoretic mobility measurements of the nanoreservoirs were performed using a Malvern Zetasizer 4.

RESULTS AND DISCUSSION

5   Corrosion inhibition of AA2024

The knowledge of the intimate details of the corrosion process of the alloy is very important for finding an appropriate defense against the corrosion attack. One of the ways to slow down the corrosion process is based on the use of inhibitive compounds. However, depending on circumstances some compounds provide inhibitive action and others don't. Therefore proper inhibitors should be found for a particular alloy.

This chapter presents a detailed study of the corrosion mechanisms of AA2024 using methods of corrosion investigation (EIS, DC polarization), localized analysis of surface (AFM/SKPFM) and methods of microstructural analysis (SEM/EDS). Several chemicals are proposed as promising corrosion inhibitors and studied using different investigation methods. The study provided the information on the mechanism of the protection action of inhibitors that is very important for the development of active corrosion protective systems on the basis of sol-gel coatings. The investigated compounds showing promising inhibitive properties were used for creating enhanced corrosion protective systems based on the sol-gel pretreatments.

5.1   Localized corrosion of AA2024

5.1.1 SEM/EDS study

A typical electron micrograph of the AA2024 surface immersed in aerated neutral 0.005M NaCl solution is depicted in Figure 5.1.1. Corrosion can already be seen even after relatively short immersion (2 hours) in such diluted electrolyte. At the beginning the localized corrosion preferentially starts in the places of intermetallic particles. The strongest corrosion attack appears in the region of the bright round inclusions. Analysis of the chemical composition (Table 5.1.1) shows that zones 1 and 4 are enriched in copper and magnesium compared to the surrounding alloy matrix (zone 5). These particles can be surely ascribed to the intermetallic S-phase with the composition Al_2MgCu [15]. However the relative concentration of magnesium in the heavily corroded zone 1 is much lower than that at intact zone 4. It seems that the intact intermetallic lies deeper and is covered with a thin layer of aluminum and native oxide film. The lower atomic ratio of Mg in the corroded intermetallic (zone 1) shows preferable dissolution of this active element from this phase. A slight increase of copper content around S-phase intermetallics (zone 6) can appear due to copper redeposition processes that occur during the dissolution of intermetallic particles. The other kind of intermetallics, darker with elongated shape (zone 3), reveals lower corrosion activity. The EDS analysis demonstrates that such particles are

composed of Al, Cu, Fe, Mn and can be associated with the Al_6(Cu, Fe, Mn) phase as reported in [15].
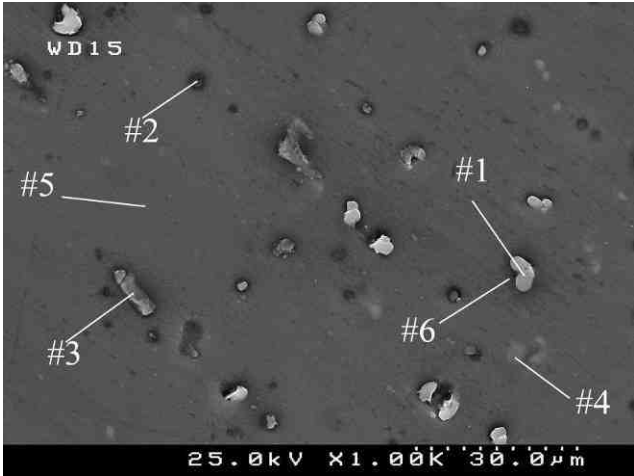
Figure 5.1.1. SEM micrograph of AA2024 immersed in 0.005M NaCl solution for 2 hours.

Table 5.1.1. Atomic ratios between the elements on different phases of AA2024 after immersion in 0.005M NaCl for 2h (see Figure 5.1.1).

	#1	#2	#3	#4	#5	#6
Mn/Al	-	0.002	0.027	-	-	-
Fe/Al	-	0.005	0.065	-	-	-
Cu/Al	0.440	0.048	0.106	0.178	0.015	0.030
Mg/Al	0.047	0.034	0.032	0.074	0.036	0.034

5.1.2 AFM/SKPFM study

Figure 5.1.2 presents topography of the polished alloy and the VPD map of the corresponding area before (a,b) and after (c,d) 2 hours of immersion in 0.005M NaCl. Two kind of localized defects can be found on the metallic surface (Figure 5.1.2c). After immersion of the aluminum specimens in NaCl dissolution of small intermetallic particles occurs. The biggest round-shape intermetallics seem also to be partially dissolved but an additional dissolution of the surrounding alloy matrix occurs as well (Figures 5.1.2c, 5.1.3a). These intermetallics, as identified by the SEM/EDS, correspond to S-phase (Al_2CuMg). Dissolution of this type of intermetallics suggests their anodic character agreeing with some previous studies [18,332]. However, analysis of the VPD distribution

118

completely refutes this suggestion. The corroded places exhibit well defined cathodic potential when compared to the aluminum alloy matrix (Figure 5.1.2d).

An important point is that the VPD map on the corroded surface has a broadened maximum without well-defined frontier compared to the maxima of the uncorroded surface where sharp borders are present (Figure 5.1.2b). The Volta potential difference over the S-phase in the case of the uncorroded alloy is about 170 mV higher than that of aluminum matrix. The maximum on the VPD map of the corroded sample is about 400 mV higher compared to the alloy matrix (Figure 5.1.3b). Increase of the VPD and broadening of the potential peaks over intermetallic zone suggest modification of the alloy surface after corrosion. One of the plausible explanations of such difference can be change of elemental composition of the surface. For example the VPD over pure copper sample is around 0 V vs. Ni reference electrode. The VPD measured on the intermetallic phase of the alloy sample increases from around -650 mV until -250 mV vs. Ni ref. (Figure 5.1.3b). Such increase can be associated with the copper enrichment on the surface. However, additional experiments must be made. Measurements of the atomic concentration of elements using the SEM coupled EDS can clarify the localized mechanism of AA2024 corrosion.

a)   b)

c)   d)
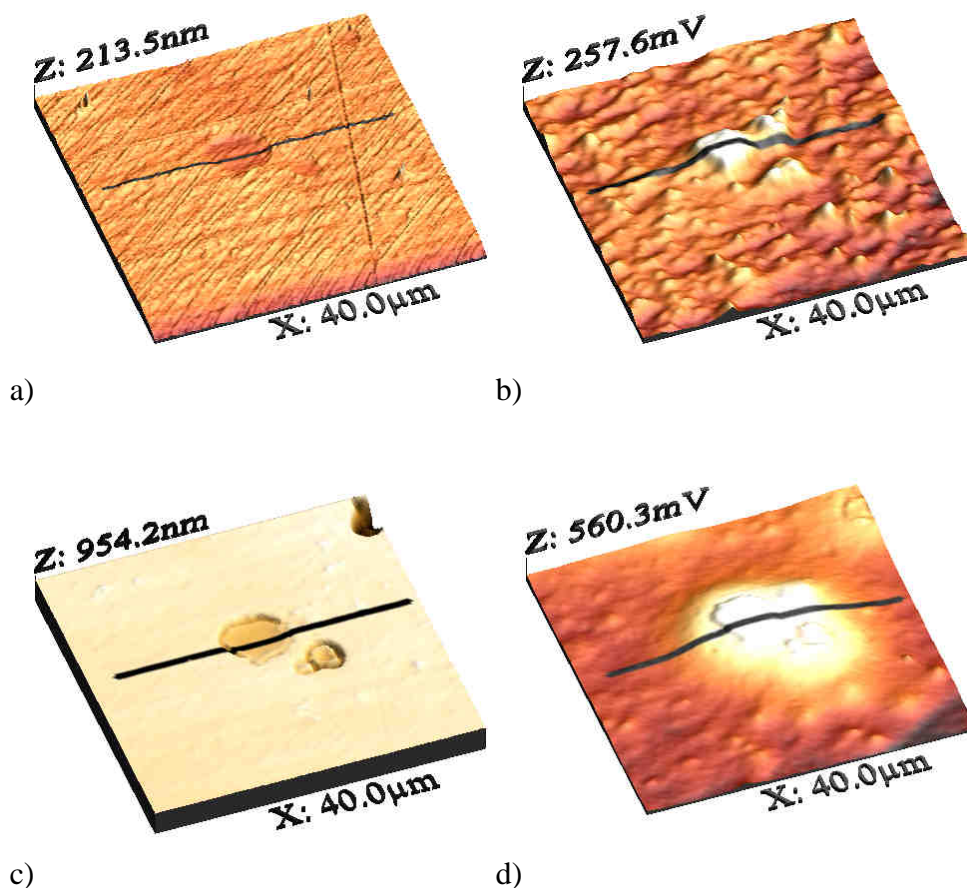
Figure 5.1.2. Topography (a) and VPD map (b) for AA2024 before corrosion; Topography (c) and VPD map (d) for AA2024 after immersion for 2 h in neutral solution 0.005M NaCl.

Figure 5.1.3 presents SEM micrograph of the surface of the alloy and EDS profiles of Al, Cu, Mg and O after immersion in neutral NaCl solution. The SEM image corresponds to the area shown in Figure 5.1.2. As can be seen, there is a significant drop in concentration of Al and Mg elements in the place of the intermetallic inclusion (Figure 5.1.3b). The S-phase is a combination of noble Cu and more active elements Al and Mg. During corrosion the electrochemically more active elements are dissolved from the phase leaving the nobler Cu element. This process is called dealloying. The signal of O is increased over the profile both in the place of the intermetallic and in the surrounding zones (Figure 5.1.3b). Such oxygen increase can be linked with the modification or growth of surface oxide films and is in good correlation with the VPD measurements that show an increase of the potential in the area of the intermetallic particle (Figure 5.1.3b lower part). These experimental results suggest two possible explanations for the VPD increase. The first one is the increase of the copper concentration due to dealloying of the intermetallic. The second one is the influence of the formed surface oxide film on the VPD. Yet additional experiments are needed in order to clarify the broadening and change of the VPD over the alloy matrix.
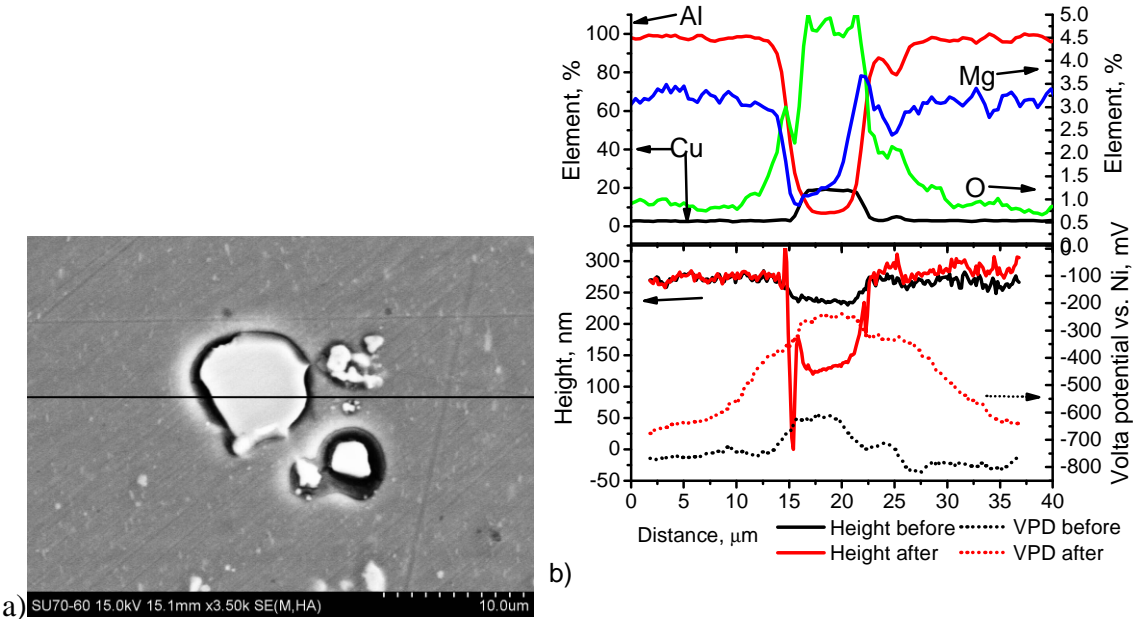
Figure 5.1.3. SEM micrograph of area presented in Figure 5.1.2c a), profiles across the black horizontal line of EDS elemental analysis upper part of (b) and Height and VPD lower part of (b).

The presence of oxide and hydroxide films on the surface can be avoided when acidic corrosion solution is used. Therefore the use of acidic electrolyte can help to clarify the influence of oxide films on VPD measured on the alloy surface. A corrosion process in 0.005M NaCl solution with pH 3 was investigated as a compliment of the study of the corrosion in neutral solution. The sample immersed in NaCl solution with pH~3 shows much higher dissolution of S-phase intermetallic around 900 nm (Figure 5.1.4c, Figure 5.1.5b) compared to neutral solution around 120 nm (Figure 5.1.3b). This indicates an increased rate of dissolution of Al and Mg from the S-phase intermetallic in acidic pH. SKPFM measurements show high value of VPD (around -200 mV vs. Ni) in the place of inclusion (Figure 5.1.5b). This value is higher compared to measurements performed in neutral pH solution (-250 mV vs. Ni). The VPD of alloy matrix has also increased after immersion. The difference between the VPD of fresh and corroded surface is around 250 mV (Figure 5.1.5b) for pH 3 and for neutral pH solution the difference is around 150 mV (Figure 5.1.3b). The increase of the VPD on the alloy matrix after immersion in acidic pH suggests the ennoblement of the surface. However the reason of such VPD increase is to be found out.

a)   b)

c)   d)
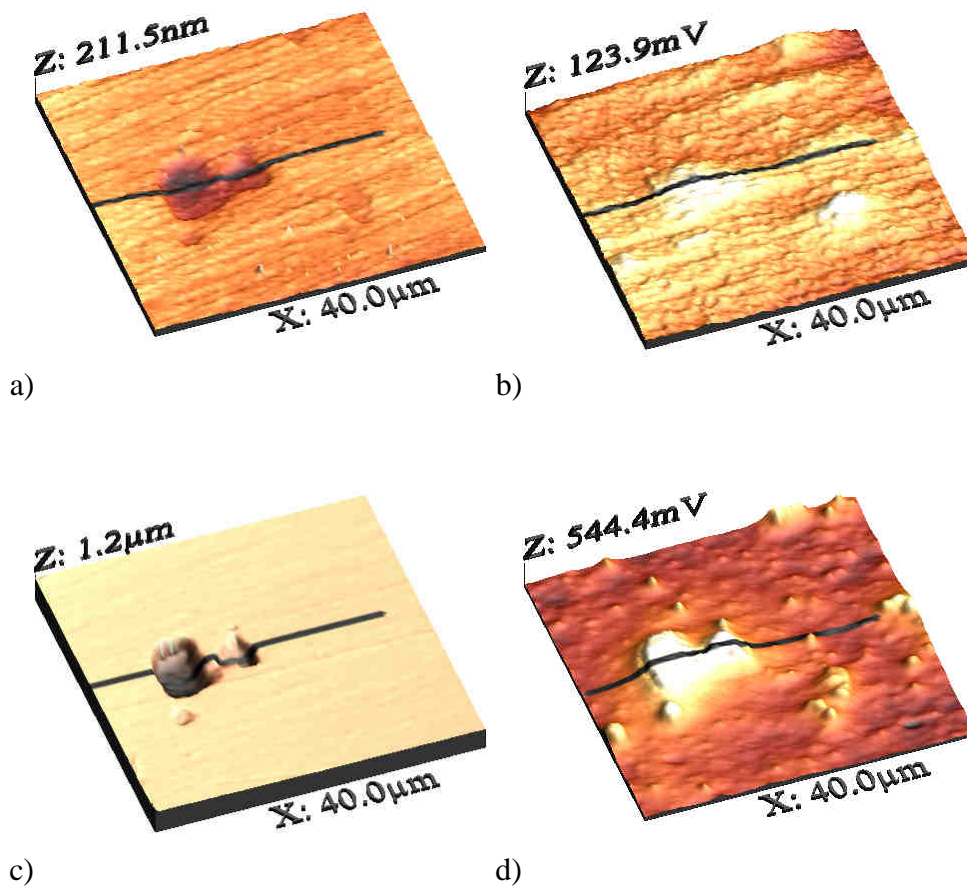
Figure 5.1.4. Topography a) and VPD map b) for AA2024 before corrosion; Topography c) and VPD map d) after immersion for 2 h in 0.005M NaCl with pH 3.
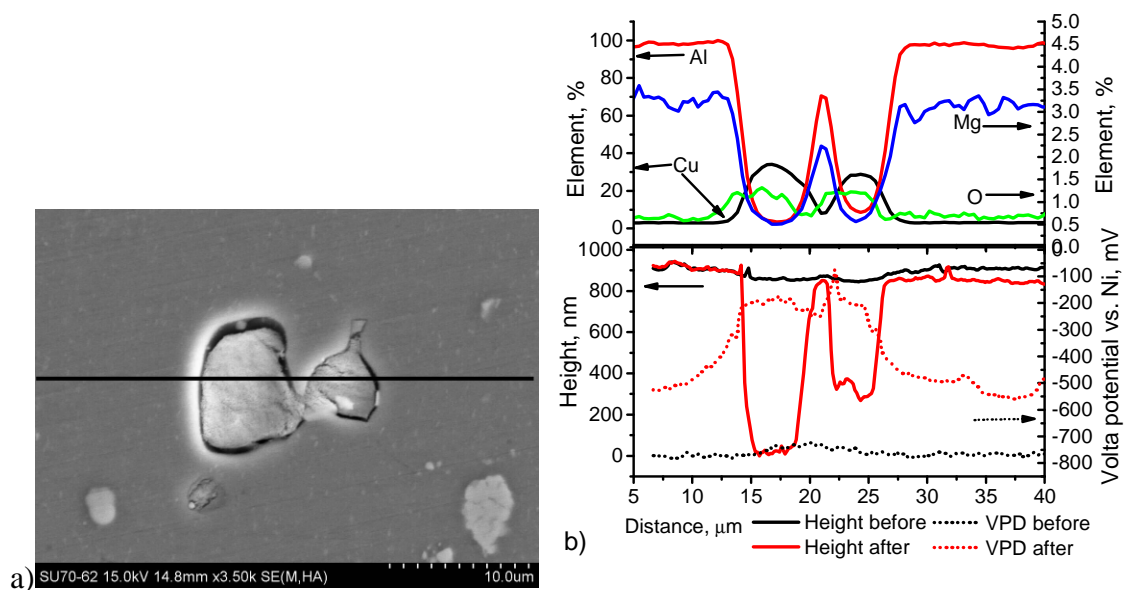
Figure 5.1.5. SEM micrograph of area presented in Figure 5.1.4, profiles across the black horizontal line of EDS elemental analysis upper part b) and Height and VPD bottom b).

SEM micrographs and EDS profiles were additionally made after corrosion in acidic electrolyte. The copper concentration is increased in the place of intermetallic up to 37 at.% that correlates with higher Al and Mg dissolution (Figure 5.1.5b upper part). The copper concentration (37 at.%) is higher compared to measurements performed after corrosion in neutral solution (20 at.%). This explains the increase of VPD measured on the dissolved intermetallic (Figure 5.1.5b). From another hand significantly lower concentration of oxygen is found on the surface after corrosion in acidic electrolyte (Figure 5.1.5b) compared to neutral one Figure 5.1.3b. Lower concentration of oxygen is a consequence of the low pH of solution at which formation of hydroxides and oxides is thermodynamically less favorable. In spite of lower oxygen content, the VPD level on the alloy matrix after corrosion in acidic pH solution is higher (Figure 5.1.5b) than in neutral pH solution (Figure 5.1.3b). One of the possible explanations for VPD increase on the alloy matrix can be related to copper redeposition over the surface. Higher level of copper from dissolved intermetallic can explain increased level of VPD after immersion in NaCl with pH~3 compared to the sample immersed in neutral NaCl solution. However the EDS method is not sensitive enough to detect the presence of very thin redeposited copper layer on the alloy surface.

The most relevant findings concerning the localized corrosion behavior are the following. The S-phase contains two active elements aluminum and magnesium in

122

combination with copper that is nobler. The higher VPD of the S-phase compared to the aluminum alloy matrix comes from the noble potential of the copper in the intermetallic phase. Increase of the VPD evidently demonstrates an enrichment of the intermetallic in copper during the corrosion tests. The dealloying of the intermetallics occurs due to selective dissolution of magnesium and aluminum from the S-phase leaving copper-rich remnants with higher VPD. The broadening of the cathodic potential peaks can happen due to the processes of copper redeposition onto the alloy matrix around the intermetallic particles, which is in good agreement with previous works [15]. The precipitation of a copper layer around the corroded intermetallics is clearly demonstrated in the optical micrograph taken after 2 hours of immersion in 0.005 M NaCl solution (Figure 5.1.6). The formation of wide cathodes around the intermetallics and the creation of copper remnants with developed surface area lead to sufficient acceleration of the cathodic processes consequently increasing the rate of the anodic dissolution of the aluminum alloy matrix around the intermetallics. Figure 5.1.7 presents Back-scattering electron micrographs made at the place of a pit after long term immersion of AA2024 in NaCl solution. White places on the pictures correspond to copper precipitates resulting from the copper redeposition process. EDS spectra made at such places clearly show a huge copper content in comparison to darker places where mostly aluminum can be found (Figure 5.1.7c). These results demonstrate how dangerous can be copper redeposition especially at later stages of corrosion where big copper cathodes significantly increase the dissolution rate of aluminum from the alloy and result in appearance of deep perforations at the surface.

The results presented above clearly demonstrate that the first stage of AA2024 corrosion in chloride medium is the dissolution of the cathodic S-phase. It can be explained in terms of the formation of local galvanic couples inside of each intermetallic. The magnesium depleted zones can play a role of cathodes whereas the rest of the intermetallic surface is an anode. The corrosion processes inside the S-phase inclusions arises in spite of the fact that the potential of the whole intermetallic is nobler than the surrounding alloy matrix.
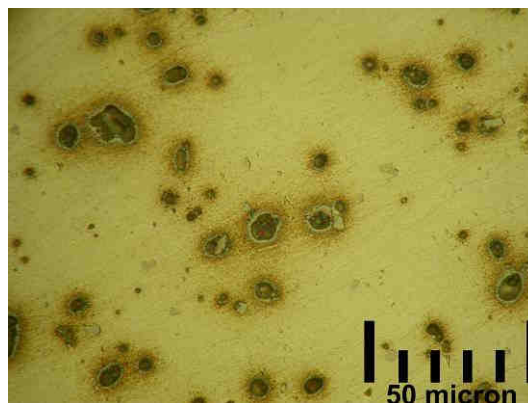
Figure 5.1.6. Optical micrograph of polished AA2024 surface after immersion in neutral 0.005M NaCl for 2 hours.
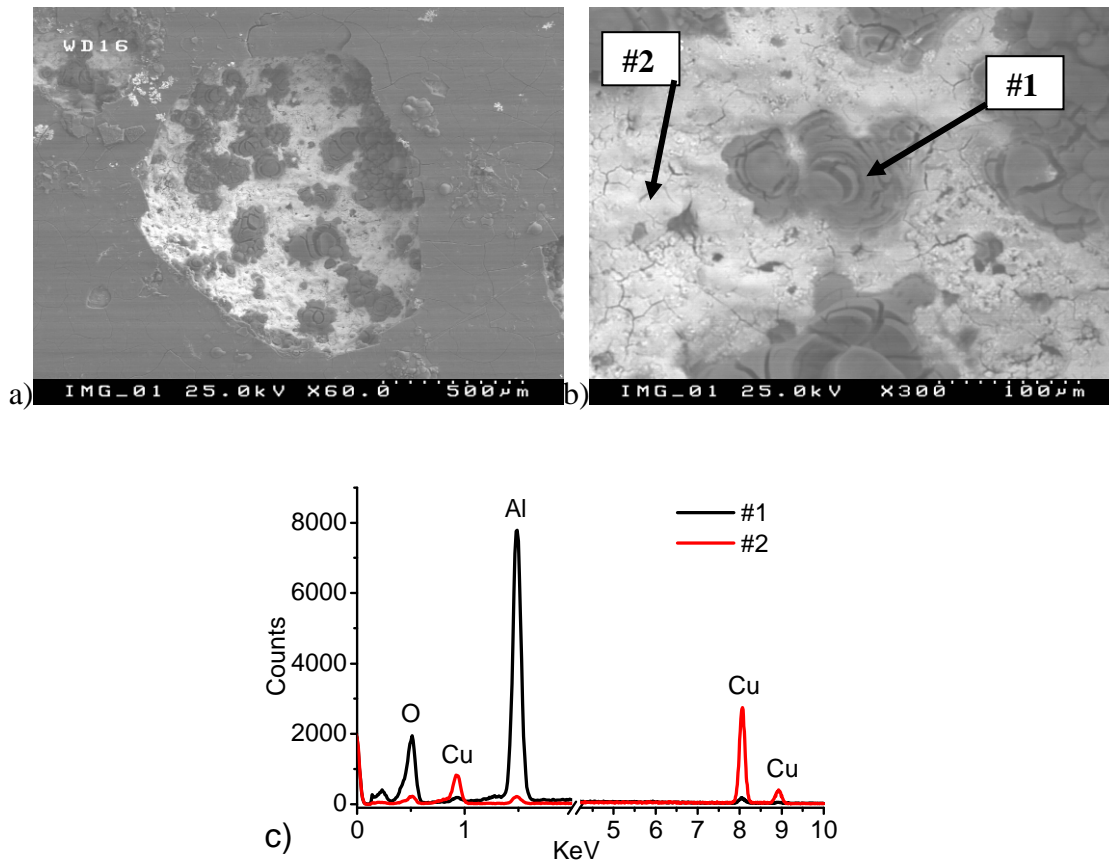
Figure 5.1.7. Back-scattering electron micrographs made on AA2024 at the place of pit after immersion in 0.5M NaCl for 2 months; EDS spectra taken at two places c); Surface of the sample was preliminary cleaned from the layer of corrosion products before the investigation.

5.1.3 Mechanism of localized corrosion of AA2024

The obtained experimental results provide evidence of complicated processes occurring during the corrosion of the alloy. It is clear that the initial step of corrosion is localized and involves the copper rich phase. Refining of the intermetallics increases copper content and corrosion of the alloy. However the experimental approaches employed in this study give only qualitative description of the obtained results. The present paragraph provides explanation of the results based on thermodynamics.

Under normal conditions the 2024 aluminium alloy as well as any other aluminium-based substrates is covered by a native oxide film. However, the intermetallics have a thinner and more defective oxide film due to the presence of different elements in the intermetallic phase. Immediately after contact of the alloy with a chloride-containing environment the chloride ions interact with the native oxide film (Figure 5.1.8a) leading to its breakdown especially in the weak places where the S-phase intermetallic precipitates

124

which are shown in Figure 5.1.1. Water contacts with the intermetallic surface after failure of the barrier oxide layer causing the chemical reaction of active aluminium and magnesium with water (Figure 5.1.8b):

$$2Al + 6H_2O \rightarrow 2Al^{3+} + 6OH^- + 3H_2 \uparrow, \tag{5.1.1}$$

$$Mg + 2H_2O \rightarrow Mg^{2+} + 2OH^- + H_2 \uparrow. \tag{5.1.2}$$
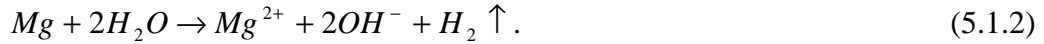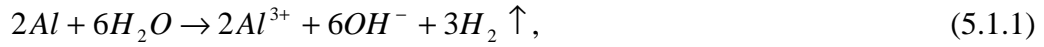
The chemical dealloying of S-phase occurs due to these processes leading to the formation of a copper-rich surface and local non-uniformities of the intermetallics composition. The possibility of chemical dealloying was not discussed before in the literature. However, clearly visible gas bubbles are formed at the initial stage of the corrosion processes at the location of pitting initiation as shown in the Figure 5.1.9. The evolution of hydrogen can be the only reason for formation of such gas bubbles. The simple chemical red/ox reaction of hydrogen evolution is a preferable way when compared with the electrochemical one since the electrochemical reduction of water can occur only at cathodic polarizations. The most likely cathodic process is the reaction of oxygen reduction due to very high overpotential of the electrochemical hydrogen evolution on copper-rich cathodes [333]. Thus the hydrogen evolution evidently proves the occurrence of reactions (5.1.1) and (5.1.2). However in parallel the electrochemical dissolution can take place at this stage as well causing faster dealloying.
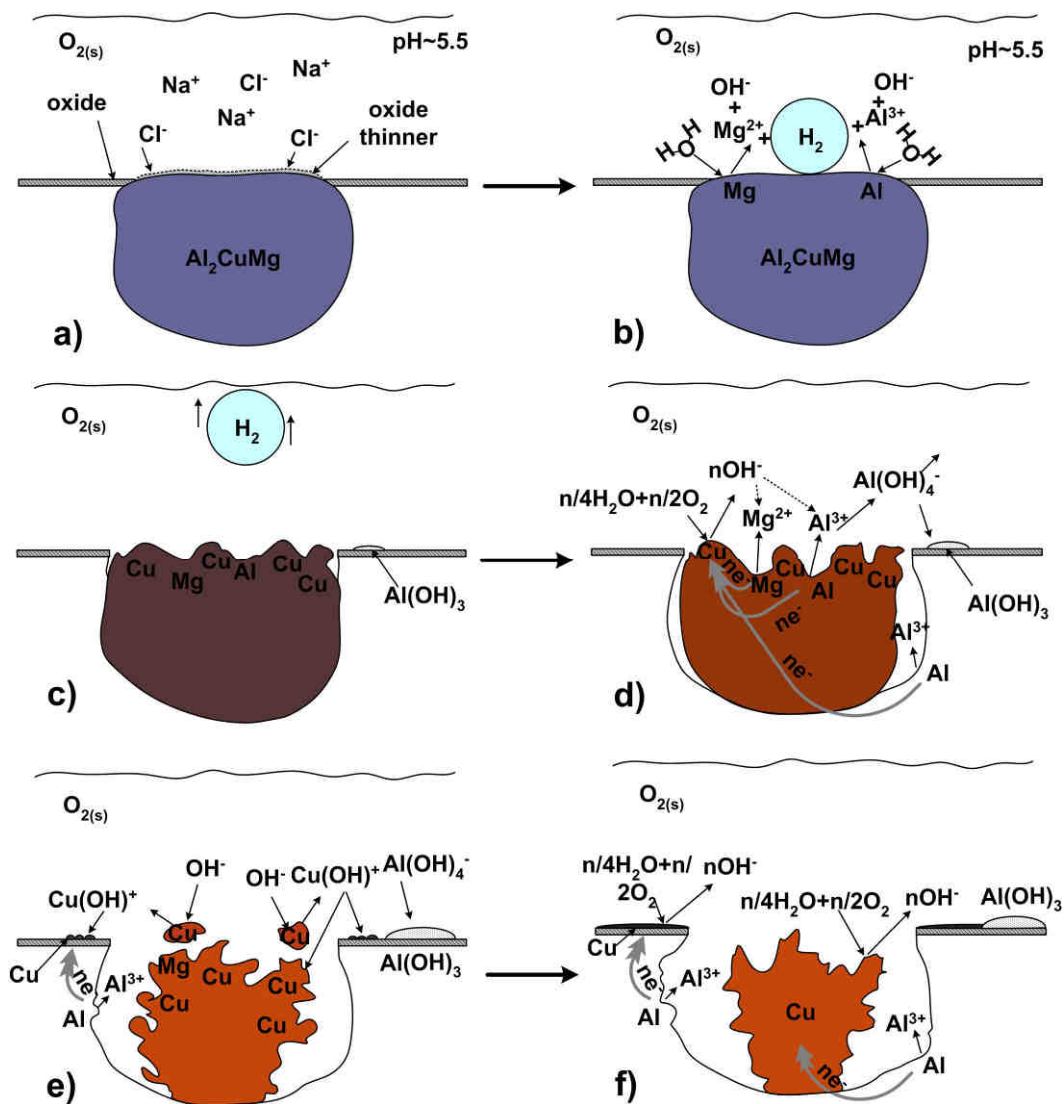
Figure 5.1.8. Schematic representation of corrosion mechanism of AA2024 in chloride solution.

a) corrosion attack of metal surface near intermetallic inclusion in chloride containing solution

b) reaction of magnesium and water with elaboration of hydrogen

c) ennoblement of the intermetallic surface with copper and dissolution of the surrounding aluminium matrix

d) dissolution of more active elements (Al, Mg) due to the galvanic coupling with copper

e) formation of copper rich remnant, copper redeposition process and aluminium matrix dissolution

f) increased area of copper stimulates cathodic process of oxygen reduction and, therefore, anodic dissolution of aluminium matrix

126

Figure 5.1.9. Optical photograph of the surface of the AA2024 at the beginning of the immersion test in NaCl solution; on the left and right sides bubbles are seen.

The local increase of pH around the S-phase particles as well as enrichment of their surface with copper lead to shifting the dissolution processes from chemical to electrochemical. The hydrogen generation on the alloy surface stops and an electrochemical dissolution starts (Figure 5.1.8c,d). The cathodic reaction occurs on copper-rich remnants by the following equation:

$$O_2 + 2H_2O + 4e^- \rightarrow 4OH^-.\qquad(5.1.3)$$

Simultaneously the oxidation of magnesium and aluminium occurs at the anodic parts of the S-phase:

$$Al \rightarrow Al^{3+} + 3e^-,\qquad(5.1.4)$$

$$Mg \rightarrow Mg^{2+} + 2e^-.\qquad(5.1.5)$$

Dissolution of aluminium and magnesium leads to deeper dealloying of the S-phase forming the porous copper remnants with "Swiss cheese"-like morphology.

An additional increase of the pH occurs due to cathodic reaction (5.1.3) at the surface of the intermetallic. This leads to formation of sufficient gradient of OH⁻ ions between the bulk solution and the surface of the intermetallic particle. The aluminium and magnesium cations can immediately react with hydroxyl ions forming insoluble hydroxide sediments or soluble hydroxy-complexes (Figure 5.1.8d) depending on pH values:

$$Al^{3+} + OH^- \rightarrow Al(OH)^{2+}, \qquad \log K = 9.03 \qquad(5.1.6)$$

$$Al^{3+} + 2OH^- \rightarrow Al(OH)_2^+, \qquad \log K = 18.7 \qquad(5.1.7)$$

$$Al^{3+} + 3OH^- \rightarrow Al(OH)_3 \downarrow, \qquad \log K = 27 \qquad(5.1.8)$$

$$Al^{3+} + 4OH^- \rightarrow Al(OH)_4^-, \qquad \log K = 33 \qquad\qquad (5.1.9)$$

$$Mg^{2+} + OH^- \rightarrow Mg(OH)^+, \qquad \log K = 2.58 \qquad\qquad (5.1.10)$$

$$Mg^{2+} + 2OH^- \rightarrow Mg(OH)_2 \downarrow, \qquad \log K = 11.33 \qquad\qquad (5.1.11)$$
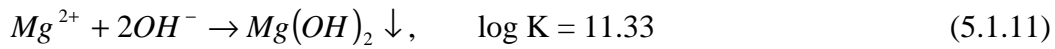
Figures 5.1.10a,b,c present the fraction of the different aluminum, magnesium and copper species in the solution depending on the pH. These fractions were calculated using thermodynamic formation constants for metal hydroxocomplexes which were taken from [17,334]. Such diagrams give a clear picture of the complexes distribution and complement the Pourbaix diagrams. Different aluminum species are present in aqueous solutions due to the possibility of formation of soluble complex compounds both in acidic and basic conditions (Figure 5.1.10a). The pH value is very high in the cathodic zones where hydroxyl ions are generated. The aluminum cations originated from anodic dissolution of the S-phase interact with the hydroxyl anions generated at the cathodic zones and form Al(OH)$_4^-$ complex ions, which diffuse to the bulk solution. Reaching the zones of the solution with lower pH (about 8) the complex anions are transformed into the insoluble Al(OH)$_3$, that is a thermodynamically preferable state at such conditions (see Figure 5.1.10a). Thus, aluminium hydroxide forms an insoluble deposit at a certain distance from the active intermetallic (Figure 5.1.8d). Longer corrosion leads to formation of a hydroxide dome covering the active pitting. Aluminum hydroxychlorides are formed at lower pH values on the periphery of the hydroxide sediments as was pointed out in [335]. The magnesium cations can also form hydroxide sediments; however a major part of magnesium is in solution due to the higher solubility of its hydroxide and the lower content of Mg in the alloy.

The electrochemical dissolution of magnesium and aluminium from the S-phase leads to the formation of a very porous structure with the copper particles connected to the copper remnants. When the neck between a copper nanosized particle and a remnant is broken the particle losses the electrical contact with the alloy [336] as demonstrated in Figure 5.1.8e. Then the chemical reaction of copper oxidation by dissolved oxygen is thermodynamically possible:

$$2Cu + O_2 + 2H_2O \rightarrow 2Cu(OH)_2, \Delta G = \text{-271.23 kJ} \cdot \text{mol}^{-1} \text{ [17]} \qquad (5.1.12)$$
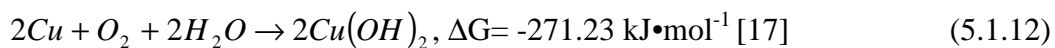
The nanosize confers even an enhanced reactivity to the copper particles. Partial dissolution of the copper hydroxide occurs due to formation of hydroxocomplexes as shown in Figure 5.1.10b. The complex ions are electrochemically reduced again to metallic copper on the surface of the aluminium alloy or on the copper remnants formed after dealloying as schematically shown in Figure 5.1.8e. The formation of chloride-based complexes can also assist the dissolution of copper particles. The reduced metallic copper redeposited on the copper remnants leads to copper "refining". When redeposited on the alloy surface around pits, it forms a thin film as it was demonstrated by optical microscopy (Figure 5.1.6). The redeposition of copper around the S-phase leads to broadening of the cathodic peaks on the VPD maps shown in Figures 5.1.2 and 5.1.4. Therefore, the SKPFM

128

technique can be used to detect the level of corrosion impact on the intermetallic particles. The effect of copper redeposition was previously discussed in the literature [336,337]. Another mechanism for this process was proposed in [18] ascribing migration of Cu particles from dealloyed intermetallic over the pit. The thin layer of copper redeposited around pits can play a role of an additional cathode accelerating the anodic processes of aluminium dissolution from the S-phase and from the surrounding alloy matrix, which is depleted in copper and is anodically active (Figure 5.1.2, 5.1.3). The localized corrosion process becomes thus autocatalytic. Therefore, redeposition of copper appears as a very important factor responsible for fast propagation of pits around intermetallics.
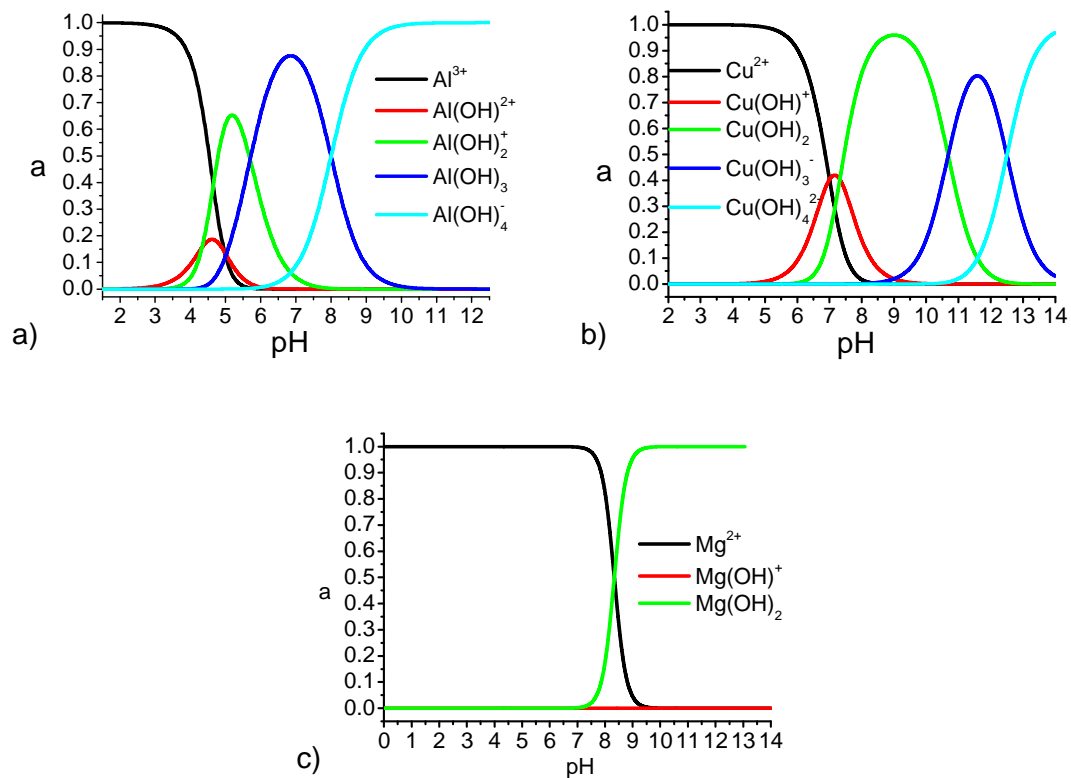
Figure 5.1.10. Fraction "a" of different metal species in the solution depending on pH.

The present results demonstrate the prime importance of the S-phase in the localized corrosion of AA2024 and show that the S-phase intermetallics do not function only as a cathode or as an anode in the corrosion processes, but play a complex role combining cathodic and anodic activity together in the same particle. Therefore, different strategies can be used to stop the localized corrosion of these intermetallics and protect AA2024 in chloride-containing environments.

Summarizing

The mechanism proposed for corrosion of AA2024 highlights an important role for the intermetallics in the localized corrosion process. The pitting corrosion begins at the places of the S-phase intermetallics, which have a cathodic potential relative to the alloy matrix. S-phase dealloying starts by the chemical attack dissolving the active aluminium and magnesium and leaving copper-rich remnants. Then the electrochemical processes take place and the S-phase intermetallics play the role of active anodes and cathodes causing at the same time deeper dealloying. The process of copper redeposition, which leads to formation of refined copper remnants and copper film deposits around pits, plays an important role in further development of the local corrosion attack. The redeposited copper increases the effective surface area of the cathodic zone, which is confirmed by the spreading of cathodic peaks on the VPD maps.

5.2 Inhibition of localized corrosion of AA2024 with Rare Earth ions

The results obtained in the previous section demonstrate the important role of the S-phase in the localized corrosion of the alloy. The main role of such intermetallics is to participate in the cathodic reaction of oxygen reduction that is coupled with the anodic process of alloy matrix dissolution. Effective blocking of the cathodic process can reduce the overall corrosion of the alloy. It is known that lanthanide salts are good inhibitors of the cathodic process on different metallic substrates and have a potential to be used as inhibitors in the sol-gel pretreatments.

In this paragraph the corrosion inhibition effect of cerium and lanthanum salts is additionally investigated for bare AA2024 substrate. Different corrosive solutions based on NaCl with or without cerium (III) and lanthanum (III) nitrates were prepared to study the effect of rare-earth cations on the localized corrosion activity of AA2024. Concentrations of Ce and La in prepared solutions were ranged from 0.001 to 0.15 M. Electrochemical techniques like DC polarization and EIS as well as microstructural (SEM/EDS) and localized techniques (AFM/SKPFM) have been used in this study.

5.2.1 SEM/EDS results

Scanning electron microscopy revealed much lower corrosion in the case of the alloy immersed during 1 hour in chloride solution with 0.15M of cerium nitrate than that for undoped chloride solution. Mainly the alloy surface is free of pitting (not shown). However, in some places signs of corrosion activity appear as depicted in Figure 5.2.1. White spherical deposits are locally formed on the alloy surface. The removal of such deposit formed after 2 hours of immersion shows the signs of localized corrosion attack under the dome (Figure 5.2.1.b). Careful EDS analysis shows that white deposits are composed mainly by cerium oxide (hydroxide) and they are located only in places of S-phase intermetallics (zone 1). The Al (Fe, Cu, Mn, Si) intermetallics (zone 2) are free of deposits and do not show any signs of corrosion activity. Some S-phase particles which are not corroded do not have cerium hydroxide domes (zone 3). Decrease of Ce concentration in solution leads to less pronounced corrosion activity and lower amount of spherical deposits (Figure 5.2.1.c). Stronger corrosion impact and deeper dissolution of S-phase in the case of the higher concentration of inhibitor can be due to lower pH values originated by hydrolysis of cerium ions. The measured pH values of 0.0015, 0.015 and 0.15M solutions of $Ce(NO_3)_3$ are 5.53, 5.12 and 4.51 respectively. The low pH values of the electrolyte can lead to faster chemical reaction of water with magnesium or aluminium from the S-phase at the initial stages.
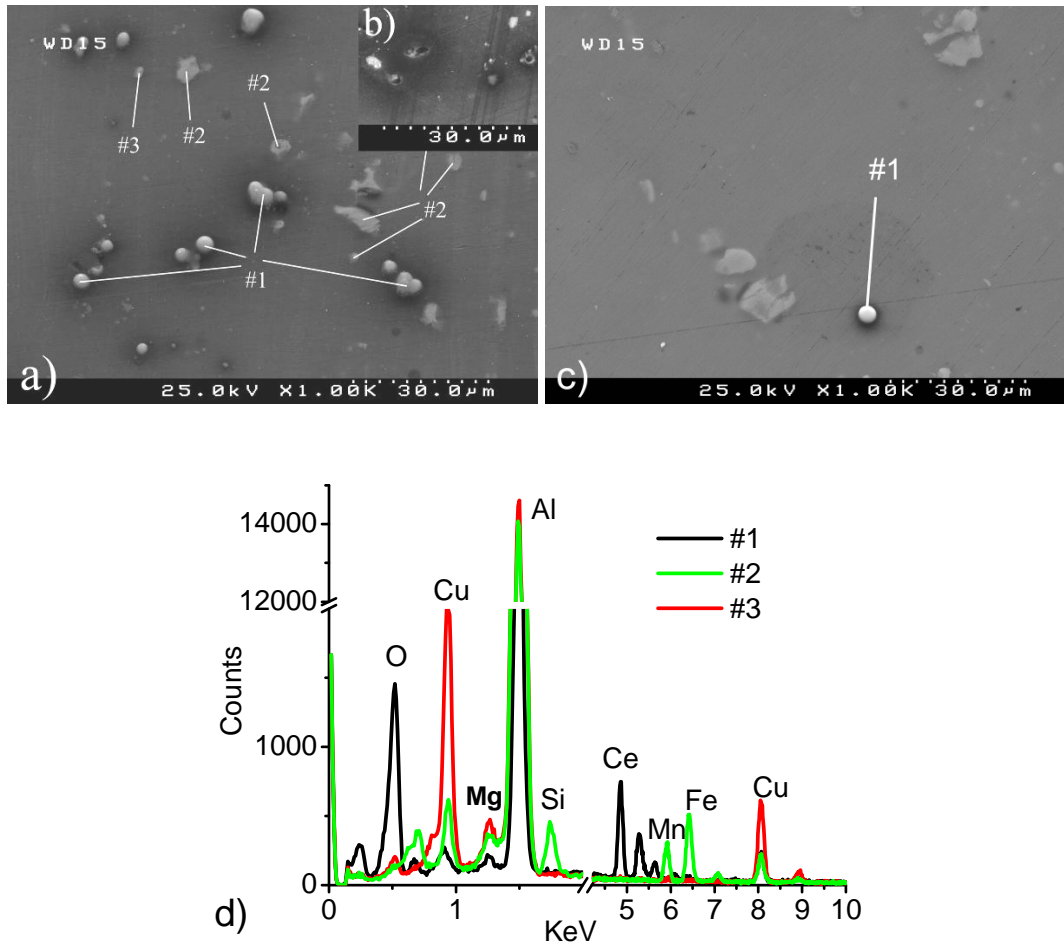
Figure 5.2.1. SEM image of the AA2024 after immersion for 1 h in 0.005M NaCl with 0.15M of Ce(NO$_3$)$_3$ a); inset picture presents micrograph after 2 h of immersion b); surface after immersion for 2 h in 0.005M NaCl with 0.0015M of Ce(NO$_3$)$_3$ is presented in picture c); EDS analysis of the areas indicated in SEM images d).

Figure 5.2.2a shows the surface of AA2024 after 1 hour immersion in the chloride solution doped with 0.15M of La(NO$_3$)$_3$. Features similar to the case of the cerium doped electrolyte are revealed on the surface of the alloy. The white deposits are formed in the places of S-phase intermetallics and the pitting-like defects are revealed under the lanthanum hydroxide domes. The EDS analysis (Figure 5.2.2c) demonstrates that the formation of lanthanum hydroxide deposits occurs only in the places of active S-phase intermetallics as in the case of cerium doped electrolytes. No signs of corrosion activity were revealed around Al(Fe, Cu, Mn, Si) intermetallics as well. The decrease of La(NO$_3$)$_3$ concentration down to 0.0015M leads to lower corrosion impact as shown in Figure 5.2.2b. Higher localized corrosion activity in the case of the electrolytes heavily loaded with lanthanum inhibitor can also be caused by the lower pH as in the case of cerium nitrate solutions.
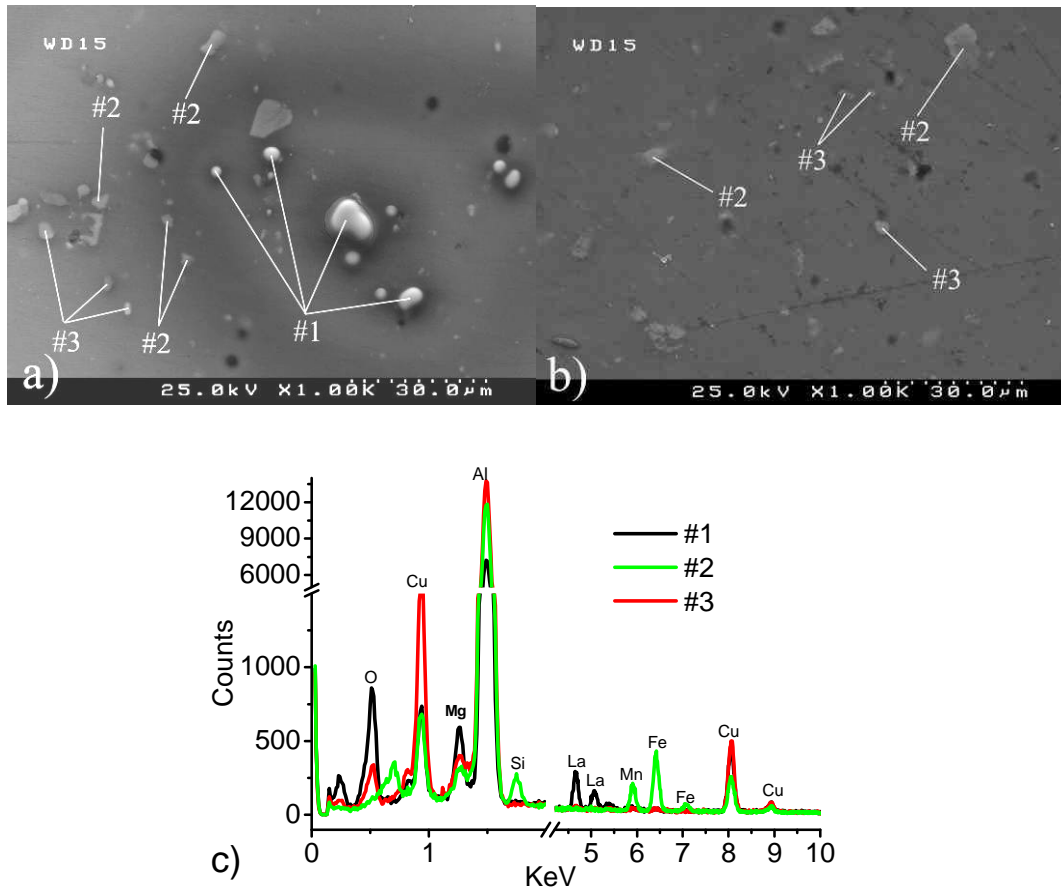
Figure 5.2.2. SEM image of the AA2024 after immersion for 1h in 0.005M NaCl with 0.15M of $La(NO_3)_3$ a) and for 2 h in 0.005M NaCl with 0.0015M of $La(NO_3)_3$ b); EDS analysis of the areas indicated c).

5.2.2 AFM and SKPFM results

The topography AFM and VPD maps presented in Figure 5.2.3a,b, confirm the selective deposition of cerium hydroxide precipitates in the cathodic places. Previous SKPFM studies also showed the cathodic nature of the intermetallic inclusions of the 2024 aluminum alloy [266]. The deposits are sharp peaks on the AFM scan (Figure 5.2.3c) after 1 hour of immersion in chloride electrolyte doped with 0.15M of cerium nitrate. They are formed only in the places of the active intermetallics which show Volta potential peaks broadened due to copper redeposition processes described above. The VPD map of AA2024 tested in the lanthanum-containing electrolyte demonstrates similar behavior (Figure 5.2.4a,b,c). The hydroxide deposits are also formed in the places of cathodic intermetallics. This suggests that the main mechanism of corrosion inhibition can be similar in the cases of different RE salts.

a)   b)

c)
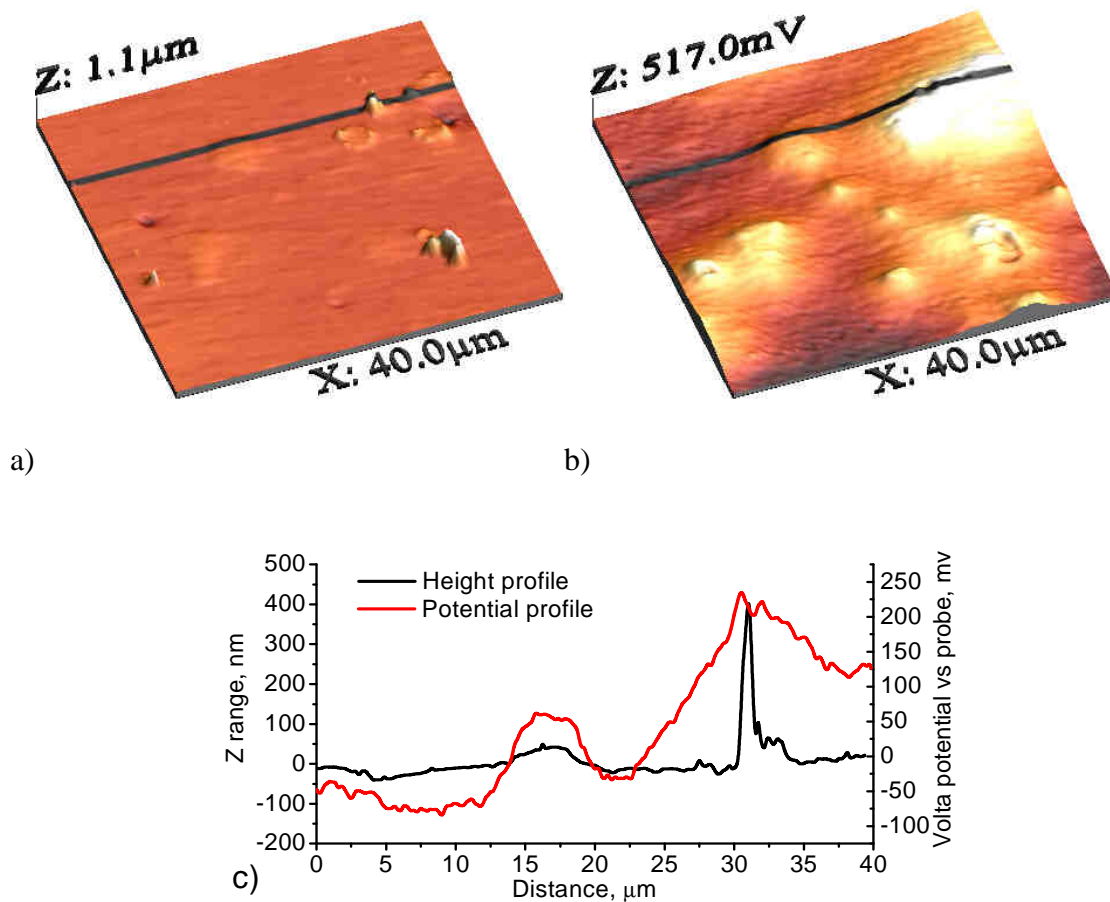
Figure 5.2.3. Topography (a), VPD map (b) and Height and VPD Profile (c) for AA2024 immersed in 0.005M NaCl solution with 0.15M $Ce(NO_3)_3$ for 1 hour.
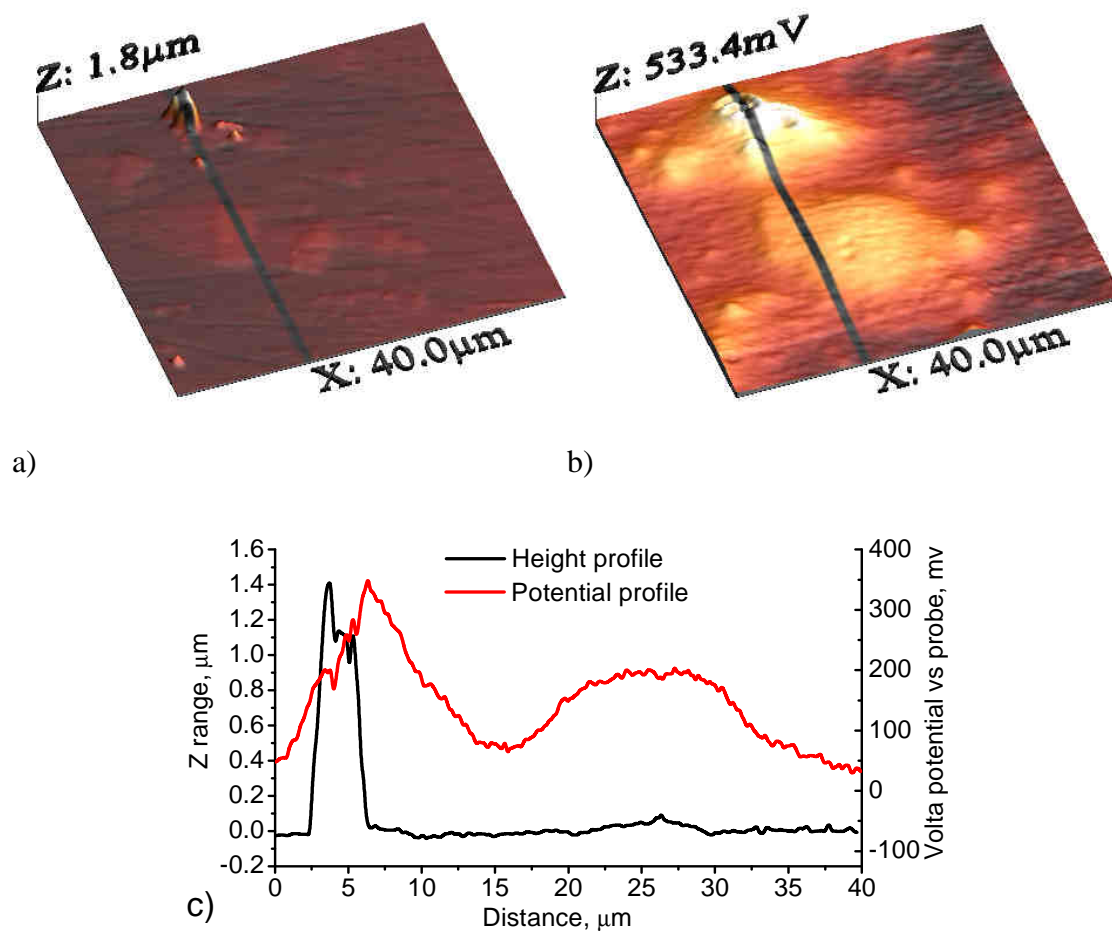
Figure 5.2.4. Topography (a), VPD map (b) and Height and VPD Profile (c) for AA2024 immersed in 0.005M NaCl solution with 0.15M La(NO$_3$)$_3$ for 1 hour.

When the corrosion process starts the broadening of the Volta potential peaks on intermetallics always occurs due to the S-phase dealloying and the copper redeposition on the surrounding alloy. Therefore the degree of peak broadening directly depends on the level of corrosion impact and can be used as a qualitative characteristic of the corrosion protection efficiency at initial stages of localized corrosion. Figure 5.2.5 demonstrates two VPD maps obtained on the AA2024 after 1 hour in 0.005 M NaCl doped with the different concentrations of cerium nitrate. The broadening of the VPD maxima is more pronounced in the case of the 0.15M Ce(NO$_3$)$_3$ electrolyte (Figure 5.2.5b) than in the case of 0.015M Ce(NO$_3$)$_3$ electrolyte (Figure 5.2.5a). These maps show that too high concentration of cerium nitrate (0.15M) leads to a higher broadening of VPD and deeper localized corrosion in the places of the S-phase intermetallics.

a)   b)
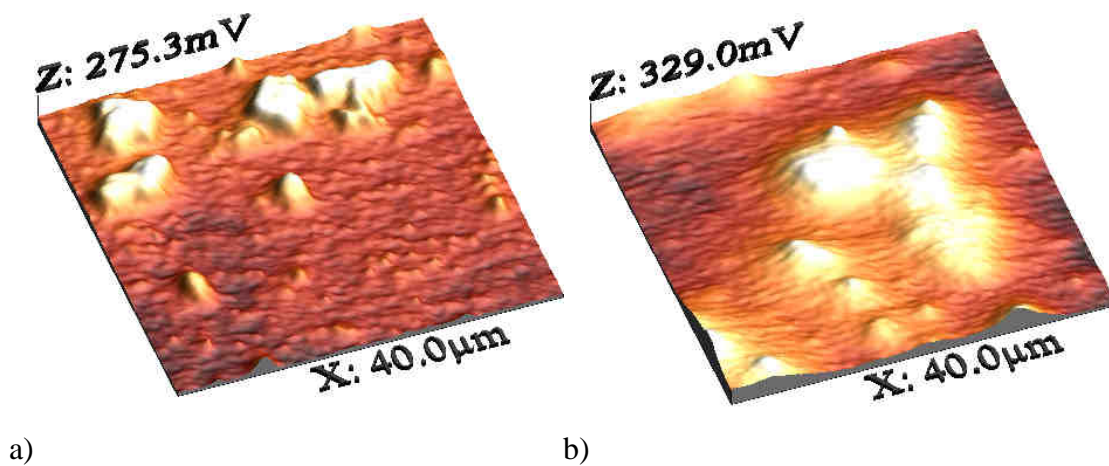
Figure 5.2.5. VPD maps for AA2024 immersed in 0.005M NaCl solution with 0.015M Ce(NO$_3$)$_3$ (a) and 0.15M Ce(NO$_3$)$_3$ (b) for 1 hour.

a)

b)

c)
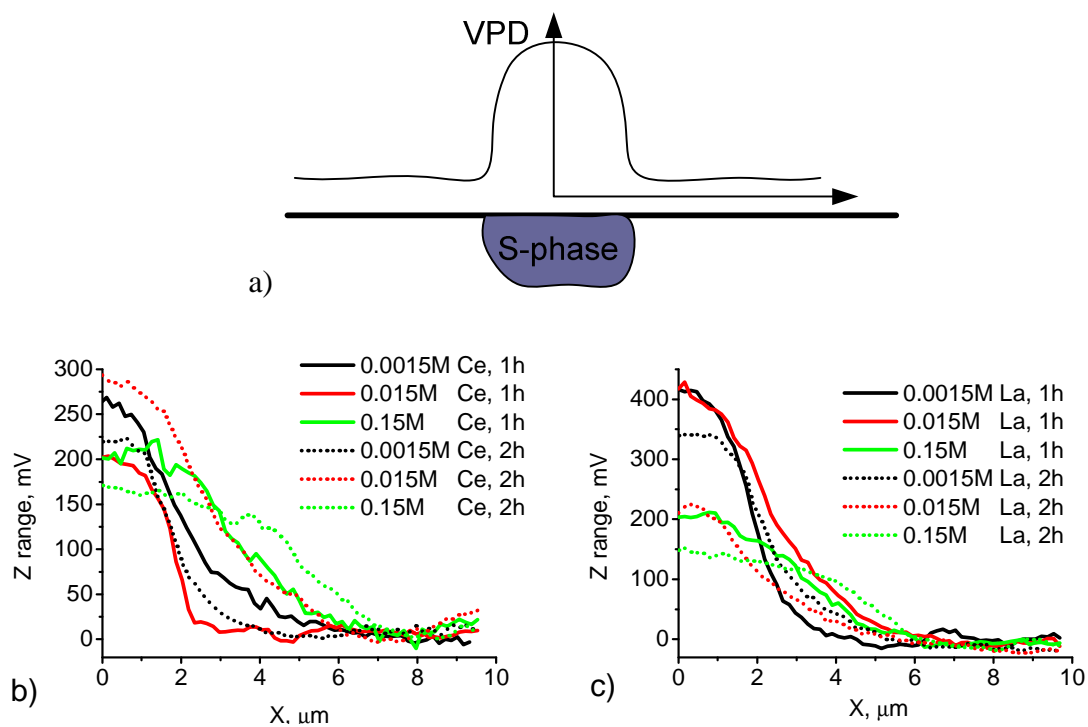
Figure 5.2.6. Evolution of the VPD profiles across the S-phase intermetallic particles (a) for the AA2024 samples immersed in 0.005M NaCl solution with 0.15M, 0.015M, 0.0015M of Ce(NO$_3$)$_3$ b), and with 0.15M, 0.015M, 0.0015M of La(NO$_3$)$_3$ c).

Profiles across the intermetallic particles were made on VPD maps for the alloy specimens after immersion in different electrolytes to compare the VPD between the intermetallic particles and alloy matrix (Figure 5.2.6). The potential profiles were recorded for alloy substrates immersed for two different periods in the chloride solution doped with different concentrations of cerium or lanthanum-based inhibitors. Figure 5.2.6a presents potential profiles for the alloy immersed in the cerium containing solutions. The increase of the immersion time tends to well-defined spreading of the transition region between the potential of the S-phase and that of the alloy matrix. This is especially seen for 0.15 and 0.015M cerium nitrate solutions (Figure 5.2.6a). The spreading of Volta potential is caused by the local corrosion process that develops in the places of cathodic S-phase intermetallics during immersion of the alloy in NaCl solution. As was mentioned above the concentration of cerium nitrate has a great influence on the inhibition efficiency. At the beginning of corrosion tests, the 0.015M solution evidences minimal potential broadening and in turn maximal efficiency in comparison with other concentrations (Figure 5.2.6a). After 2 hours of immersion the broadening of Volta potential is smaller when using 0.0015M inhibitor compared to 0.15M inhibitor. The VPD peak does not have a well-defined frontier between the potential of the S-phase and that of the alloy matrix when AA2024 is immersed in 0.15M $Ce(NO_3)_3$ for two hours. Careful analysis of VPD profiles (Figure 5.2.6a) clearly shows the higher corrosion inhibition efficiency when the electrolyte with concentration of cerium nitrate of 0.0015M to 0.015M is used. The VPD profiles of the alloy immersed in the chloride solution doped with lanthanum-based inhibitor (Figure 5.2.6b) demonstrate similar behavior to that reported above for Ce. Spreading of the VPD maxima slightly increases with immersion time. The concentration of inhibitor also has strong influence on the shape of the potential profiles as in the case of cerium nitrate. However a maximal inhibition efficiency was revealed when the electrolyte with lower concentration 0.0015M of $La(NO_3)_3$ was used. The optimal concentration of the RE cation inhibitors obtained with the SKPFM method is in good agreement with results reported elsewhere obtained by other methods for other aluminium alloys [46,338].

5.2.3 In-situ AFM study

In-situ AFM measurements of the AA2024 surface during immersion in the electrolyte doped with different concentrations of cerium or lanthanum-based inhibitors were performed in order to study the kinetics of hydroxide deposits formation on the cathodic S-phase particles. Figure 5.2.7 presents the evolution of the alloy topography in the place of cathodic intermetallics during immersion in La-doped NaCl solution. The topography of the alloy exhibits a weakly defined hill after 24 minutes of immersion (Figure 5.2.7a), which can be ascribed to the precipitate formed on the intermetallic. The substrate was immersed during 5 hours and 23 minutes in the electrolyte containing 0.005 M NaCl and 0.015M of $La(NO_3)_3$. Then the electrolyte with higher concentration of chloride (0.5 M) and same concentration of inhibitor was introduced in the AFM cell

instead of the diluted one and scanning of topography was continued for about one hour. The relatively high deposit (about 800 nm) is formed on this intermetallic after 6 hours and 20 minutes of continuous immersion (Figure 5.2.7b). Figure 5.2.7c presents the evolution of the height profile across the hydroxide deposit formed on the surface in the places marked by black lines on the AFM scans. Relatively slow growth of the deposit occurs during the first period of immersion (in weak electrolyte). Two orders of magnitude increase in chloride concentration leads to higher rate of lanthanum hydroxide deposition.
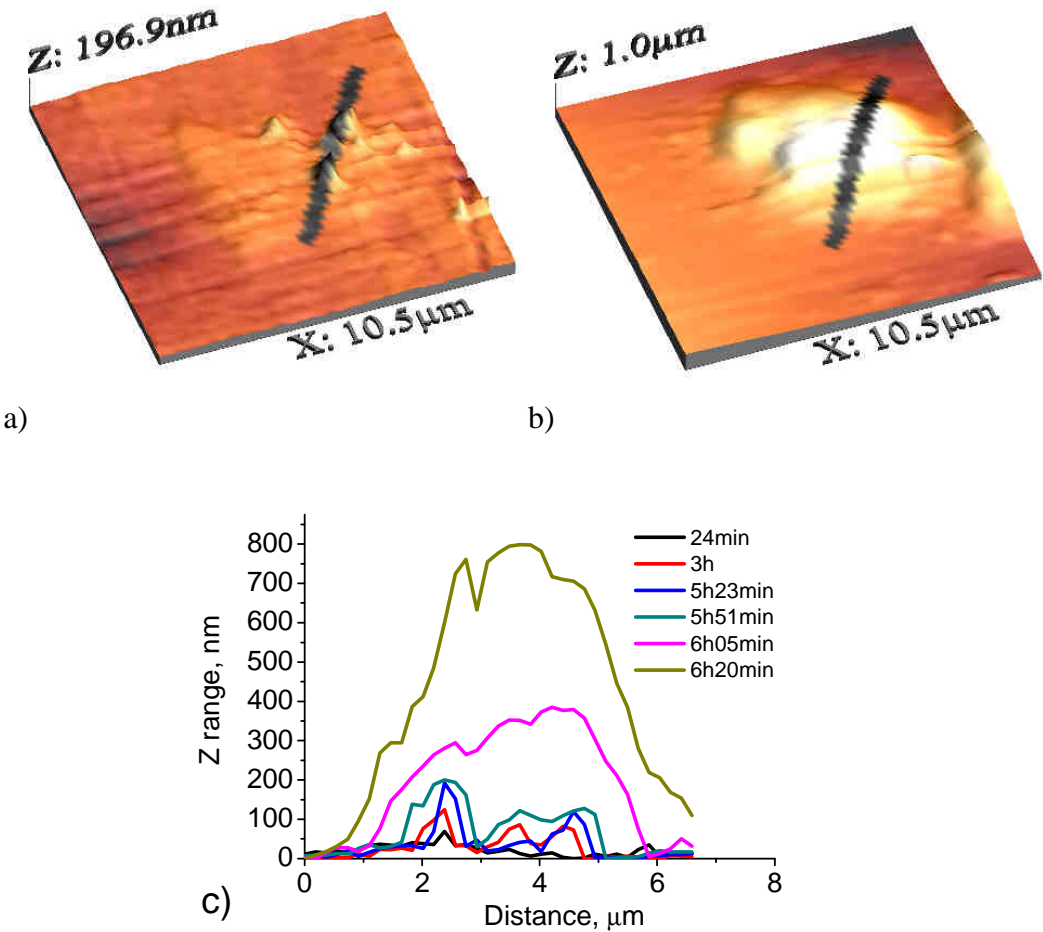
Figure 5.2.7. In-situ AFM scans of the AA2024 surface after 3h of immersion in 0.005M NaCl with 0.015M $La(NO_3)_3$ a) and at the end of immersion in 0.5M NaCl with 0.015M $La(NO_3)_3$ solution (b) and evolution of height profile in the solution of 0.005M and 0.5M NaCl with time (c).

Figure 5.2.8 shows the kinetics of the La(OH)$_3$ precipitate formation at the place presented in the Figure 5.2.7. A linear kinetic law can be used to describe the rate of the deposits formation. The estimated rate of the precipitate growth is about 0.4 nm/min in the weak chloride-based electrolyte. However, the rate is increased by almost 50 times reaching 20 nm/min when concentrated solution is used. These results indicate a very important role of the chloride ions in the kinetics of the hydroxide deposits formation. Obviously the increase of chloride concentration leads to enhanced corrosion activity which consequently increases the pH in the places of active intermetallics leading to faster local deposition of hydroxide precipitates. Thus, the RE salts work as an "intelligent" inhibition system with an active feedback to the corrosive medium.
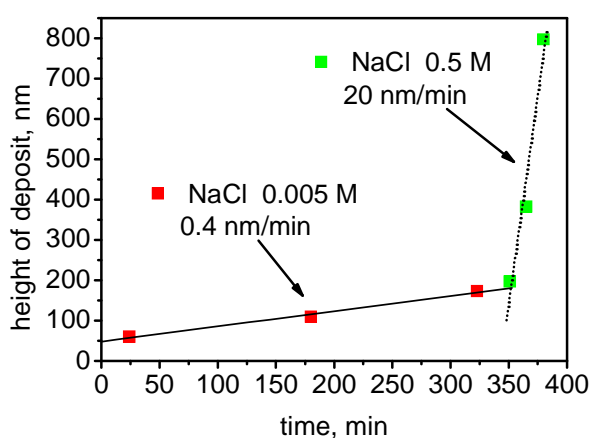
Figure 5.2.8. Rate of the lanthanum hydroxide precipitation at the place showed in Figure 5.2.7 in 0.005M NaCl at the beginning (red squares) and in 0.5M NaCl (green squares) at the end of in-situ AFM measurement.

5.2.4 DC polarization

Potentiodynamic polarization measurements were carried out in the potential range from -0.25 V to 0.2 V vs. open circuit potential to estimate the effect of the different inhibitors on the anodic and cathodic partial electrode reactions. To clarify kinetic features of the inhibition process the polarization curves were recorded after different periods of immersion at the open circuit potential in 0.05 M chloride electrolyte doped with 0.0015M of Ce or La nitrate inhibitors. Alloy substrates prior to polarization were prepared according to the procedure described in paragraph 4.2.3.

Figure 5.2.9a presents the DC polarization curves for AA2024 in the undoped and in cerium-doped solutions. The anodic branch shows two well defined breakdown

potentials corresponded to the S-phase dissolution (in case of AA2024 at lower polarization) and to the beginning of the intergranular corrosion (higher polarization) as was shown in ref. [339] and in ref. [340] for AA7075 alloy. Doping of chloride electrolyte with cerium nitrate leads to remarkable decrease of cathodic and anodic currents. After only 10 minutes of immersion in doped solution at the open circuit potential the cathodic current during polarization drops almost by one order of magnitude. Increase of the immersion time leads to further decrease in cathodic current showing that interaction of cerium cations with the cathodic centers is a relatively slow process which can take several hours to achieve maximal inhibition of the cathodic reaction. The oxygen reduction is the main process in the cathodic region of the polarization curves.

The anodic processes are also influenced by the cerium-based inhibitor. Remarkable decrease of anodic current between the two breakdown potentials already occurs after only 10 minutes of immersion. This current is related with the dissolution of Al and Mg from Al_2CuMg intermetallics. After longer immersion time the anodic current decreases in this region almost by two orders of magnitude when compared with that of the undoped chloride solution. An important shift of the second breakdown potential toward positive potentials occurs with increase of the immersion time. Decrease of cathodic and anodic currents is originated from the formation of cerium hydroxide deposits in the places of S-phase intermetallics. This confirms that anodic and cathodic reactions at low polarizations occur mainly at the Al_2CuMg precipitates in the AA2024 matrix. The longer immersion time before polarization leads to formation of larger deposits on the S-phase hindering the cathodic reduction of oxygen on Cu-rich intermetallics as well as anodic dissolution of Al and Mg from these intermetallics.

The influence of lanthanum nitrate on the corrosion of AA2024 was also studied by DC polarization (Figure 5.2.9b). The behavior of the alloy in the La-doped chloride solution is similar to that of the Ce-doped one. However, the inhibition effect of lanthanum cations for cathodic reactions is lower than in the case of cerium-based inhibitor. The hindering of anodic dissolution of the S-phase is also less effective when compared with the cerium doped electrolyte. While, the inhibition effect appears almost immediately after starting the immersion (10 minutes) and keeps constant value even after 2 hours, demonstrating a faster kinetics of the hydroxide deposits formation.
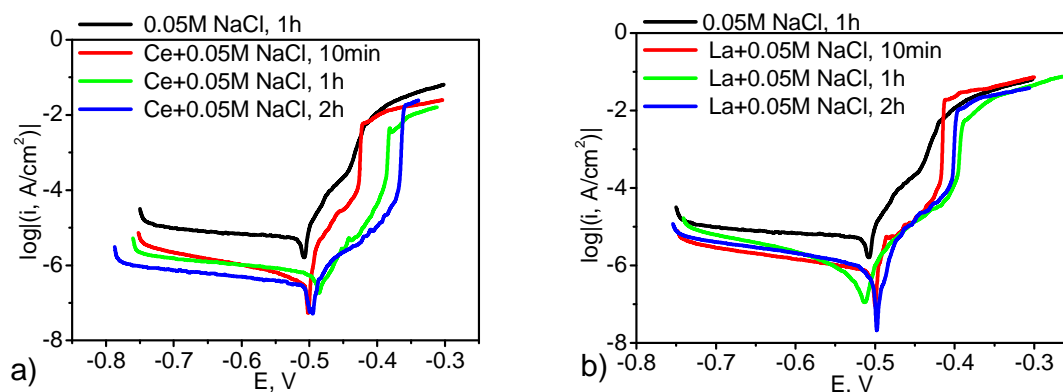
Figure 5.2.9. Potentiodynamic polarization curves for the AA2024 in 0.05M NaCl solution without cerium nitrate (after 1 hour of immersion) and with 0.0015M of $Ce(NO_3)_3$ inhibitor after 10 min, 1 h and 2 h of immersion a), and 0.0015M of $La(NO_3)_3$ after 10 min, 1 h and 2 hours of immersion b).

5.2.5 EIS study

Impedance measurements were carried out in 0.05M NaCl solution with Ce or La nitrate salts added as inhibitor during 2 weeks of immersion to supplement the results of DC polarization tests. A concentration 1 mM of Ce or La species was used in the study. Alloy substrates prior to investigation were prepared according to the procedure described in paragraph 4.2.4.

Figure 5.2.10 presents impedance spectra of AA2024 during immersion in 0.05M NaCl solution with and without addition of Ce or La salts. The use of 1mM Ce in the solution provides a good corrosion inhibition during 1 week of immersion (Figure 5.2.10a). EIS spectra after 1 week of immersion show the presence of only one clearly defined relaxation process near 10 Hz ascribed to the barrier oxide film. A longer immersion time leads to decrease of low frequency impedance and appearance of small pits on the surface (Figure 5.2.11a). Such behaviour is consistent with the appearance of a second time constant near 0.01 Hz that is related to the corrosion of the alloy though a time constant associated with the barrier oxide film is still visible at higher frequency (Figure 5.2.10a).

After one day of immersion in 1mM La containing solution impedance at low frequency is lower than in Ce containing solution (Figure 5.2.10a). Barrier oxide film is quickly degraded during immersion in La solution and after 14 days impedance lowers until around 20 kOhm cm^2 (Figure 5.2.10a). Such behaviour is accomplished with a strong pitting attack shown in Figure 5.2.11b.

Impedance spectra of alloy during immersion in NaCl solution only are presented in Figure 5.2.10b. As can be seen a corrosion progress is fast and after 1 day of immersion the

response from the native oxide film almost disappears and is overwhelmed by the corrosion process. A time constant that appears at lower frequencies is most probably associated with mass transport limitations. Impedance modulus at longer immersion time decreases compared to initial immersion time. EIS spectrum shows two time constant elements at around 2Hz that is related to corrosion and at low frequencies that is associated with diffusion limitations. Optical photograph after 2 weeks of immersion in NaCl solution only shows strong pitting activity and the surface is totally covered by a layer of white corrosion products (Figure 5.2.11c).
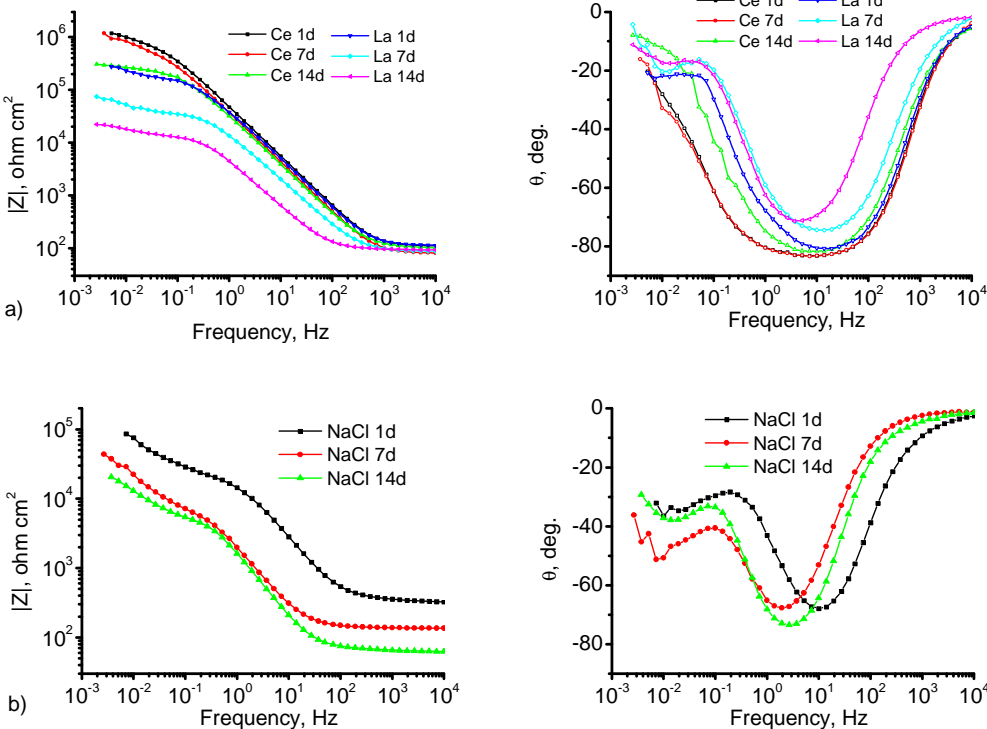
Figure 5.2.10. Bode plots of AA2024 recorded during different time of immersion (1, 3, 7, 14 days) in 0.05M NaCl solution with 1mM Ce or La salts a); bode plots of alloy immersed in 0.05M NaCl solution b).
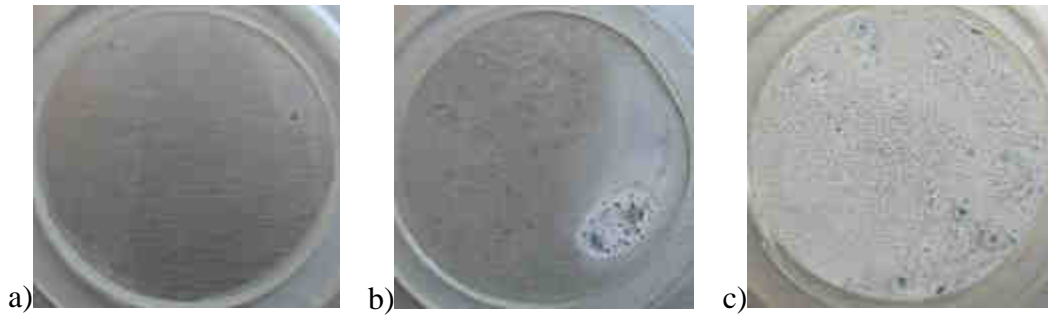
Figure 5.2.11. Optical photographs of AA2024 made after 14 days of immersion in 0.05M NaCl solution with 1mM Ce a) and 1mM La b); photo c) shows alloy surface after corrosion in 0.05M NaCl solution.

The impedance measurements demonstrate a superior inhibiting of cerium compared to lanthanum. Such results are in accordance with DC polarization and localized methods of analysis. However, experimental techniques do not give a clear explanation of the inhibiting efficiency. The obtained inhibition difference between cerium and lanthanum salts can be understood more clearly using the thermodynamical analysis which is performed in the next section.

5.2.6 Mechanism of corrosion inhibition with RE compounds

Introduction of lanthanum or cerium nitrate into the corrosion environment sufficiently changes the corrosion susceptibility of alloy due to blocking the cathodic intermetallics with insoluble deposits of the respective hydroxides. Figure 5.2.12 presents the pH range at which the different lanthanum and cerium hydroxides species can be formed in the solution. The relative compositions of water-based solutions doped with cerium and lanthanum salts presented in Figure 5.2.13 were calculated using the thermodynamic equilibrium constants for the following reactions:

$$La^{3+} + OH^- \rightarrow La(OH)^{2+} \qquad \log K = 2.7 \qquad (5.2.1)$$

$$La^{3+} + 3OH^- \rightarrow La(OH)_3 \downarrow \qquad \log K = 22 \qquad (5.2.2)$$

$$Ce^{3+} + OH^- \rightarrow Ce(OH)^{2+} \qquad \log K = 5.57 \qquad (5.2.3)$$

$$Ce^{3+} + 2OH^- \rightarrow Ce(OH)_2^+ \qquad \log K = 10.4 \qquad (5.2.4)$$

$$Ce^{3+} + 3OH^- \rightarrow Ce(OH)_{3(sol)} \qquad \log K = 14.71 \qquad (5.2.5)$$

143

$$Ce^{4+} + OH^{-} \rightarrow Ce(OH)^{3+} \qquad \log K = 14.76 \qquad (5.2.6)$$

$$Ce^{4+} + 2OH^{-} \rightarrow Ce(OH)_{2}^{2+} \qquad \log K = 28.04 \qquad (5.2.7)$$

$$Ce^{4+} + 3OH^{-} \rightarrow Ce(OH)_{3}^{+} \qquad \log K = 40.53 \qquad (5.2.8)$$

$$Ce^{4+} + 4OH^{-} \rightarrow Ce(OH)_{4} \downarrow \qquad \log K = 51.86 \qquad (5.2.9)$$

Formation constants for lanthanum hydroxocomplexes were taken from [17,334]. Formation constants for cerium species were calculated using free Gibbs energies of formation of cerium hydroxocomplexes, which were taken from [341]. In $0.15 - 0.001$M solutions of $La(NO_3)_3$, lanthanum is mainly present in the form of free hydrated La^{3+} ions. When the S-phase is activated by chloride-containing solution the pH value is locally growing up. Increase of pH values up to 9 leads to formation of lanthanum hydroxide via reaction (5.2.2) (Figure 5.2.13a). The lanthanum hydroxide is deposited immediately on the top of the active copper-rich intermetallics as shown in Figure 5.2.2. Formation of sediments occurs directly on the cathodic zones (Figure 5.2.2) since much higher pH can not be achieved far from the source of the hydroxyl ions due to fast diffusion processes, which equalize the concentration of OH^{-} at the cathode surface and in the bulk solution. The continued cathodic reaction generates hydroxyl ions causing further growth of lanthanum hydroxide deposits (Figure 5.2.2, 5.2.7). The hydroxides formed on the top of copper-rich intermetallics significantly hinder the corrosion processes in the active S-phase. The decrease of the corrosion activity is confirmed by the linear polarization measurements, which show a sufficient decrease of the cathodic and anodic currents at low polarization when lanthanum nitrate is added to the electrolyte (Figure 5.2.9b). The anodic current at low polarization is related with dissolution of magnesium and aluminum from the copper-rich intermetallics. Decrease of the anodic current for one order of magnitude confirms an effective suppression of the S-phase dealloying due to the lanthanum inhibitor. However, the anodic processes originated from intergranular corrosion at higher polarization are not influenced by the lanthanum (III) compounds.

The analysis of the VPD distribution shows that 0.0015M of $La(NO)_3$ is an optimal concentration for inhibition of the S-phase dissolution in AA2024 immersed in the chloride solution, which is in a good accordance with literature data for the inhibiting action of La compounds [46,341]. A high concentration of La^{3+} in solution leads to decrease of its pH due to a hydrolysis reaction. A lower pH of the electrolyte in turn can be responsible for faster chemical dealloying of intermetallics (according to equations 5.1.4, 5.1.5). Decrease of pH leads also to a delay in the formation of lanthanum hydroxide deposits.
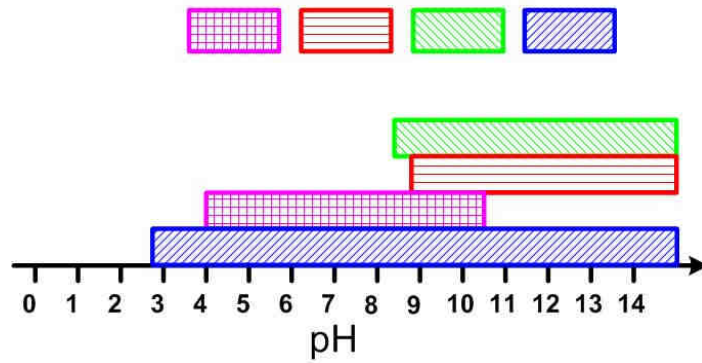
Figure 5.2.12. Diagram of the pH range of the respective hydroxides existence. Range of existence of different insoluble hydroxides was calculated using Solubility Products constants.
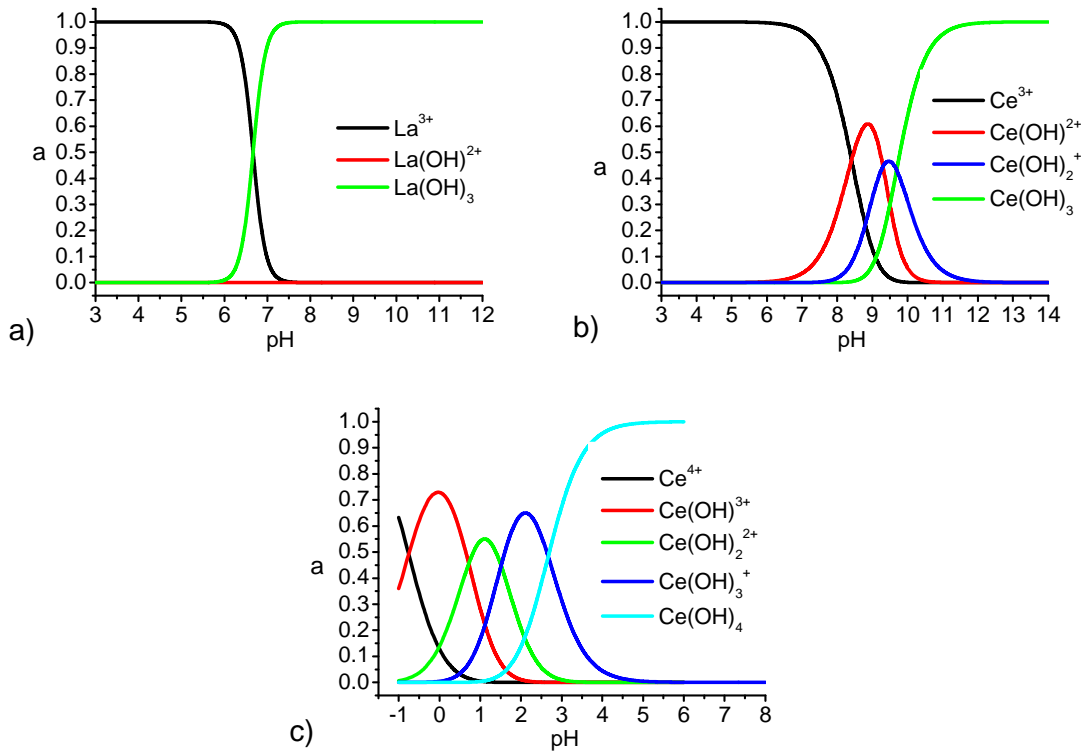
Figure 5.2.13. Fraction "a" of different metal species in the solution depending on pH.

Cerium (III) shows similar effect to that of the lanthanum-based inhibitor. The relative composition of Ce(III) species in solution at different pH's is shown in Figure 5.2.13b. Cerium (III) is present mainly in the form of free Ce^{3+} in neutral solutions. Increase of pH leads to formation of hydroxocomplexes (Figure 5.2.13b) at first and when the pH reaches 10 the hydroxide sediments can be formed as in the case of lanthanum. The formation of hydroxide domes occurs also selectively on the top of the S-phase intermetallics (Figure 5.2.1) hindering the corrosion. Both cathodic and anodic processes on the S-phase intermetallics are suppressed in accordance to the DC polarization results (Figure 5.2.9a). The suppression of cathodic processes in the case of cerium is higher than for lanthanum doped electrolytes. The anodic current due to S-phase dealloying is also one order of magnitude lower than in the case of lanthanum. The more effective inhibition of the corrosion processes in the case of the cerium inhibitor can not be explained only by difference in solubility of cerium (III) hydroxide and lanthanum (III) hydroxide since they are very similar.

An additional important feature of corrosion inhibition by cerium cations was found. The DC polarization curves presented in Figure 5.2.9a clearly demonstrate that the corrosion inhibition efficiency increases with the increase of the immersion period before the polarization tests. It seems that deposits with excellent protective characteristics are not immediately formed on the S-phase particles in contrast to the case where lanthanum nitrate was used as corrosion inhibitor. This relatively long process can be related to the ability of trivalent cerium to be oxidized to the tetravalent state. The tetravalent cerium forms extremely insoluble hydroxides already at pH about 3 as exhibited in Figure 5.2.13c. As was discussed elsewhere [45,341] the oxidation of cerium (III) can be caused by hydrogen peroxide, which is originated from the cathodic reaction of two electron reduction of oxygen:

$$O_2 + 2H_2O + 2e^- \rightarrow H_2O_2 + 2OH^- \qquad (5.2.10)$$
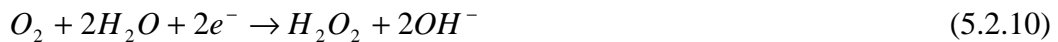
The generated peroxide can in turn oxidize trivalent cerium by one of the following reactions:

$$Ce^{3+} + H_2O_2 + 2OH^- \rightarrow Ce(OH)_4 \quad (CeO_2 \cdot 2H_2O)\downarrow \qquad (5.2.11)$$

$$Ce(OH)^{2+} + H_2O_2 + OH^- \rightarrow Ce(OH)_4 \quad (CeO_2 \cdot 2H_2O)\downarrow \qquad (5.2.12)$$

$$Ce(OH)_2^+ + H_2O_2 \rightarrow Ce(OH)_4 \quad (CeO_2 \cdot 2H_2O)\downarrow \qquad (5.2.13)$$
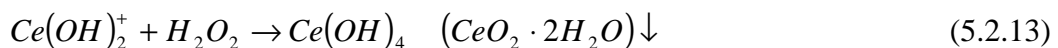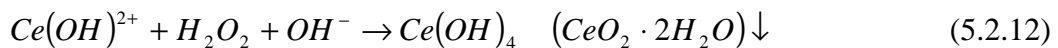
Reactions (24) and (25) are preferable at high pH values near the cathode surface. On the other hand the reaction of cerium (III) oxidation proposed elsewhere [342]:

$$Ce^{3+} + 1/2 H_2O_2 + OH^- \rightarrow Ce(OH)_2^{2+} \qquad (5.2.14)$$

seems questionable since the $Ce(OH)_2^{2+}$ complex ions can exist only at extremely low pH as presented in Figure 5.2.13c, which can not be achieved in the system under study.

The formed hydroxide of tetravalent cerium is also deposited on the cathodic parts providing additional hindering of the corrosion processes. Therefore the obtained difference in the inhibiting efficiency of Ce and La salt is attributed to a slightly different mechanism of the corrosion protection in case of Ce.

The corrosion inhibition process studied by SKPFM/AFM technique demonstrates important information on the mechanism of localized corrosion and inhibition. When making VPD maps at the place with Ce or La hydroxides deposits the difference between the values of VPD at the place of deposit and aluminum matrix are higher than 500 mV (Figures 5.2.3 and 5.2.4). This difference is sufficiently higher compared to the difference between the uncorroded S-phase and alloy matrix (150-250 mV) (Figures 5.1.3 and 5.1.5). The increase of VPD in the place of deposit is related with the localized corrosion activity of S-phase intermetallic and copper enrichment prior to the formation of a deposit. According to the mechanism of the hydroxide precipitation the source of hydroxyl anions is needed for the formation of insoluble hydroxides. Therefore the initial localized corrosion process must occur on the intermetallic inclusion in order to produce hydroxyl anions that are consumed locally by the precipitation of hydroxides in the presence of Ce or La salts. The ability of SKPFM to sense changes of the VPD even in places with precipitates is important and allows deeper understanding the localized corrosion processes and mechanisms of inhibition.

Summarizing

The addition of lanthanum (III) or cerium (III) leads to formation of the respective hydroxide deposits in the S-phase locations hindering the anodic and the cathodic processes. The formation of hydroxides occurs due to an increase of the pH in such locations resulting from the cathodic processes. The formation of the deposits decelerates the redeposition of copper and the broadening of cathodic VPD peaks. Thus, the SKPFM technique was found to be an effective method to estimate the protection performance of the RE salts and to find the optimal concentrations of inhibitor. The VPD of S-phase increases in the place of deposit formation because of initial localized corrosion process that leads to ennoblement of the intermetallic particle. During the initial localized activity copper enrichment occurs that is responsible for VPD growth.

Too high concentration of cerium or lanthanum nitrates leads to deeper localized corrosion in the places of the S-phase intermetallics. The growth of hydroxide deposits studied by the in-situ AFM technique exhibit linear time dependence indicating that the corrosion process is progressing in stationary state that results from a balance between diffusion and electrochemical reaction. The chloride ions strongly influence the rate of the corrosion processes and in turn the rate of the hydroxide deposits formation. The cerium nitrate shows superior inhibition properties in comparison with lanthanum nitrate probably due to consecutive formation of the extremely insoluble cerium (IV) hydroxide. The

proposed mechanisms of pitting corrosion and corrosion inhibition with RE salts are supported by thermodynamic analysis.

Cerium salts can be good inhibiting additives to the pretreatments because of their superior inhibiting properties compared to La salts. Fast inhibition of the corrosion process can allow active protection of the coated metal during the exposure to the corrosion environment.

5.3   Corrosion inhibition of AA2024 by Cerium molybdate nanowires

Highly soluble salts provide fast delivery rate of the inhibiting ions to the place where corrosion starts. As a result the corrosion process becomes efficiently and quickly inhibited. However, the disadvantage of highly soluble inhibitors might be their quick release when they are incorporated in the protection system. When an inhibitor is fully released from the coating to the corrosion solution there will be no protection of the underlying metal. Blistering is another problem that appears on the coated metallic systems when using soluble inhibitive pigments. Due to high osmotic pressure water penetrates inside the organic coatings with the pigment and causes blisters and delamination of the coating. Therefore solubility and release properties of inhibitors play an important role in the efficiency of the coating system with such additives.

One of the perspective approaches for the role of inhibitive additive could be a combination of inhibitive cations and inhibitive anions in one compound that will possess low solubility and inhibitive abilities. In this paragraph a new compound based on Cerium molybdate have been investigated as a potential inhibitor of AA2024 corrosion.

5.3.1 Characterization of cerium molybdate compound

Nanoparticulated Cerium molybdate was produced by Leibniz - Institut fuer Neue Materialien gGmbH. The reagents used in the synthesis were sodium molybdate and cerium (III) sulphate. The synthesized cerium molybdate compound appears as a gray slurry with about 14 wt.% of the compound in ethanol. The XRD analysis performed for dried powder didn't show any defined crystalline structure therefore it is difficult to ascribe any chemical formula to the compound. In the text the compound will be called cerium molybdate. However, the real chemical composition of powder might be different.

A yellow suspension is formed when dispersing the cerium molybdate in water. The suspension is stable without precipitation at least several hours after preparation. Figure 5.3.1 presents the results of the microscopical analysis and particle size measurements of the dried suspension containing cerium molybdate. For microscopical analysis a drop of suspension of cerium molybdate was deposited on the cleaned surface and dried at 60ºC. The obtained micrograph shows tiny filaments made of cerium molybdate approximately 50 nm thick and more than 500 nm long (Figure 5.3.1a). The light scattering measurements show that two populations of nanoparticles with average size around 90 nm and 300 nm can be found in the spectra (Figure 5.3.1b). The presence of two peaks in spectra can be attributed to different orientation of the particles during the measurement since the particles are not round shaped. Nevertheless, the size of nanoparticles is small enough for introduction of the compound into the protective coatings.

a)

b)
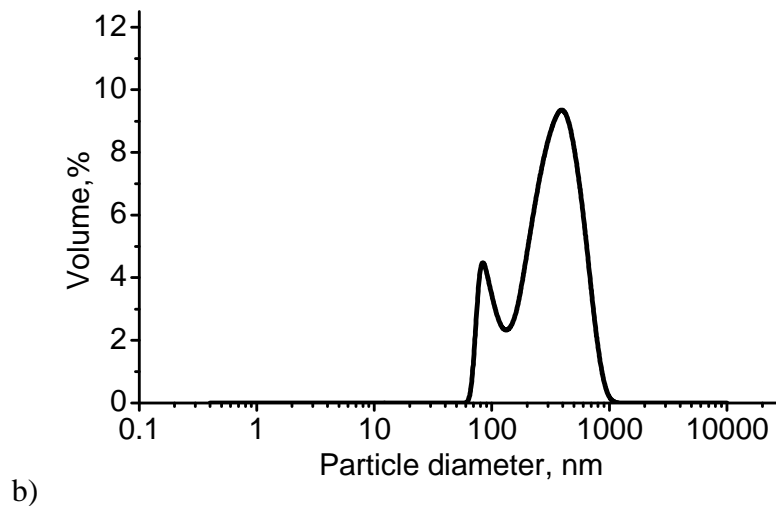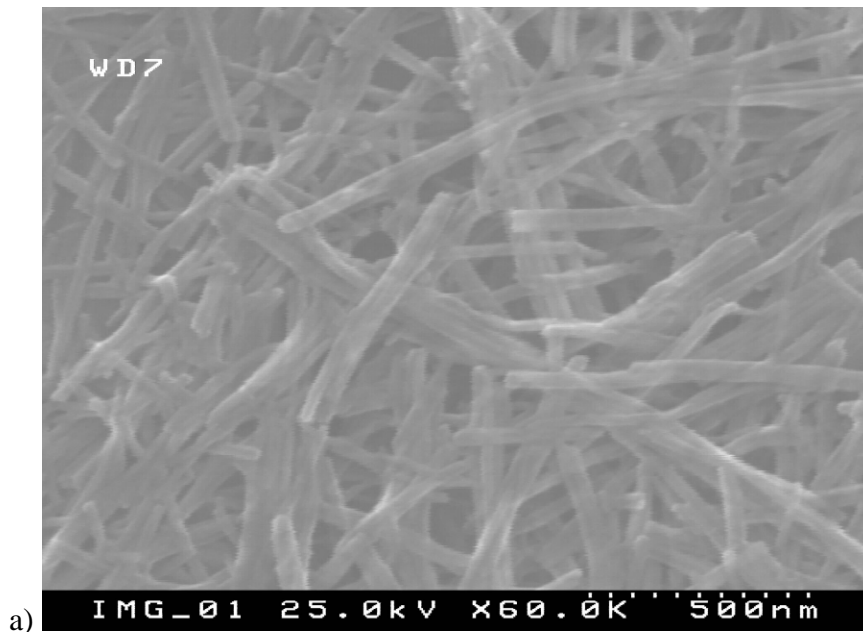
Figure 5.3.1. SEM micrograph of the dried suspension a) and size distribution of a suspension based on cerium molybdate compound b).

5.3.2 Experimental procedure and corrosion solutions preparation

2024 aluminum alloy was used in this study. Panels 3x4.5 cm, 1 mm thick were chemically etched according to the procedure (paragraph 4.2.4) and used for EIS testing. For DC polarization experiments samples were prepared according to the polishing procedure (paragraph 4.2.2). Localized analysis by means of SEM and EDS was performed on polished alloy samples prepared according to paragraph 4.2.1.

For testing of cleaned alloy substrates corrosion solutions with addition of cerium molybdate were prepared. At first a corrosion solution was prepared adding 3.57 g of cerium molybdate slurry to 100 ml of 0.05M NaCl solution followed by ultrasonic agitation during 10 minutes. This testing solution is called Suspension #1 and used for corrosion measurements during 30 min after preparation (Table 5.3.1). The other two corrosion solutions were obtained after centrifugation of a suspension with cerium molybdate. The suspensions containing 0.714g or 3.57g of the compound in 100 ml of 0.05M NaCl solution were ultrasonically agitated during 10 min and let stay during 1 day. After 1 day the suspensions were centrifuged and the clear solutions, namely Centrifugate #1 and Centrifugate #2, were used for measurements. The amount of additives and conditioning are summarized in Table 5.3.1.

Table 5.3.1. Compositions of different solutions and respective reference name.

Composition	Condition	Sample reference name
0.05M NaCl	bare	0.05M NaCl
3.57g cerium molybdate in 100ml 0.05M NaCl	suspension	Suspension #1
0.714g cerium molybdate in 100ml 0.05M NaCl	centrifugate	Centrifugate #1
3.57g cerium molybdate in 100ml 0.05M NaCl	centrifugate	Centrifugate #2

5.3.3 Localized corrosion inhibition of AA2024

The analysis of the localized inhibitive behavior was performed on polished substrates after 2h immersion in the corrosive solutions (Table 5.3.1). Initially SEM photographs were acquired to locate the S-phase intermetallic inclusion on both samples (Figure 5.3.2a,b). The pictures show intact S-phase intermetallics before corrosion. Then the first sample was immersed in NaCl solution only and the second one was immersed in Centrifugate #1 solution for 2 hours. The electron micrographs showing the surface of samples after 2h of immersion are presented in Figure 5.3.2c,d. Localized corrosion attack is clearly visible around the S-phase intermetallic in case of sample immersed in NaCl solution only Figure 5.3.2c. The EDS spectra taken at the S-phase are shown in Figure 5.3.2e. There can be clearly seen low signal of Mg that was dissolved from the intermetallic during the localized corrosion and increased signal of copper due to the copper refining. On the contrary to the NaCl solution only a corrosion attack was not found in case of sample immersed in Centrifugate #1 solution, what obviously demonstrates its inhibitive properties (Figure 5.3.2d). EDS spectrum shows high magnesium and low copper contents that testifies for inhibition of the S-phase localized corrosion in NaCl solution (Figure 5.3.2e). In the EDS spectrum there is a small peak attributed to molybdenum that most probably came from the precipitates forming atop the intermetallic. When performing observations at higher magnification a formation of precipitates on the top of S-phase intermetallic particle is clearly seen after immersion in Centrifugate #1 and

Suspension #1 solutions (Figure 5.3.3a,b). The precipitates formed at the top of S-phase intermetallics can block the cathodic process that occurs in such places and decrease the localized corrosion attack. However, more experiments are needed to support such assumption. Therefore polarization measurements have been performed on alloy substrates in order to reveal the inhibiting nature of cerium molybdate compound.
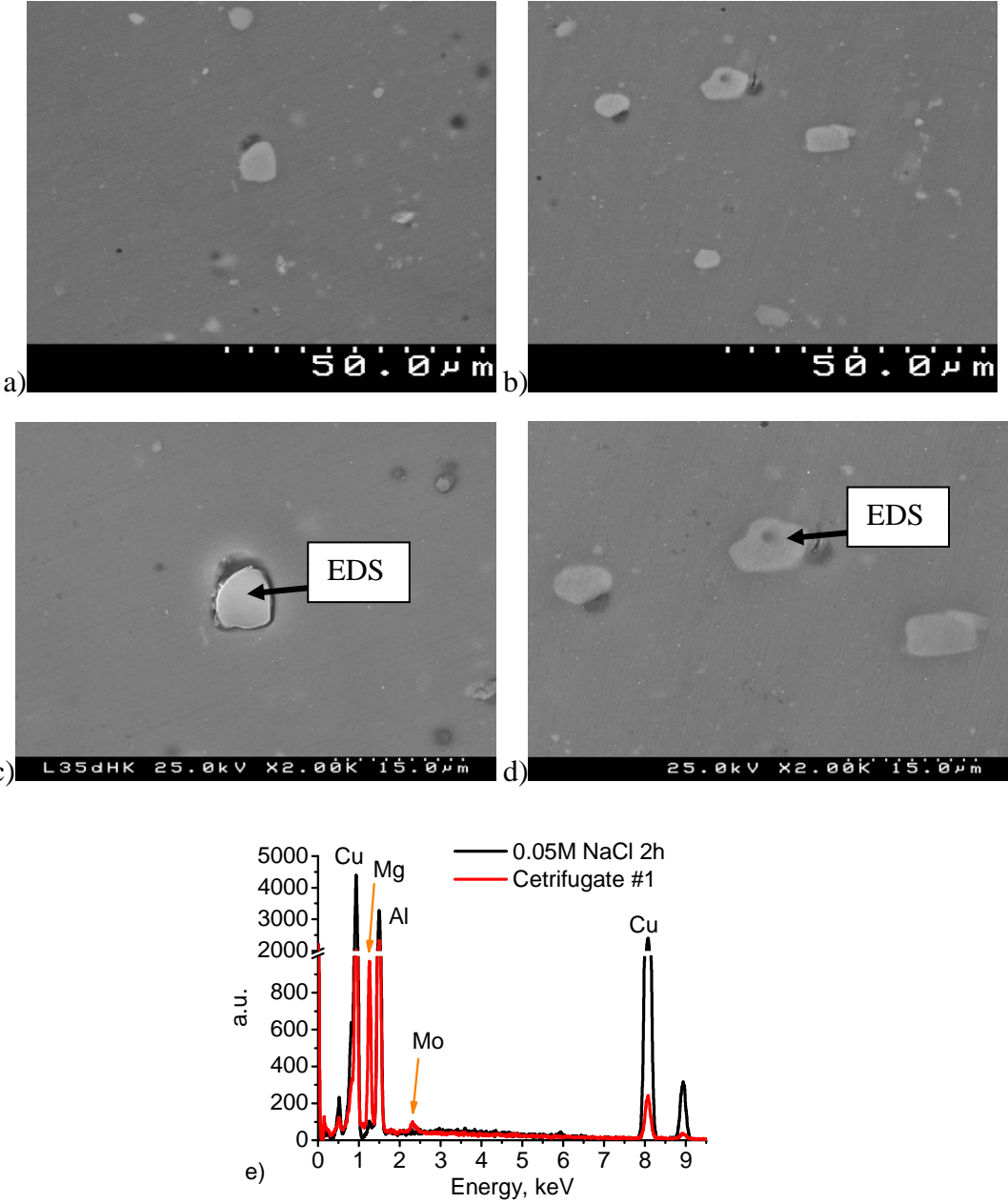
Figure 5.3.2. SEM micrographs made on polished AA2024 substrates before a), b) and after 2h of immersion in undoped 0.05M NaCl c) and in Centrifugate #1 solution d); EDS spectra taken after corrosion exposure on the intermetallics in the middle e).
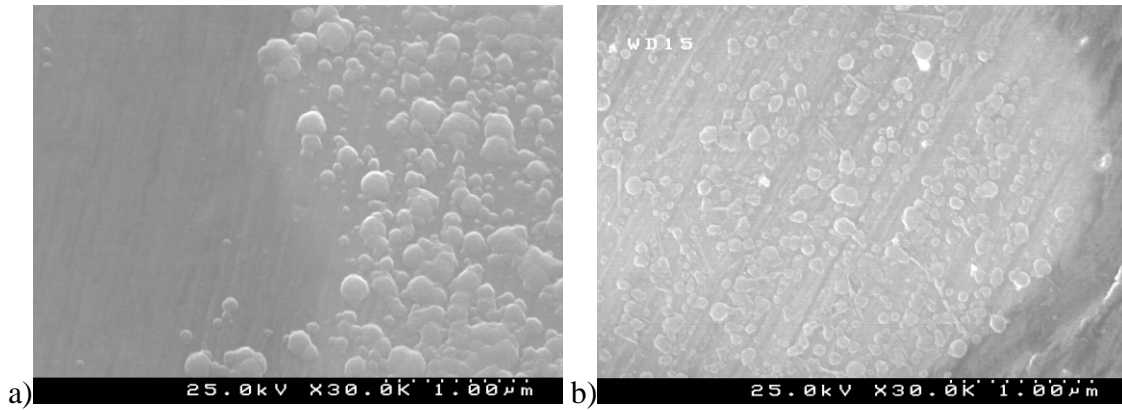
Figure 5.3.3. SEM micrographs made on polished AA2024 substrates after 2h immersion in Centrifugate #1 solution a) and Suspension #1 b).

5.3.4 DC polarization

In order to estimate the inhibiting action of cerium molybdate on cathodic and anodic process, polarization curves were recorded in the potential range -1.4 to -0.2 V vs SCE. Figure 5.3.4 presents cathodic and anodic curves made in pure 0.05M NaCl and inhibitor doped electrolytes. A cathodic curve for bare NaCl electrolyte shows a diffusion limited plateau of oxygen reduction starting from -0.6 V vs. SCE and a limiting current density around 10^{-5} A/cm^2. At more negative polarization hydrogen reduction process starts increasing the cathodic current. It is clearly seen that the inhibitive solutions decrease the cathodic current at the beginning of the cathodic scan (Figure 5.3.4) compared to NaCl solution only. Therefore cerium molybdate acts preferably as cathodic inhibitor of AA2024 corrosion. The cathodic current is smaller for Centrifugate #2 solution which confirms its higher inhibiting efficiency. However, at higher cathodic polarizations the difference between the current densities becomes smaller. The anodic part of the polarization curves appeared to be almost unchanged in case of centrifuged solutions. However, a slight step (around -0.5V vs SCE) is noticeable and associated with the change from anodic dealloying of active intermetallics to intergranular corrosion of the alloy. The appearance of such step can be connected with the small shift of the corrosion potential to the negative direction or to the partial inhibition of dealloying of active intermetallics by cerium molybdate.
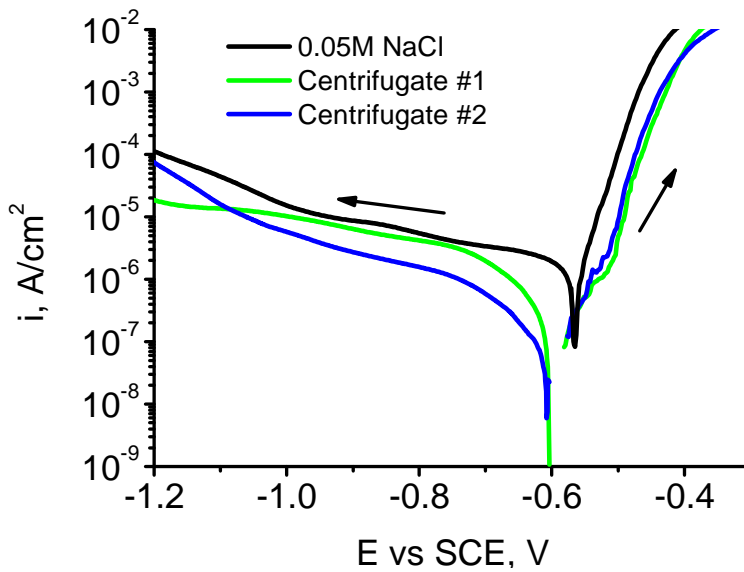
Figure 5.3.4. Polarization curves made on polished AA2024 samples obtained after 1 h of immersion in bare 0.05M NaCl solution, Centrifugate #1 and Centrifugate #2 solutions.

5.3.5 Optical characterization of AA2024 after corrosion.

Samples after 2 weeks immersion in different electrolytes were characterized by optical microscopy. Figure 5.3.5 presents the appearance of alloy surface after immersion tests. Although pitting activity is present on the surface of alloy samples, all three inhibitive solutions provide some degree of corrosion protection compared to NaCl solution (Figure 5.3.5a,b,c,d). A thick layer of white corrosion products completely covers the surface of alloy after immersion in NaCl solution only unlike for the samples after immersion in inhibitive solutions. The surface of alloy after immersion in Centrifugate solutions (Figure 5.3.5b,d) shows noticeable yellowish stain that can be associated with the presence of corrosion products layer on the surface. The presence of the stain is less noticeable for the sample after immersion in Suspension electrolyte. Nevertheless, the difference between the samples is very small and other methods of investigation must be used to distinguish the corrosion protective performance of different systems. More detailed analysis of the corrosion protection efficiency of different inhibiting solutions has been performed in the following paragraph using EIS method.
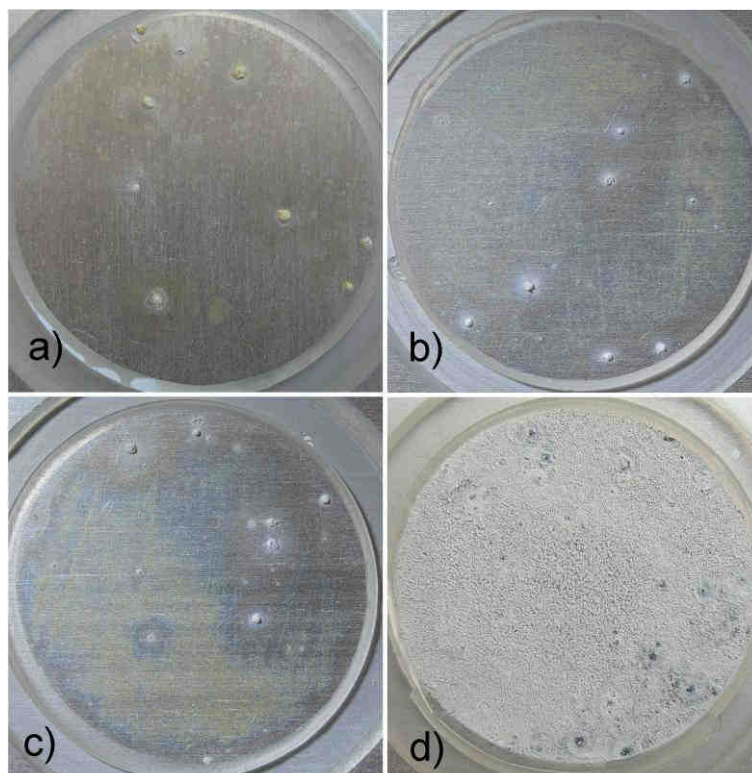
Figure 5.3.5. Optical photographs of AA2024 substrates after 14 days of immersion in Suspension #1 a), Centrifugate #1 b) and #2 c), and undoped 0.05M NaCl d).

5.3.6 Corrosion characterization of AA2024 using EIS.

The corrosion protection of bare AA2024 substrates was assessed using the EIS technique during immersion in 0.05M NaCl solution with or without cerium molybdate. Figure 5.3.6 presents the Bode plots of AA2024 after 7 days of immersion in Suspension #1, Centrifugate #1, #2 or 0.05M NaCl solution only. As can be seen from the spectra the low frequency impedance during immersion in all inhibitive solutions is 1 order of magnitude higher than for NaCl solution only. When comparing impedance at low frequencies between the inhibitor containing solutions the best behavior is attributed to the solution Centrifugate #1 that was prepared using lower amount of the compound (Figure 5.3.6). The lowest impedance is attributed to the Suspension #1 electrolyte. Nevertheless the difference in impedance for the inhibited samples is small.

Numerical characteristics of the inhibiting efficiency and corrosion progress such as oxide layer resistance and polarization resistance can be obtained after fitting the impedance spectra. In such a way we can make a clear distinction between the corrosion protection efficiency of doped and undoped NaCl electrolytes.

After 7 days of immersion the impedance spectrum obtained in Suspension #1 shows two time constants associated with native oxide film on the aluminum surface (around 20 Hz) and with the corrosion process (around 1 Hz) (Figure 5.3.6). The oxide layer (R_{ox}) provides protection of underlying metal and is the last barrier between corrosive species and the metallic substrate. Changes of the oxide layer during immersion in NaCl solution reflect resistance to corrosion attack of metal and, therefore, can be used to describe the efficiency of the corrosion protection. The corrosion activity can be expressed as polarization resistance and double layer capacitance (R_{polar} and C_{dl}). A low frequency time constant (around 0.01) Hz is attributed to the mass transfer limitations. The spectra recorded in Centrifugate solutions do not differ much, however present an additional component. At high frequencies (around 7000 Hz) it can be seen a new time constant associated with the formation of inhibitive layer on the surface of alloy (Figure 5.3.6). In contrast to inhibited solutions impedance spectra made in pure NaCl solution present one clearly defined time constant around 1 Hz that is associated with the corrosion process. A lack of the oxide layer response in the spectra points out high corrosion degradation of the alloy. The low frequency part of the spectrum is attributed to the diffusion related processes.

Equivalent circuits presented in Figure 3.3.13 a,b have been mainly used for fitting the impedance spectra during immersion in NaCl electrolyte. The corrosion progress is very rapid and the response from the oxide layer (R_{ox}) quickly disappears eliminating the need of using elements describing the oxide film (Figure 5.3.7a). Due to the pitting activity a Warburg element was introduced in the circuit to describe diffusion limitations of the corrosion process (Figure 5.3.6). The diffusion element introduced in the fitting model increases the quality of fitting. Fitting curves presented in Figure 5.3.6 as solid lines adequately describe the impedance spectra for all samples and allow plotting the changes of fitting parameters during the immersion time. The evolution of R_{polar} is presented in Figure 5.3.7b. Stable corrosion activity of alloy starts since the first day of immersion as the polarization resistance does not significantly change with time.

Impedance spectra of the alloy during immersion in inhibited solutions were fitted using models presented in Figure 3.3.13 c,d,e,f. The results of fitting of samples during immersion in Suspension #1, Centrifugate #1 and #2 are presented in Figure 5.3.7. For all inhibitive solutions there is the same trend of R_{ox} change during immersion. During the first hours of immersion the resistance increases followed by a decrease until around $8*10^4$ Ohm*cm^2. After two days of immersion the R_{ox} was stable for Suspension #1 and Centrifugate #2 solutions and slightly increased in case of Centrifugate #1 solution (Figure 5.3.7a). The maximal degree of corrosion protection was conferred by Centrifugate electrolytes (Figure 5.3.7b) and R_{polar} was maintained around $2*10^5$ Ohm*cm^2 during immersion. For Suspension #1 electrolyte R_{polar} was monotonously decreasing until around 10^5 Ohm cm^2 during immersion.
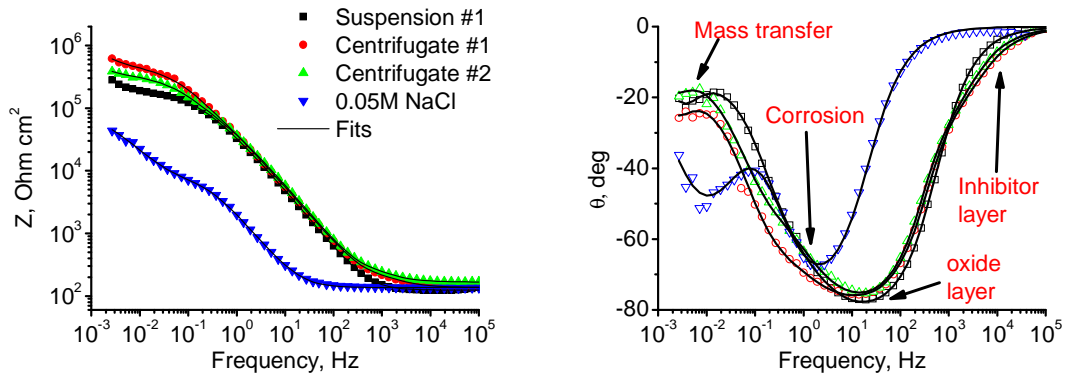
Figure 5.3.6. Bode plots for AA2024 after 7 days of immersion in Suspension #1, Centrifugate #1 and #2 and uninhibited 0.05M NaCl solution.
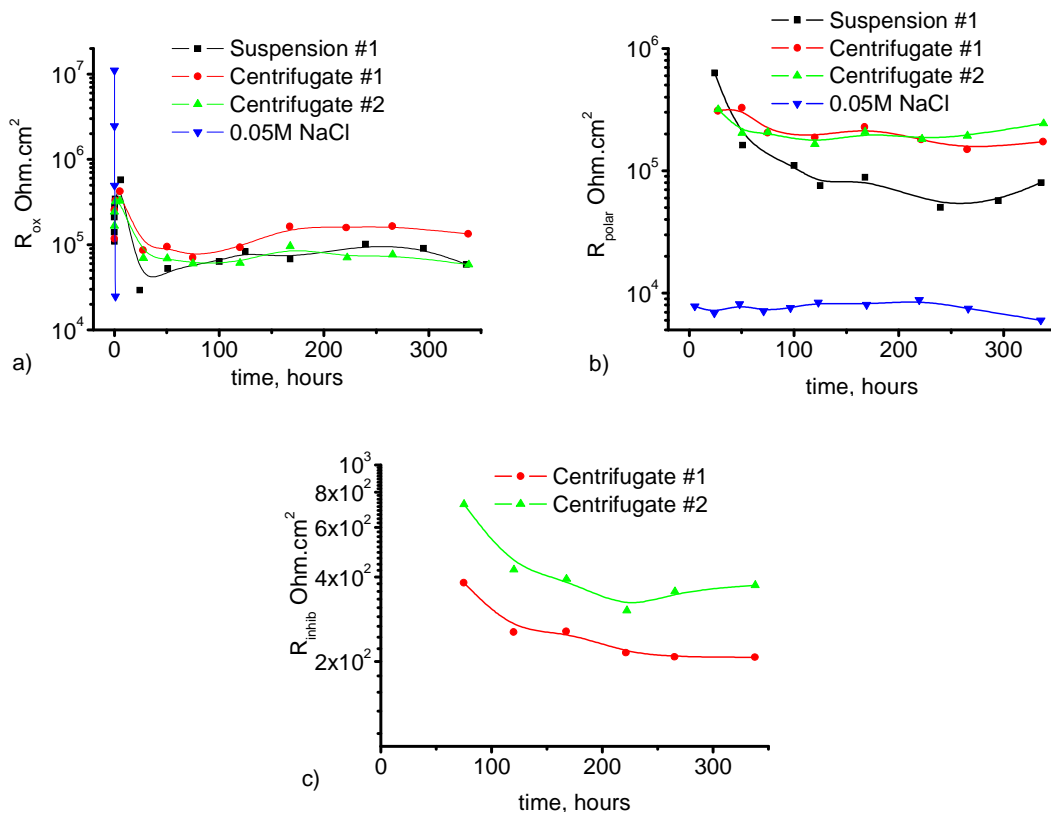
Figure 5.3.7. Evolution of oxide layer resistance (R_{ox}) a), oxide layer capacitance (C_{ox}) b), polarization resistance (R_{polar}) c) for bare AA2024 substrates during immersion in Suspension #1, Centrifugate #1 and #2 and 0.05M NaCl.

The modifications of the equivalent circuit were made especially for samples immersed in Centrifugate solutions due to the appearance of a new time constant ascribed to the presence of inhibitor layer (Figure 5.3.6, 5.3.7c). The addition of resistance of inhibitor layer R_{inh} and its capacitance C_{inh} was necessary in this case to fit a high frequency part of impedance spectra (Figure 5.3.6). The highest obtained R_{inh} is attributed to the Centrifugate #2 solution and is most probably associated with the higher concentration of inhibitor in the solution.

5.3.7 Mechanism of corrosion inhibition

The results of the corrosion testing of bare substrates clearly show enhanced protection conferred by cerium molybdate compound either in the form of suspension or after centrifugation of the suspension. The inhibiting effect is related to the decrease of the cathodic activity of the intermetallic inclusions as was shown performing DC-polarization measurements (Figure 5.3.4). The inhibition can occur because of formation of precipitates atop the active surface that create a diffusion barrier against oxygen. Another possible scenario of inhibition is the formation of an adsorbed layer of molybdate that can block adsorption sites of oxygen. It is surprising that the EDS analysis made in places of local deposits on S-phase intermetallics did not reveal any detectable amount of cerium (Figure 5.3.2e) and only molybdenum signals were found in the EDS spectra. Therefore the initial precipitates formed after some hours of immersion in NaCl solution containing cerium molybdate are most probably of molybdenum as a main element.

The thermodynamic analysis can help to understand why the formation of deposits based on Mo occurs. Figure 5.3.8 presents the Pourbaix diagram for the system Mo-H_2O [19]. The Figure shows that at neutral or more acidic pH and at potentials around -0.2V (SHE) molybdenum is in passive state due to formation of MoO_2 protective oxide film. At high pH molybdenum is in its soluble form MoO_4^{2-}. The following experimental data was obtained during the preparation of the inhibitive solutions and corrosion study of the alloy substrate. The pH of the Suspension or Centrifugate solutions was around 6 after the preparation and has not changed significantly after EIS corrosion testing. The corrosion potential of the alloy during immersion before polarization measurements was near -0.6V vs SCE (around -0.35V vs SHE at 20ºC). According to E-pH diagram at such potential and pH the formation of MoO_2 oxide is possible via reduction of molybdate ions according to the following reaction:

$$MoO_4^{2-} + 4H^+ + 2e^- \rightarrow MoO_2 + 2H_2O \qquad (5.3.1)$$

This process is thermodynamically possible to occur on the cathodic intermetallic inclusions of AA2024 even at OCP conditions during immersion in cerium molybdate containing solutions. The formed molybdenum (IV) oxide has low solubility ($pK_{sp}=13.39$)

according to [55] and can decrease the S-phase intermetallics surface in the alloy or provide formation of a barrier that impedes transport of oxygen to the surface of copper-rich intermetallics [47]. When increasing the pH of the electrolyte the formed MoO_2 can undergo the oxidative dissolution according to the E-pH diagram (Figure 5.3.8). Therefore the protective film may dissolve at more negative cathodic polarization due to the increased pH associated with oxygen reduction reaction.
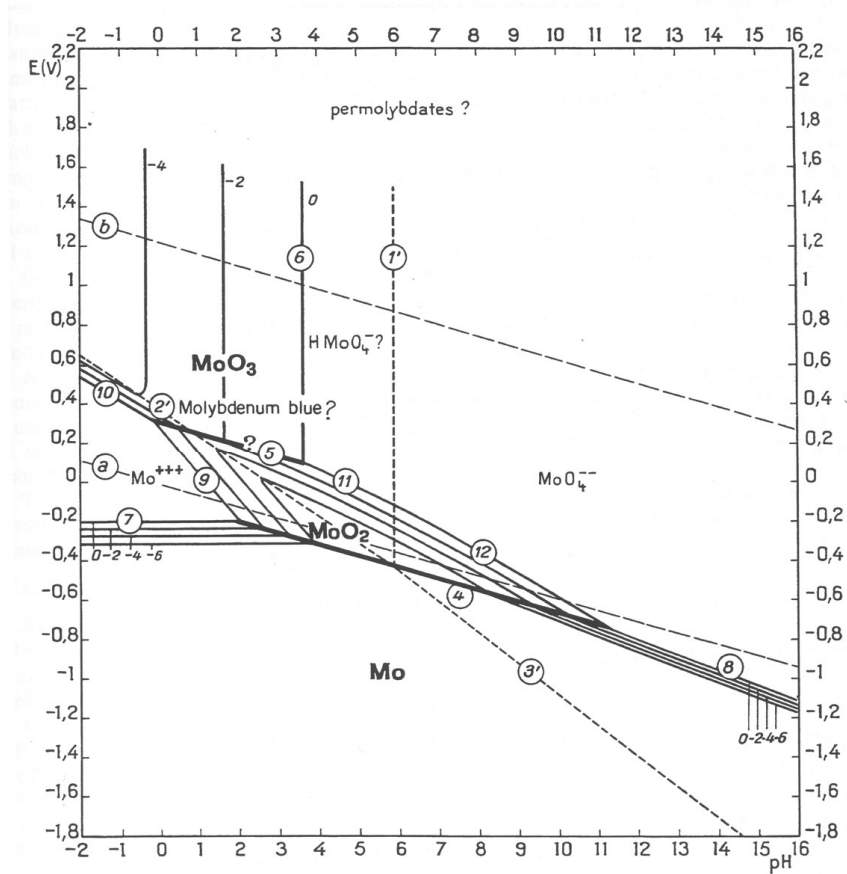
Figure 5.3.8. Potential-pH equilibrium diagram for the system Mo-water, at 25ºC [19].

Impedance results made in the presence of cerium molybdate compound present an additional feature associated with the action of inhibitor. The EIS spectra show the presence of an inhibiting layer on the surface of alloy during immersion in the Centrifugate solutions. The formation of such layer can be attributed to the oxidative reduction of molybdate to Mo (IV) oxide on the surface of aluminium as was suggested in ref. [52]. When formed on the surface the oxide film protects the underlying metal from the corrosion attack. However, the impedance spectra taken from sample immersed in Suspension #1 electrolyte do not show the formation of such inhibiting layer. In order to clarify the existence of such layers SEM micrographs have been taken on the two samples after immersion in Suspension #1 and Centrifugate #2 electrolytes (Figure 5.3.9). The left picture (Suspension #1) shows that the surface of alloy is coated with round shaped precipitates around 100-300 nm in diameter (Figure 5.3.9). The right picture (Centrifugate #2) shows the presence of precipitates with smaller size around 100-200 nm. However the important difference between the two pictures is that the precipitates layer in the case of Centrifugate #2 solution is much denser than in the other case. The alloy surface is barely visible on SEM micrograph (Figure 5.3.9b). The most plausible explanation of such difference is that the dense inhibitive film could form in conditions closer to the equilibrium in Centrifugate solution than in the case of Suspension solution. Therefore the more dense film has higher resistance and thus can be distinguishable in EIS spectra.

When performing the impedance measurements on the alloy, cerium molybdate demonstrates the corrosion protection either as Suspension or as clear Centrifugate solution. In previous section the protective properties of Ce containing solutions were investigated in detail. It was found that even at low concentration Ce effectively blocks the cathodic process of ORR. In order to understand the role of molybdate anions on corrosion protection of AA2024 additional experiments have been performed. Figure 5.3.10 shows the Bode plots of AA2024 after 7 days of immersion in 0.05M NaCl solution with cerium molybdate and in solution containing 1 or 50 mM of Na_2MoO_4. At any concentration sodium molybdate does not provide any corrosion protection of alloy substrate. The impedance magnitude is very similar to the uninhibited NaCl solution. This in not surprising since the concentration that provides inhibition of aluminium or aluminium alloy has to be as high as about 0.1 M [47,54].

The mechanism of the corrosion protection by cerium molybdate compounds has not been understood completely. Apparently there is a synergetic effect between the cerium and molybdate that results in appearance of species that act as inhibitors of AA2024 corrosion process. This is supported by the corrosion analysis of the alloy in the presence of only Na_2MoO_4 that does not provide any corrosion protection of alloy.
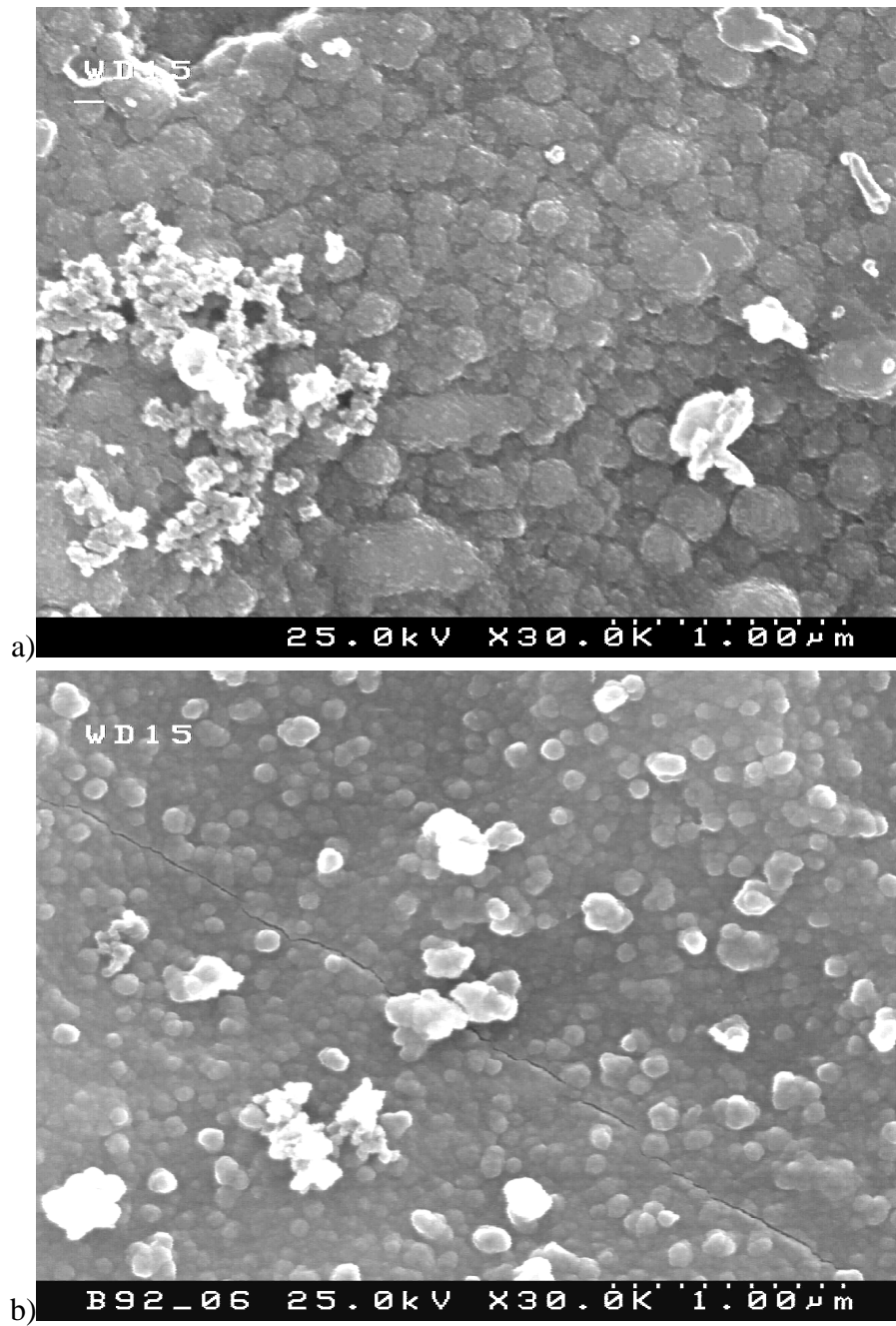
Figure 5.3.9. SEM micrographs made on AA2024 substrates after EIS testing in Suspension #1 electrolyte a) and in Centrifugate #2 electrolyte b).
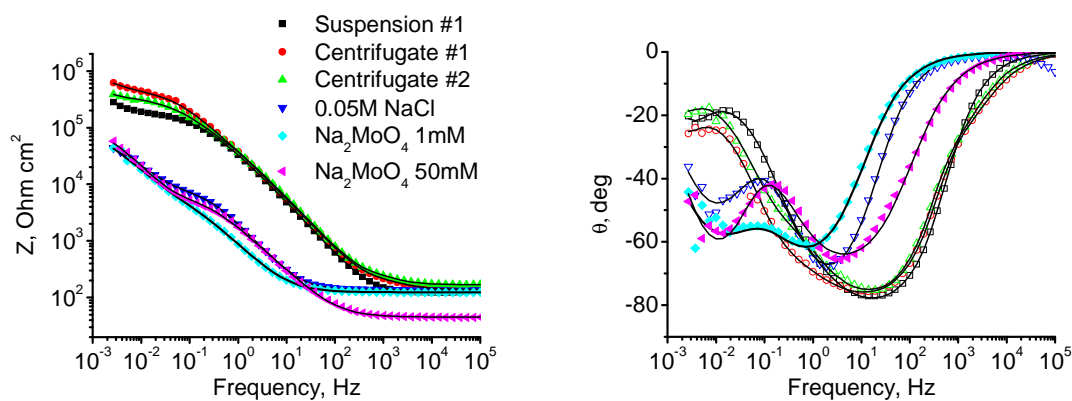
Figure 5.3.10. Bode plots for AA2024 after 7 days of immersion in Suspension #1, Centrifugate #1 and #2 and uninhibited 0.05M NaCl solution in comparison with the solutions of 1 or 50 mM of Na_2MoO_4 in 0.05M NaCl.

Summarizing

A new prospective compound has been investigated as a potential corrosion inhibitor for AA2024 corrosion using methods of microstructural and electrochemical analysis.

The inhibition performance of cerium molybdate was attributed to the formation of precipitates atop the S-phase intermetallics that create a barrier and block the ORR. A current density at the beginning of cathodic polarization in inhibited solutions is lower compared to NaCl solution only. Inhibition takes place either when inhibitor was in the form of suspension in the corrosive media or as a clear solution after centrifugation of the suspension. The formation of precipitates is thermodynamically possible through the reduction reaction of molybdate anions to Mo (IV) oxide that is formed on the cathodic intermetallic particles.

The corrosion protection of AA2024 alloy was accessed using the EIS method. The obtained results demonstrate a superior performance of cerium molybdate for the inhibition of the alloy corrosion compared to sodium molybdate with different concentrations. In case of the Centrifugate solutions the EIS spectra after some days of immersion show the formation of inhibiting layer on the surface of alloy. The formation of such inhibiting layer is most probably related with the reduction of molybdate species at the aluminium surface.

5.4   Corrosion inhibition of AA2024 by organic corrosion inhibitors

The corrosion mechanism of AA2024 clearly demonstrates an important role of copper-rich intermetallics in accelerated localized corrosion attack that results in copper redeposition and intermetallic dealloying. The electrochemical activity of copper can be reduced using organic compounds which can be adsorbed on the metal surface and form strong complexes with copper or other constituents of the alloy. In this paragraph several organic inhibitors (1,2,4-triazole, 3-amino-1,2,4-triazole, BTA and MBT) effective for copper corrosion inhibition are studied as possible candidates for AA2024 protection.

Aluminum alloy samples for EIS and DC-polarization experiments were prepared according to procedure described in paragraph 4.2.3; for AFM/SKPFM experiments samples were polished according to the procedure described in paragraph 4.2.1. The concentration of inhibitors in 0.005M NaCl corrosive solution was following for different inhibitors: 1,2,4-triazole – 3.5 g/l; 3-amino-1,2,4-triazole – 15 g/l; BTA – 3.5 g/l; MBT – 0.3 g/l. A higher concentration of 3-amino-1,2,4-triazole was used to enhance the effect of this inhibitor, since preliminary experiments with lower concentration didn't show an effective inhibiting action. The concentration of MBT was limited by the low solubility of this inhibitor in water.

5.4.1 EIS measurements

Preliminary screening of the inhibiting efficiency has been performed using EIS technique. The impedance spectra were taken on AA2024 samples during immersion in 0.005 M NaCl solution or in the same solution with different inhibitors. As shown in Figure 5.4.1, the addition of organic compounds to the corrosive solution increases corrosion resistance of the alloy. The value of impedance modulus in 1,2,4-triazole and 3-amino-1,2,4-triazole-containing electrolytes is higher than that in chloride solution only after longer immersion time. For MBT and BTA, the impedance at low frequencies is one order of magnitude higher than for uninhibited solution showing the highest inhibition efficiency among the tested compounds.

A deeper analysis of Figure 5.4.1a,b reveals the presence of two well-defined time constants for the alloy in inhibitor-free solution after 2 days of immersion. The time constant at 10 Hz can be attributed to the corrosion process which was developed very fast during 2 days of immersion. A low frequency part of the impedance spectra is most likely related to a diffusion process.

Impedance spectra of alloy during immersion in inhibitive solutions are more complex. In case of BTA and MBT inhibitors there are two well visible time dependent elements. The low frequency time constant develops at around 1 Hz and is ascribed to the corrosion process. High frequency time constant appeared around 100 Hz and is related to the presence of native oxide film. The part of the spectra close to 0.01 Hz presents signs of

another relaxation process which can be related to the mass transport limitations. This is visible especially in the case of 1,2,4-triazole inhibitor.

The presented results demonstrate that the organic compounds under study confer remarkable inhibition effect. However deeper study is needed to understand the mechanisms of these inhibition processes.
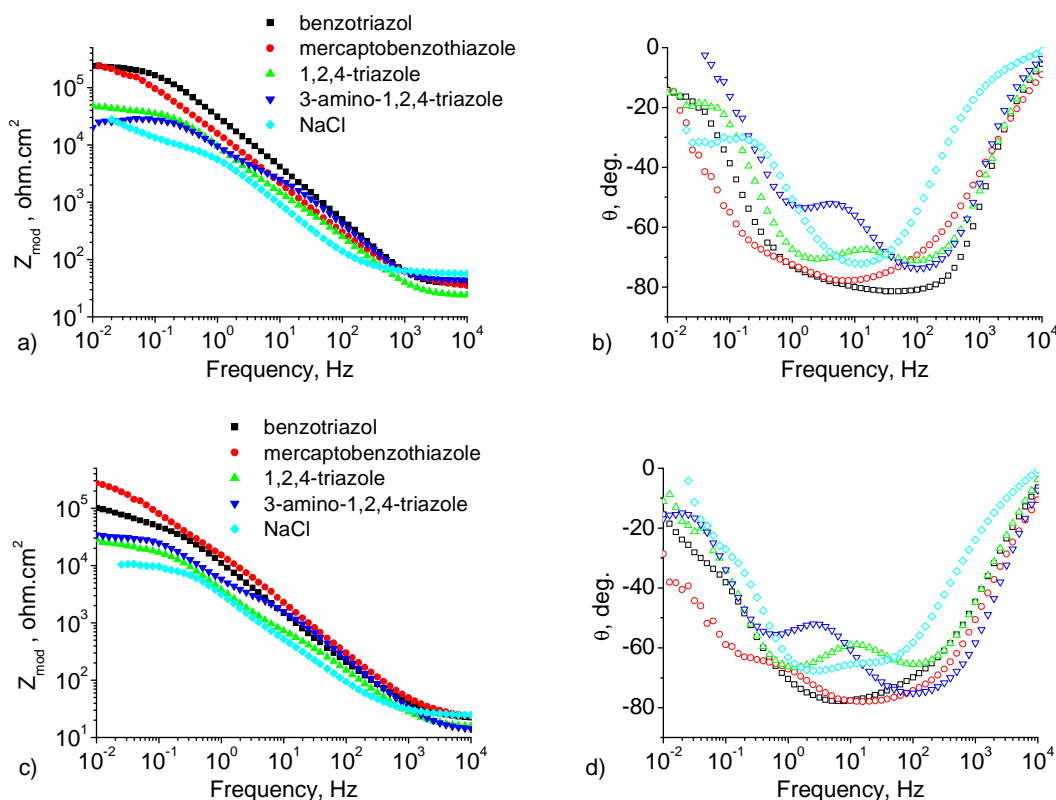
Figure 5.4.1. Bode plots for AA2024 after 2 a) and 12 days b) of immersion in 0.005 M NaCl electrolyte without and with different inhibitors.

5.4.2 DC polarization measurements

To estimate the effect of different inhibitors on the anodic and cathodic electrode reactions, Potentiodynamic polarization measurements were carried out in the potential range from -0.25 V to 0.2 V vs. open circuit potential. The cathodic polarization curve in the inhibitor-free chloride solution shows a diffusion-limited plateau of the cathodic current about $1*10^{-5}$ A/cm^2 (Figure 5.4.2). The diffusion limitations are related to the transport of the oxygen dissolved in the electrolyte to an electrode surface. Introduction of the inhibitors into solution leads to a decrease of the cathodic current (Figure 5.4.2). For

example, 2-mercaptobenzothiazole suppresses the cathodic current by about one order of magnitude compared to the inhibitor-free electrolyte.

To clarify this effect, cathodic polarization plots were recorded on Cu electrodes in the same solutions. Copper was chosen because this metal is a main component in the intermetallic inclusions of the alloy where the cathodic process of electrochemical oxygen reduction occurs. As can be seen in Figure 5.4.3, adding BTA and MBT inhibitors into the solution results in a significant decrease of the cathodic current at E > -0.9 V, in contrast to NaCl solution only, in which a diffusion-limited current plateau is observed in the potential region between -0.9 V and -0.5V. The slope of the polarization curve antecedent to the diffusion-limited plateau has comparable values in the case of the copper (250 mV/dec) and in the case of the aluminium alloy (210 mV/dec) in inhibitor-containing solutions. These similar slopes indicate that the cathodic process on the copper inclusions may determine the electrochemical behavior of the alloy in the negative potential region. The higher diffusion limiting current density in the case of the copper electrode in comparison with AA2024 substrate (Figure 5.4.2) is due to the alkali cleaning of the alloy plates which leads to partial removal of the copper-containing intermetallics from the alloy surface.

The inhibitors influence the anodic partial reactions as well (Figure 5.4.2). The anodic polarization curves in the presence of inhibitor show different sections. The first section with a fast current increase at low polarization can be assigned to the dissolution of aluminium and magnesium contained in Al_2MgCu particles [339]. The second section at higher polarization has a current stabilization region, which is more pronounced in the case of benzotriazole and 2-mercaptobenzothiazole-containing solutions. The third section is observed at even more positive potentials where intergranular corrosion in the aluminum matrix also takes place [339].

The current densities at given anodic potentials (overpotential of 50 mV vs. open circuit potential) were compared in different electrolytes. The AA2024 anodically polarized in inhibitor-free NaCl solution shows a relatively higher current density about $3.6*10^{-3}$ A/cm^2. Addition of 3-amino-1,2,4-triazole decreases drastically the current density to 1.2×10^{-4} A/cm^2. The other inhibitors under study show even more significant decrease of the anodic current (1,2,4-triazole ($1.4*10^{-5}$ A/cm^2), MBT ($1.7*10^{-5}$ A/cm^2), BTA ($2.3*10^{-5}$ A/cm^2) conferring an additional corrosion protection.
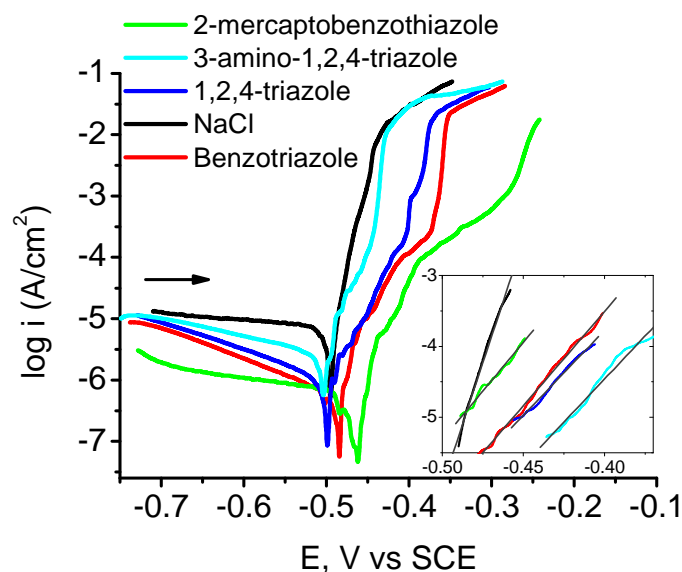
Figure 5.4.2. Anodic and cathodic polarization curves for 2024 aluminium alloy in 0.05 M NaCl with different inhibitors. The potential was scanned in the positive direction. (Inset shows linear Tafel parts on the first section of the anodic branches). The samples were immersed in solutions for 20 min prior the measurements.
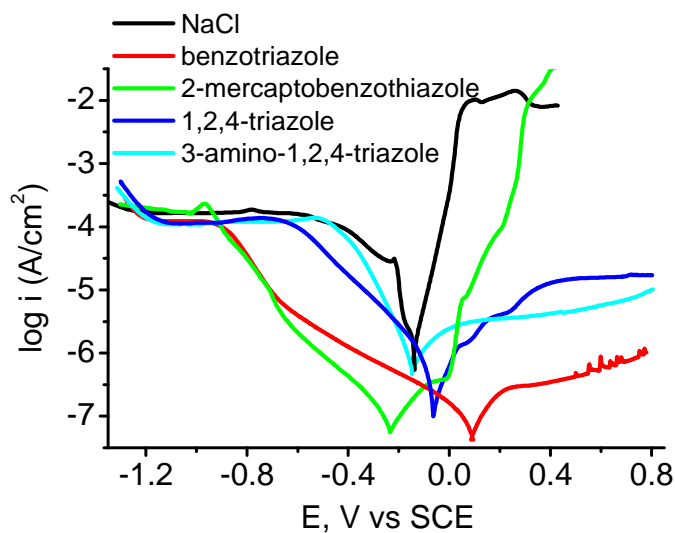
Figure 5.4.3. Anodic and cathodic polarization curves for copper in oxygen saturated 0.05 M NaCl electrolyte. The potential was scanned from open circuit potential to the respective direction.

The anodic Tafel slopes were calculated using linear parts of the log i vs. E curves between the OCP potential and the current stabilization region (insert in Figure 5.4.2). The slopes increase when an inhibitor is added to NaCl solution (pure solution (14.5 mV/dec), 3-amino-1,2,4-triazole (36 mV/dec), 1,2,4-triazole (38 mV/dec), MBT (41 mV/dec), BTA (42 mV/dec)). The increase of the Tafel slopes confirms the retarding effect of the inhibitors on anodic processes for the alloy in neutral chloride solutions. The anodic polarization measurements performed on copper have shown that the introduction of inhibitors into solution drastically slows down the anodic processes on Cu electrodes except for MBT inhibitor (Figure 5.4.3). Thus, the contribution of the anodic dissolution of copper in the total anodic process on the AA2024 alloy should be negligible. This fact allows us to assume that the main anodic process on the alloy at relatively low overpotentials is the dissolution of aluminium and magnesium from intermetallic particles, which is in a good accordance with the results presented in the literature [339].

5.4.3 Surface evolution

The polished AA2024 substrate was immersed in 0.005 M NaCl solution with different inhibitors to estimate the evolution of the alloy surface. Optical micrographs of the substrate after 2 hours of testing are presented in Figure 5.4.4. The sample in chloride solution only shows drastic changes of the surface due to localized corrosion processes. Dark areas formed around the pits indicate redeposition of copper dissolved from the intermetallic particles (Figure 5.4.4a). On the contrary to bare NaCl solution the surface after immersion in BTA and MBT inhibitive solutions appears to be without any signs of localized corrosion (Figure 5.4.4b,c). Immersion in 3-amino,1,2,4-triazole did not show corrosion activity as well (Figure 5.4.4d). These results prove inhibition of the localized corrosion of AA2024 in the presence of organic compounds under study during the first 2 hours of immersion in corrosive environment. However, as was demonstrated above, after longer immersion the corrosion process begins.
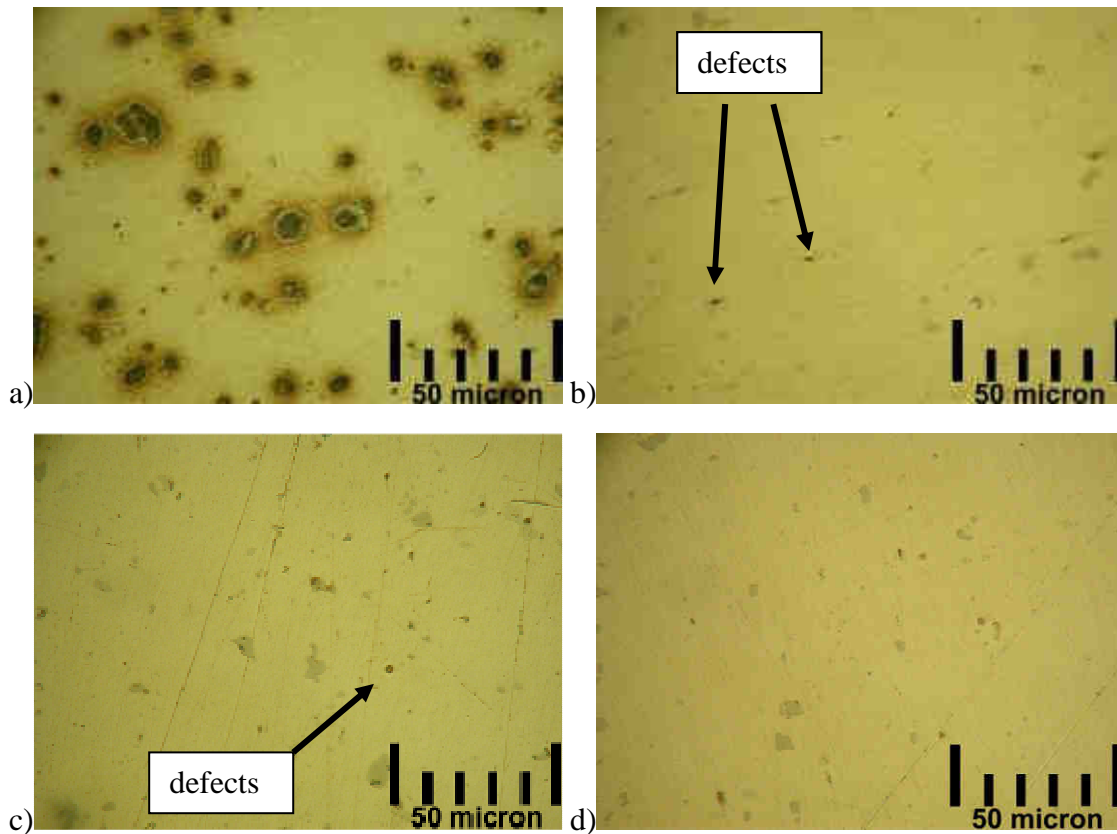
Figure 5.4.4. Optical micrographs of the polished alloy immersed for 2 h in 0.005 M NaCl a), and in the solution containing BTA b), MBT c) and 3-amino1,2,4-triazole d) inhibitors.

5.4.4 AFM/SKPFM study

The AFM and SKPFM techniques were used in the work as complimentary methods to reveal the evolution of the surface topography and VPD after corrosion tests. This information can be extremely helpful for understanding the corrosion and inhibition mechanisms. Figure 5.4.5 depicts topography and VPD scans for the AA2024 after 2h immersion in BTA and MBT containing electrolyte. The surface topography does not show any signs of corrosion activity (Figure 5.4.5a,c) in comparison to uninhibited solution (Figure 5.1.2a) and the Volta potential distribution keeps the same character as in the case of the surface before immersion (Figure 5.1.2b) that confirms retardation of the localized corrosion activity on S-phase inclusions. The only defects on the alloy surface are hole-like defects that are visible on both topography maps (cavities Figure 5.4.5a,c) and optical pictures (black dots Figure 5.4.4). Such holes are left by the intermetallics removed during polishing and are not related to the pitting as confirmed by VPD measurements. Any signs of intermetallics or potential change are not observed in such areas. Careful analysis of the

168

surface topography shows that some deposits appear on the top of the copper-rich intermetallic particles after immersion in MBT solution (Figure 5.4.5c,f). The use of BTA does not provide this effect of selective deposition of inhibitor (Figure 5.4.5a,e). Surface topography and VPD maps in the case of 1,2,4-triazole and 2amino-1,2,4-triazole containing electrolytes (not shown) are similar to BTA and MBT inhibitors.
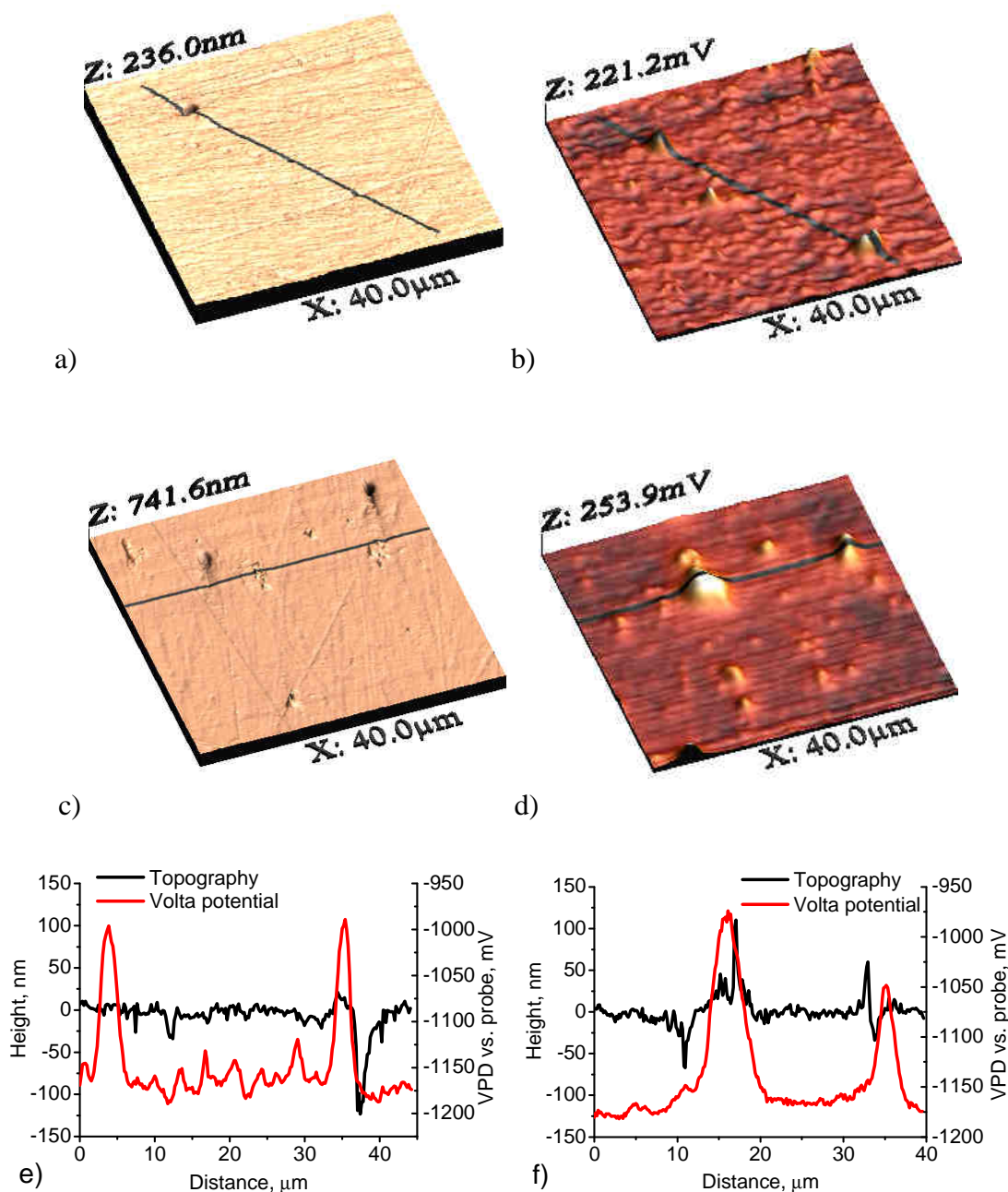
Figure 5.4.5. Topography (a, c) and VPD map (b, d) of AA2024 after 2 h of immersion in 0.005 M NaCl solution containing BTA (a, b) and MBT (c, d). Black lines on the maps correspond to profiles of the topography and VPD which are presented on the graphs e) for BTA and f) for MBT.

5.4.5 Mechanism of corrosion inhibition

The results described above can clarify some details of the mechanism of corrosion inhibition by the triazole and thiazole derivatives used in this study. Introduction of the triazole or thiazole compounds into the corrosive media leads to retardation of the corrosion processes on AA2024. EIS measurements have shown increased impedance during immersion in inhibitive solutions containing BTA and MBT compared to NaCl solution only. Such effect was caused by slowing down the kinetics of oxygen reduction on copper containing intermetallics that are major cathodic particles in the alloy. The inhibitor is quickly adsorbed on the intermetallics providing effective protection. The adsorption process occurs during the first hour of immersion as follows from optical imaging (Figure 5.4.4) and AFM/SKPFM measurements (Figure 5.4.5). Furthermore MBT forms precipitates on the copper-rich intermetallic inclusions (Figure 5.4.5c). The formation of the precipitates was not observed for other inhibitors.

In the case of BTA the mechanism of inhibition is related to the formation of an inhibiting layer (complex CuBTA) atop the copper surface [343,344]. The formation of an inhibiting layer proceeds through the following reactions [345]:

$$Cu + Cl^- \leftrightarrow CuCl + e^- \tag{5.4.1}$$

$$CuCl + Cl^- \leftrightarrow CuCl_2^- \tag{5.4.2}$$

$$CuCl_2^- + BTAH \leftrightarrow CuBTA + H^+ + 2Cl^- \tag{5.4.3}$$
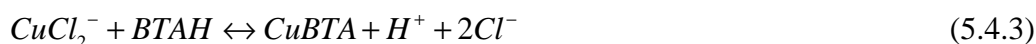
In chloride solution copper (I) is stabilized by the formation of a complex with chloride anions. When an inhibitor is introduced in the system the reaction (5.4.3) occurs. It follows from the thermodynamical data [345] that the acidic environment destabilizes the CuBTA complex, therefore the inhibiting efficiency of BTA is lower at low pH. Such behavior is a common feature for the heterocyclic organic derivatives having a hydrogen atom in position one in the heterocyclic ring [59]. For corrosion inhibition by MBT the mechanism is also related to the formation of complexes with cuprous ions that reacts with adsorbed molecules of MBT in analogy with 2-Mercaptobenzoxazole [346] according to the following reaction [347]:

$$CuCl_2^- + MBT \leftrightarrow CuMBT + 2Cl^- \tag{5.4.4}$$

Selective deposition of inhibitor molecules can be caused by the formation of stable covalent Cu-S- bonds that provide corrosion inhibition of copper [348].

Triazole and thiazole derivatives have common mechanism of inhibition related to the formation of a protective film on the copper surface by means of reaction with cuprous species formed at the surface of metal in chloride containing environment. The Cu-(inhibitor) complexes and adsorbed inhibitor molecules decrease the rate of both anodic and cathodic processes on the AA2024 surface. Particularly, MBT, in spite of a low concentration in solution, decreases the cathodic current by an order of magnitude (Figure

5.4.2) due to blocking the oxygen reduction processes on copper-rich intermetallics (Figure 5.4.3). All inhibitors also decrease the rate of the anodic reaction of intermetallics and aluminum matrix dissolution and increase the Tafel slope by about two-three times compared to pure chloride solution (Figure 5.4.2).

Summarizing

The triazole and thiazole derivatives used as additives to the NaCl containing solutions decrease the rate of the anodic reaction, increasing the Tafel slope for about two-three times compared to uninhibited corrosion solution. Such action provides additional effect against intermetallics dealloying and copper redeposition, therefore decreasing the susceptibility of the alloy toward localized corrosion attack.

Using a combination of different techniques such as EIS, DC-polarization and AFM/SKPFM measurements one can conclude that 2-mercaptobenzothiazole and benzotriazole can be used as effective corrosion inhibitors conferring long-term corrosion protection to the 2024 aluminum alloy in neutral chloride solution. Introduction of these inhibitors into "intelligent" storage/release reservoirs could be a promising way to provide active corrosion protection to copper containing aluminum alloys.

5.5   Other effective organic corrosion inhibitors for AA2024

Previous results demonstrate a good corrosion protection of AA2024 in NaCl solution conferred by BTA and MBT inhibitors even at low concentration for MBT. In addition to the above indicated experiments the inhibiting effect of several new candidates to be used as corrosion inhibitors for AA2024 was investigated as well. The main decisive factor to choose the inhibitors was the ability to form insoluble complexes with Mg and Cu at different conditions (pH and concentration). The concentration of organic compounds used as inhibitors for AA2024 corrosion is presented in Table 5.5.1.

For the visual observation and EIS measurements the bare metal substrates were cleaned using the procedure described in paragraph 4.2.3. Samples for DC polarization investigations were prepared according to the polishing procedure described in paragraph 4.2.2. The specimens used for SKPFM, XPS and SEM/EDS were prepared according to procedure described in paragraph 4.2.1. The polishing with diamond paste was employed to reduce roughness of the alloy surface down to the values required for AFM measurements as well as for XPS and SEM/EDS analysis.

Table 5.5.1. Concentrations of reagents used for testing in 0.05M NaCl solution.

	Inhibidor	Concentration
1	Salicylaldoxime (SAL)	0.5g/l
2	Dithizone	Saturated (<0.5g/l)
3	8Hydroxyquinoline (8HQ)	Saturated (<0.5g/l)
4	5,7 -Dibromo-8HQ	Saturated (<0.5g/l)
5	Thioacetamide	0.5g/l
6	Quinaldic acid (QA)	Saturated (<0.5g/l)
7	α-Benzoinoxime	Saturated (<0.5g/l)
8	2-(2-Hydroxyphenyl)benzoxazole	Saturated (<0.5g/l)
9	Cupferron	0.5g/l
10	Cuprizone	0.5g/l
11	Dithiooxamide	Saturated (<0.5g/l)

5.5.1 EIS measurements

A screening test using 0.05M NaCl electrolyte doped with different active agents was performed by means of EIS as in the case of triazole and thiazole based inhibitors. Figure 5.5.1a,b demonstrate Bode plots of AA2024 specimens after 2 weeks of immersion in 0.05M NaCl solution in the presence of the organic compounds listed in Table 5.5.1. As shown in Figure 5.5.1a,b the lowest value of impedance at low frequency corresponds to the sample immersed in NaCl solution only. Thus, all tested reagents reveal a certain inhibiting action conferring different protective efficiency. The value of the low frequency impedance, which is related to the corrosion process, is one to two orders of magnitude

higher for the specimens immersed in chloride containing solution doped with 8HQ, SAL and QA than for the alloy immersed in the undoped electrolyte.

Evolution of impedance spectra was analyzed in more detail for the three most effective inhibitors. Figure 5.5.2 presents Bode plots of the alloy after 1 and 14 days of immersion in NaCl solution with or without different inhibitors. The impedance spectrum of the alloy immersed in NaCl solution only reveals two time constants at 10 Hz and inchoate one at about 0.01 Hz (Figure 5.5.2a). The high frequency time-constant can be assigned to the corrosion process developed very fast on the bare alloy. The low frequency one can be related to the mass transfer limitations accompanying the corrosion process. The fitting curve using the equivalent circuit presented in Figure 3.3.13d adequately describes the impedance spectrum of alloy in NaCl solution (Figure 5.5.2a). It should be noted that after one day of immersion, the sample immersed in NaCl solution only does not show the presence of the native oxide layer due to the strong corrosion attack. Thus the impedance spectra can be fitted with the circuit shown in Figure 3.3.13b.

After one day of immersion the samples immersed in inhibitive solutions do not show visible corrosion. The impedance spectra present two overlapping time constants in a middle frequency range (1 - 200 Hz) (Figure 5.5.2a). In case of SAL inhibitor two processes are not clearly visible after one day of immersion though distinguishable after longer period. A time constant located around 100Hz can be ascribed to a layer of inhibitor formed on the alloy surface (especially noticeable for 8HQ and QA inhibitors). A time constant around 1 Hz can be ascribed to the native oxide film. A low frequency part of the impedance spectra (around 0.01Hz) shows signs of corrosion process. The fitting procedure was performed using the equivalent circuit presented in Figure 3.3.13e. The results of fitting are shown in Figure 5.5.2a as black lines. As can be seen the used equivalent circuit adequately describes the impedance curves. Though, it should be noted that the circuit has a third time constant related to corrosion which increases the quality of the fitting at low frequency. However the numerical errors exceed the fitted values therefore the corrosion process was not considered in the discussion.

An example of the impedance fitting after 14 days of immersion can be seen in Figure 5.5.2b. Longer immersion results in separation of the two time constants. Growth of the inhibitor layer is mostly pronounced in case of 8HQ (Figure 5.5.2b). Signs of the corrosion process become more visible in the low frequency part of the impedance spectra (Figure 5.5.2b) especially for 8HQ inhibitive solution. More detailed information on the behavior of the alloy during immersion in the corrosive solution can be obtained from the fitting data.
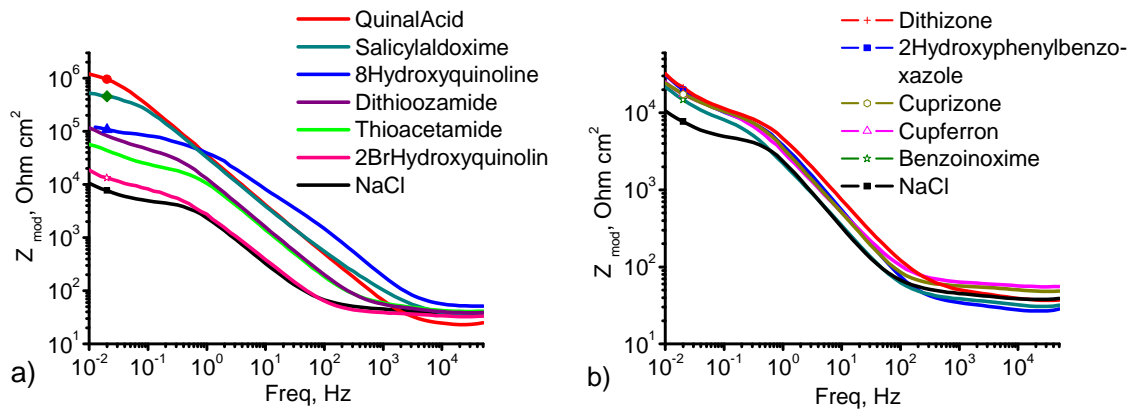
Figure 5.5.1. EIS spectra obtained for AA 2024 after 14 days of immersion in 0.05 M NaCl with or without inhibitors.
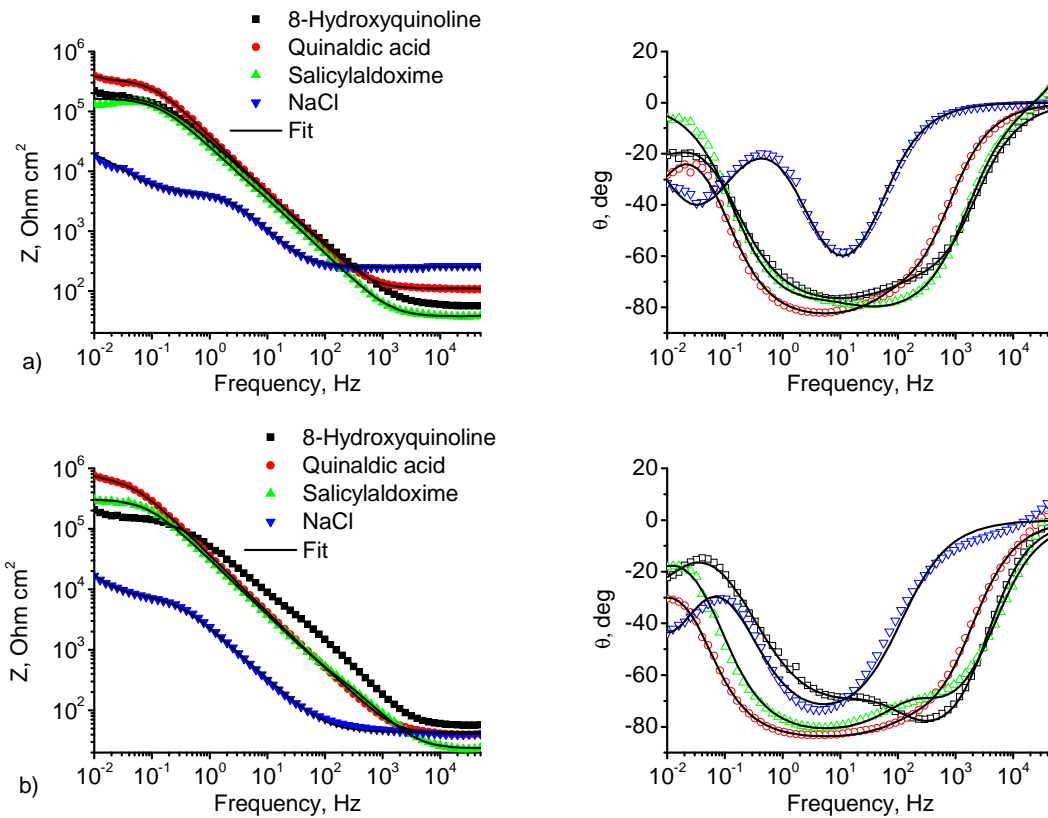
Figure 5.5.2. Bode plots for AA 2024 after 1 day a) and 14 days b) of immersion in 0.05 M NaCl with 8HQ, QA and SAL inhibitors; solid lines present fitting curves.

Figure 5.5.3 presents the evolution of different parameters after fitting the impedance spectra. The capacitance of the inhibiting layer stays almost without changes with the immersion time for SAL and QA inhibitive additives (Figure 5.5.3a). This can be attributed to the relatively fast formation of a dense and stable inhibitor containing layer on the surface of the alloy. The behavior of the specimen immersed into 8HQ containing solution is different. A prolonged decrease of capacitance shows continuous increase of thickness of the inhibitor layer (Figure 5.5.3a). The resistance of inhibitor film increases in the case of 8HQ until around $4*10^3$ Ohm*cm^2 which is consistent with the change of capacitance. For other inhibitors the changes of inhibitive film resistance are uneven. The resistance is changing around $2*10^3$ Ohm*cm^2 for QA and $9*10^2$ Ohm*cm^2 for SAL inhibitors.
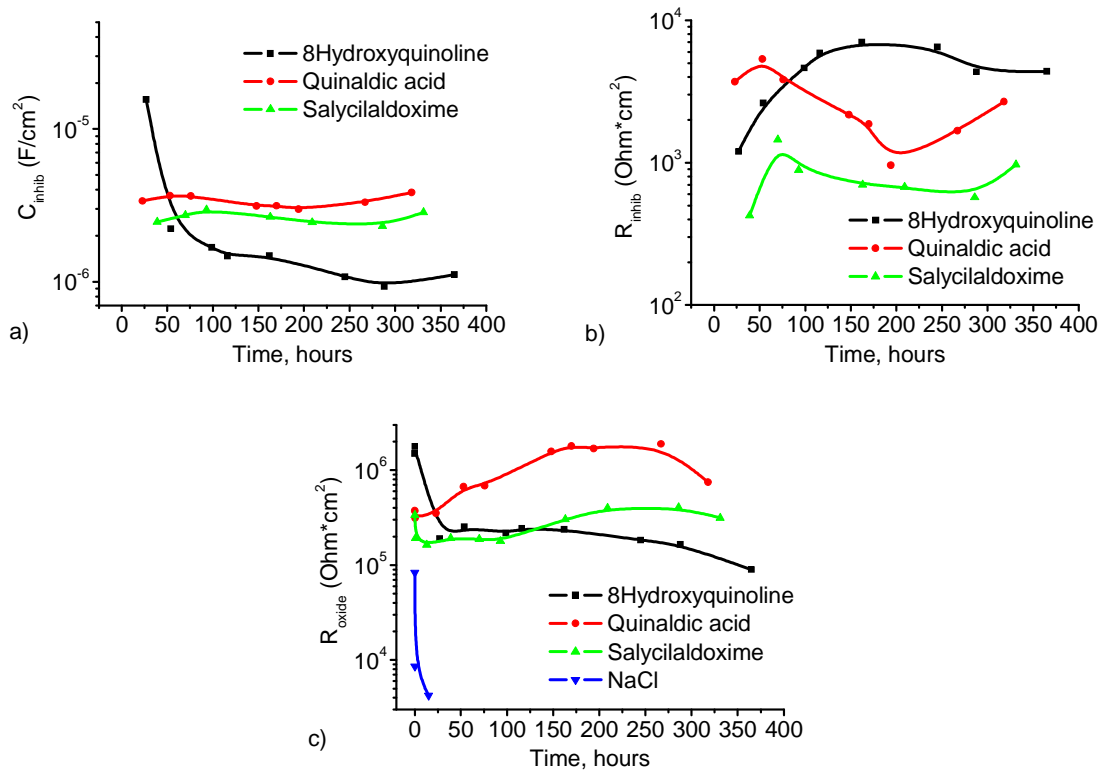
Figure 5.5.3. Evolution of capacitance a) and resistance b) of inhibitor layer; resistance of the oxide layer c) during the immersion time in 0.05M NaCl with or without inhibitors.

The native aluminum oxide has an important role on the corrosion resistance of the aluminum-based alloys. Monitoring the oxide layer during immersion can give an indication of the protection efficiency of different inhibitors. For pure NaCl solution the oxide resistance drops during the first day of immersion and then disappears completely from the spectra (Figure 5.5.3c). Different behaviour can be found when using QA and SAL inhibitors. The resistance of oxide increases during the immersion until around $1.5*10^6$ Ohm*cm^2 for QA and $4*10^5$ Ohm*cm^2 for SAL inhibitor (Figure 5.5.3c). Rapid decrease of the resistance until about $2.5*10^5$ Ohm*cm^2 can be seen during the first day of immersion for 8HQ followed by a slow decrease until around $1*10^5$ Ohm*cm^2 by the end of immersion (Figure 5.5.3c). Nevertheless, the resistance remains in the range of 10^5- 10^6 Ohm*cm^2 which is significantly higher than in the case of inhibitor-free solution.

5.5.2 Optical observations

Optical images of the alloy after 2 weeks of immersion are shown in Figure 5.5.4. The sample immersed in pure chloride solution has many pits on the surface and is significantly corroded (Figure 5.5.4d). Moreover, the corrosion has already started after only one day of immersion in NaCl containing electrolyte. Unlike for pure NaCl solution, the surface of alloy samples immersed in the electrolyte doped with inhibitors is much cleaner showing low visual corrosion attack especially in the case of 8HQ where the surface seems to be intact after the immersion test. In case of QA and Sal inhibitors metal surface shows some pits. However a zone around pits doesn't have any significant amount of the corrosion products of aluminum. Nevertheless, the alloy surface shows slightly yellowish coloration which can be associated with the presence of an insoluble layer containing inhibitor. The coloration is more noticeable for QA containing electrolyte compared to SAL containing electrolyte and almost not noticeable for HQ electrolyte. These results are in close agreement with the impedance data presented in Figure 5.5.3 where the most defined response from the organic layer was revealed in the case of 8HQ.

Quinaldic acid, 8Hydroxyquinoline and Salicylaldoxime organic substances revealed superior corrosion suppression and were selected for additional testing to confirm their inhibiting action and get understanding of the mechanism of protection.

a) 8HQ   b) QA   c) SAL

d) NaCl 0,05M
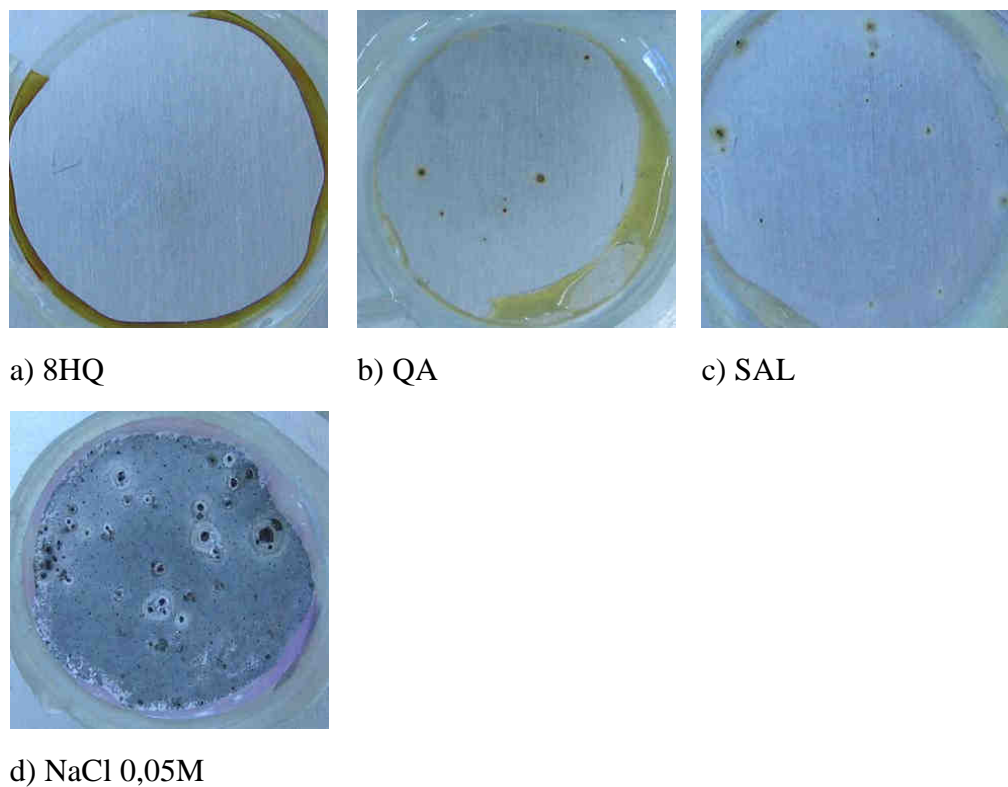
Figure 5.5.4. Photos of the AA2024 samples immersed for two weeks in 0.05 M NaCl with and without inhibitors.

5.5.3 DC-polarisation

Potentiodynamic polarization measurements were carried out in the potential range of -0.8 V to 0.6 V vs open circuit potential to characterize the effect of the different inhibitors on the anodic and cathodic partial electrode reactions. Values of pH measured for the solutions with or without inhibitors were in the range of 5.7±0.5.

The polarization curves presented in Figure 5.5.5a were recorded after 1 hour (Figure 5.5.5 a) and 24 hours (Figure 5.5.5 b) of immersion at the open circuit potential in pure 0.05M NaCl or in the same solution doped with inhibitors. Doping of chloride electrolyte with the inhibitors leads to decrease of the cathodic current which can be seen after one hour of immersion (Figure 5.5.5a). However, the decrease is more pronounced in the more negative potential range where hydrogen evolution occurs. Increase of immersion time prior to polarization increases inhibiting efficiency, suppressing the cathodic current by more than one order of magnitude (Figure 5.5.5b). The results show that the interaction of the inhibitors with the aluminium alloy including the cathodic particles is, most probably, a relatively slow process which takes several hours.
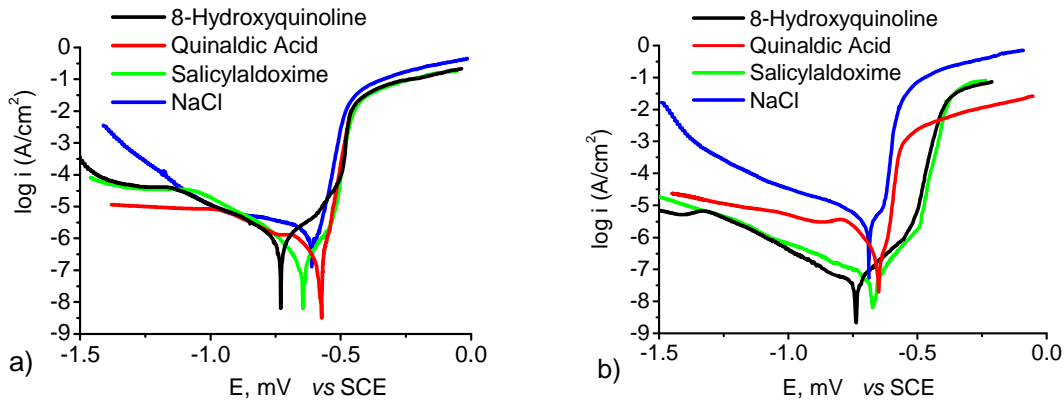
Figure 5.5.5. Polarization curves made on AA2024 in 0.05 M chloride solution with different inhibitors. The curves were taken after 1 hour of immersion a) and 24 hours of immersion b).

The anodic partial reactions are also influenced by inhibitors. After one hour there is almost no difference in the anodic currents due to the addition of inhibitor. The difference is much more defined after longer immersion time. The anodic branch of the polarization curve on AA2024 has two breakdown potentials accompanied with sharp growth of the current. The first breakdown is due to the dissolution of S-phase intermetallics and the second one at more positive potentials is caused by intergranular attack. Addition of QA decreases the maximal current density at high anodic potentials. However the second breakdown potential is not shifted in this case. SAL and 8HQ act differently. They decrease the anodic dissolution of the S-phase intermetallic inclusions leading to lower current densities in the potential range between the two breakdown potentials. The second breakdown potential is also shifted to the more positive direction demonstrating inhibition of the intergranular attack as well.

The longer immersion time before polarization could lead to formation of denser protection layer on the metal surface. EIS data supports this assumption because the presence of inhibitive layer could not be detected before one day of immersion (Figure 5.5.3). The inhibiting layer decreases the cathodic reduction of oxygen and anodic dissolution of Mg and Al on copper rich intermetallic zones. This is in agreement with results of long-term EIS measurements, which indicate the growth of inhibitive film on the surface. In case of SAL and QA inhibitive layers were noticeable after 1 day of immersion being in good correlation with polarization measurements.

5.5.4 XPS characterisation

The chemical composition of the surface of the samples immersed in the blank NaCl solution or into the same solution with QA, SAL or 8HQ was studied by XPS analysis. Figure 5.5.6a shows the Al2p ionization obtained on immersed substrates. The main Al2p peak, with binding energy of approximately 74.6 eV can be assigned to Al-O bonds due to the presence of $Al_2O_3/Al(OH)_3$ constituents [349].

The minor Al2p peak with binding energy of about 71.8 eV is related to the presence of metallic aluminum and it was detected only on the samples immersed in the inhibitor containing solutions. Such effect can be explained by the inhibiting action of organic compounds that delay the formation of a layer of corrosion products on the alloy surface. In the undoped NaCl solution the electrochemical activity of intermetallics inclusions is faster, which promotes corrosion activity of the whole alloy thus blocking the surface with a layer of corrosion products.

The presence of organic inhibitors on the surface of the immersed specimens can be characterized by the N 1s ionization peaks that are presented in Figure 5.5.6b. This ionization is composed by a main peak, at binding energies between 400 and 401 eV that can be assigned to the C-N bonds present in the inhibitor molecules. In the case of the SAL a small peak was also detected in the higher binding energy side of the N1s spectrum and can be related to the N-OH bonds.

Copper and magnesium were also detected on the surface of all AA2024 samples. The Cu 2p ionization for all the samples is depicted in Figure 5.5.6c. The relative atomic contents of Cu in the samples are presented as well. The total amount of different forms of Cu is 1.5 -2.4 times higher for the specimens immersed in inhibitor free NaCl solution.

The Cu 2p envelope for the sample exposed to blank NaCl presented a Full width at half maximum of about 6 eV, revealing the contribution of different forms of copper. These can be linked to both Cu(I) and Cu(II), although the shake-up satellites above 938.0 eV and characteristic of Cu(II) could not be detected [350]. Therefore, the composition of the Cu envelop can be related with Cu (I)-Cl complexes and Cu (I)-O species. The FWHM of the Cu2p ionization decreased for the samples exposed to the solutions of NaCl with inhibitors and for the QA and 8HQ only one Cu peak was observed, which may correspond to the Cu present in the precipitates.

The Mg 2p ionization showed a very low signal to background ratio. However, two peaks can be observed. The first one is at binding energies of approximately 48.0 eV, corresponding to metallic Mg and second one is at about 51 eV, traceable to the Mg-O bonds arising from inhibitor-Mg^{2+} complexes or Mg oxide/hydroxide [351] (Figure 5.5.6d). The peak obtained in the blank NaCl solution is slightly different and seems to present only one contribution, at 49.8 eV probably due to magnesium corrosion products. Relative atomic percentage of Mg is depicted in the Figure label. The sample immersed in

the blank NaCl solution presents the lowest amount of Mg, which gives an evidence of more intense corrosion processes.

The trends observed in the Cu2p and Mg2p ionizations are in a good agreement with the corrosion mechanism for the AA2024 discussed in paragraph 5.1 and supports the mechanism of localized corrosion that includes magnesium dealloying from the S-phase intermetallics and copper redeposition. The XPS data also proved the presence of adsorbed N containing layers and the absence of significant corrosion activity on the surface of the specimens exposed to the solutions containing inhibitor in contrast to features observed in blank NaCl where corrosion activity is much more intense.
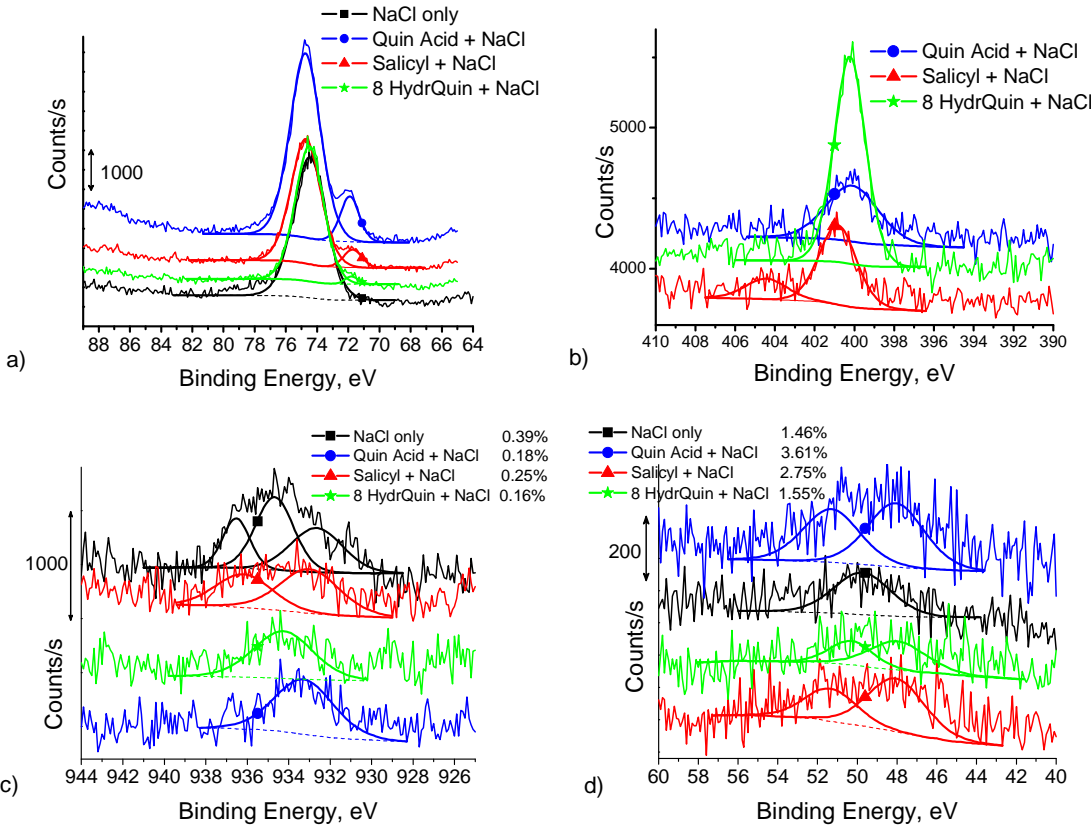
Figure 5.5.6 XPS spectra corresponded to ionizations of Al 2p a), N 1s b), Cu 2p c) and Mg 2p d) obtained on the AA2024 immersed for 5 hours into pure NaCl solution, or NaCl with different inhibitors.

5.5.5 AFM/SKPFM investigation

Figure 5.5.7 presents the topography and VPD profiles across the copper rich intermetallic inclusions before and after 5 hours of immersion in 0.05M NaCl solution with or without different inhibitors. No changes can be found for topographic profiles corresponding to for absence of the localized corrosion activity on the surface in the presence of inhibitors (Figure 5.5.7a,b,c). The absence of even minor changes at the height profile testifies the stability of the intermetallic particles in the solution doped with inhibitors. On the contrary, evolution of profiles for NaCl solution only shows signs of pitting on the surface (a hole in the center) as well as a layer of corrosion products of aluminum being noticeable in the left and right parts of the topographic profile (Figure 5.5.7d).
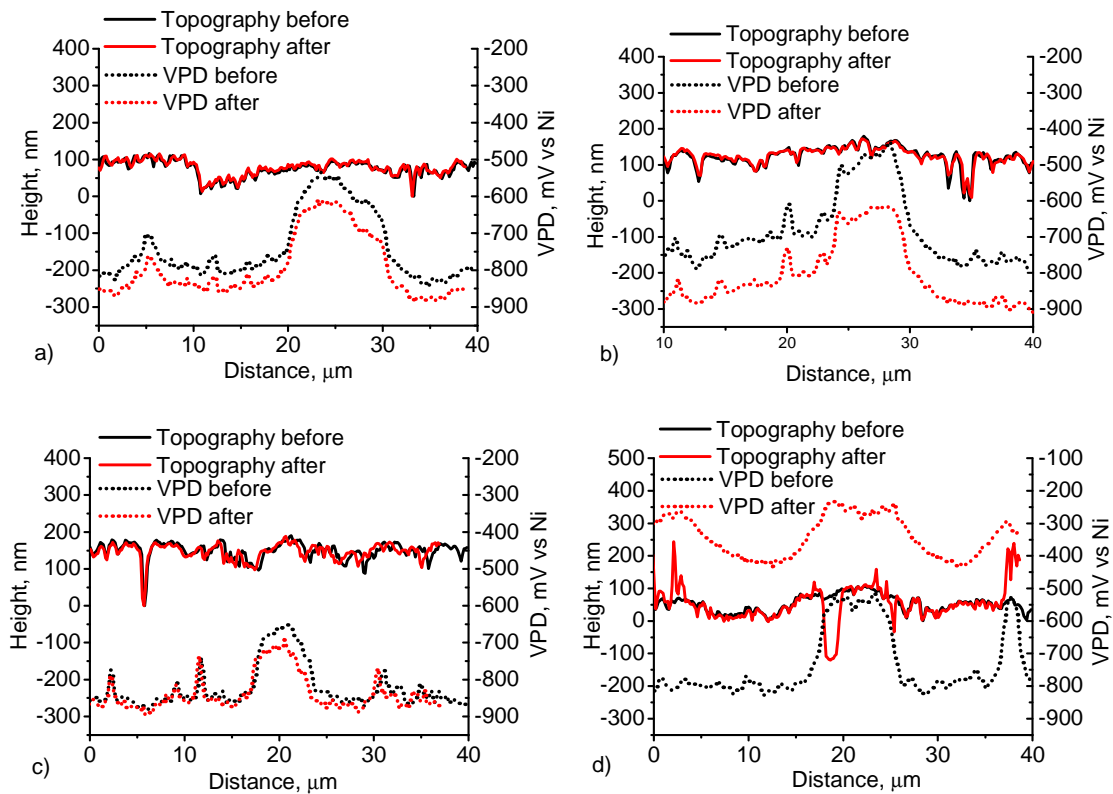
Figure 5.5.7 Topography and VPD profiles of the polished specimens of AA2024 before and after 5h immersion in 0.05 M NaCl solution with SAL a), QA b), 8HQ c) and NaCl solution only d).

The VPD profiles before immersion (Figure 5.5.7) display well defined peaks indicating copper rich intermetallic zones. After immersion in NaCl electrolyte with inhibitors the shape of VPD profiles has not changed, indicating the absence of localized corrosion attack (Figure 5.5.7a,b,c). However, the relative position of the profiles after immersion was changed compared to as polished substrates (Figure 5.5.7a,b,c black profiles). In case of SAL and QA inhibitors these changes were about 50mV and 100 mV respectively in the negative direction (Figure 5.5.7a and Figure 5.5.7b respectively). Almost no change was observed for 8HQ (Figure 5.5.7c). The negative offset of the VPD level for different inhibitors can be attributed to a charged or polar layer formed on the surface.

After immersion of the aluminum sample in NaCl solution only there is a huge broadening and positive shift of the VPD that is caused by copper redeposition on those zones (Figure 5.5.7d). The increase of potential of the matrix can be explained by the presence of the aluminum corrosion products layer and by the total increase of Cu content on the surface of the alloy resulting from redeposition processes around dissolved S-phases. This is confirmed by data of XPS analysis presented above, which shows the increase of copper content on the surface of alloy immersed in NaCl solution only (Figure 5.5.7c) compared to lower amount of Cu on the surface of specimens immersed into inhibitor-containing solutions.

5.5.6 Mechanism of the corrosion inhibition

The effectiveness of corrosion inhibition of AA2024 is mainly determined by the mechanism of action of the studied compounds on the activity of the S-phase inclusions. One of the possible mechanisms is the formation of hardly soluble chelate compounds on the alloy surface. The results of the EIS measurements showed the presence of a high frequency time-constant on the impedance spectra of samples immersed into inhibitor-containing solutions. This time constant was attributed to the presence of the adsorbed layer of inhibitor or complexes containing Al^{3+}, Mg^{2+} or Cu^{2+} cations. XPS data demonstrate the presence of nitrogen on the surface of all specimens immersed into inhibitor-containing solutions which can be explained only by the presence of inhibitor or insoluble complexes of inhibitor with metals on the surface of the alloy.

Analytical data regarding the conditions of formation, composition and properties of complexes of the investigated inhibitors with cations of Mg, Cu and Al occasionally exist in literature [17,352-354] and are presented in Table 5.5.2. The 8HQ forms very insoluble precipitates with all the components of the S-phases. Such low values of product solubility and wide pH range of stability of the complexes result in the formation of insoluble $Al(C_9H_6ON)_3$, $Mg(C_9H_6ON)_2$ and $Cu(C_9H_6ON)_2$ compounds at the very beginning of the corrosion process when only the first products of corrosion appeared at

low concentration. Moreover, the layers of deposited chelates prevent adsorption of chloride ions on the surface covered with native aluminum oxide, which remains intact. Although formation of chelate 8-hydroxyquionoline complexes on the surface of aluminum [61] and copper [355] was described, the inhibiting action of 8HQ on the dissolution of magnesium from the intermetallic inclusions, which was presented above has not been mentioned earlier. SAL and QA have never been mentioned before in literature as inhibitors of copper, magnesium or aluminium corrosion process. There is no strict analytical data on numerical values of solubility or stability constants for complexes of copper with SAL or Al with SAL except for Cu with QA (Cu(L)$_2$ PS = 1.6·10^{-17}) [17]. However, there is information on gravimetric [356-359] and conductimetric [360] determination of Cu and Al in the form of their QA or SAL complexes. Thus, Al and Cu are able to form insoluble complexes with SAL and QA as well as 8HQ. Formation of water insoluble complex layers on the entire metal surface and on the active sites of AA2024 alloy stops the extension of the corrosion and is most probably responsible for the effective inhibition of the localized corrosion processes.

The number of investigations aimed at the exploration and development of effective substitution of chromates has considerably increased since the prohibition of the use of chromate-containing anticorrosion coatings. Undoubtedly, the environmental friendliness of newly-discovered inhibitors is an issue. According to the MSDS (Material Safety Data Sheet) of ChemExper data base [361] carcinogenicity of 8HQ, SAL and QA are not listed by ACGIH, IARC, NIOSH, NTP, OSHA in contrast with compounds of Cr(VI) which is a known carcinogen. However, exact toxicological tests should be carried out before wide industrial use of the investigated inhibitors.

The corrosion inhibitors in the case of the aeronautical applications, where AA2024 is mainly used, can not be added to the corrosive environment like in some technological cases where metallic constructions are employed. Another way is to introduce the organic inhibitor into the coating system. The main concept of prospective application of SAL, QA and 8HQ is their embedding as active components into thin hybrid organic-inorganic sol-gel coatings or primer.

Table 5.5.2. The properties of insoluble complexes of Cu, Mg and Al with 8HQ.

Me	pH	PS*	Compound	Reference
Al – 8-HQ	4.2 - 9.8	1.03·10^{-29}	Al(L)$_3$	[352]
Mg – 8-HQ	9.4 - 12.7	6.8·10^{-16}	Mg(L)$_2$	[353]
Cu – 8-HQ	5.3 - 14.6	4.2·10^{-24}	Cu(L)$_2$	[354]

$*PS = a_{Kt}^{m} a_{An}^{n}$, where a is activity of ion when dissociation of low soluble Kt$_m$An$_n$ occurs: Kt$_m$An$_n$ = mKt + nAn.

Summarizing

Three organic inhibitors SAL, 8HQ and QA are proposed for effective corrosion protection of AA2024.

The results of corrosion tests using EIS, DC polarization and localized techniques (AFM/SKPFM) demonstrate a stable and prolonged corrosion inhibiting effect of AA2024 conferred by the tested organic compounds.

The presence of inhibitors in the corrosive medium leads to significant decrease of the corrosion processes as a result of formation of a thin adsorption protective layer on the surface of the alloy. However, the formation of the layer takes time. Impedance measurements clearly demonstrate the formation of layer only after approximately one day of immersion. DC polarization measurements also show that the protection is more efficient after longer immersion time prior to the measurements. The inhibiting action is based on the passivation of active intermetallic zones preventing the dissolution of Mg and Al as well as dissolution and redeposition of Cu. Moreover, the insoluble layer prevents the adsorption of aggressive chloride ions on the surface of the alloy.

The presence of layers of inhibitors on the surface is proven by XPS and EIS analysis. Quantitative considerations of results of XPS and EIS analysis show that 8HQ forms a thicker layer on the surface compared to SAL and QA. Chemisorption and precipitation of complexes occur on the surface alloy including the active S-phase.

The 8HQ and SAL decrease the rate of the anodic reaction. The cathodic process occurring mainly on the intermetallic particles is slowed down as well by all inhibitors.

The 8HQ, SAL and QA are promising candidates to be added to the coating systems as active anti-corrosion components for long-term corrosion protection of 2024 aluminium alloy.

6 Sol-gel coatings

6.1 Hybrid sol-gel coatings as pretreatments for corrosion protection of AA2024

In conventional coating systems used for different metallic substrates the adhesion between the metal and organic paints is mainly based on the mechanical interlocking between the pre-treated metal surface and the organic coating. In the case of sol-gel pre-treatments mechanical interlocking is difficult to achieve because the surface of the sol-gel coating is very smooth compared to anodized layers or conversion coatings. Nevertheless, sol-gel systems are chemically reactive and can provide chemical bonding to the hydroxide functionalities existing on the oxide covered metal surface and to the organic functionalities existing in different polymer coatings thus enhancing the adhesion. Appropriate functionalized groups are necessary for the sol-gel systems to provide chemically bonded interface between the metal and the organic paints. Sol-gel systems stabilize two interfaces. The first one is metal/sol-gel interface and the second one sol-gel/organic paint. The stabilization of the first interface is mainly attributed to the formation of covalent bonds between Si and metal through the oxygen bridge. Such bonding is very strong and can provide necessary degree of adhesion to metallic substrate. The stabilization of the second interface between the sol-gel/organic paints can be achieved by the introduction of specific functional groups like epoxy-, methacryl-, amino- and others to the sol-gel systems. For example organic paints used in aerospace industry typically contain epoxy and amino based components in order to provide crosslinking. Therefore chemical reactivity between the functional groups of paints and sol-gel confers effective bonding of the two layers. In addition to quality of adhesion, pretreatments should provide necessary degree of barrier protection. This can be achieved by variation of the crosslinking and condensation degree of the sol-gel network. Sol-gel pretreatments are therefore promising candidates for substitution of conventional pretreatments like conversion coatings or anodized layers in industry.

In this study two hybrid sol-gel systems were synthesized, optimized and investigated as pretreatments for corrosion protection of AA2024. The first system is based on the combination of Zirconium (IV) propoxide (TPOZ) and organofunctional silane 3-glycidoxypropyltrimethoxysilane (GPTMS). The second system is a combination of Titanium (IV) propoxide (TPOT) and GPTMS. The procedures of the sol-gel synthesis are described in paragraphs 4.3.1 and 4.3.2. However, some observations and details of the sol-gel processing will be presented further.

6.1.1 Sol-gel synthesis

Two main components have been used for the sol-gel synthesis, namely TPOZ or TPOT (metalorganic compounds) and GPTMS (organofunctional silane). The metalorganic compounds were employed to build an inorganic network and for in-situ formation of oxide nanoparticles which normally reinforce the sol-gel matrix and provide necessary mechanical strength. However, due to high reactivity of the metalorganic precursors it is essential to introduce additional complexants that inhibit the hydrolysis of TPOZ and TPOT. Two different complexing agents such as Acetylacetone (AcAc) and Ethylacetoacetate (EtAcAc) were used for the preparation of Zr and Ti based sol-gel systems. The organofunctional silane (GPTMS) provides required functionality for the stabilization of the two interfaces. Hydrolyzed silanol groups can react with the metal interface forming covalent oxygen bridges and inorganic network. Epoxy functionalized organic part provides necessary cross linking degree with organic paints ensuring good adhesion between the two layers. Table 6.1.1 shows the composition and reference number of different sol-gel systems prepared in this study.

Table 6.1.1. Compositions of different sol-gel systems and their reference name.

Component/Reference	SgZr1	SgZr2	SgTi1	SgTi2
TPOZ	+	+	-	-
TPOT	-	-	+	+
EtAcAc	+	-	+	-
AcAc	-	+	-	+
GPTMS	+	+	+	+
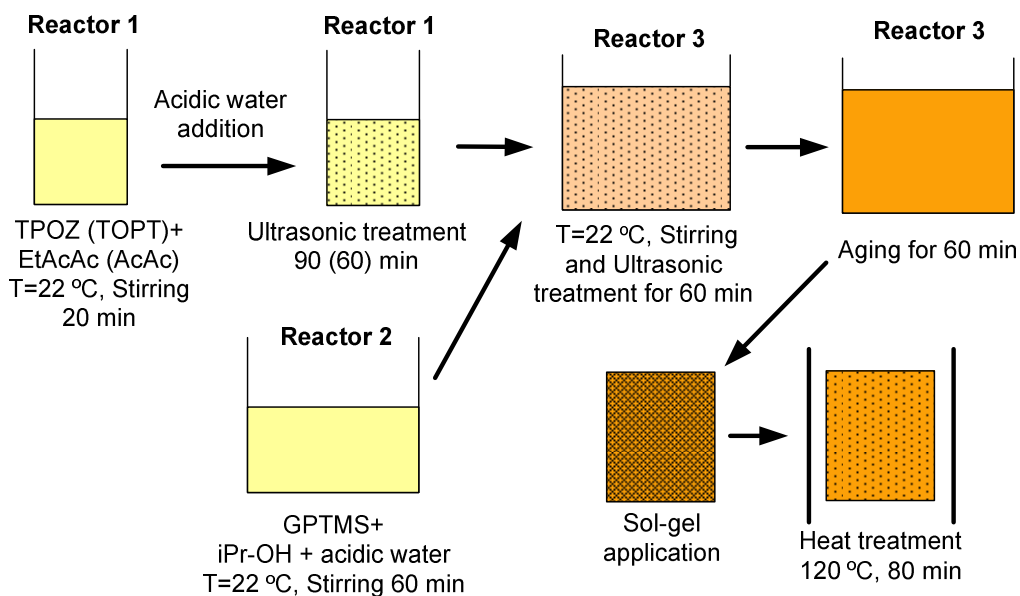
Figure 6.1.1. Schema of the sol-gel synthesis route.

Sol-gel formulations were prepared in three steps as described in the synthesis procedure (paragraphs 4.3.1 4.3.2). The schematic representation of the sol-gel synthesis route is presented in Figure 6.1.1. The first step of the synthesis includes the synthesis of alkosol 1 based on metalorganic precursors (TPOT or TPOZ) which is performed in Reactors 1. The second step includes the preparation of alkosol 2 containing GPTMS in Reactor 2. At the third step the obtained two alkosols are mixed in Reactor 3 giving the alkosol 3. After ageing the sol-gel is applied at alloy substrates and then cured in an oven.

Different transformations occur at each step of the sol-gel synthesis. The following observations were made during the synthesis of titania-containing organosiloxane sols (alkosol 1). The use of TPOT and AcAc as starting compounds in the first sol system results in the formation of pale yellow suspension after water addition and about 10 min of ultrasonic agitation (Figure 6.1.2a). After 35 min of intense ultrasonic treatment, the yellow suspension gelates. Therefore to avoid gelation the first sol was ultrasonically treated for 25-30 min and then only mechanically stirred for 30-35 min before mixing with the second alkosol. Combining of this suspension with the second organosiloxane alkosol gives a transparent straw-colour agile sol (SgTi2) even after several minutes of ultrasonic treatment (Figure 6.1.2b). On the contrary the use of EtAcAc as a complexant-stabilizer for TPOT hydrolysis does not lead to formation of a suspension during the first alkosol synthesis. The colour of the first alkosol is a tee like (Figure 6.1.3a) with no visible turbidity. After mixing the first alkosol with the second alkosol the resulting colour of the final sol-gel (SgTi1) is yellow (Figure 6.1.3b) and is very similar to SgTi2 (Figure 6.1.2b).

By the analogy with the titanium organic precursors, the combination of TPOZ and AcAc with water also gives a suspension after their mixing (Figure 6.1.4a). A crystalline compound was apparently formed as a result of reaction between the two reagents. Continuous ultrasonication of the suspension for 60 and more minutes does not increase the viscosity of the suspension. After mixing alkosol 1 and 2 a transparent light yellow sol is formed without visible turbidity (SgZr2) (Figure 6.1.4b). The alkosol obtained after mixing of TPOZ and EtAcAc with water is clear with no signs of gelation and turbidity even after long ultrasonic agitation time. A clear sol with brownish colour is formed in this case (Figure 6.1.5a). The mixing of the first and the second alkosols gives transparent almost colourless sol (SgZr1) (Figure 6.1.5b).
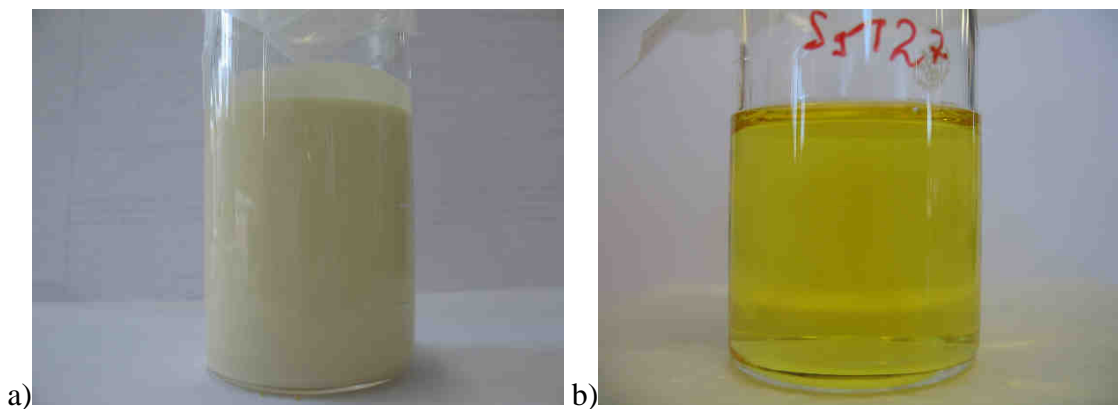
Figure 6.1.2. Optical photograph of the suspension formed in alkosol 1 with TPOT, AcAc and water after ultrasonic agitation a), and the final sol-gel mixture alkosol 3 (SgTi2) b).
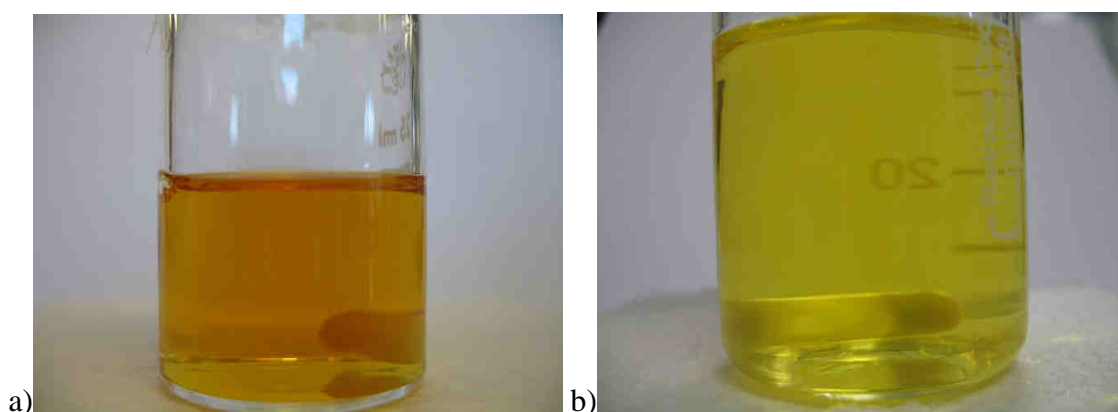
Figure 6.1.3. Optical photograph of the suspension formed in alkosol 1 with TPOT, EthAcAc and water after ultrasonic agitation a), and final sol-gel mixture alkosol 3 (SgTi1) b).
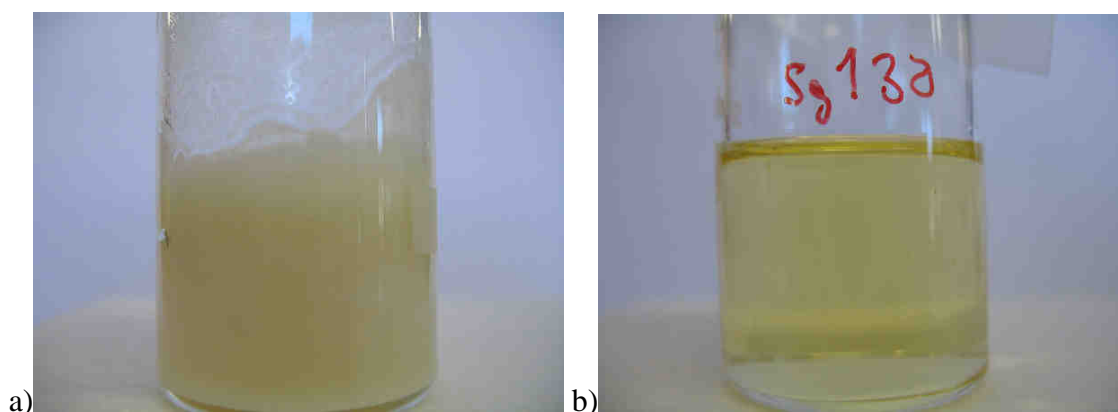
Figure 6.1.4. Optical photograph of the suspension formed in alkosol 1 with TPOZ, AcAc and water after ultrasonic agitation a), and final sol-gel mixture alkosol 3 (SgZr2) b).

188
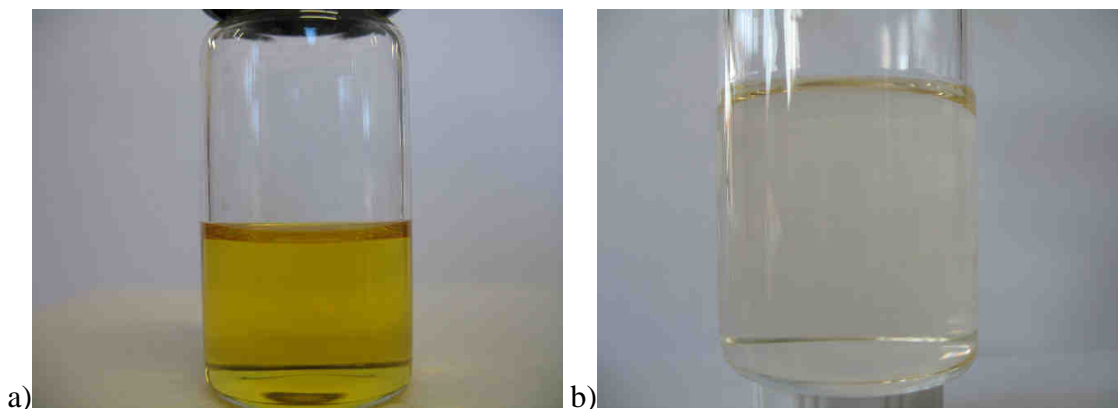
Figure 6.1.5. Optical photograph of the suspension formed in alkosol 1 with TPOZ, EthAcAc and water after ultrasonic agitation a), and final sol-gel mixture alkosol 3 (SgZr1) b).

The colour alterations suggest that the complex chemical interactions occur during the synthesis of the alkosols. According to the previously obtained data on the titanium alkoxide hydrolysis/condensation reactions [362-365], the formation of metal oxide nanoparticles in the first sol can proceed with participation of different complexes such as $Ti(OPri)_3(acac)$ and $Ti(OPri)_2(acac)_2$. Moran *et al.* found that the clusters $Ti_4O_2(OPri)_{10}(acac)_2$ can be obtained by slow hydrolysis of a mixture of $Ti(OPri)_4$ and AcAc [366]. Further linking between these organo-inorganic bricks can be accomplished through the hydrolysis-condensation reactions promoted by residual water and protons.

The appearance of the suspension in the case of AcAc complexing agent might be associated with the formation of oxo-compounds with the following formulas $TiO(AcAc)_2$ and $[TiO(AcAc)_2]_2$ [367,368]. To support this assumption, we performed XRD analysis of the powder obtained after centrifugation of this suspension (Figure 6.1.6). Results obtained show that titanium oxo bis(acetylacetonate) ($TiO(AcAc)_2$) is actually a dominant component of the precipitate. Introduction of these pre-hydrolized acetylacetonate complexes into the organosiloxane sol gives transparent hybrid sol under US agitation. The formation of heterometal Si-O-Ti bonds takes place during this stage. Further chemical transformations occur also during the stage of hybrid alkosol aging. Colour alternation of the titania-containing sols from light-yellow to yellow support this assumption.
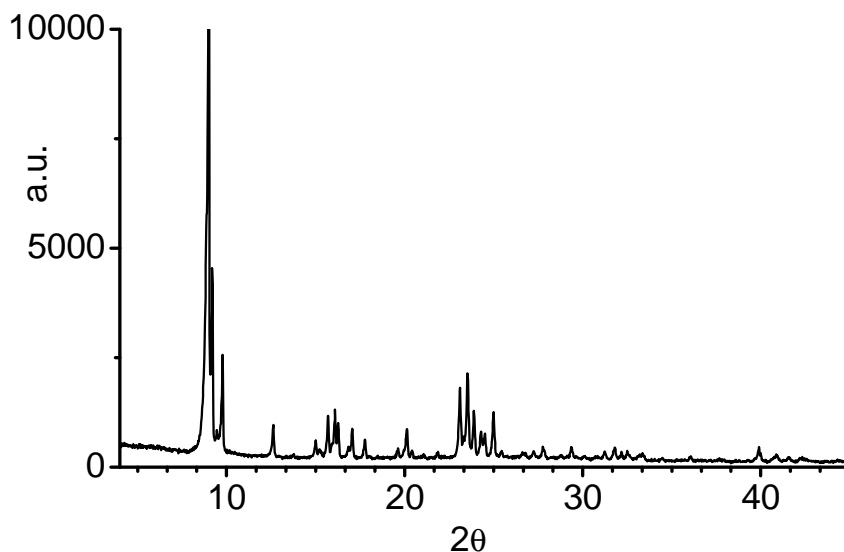
Figure 6.1.6. XRD spectra of $TiO(AcAc)_2$ compound obtained after centrifugation of the alkosol 1 containing TPOT and AcAc.

Less information on the structure of the Zr-containing complexes can be found in the literature. The complex $Zr_4O(OiPr)_{10}(AcAc)_4$ which is the primary hydrolysis product of $Zr(OPr)_3(acac)_2$ can be obtained in the system with Zr (IV) precursors and AcAc [369]. The composition of a Zr complex depends on the ratio between the ligand and the metal. When this ratio is low then larger clusters can be obtained. The appearance of crystalline precipitates when mixing TPOZ and AcAc can be related to the initial formation of $Zr(OiPr)(AcAc)_3$ complexes that are transformed to a more stable form $Zr(AcAc)_4$ [370,371].

6.1.2 TG/DTA characterization of the hybrid sol-gel polymers

To study thermal behavior of the sol-gel materials obtained from the prepared sols and to select proper heat-curing temperature for the preparation of the films DTA/TGA analysis was performed on powdered xerogel samples. Before these measurements the xerogels were dried at 60 °C for 7 days to ensure deep polymerization. Figure 6.1.7 shows the DTA/TGA curves for Zirconium and Titanium based hybrid sol-gels. For comparison reasons, similar experiments were made for xerogels prepared from the first Alkosol solution 1 containing TPOZ, EtAcAc with water and second Alkosol solution 2 containing GPTMS, 2-propanol and water (Figure 6.1.7).

The xerogel prepared from GPTMS (alkosol 2) gives first distinctly steep weight loss at 170-230°C with a sharp exothermic peak at 180 °C followed by a second steep weight loss at 250-450 °C and broad exothermic peak that starts from 250 °C. The first weight loss may be assigned to the elimination of chemically bound water from the inorganic network and additional condensation of the siloxane groups [372,373]. Whereas the second weight loss is ascribed to the decomposition of organic part [256].

As compared with the xerogel prepared using GPTMS (Alkosol 2) (Figure 6.1.7), the TGA curves for the binary oxide systems (SgZr1 and SgTi2) demonstrate very small weight losses in the temperature range up to 150 °C with small endothermic effects near 100 °C which are characteristic of the desorption of physically adsorbed water molecules. There are several steps of a strong weight loss between 150 and 350 °C, which can be attributed to the release of chemically bounded water (around 200 °C) and to decomposition of the organic components (around 300 °C). Moderate exothermic effects accompany this weight loss. Exothermic effects and weight loss at temperatures higher 400 °C both for (1) and (2) xerogels can be associated with an additional decomposition of the organic matrix as well as structural transformations of Zr or Ti oxides. More detailed analysis of high temperature part of TG and DTA curves can be studied for xerogels based on metal alkoxides in order to clarify existence of broad exothermic peaks at high temperatures.

Thermal behavior of metalorganic precursors, as an example for TPOZ based xerogel (4), shows appearance of the exothermic peak near 440 °C (Figure 6.1.7). Such increase is associated with the crystallization process of a partially hydroxylated amorphous oxide [374]. For TPOT based xerogel (data are not presented) there is an exothermic peak at around 500 °C that is similar to xerogel (4). Such exothermic peak can be attributed to the structural transformation of anatase to rutile [374]. Therefore the broadening on DTA curves for the sol-gel systems (1) and (2) is a mixture of decomposition of organic matrix and structural changes of the metal oxides.

These results indirectly show that the hydrolysis and condensation reactions are more complete in the binary oxide systems as compared to single alkosol 1 or 2 systems. The binary oxide xerogels are more thermo-stable than those containing individual oxides only. Results of TGA measurements show that sol-gel systems based on Zr- and Ti-propoxides are relatively stable up to 150°C. Therefore temperature of curing of the sol-gel coatings should not exceed this value.
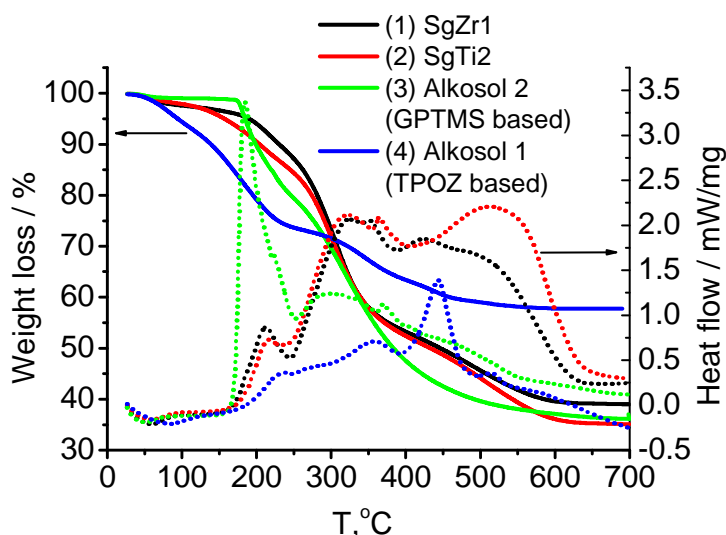
Figure 6.1.7. TGA/DTA curves for zirconia - (1) and titania - (2) based hybrid xerogels; for xerogels prepared from alkosol 2 containing GPTMS, 2-propoxide and water (3); for xerogels from alkosol 1 containing TPOZ, EtAcAc and water (4).

6.1.3 Microstructural characterisation of the sol-gel coatings

To find more information about the micro- and nanostructure of the sol-gel coatings, two model systems based on Zr and Ti hybrid sol-gels were deposited on glass substrates and studied by AFM. Prior to the deposition the glass was carefully cleaned to avoid artifacts on the topographic maps. The AFM measurements of the two systems are presented in the Figure 6.1.8. Well uniform coatings are formed in case of hybrid sol-gel systems based on Zr and Ti precursors (Figure 6.1.8). At closer observation one can see that the surface of the coatings is composed of nanostructured particles that are formed during hydrolysis and condensation of metal organic and silicon based compounds (Figure 6.1.8 b,d). The average size of nanoparticles in both coatings is around 50 nm.

SEM was also used to characterize microscopic properties and thickness of the sol-gel films after deposition on chemically cleaned AA2024 substrates. The deposited sol-gel films have homogeneous glass-like structure and defect and crack free surface (Figure 6.1.9 a,c). Dark spots around 10-20 µm on the SEM images correspond to the sol-gel filled voids that were formed in the alloy after chemical pretreatment of the alloy surface (Figure 6.1.9a,c). At high magnifications SEM shows the nanostructured surface which is in agreement with AFM topographic measurements. The diameter of the particles is less than 100 nm (Figure 6.1.9b,d). The particles are uniformly distributed in the hybrid matrix without visible signs of agglomeration. However, whether these particles are composed by oxides of Zr, Ti or Si is not yet resolved. Another important characteristic of the deposited

192

coatings is their thickness. The thickness of the films was estimated by the cross section SEM analysis presented in Figure 6.1.10. For Zr and Ti based films thickness varies between about 1.5 to 2 µm. Such deviation of thickness can be a result of the nonuniform alloy surface and dipcoating process in which the coating thickness slightly changes from the top to bottom of the sample.
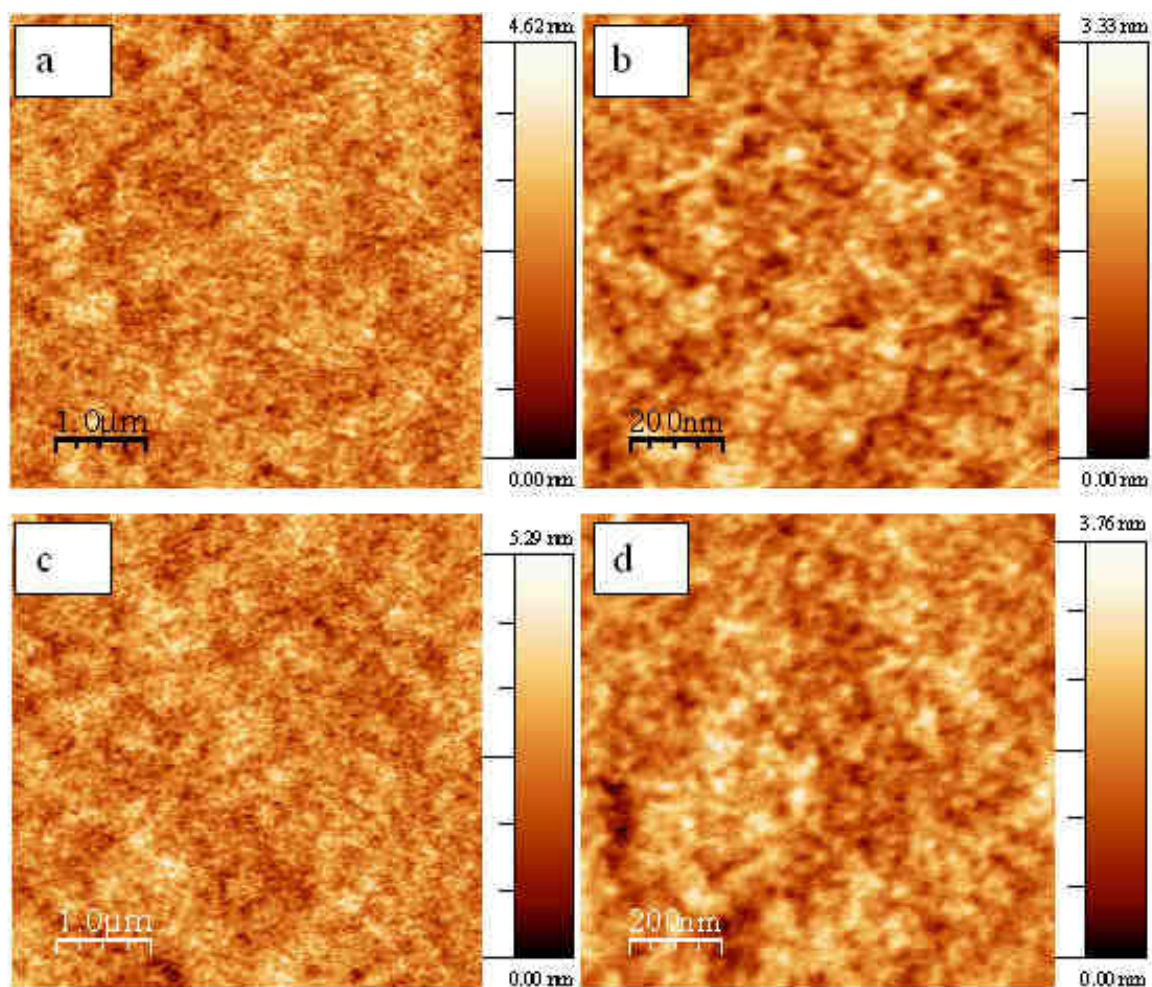
Figure 6.1.8. Topography of hybrid sol-gel coatings SgZr1 a), b) and SgTi2 c), d).
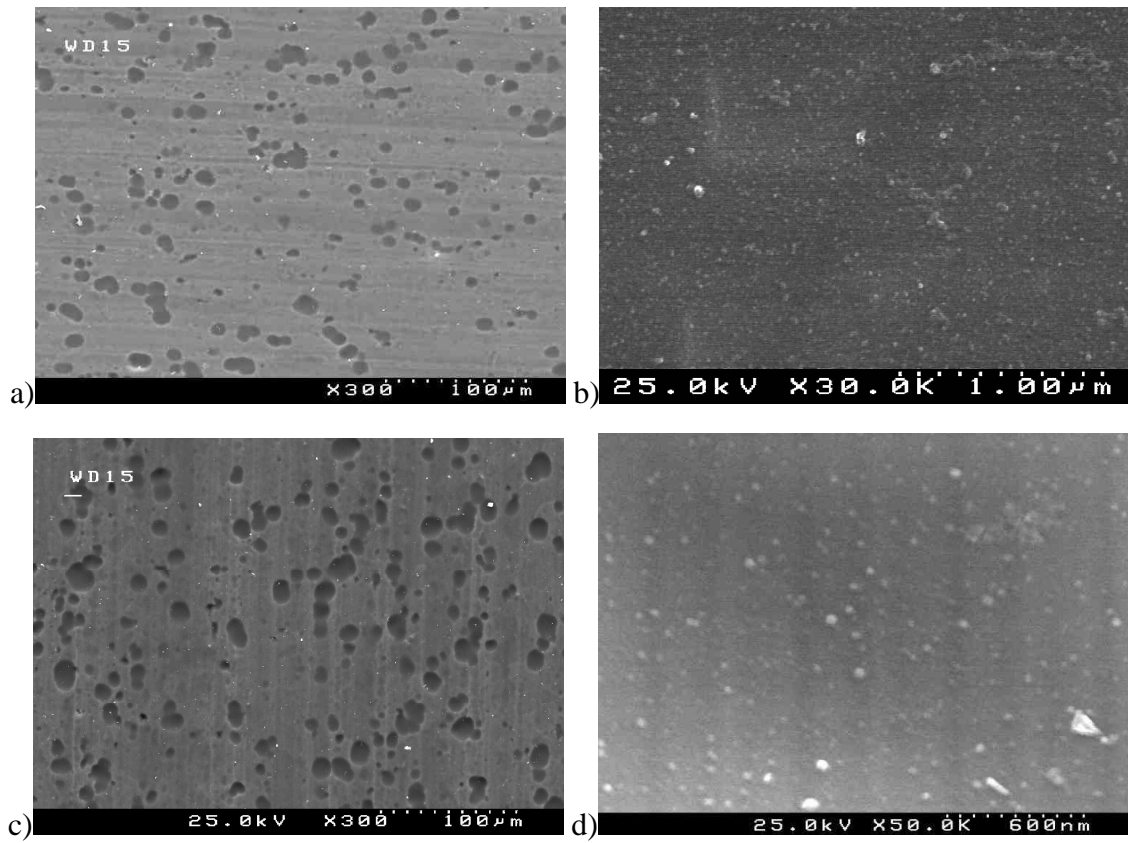
Figure 6.1.9. SEM micrographs of SgZr1 (a,b) and SgTi2 (c,d) sol-gel coatings deposited on AA20204 substrates.
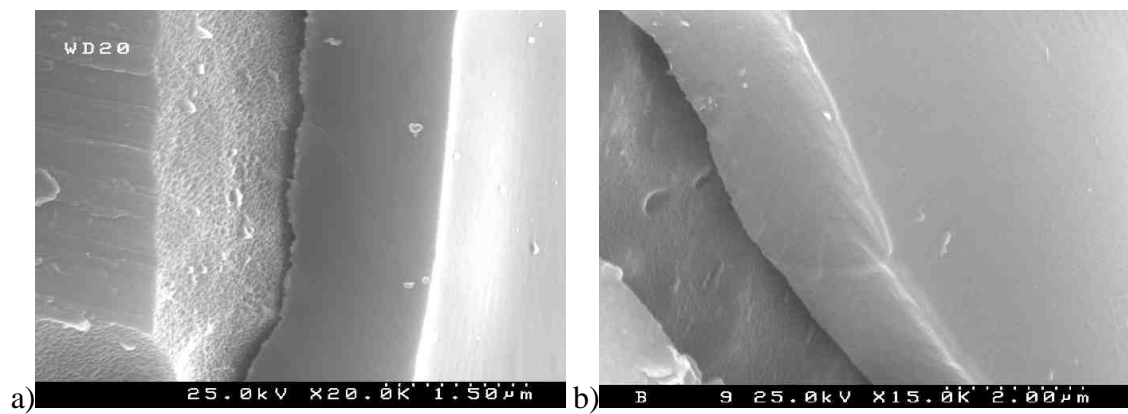
Figure 6.1.10. SEM cross-section micrographs of SgZr1 a) and SgTi2 b) sol-gel coatings deposited on AA2024 substrates.

A TEM investigation has been performed in order to get information on micro- and nanostructural properties of the sol-gel coatings applied on AA2024 substrate. Figure 6.1.11 presents cross-section images of sol-gel coatings. The coatings are dense, homogeneous and uniformly cover the alloy surface. Sol-gel penetrates inside the voids in the metal surface as can be seen as an example for SgZr1 coating (Figure 6.1.11a). This indicates good wettability of the alloy by the sol-gel solution. An interface between the alloy and sol-gel coatings at higher magnification is presented in Figure 6.1.11b. Micrographs clearly show the presence of an intermediate layer between the alloy matrix (bottom) and sol-gel coating (top). The layer has different gray tone compared to alloy and sol-gel and most probably is composed by aluminum oxide. Such oxide is naturally formed after the alloy cleaning procedure. The sol-gel layer tightly adheres to the oxide layer forming a stable interface (Figure 6.1.11b).

The nanoparticulated structure of the coating is visible at higher magnifications over 150k times. Figures 6.1.11 present cross-sectional micrographs of the Zr (c) and Ti (d) sol-gel coatings. Dark spots on the Figures most probably indicate the presence of nanoparticles of ZrO_2 and TiO_2. Since Zr and Ti elements have higher molecular weight the scattering and absorption of electron beam by these atoms is higher when compared to silicon and TEM image gets darker in the places of metal nanoparticles as can be seen on Figure 6.1.11c,d. The size distribution of nanoparticles varies between about 10 to 20 nm for Zr and Ti based systems. However, the presence of SiO_2 nanoparticles is not possible to resolve by TEM because silicon is the major element in the sol-gel and is distributed homogeneously in the matrix. Nevertheless, AFM images (Figure 6.1.9) and SEM images (Figure 6.1.10) clearly show the nanostructured properties of the coatings which can be associated with the presence of both silica and metal-oxide nanoparticles. From another hand, the higher size of nanoparticles observed by AFM and SEM (around 50nm) can be related to the fact that those nanoparticles have a kind of core-shell structure when core is titania or zirconia and shell is constituted by the siloxane chains. However, neither TEM nor AFM methods can prove the presence of silica nanoparticles.
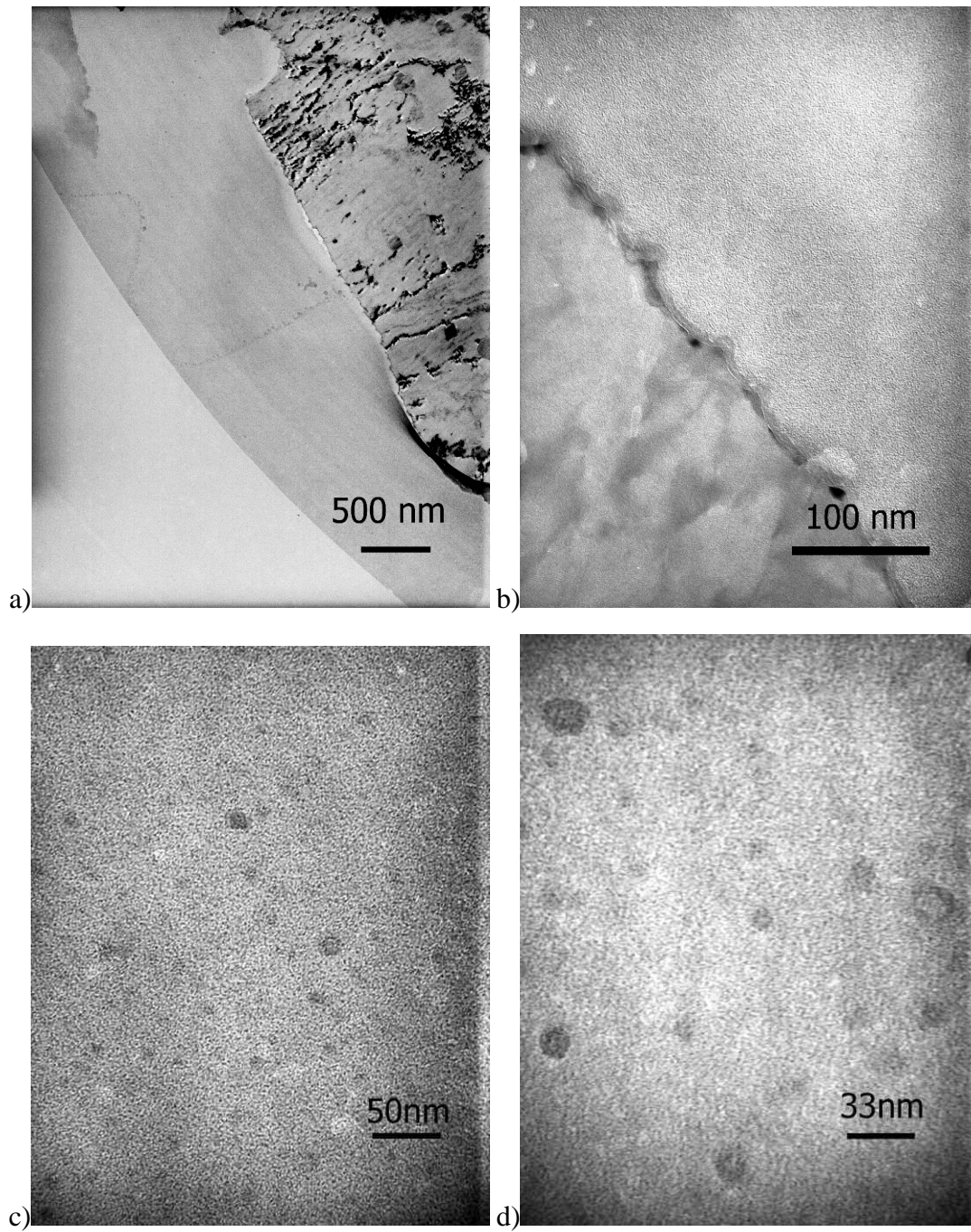
Figure 6.1.11. TEM cross-section micrographs of SgZr1 a), b), c) and SgTi2 d) sol-gel coatings deposited on AA2024 substrates.

6.1.4 Corrosion protection properties of the sol-gel coatings

Equivalent circuit modeling and analysis of impedance spectra

The impedance measurements provide valuable information on the physicochemical processes that occur in coated metal samples during immersion in corrosive electrolytes. Creating an appropriate physical model and using it for fitting of impedance spectra helps to get information on corrosion protection efficiency and study the kinetics of corrosion. Figure 6.1.12 presents evolution of impedance spectra after one hour, one day, two weeks and 1 month of immersion in 0.5M NaCl electrolyte for Zr-based sol-gel coating deposited on AA2024 substrate. Two well-defined time constants can be observed on the Bode plots after 1 hour of immersion. The high frequency time constant (around 10^5 Hz) is associated with capacitance and resistance of the sol-gel layer (C_{coat}). The second relaxation process observed in the 0.1-1 Hz frequency range is ascribed to the presence of intermediate oxide film (C_{ox}) at the metal/coating interface. The spectra show one clearly visible resistive component near 10^2-10^3 Hz which corresponds to a resistance of the sol-gel film (R_{coat}). A model presented in Figure 3.3.14a can be used for fitting of the impedance spectra after short immersion time in NaCl solution. The result of fitting is shown as a solid line (Figure 6.1.12 1hour). The increase of the immersion time results in decrease of the (R_{coat}) due to the development of cracks and pores in the sol-gel film (Figure 6.1.12). The capacitance of the coating increases with the immersion time (Figure 6.1.12). Such behavior can correspond to the penetration of water in the film and partial hydrolytic destruction of the coating.
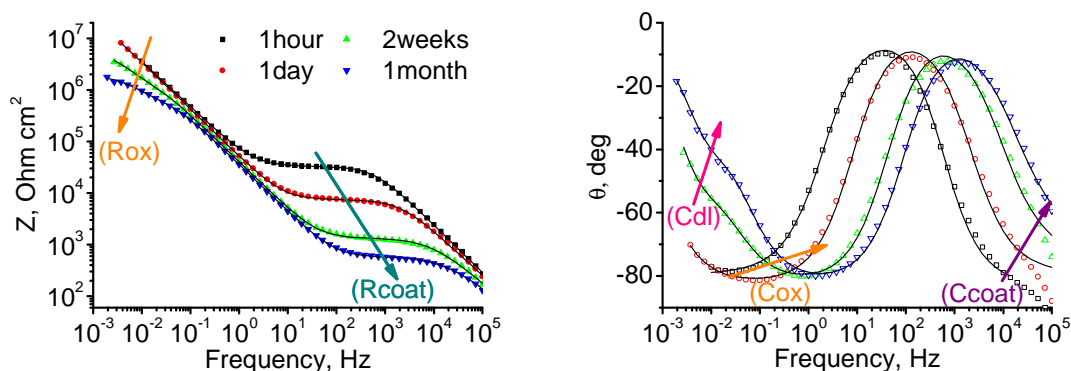
Figure 6.1.12. Impedance spectra of AA2024 coated with Zr based hybrid sol-gel film taken after 1 hour, 1 day, 2 weeks and 1 month of immersion in 0.5 M NaCl. Solid lines present fit using appropriate equivalent circuits.

After 1 day of immersion a new resistive component appears in low frequency part of the spectra and is ascribed to a resistance of the intermediate oxide layer (R_{ox}). Corrosive species progress through the coating and defects in the oxide layer forming a conduction path to the metal substrate thus developing a resistive behavior in the low frequency part of the impedance spectra. Oxide layer resistance decreases with immersion time. The corresponding spectra can be fitted using the equivalent circuit presented in Figure 3.3.14b. Solid line in Figure 6.1.12 presents the fitting results.

Signs of a corrosion process can be detected in the impedance spectra after several days of immersion. An additional time constant appears on the spectra in the low frequency region due to started corrosion attack (Figure 6.1.12 2 weeks). Therefore additional elements associated with double layer capacitance (C_{dl}) and polarization resistance (R_{polar}) should be added to the equivalent circuit model (Figure 3.3.14c). As can be seen from Figure 6.1.12 the fitting curves adequately describe impedance spectra after 2 weeks and 1 month of immersion.

The presented equivalent circuit models and fitting procedure are valid and can be used for fitting of impedance spectra obtained on the sol-gel coated alloy substrates. In the following paragraph EIS measurements will be performed on several sol-gel coated samples in order to determine the kinetics of the coating degradation and corrosion protection efficiency.

Corrosion protection of AA2024 by Zr and Ti based hybrid sol-gel coatings

Four different Zr and Ti based sol-gel coatings were applied on the alloy samples and studied using EIS during 1 month of immersion in 0.5M NaCl solution. Numerical fittings of impedance spectra employing appropriate equivalent circuits were performed in order to estimate the evolution of corrosion protection properties of different coatings under study. These equivalent circuits were selected for fitting the experimental results basing on the physico-chemical model of the corrosion process on coated metals. Only models that obtained high goodness were used to fit experimental results and to extract parameters of the investigated systems. The evolution of the parameters of the coated systems with time was analyzed in order to assess the corrosion protection properties of different sol-gel pre-treatments.

The evolution of the sol-gel coatings capacitance (C_{coat}) during 1 month of immersion in chloride-containing solution is presented in Figure 6.1.13a. The initial values of capacitance of SgZr1 and SgZr2 sol-gel films calculated form the first recorded impedance spectra are around $8.20*10^{-9}$ F/cm^2 for both coatings. Dielectric permittivity (ε) of the Zr based sol-gel coatings can be easily estimated using the thickness measurements. The results of ε calculation are presented in Table 6.1.2 for coating thickness 1.5 and 2 μm. Values of dielectric permittivity of the sol-gel coatings are about 13.9-18.5 and higher than

for organic materials. The presence of inorganic constituents in the sol-gel coatings can explain the increased dielectric permittivity. During the 2 days of immersion there is a rapid increase of capacitance until about $1.2*10^{-8}$ F/cm^2 followed by a linear increase until the end of immersion (Figure 6.1.13a). The rapid increase of the capacitance of the sol-gel coating can be explained by a water penetration inside the coating. Water uptake is estimated using the values of the coating capacitance at the beginning and in the end of immersion. Brasher-Kingsbury equation (3.3.22) was used for calculations and results are presented in Table 6.1.2. For SgZr1 and SgZr2 coating the estimated water uptake is 12.5% and 11.8% respectively after 1 month of immersion. However, the results of water uptake calculation might include an error because the obtained values are relatively high for thin coatings. This can be associated with the hydrolytic instability of the sol-gel coating during immersion in electrolyte and partial decomposition of the siloxane bonds. The sol-gel matrix destruction results in additional growth of capacitance and apparent increase of the water uptake.

The initial capacitance for Ti-based coatings is lower than for Zr-based ones and is around $7.58*10^{-9}$ F/cm^2 and $7.39*10^{-9}$ F/cm^2 for SgTi1 and SgTi2 coatings respectively (Table 6.1.2). The calculated dielectric permittivity is also lower and varies from 12.5 to 17.1 at thickness 1.5 and 2 µm respectively. In contrast to Zr based coatings during immersion there is a difference between the capacitance of SgTi1 and SgTi2 coatings. For SgTi1 sample the capacitance increases until about $1*10^{-8}$ F/cm^2 after two days of immersion. For SgTi2 sample the increase is higher until about $1.31*10^{-8}$ F/cm^2. A longer immersion time is accompanied by an additional increase of capacitance until approximately $1.65*10^{-8}$ F/cm^2. The calculations show that water uptake for Ti coatings is higher than for Zr based ones (Table 6.1.2). However, as was pointed out before, a high water uptake is rather attributed to the degradation of the sol-gel than to physical ingress of water in the coating.

The obtained results show that the use of various complexants for the sol-gel preparation results in different properties of the coatings especially for Ti based sol-gels. A variation in capacitance between SgTi1 and SgTi2 samples can evidence the different stability of the sol-gel coatings in water solution. In contrast to that, Zr based systems show very similar behavior.

Table 6.1.2. Numerical data of capacitance (C), dielectric permittivity ε, and water uptake for different sol-gel coatings.

	SgZr1	SgZr2	SgTi1	SgTi2
C F/cm^2 initial	$8.20*10^{-9}$	$8.20*10^{-9}$	$7.58*10^{-9}$	$7.39*10^{-9}$
C F/cm^2 after 1 month	$1.42*10^{-8}$	$1.38*10^{-8}$	$1.47*10^{-8}$	$1.65*10^{-8}$
ε, thickness 1.5 µm	13.9	13.9	12.8	12.5
ε, thickness 2 µm	18.5	18.5	17.1	16.7
Water uptake %	12.5	11.8	15.1	18.3

The information on the capacitance of coating is not sufficient for the analysis of the corrosion protective properties. Another important parameter of the coating is the pore resistance (Rcoat) that characterizes its barrier properties. The pore resistance consists of the resistance of electrolyte in pores, cracks and pits connected in parallel to each other. Figure 6.1.13b shows the evolution of the pore resistance of coatings under study during 1 month of immersion in 0.5M NaCl solution. Hybrid coatings demonstrate the highest resistance at the beginning of immersion with following fast decrease during the first 24 hour of contact with electrolyte. Fast penetration of water and ions into the finest pores of the film is most probably responsible for this resistance drop. The initial coating resistance and the following resistance drop after 1 day of immersion are significantly higher for coatings prepared using AcAc (SgZr2, SgTi2) as compared with EtAcAc (SgZr1, SgTi1) complexing agents (Table 6.1.3).

After the first minutes of immersion, SgZr1 and SgZr2 systems have almost two orders of magnitude difference in the initial R_{coat} (Table 6.1.3). However, after 100 hours of immersion, the lowest resistance was revealed for the SgZr2 coating which had the highest initial resistance (Figure 6.1.13b). Probably, a higher reactivity of the sol-gel system prepared using AcAc is responsible for such behavior. During the longer immersion time a well-defined linear decrease of R_{coat} occurs for all the coatings (Figure 6.1.13b). However, in spite of high initial resistance of SgZr2 coating the better behavior is attributed to another coating, namely SgZr1. This coating demonstrates better barrier protection during longer immersion in corrosive electrolyte.

Ti based coatings have opposite tendency compared to Zr based coatings. Sol-gel film prepared with AcAc (SgTi2 sample) has higher resistance at the beginning of immersion. However, unlike for sample SgTi1, sample SgTi2 shows higher resistance in the end of immersion as well (Figure 6.1.13). These results demonstrate that the complexing agents have different influence on the barrier properties of Zr and Ti bases sol-gel coatings.
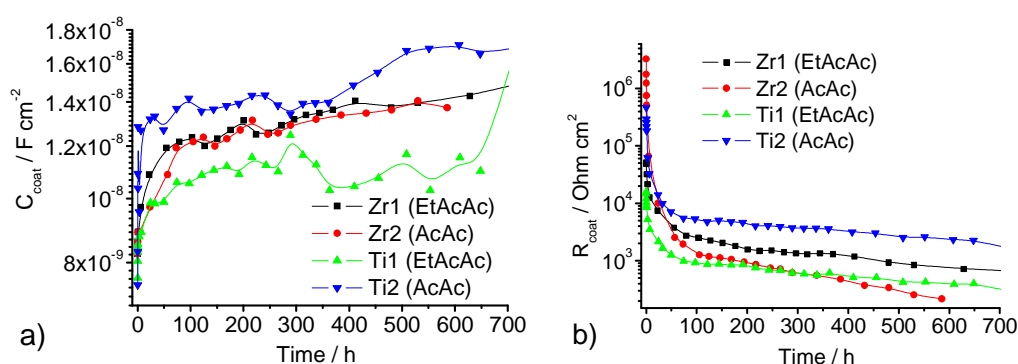
Figure 6.1.13. Evolution of capacitance C_{coat} a) and resistance R_{coat} b) for different hybrid coatings on AA2024 during immersion in 0.5 M NaCl solution.

Table 6.1.3. The resistance of different coatings at the beginning of immersion and after 24 hours of immersion in 0.5 M NaCl.

Coating reference	Initial R_{coat}, Ohm cm^2	R_{coat} Ohm cm^2 after 24 h of immersion	$R_{coat\ init.}$ / $R_{coat\ 24h}$
SgZr1	$5.0*10^4 \pm 4.8*10^2$	$7.5*10^3 \pm 7.8*10^2$	6.7
SgZr2	$3.3*10^6 \pm 2.9*10^4$	$1.0*10^4 \pm 1.3*10^2$	330
SgTi1	$1.6*10^4 \pm 1.5*10^2$	$2.2*10^3 \pm 4.8*10^2$	7.3
SgTi2	$4.6*10^5 \pm 4.2*10^3$	$1.4*10^4 \pm 2.8*10^1$	32.8

The compactness of the intermediate oxide layer formed between the sol-gel film and the metallic substrate is very important from the point of view of corrosion protection. A breakdown of this oxide layer allows direct ingress of the corrosive agents to the metallic surface. Figure 6.1.14a presents the evolution of the intermediate oxide layer resistance (R_{ox}). Samples SgZr2 and SgTi1 show fast drop of the oxide resistance from approximately $1*10^8$ Ohm*cm^2 to about $3*10^6$ Ohm*cm^2 during the first four days of immersion. Resistance continues to decrease at longer immersion time until about $5*10^5$ Ohm*cm^2 for SgZr2 coating and $8*10^5$ Ohm*cm^2 for SgTi1 coating. An initial resistance of SgZr1 and SgTi2 samples is about $1*10^8$ Ohm*cm^2 which is similar to other sol-gel systems (Figure 6.1.14a). At longer immersion the resistance of the oxide layer decreases to about $1*10^6$ Ohm*cm^2 and $2*10^6$ Ohm*cm^2 for SgZr1 and SgTi2 samples respectively. The results of evolution of intermediate oxide resistance are in accordance with the evolution of sol-gel coating resistance presented in Figure 6.1.13b. Sol-gel coatings SgZr1 and SgTi2 demonstrate higher barrier protection and higher intermediate oxide resistance. However, the high resistance of intermediate oxide does not only depend on the barrier protective properties of the coating. The stability of the interface between the sol-gel and metal plays an important role as well. The impedance results show that the initial values of resistance (R_{ox}) are similar for all samples. However, at longer immersion there is a significant difference. When a metal and sol-gel are tightly bonded, less corrosion species can ingress through the sol-gel matrix to this interface. Therefore oxide layer has higher stability. Apparently interface formed by SgZr1 and SgTi2 sol-gel systems is more stable compared to other sol-gel systems.

The rate of the corrosion processes ongoing on the metal surface can be estimated measuring the polarisation resistance of the sol-gel coated alloy. Figure 6.1.14b presents evolution of the polarization resistance R_{polar} calculated from EIS spectra for different coatings. A time constant associated with corrosion process becomes visible on impedance spectra only after some days of immersion. SgZr1 and SgZr2 coatings show very similar behaviour of R_{polar} that evenly decreases from around $1*10^7$ Ohm*cm^2 to $2*10^6$ Ohm*cm^2 during 1 month of immersion. In contrast to Zr based sol-gel coatings, behavior of R_{polar} is different for SgTi1 and SgTi2 coatings (Figure 6.1.14b). SgTi2 sample shows superior performance over other samples. These results demonstrate that different Zr- and Ti-based

sol-gel coatings delay starting of the corrosion process, though no decrease of the corrosion was found during the tests. Therefore the sol-gel coatings provide only passive corrosion protection to the substrate.
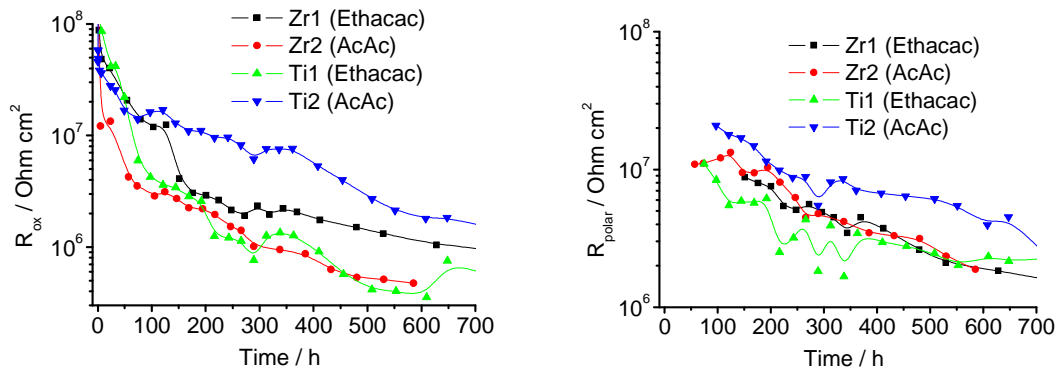
Figure 6.1.14. Evolution of resistance of the intermediate layer R_{ox} a) and polarization resistance of corrosion process R_{polar} b) for different hybrid coatings deposited on AA2024 during immersion in 0.5 M NaCl solution.

6.1.5 Optical and microstructural characterization of sol-gel coatings after corrosion.

Optical microscopy and SEM were used for macro- and micro- visualization of corrosion impact on sol-gel coated samples. Figure 6.1.15 shows the appearance of AA2024 samples coated with different sol-gel films after 1 month immersion in 0.5 M NaCl solution. All coatings demonstrate rather good protection against corrosion in chloride solution. Only several corrosion pits can be seen on the surface. However, two samples SgZr1 and SgTi2 show less pits and corrosion products compared to other samples. Low corrosion degradation is in a good agreement with the results obtained by EIS measurements.
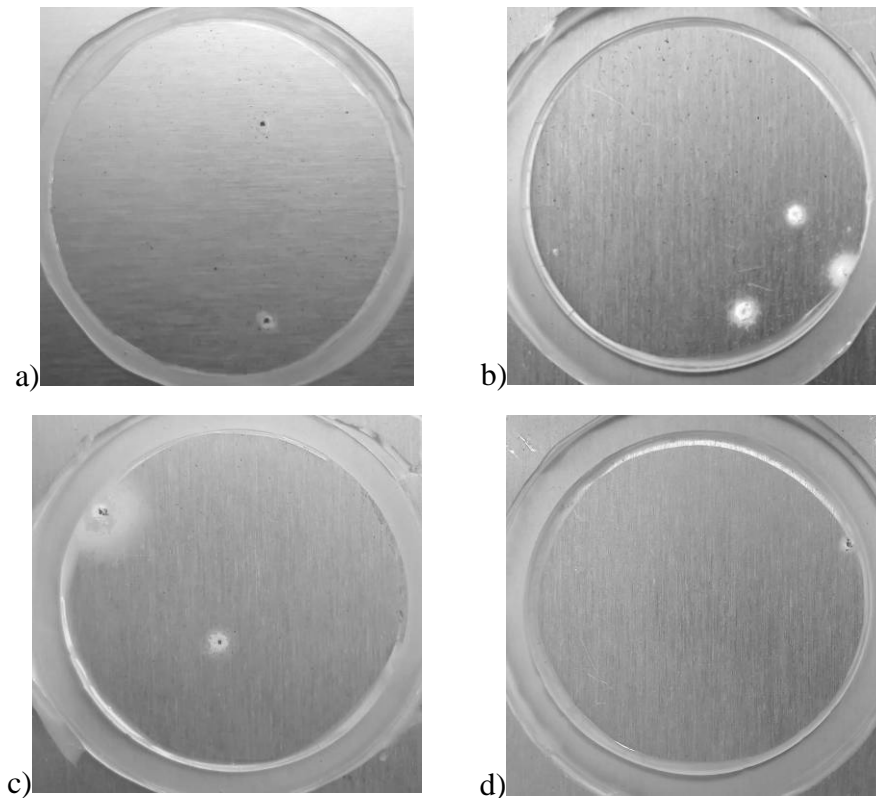
Figure 6.1.15. Optical photographs of AA2024 samples coated with different sol-gel films SgSgZr1 a) and SgZr2 b), SgTi1 c) and SgTi2 d) after 1 month immersion in 0.5 M NaCl solution.

SEM measurements provide additional information on the microstructural changes of the sol-gel surface after long-term corrosion testing. Inspection of the sample surface after 1 month immersion in 0.5 M NaCl solution shows no delamination or significant deterioration. However, small defects can be seen on the surface of the SgZr1 and SgTi1 coatings (Figure 6.1.16a,b). These defects appear particularly around the big corrosion pits presented in Figure 6.1.15. Similar defects can also be seen on the surface of SgZr2 sample (not shown). In contrast to that, SgTi2 sample contains much less microstructural defects except for a couple of them near the pit as in the case of SgTi1 coating (Figure 6.1.16b). However, the surface of SgTi2 sample is relatively clean away from the pits as can be seen in Figure 6.1.16c. The found defects look like blisters around 30-50 µm in diameter at higher magnification (Figure 6.1.16d). The figure also shows cracks in the sol-gel film near blisters that could be formed due to mechanical stress of the sol-gel during immersion.
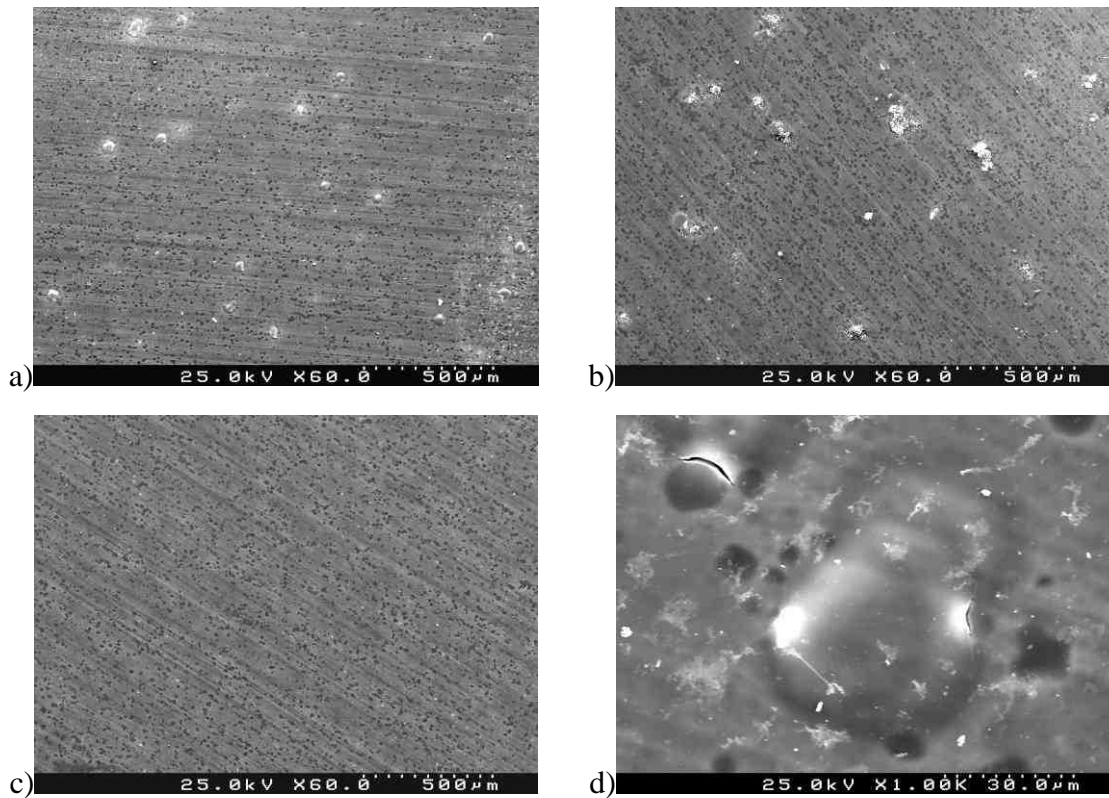
Figure 6.1.16. SEM micrographs of SgZr1 (a), SgTi1 (b) and SgTi2 (c) sol-gel after 1 month immersion in 0.5 M NaCl solution (plane view). Picture d) shows blister at higher magnification.

6.1.6 Salt spray tests

Titania- and zirconia-containing sol-gel coatings that showed the best performance in corrosion tests were deposited on large AA2024 specimens (150 x 80 mm) and investigated using standard accelerated corrosion tests such as neutral salt spray test (ISO 9227) and paint adhesion test (according to ISO 2409).

Table 6.1.4 shows the salt spray test results of chromate conversion coating (CCC), used as a reference, and selected sol-gel coatings (SgZr1 and SgTi2 without additional organic coat) after 168 h and 336 h test duration. A scratch with dimensions 1 mm width and 150 μm deep was made on all panels prior to testing. All the investigated samples do not show creepage from the scratch after 168 h and 336 h of testing. The chromate conversion coating demonstrates no defects after 168 h and only slight coloration of the surface appears after 336 h testing time. On the other hand the sol-gel coatings show some pits after 168 h and a stronger corrosion attack after 336 h (Figure 6.1.17b,c). SgTi2 coating shows less pits compared to SgZr1 film after both testing periods (Table 6.1.4).

Although both coating did not fulfill the requirement according to MIL 5541 E specification, it's a promising approach towards replacement of chromate conversion coatings.

Figure 6.1.18 shows photos of the scratch area of the test specimens after 168h and 336h of salt spray testing. The chromate conversion coating provides good active corrosion protection due to leaching of chromates. Therefore the scratch remains almost shiny after the test duration of 336h. The sol-gel coatings provide adequate protection of the scratch until 168h with coloration but no visible pits. After 336 h, the sol-gel samples offer lower degree of corrosion protection compared to CCC. Some pits with corrosion products are detectable in the scratch area of the two specimens. However, SgTi2 coating shows a slightly lower amount of pits than SgZr1 one. The results of the accelerated corrosion testing show the lack of active corrosion protection of the sol-gel coatings.

Table 6.1.4. Results of the salt spray test of different coatings after 168 h and 336 h.

Coating reference	Test duration	Creepage from scratch max. [mm]	Evaluation of sample surface	Evaluation of scratch area
CCC	168 h	0	no defects	no corrosion
SgZr1	168 h	0	8 pits, 30 evolving pits	coloration
SgTi2	168 h	0	6 pits, 20 evolving pits	coloration
CCC	336 h	0	slight coloration	slight coloration
SgZr1	336 h	0	15 pits, 40 evolving pits	visible pits
SgTi2	336 h	0	10 pits, 30 evolving pits	visible pits

| a) 168 h | b) 168 h | c) 168 h |

| a) 336 h | b) 336 h | c) 336 h |
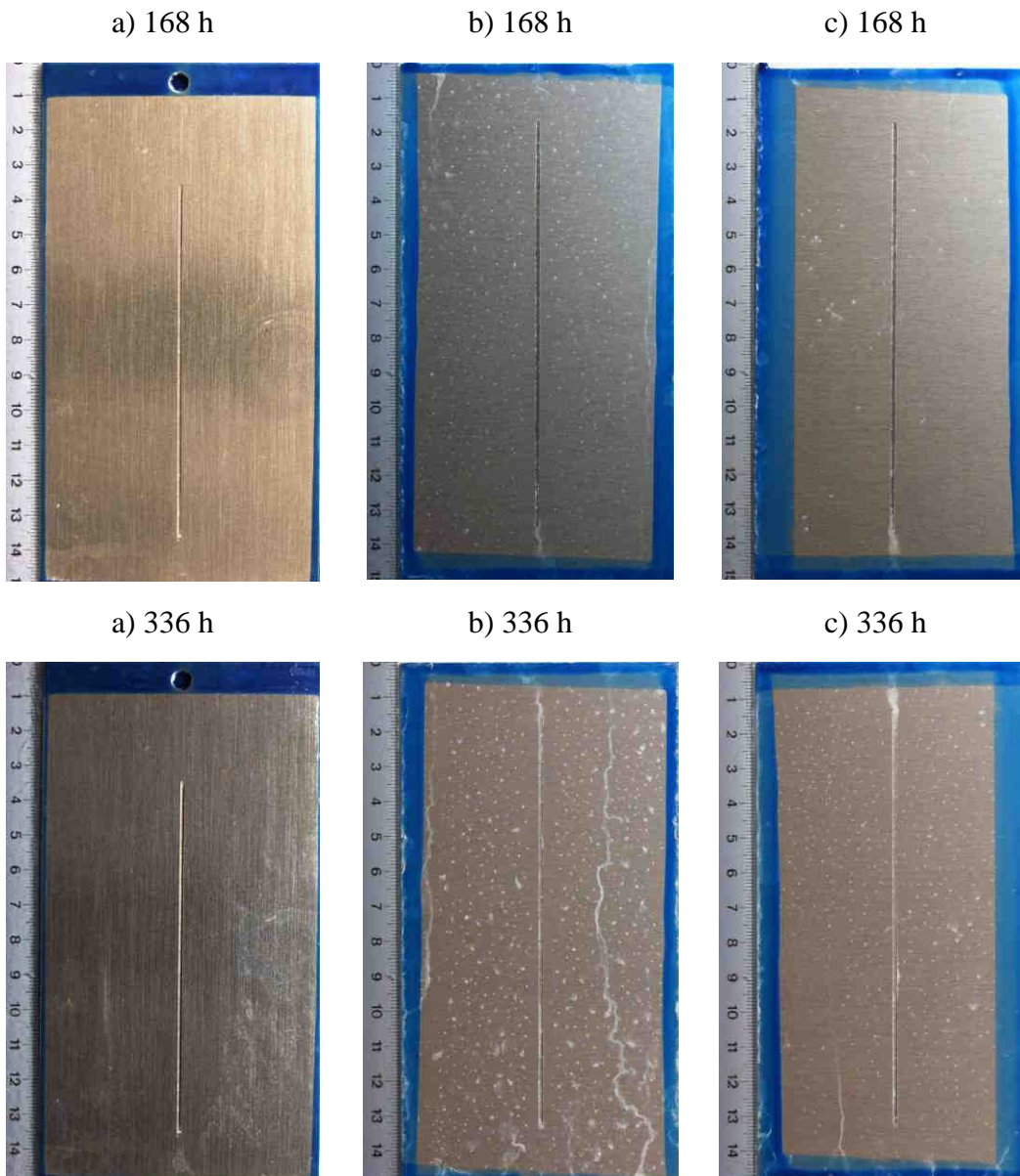
Figure 6.1.17. Photos of AA2024 samples coated with chromate conversion coating (a), SgZr1 (b), SgTi2 (c) after 168 h and 336 h in neutral salt spray test according to ISO 9227.
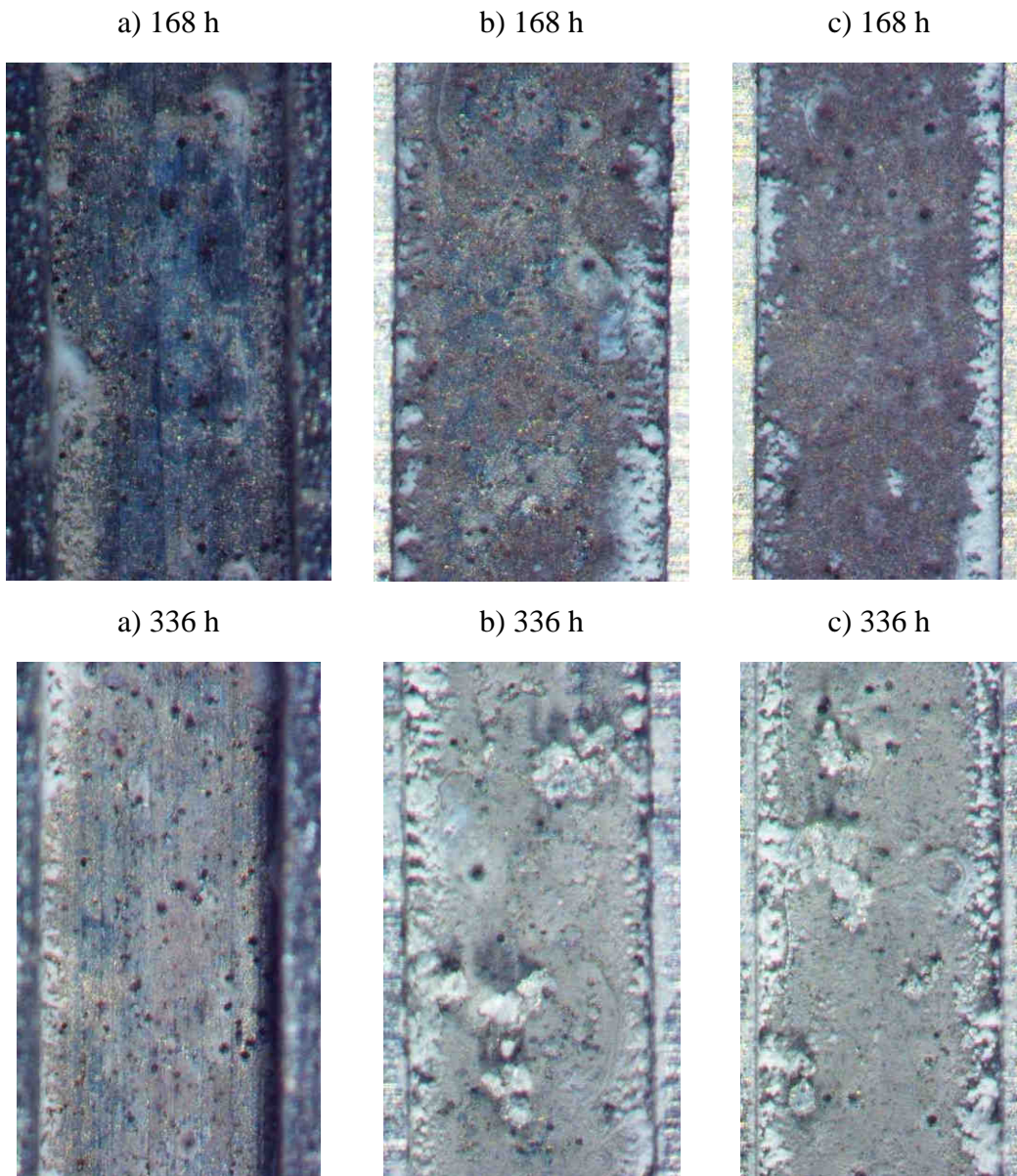
Figure 6.1.18. Photos of the scribe area (1 mm scribe width) of AA2024 samples coated with chromate conversion coating (a), SgZr1 (b), SgTi2 (c) after 168 h and 336 h in neutral salt spray test according to ISO 9227.

6.1.7 Paint adhesion tests

Figure 6.1.19 and Table 6.1.5 present results of paint adhesion test before immersion and after 14 days of immersion in deionized water of SgZr1 and SgTi2 samples coated with epoxy based primer and top coat. Both sol-gel coatings show excellent adhesion properties (substrate/sol-gel and sol-gel/paint interface). There is no coating damage or delamination on both test samples for dry and wet testing conditions (Figure

207

6.1.19). Furthermore, no blisters are formed on the test samples during immersion in DI water proving a very stable sol-gel/paint interface.

The results of the adhesion test demonstrate a very good compatibility of the sol-gel coatings with paint under study. The use of organic epoxy functional groups provides necessary bonding strength between the sol-gel coating and primer as can be seen from the Figure 6.1.20. The cross-sectional TEM micrograph shows excellent interface between the sol-gel coating (SgZr1 as an example) and a primer coating. The development of such interface is attributed to the chemical bonds formed between the functional groups present in both sol-gel and primer.

Table 6.1.5. Results of the paint adhesion test (ISO 2409) before and after 14 days immersion in DI water. The results are classified in classes, with class 0 (GT 0) representing no removal of paint and class 5 (GT 5) severe loss of paint. The number of blisters (m) is ranked from 0 (no blisters) to 5 (covered with blisters), the size of blisters g is ranked from 0 (not visible) to 5 (more than 5mm).

Coating reference	GT value before immersion in DI water	GT value after 14d immersion in DI water	Evaluation of paint surface (after 14d immersion in DI water)
SgZr1	GT 0	GT 1	m0/g0
SgTi2	GT 0	GT 1	m0/g0

a) Before exposure to DI water   b) Before exposure to DI water

a) After 14d exposure to DI water   b) After 14d exposure to DI water
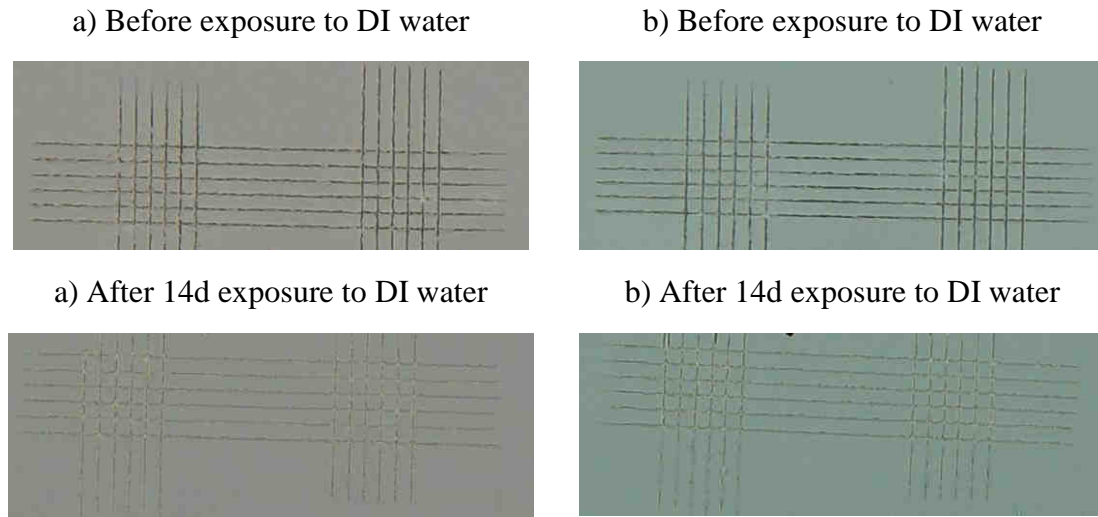
Figure 6.1.19. Crosscut adhesion tape test of the SgZr1 (a), SgTi2 (b) sol-gel coatings on AA2024 samples coated with water based epoxy primer and water based epoxy topcoat before and after 14d immersion in DI water.
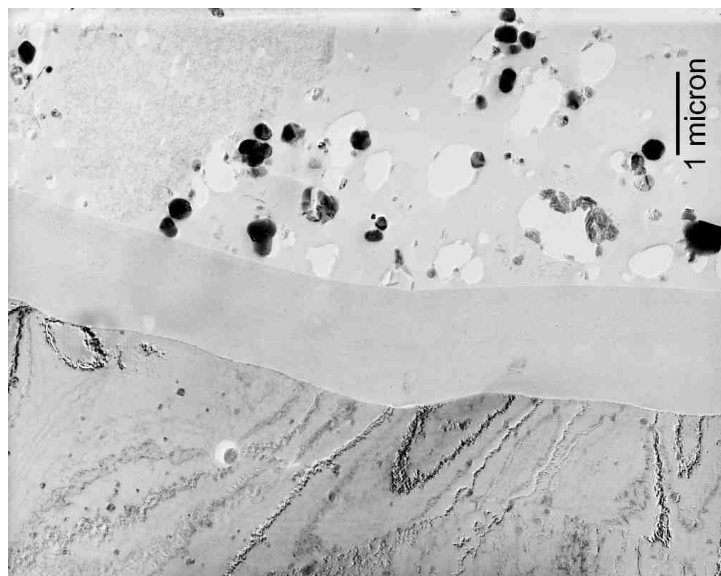
Figure 6.1.20. TEM micrograph shows a cross-section of a primer coating and SgZr1 sol-gel coating deposited on AA2024 sample. Alloy is on the bottom, sol-gel coating is in the middle and primer is on the top of the image.

Summarizing

Different sol-gel coating systems were prepared and tested as corrosion protective pretreatments for AA2024. Stable sol-gel formulations are obtained when combining Ti (IV) and Zr (IV) alkoxides with epoxy-organosiloxane alkosol. Such hybrid systems can be used for deposition of thin pretreatment films for protection of aluminum alloy against corrosion and for increasing a bonding strength between the alloy and organic paints. The obtained films are dense, uniform and crack free with a thickness around 1.5-2 µm.

The corrosion resistance of the AA2024-T3 coated with hybrid sol-gel films were evaluated using EIS. The EIS method can be used to model the degradation of the sol-gel and metal/coating interface during the corrosion exposure.

The nature of metal oxide nanoparticles incorporated into the hybrid silica sol-gel network as well as the nature of complexing agents used for hydrolysis strongly influence the anticorrosive performance of the prepared coatings. The best corrosion protective properties are demonstrated by the hybrid titania-silica films prepared using acetylacetone as complexant. For zirconia-containing films, better protective properties are showed by coatings prepared using ethylacetoacetate as a complexing agent. The developed sol-gel films have good anticorrosive performance and adhesion both to the metallic substrate and to the organic paint. Although the films lack active corrosion protection, they can be promising candidates for replacement of chromate conversion coating.

6.2 Influence of ageing of Ti-based sol-gel formulation on the corrosion protection performance

Sol-gel systems applied as pretreatments demonstrate good adhesion to the alloy substrate and organic protective systems. Coatings have relatively small thickness and provide significant degree of passive protection of alloy. However, in spite of good properties of the sol-gel layers there are certain important limitations. The major problem associated with the use of sol-gel formulations is their ageing stability. In the case of industrial application shelf-life of the coating formulation becomes an important factor. The results presented above were obtained on the sol-gel coatings aged only for one hour prior application of the coatings. This is clearly not sufficient aiming at industrial applications. The present chapter will shortly describe optimization of the ageing properties of the sol-gel formulations varying several process parameters.

During the sol-gel synthesis and ageing different chemical reactions take place. The hydrolysis process of alkoxides occurs in the sol-gel system in the presence of water. The formation of partially hydrolyzed precursors and condensation reactions accompany this step. However, chemical reactions are not stopped in the system during its ageing and continue to propagate following a condensation step in which partially hydrolyzed precursors are polymerized. Another important process associated with the chemical reactivity of hybrid sol-gel system is the stability of the organic functional groups. It is known that the epoxide ring in GPTMS can be opened with the formation of diol- groups or polymerization. This process is actually undesirable for the adhesion strength between the metal/sol-gel and sol-gel/organic layers and reduces the shelf-live of the sol-gel systems. In order to better understand issues that reduce the stability of the sol-gel a more clear insight should be given on chemical transformations occurring in the sol-gel and parameters that influence the reactivity of the system.

There are several main factors that can affect the hydrolysis and condensation processes in the sol-gel systems, namely: temperature, pH, water to precursor ratio, concentration of reagents. Optimization of these factors can be helpful to extend the life time of the sol-gel reducing the condensation degree and avoiding undesirable modification of organo-functional groups in the hybrid sol-gel systems. Therefore the idea of this section is to study the effect of ageing time, temperature and water ratio as parameters that influence the chemical reactivity of the sol-gel system and corrosion protective properties of the resulting sol-gel coatings.

6.2.1 Influence of temperature, ageing time and water to alkoxides ratio

The Titania based hybrid sol-gel formulation (SgTi1) was used as a model system in this study because there is a lot of information in literature concerning the hydrolysis and behavior of the Titania based sol-gel systems unlike for Zirconia based ones. The sol-gel synthesis was performed in accordance to the procedure described in paragraph 4.3.2.

Aluminum alloy samples prior to the coating application were prepared using the chemical cleaning procedure described in paragraph 4.2.4.

The coatings were applied using sol-gel formulations aged for different time periods at different temperatures. After the sol-gel synthesis the final formulation was divided in two containers. The first one was stored at 25 ºC and the second one at -6 ºC. After different time of ageing the sols were applied to AA2024 substrates. The deposition was carried out at room temperature. Sol-gel formulation stored at -6 ºC prior to deposition was held in a water bath for some time at room temperature. The conditions and reference names of the prepared samples are presented in Table 6.2.1. Water to OR ratio indicates the total amount of water with respect to all hydrolysable alkoxy groups present in the sol-gel formulation after the synthesis.

Table 6.2.1. Compositions of different sol-gel systems and respective reference name of the samples.

Reference name	Storage temperature, ºC	Ageing time	$H_2O/(OR)$Ratio, r
SgTi1_A	+25	1hour	0.73
SgTi1_B	+25	1week	0.73
SgTi1_C	-6	1day	0.73
SgTi1_D	-6	12days	0.73
SgTi1_E	-6	52days	0.73

The EIS results of the corrosion testing of different sol-gel coatings after two weeks of immersion in 0.5M NaCl are presented in Figure 6.2.1. The sample aged at room temperature during 1 week (SgTi1_B) shows the lowest performance. The impedance modulus at low frequency for this sample is almost one order of magnitude lower compared to others. Such behaviour is unambiguously associated with the influence of the ageing temperature on the barrier properties of the final coating. EIS spectra for samples after ageing at -6ºC are very similar to sample SgTi1_A obtained directly after the sol-gel synthesis. More detailed information on the evolution of different parameters of the sol-gel coated samples can be extracted from the fitting of the spectra using equivalent circuits presented in Figure 3.3.14. The fitting procedure and interpretation of impedance spectra of the sol-gel coated substrates were explained in details in paragraph 3.3.5, therefore only relevant results will be presented in this discussion.
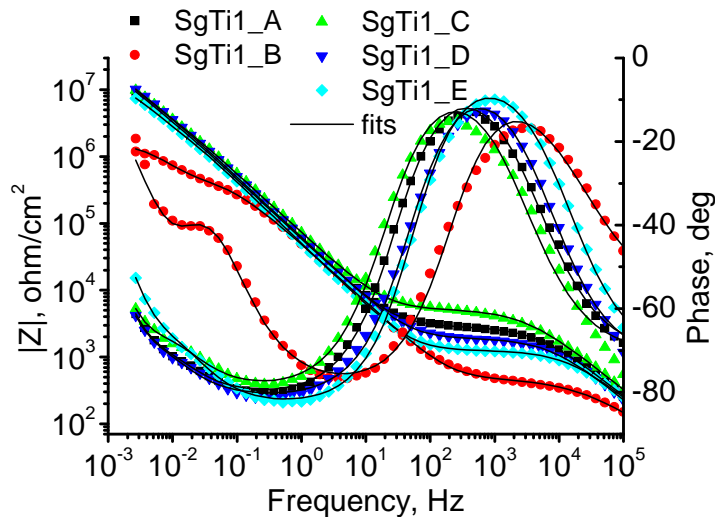
Figure 6.2.1. Bode plots for sol-gel coatings applied after different aging time at 25ºC and -6ºC. EIS spectra correspond to the sol-gel coated AA2024 samples after 14 days of immersion in 0.5M NaCl. Solid lines present fits of the spectra using an appropriate model.

The evolution of the resistance of the sol-gel films is presented in Figure 6.2.2a. The initial values of the resistance are higher for samples stored at -6ºC being $2*10^6$ (SgTi1_E), $8*10^5$ (SgTi1_D) and $5*10^5$ (SgTi1_C) Ohm*cm^2. The lowest initial resistance (around $3*10^5$ Ohm*cm^2) is attributed to the sample SgTi1_B stored during 1 week at 25ºC. During the first two days of immersion the coating resistance of all samples drops very fast followed by a monotonous decrease (Figure 6.2.2a). The lowest value of the resistance at the end of immersion is ascribed to a sample SgTi1_B demonstrating its low barrier properties. The values of the coating resistance at the end of immersion are decreasing in the following order SgTi1_C, SgTi1_D and SgTi1_E. The resistance decrease is consistent with the increase of the ageing time of the sol-gel formulations prior to coating deposition. The time of ageing of the sol-gel decreases the barrier protection of the coatings. The increase of temperature of ageing also decreases the protection as can be seen when comparing the samples SgTi1_B and SgTi1_D.

The highest value of the initial sol-gel resistance of sample SgTi1_E (being around $2.2*10^6$ Ohm.cm^2) is consistent with the coating capacitance (Figure 6.2.2b). The initial value of the capacitance for SgTi1_E is around $4*10^{-9}$ F/cm^2. The lower initial capacitance can be attributed to a thicker sol-gel coating formed in the case of the longest ageing time. This could happen because of increased crosslinking degree of the sol-gel and, as a consequence, slightly higher viscosity of the sol-gel formulation. For other samples the initial capacitance is around $6*10^{-9}$ F/cm^2. During the first two days of immersion the capacitance rapidly grows followed by a small increase until the end of immersion (Figure

6.2.2b). The increase of capacitance at the beginning is most probably associated with the rapid water uptake from electrolyte. At longer immersion time the increase of capacitance may be attributed to hydrolytic degradation of the coating and/or to additional water uptake. For SgTi1_B the increase of capacitance is higher comparing to other samples indicating higher deterioration of the coating (Figure 6.2.2b).

Evolution of the intermediate oxide layer resistance is presented in Figure 6.2.2c. SgTi1_A, SgTi1_C and SgTi1_D samples have highest values of oxide resistance during immersion indicating stability of a metal/coating interface. Values of the resistance R_{ox} for sample SgTi1_E are 3-5 times lower (Figure 6.2.2c). The sample SgTi1_B shows the worst behaviour having more than one order of magnitude lower R_{ox}. The trend of polarization resistance change (R_{polar}) for all samples is consistent with the other fitting parameters. The corrosion protection decreases in the line SgTi1_C, SgTi1_A, SgTi1_D, SgTi1_E, SgTi1_B (Figure 6.2.2d).
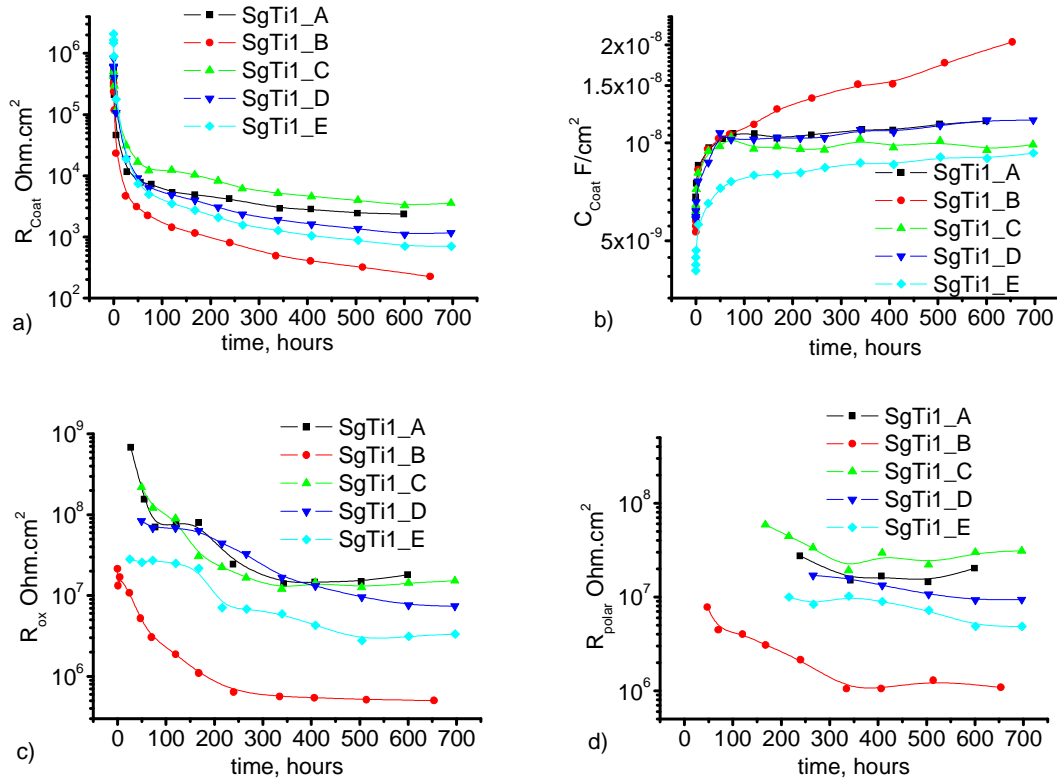
Figure 6.2.2. Evolution of the sol-gel coating resistance a) and capacitance b); intermediate oxide film resistance c) and polarization resistance d) obtained after fitting of impedance spectra.

These results demonstrate the high importance of the storage conditions such as temperature and duration of the sol ageing on the barrier and corrosion protective properties of the sol-gel coatings. The decrease of the temperature during the ageing increases the life time of the sol-gel formulation. On the other hand, the increase of ageing time has negative effect on the sol-gel coating protection efficiency. In the order SgTi1_C, SgTi1_D and SgTi1_E the corrosion protection is decreasing. Figure 6.2.2 demonstrates that coating SgTi1_C prepared after 1 day of ageing at -6ºC is somewhat better than the coating SgTi1_A prepared from the fresh sol-gel. Such difference can be attributed to the change of the rate of the hydrolysis/condensation reactions during the ageing at low temperature. A sol-gel with higher degree of hydroxylated species (Si-OH or Ti-OH) theoretically can form better coating which can be the seen in the case of sample SgTi1_C (Figure 6.2.2).

The previous results have shown that the sol-gel ageing at ambient temperature (25ºC) negatively influences the corrosion protection properties of the coatings. The ratio of water to alkoxides is another parameter that influences the kinetics of hydrolysis and condensation reactions occurring in the sol. The variation of this ratio controls the condensation degree of the final sol-gel formulation and can reduce the unfavorable effect of ageing on the properties of the sol-gel coatings. The influence of lower water/OR ratio, during ageing of the sol-gel on the corrosion protection properties of Ti based sol-gel coatings was also studied.

A standard procedure of the Ti-based sol-gel synthesis (paragraph 4.3.2) was modified in order to reduce rate of reactions during ageing of the sol-gel. During the sol-gel synthesis the water to all hydrolysable groups ratio $H_2O/(OR)$ was 0.073 (Table 6.2.2) which is 10 times lower compared to the ratio in the initial synthesis (Table 6.2.1). The other parameters of the synthesis procedure were kept unchanged. The obtained sol-gel was separated in two parts. The first one was stored at 25ºC and the second one at -6ºC during one month. After ageing the rest of water was added to achieve a $H_2O/(OR)$ ratio 0.73 used in the initial sol-gel synthesis procedure (paragraph 4.3.2). Sol-gel was continuously stirred during 2 h after water addition followed by the coating of alloy samples. Table 6.2.2 shows the reference names of samples and the conditions of the sol-gel ageing.

Table 6.2.2. Compositions of different sol-gel systems and respective reference name.

Reference name	Storage temperature, ºC	Ageing time	$H_2O/(OR)$ ratio during ageing
SgTi1_F	+25	30days	0.073
SgTi1_G	-6	30days	0.073

Figure 6.2.3 presents Bode plots of the sol-gel coated samples after 14 days immersion in 0.5M NaCl solution. Impedance spectra of the samples SgTi1_F and SgTi1_G were compared with samples after 1h and 1 week of ageing SgTi1_A and SgTi1_B respectively. The results do not show any significant difference between the impedance spectra of SgTi1_F and SgTi1_G samples. The corrosion protective properties of the coatings are influenced by the water content regardless of the temperature used during the ageing of the sol-gel formulation. Therefore stability of the sol-gel system can be altered changing the water ratio r during the synthesis and ageing. More detailed information on the changes of barrier properties and corrosion protection are obtained after fitting the impedance spectra.

The evolution of the parameters obtained after fitting the impedance spectra during immersion in NaCl solution are presented in Figure 6.2.4. The barrier protection (Rcoat) of the two samples (SgTi1_F and SgTi1_G) is similar to sample SgTi1_A (Figure 6.2.4a). This indicates that lower amount of water during ageing drastically reduces the negative effect of ageing even at higher temperatures. In addition, the temperature of ageing does not have a significant influence on the barrier properties. Therefore the degree of condensation and hydrolysis occurring in the sol-gel during the ageing are limited by amount of available water.

The initial capacitance of the coatings SgTi1_F and SgTi1_G is around $4.6*10^{-9}$ F/cm^2 and is lower compared to sample SgTi1_A ($5.7*10^{-9}$ F/cm^2). The lower capacitance of the sol-gel films might be associated with slightly higher thickness of the coating. During immersion the capacitance increases until approximately $1.15*10^{-8}$ F/cm^2 and $9.2*10^{-9}$ F/cm^2 for SgTi1_F and SgTi1_G respectively.

The corrosion protective properties of the sol-gel coatings after ageing at water ratio 0.073 are worse than for sample SgTi1_A. The evolution of oxide layer resistance R_{ox} during immersion time (Figure 6.2.4c) resembles the behavior of sample SgTi1_E aged during 52 days (Figure 6.2.2c). R_{ox} in the end of immersion is around $3*10^6$ $Ohm*cm^2$ and almost one order of magnitude lower compared to sample SgTi1_A (Figure 6.2.4c). Polarization resistance (R_{polar}) is lower on about 2-3 times compared to sample SgTi1_A (Figure 6.2.4d). Nevertheless, the protection conferred by the sol-gel coatings is enhanced when lower amount of water is added during the sol-gel ageing in contrast to sample SgTi1_B obtained after 1 week of ageing with normal water content.
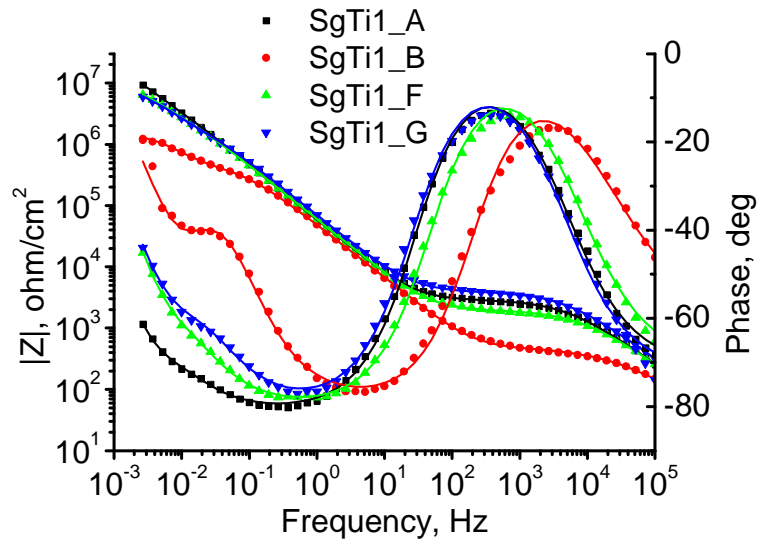
Figure 6.2.3. Bode plots for sol-gel coatings applied after different aging time at 25ºC and -6ºC. EIS spectra correspond to the sol-gel coated AA2024 samples after 14 days of immersion in 0.5M NaCl. Solid lines present fits of the spectra using appropriate model.
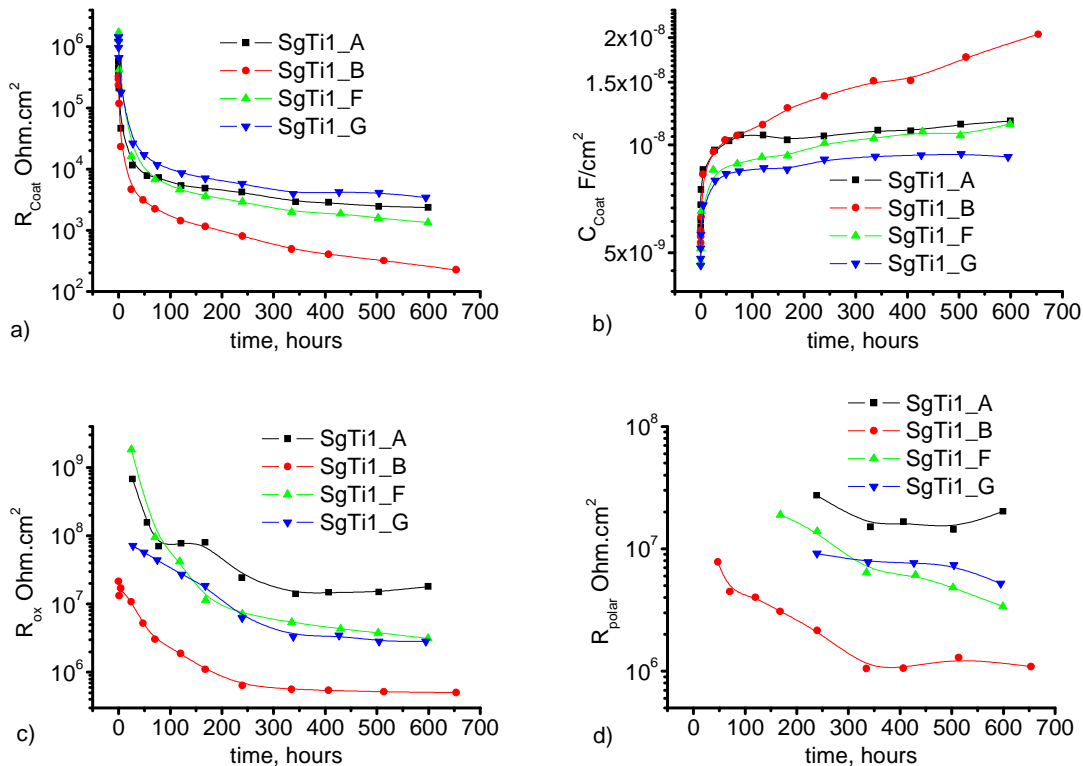
Figure 6.2.4. Evolution of coating resistance a), capacitance b) intermediate oxide film resistance c) and polarisation resistance d) obtained after fitting of impedance spectra.

6.2.2 Discussion

The results of corrosion tests demonstrate the important influence of temperature and water ratio on the stability of the hybrid sols during ageing and consecutively on the corrosion protection of the resulting coatings. The decrease of temperature or water ratio during ageing positively influences the corrosion protective properties of films. This fact is unambiguously related to the chemical reactivity of the sol-gel system during the ageing. Both temperature and water ratio influence the rate of the chemical reactions that occur in the sol-gel system containing TPOT and GPTMS. The increase of temperature leads to a faster hydrolysis, condensation and other chemical reactions according to Arrhenius dependence. A low amount of water reduces rate of hydrolysis reaction mainly. In order to understand the role of temperature and water ratio on the properties of the sol-gel coatings, chemical reactivity of the sol-gel must be discussed in more details. Typical chemical reactions of hydrolysis occurring in the system containing TPOT and GPTMS in the presence of water are the following:

$$
C_3H_7-O-\underset{\underset{C_3H_7}{|}}{\overset{\overset{C_3H_7}{|}}{\underset{|}{\overset{|}{Ti}}}}-O-C_3H_7 \xrightarrow[-C_3H_7OH]{+\ H_2O,\ H^+} H-O-\underset{\underset{H}{|}}{\overset{\overset{H}{|}}{\underset{|}{\overset{|}{Ti}}}}-O-H
$$

(6.2.1)

$$
H_3C-O-\underset{\underset{CH_3}{|}}{\overset{\overset{CH_3}{|}}{\underset{|}{\overset{|}{Si}}}}-(CH_2)_3-O-\underset{H}{\overset{O}{C}}-CH_2 \xrightarrow[-CH_3OH]{+\ H_2O\ H^+} HO-\underset{\underset{OH}{|}}{\overset{\overset{OH}{|}}{Si}}-(CH_2)_3-O-\underset{H}{\overset{O}{C}}-CH_2
$$

(6.2.2)
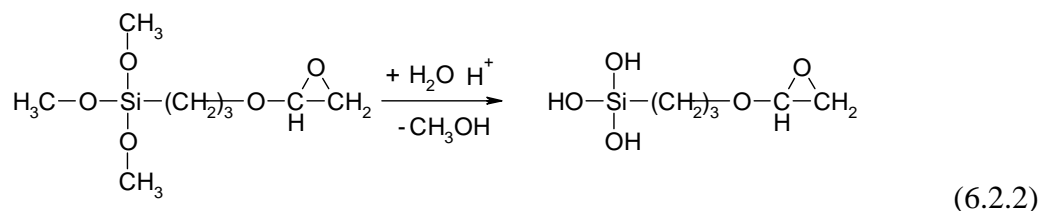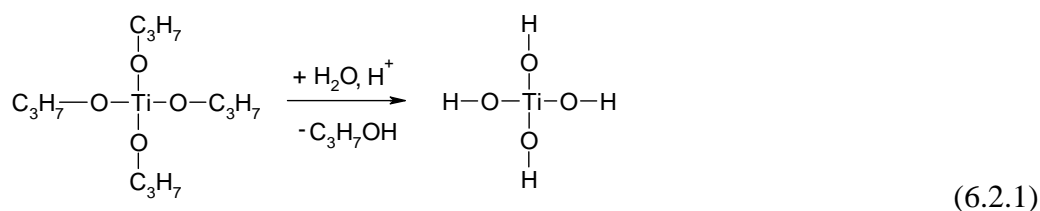
The reaction of hydrolysis of metal alkoxides occurs rapidly when water is added and the presence of acid catalyst in this case may not be necessary. Hydrolysis of Si alkoxide is slow therefore acid is needed to assist the reaction. Water to alkoxide ratio plays an important role in the hydrolysis reaction. When the ratio is small a partial hydrolysis occurs and only one or a couple of alkoxide groups are hydroxylated. When the ratio is high a hydrolysis is complete and all alkoxy groups are hydrolyzed according to reactions 6.2.1 and 6.2.2. The condensation reaction follows the hydrolysis and can proceed through different ways. A homo-condensation normally occurs between the same hydroxylated species according to reactions 6.2.3 and 6.2.4. However, two different species of metal and silicon hydrolyzed precursors can be combined in hetero-condensation process (reaction 6.2.5).

$$
H-O-\underset{\underset{H}{|}}{\overset{\overset{H}{|}}{\underset{|}{\overset{|}{Ti}}}}-O-H\ +\ H-O-\underset{\underset{H}{|}}{\overset{\overset{H}{|}}{\underset{|}{\overset{|}{Ti}}}}-O-H \longrightarrow -O-\underset{|}{\overset{|}{Ti}}-O-\underset{|}{\overset{|}{Ti}}-O-
$$

(6.2.3)

$$\text{(6.2.4)}$$

$$\text{(6.2.5)}$$

The reactivity of alkoxy silane in the presence of acidified water is very low. The hydrolysis and condensation reaction can take hours before any significant degree of condensation is achieved. However, in the presence of Me alkoxides (Me stands for Sn, Zr, Al, Ta, Ti etc.) the behavior of the system containing GPTMS is quite different. The condensation reactions of alkoxy silane are significantly accelerated by Me alkoxides as discussed before in [185,375,376]. Using NMR technique the condensation degree of GPTMS was analyzed in the presence of 10 % mol. of Me alkoxides and water. The condensation degree of GPTMS in hybrid sols with Me alkoxides increases according to the following order: $Sn(OBu^t)_4 < Zr(OBu^n)_4 \ Al(OBu^s)_3 < Ta(OEt)_5 < Ti(OEt)_4$ [376]. In contrast to that the addition of $Si(OEt)_4$ in the mixture of GPTMS and water resulted in about 5% of the condensation degree of GPTMS compared to 50-80% increase of condensation degree when Me alkoxides were used. These results testify for the important role of Me alkoxides in the reaction of condensation of alkoxy silanes. However, condensation is not only the reaction that can be affected by metal alkoxides.

The experimental results provide evidence that metal alkoxides catalyze the epoxide ring opening and polymerization reaction at room temperature [185,375]. The catalytic activity of Zr alkoxide is higher compared with Ti alkoxide and moreover the catalytic action can be promoted by light and temperature [375]. In regard to the chemistry of the process the following reactions of the epoxide group occur:

$$\text{(6.2.6)}$$

The nucleophilic and electrophilic attack at the epoxide group can lead to the opening of the ring and the formation of diol groups (upper reaction) or poly(ethylenoxide) chains (bottom reaction) (6.2.6). Furthermore, due to the presence of acidic water, alcohols and metal alkoxides there are also possible reactions of etherification and esterification of diol groups that lead to formation of more complicated species.

218

The temperature can significantly affect the rate of hydrolysis, condensation and epoxide ring opening reactions. As was shown in ref [33] the increase of temperature by 25ºC increases the rate of the hydrolysis reaction by 10 times. Gelation of mixture of TEOS in methanol in the presence of HF occurs in 49h at 4ºC and in 0.3h at 70ºC and this shows an important influence of temperature on the gelation time [377]. Therefore the reduction of temperature of ageing plays a significant role decreasing rate of condensation and hydrolysis reactions. The results of electrochemical measurements presented in Figure 6.2.1 and 6.2.2 demonstrate that the sol-gel coatings (SgTi1_C and SgTi1_D) deposited after 1 and 12 days of ageing of sol at -6ºC retain the corrosion protective properties compared to freshly deposited film. A decrease of corrosion protection is noticeable for the sample SgTi1_E deposited after 52 days of ageing (Figure 6.2.2), nevertheless the protection is superior compared to sample (SgTi1_B) stored at 25 ºC.

The water/alkoxide ratio significantly influences the process of epoxide ring opening [185]. The effect of water ratio was studied for the sol-gel mixtures of Ti tetraethoxide and GPTMS. Using NMR method the presence of epoxide rings was determined after 24h of ageing of different sols. It was established that at water/OR ratio less than 0.12 the reaction of epoxide ring opening is very slow. Only when sufficient amount of water is added (i.e. at water/OR ratio >0.5) the reaction of epoxide opening is accelerated. When low amount of water is present in the system the hydrolysis reactions (6.2.1 and 6.2.2) are incomplete and the amount of Ti oxo-species is small. Therefore the epoxy ring opening reaction is retarded. In fact this is in accordance with the results of the corrosion testing of different sol-gel coatings presented in Figures 6.2.3 and 6.2.4. At wide range of temperature conditions of ageing (-6 – 25ºC) of the sol-gels there is almost no difference between the sol-gel coatings (SgTi1_F, SgTi1_G) obtained after the addition of the remaining water for the hydrolysis of the sol-gel formulations. All electrochemical parameters related to the coating, intermediate oxide layer and corrosion process are similar for the two samples. In this case temperature does not influence the reactivity of the sol-gel systems. The rate of hydrolysis, condensation and epoxy opening reactions are controlled by the concentration of the reagents and water/OR ratio.

The decrease of water content during the sol-gel ageing helps to enhance the corrosion performance of the coatings. Nevertheless the corrosion performance of coatings SgTi1_F and SgTi1_G is lower compared with the coatings SgTi1_C and SgTi1_D prepared with normal amount of water and aged at -6ºC (Figures 6.2.1 and 6.2.3). There is a significant oxide resistance drop during immersion (Figures 6.2.4c). Such drop can be associated with the low stability of the metal/sol-gel interface. As well known, covalent bonding Al-O-Si greatly improves the adhesion and stability of the metal/sol-gel interface [218]. The condensation reaction between hydrolyzed Si alkoxide groups (Si-OH) and hydroxylated metal (Me-OH) produces Al-O-Si bonds. However, when there are not enough Si-OH groups the bonding strength with aluminum is lower. From another hand, higher condensation degree of the sol-gel reduces the mobility of Si-OH units and also

lowers their concentration, which can negatively influence the bonding between the sol-gel and metallic substrate.

One of the possible explanations of lower oxide resistance of the sol-gel coated samples SgTi1_F and SgTi1_G is the following. A lower water/OR ratio (0.073) retards the hydrolysis reaction of both TPOT and GPTMS during the sol-gel synthesis. This is especially important since during the TPOT hydrolysis the formation of clusters and nanoparticles is retarded. The complexant (AcAc) interacts stronger with the TPOT in the absence of water and retards the condensation of Ti-OH units. After 1 month of ageing the sol-gel synthesis was finalized in the presence of additional water. At this stage a fast hydrolysis reaction of Ti alkoxides occurs and more Ti-OH species are formed. Hydroxylated Ti species (Ti-OH) promote the condensation reaction of GPTMS. The results of capacitance calculation presented in Figure 6.2.4b support such assumption. The capacitance of the sol-gel coatings SgTi1_F and SgTi1_G at the beginning of testing is lower that might testify for the increased thickness caused by higher condensation degree of the sol-gel which is similar to the coating SgTi1_E obtained after 52 days of ageing of the sol-gel at -6ºC (Figure 6.2.2b). The increase of condensation degree leads to decrease of silanol groups available for the bonding with the metal surface. In addition, the condensed species have sterical limitations which impede the reaction between the silanol groups and the aluminum surface. Thus the oxide layer resistance drops very fast and is lower for samples SgTi1_F and SgTi1_G (Figure 6.2.4c).

Summarizing

The influence of temperature, water content and ageing time of the Ti-based sol-gel system on the properties of coatings has been studied using the EIS technique. The impedance results demonstrate an important influence of the conditions of ageing on the corrosion protective properties of the obtained coatings. Ageing of the sol-gel at room temperature significantly deteriorates corrosion protection of the hybrid films. In contrast to that, low temperature used during ageing of the sol-gels decreases the negative effect of ageing. The corrosion behavior of the coating obtained after 12 days of ageing at -6ºC is comparable to that of the coating deposited from the fresh sol-gel formulation. A longer ageing time results in increased condensation of the sol-gel and decrease of protection conferred by the coating.

The water ratio affects the chemical reactivity of the sol-gel during the ageing. Coatings obtained after 1 month of ageing with lower water content demonstrate increased protection performance. In this case the temperature during the ageing does not significantly influence the protection. Nevertheless, the protection properties of such coatings are less efficient compared to coatings obtained after aging at low temperature and nominal water ratio. This discrepancy is directly related with the chemical transformations occurring in the sol-gel system during the synthesis and ageing.

6.3 Influence of alloy surface preparation on the corrosion protection conferred by sol-gel coatings

Adhesion of organic paints to metallic substrates is often poor which results in rapid delamination of applied paints. Therefore there is a need of using special pretreatments which increase adhesion between the metal and organic paints. Hybrid sol-gel pretreatments applied on aluminum alloys stabilize the interface between the alloy and organic coatings. The adhesion to metal substrate is promoted by covalent bonds Me-O-Si that are formed during the sol-gel coating application and curing. Organic functional groups of silane derivatives greatly enhance adhesion to organic paints. Nevertheless, the metal surface must be adequately cleaned in order to provide a good bonding between the metal and the sol-gel. The cleaning procedure removes grease, scale and other contaminations and makes metal surface more hydrophilic. In this paragraph two cleaning procedures applied to AA2024 were investigated from the point of view of microstructure of the surface and corrosion protection properties of the sol-gel coated alloy.

6.3.1 Characterization of the surface of AA2024 after different cleaning procedures

Influence of cleaning procedures of AA2024 on the appearance and microstructure of the surface has been studied by SEM. Two cleaning procedures were used. The first one (alkaline cleaning) is described in paragraph 4.2.3. It has two stages based on alkaline cleaner and in 20 wt % nitric acid. The scheme of the process is presented in Figure 6.3.1. The second procedure (chemical etching) (paragraph 4.2.4) is different. After the first cleaning step in alkaline cleaner the alloy samples are immersed in alkaline etching solution followed by a treatment in deoxidizing solution (Figure 6.3.1).

SEM micrographs of alloy surface after alkaline cleaning are presented in Figure 6.3.2. The surface of alloy after alkaline cleaning shows the presence of small holes formed due to dissolution of intermetallic inclusions on the surface. The used procedure does not remove completely all the intermetallics and some of them are still present on the surface which can be clearly seen in Figure 6.3.2b. The surface of aluminum matrix has visible signs of etching as well (Figure 6.3.2c).

Micrographs of the alloy surface after the chemical etching procedure are presented in Figure 6.3.3. The cleaning procedure significantly etches aluminum matrix and the surface has lots of craters and holes (Figure 6.3.3a). The craters most probably correspond to places where intermetallics were before the etching. The appearance of pits or holes is associated with the dissolved intermetallics from the alloy matrix (Figure 6.3.3b). Another important feature of the aluminum surface after etching is the appearance of a nano-sized network which is visible at higher magnification (Figure 6.3.3c). Such network provides better mechanical interlocking between the sol-gel and metal surface, which improves the stability of the interface and the corrosion protection of the coated substrate. Moreover the

removal of the intermetallics can delay the corrosion progress and decreases the active sites where localized corrosion starts.

Alkaline cleaning

| Tank 1 | Tank 2 | Tank 3 | Tank 4 |
| Alkaline Cleaning Turco 4215 60-70 °C 25-35 min | Distillated water washing | 20% nitric acid 20-40 °C 5-10 min | Distillated water washing |

AA2024-T3

Drying in air stream after etching procedure

Chemical etching

| Tank 1 | Tank 2 | Tank 3 | Tank 4 | Tank 5 | Tank 6 |
| Alkaline Cleaning Metaclean T2001 60-70 °C 15-25 min | Distillated water washing | Alkaline Etch Turco Liquid Aluminetch Nr.2 55-65 °C 1 min max | Distillated water washing | Acid Etch Turco Liquid Smutgo NC 20-40 °C 5-10 min | Distillated water washing |

AA2024-T3

Figure 6.3.1 Schematic representation of AA2024 cleaning procedures (paragraph 4.2.3, 4.2.4).

In the first process the alloy plates are treated in Alkaline cleaning solution and nitric acid solution; the washing in distilled water is used after each cleaning step. The samples were dried in air flow after etching.

In the second process the alloy plates are treated in Alkaline cleaning solution, Alkaline etch solution and Acid etch solution; the washing in distilled water is used after each cleaning step. The samples were dried in air flow after etching.
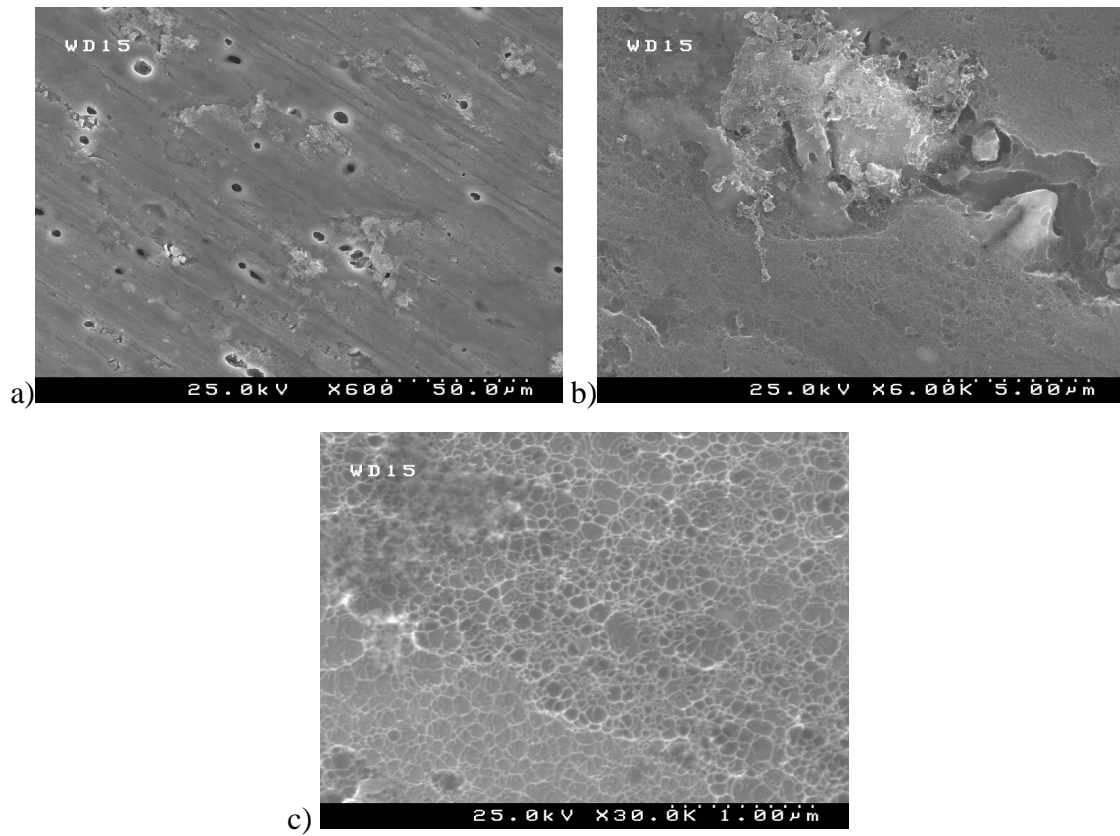
Figure 6.3.2 SEM micrographs of AA2024 surface after alkaline cleaning procedure (paragraph 4.2.3).
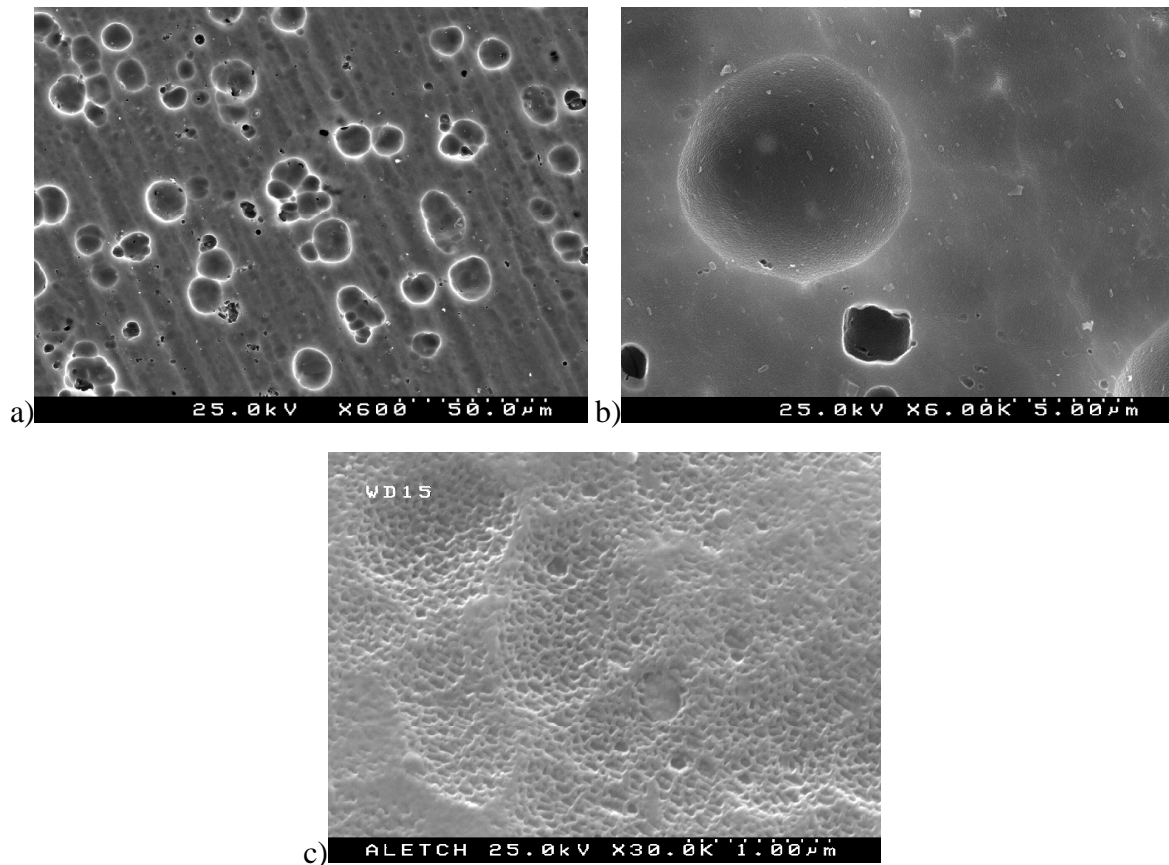
Figure 6.3.3 SEM micrographs of AA2024 surface after chemical etching procedure (paragraph 4.2.4).

6.3.2 Corrosion protection properties of AA2024 coated with Zr based sol-gel system. Influence of the surface preparation.

The influence of surface preparation has been studied using the EIS technique on the sol-gel coated alloys samples during immersion in 0.5M NaCl solution. SgZr1 sol-gel formulation was used for the coating preparation. Figure 6.3.4 presents Bode plots of the sol-gel coated AA2024 substrates with different methods of surface preparation. Difference between the two impedance spectra is clearly visible even after 1 day of immersion (Figure 6.3.4). The sample prepared using alkaline cleaning procedure (sample A) has almost two times lower sol-gel film resistance at middle frequency (3 kHz) part compared to sample C (Figure 6.3.4). The corrosion protective properties of the samples are presented at lower frequency on the Bode plot. The impedance spectra of sample A clearly show the presence of a time constant associated with the corrosion activity at around 10^{-2} Hz (Figure 6.3.4). On the other hand, sample C shows only a resistive response of the intermediate oxide layer (Figure 6.3.4). The corrosion protective properties of the

224

coatings show high degradation for one month of immersion in NaCl solution. Nevertheless, the difference between the two samples is clear. The sample (A) prepared using alkaline cleaning definitely shows worst behavior.

The results of the impedance test of the second sample can be explained by a fast deterioration of the intermediate oxide layer and starting of the localized corrosion activity of alloy. The developed corrosion process results in appearance of pits that lead to deterioration of the sol-gel matrix and decrease of its barrier properties. Optical pictures taken after one month of testing are presented in Figure 6.3.5 and show stronger pitting activity in the case of sample (A) compared to sample (C). Such different corrosion performance is associated with the surface preparation of alloy before the coating application. A microstructural analysis clearly shows that some intermetallics were not removed after alkaline cleaning procedure (Figure 6.3.2b). Heterogeneous places may be potentially a source of the localized corrosion activity of alloy. A corrosion process starts faster for the sample (A) compared to the sample C as shown by EIS measurements (Figure 6.3.4). Apparently, the removal of intermetallics delays the corrosion process and increases the corrosion resistance of the alloy. Moreover, etching of the alloy surface and intermetallics removal makes the surface rougher that increases the bonding strength between the sol-gel coating and the metal.
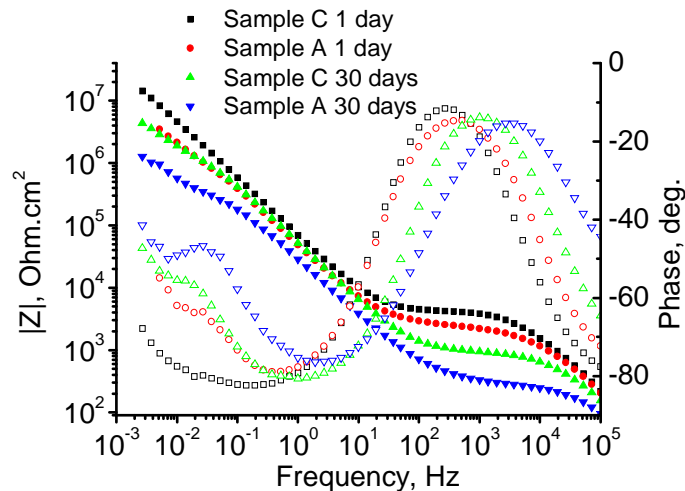
Figure 6.3.4. Bode plots of AA2024 coated with SgZr1 sol-gel coatings after 1 day and 1 month of immersion; alloy substrate was etched using alkaline cleaning procedure (sample A) (paragraph 4.2.3) and chemical etching procedure (sample C) (paragraph 4.2.4).
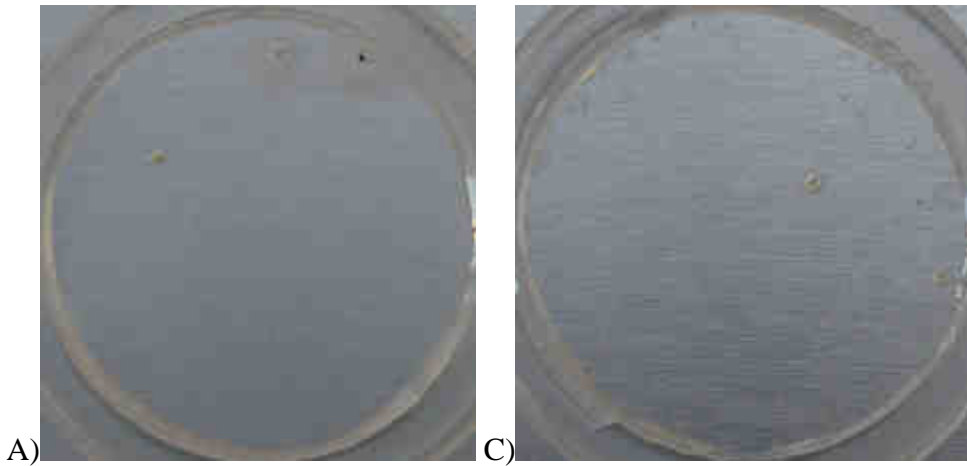
Figure 6.3.5. Optical photographs of AA2024 coated with SGZr1 hybrid sol-gel coatings after 1 month of immersion; alloy substrates were etched using alkaline cleaning procedure (Sample A) described in paragraph 2.3.3, and chemical etching procedure (Sample C) described in paragraph 2.3.4.

Summarizing

The importance of the surface preparation of the alloy is demonstrated using methods of microstructural and electrochemical analysis. The use of alkaline cleaning procedure does not provide adequate removal of the intermetallics from the alloy surface. Therefore, the presence of intermetallics on the surface increases susceptibility to the localized corrosion of the sol-gel coated alloy and leads to faster corrosion degradation as was demonstrated by EIS measurements.

Chemical etching procedure removes the majority of the intermetallics from the surface, therefore increasing corrosion resistance of the sol-gel coated alloy. The increased roughness provides a good interface and adhesion to the sol-gel coating which is of prime importance for application of the sol-gel pretreatments.

6.4 Mechanism of corrosion attack on AA2024 coated with sol-gel films

6.4.1 Corrosion activity of the sol-gel coated alloy

The application of the sol-gel coating on the alloy substrate increases its corrosion protection in aggressive electrolytes. Coating provides a barrier against corrosion species. However there is no perfect coating because defects and micropores are always present in the coating. After some time of immersion the electrolyte penetrates through the pores, micro cracks and other defects. When the corrosive environment comes into a contact with the metal surface it results in corrosion activity. The ingress of the corrosion species to the metal substrate can be visualized using the measurements of the OCP of the sol-gel coated alloy during immersion in NaCl solution (Figure 6.4.1). It can be seen that during some hours the corrosion potential is in the passive region around -0.25 V vs SCE because of the barrier properties of the intact coating. However, the moment when electrolyte comes to the contact with the metal is accompanied by a decrease of the potential to approximately (-0.68 V vs SCE). Such decrease usually comes along with the development of pitting.

The pitting activity is localized and generally starts near the second phase inclusions. The development of pitting is accompanied by dealloying of active intermetallics and copper redeposition process that increase the cathodic area and, therefore, the corrosion impact. During the growth of pit a perforation appears in the sol-gel layer surrounded by a net of cracks and micro defects as can be seen in Figure 6.4.2. However, with time the corrosion increases and the pitting expands its area (Figure 6.4.3a). An EDS analysis made inside the pit shows an increased signal of copper compared to the zone outside of the pit (Figure 6.4.3b). Such macro agglomeration of copper inside the pit provides an effective cathode that increases anodic dissolution of the surrounding aluminum matrix. The coupled cathodic and anodic corrosion activity of the pit can be confirmed by the methods of localized corrosion investigation.

Afterwards experiments have been performed in order to characterise the localized corrosion activity of AA2024. Two artificial micro defects were made on the sol-gel coated AA2024 sample as shown in Figure 6.4.4a. Then the sample was immersed in 0.05M NaCl solution and maps of ionic currents were acquired. The ionic currents are presented as profiles (Figure 6.4.4b) obtained at the distance of 100 µm from the surface across the line indicated in Figure 6.4.4a. Typically positive currents are associated with the upward flux of aluminium cations from the place with anodic activity and negative currents are associated with the upward flux of anions from the cathodic place (Figure 6.4.4b). The black line presents the profiles of the ionic current made in NaCl solution only after approximately one day of immersion. The right defect shows an anodic activity (positive current) whereas the left defect shows a cathodic activity (negative current).
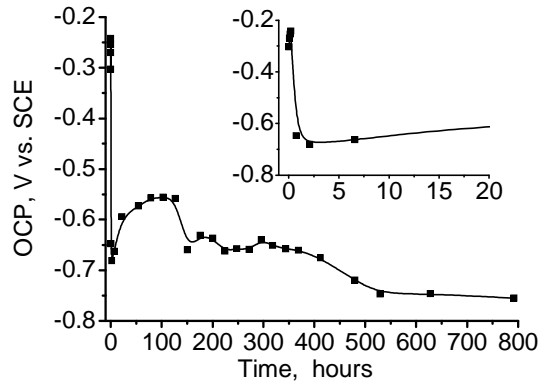
Figure 6.4.1. Evolution of OCP of AA2024 coated with Zr1 sol-gel during immersion in NaCl solution.
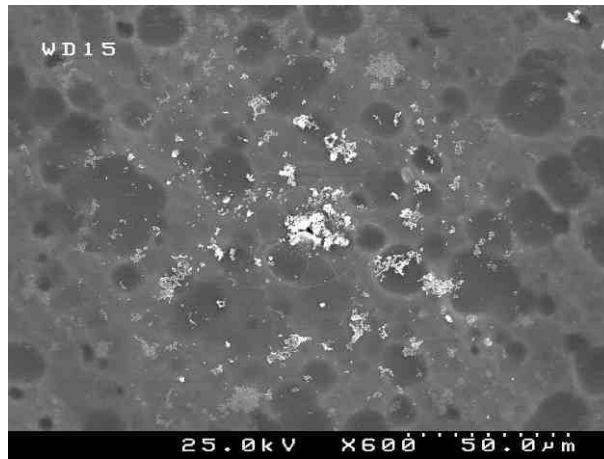
Figure 6.4.2. SEM image of AA2024 coated with Zr1 sol-gel after short exposure to NaCl solution.
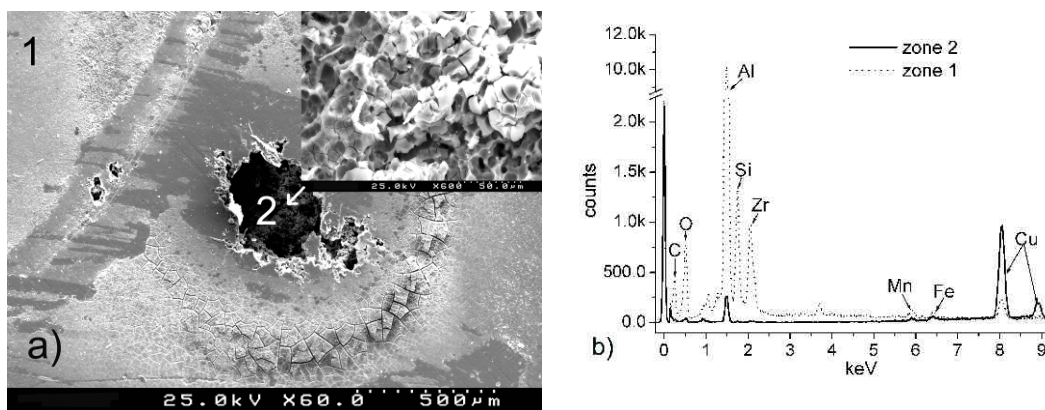
Figure 6.4.3. SEM Micrograph of pit a) and EDS spectra b) of two different zones.
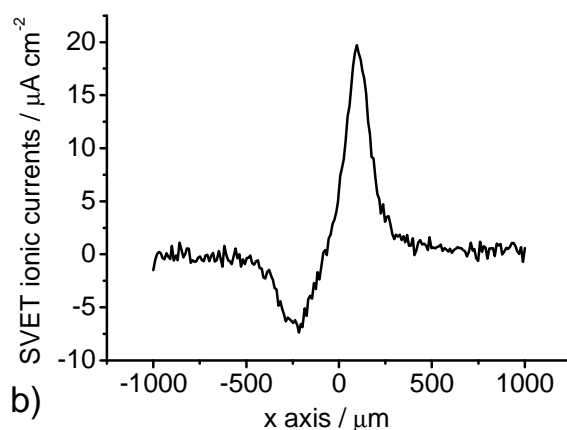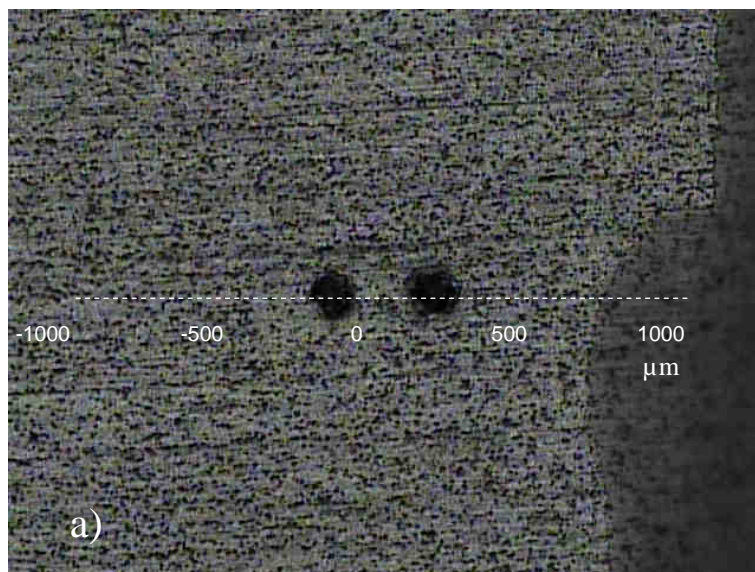
Figure 6.4.4. Optical photograph of the micro defects made on the sol-gel coated AA2024 sample a). Profile of ionic current b) measured at 100 µm away from the surface across the line indicated in optical picture.

The results of SVET measurements presented above give information only about the fluxes of cations and anions originated from the corrosion processes in defects with no information about their chemical nature. In order to get more information about the chemical environment in the corroding sites, a combination of micro-potentiometry and micro-amperometry was additionally used to measure local variations of pH and to probe the dissolved oxygen concentration in solution.

Figure 6.4.5 shows the variation of ionic currents as detected by SVET (a), pH (b) and the reduction current of dissolved oxygen (c). The distance to the point at which detection with the probe was made is 50 µm for pH and O_2 and 100 µm for SVET. The

additional details concerning the preparation of electrodes, calibration and measurements of pH and oxygen concentration are thoroughly discussed in paragraphs 3.4.1 and 3.4.2. SVET profiles show the negative and positive peaks above the cathodic and anodic defects respectively. The values of pH in solution are significantly increased close to the cathode and no variation was detected above the anode. The measured oxygen reduction current was lower in the places with both defects.
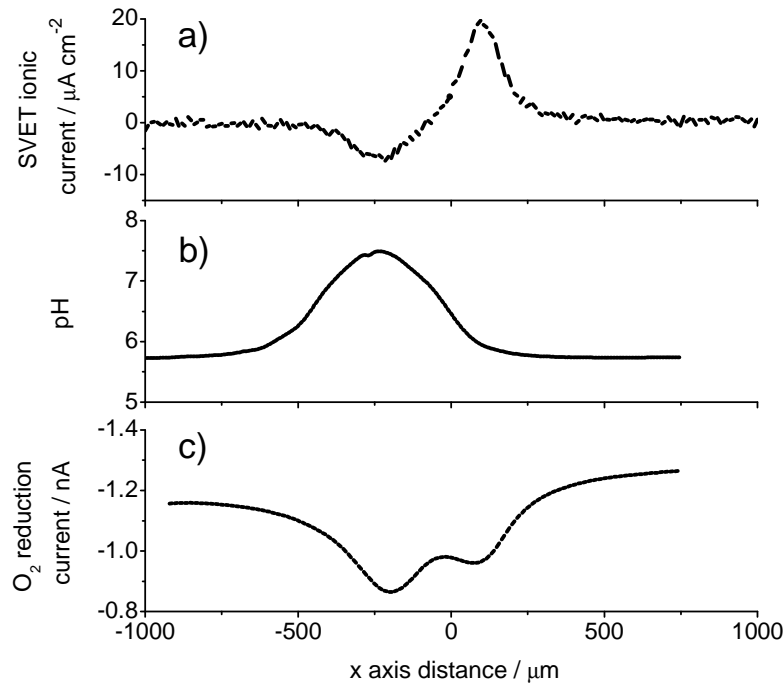
Figure 6.4.5. Line scans of ionic current (SVET) a), pH b) and dissolved oxygen c) obtained at 50 µm (100 µm for SVET) above the surface of the sol-gel coated alloy with two artificial defects during immersion in 0.05M NaCl solution.

The presented results open an additional discussion concerning the localized corrosion behaviour in micro confined defects. The corrosion processes that occur at the anodic place (right place Figure 6.4.5a) can be generally characterised by the equation presenting the dissolution of aluminium from the matrix or magnesium from the S-phase intermetallics:

$$M(s) \rightarrow M_{aq}^{n+} + ne^-. \tag{6.4.1}$$

The upward flux of (Al^{3+} or Mg^{2+}) cations gives positive current that is detected by SVET.

In the case of cathodic process (left place Figure 6.4.5a) two reactions are possible namely the reduction of water that produces hydrogen gas and hydroxyl ions and reduction of the dissolved oxygen that gives hydroxyl ions according following the two reactions:

$$2H_2O + 2e^- \rightarrow H_2(g) + 2OH_{aq}^-.$$ (6.4.2)

$$2H_2O + O_2 + 4e^- \rightarrow 4OH_{aq}^-.$$ (6.4.3)

The measurements of pH presented in Figure (6.4.5b) indeed show the increased pH over the cathodic defect on the left side. This is perfectly correlated with the cathodic nature of the defect. However, when microamperomenty was used to detect a concentration of the dissolved oxygen it showed significant drop of oxygen concentration in the place of cathodic and anodic defects (Figure 6.4.5). Reaction (6.4.3) seems to be the main cathodic process that occurs in the defect. The influence of the reaction (6.4.2) is not excluded yet is not supported by visual observations of the gas evolution during the corrosion. The drop of oxygen concentration in two defects contradicts the initial assumption given by SVET of a sole cathode and a sole anode nature of the defects. One defect is predominantly cathodic and the other is predominantly anodic but cathodic activity exists in both.

The results of the localized corrosion analysis show that the anodic defect can also supply the cathodic process. However, a pit that is formed during corrosion of the sol-gel coated alloy does not take all anodic and cathodic activity of the sample. There are other defects that can show localized corrosion behavior. The appearance of small blisters on the sol-gel surface is another sign of the localized corrosion activity of the coated alloy. Blisters have dimensions around 20-50 um in diameter and typically appear on the surface of sol-gel coatings after corrosion testing in NaCl solution (Figure 6.4.6a). The appearance of blisters (Figure 6.1.14d) can be the result of the localized cathodic activity of the alloy. The cathodic activity can be easily supported by the diffusion of oxygen which occurs through the cracks in the sol-gel film and through the sol-gel film (Figure 6.4.6a). The main cathodic activity of the alloy is the reduction of oxygen taking into the account the OCP potential of the sol-gel coated alloy and results of the polarization measurements made on bare alloy. The cathodic activity produces hydroxyl ions that increase the pH in the area inside the defect. Such increase of pH can negatively influence the hydrolytic stability of the Si-O-Si or Al-O-Si bonds. During the cathodic process there is an ingress of positively charged species from the electrolyte (sodium in case of NaCl) to the metal/coating interface in order to balance the negative charge due to the excess of OH- ions [378,379]. The appearance of sodium in blisters can be clearly seen when performing an EDS analysis on the top of blister and on the sol-gel matrix nearby (Figure 6.4.6b). As can be seen from the spectra there is a higher concentration of sodium on the blister zone and no signs of chlorine that supports the above assumption of the cathodic nature of such blisters. The cathodic process can also occur in the defected sol-gel film in the place of cracking and delamination (Figure 6.4.7). Such defects develop around a big pit during the corrosion and may assist the cathodic process.
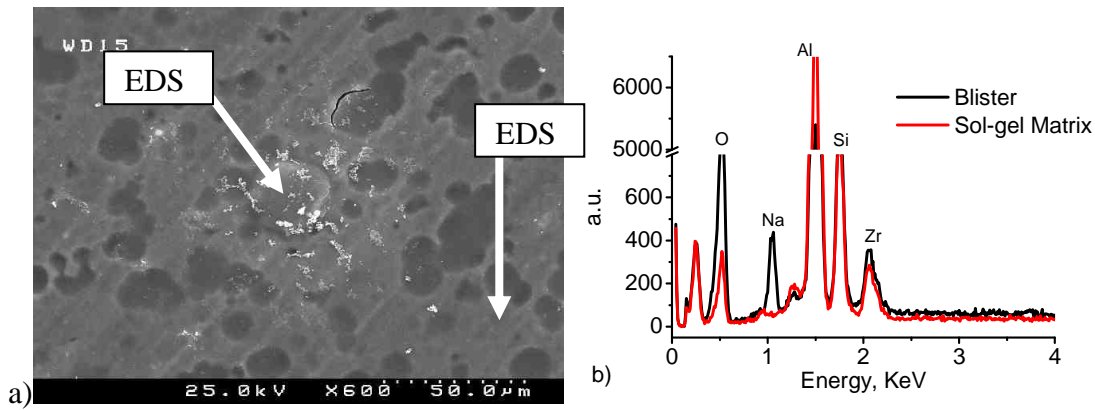
Figure 6.4.6. SEM image a) and EDS spectra on the blister and on the sol-gel matrix after immersion in NaCl solution.
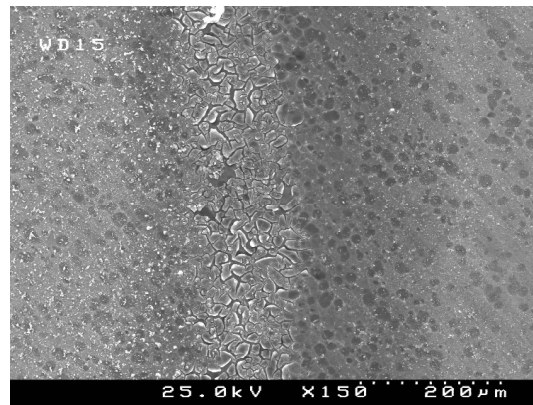
Figure 6.4.7. SEM image of the delaminated part of the sol-gel coating around a big corrosion pit after immersion in NaCl solution.

The scheme of the corrosion behaviour of sol-gel coated alloy presented in Figure 6.4.8 generalizes the results of the corrosion testing and microstructural analysis. The anodic process of alloy matrix dissolution mainly occurs in the pits developed during immersion in NaCl solution. On the left part of the picture the pitting is schematically presented as a copper enriched zone in the centre and dissolved aluminium matrix around it. During the pitting growth the aluminium dissolves from the pit. A low pH is formed inside the pit due to hydrolysis reactions of aluminium cations in the presence of chloride ions. A low pH inside the pit prevents the deposition of insoluble corrosion products of aluminium. Therefore soluble aluminium species diffuse to the bulk solution where pH is close to neutral and precipitate as hydroxides and oxychlorides corrosion products on the periphery of a pit as schematically shown in the Figure 6.4.8. When corrosion progresses

the pit becomes covered by a dome made of corrosion products of aluminium. The copper enriched zone on the bottom of the pit plays a role of local cathode surrounded by alloy matrix that becomes an anode. Therefore a pit can be self sustained. However, when oxygen diffusion to copper rich zone becomes limited by corrosion products precipitates, the development of the cathodic activity can start at the places with other defects in order to balance the current demand between the anodic and cathodic processes. Such places are represented by cracks and blisters schematically shown in Figure 6.4.8. In such places there is a free access of oxygen from the bulk electrolyte to support the cathodic activity. More pitting growth and expansion of the delaminated zone occurs during longer immersion time.
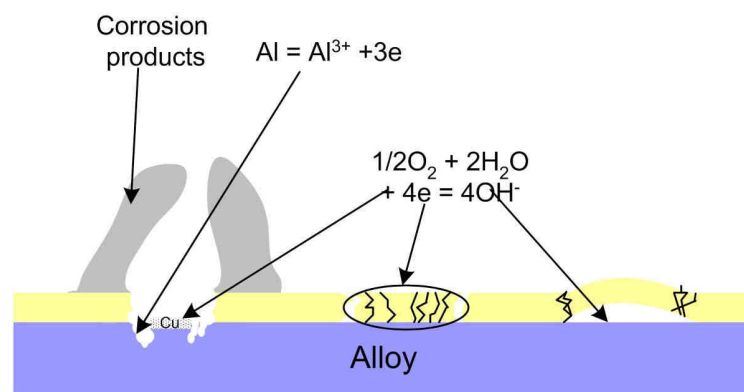
Figure 6.4.8. Localized corrosion of sol-gel coated alloy presenting pitting, cracking and blistering.

Summarizing

Sol-gel coatings provide passive barrier corrosion protection to the alloy substrate and block the ingress of corrosion species to the metal surface. However, corrosion starts when the aggressive environment reaches the metal surface. Typical corrosion features present on the sol-gel coated alloy are pits, blisters and cracks. Pits mainly show anodic activity, however the copper enriched zone inside may support cathodic activity. The cathodic process of oxygen reduction also occurs in damaged zones of the coating such as cracks and blisters.

The results obtained using microelectrode techniques revealed dual electrochemical nature of a local anode. In spite of positive currents measured by SVET technique at local anode there is a noticeable drop in oxygen concentration that suggests a cathodic process of oxygen reduction going also in anodic place. This is not revealed by SVET and shows the limitations of SVET for investigation of the localized corrosion activity on the sol-gel coated alloy.

6.5   Methods of investigation of self-healing effects on the sol-gel coated AA2024

The "self-healing" in corrosion protection can be defined as the complete or partial recovery of the corrosion protective properties of the coated or uncoated metallic substrate. For aluminium based alloys the corrosion protection is directly related to the presence and integrity of the intermediate oxide film on the metal surface. Damaging of this layer leads to the development of corrosion. Therefore coatings are used for corrosion protection of aluminium alloys. Normally coatings provide "passive" barrier for alloy against the corrosive species from the electrolyte. However, when corrosion starts and integrity of the coating is disturbed the coating can not provide "passive" protection anymore. Therefore coatings are impregnated with inhibitive additives in order to reduce the corrosion rate of metal and provide "active" corrosion protection of alloy.

Corrosion protection efficiency of the coatings can be studied by different electrochemical techniques. EIS and SVET techniques make available monitoring the corrosion activity of alloys during immersion in the corrosive electrolyte. EIS is used to monitor general corrosion activity of metals. On the other hand SVET is used to characterize the localized corrosion activity of metals. The increase of impedance of the coated metallic substrate measured by EIS and the decrease of ionic currents measured by SVET can be correlated with the "self-healing" effect provided by inhibitor addition in the coatings. However, such effect can be caused by other factors and not only by the inhibitor. For example the deposition of the corrosion products can "close" the pores of the coating and decrease the penetration of the corrosive electrolyte to the metal surface which can be interpreted as self-healing. In order to understand the role of inhibitive additives in the sol-gel coatings on the corrosion activity of the coated alloy some model experiments must be performed to ensure that the addition of inhibitor to the sol-gel coating can affect the corrosion process monitored by EIS and SVET.

6.5.1 Application of EIS and SVET technique for studying the self-healing on the sol-gel coated alloy

In this work series of model experiments were performed to correlate the evolution of impedance spectra of the sol-gel coated alloy substrate measured by EIS and local currents measured by SVET with self-healing action of a corrosion inhibitor added to the corrosive solution. Figure 6.5.1 presents the evolution of impedance spectra for two sol-gel coated samples. The first one was immersed in 0.5M NaCl solution before and after defect formation (Figure 6.5.1a). It can be seen that at initial period there are two time constants in EIS spectra. The first one related to the sol-gel coating is at high frequencies (10^5 Hz) and the second is at low frequencies (1 Hz) indicating the presence of the intermediate oxide layer. Spectrum does not show significant signs of corrosion which could not develop during short immersion time. After defect formation a new low frequency time constant attributed to the corrosion process appears in the spectrum near 1 Hz (Figure

6.5.1a). The formation of defect causes the decrease of the low frequency part of impedance during immersion in NaCl solution (Figure 6.5.1a). The decrease of Z_{mod} is caused by the permanent development of the corrosion processes in the defected zone.
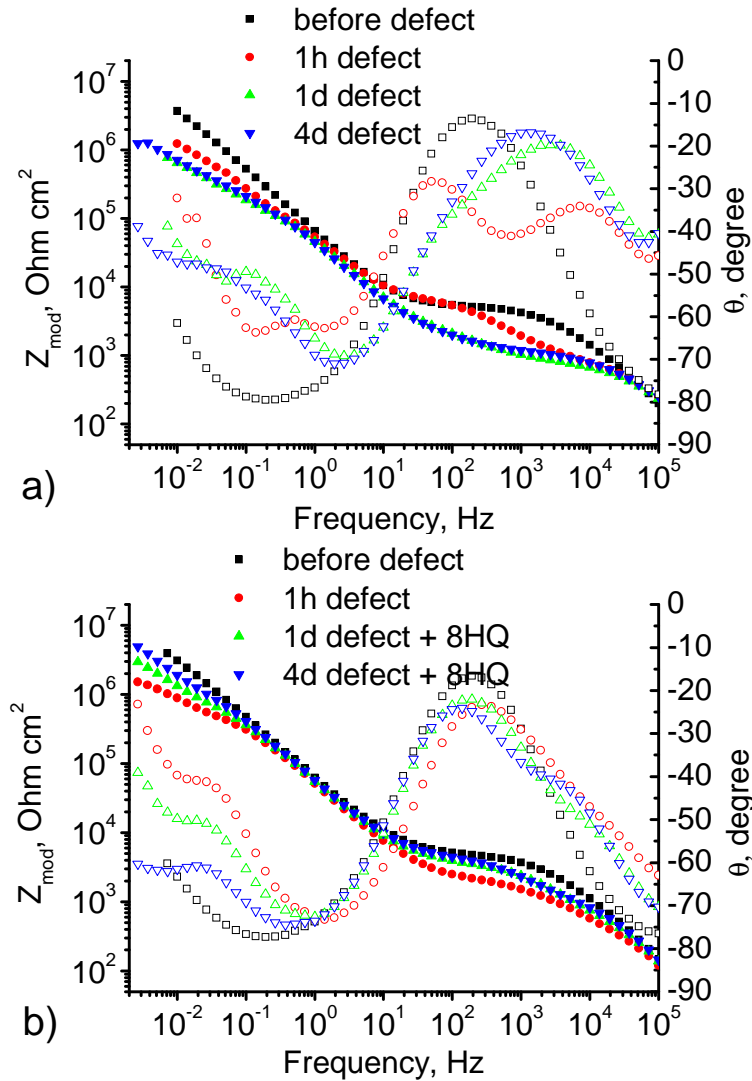
Figure 6.5.1. Evolution of impedance spectra of undoped sol-gel coated alloy during immersion in 0.5M NaCl before and after defect formation a) and in undoped 0.5M NaCl during 1 day after defect formation with following 4 days in electrolyte containing 0.5M NaCl and 0.1mM 8HQ b).

The second sample was initially immersed in 0.5M NaCl solution before and after 1h of the defect formation and then 8HQ inhibitor was introduced at concentration 0.1mM and measurements were continued at 1 and 4 days of immersion (Figure 6.5.1b). After 1h of defect formation the impedance decreased and an additional time constant appeared at

low frequencies (Figure 6.5.1b). However, the addition of inhibitor increased the impedance and lowered a phase angle of the third time constant at low frequency after 1 day. This effect becomes even more pronounced after 4 days of measurements (Figure 6.5.1b). This experiment undoubtedly confirms that the increase of the low frequency impedance is related to the healing of the defect by the corrosion inhibiting species.

The Scanning Vibrating Electrode Technique was additionally used to investigate the self-healing processes on the micro-level providing extra information for the EIS experiments and proving the conclusions made above.

The results presented in Figure 6.5.2 correspond to the case when a sol-gel coated sample was immersed during one day after the scratching in an undoped 0.05 M NaCl and then one day more in the same electrolyte doped with a 0.1 mM 8-hydroxyquinoline. These measurements correspond to the conditions of the EIS experiment presented in Figure 6.5.1b. During the first day of immersion once the scratch is created the anodic corrosion activity is continuously growing from 1.6 μA/cm^2 after 1 h to about 20 μA/cm^2 after one day of testing (Figure 6.5.2b and c). This corresponds to the remarkable drop of the impedance on the Bode plot taken after defect formation (Figure 6.5.1b). The change of the electrolyte to the doped one leads to a slight increase of the corrosion activity especially in the cathodic region (Figure 6.5.2d). This increase can be related to the increased concentration of oxygen in the fresh electrolyte favoring the cathodic reduction of oxygen. It is also possible that the addition of 8HQ increases a dissolution rate of aluminum from the anodic zone in the middle of the defect due to the strong complexing action of 8HQ to Al^{3+} ions. However, one day later the corrosion activity lowers at least twice showing a decrease of the activity in the scratched area (Figure 6.5.2e). This reduction of the currents related to the active anticorrosion effect of the inhibitor explains the increase of the low frequency impedance in the case of Figure 6.5.1b. It should be noted that the corrosion activity is not hindered completely leading to only partial reduction of the impedance without reaching the initial values.

The presented SVET results clearly confirm on micro-level the conclusions made from the EIS macro-level tests. It is undoubtedly shown that the decrease of the low frequency impedance after the defect formation is related with the disruption of the coating and the oxide barrier and the corresponded localized corrosion activity in the defected area. The addition of the corrosion inhibitor heals the defect leading to lower corrosion currents and the increase of impedance.
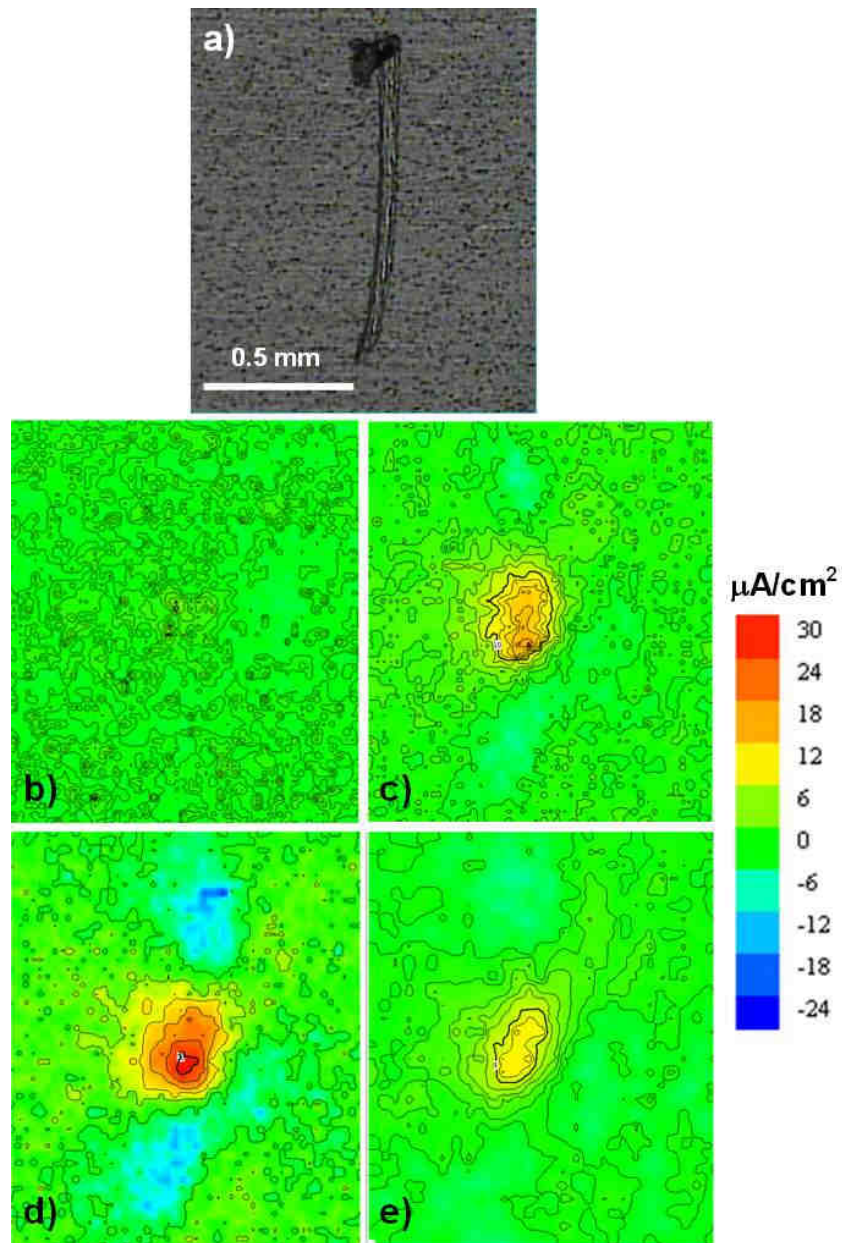
Figure 6.5.2. Optical photo (a) and the SVET maps taken in the corresponding zone of AA2024 coated with sol-gel film after 1 hour (b) and 1 day (c) of immersion in 0.05M NaCl electrolyte. The electrolyte was changed to the 0.05M NaCl + 0.1mM 8-hydroxyquinoline and the SVET maps were obtained after 1 hour (d) and 1 day (e).

Summarizing

The development of the sol-gel pretreatments with active corrosion protection requires methods to investigate and prove the ability to "heal" the corrosion process on the coated metal. In this study two electrochemical methods, namely EIS and SVET, have been used to investigate the self-healing processes in AA2024 substrate with protective sol-gel coating in the presence of corrosion inhibitor.

The particular experimental results show that the increase of the low frequency impedance during immersion can be correlated to the active corrosion protection originated from the self-repairing of the defects in the presence of the corrosion inhibitor. The SVET results obtained on micro-level are in good accordance with the EIS measurements. The decrease of the low frequency impedance after the defect formation is related to the disruption of the coating and the oxide barrier and the consequent localized corrosion activity in the defected area. The addition of the corrosion inhibitor heals the defect leading to lower corrosion currents and high impedance.

The overall outcome of the obtained results is that corrosion investigating methods such as EIS and SVET can be applied to study the self-healing processes in the sol-gel coatings doped with different inhibitors and nanocontainers with inhibitors which will be presented in the following sections.

7 Sol-gel coatings with corrosion inhibitors

7.1 Inhibitor-containing hybrid sol-gel coatings

This part of the work presents the results of investigation of hybrid sol-gel coatings doped with corrosion inhibitors. A certain number of corrosion inhibitors for AA2024 studied in section 5 were used as additives to the hybrid sol-gel formulations in order to confer active corrosion protection properties and enhance protection of the sol-gel coated alloy. Organic inhibitors 8-hydroxyquinolin (8HQ), benzotriazole (BTA) and inorganic cerium nitrate ($Ce(NO_3)_3$) were added at different stages of the sol-gel synthesis process to understand the role of possible interaction of inhibitor with components of the sol-gel system. Sol-gel coating without inhibitor addition was prepared and used as a reference. The sol-gel coatings were studied using different electrochemical and microstructural techniques.

7.1.1 Synthesis and characterisation of hybrid sol-gel coatings

Hybrid sols were prepared on the basis of the sol-gel formulation SgZr1 (synthesis is described in details in paragraph 4.3.1). Organic compounds (BTA, 8HQ) and inorganic $Ce(NO_3)_3$ were chosen as effective corrosion inhibitors for AA2024 based on the investigations performed in chapter 5 and added to the Zr-based sol-gel system at different synthesis steps. Preliminary concentrated solutions of inhibitors were made using the components of the sol-gel system as solvents and necessary amount of the concentrated inhibitor solutions was introduced drop wise in the alkosols 1, 2 or 3 during the sol-gel synthesis. The synthesis steps where inhibitors were introduced are shown in Table 7.1.1 and Table 4.3.1. The molar concentration of inhibitor in the final sol-gel solution was the same for all inhibitors (0.054 M). The reference coating without any additives was also prepared for the comparison reason.

The obtained sol-gel coatings were characterized by the SEM in order to reveal the surface microstructure of the sol-gel coatings doped with different inhibitors after synthesis. Figure 7.1.1 shows typical plane and cross-section views of the sol-gel coating doped with organic (BTA, 8HQ) and inorganic $Ce(NO_3)_3$ inhibitors. The stage at which inhibitor is introduced to the sol-gel does not influence significantly the appearance of the coatings surface. Therefore only samples doped at stage 3 are presented in the Figure. It can be seen, that deposited sol-gel films are uniform, defect- and crack-free. The addition of inhibitors does not notably change thickness of the sol-gel films which is around 1.5 – 2 µm for all the coatings. Such thickness is essentially similar to that of undoped sol-gel films (Figure 6.1.8).

Table 7.1.1. Addition step of inhibitor during preparation of Zr based sol-gel and respective reference names of coatings applied on AA2024 substrates.

Inhibitor 0.0536 M	(Alkosol 1) TPOZ	(Alkosol 2) GPTMS	(Alkosol 3) TPOZ+GPTMS	Reference name
-	-	-	-	SgZr1
BTA	+	-	-	SgZr1BTA1
BTA	-	+	-	SgZr1BTA2
BTA	-	-	+	SgZr1BTA3
8HQ	+	-	-	SgZr1HQ1
8HQ	-	+	-	SgZr1HQ2
8HQ	-	-	+	SgZr1HQ3
$Ce(NO_3)_3$	+	-	-	SgZr1Ce1
$Ce(NO_3)_3$	-	+	-	SgZr1Ce2
$Ce(NO_3)_3$	-	-	+	SgZr1Ce3
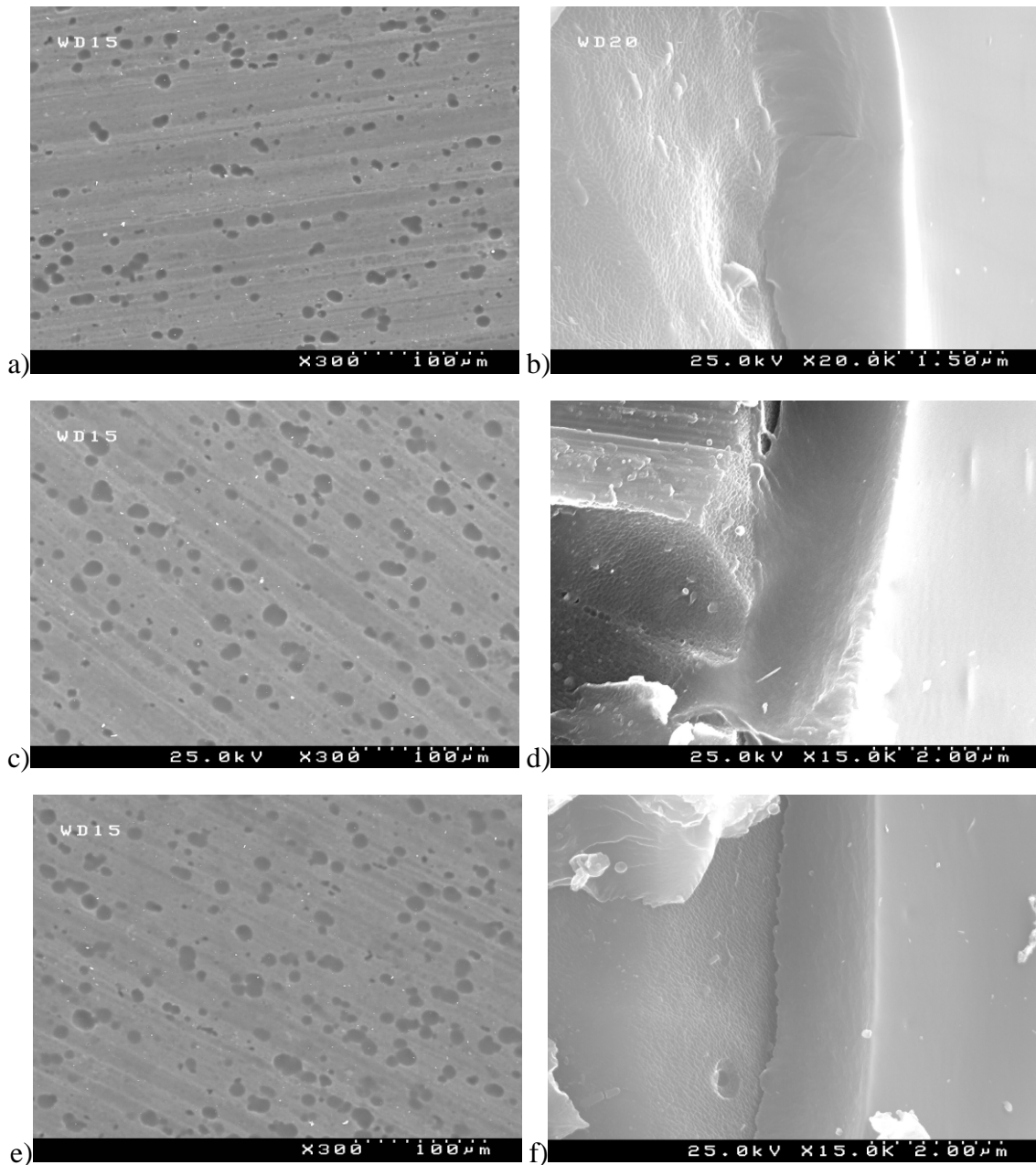
Figure 7.1.1. Plane and cross-section views obtained by SEM of the sol-gel coatings deposited on AA2024 before corrosion exposure SgZr1BTA3 (a,b), SgZr18HQ3 (c,d), SgZr1Ce3 (e,f).

7.1.2 Surface characterisation after corrosion

To reveal changes of microstructure of the sol-gel coatings after corrosion the immersed samples were examined by SEM technique. Figure 7.1.2 presents SEM images for different samples after 25 days of corrosion exposure in 0.5M NaCl solution. As can be seen the appearance of surface is changed after immersion in NaCl solution compared to initial state before immersion (Figure 7.1.1). Sol-gel coatings containing BTA show dramatic changes of the surface (Figure 7.1.2a). A lot of small pits and blisters cover entirely all the surface. In contrast to BTA the surface of samples doped with 8hydroxyquinolin and cerium nitrate shows much less corrosion impact (Figure 7.1.2b,c). The main features associated with the corrosion activity are small blisters that are delaminated parts of the sol-gel film caused by the local corrosion process. Such features were also found in case of undoped sol-gel coatings. Blisters can be found on all the surface of SgZr1BTA samples. On the other hand, the appearance of blisters on samples SgZr18HQ3 and SgZr1Ce3 is rare and mostly concentrated around big pits. Most probably, BTA added to the sol-gel formulations chemically interacts with the components of the sol-gel weakening the coating stability. Such interactions negatively influence the crosslinking degree and adhesion to the metal surface. When stability of the coatings and metal/coating interface is low corrosion quickly develops which results in appearance of many blisters and pits (Figure 7.1.2a).

An additional analysis of the sol-gel surface close to big pit shows some aspects of the localized corrosion as example for SgZr1BTA3 sample. A zone close to the pit (Figure 7.1.3a) shows lower amount of the corrosion products with visible cracking of the sol-gel film (Figure 7.1.3b). This cracking becomes clearer seen at higher magnification (Figure 7.1.3c). A corrosion activity developed in such area can be responsible for the damage of the coatings. A most plausible explanation of the sol-gel film cracking is due to the cathodic processes in such place. The reduction of oxygen produces hydroxyl ions that can negatively affect the hydrolytic stability of the sol-gel coating which results in appearance of cracks and significant delamination. In contrast to the sol-gel films with BTA inhibitor, the other coatings containing cerium nitrate or 8HQ did not show cracking in the vicinity of big pits.

The results of microstructural investigation showed that the main damaging that occurs during the corrosion of the sol-gel coated samples is the formation of blisters, delamination areas and pits. However, microstructural analysis can not provide a clear distinction of the corrosion protection conferred by different sol-gel systems. Therefore electrochemical techniques such as EIS can be used to characterize the corrosion protection efficiency.
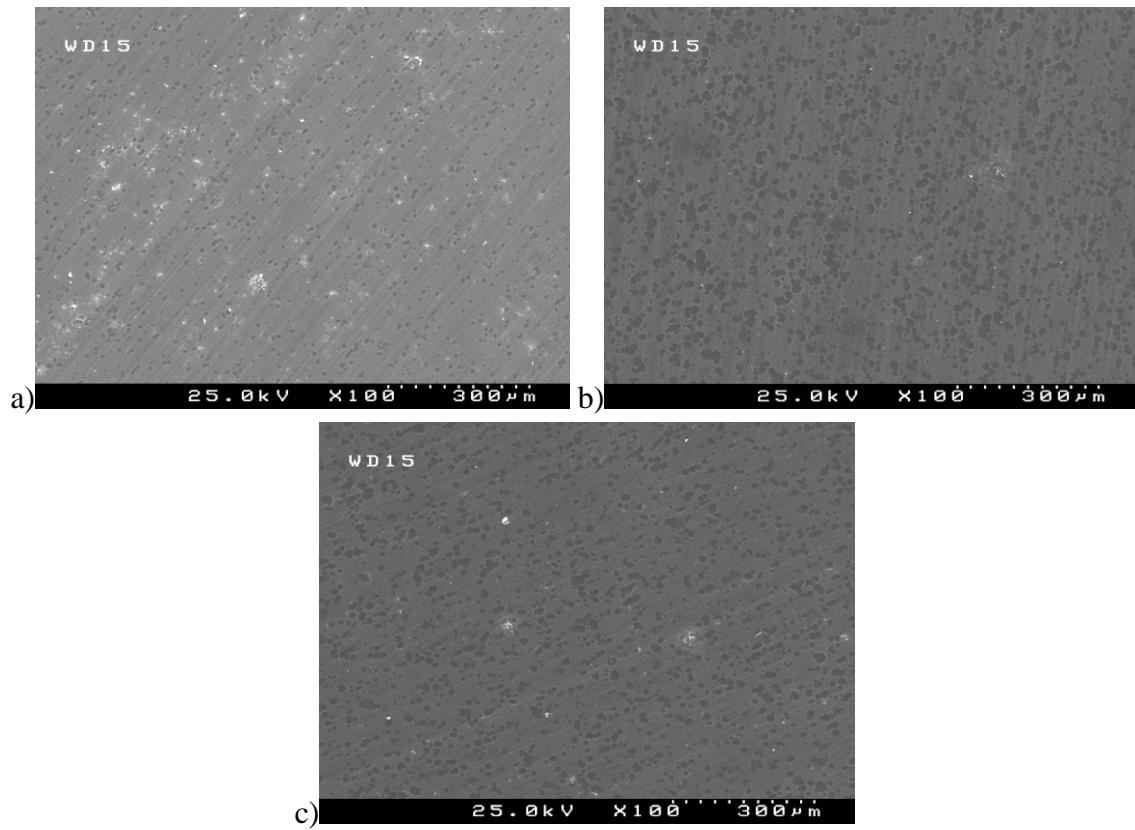
Figure 7.1.2. SEM images of sol-gel coated samples after 25 days of immersion in 0.5M NaCl, SgZr1BTA3 a), SgZr18HQ3 b) and SgZr1Ce3 c).
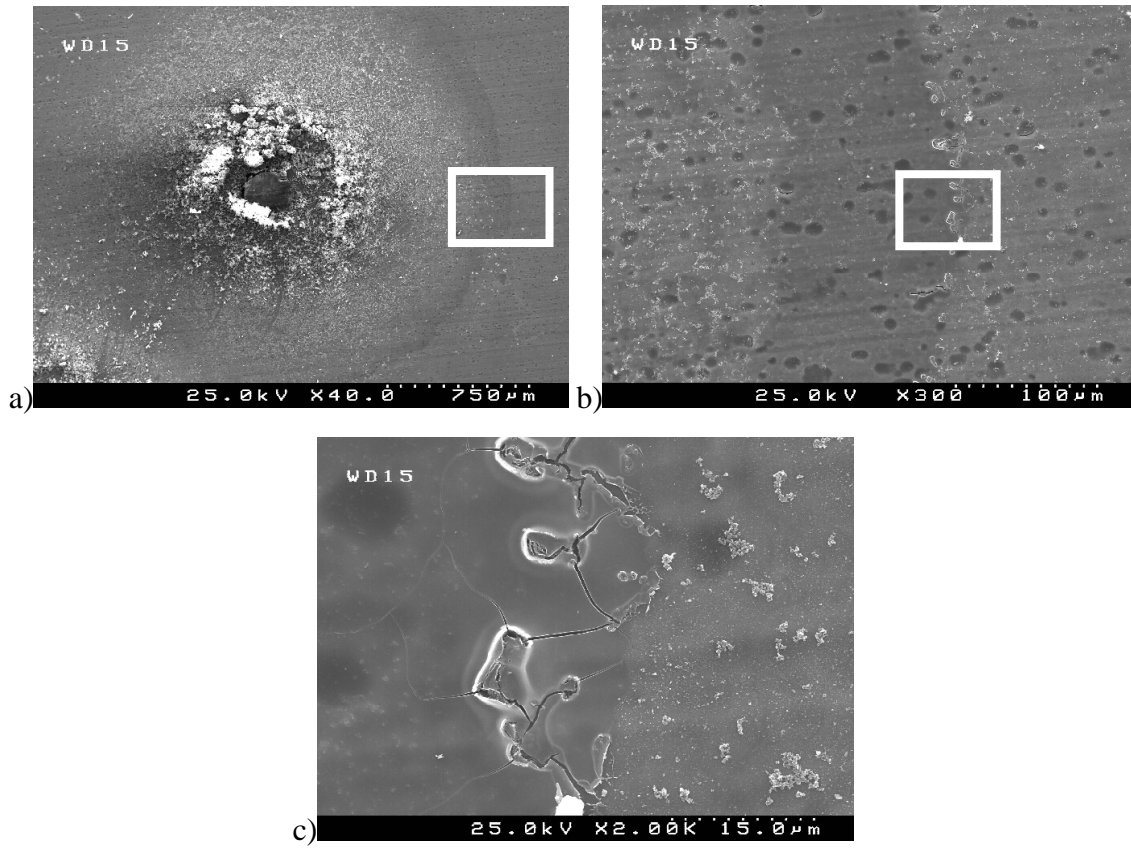
Figure 7.1.3. SEM images of SgZr1BTA3 sample after 25 days of immersion in 0.5M NaCl, pit a), zone on the periphery of the pit at higher magnification b), zone of cracking at higher magnification c).

7.1.3 Study of the corrosion protection of the sol-gel coatings by EIS

Corrosion protection efficiency of the sol-gel coatings was evaluated during 25 days of immersion in 0.5M NaCl solution. Figure 7.1.4 shows Bode plots of the sol-gel coatings doped by BTA, 8HQ and $Ce(NO_3)_3$ inhibitors after 7 day of immersion in NaCl solution. The impedance spectra show three typical time constants that are usually observed on the sol-gel coated aluminum alloys as previously discussed in paragraph 6.1. The capacitive response of the sol-gel coating appears at high frequencies about 10^5 Hz. The relaxation process at middle frequencies (10^{-1}-10 Hz) is ascribed to the intermediate oxide layer present on the alloy surface. The time constant at low frequencies $<10^{-1}$ Hz is associated to the developed corrosion activity.
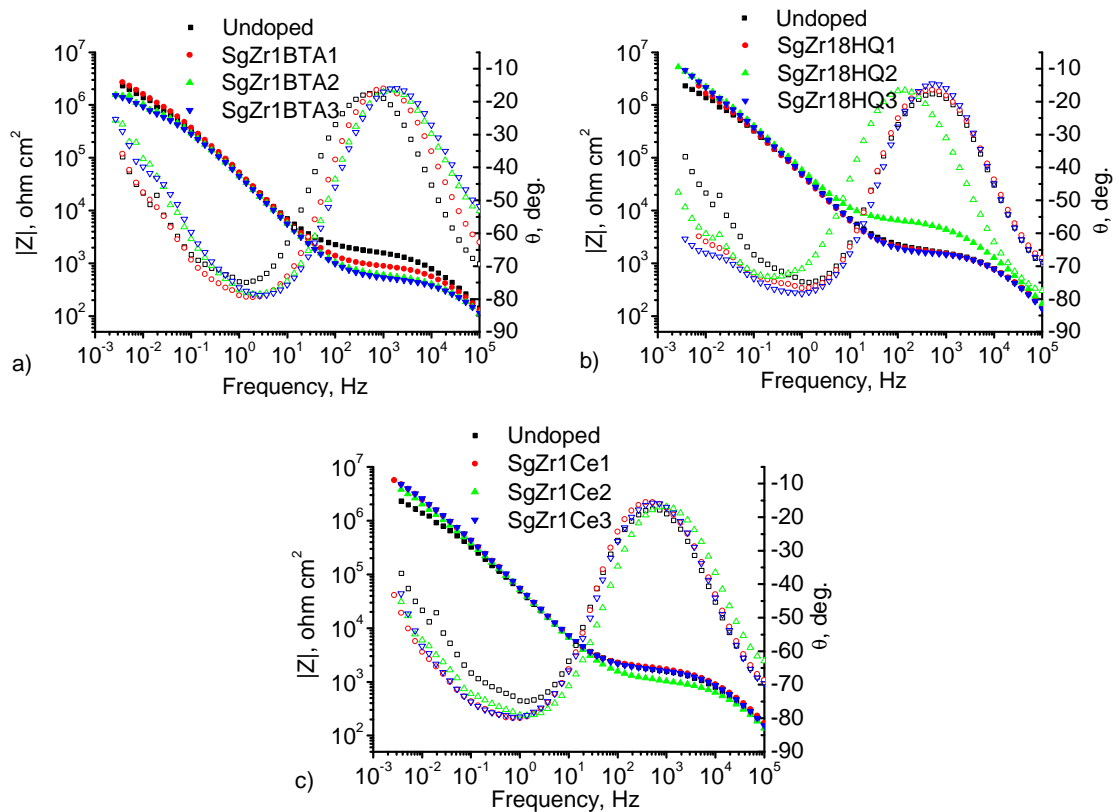
Figure 7.1.4. EIS spectra of different sol-gel coatings doped with BTA a), 8HQ b) and $Ce(NO_3)_3$ c) inhibitors. Spectra were obtained after 7 days of immersion in 0.5M NaCl solution.

A rough evaluation of impedance data shows that the addition of BTA inhibitor to the sol-gel at any stage of hydrolysis leads to a significant degradation of the sol-gel film compared to the undoped one (Figure 7.1.4a). Sol-gel coatings with 8HQ and $Ce(NO_3)_3$ inhibitors have higher values of low frequency impedance compared to the undoped film (Figure 7.1.4b,c). The impedance increase testifies for enhanced corrosion protection of the alloy. However, a more detailed analysis of the corrosion protection properties of different sol-gel coatings is needed in order to better indentify the difference in protection effectiveness. This can be achieved by fitting the impedance data with the appropriate equivalent circuits presented in Figure 3.3.14.

Evolution of the sol-gel film

The rate of water uptake and the hydrolytic stability of coatings during immersion in aqueous solutions can be determined from the change of the capacitance of the sol-gel films. The results on capacitance evolution (C_{coat}) for different coatings are presented in Figure 7.1.5. During first 3 days of immersion the capacitance for BTA-doped samples is lower compared to undoped sample (Figure 7.1.5a). At longer immersion there is a linear increase of capacitance. During immersion the capacitance for the BTA doped sol-gel coating changes from around $8.5*10^{-9}$ F/cm^2 to $3.6*10^{-8}$ -$6.6*10^{-8}$ F/cm^2 (Figure 7.1.5a). The calculated water uptake using the Brasher-Kingsbury equation (3.3.22) is presented in Table 7.1.2. It can be seen that for BTA doped sol-gel coatings a water uptake reaches 47%. Such huge value is too high for a small and dense coating. Most likely the increase of the capacitance can not be related only to the water uptake. Degradation and hydrolytic decomposition of the sol-gel systems should be taken into account in this case as well. The condensation process of the siloxane groups is reversible and a hydrolytic reaction can lead to cleavage of Si-O-Si bonds in alkaline environment. Thus the change of capacitance during water absorption can not follow classical Brasher-Kingsbury relation used for typical organic coatings. This explains the abnormal increase of capacitance for BTA doped samples. Moreover, the thickness of sol-gel film can also be decreased due to partial removal of the degraded sol-gel layer. This adds an additional error for calculation of capacitance. Nevertheless, at the beginning of immersion the capacitance increase can be attributed to the water absorption. However, the longer immersion time most probably leads to the hydrolytical decomposition of the coating.

Sol-gel coatings doped with 8HQ do not show significant difference of the capacitance compared to the undoped films at the beginning of immersion (Figure 7.1.5b). During the first two days there is a fast growth of the capacitance from $1.0*10^{-8}$ F/cm^2 to $1.6*10^{-8}$ F/cm^2. At longer immersion time the capacitance steady grows until around $1.9*10^{-8}$ F/cm^2 and is slightly higher than for undoped coating. The water uptake of the sol-gel coatings with 8HQ presented in Table 7.1.2 shows practically the same values as for undoped sample (12.5%). The sample SgZr18HQ1 where the additive of inhibitor was introduced to Zr-propoxide solution (Alkosol 1) during the sol-gel synthesis shows higher

values of water uptake (15.6%) (Table 7.1.1). The higher water uptake in this case can be attributed to the interactions of the inhibitor with TPOT or EtAcAc which cause modification of the sol-gel system.

The evolution of the capacitance of cerium nitrate doped sol-gel coatings demonstrates behavior close to the undoped system (Figure 7.1.5c). A slightly lower increase of capacitance is notable at the beginning of immersion compared to undoped sample (Figure 7.1.5c). However, after few days the trend becomes similar to the undoped layer. Capacitance increases from around $1.0*10^{-8}$ F/cm^2 until $1.9*10^{-8}$ F/cm^2. The sample SgZr1Ce1 shows somewhat low capacitance ($9*10^{-9}$ F/cm^2) at the beginning of immersion compared to other samples. This may testify for a slighter thicker sol-gel film formed in this case. The calculated water uptake varies from 11.6 to 15.6 % for different $Ce(NO_3)_3$ doped samples (Table 7.1.2). The addition of soluble salt to the sol-gel coating might increase ingress of water into it which explains higher values of water uptake.
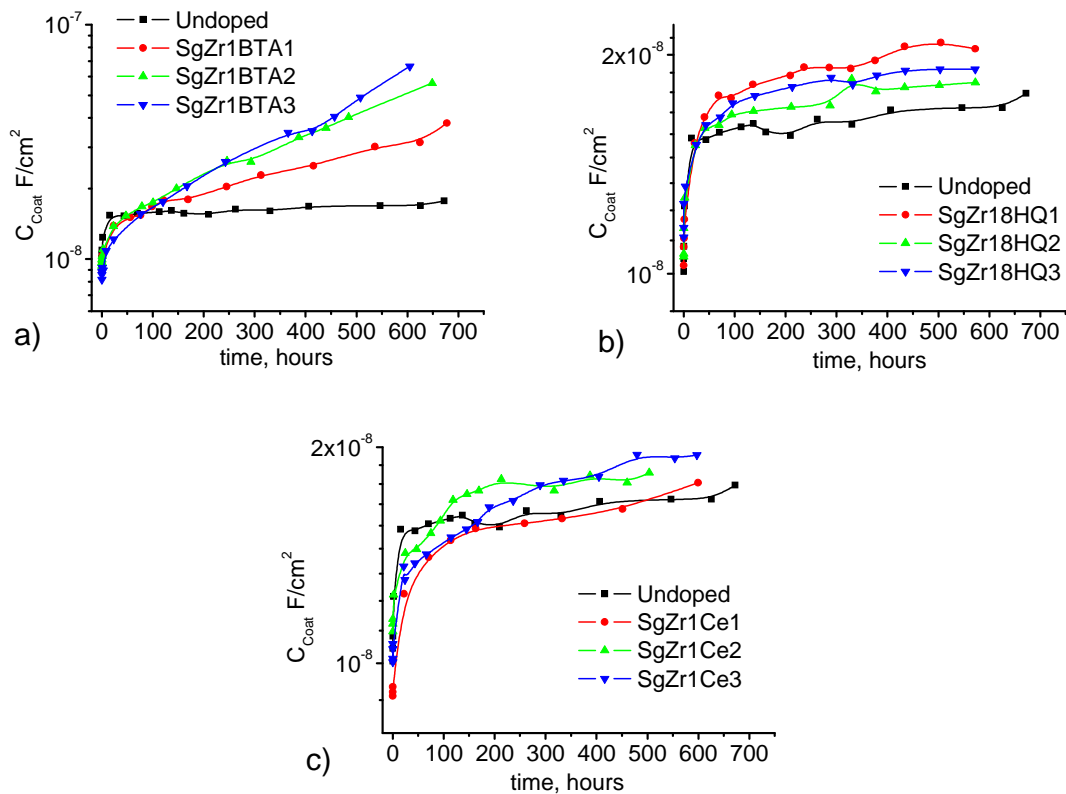
Figure 7.1.5. Evolution of Sol-gel films capacitance for coatings doped by BTA a), 8HQ b) and $Ce(NO_3)_3$ c) during immersion in 0.5M NaCl solution.

Table 7.1.2. Numerical data of capacitance and water uptake for different sol-gel coatings with inhibitors.

Sample	Undoped	SgZr1BTA1	SgZr1BTA2	SgZr1BTA3	SgZr18HQ1
C F/cm^2 initial	$1.01*10^{-8}$	$8.96*10^{-9}$	$9.35*10^{-9}$	$8.17*10^{-9}$	$1.03*10^{-8}$
C F/cm^2 end	$1.77*10^{-8}$	$3.80*10^{-8}$	$5.63*10^{-8}$	$6.64*10^{-8}$	$2.04*10^{-8}$
Water uptake %	12.8	32.9	40.9	47.7	15.6

Sample	SgZr18HQ2	SgZr18HQ3	SgZr1Ce1	SgZr1Ce2	SgZr1Ce3
C F/cm^2 initial	$1.06*10^{-8}$	$1.12*10^{-8}$	$9.01*10^{-9}$	$1.11*10^{-8}$	$1.05*10^{-8}$
C F/cm^2 end	$1.83*10^{-8}$	$1.91*10^{-8}$	$1.78*10^{-8}$	$1.84*10^{-8}$	$1.95*10^{-8}$
Water uptake %	12.5	12.1	15.6	11.6	14.1

The addition of inhibitive species during different steps of synthesis can result in the specific chemical interaction of inhibitor with the components of the sol-gel system like GPTMS, Zr(IV) propoxide and others. Consequently, such interaction can cause notable changes of the hydrolytic stability, barrier properties and adhesion of sol-gel coatings. Figure 7.1.6 presents evolution of the sol-gel film resistance (Rcoat) doped by different inhibitors. Sol-gel coatings doped by BTA show very fast decrease of the resistance during the first two days of immersion compared to the undoped sample. After three days of immersion resistance decreases linearly with time and in the end of immersion the difference of R_{coat} between the undoped and BTA doped coatings is almost an order of magnitude (Figure 7.1.6a). The decrease of the sol-gel film resistance and huge increase of capacitance provide evidence of a significant hydrolytic instability of BTA doped sol-gel systems. In the case of 8HQ and Ce(NO$_3$)$_3$ doped sol-gel coatings the evolution of coating resistance is almost the same as for undoped coating (Figure 7.1.6b,c) that can account for chemical stability of the sol-gel systems. It should be noted that coating SgZr18HQ2 shows higher resistance which is probably associated with the influence of 8HQ on he hydrolysis and condensation reactions of GPTMS based Alkosol 2. A lower R_{coat} in the other two cases suggests possible chemical interactions between molecules of 8HQ and either TOPZ or EthAcAc that might block the inhibitor.

These results show that addition of 8HQ and Ce(NO$_3$)$_3$ does not influence significantly the hydrolytic stability of sol-gel films unlike for BTA doped ones. A chemical interaction of inhibitor with the components of the sol-gel system is the most likely process that results in decrease of the barrier properties of the sol-gel coatings in the last case.
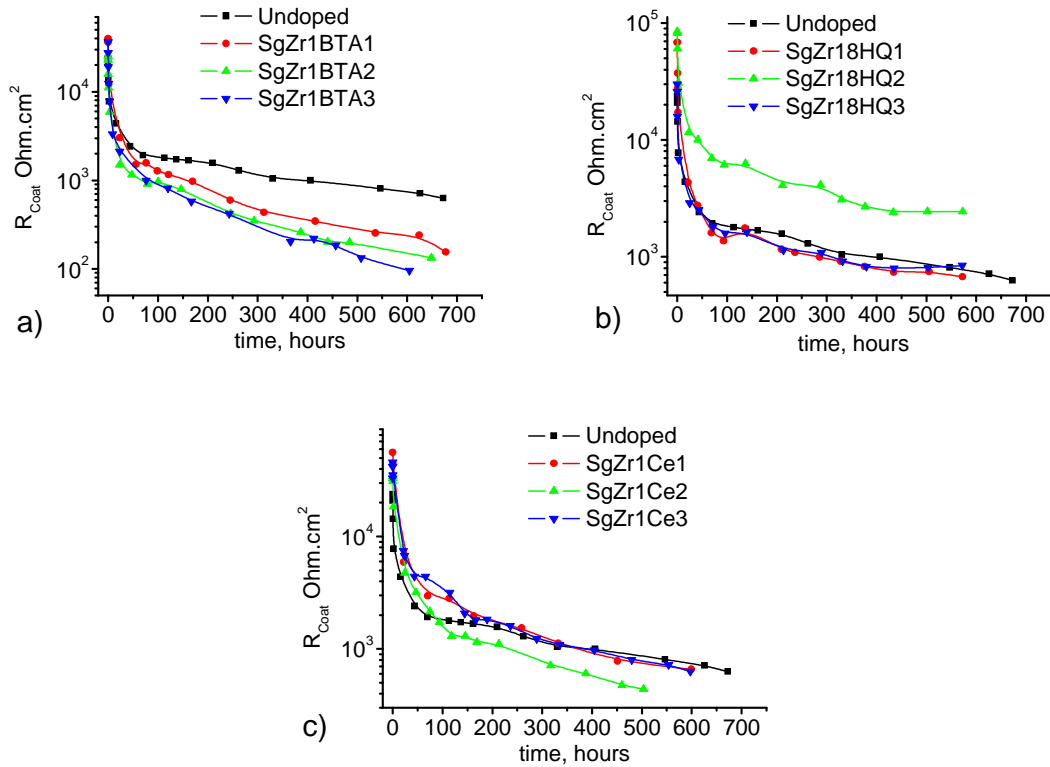
Figure 7.1.6. Evolution of sol-gel films resistance for coatings doped by BTA a), doped by 8HQ b) and $Ce(NO_3)_3$ c) during immersion in 0.5M NaCl solution.

Evolution of the intermediate oxide layer

The intermediate oxide layer is the last barrier between the corrosive species and the metal surface. Its integrity is very important from the standpoint of the corrosion protection since defects in it allow direct ingress of the corrosive species to the metal. Therefore the monitoring of the evolution of the oxide layer during corrosion exposure can give information on the corrosion progress. Evolution of the resistance of oxide layer (R_{ox}) for different sol-gel coatings during immersion in 0.5M NaCl solution is presented in Figure 7.1.7. During the first 2 days of immersion R_{ox} is higher for SgZr1BTA samples. This effect is most probably provided by the rapid inhibiting action of BTA. However, longer immersion results in a failure of oxide resistance and decrease of corrosion protection. At the beginning of immersion the initial value of R_{ox} is around $1.5*10^7$ $Ohm*cm^2$ gradually decreasing during the immersion until $3.5*10^5$ $Ohm.cm^2$ at the end of immersion (Figure 7.1.7a).
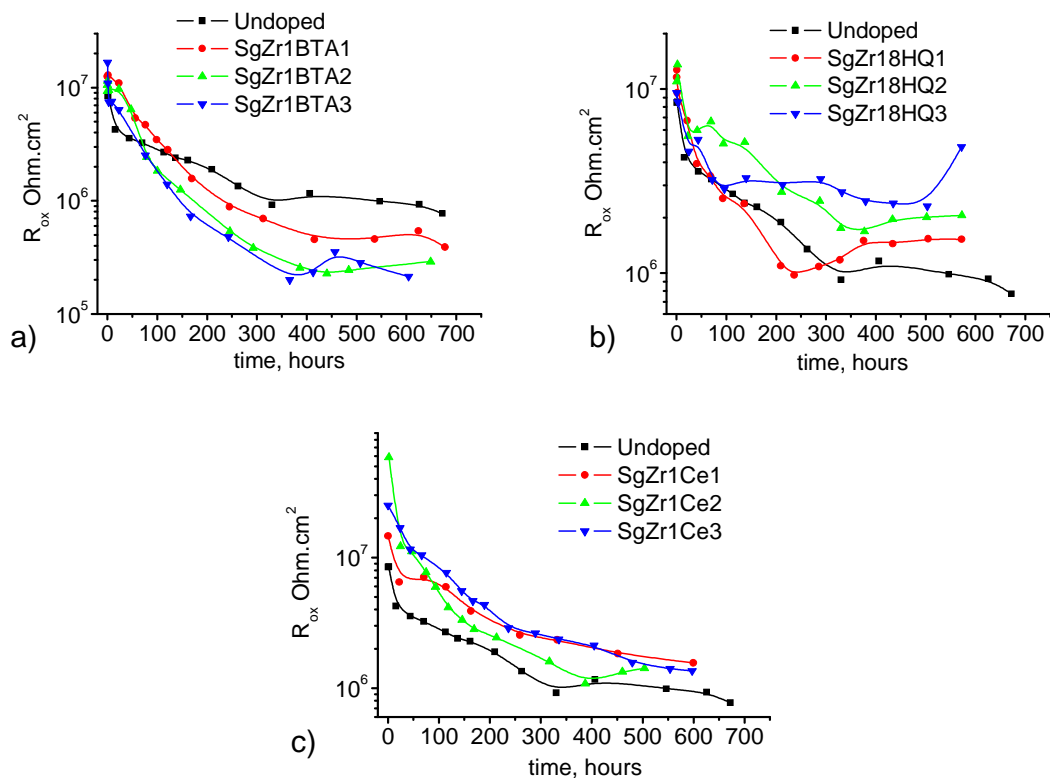
Figure 7.1.7. Evolution of intermediate oxide layer resistance for sol-gel coatings doped by BTA a), 8HQ b) and Ce(NO₃)₃ c) during immersion in 0.5M NaCl solution.

On the contrary to BTA, doping by 8HQ and $Ce(NO_3)_3$ leads to the increase of the intermediate oxide film resistance compared to undoped sample. For instance, initial values of R_{ox} for all $Ce(NO_3)_3$ doped sol-gel coatings are higher than for undoped one (Figure 7.1.7c). The evolution of the oxide resistance shows that the corrosion protection during first 6 days of immersion remains higher in the case of Ce-doped sol-gel films (Figure 7.1.7c).

In contrast to Ce-containing ones, the sol-gel samples doped with 8HQ show almost the same values of R_{ox} as for undoped one at the commencement of immersion (Figure 7.1.7b). This can support the low release of inhibitor during initial immersion. Although, the trend of the R_{ox} change is very similar to undoped sample at the beginning of immersion, the difference between the R_{ox} of inhibited and undoped samples can be observed at longer immersion time. The best corrosion protection was achieved when 8HQ was introduced to the Alkosol 2 (sample SgZr18HQ2) and Alkosol 3 (sample SgZr18HQ3) during the synthesis (Figure 7.1.7b). The addition of 8HQ during hydrolysis of zirconia-precursor in Alkosol 1 (sample SgZr18HQ1) leads to decrease of the intermediate oxide layer resistance. This can be caused by a strong interaction of the zirconia-precursor with 8-hydroxyquinoline, which is a good complexing agent [380]. The formation of the

250

complexes between the zirconium alkoxide and/or its partially hydrolyzed form with 8-hydroxyquinoline when inhibitor was added in the Alkosol 1 can influence the hydrolysis and condensation reaction of metalorganic precursor and deactivate inhibiting action of 8HQ that becomes chemically bonded to the precursor. This demonstrates the importance of the sol-gel synthesis stage at which inhibitor is added.

7.1.4 Active corrosion protection of the sol-gel coatings, SVET study

The undoped sol-gel film confers adequate corrosion protection to AA2024 due to good adhesion and formation of stable barrier against aggressive corrosive species. Addition of cerium nitrate and 8HQ to the sol-gel composition has no significant influence on the barrier properties of the coatings. However, in general corrosion protection is improved demonstrating that another factor than just passive protection is responsible for this. The main plausible explanation of this effect is active corrosion protection conferred by the corrosion inhibitor released from the sol-gel coating. To confirm the active corrosion protection effect and the ability to heal the defects in the coating the Scanning Vibrating Electrode Technique (SVET) was employed. The SVET method is a powerful tool to measure the local ionic currents originated from the active surface. In the case of localized corrosion processes the flows of ions appear in the active zone being directly related to the local cathodic and anodic corrosion activities.

To investigate the self-healing ability of different sol-gel coatings two equal artificial defects were made on the surface of different sol-gel films. After defect formation, a local distribution of currents was measured during immersion in 0.05M NaCl solution for 4 days.

The results of SVET measurements are presented in Figure 7.1.8. After 4 hours of defect formation both cathodic and anodic activities can be seen on the surface of all samples (Figure 7.1.8a,c,e). Following one day of immersion all samples show increase of activity. Nevertheless, the longer immersion causes decrease of activity for inhibitor-doped samples, whereas for the undoped one corrosion becomes rather high. After 4 days of immersion such a difference can be clearly seen (Figure 7.1.8b,d,f). Anodic and cathodic currents measured on the undoped sample (Figure 7.1.8b) are higher compared to the Ce or 8HQ doped samples. The results show that coatings doped by 8HQ and cerium nitrate decrease corrosion activity in the zones of local defects demonstrating well-defined signs of self-healing ability.
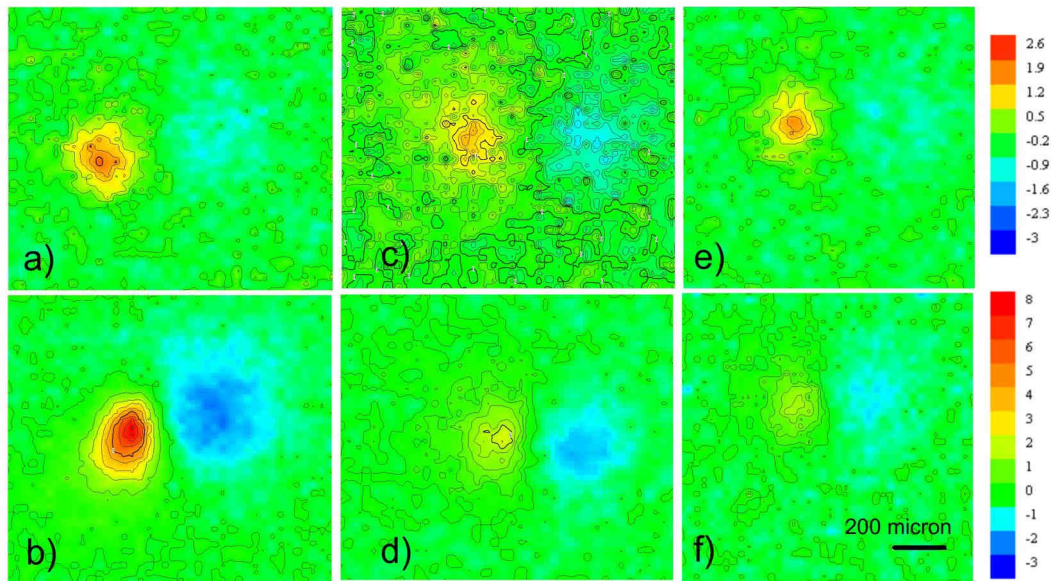
Figure 7.1.8. SVET maps of the local current fluxes after 4h and 4 days of immersion in 0.05M NaCl for undoped sample (a, b), SgZr18HQ3 sample (c, d) and SgZr1Ce3 sample (e, f). Scale units: $\mu A \, cm^{-2}$.

7.1.5 Mechanism of the corrosion attack on AA2024 coated with sol-gel films containing inhibitors

Pits, blisters and cracks are formed in the coating during immersion of the alloy coated by sol-gel coatings containing inhibitors. The corrosion develops in similar fashion as in the case of undoped sol-gel coatings. In the place of defects an aggressive environment penetrates the sol-gel film until the metallic substrate and activates the corrosion process. However, the presence of inhibitors in the coating can decrease the started corrosion activity. Figure 7.1.9 schematically presents the corrosion inhibition process in a micro defect. When cracks appear in the sol-gel coating they become flooded with the electrolyte that induces corrosion at the metal surface. On the other hand, electrolyte also provides a pathway for inhibitor that leaches out from the sol-gel coating close to the defect as shown by the blue arrows in Figure 7.1.9. When inhibitor reaches the metal surface it reduces the corrosion process affecting either the cathodic or anodic activity (Figure 7.1.9).
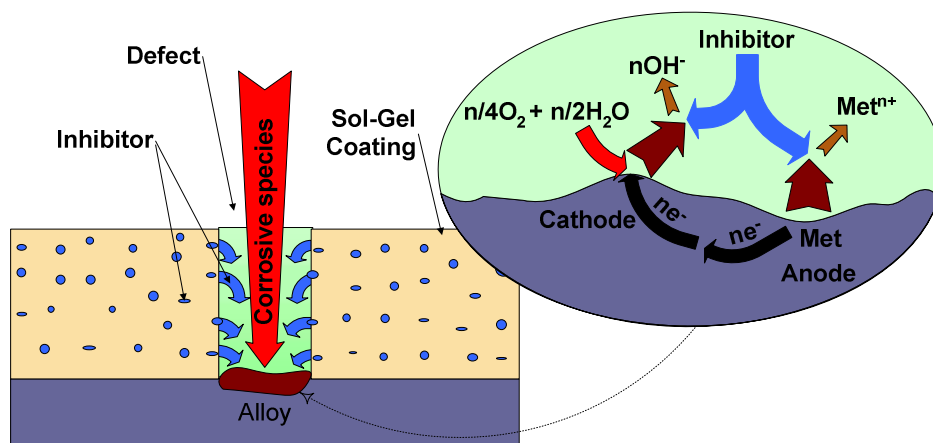
Figure 7.1.9. Localized corrosion inhibition in the sol-gel coating with micro defect.

The addition of 8HQ and cerium nitrate to the sol-gel coating results in a decrease of the corrosion activity as was demonstrated by EIS (Figure 7.1.4) and SVET (Figure 7.1.8) measurements. In particular the increase of resistance of the intermediate oxide layer was found in the case of sol-gel coatings doped by inhibitors (Figure 7.1.7). The higher stability of the intermediate oxide layer testifies for enhanced corrosion protection conferred by the inhibitive additives. The corrosion process is also diminished during the initial immersion time as was demonstrated by SVET measurements. The corrosion inhibition mainly occurs in the places with cathodic activity such as cracks and blisters due to cathodic inhibitive nature of 8HQ and cerium ions. However, as was discussed in paragraph 5.5, 8HQ can provide in some extent an anodic inhibition as well. Such inhibition mechanism is based on the formation of poorly soluble chelates complexes with copper or aluminum in neutral media which can be represented by the following reactions:

$$Cu^{2+} + 2(8-HQ) \Rightarrow Cu(8-Q)_2 + 2H^+, \tag{7.1.1}$$

$$Al^{3+} + 3(8-HQ) \Rightarrow Al(8-Q)_3 + 3H^+. \tag{7.1.2}$$
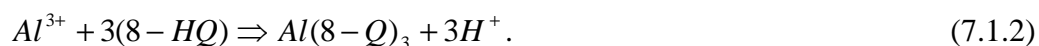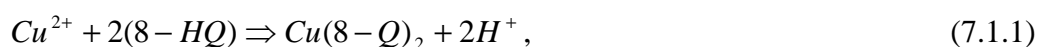
In acidic solution with pH~3 the equilibrium of the reactions (7.1.1) and (7.1.2) is shifted to the left, and the stability of the protonated form of 8-hydroxyquinoline and positively charged complexes is higher than of the insoluble products. Therefore, 8HQ can not inhibit the corrosion in developed deep pits because of the low pH that favors dissolution of chelates with copper and aluminum [381,382]. However, the localized attack at the cathodic intermetallics and aluminum matrix during initial stage of corrosion can be significantly suppressed.

Inhibition nature of cerium nitrate is attributed to the formation of highly insoluble hydroxides with solubility constants less than $1*10^{-19}$, which can be formed in places with cathodic process of oxygen reduction needed for the production of hydroxyl ions:

$$Ce^{3+} + 3OH^- \Rightarrow Ce(OH)_3 \downarrow \qquad\qquad (7.1.3)$$

Such limitation does not allow cerium to inhibit the corrosion process in pits with acidic environment inside. Therefore, when the pitting corrosion has started, the inhibition of the cathodic process in micro defects is the only way to decrease the corrosion activity. The corrosion will be reduced since the inhibition of the cathodic process affects the anodic process as well.

7.1.6 Limitations and perspectives of direct inhibitor introduction in the sol-gel coatings

In spite of the increased corrosion protection conferred by inhibitor containing sol-gel coatings there are certain drawbacks that limit active corrosion protection properties of such systems. The first disadvantage is the chemical interactions that can occur between the inhibitive compound and components of the sol-gel systems. The addition of BTA inhibitor is evident example of such issue. Although BTA is a good cathodic inhibitor for copper corrosion, the addition of BTA to the sol-gel coatings significantly decreases their barrier properties. The decrease of the barrier protection tremendously increases the corrosion degradation of the sol-gel coated samples with additives of BTA.

The second drawback is associated with the limited amount of inhibitor in the sol-gel coating. For low (safe) concentration of inhibitors there is no decrease of the barrier properties of the sol-gel coatings. When exciding this concentration the barrier properties of the coatings are significantly reduced. Therefore the maximal concentration of inhibitor in sol-gel systems is limited by the chemical stability of the sol-gel components with inhibitor. For example the acceptable concentration of cerium nitrate inhibitor in the sol-gel formulation is 0.034 mol/L. In the sol-gel coating the concentration of inhibitor is higher because of the drying of the sol-gel and is around 0.1 mol/L. The concentration per unit of volume is relatively high. However, due to the small thickness of the sol-gel coating the total inhibitor content is very low. Such a low concentration in the coating cannot confer long term protection to the underlying alloy substrate. Nevertheless, the corrosion protection can be effective in micro defects at the initial stages of the corrosion process. When the micro defect appears it can be healed by inhibitor that diffuses from the nearest matrix. However, at longer immersion time the concentration of inhibitor in the surrounding matrix may be insufficient for effective inhibition, which leads to the corrosion progress.

When the concentration of inhibitor in the coating is low another issue appears to be significant. The increased release of inhibitor from the undamaged sol-gel coating can

extensively decrease the positive effect of the inhibiting compound in the coating. During few hours of immersion the concentration of inhibitor can be reduced below the effective limit therefore making the substrate susceptible to corrosion attack. The results of EIS measurements show that cerium nitrate incorporated into the sol-gel films affects the intermediate oxide resistance more efficiently at the beginning of immersion as can be seen in Figure 7.1.7c. This implies fast release of inhibitor from the coating. On another hand the intermediate oxide resistance in case of 8HQ addition in the sol-gel coating is not much higher compared to undoped coating at the beginning of immersion Figure 7.1.7b. Such effects are more likely associated with the release of inhibitors from the sol-gel coatings. For cerium ions the release might be faster than for 8HQ as follows from the values of oxide layer resistance at the beginning of immersion.

It is important to consider such limitations and perform a more complete study of particular inhibiting compounds as additives to the sol-gel coatings in order to create more efficient corrosion protection of alloys. Taking into account such disadvantages a possible way to avoid the interaction of inhibitor with the sol-gel and restrict the release is the incorporation of inhibitor in nanocontainers. The containers have to be small enough to not decrease the sol-gel matrix barrier properties and at the same time to provide a controlled release of inhibitor. Some examples of such approaches will be addressed in the next chapter.

Summarizing

The addition of corrosion inhibitors to the hybrid sol-gel coatings confers additional corrosion protection when an appropriate inhibitor is used. Cerium salts and 8-hydroxyquinoline are demonstrated here as possible additives which can provide some self-healing ability in supplement to the good barrier properties of the sol-gel films. These two dopants, being added at different stages of sol-gel synthesis, do not influence sufficiently the barrier properties of the films. However, the overall corrosion protection can be affected depending on the stage where inhibitor was added.

The addition of 8HQ during hydrolysis of zirconia-precursor leads to a decrease of corrosion protection properties in particular to low values of the intermediate oxide layer resistance. This effect can be caused by the interaction of the zirconium alkoxides or their partially hydrolyzed form with 8HQ and formation of complexes that in turn can negatively influence the hydrolysis and condensation reactions during the sol-gel synthesis and film formation. Addition of cerium-based inhibitor at any hydrolyzing step improves the corrosion protective properties of the coatings.

In contrast to 8HQ and cerium nitrate inhibitors, BTA added to the sol-gel film significantly decreases its barrier properties and results in fast corrosion activity. The

inhibiting action of BTA is outweighed by the fast degradation of the coating thus reducing corrosion protection of the sol-gel system with the inhibitor.

The mechanism of the corrosion protection of AA2024 by the inhibitor doped sol-gel coatings is related to the inhibition of the corrosion process in the micro defects. After corrosion started the leached inhibitor diffuses to the place where corrosion appears and slows down or stops the activity in that place thus providing protection of the alloy. However, there are certain limitations associated with the chemical nature, maximal concentration and release rate of inhibitors from the sol-gel coating.

7.2 Hybrid sol-gel coatings with nanostructured reservoirs of inhibitors

The investigation carried out in previous chapter showed that the sol-gel coatings with directly introduced inhibitors possess certain drawbacks like decrease of hydrolytic stability, slow release or fast leaching of inhibitors. Therefore, a successful incorporation of inhibiting compounds in the sol-gel coatings requires additional strategies. In this chapter several new approaches will be presented that intend to eliminate the drawbacks associated with direct inhibitor addition to the sol-gel systems.

In the first approach an inhibitor was introduced in nano-porous Titania based (TiOx) intermediate layer coated by a hybrid sol-gel film. The use of TiOx nano-porous layer for storage and release of corrosion inhibitors eliminates the negative effect of inhibitors on the stability of the hybrid sol-gel matrix. The corrosion protective properties and self-healing abilities of such "sandwich"-like system were investigated in comparison to single layered Zr-containing hybrid sol-gel coatings.

A new method of corrosion inhibitor delivery on demand is proposed conferring "intelligent" self-healing ability to the hybrid sol-gel protective films. Controllable delivery is achieved by incorporating nanocontainers of benzotriazole inhibitor in the hybrid sol-gel pre-treatments. The nanocontainers were formed using silica nanoparticles layer-by-layer coated with different shells of polyelectrolyte molecules acting as nanocontainers of corrosion inhibitor. The impregnation of the hybrid sol-gel films with nanocontainers increases their long-term corrosion protection performance. Moreover the introduction of the inhibitor in the form of nanocontainers instead of the direct addition to the sol-gel matrix prevents the interaction of benzotriazole with components of the coating, which can negatively influence barrier properties of the hybrid film and lead to the deactivation of the corrosion inhibitor.

Another type of nanocontainers that can be used for inhibitor storage and release is a naturally formed mineral, namely, halloysites. Single elements of this mineral have shape of hollow cylinder that allows incorporation of materials inside for storage and release purpose. Mercaptobenzothiazole was tried as an inhibitor for incorporation in halloysites nanocontainers. To achieve the prolonged and intelligent release of inhibitor from nanocontainers, halloysites were coated by different polyelectrolyte shells and then incorporated in the sol-gel system.

The use of soluble compounds as inhibitors has its disadvantages such as fast delivery to the place of localized corrosion and homogeneous distribution in the coating. However, coatings with soluble inhibitors show significant blistering and delamination when performing corrosion tests. Such negative effect is caused by high solubility of inhibitors. In contrast to that, coatings with partially soluble compounds passed corrosion tests with good results. Therefore the idea of another approach is to use partially soluble environmentally acceptable inhibitive compound as an additive to the sol-gel formulations. In this study a nanoparticulated compound based on amorphous cerium molybdate was

used as an inhibitive additive to the sol-gel. The influence of the addition step in the sol-gel formulations and concentration of inhibitor on the corrosion protective properties and self-healing abilities of the coatings have been studied using corrosion investigation methods and methods of microstructural analysis.

7.2.1 Nanoporous titania based interlayer with inhibitor for enhanced corrosion protective properties of the sol-gel coatings

A novel approach is proposed that aims at developing a nanostructured porous reservoir that stores a corrosion inhibitor at the metal/hybrid sol-gel film interface. The template based reaction of controlled hydrolysis of titanium alkoxides was used to create self-assembled porous nets composed by TiOx nanoparticles. SEM and AFM techniques were used to characterize the structure of the formed nanoreservoirs. EIS and SVET were employed to study the evolution of the corrosion protection performance of different pre-treatments and to reveal their self-healing properties.

7.2.1.1 Preparation and characterisation of nanostructured titania layer on AA2024

Aluminum alloy 2024 samples were etched according to procedure described in paragraph 4.2.3 using alkaline cleaning and acid desmutting steps prior to the deposition of the oxide layer. The procedure of synthesis and formation of TiOx nanoporous layer on the AA2024 is described in details in paragraph 4.3.3. Synthesis includes controllable hydrolysis of TPOT in the presence of a templating agent (Puronic F127). Additional aspects of the TiOx synthesis and preparation are presented below.

Chemical evolution of titanium precursors during the sol-gel process can be described in following way. Common reactions of hydrolysis, alcohol and water condensation with titanium precursor take place in a reaction system inasmuch as condensation process starts before the ending of the hydrolysis:

$$2 \; \underset{C_3H_7O}{\overset{C_3H_7O}{\diagdown}} Ti \underset{OC_3H_7}{\overset{OC_3H_7}{\diagup}} \xrightarrow[-5C_3H_7OH]{+5\,H_2O} \; \underset{HO}{\overset{C_3H_7O}{\diagdown}} Ti \underset{OH}{\overset{OC_3H_7}{\diagup}} \cdots \; Ti \underset{OC_3H_7}{\overset{OH}{\diagup}} \xrightarrow[-H_2O]{-C_3H_7OH} \; \underset{HO}{\overset{C_3H_7O}{\diagdown}} Ti \underset{O}{\diagdown} Ti \underset{OC_3H_7}{\overset{OH}{\diagup}}$$
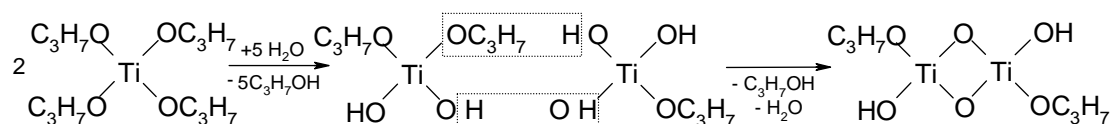
$$(7.2.1)$$

The formation of other products of polycondensation, such as partly hydrolyzed titanium oxo-propoxide as presented in equation (7.2.2), with coordination number of Ti more than its valence is a likely event [363] due to the fact that the titanium alkoxides are Lewis acids and can interact with the compounds which have unshared electron pairs with the formation of Lewis acid-based complexes. However the hydrolysis and condensation

reactions of the titanium alkoxides are usually very fast and must be controlled by the use of inhibitors. Different β-diketones, β-ketoesters, diethylene-glycol, carboxylic acids or other complexing agents, which inhibit the condensation reaction, are commonly used. Changing the concentration of water and the complexing agent leads to modification of the sol-gel systems structure, and consequently, the coatings properties.
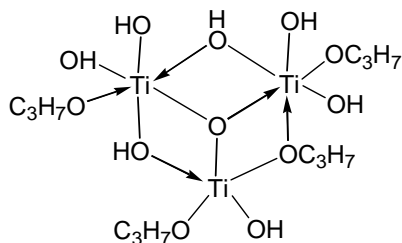
(7.2.2)

The addition of a templating agent to the solution can control the hydrolysis of titanium propoxide and play two important roles. A prime function of block-copolymer molecules is the formation of micelles with titanium alkoxide. Moreover an inhibition of the hydrolysis/condensation reaction can occur providing the controllable synthesis. The templating and inhibition effects can be originated from the formation of the complexes between template agent block-copolymer type and a titanium oxide based complex as was described in [383]. In the case of Pluronic F 127 this structure can be present as following:
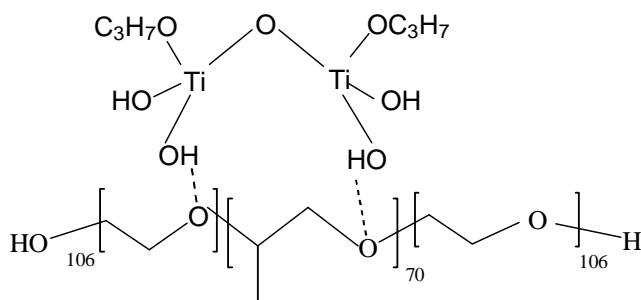
(7.2.3)

Chemical transformations such as hydrolysis and alcohol condensation that occur during mixing of the reagents can be uncovered by means of FTIR spectroscopy. FTIR spectra of initial substances ($Ti(OPri)_4$, Pluronic F 127 and $CHCl_3$ used as a solvent) are shown in Figure 7.2.1. In the high wave number range there can be noticed some peaks at 3010, 2972 2870cm^{-1} which correspond to symmetric and antisymmetric vibration modes of -CH_2- and -CH_3 groups coming from either pluronic or alkoxides [384]. At the middle wave numbers there are bands around 1450 and 1379 cm^{-1} associated with C-H asymmetric deformation and -CH_2- scissors vibration and a characteristic doublet of the gem-dimethyl structure of isopropoxides [385]. Well-defined absorbance peaks are also observed at 1120, 1001, 948, 852, 621cm^{-1} before the hydrolysis of $Ti(OPri)_4$. The very strong band in the 1000 cm^{-1} region is a common feature of transition metal isopropoxides and was assigned to C-O stretch vibration [386]. The band at 852 cm^{-1} was also related to the vibration of the C---C skeleton coming from isopropoxy group [385].
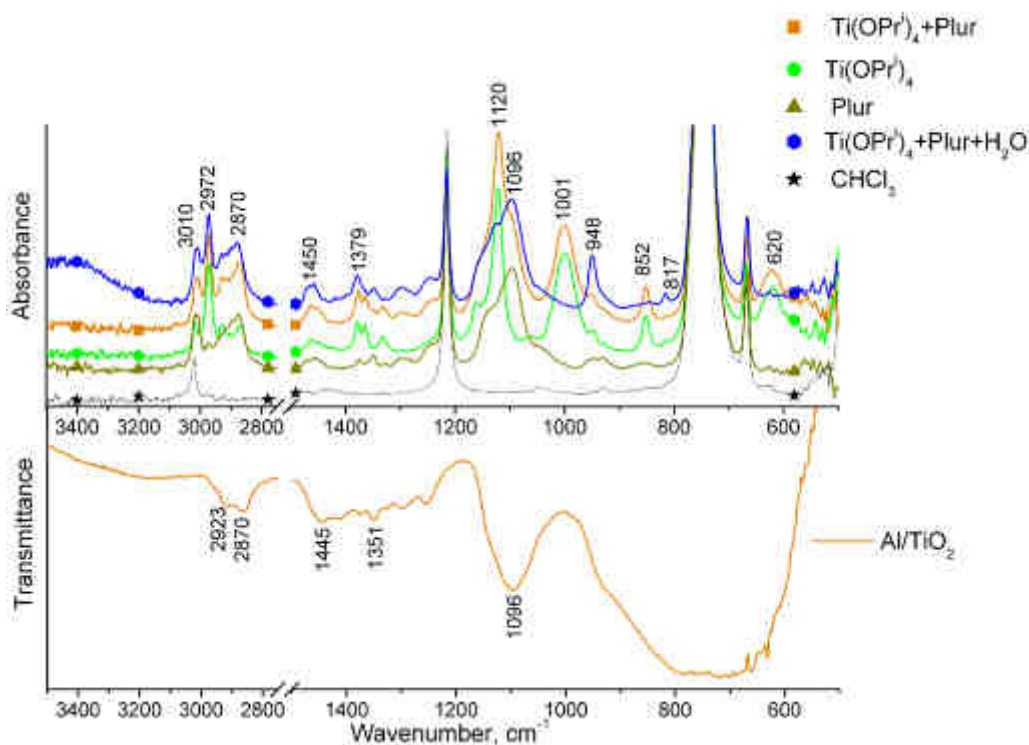
Figure 7.2.1. FTIR spectra of individual components and model reactive mixture of semihydrolyzed Ti(OPri)$_4$ with Pluronic F127 as well as transmittance spectra of the aluminium alloy substrate covered with TiOx layer after heat treatment.

After interaction of Ti(OPri)$_4$ with Pluronic F 127 and water hydrolysis, most of the changes occurred in the 550-1200 cm^{-1} region due to the partial opening of (R-O)-Ti bonds and the formation of new Ti-O-Ti bridges. Thus the absorbance of the most intensive peak in this group at 1120 cm^{-1} was essentially decreased and a wide peak from ν C-O-C vibration of Pluronic located at 1160 - 1060 cm^{-1} became more pronounced again. Weaker peaks located at 1001, 852 and 621 cm^{-1} almost disappeared which suggests that TPOT has reacted already. The peak at 948 cm^{-1} was doubled. Moreover, a rise of the absorbance at 817 and 948 cm^{-1} can be explained by liberation of free iso-propanol in the reaction solution [384]. Peaks at 820 and 948 cm^{-1} are the most intensive in its spectrum. Both processes Ti-O-Ti bonds formation and 2-propanol evolution are likely to contribute in the appearance of these peaks, since they run in the direction of Ti(OPri)$_4$ polycondensation.

Analysis of the position alteration of the diagnostic peaks in 1200 – 550 cm^{-1} region allows to conclude that the solution of the titanium sol, deposited on aluminium substrates, contains the products of the titanium tetraisopropoxide hydrolysis and polycondensation and likely some amount of unhydrolyzed Ti(OPri)$_4$. The formation of complexes of Pluronic with semi-hydrolyzed Ti(OPri)$_4$ is accompanied by appearance of hydrogen bonds between OH groups of hydrolyzed Ti(OPri)$_4$ and oxygen of Pluronic.

Based on the presented spectra, which reflect the reactive mixture where O-H stretching can correspond to TiOH, PrOH groups as well as H_2O, discussion about formation of hydrogen bonds seems not appropriate. Nevertheless, strong interaction under similar conditions between the titania sub-units and the polymer has been reported in literature [387-389].

Although characteristic peaks of pure TiO_2 (wide intensive peaks for anatase at 650 and rutile at 660 cm^{-1}) were not exhibited in the spectra of model solutions, its presence became evident on the aluminum substrate after depositing TiOx film on aluminum substrate (Figure 7.2.1). A wide peak at 600 - 900 cm^{-1} can be explained by overlapping of the stretching mode of vibration frequencies of Al-O at 750-850 cm^{-1} with those of Ti-O at 750-650 cm^{-1} [390]. Template signals of ν CH at 2923 and 2870 cm^{-1} and of δ CH at 1470 – 1230 cm^{-1} and a wide intensive ν C-O-C peak at 1096 cm^{-1} are also presented on the surface of aluminum substrate after heat treatment.

In order to reveal the micro- and nano-structure of the TiOx layer titanium isopropoxide was hydrolysed in the presence of templating agent and deposited onto polished AA2024 substrate prepared according to procedure (paragraph 4.2.1). AFM maps (Figure 7.2.2) present the topography of the polished alloy surface and the alloy surface after TiO$_x$ layer deposition. The titania-based nanoparticles completely cover the alloy surface with the uniform layer. The average diameter of the formed nanoparticles is about 30 nm demonstrating a narrow size distribution. A well-defined nanoparticulated structure shown in Figure 7.2.2 is most probably conferred by the effect of block-copolymer molecules of the Pluronic F 127 templating agent.
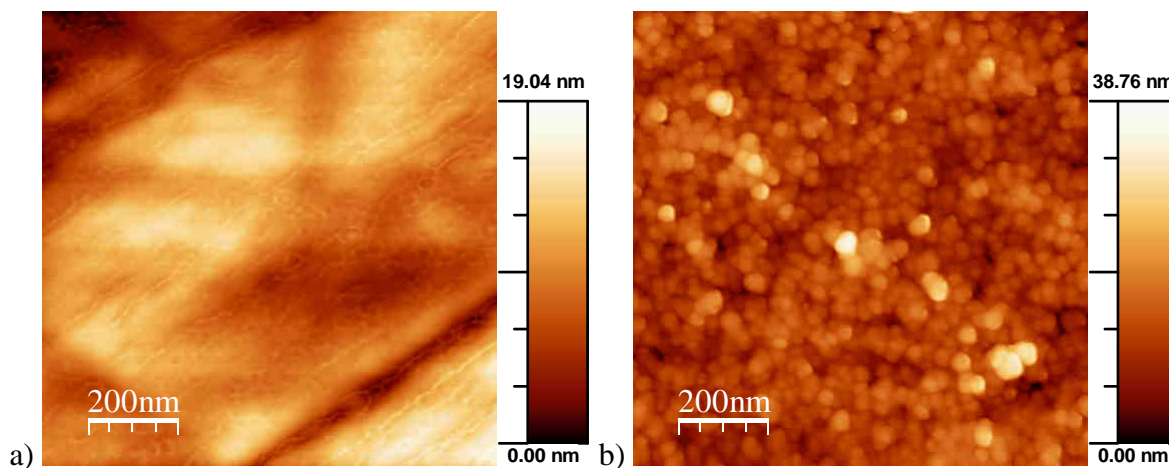
Figure 7.2.2. AFM images of the surface morphology for polished aluminium AA2024 a) and for polished aluminium AA2024 treated with TiO$_x$ layer b).

Significantly different structures are formed on the surface when the etched alloy is used as a substrate. The alkaline etching followed with nitric acid desmuting leads to partial dissolution of alloy forming a porous structure on the substrate as shown in Figure 7.2.3a. The TiO_x-based layer in the case of etched alloy forms net-like structure with wires on the edges of pores in the alloy matrix. The TiO_x net completely replicate the native porous aluminium alloy structure as demonstrated on SEM image depicted in Figure 7.2.3b. The EDS analysis confirms the presence of titanium-containing film on the top of aluminum alloy (Figure 7.2.3c). It seems that templating agent can play an important role in the formation of the net-like oxide replica of the etched aluminum alloy surface. The formation of a net-like oxide-based structure with high developed surface area on the metallic substrates open a great opportunity for loading of this layer with active substances.
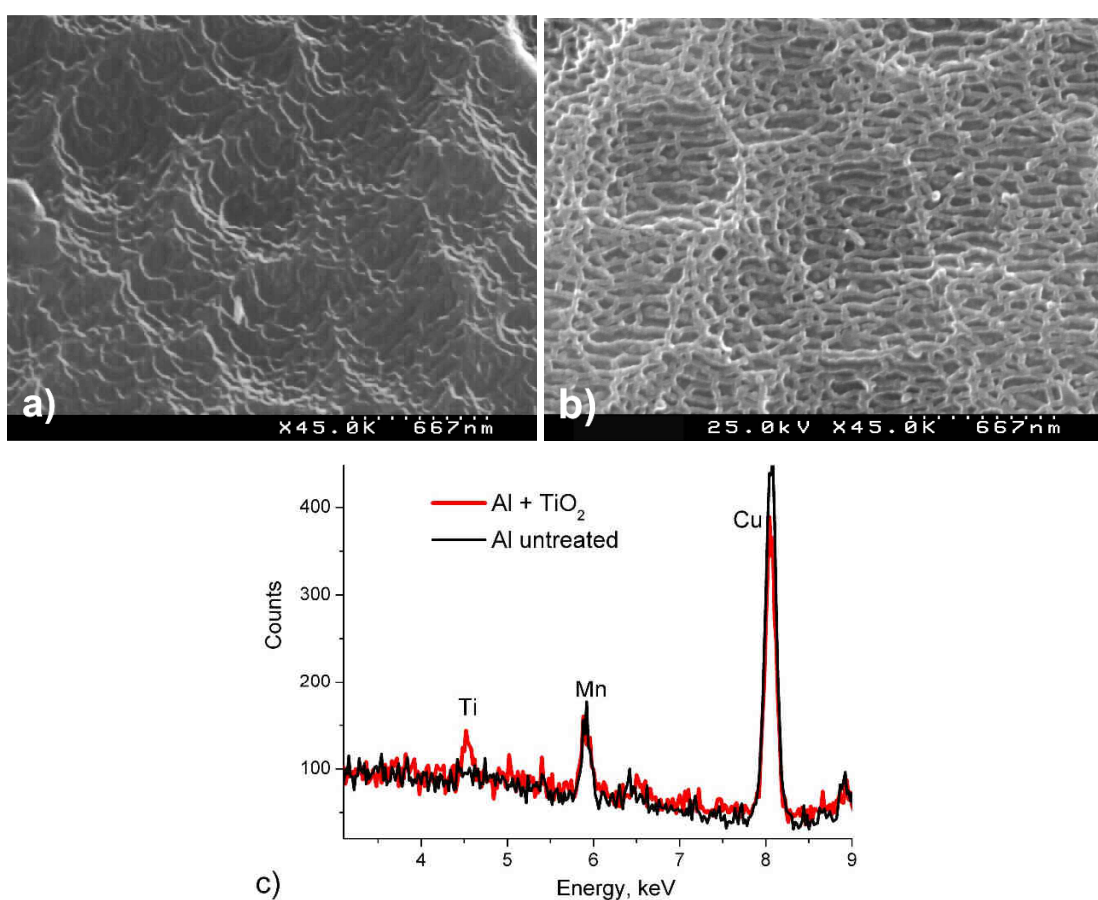
Figure 7.2.3. SEM micrographs for AA2024 etched bare substrate a), etched alloy coated with TiOx film b) and fragment of the EDS spectra of the materials presented in a) and b) pictures c).

7.2.1.2 Corrosion protection

For corrosion characterisation different samples were prepared. The first one includes TiOx networks as an intermediate layer with incorporated BTA inhibitor and standard hybrid sol-gel coating was used as a top layer (Table 7.2.1). The samples with single sol-gel coating and sol-gel coating doped with BTA inhibitor were made for comparison purpose (Table 7.2.1). Sol-gel coatings were prepared according to SgZr1 formulation described in paragraph 4.3.1.

Table 7.2.1. Composition of different coatings tested on AA2024

Reference name	TiOx layer	BTA in TiOx	SGZr1 sol-gel coating	BTA in sol-gel
TiOxBTSGZr1	+	+	+	-
SgZr1	-	-	+	-
SgZr1BT1	-	-	+	+

The electrochemical impedance spectroscopy was used to evaluate the corrosion protection performance conferred by the different pre-treatments on AA2024. Figure 7.2.4 depicts the Bode plots for the different sol-gel coatings after 14 days of immersion in chloride-containing electrolyte. The alloy sample treated with TiO_x porous layer doped with BTA shows high corrosion protection with impedance value about $4*10^6$ Ohm*cm^2 at 0.01 Hz. The low frequency impedance in the case of SgZr1 sol-gel film deposited directly on the alloy surface is about one order of magnitude lower in comparison with the previous sample. The weakest corrosion protection is revealed when the aluminium alloy was pre-treated with the hybrid film containing BTA inhibitor (SgZr1BT1) showing the impedance values only 10^5 Ohm*cm^2 at low frequencies in spite of lower electrolyte concentration (0.005M NaCl) used for immersion in this case.

Tree time constants are disclosed in the Bode plots at high frequencies and at low frequencies for the most stable sample TiOxBTSgZr1. These relaxation processes can be assigned to the sol-gel film capacitance (around 10^5 Hz), oxide layer capacitance (around 10 Hz) and starting corrosion process (around 0.1 Hz). A resistive plateau appears at about 100 Hz related with pore resistance of the sol-gel film. The sample treated with undoped sol-gel film without TiOx layer shows similar behavior. The resistance of the sol-gel film for both samples is close after 14 days of immersion demonstrating that the barrier properties of sol-gel coatings in cases of undoped sol-gel sample and TiOx treated are the same. Moreover a first sign of another time constant related with mass transfer limitations appears at 0.01 Hz for SgZr1BT1 sample. The presence of well-defined low-frequency relaxation process ascribed to the diffusion limitations on the spectra of sample directly doped with BTA confirms its poorer corrosion protection compared to other samples.
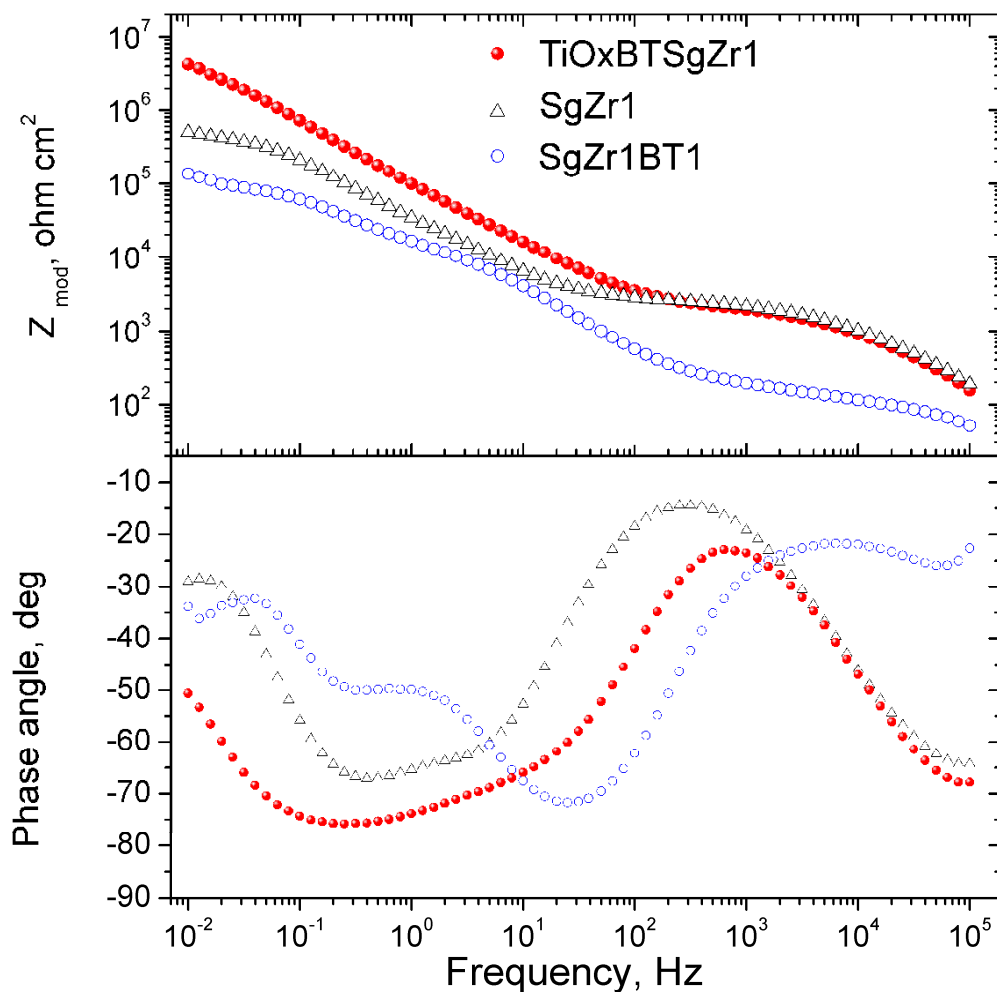
Figure 7.2.4. Bode plots of AA2024 substrates covered with different sol-gel pretreatments after 14 days of immersion in 0.05 M NaCl solution. Sample coated with benzotriazole doped sol-gel was immersed in 0.005M NaCl solution.

A fitting of the experimental spectra was made taking different equivalent circuits presented in Figure 3.3.14 in order to separate different elements attributed to the physico-chemical processes occurring at the metal/coating interface and in the coating. Figure 7.2.5 shows evolution of the resistance of the sol-gel films for different samples in NaCl solution. The fast decrease of the film resistance at the beginning of immersion is related with penetration of the electrolyte into micro- or nano-pores of sol-gel film. The further slower decrease of the hybrid film resistance is caused by the hydrolytical degradation of the coating. The hydrolytical cleavage of Si-O-Si bonds can be accelerated due to change of solution pH leading to faster degradation as was suggested in paragraph 6.4.1. Local change of pH always takes place when the corrosion processes are started on the metal causing the corrosion induced degradation of the coating. Almost equal stability of the film resistance was revealed in the case of pure sol-gel film and sol-gel deposited on TiOx

reservoir layer doped with benzotriazole. The hybrid coating impregnated with benzotriazole during sol-gel synthesis shows sufficiently higher porosity and faster degradation of the matrix (Figure 7.2.5).

The low-frequency impedance originated from resistance of the mixed oxide layer is directly related with corrosion protection conferred by the coating system since formation of defects in this layer opens the immediate access of corrosive medium to the alloy surface leading to fast development of the corrosion activity. Figure 7.2.6 shows evolution of the intermediate oxide layer resistance for the different samples. The lowest resistance of the oxide layer around $4*10^4$ Ohm*cm^2 after corrosion tests was revealed in the case of sol-gel film directly impregnated with benzotriazole (SgZr1BT1). The low resistance confirms high density of defects induced by corrosion on the alloy surface during immersion in NaCl solution. The AA2024 coated with undoped hybrid film (SgZr1) has sufficiently higher and more stable resistance of the mixed oxide film around $1*10^6$ Ohm*cm^2 at the end of immersion. The resistance of oxide layer in the case of pre-treatment with TiO$_x$ self-assembled layer (TiOxBTSgZr1) can not be measured precisely at the beginning of the immersion due to purely capacitative behavior originated from intact character of the oxide layer. Only after about 100 hours of immersion a change of the phase angle occurs, allowing calculation of the oxide resistance. The value of the intermediate layer resistance during 300 hours of immersion in this case is sufficiently higher around $1*10^7$ Ohm*cm^2 than in both previous cases (Figure 7.2.6). However after 330 hours immersion the first breakdown of the oxide film occurs. Nevertheless the resistance increases almost immediately again achieving the values before breakdown. Breakdown of the oxide layer happens several times with consequent recovering of the impedance.

The Complex plane plots presented in Figure 7.2.7a clearly demonstrate the periodic decrease and increase of the complex impedance originated from the breakdown of the intermediate layer followed by recovering of impedance for sample TiOxBTSgZr1. The increase of the impedance can be explained in terms of self-healing originated from the inhibiting effect of BTA released from the Titania network as schematically shown in Figure 7.2.8. When a defect is formed in the coating the resistance of the oxide layer drops as was shown in Figures 7.2.6. However, the inhibitor incorporated in the intermediate TiOx network heals the started corrosion process and leads to partial recovering of the oxide resistance. The results obtained for undoped sol-gel film are opposite showing a continuous decrease of the impedance during the all immersion time (Figure 7.2.7b).
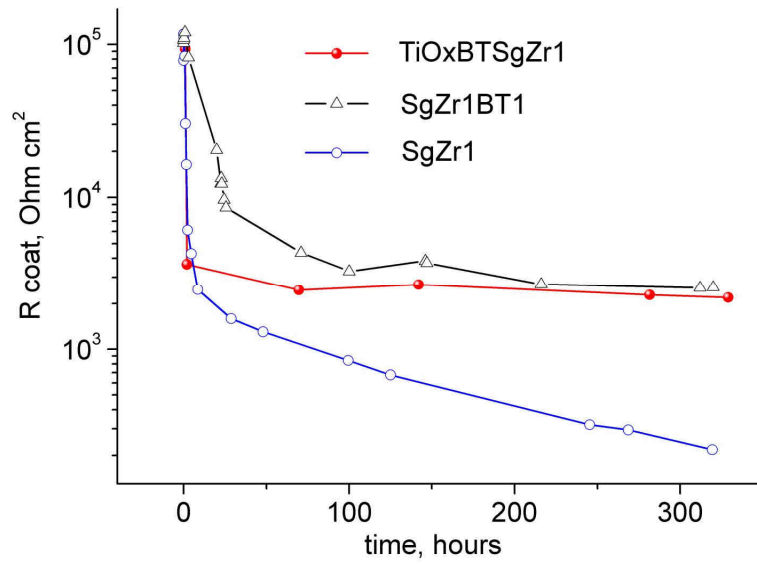
Figure 7.2.5. Evolution of the sol-gel coating resistance during the immersion.
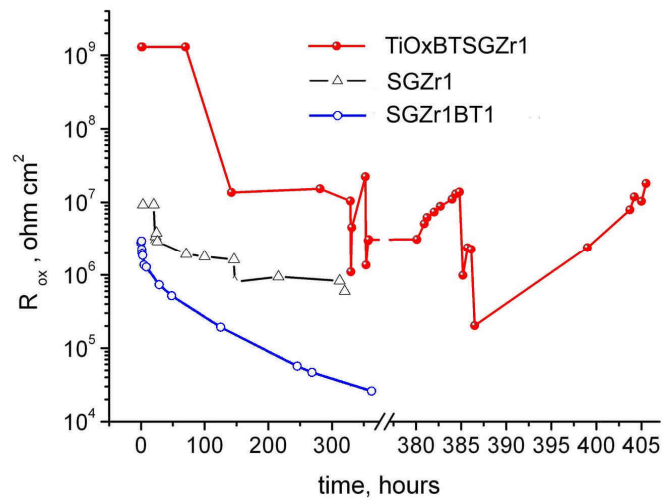
Figure 7.2.6. Evolution of the oxide layer resistance during the immersion.
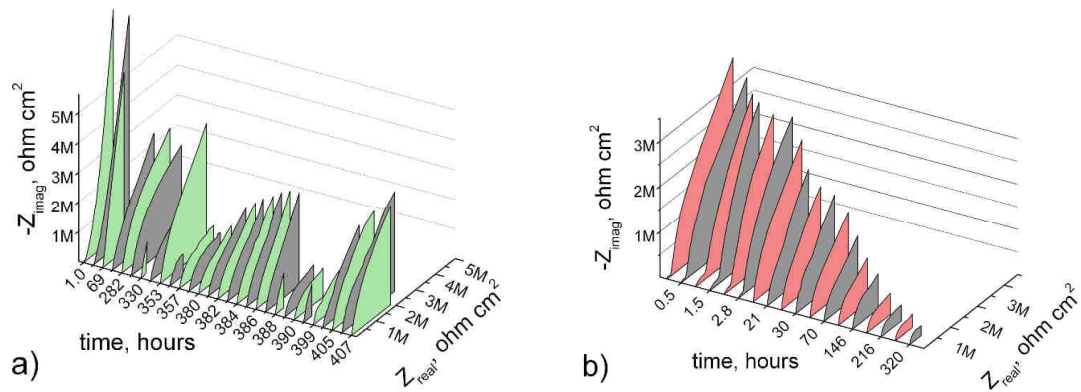
Figure 7.2.7. Evolution of the Complex plane plots during immersion in 0.05 M NaCl obtained for the aluminium AA2024-T3 treated with formulation TiOxBTSgZr1 a) and undoped sol-gel coating SgZr1 b).
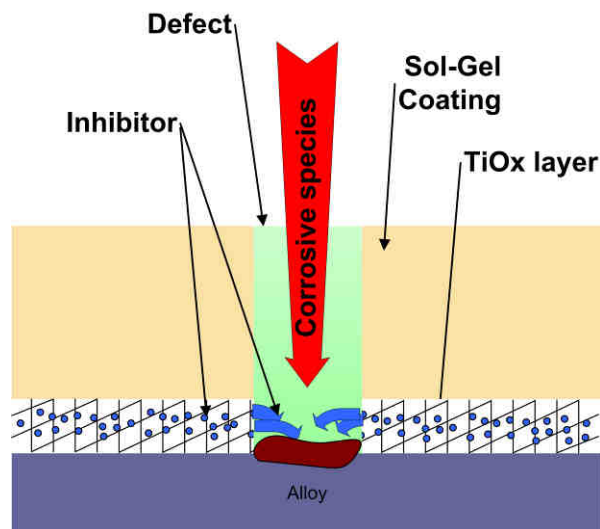
Figure 7.2.8. Schematic view of the self-healing process when defect is formed on sol-gel coated alloy with TiOx network loaded with inhibitor.

SVET technique was then employed to confirm the self-healing effect of the pre-treatment with TiOx nanoreservoir layer. The distribution of local currents along the alloy surface was measured. The AA2024 coated with undoped sol-gel film was used as a reference sample. No local current activity was revealed during the 24 hours of immersion in the 0.05M NaCl solution on both samples (Figure 7.2.9 a,e) revealing the absence of

corrosion activity. Then defects were made in the hybrid films as shown in Figure 7.2.9 b,f. Almost immediately, well-defined cathodic activity due to active corrosion processes appears at the defect formed on the surface of the AA2024 treated with undoped sol-gel. At the same time no corrosion activity appeared on alloy pre-treated with TiOx net layer (Figure 7.2.9 c, g), although a larger defect was formed in this case when compared with previous sample. Even after 3 hours of immersion the defect is almost inactive while the cathodic current density increased in the case of reference sample (Figure 7.2.9 d,h).
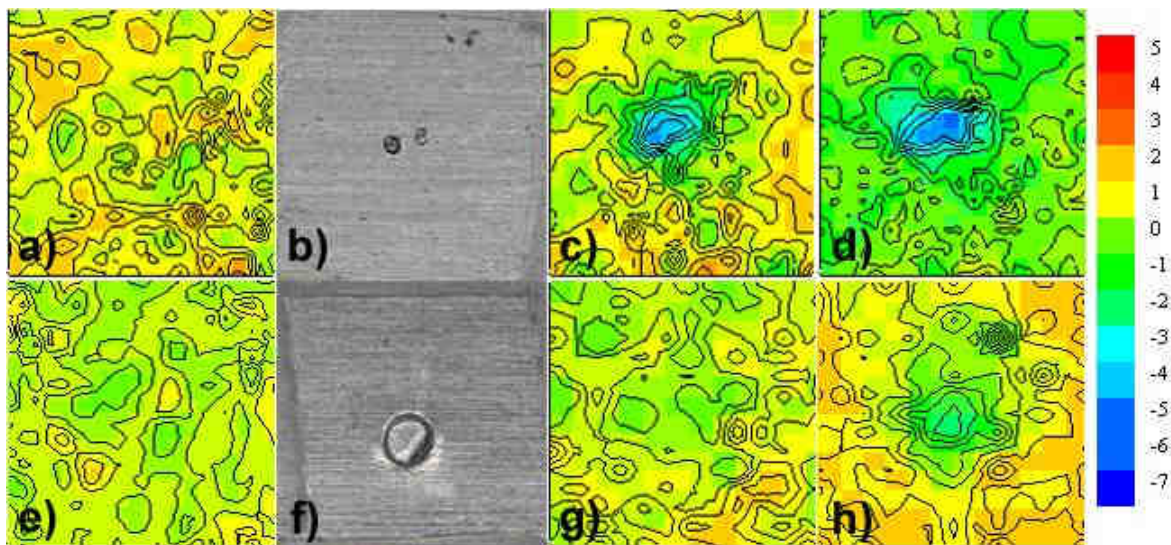
Figure 7.2.9. SVET maps of the ionic currents measured 200 µm above the surface of the AA2024 coated with SgZr1 hybrid film (a, c, d) and with TiOxBTSgZr1 coating (e, g ,h) exposed to 0.05M NaCl; for 1 day (a,e). The defects were made after 1 day (b, f). SVET scans were taken in 5min after defect formation (c,g) and 3h after defect formation (d,h). Scale units: µA cm^{-2}. Scanned area: 2 mm × 2 mm.

Summarizing

A new approach for creation of anticorrosion pre-treatments with self-healing ability is proposed. A TiOx nanostructured reservoir layer for storage and release of corrosion inhibitor is suggested to impart self-repair properties to the hybrid sol-gel pre-treatments deposited on 2024 aluminium alloy.

The nanostructured porous reservoir layer was obtained by the controllable hydrolysis of titanium alkoxide in the presence of a templating agent leading to formation of TiOx self-assembled nets replicating the structure of the etched alloy. The formation of the self-assembled nanostructured oxide net opens the possibility of loading such layer with corrosion inhibitors.

The novel pre-treatment based on TiOx layer doped with BTA and sol-gel coating on the top shows enhanced long-term corrosion protection and well-defined self-healing effects confirmed by EIS and SVET measurements. The incorporation of BTA in the nanoreservoir layer eliminates the negative effect of the inhibitor on the stability of the hybrid sol-gel matrix.

7.2.2 Anticorrosion sol-gel coatings loaded with LbL nanocontainers with inhibitor

In this paragraph the possibility to employ SiO_2 nanoparticles coated with polyelectrolyte shells (poly(ethylene imine)/poly(styrene sulfonate) (PEI/PSS) layers) is demonstrated as promising nanocontainers embedded in hybrid epoxy-functionalized hybrid sol-gel coatings. The inhibitor (BTA) was entrapped within polyelectrolyte multilayers on the assembly step as shown in Figure 7.2.10. The nanocomposite coatings were investigated using methods of surface and corrosion analysis.
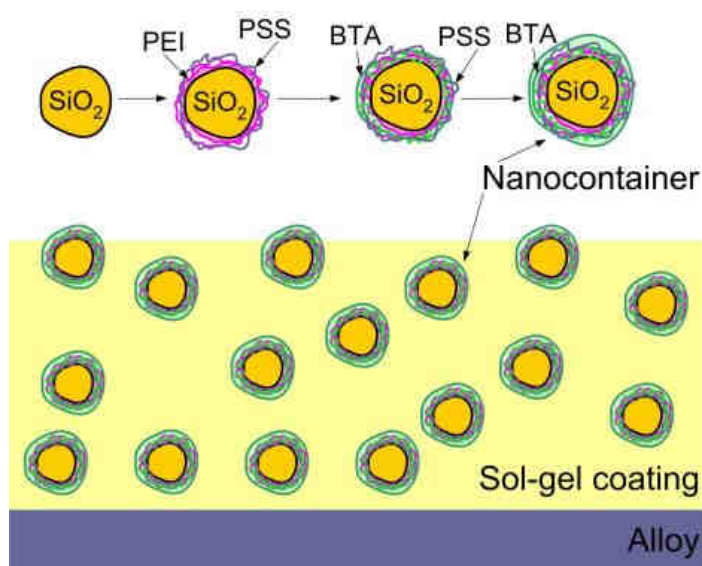
Figure 7.2.10. Schematic view of the nanocomposite sol-gel coating with inhibitor.

7.2.2.1   Preparation and characterization of nanocontainers

A more detailed procedure of nanoparticles preparation is described in paragraph 4.3.4. However certain aspects of the process of layer assembling merit an additional discussion. When performing electrophoretic measurements after deposition of a single polyelectrolyte layer the charge of nanoparticles was changed. Figure 7.2.11a represents a drastic increase of the surface charge after deposition of the first PEI layer (65 mV) followed by a similar (68 mV) decrease after PSS adsorption in the next stage. Benzotriazole deposition leads to a less pronounced increase of the ζ-potential without complete recharging of the surface. This is caused by the different molecular weight, charge and size of the layer components. Large multicharged chains of PEI or PSS have stronger electrostatic forces and can be adsorbed in quantities sufficient to completely recharge the surface while small molecules of monocharged benzotriazole only

270

compensate the excess of negative charge resulting in a PSS/benzotriazole complexes insoluble in slightly acidic and neutral water solutions.
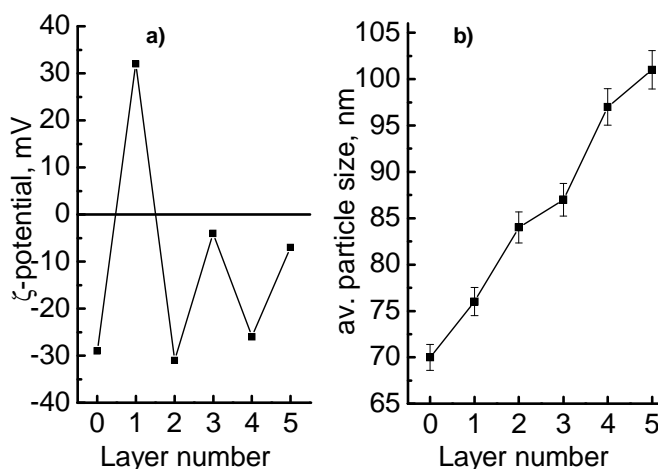
Figure 7.2.11. Electrophoretic mobility measurements of nanocontainers a) and diameter of the nanocontainers vs. LbL assembly step b); (0 layer - initial SiO_2 particles), 1 layer - SiO_2/PEI, 2 layer - SiO_2/PEI/PSS, 3 layer - SiO_2/PEI/PSS/BTA, 4 layer - SiO_2/PEI/PSS/BTA/PSS, 5 layer - SiO_2/PEI/PSS/BTA/PSS/BTA.).

The average diameter of the nanoreservoirs obtained from light scattering measurements increases with the layer number (Figure 7.2.11b), which clearly indicates the LbL assembly of polyelectrolytes and inhibitor molecules. For the first PEI and PSS monolayers the size increment is about 8 nm per layer. The benzotriazole layers increase the size of nanoreservoirs by a smaller about 4 nm step confirming the electrophoretic mobility data on a lower amount of deposited benzotriazole as compared to the polyelectrolytes. The optimal number of the PSS/benzotriazole bilayers deposited onto silica nanoparticles is two. One bilayer is not sufficient for the self-healing effect of the final protective coating while three or more bilayers drastically increase the aggregation of nanocontainers during assembly and coating deposition, which affects the integrity of the protective coating and nanocontainers distribution in the coating matrix adversely.

7.2.2.2   Preparation and characterization of sol-gel coatings loaded with nanocontainers

AA2024 panels cleaned according to the procedure (paragraph 4.2.3) were used as substrate for sol-gel coating deposition. A standard Zr based sol-gel system (SgZr1) was used as a hybrid matrix. Different sol-gel coatings were prepared including BTA inhibitor

directly incorporated in the sol-gel matrix (SgZrBT1) and nanoreservoirs of BTA incorporated in the sol-gel matrix (SgZr1NCBT1) as presented in Table 7.2.2.

Typical SEM micrographs in plane and cross-section view of the sol-gel coating doped with BTA nanocontainers are presented in Figure 7.2.12. The coating is homogeneous and free of defects. The thickness of the sol-gel layer is around 1.5 µm that is comparable with the undoped coatings (Figure 6.1.10).

Table 7.2.2. Composition and name of different coatings applied on AA2024

Name	Zr based sol-gel coating	BTA in sol-gel	BTA nanocontainers
SGZr1	+	-	-
SGZr1BT1	+	+	-
SGZr1NCBT1	+	-	+
SGZr1NCBT1x2	+	-	+ 2x concentration

A AFM scan taken before immersion of the coated alloy in NaCl solution reveals the topography of the hybrid film doped with nanocontainers (Figure 7.2.13a). Only a few round shaped features with a diameter about 100 nm can be seen on the surface. This evidences the occlusion of the majority of the nanocontainers inside the film volume confirming good affinity of SiO_2-based nanocontainers to sol-gel film. The same sample was also examined by AFM after 2 weeks of immersion in NaCl solution. Figure 7.2.13b,c demonstrates the topography of the composite film after treatment in aggressive media. A high population of nanoparticles is present on the surface. The image (Figure 7.2.13c) acquired at higher magnification shows that these particles are 70-100 nm in diameter, which is close to the diameter of the nanocontainers before loading in the coating. The increased number of nanocontainers visible in the AFM image upon NaCl treatment can be caused by the modification of the top layer of the sol-gel film revealing the embedded nanocontainers. These nanocontainers are uniformly distributed in the sol-gel film showing low degree of aggregation.
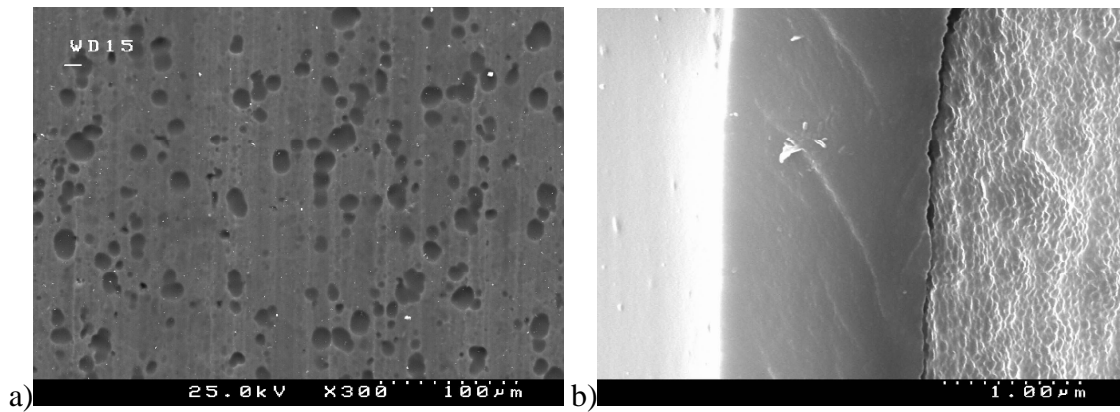
Figure 7.2.12. Plane a) and cross-sectional b) electron micrographs of the sol-gel film loaded with BTA nanocontainers and deposited on AA2024 substrate.
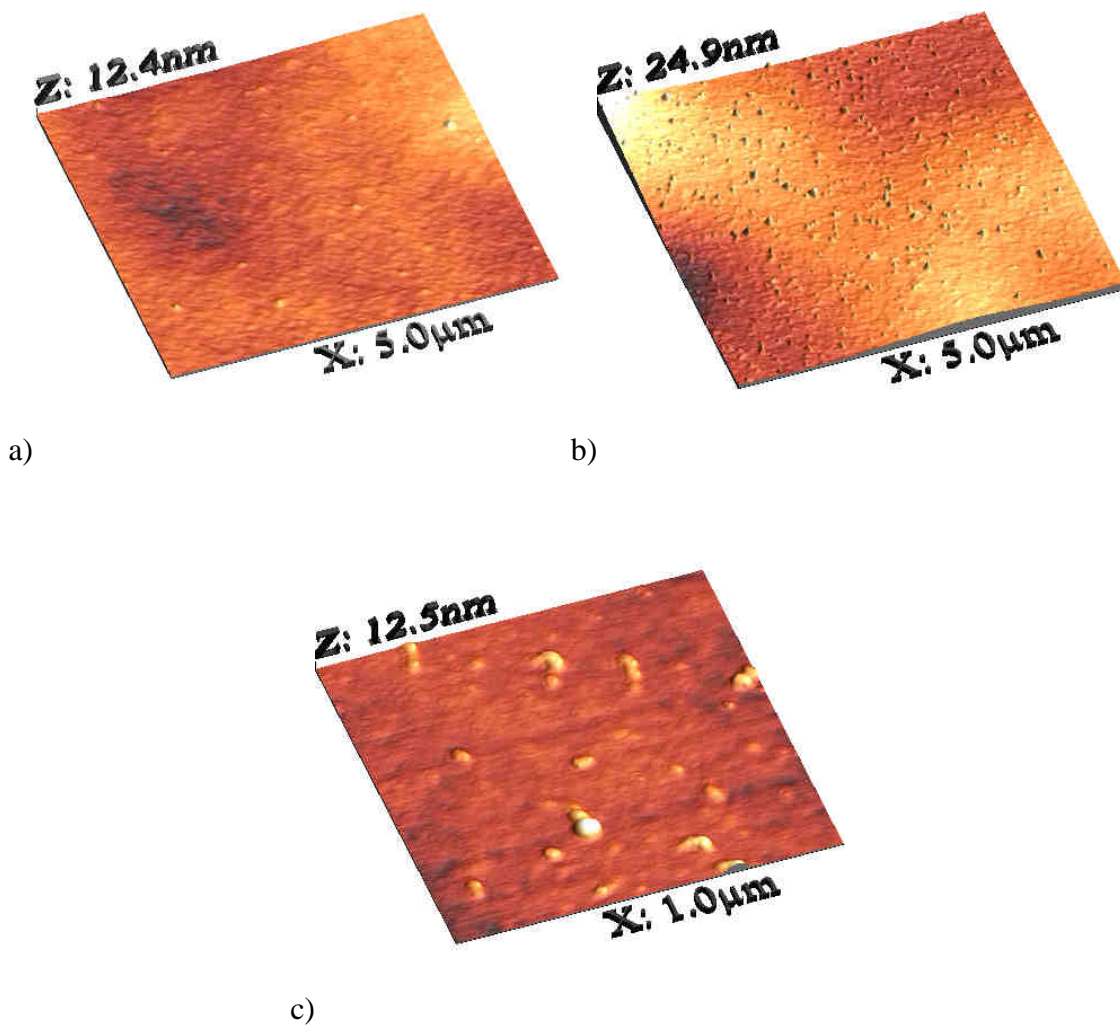
Figure 7.2.13. Topography of the hybrid film SgZr1NCBT1x2 obtained by AFM before a) and after 14 days b,c) of immersion in NaCl solution.

7.2.2.3 Corrosion protection conferred by nanocontainers loaded sol-gel coatings

Electrochemical impedance spectroscopy was employed to quantify the corrosion protection obtained by the different composite coatings under study. The dependence of the complex impedance of the coated aluminium on the applied frequency permits the separation of the response of the different components of the system such as capacitance and resistance of the protective layers, polarization resistance and double layer capacitance. The evolution of such parameters can distinguish passive and active corrosion protection of the coatings. Figure 7.2.14 depicts the impedance spectra of the different sol-gel coated samples after 190 hours of immersion in 0.005M NaCl. The undoped hybrid film (SgZr1) and the coatings doped with different concentrations of nanocontainers (SgZr1NCBT1) show very similar behaviour at frequencies higher than 0.1 Hz revealing the same barrier properties. The capacitance of the oxide layer is also comparable for those samples. A significant difference appears only at low frequencies, which is related to the open defects in the intermediate oxide layer and, consequently, corrosion activity. The sample with highest concentration of nanoreservoirs in the matrix shows almost pure capacitative behaviour at low frequencies demonstrating excellent protective properties even after long immersion time. This confirms the absence of large defects. The sample with lower concentration of nanocontainers also demonstrates a good corrosion protection performance. However, the resistive part appears at low frequencies demonstrating the formation of active defects in the oxide film (Figure 7.2.14). The AA2024 coated with undoped film shows lower corrosion resistance than in both previous cases. The results clearly illustrate the positive effect of the nanocontainers loaded with benzotriazole on the corrosion protection performance of the sol-gel films. The positive effect increases with the increase of the loading degree of the nanocontainers.

Direct doping of BTA in the sol-gel matrix doesn't reveal any good corrosion protective properties as was shown before. The sample (SgZr1BT1) has one order of magnitude lower resistance demonstrating defective character of the film compared to other coating systems (Figure 7.2.14).

A low concentration of NaCl was used in this study in order to decrease the rate of the corrosion processes in the case of the samples with weak corrosion protection performance. The decrease of the salt concentration decreases the rate of the corrosion processes and allows the estimation of its kinetics.
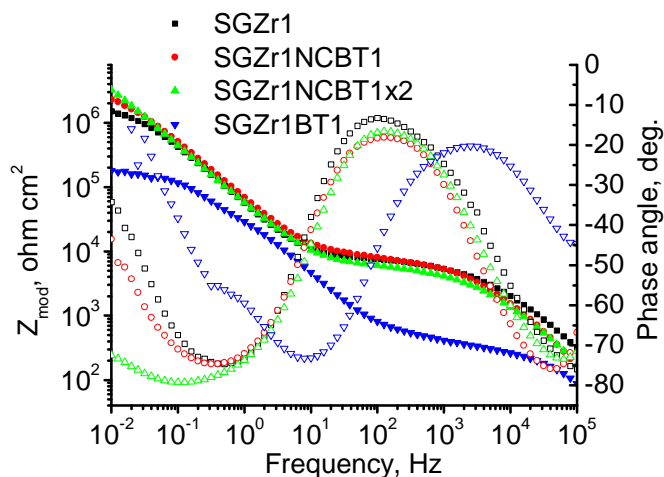
Figure 7.2.14. Impedance spectra of different sol-gel films after 190 hours of immersion in 0.005 M NaCl.

The time-dependent evolution of the resistance of the composite sol-gel films is depicted in Figure 7.2.15a. At the beginning the sol-gel films have similar resistance about $1*10^5$ Ohm*cm^2. However, a fast decrease occurs during the first hours of immersion. This drop is caused by the filling of the pores of the film with electrolyte. The undoped sol-gel film and the coatings doped with different amounts of nanocontainers demonstrate very close values of pore resistance confirming that the introduction of the nanoreservoirs does not influence the porosity and density of the composite matrix. On the contrary the direct doping of sol-gel coating by BTA leads to the well-known deterioration of barrier properties (Figure 7.2.15a).

The role of the nanocontainers is not only to diminish the negative effect of the inhibitor on the polymer film but also to provide delivery of inhibitor on demand and to ensure the active corrosion protection when defects are formed in the coating. The resistance of the oxide layer can be a parameter, which permits monitoring the corrosion protection, because it is proportional to the metal surface area in contact with the electrolyte. Figure 7.2.15b demonstrates the evolution of the oxide layer resistance for all samples during immersion in the chloride-based electrolyte. The highest values of the oxide resistance were found for samples doped with nanocontainers. This superior corrosion protection performance evidently originates from the inhibiting effect of the BTA released from the nanocontainers. However, the resistance of sample loaded with lower content of nanocontainers (SgZr1NCBT1) decreases by one order of magnitude after about 150 hours due to the release and consumption of the inhibitor while the coating with higher loading (SgZr1NCBT1x2) has very stable long-term behavior (Figure 7.2.15b). This difference remains even after 300 hours of immersion demonstrating effective long-term corrosion protection of nanocontainers impregnated sample.

275

The self-healing ability is the most important attribute of the effective pre-treatment. Therefore, the self-healing efficiency of the sol-gel films impregnated with inhibitor-loaded nanocontainers was investigated by SVET. Figure 7.2.16 presents the local current maps over the AA2024 alloy surface covered with both the undoped sol-gel film and the sol-gel film loaded with the maximal amount of nanocontainers. A typical current map along the intact sol-gel film is depicted in Figure 7.2.16a illustrating the absence of local corrosion processes for both coatings. Artificial defects (around 200 µm in diameter) were formed on the surface of both coatings after 24 hours of immersion in 0.05 M NaCl as shown in Figure 7.2.16b,f. Well defined cathodic activity appears in the place of the induced defect on the alloy coated with the undoped hybrid film (Figure 7.2.16c). This activity becomes even more intense with the immersion time (Figure 7.2.16d,e). Sufficiently different behavior was revealed after defect formation on the substrate coated with sol-gel film doped with nanocontainers. No corrosion activity appears in this case after 4 hours following the defect formation (Figure 7.2.16g). Only after about 24 hours the well defined cathodic activity appears in the zone of the induced defect (Figure 7.2.16h). The rest of the surface generates an anodic flow. However, the defect becomes passivated again two hours later and remains healed even after 48 hours (Figure 7.2.16i).
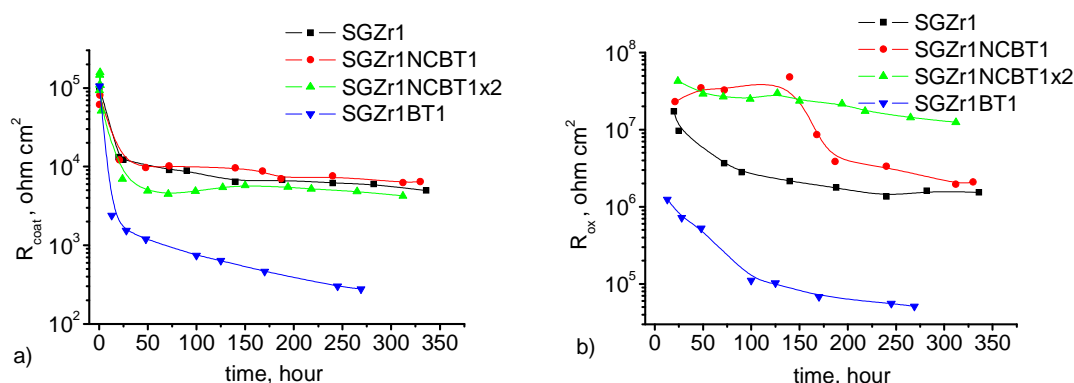
Figure 7.2.15. Evolution of the sol-gel film resistance a) and resistance of the intermediate oxide layer b) during immersion in 0.005M NaCl electrolyte for AA2024 coated with different hybrid films.
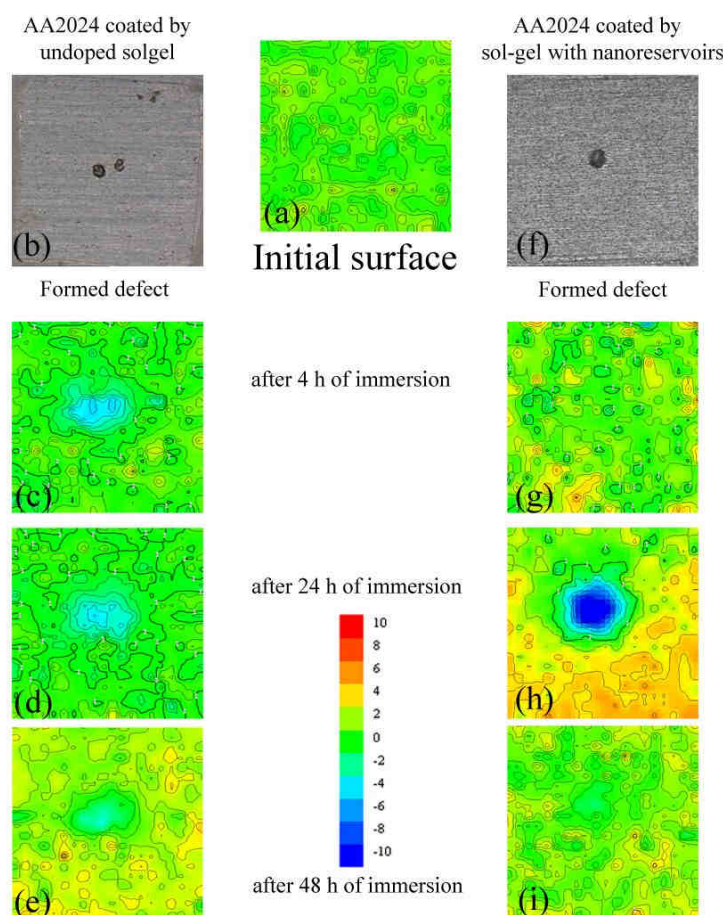
Figure 7.2.16. SVET maps of the ionic currents measured above the surface of the AA2024 coated with undoped sol-gel film (SgZr1) (a,c,d,e) and with film doped by nanocontainers (SgZr1NCBT1x2) (g,h,i). The maps were obtained before defect formation a) after defect formation for 4h (c,g), 24h (d,h) and 48h (e,i). Scale units: $\mu A\ cm^{-2}$. Scanned area: 2 mm × 2 mm.

7.2.2.4 Mechanism of corrosion protection

The started local corrosion activity in the defective area of nanocomposite containing sol-gel coating (Figure 7.2.16) hinders after longer immersion time. Such "self-healing" effect can be originated from the active feedback between the coating and the localized corrosion processes. The most probable mechanism is based on the local change of pH in the damaged area due to the corrosion processes. The permeability of the polyelectrolyte shells strongly depends on pH [391-394]. In acidic or alkali conditions the polyelectrolyte shell increases its permittivity due to the charge redistribution in polyelectrolyte layers which can lead to electrostatic repulsion between the layers and swelling. Swelling of the polyelectrolyte shell increases its permeability to ions and molecules from its interior to the bulk solution. Swelling is a reversible process and when

pH restores to neutral polyelectrolyte shell closes. This property of polyelectrolyte layers can be used to control the release of the encapsulated chemical. When the corrosion process starts, the local pH value is changed due to the cathodic or anodic activity, which opens the polyelectrolyte shell of the nanocontainers in a local area followed by release of BTA (Figure 7.2.17). Then, the released inhibitor suppresses the corrosion activity. As a result, the pH value recovers closing the polyelectrolyte shell of the nanocontainers and terminating further release of the inhibitor. The pH is not only one factor that controls the permeability of the polyelectrolyte layers. The increase of ionic strength of the solution can increase the permeability of polyelectrolyte layers like PSS/PAH [395]. When sol-gel coating is penetrated by corrosive electrolyte in the places of defects the increased ionic strength can affect the polyelectrolyte nanocontainers and increase the permeability. The released BTA inhibitor will migrate to the defect decreasing the corrosion activity of the alloy. Thus the introduction of nanocontainers to the sol-gel film leads to active corrosion protection originating from "smart" self-healing ability as schematically demonstrated in Figure 7.2.17.
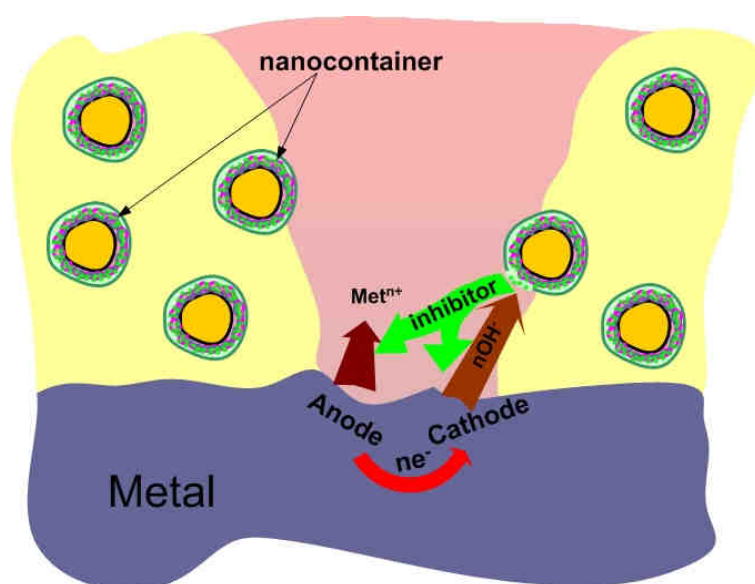
Figure 7.2.17. Scheme of the controllable release of inhibitor from the nanocontainers and the "smart self-healing" process.

Summarizing

A new method of corrosion inhibitor delivery on demand is proposed conferring "intelligent" self-healing ability to the hybrid sol-gel protective films. Controllable delivery is achieved incorporating nanocontainers of benzotriazole inhibitor in the hybrid pre-treatments. The nanocontainers were formed using silica nanoparticles layer-by-layer coated with polyelectrolyte molecules acting as nanoreservoirs of corrosion inhibitor.

The impregnation of the hybrid sol-gel films increases their long-term corrosion protection performance for metallic substrates. Moreover the introduction of the inhibitor in the form of nanocontainers instead of the direct addition to the sol-gel matrix prevents the interaction of the benzotriazole with components of the coating, which can negatively influence the barrier properties of the hybrid film and lead to the deactivation of the corrosion inhibitor. The resulting hybrid films have pronounced protective efficiency and possess self-healing ability. Intelligent corrosion protection was achieved by the inherited property of the polyelectrolyte layers that are sensitive to pH and ionic strength changes. Thus when there is a change of pH in defective areas and there is ingress of the aggressive electrolyte during corrosion of AA2024 polyelectrolyte layers open and provide release of incorporated inhibitor which heals the corrosion process.

The use of the nanocontainers approach creates a new opportunity to substitute the carcinogenic chromates allowing the development of a new generation of active corrosion protective systems possessing effective self-repairing capacity of the corrosion defects.

7.2.3 Anticorrosion sol-gel coatings loaded with Halloysites nanocontainers of inhibitor

The large-scale implementation of the nanocontainer-based coatings is limited by the nanocontainer price, which is too high to make self-healing coatings commercially competitive. This calls for finding low-cost nanocontainers, which can be successfully employed in self-healing coatings. One of the perspective future containers can be industrially mined halloysite nanotubes.

The possibility to employ halloysite nanotubes as perspective nanocontainers for anticorrosion coatings with corrosion protection is demonstrated in this paragraph. Halloysite nanotubes were loaded with the corrosion inhibitor 2-mercaptobenzothiazole (MBT), which is poorly soluble in water, however is well-soluble in ethanol or acetone, and then incorporated into hybrid sol-gel coating. To prevent undesirable leakage of the loaded inhibitor from the halloysite interior, the outer surface of the MBT-loaded halloysite nanotubes was modified by deposition of several alternating polyelectrolyte multilayers poly(allylamine) hydrochloride (PAH) and poly(styrene sulfonate) PSS. The halloysite nanocontainers and sol-gel coatings were characterised from the point of view of corrosion protection and microstructure.

7.2.3.1   Preparation and characterization of nanocontainers

Halloysite is defined as a two-layered aluminosilicate, chemically similar to kaolin, which has predominantly hollow tubular structure in the submicron range. The neighboring alumina and silica layers create a packing disorder causing them to curve. As for most natural materials, the size of halloysite particles varies within 1-15 µm of length and 10-150 nm of inner diameter depending on the deposits. The ζ-potential of halloysite particles is negative at pH 6-7 and similar to the surface potential of SiO_2 with a small contribution from the positive Al_2O_3 inner surface [396]. At pH 8.5 the tube lumen has a positive surface promoting loading by negatively charged macromolecules and preventing their adsorption on the negatively charged outer surface.

The initial appearance of the nanocarriers before loading with 2-mercaptobenzothiazole is presented in Figure 7.2.18. Figure 7.2.18a shows a SEM image of the separated halloysite nanotubes. Initial halloysite material consists of well-defined nanotubes with size varying between 1-15 µm. The hollow lumen of the halloysite nanotubes before loading is clearly visible in Figure 7.2.18b and can be estimated as 15-40 nm in diameter. The calculated inner space provides the ability of loading 12 % of the total volume of the halloysite.

Embedding of the MBT inside the inner volume of the halloysite nanotubes (see overall scheme of nanocontainer fabrication in Figure 7.2.19) was performed adapting the procedure described by Price *et al.* [397]. Dispersed halloysite powder was mixed with 10 mg/ml solution of MBT in ethanol. A vial containing the mixture was transferred to a vacuum jar and then evacuated using a vacuum pump. Slight fizzing of the suspension

indicates the air being removed from the halloysite interior. After the fizzing was stopped, the vial was sealed for 30 min to reach equilibrium in MBT distribution. The halloysite suspension was centrifuged to remove excess of the dissolved MBT, cleaned in water three times, and dried. This process was repeated four times to ensure the saturation of the inner halloysite cavity with precipitated MBT. During the first three cycles the loading of MBT into halloysites was gradually increased with the increment of 25 mg of MBT per 1 g of the halloysite. The saturation loading level was achieved after the fourth loading step. The maximum MBT quantity loaded into halloysite tubes is 5 % wt.
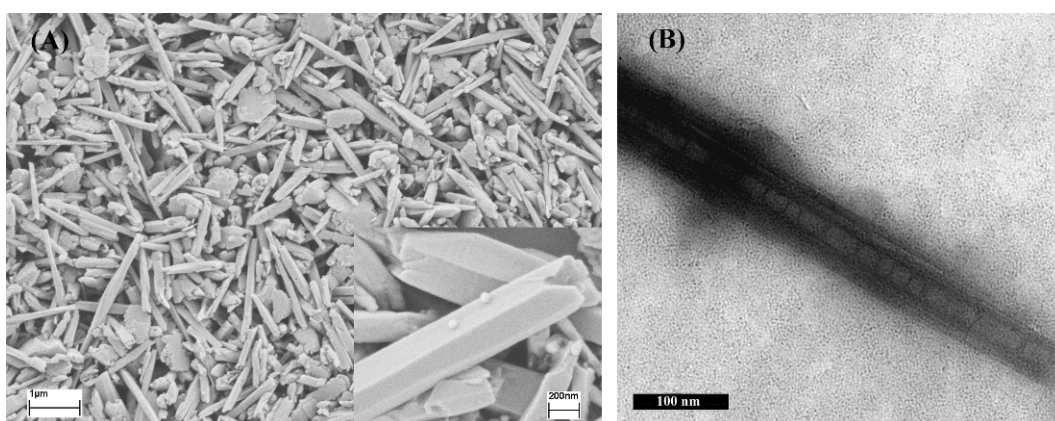
Figure 7.2.18. SEM a) and TEM b) images of the halloysite nanocontainers.
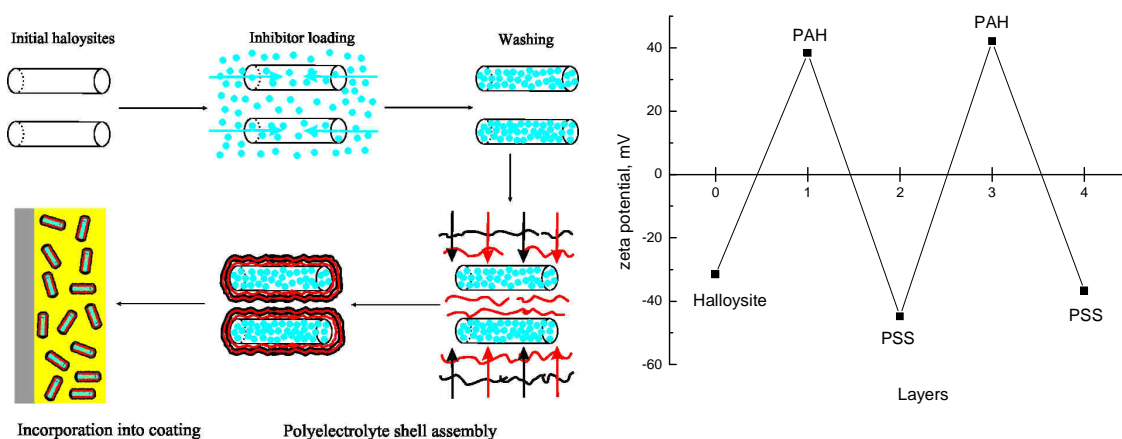
Figure 7.2.19. Left: schematic illustration of the fabrication of MBT-loaded halloysite/polyelectrolyte nanocontainers. Right: zeta-potential data for sequential deposition of PAH and PSS polyelectrolytes on halloysite nanotubes, pH 7.5.

Figure 7.2.19 shows a drastic increase of the surface charge after deposition of the first PAH layer (+70 mV) followed by a similar (-82 mV) decrease after PSS adsorption on the next stage. The final nanocontainers have inhibitor/halloysite/PAH/PSS/PAH/PSS layer structure. The SEM image of halloysites doped with MBT and coated with polyelectrolyte layers, the final product which was added into the sol-gel coating, is presented in Figure 7.2.20. Polyelectrolyte-coated halloysites material composed of well-defined single tubes 0.2-1.5 µm long and 100-300 nm thick as well as fractured small pieces of nanotubes. The polyelectrolyte shell formed provides controlled release properties to the halloysite nanotubes.

Figure 7.2.20. SEM image of halloysites doped with 2-mercaptobenzothiazole and coated with PAH/PSS/PAH/PSS polyelectrolyte layers.

7.2.3.2   Preparation and characterization of sol-gel doped with halloysite nanocontainers

Zr based sol-gel formulation (SgZr1) has been used for the preparation of the sol-gel (paragraph 4.3.1). Necessary amount of halloysites (0.04g) was introduced in the alkosol 3 during the sol-gel synthesis procedure (Table 7.2.3). Two sol-gels have been prepared using halloysite nanocontainers with or without MBT inhibitor. The respective reference names are shown in Table 7.2.3. Figure 7.2.21 presents an optical photograph of the sol-gel formulation doped with halloysites. As can be seen the halloysites are homogeneously dispersed in the sol-gel. The suspension was stable for at least 5 hours after preparation.

SEM image (Figure 7.2.22) shows plane view of a halloysite-doped sol-gel film applied on AA2024. Neither cracks nor other defects induced by addition of halloysites were visualized on the surface of the coating. Using SEM it was difficult to find any features related to the halloysite presence on the surface. Just single fragments of the

halloysites can be seen on the surface at higher magnification (Figure 7.2.22b). The observed feature is a halloysite tube about 1.9 µm long and 0.2-0.4 µm thick. The SEM image of the halloysite is blurred and not clear which indicates that the tube is under the sol-gel layer.

Table 7.2.3. Compositions of different sol-gel systems and respective reference name.

	TPOZ/GPTMS (alkosol 3)	Reference name
0.04g Halloysites with MBT	+	SgZrHSMBT
0.04g Halloysites empty	+	SgZrHS

Figure 7.2.21. Optical photograph of the sol-gel formulation doped with halloysites.
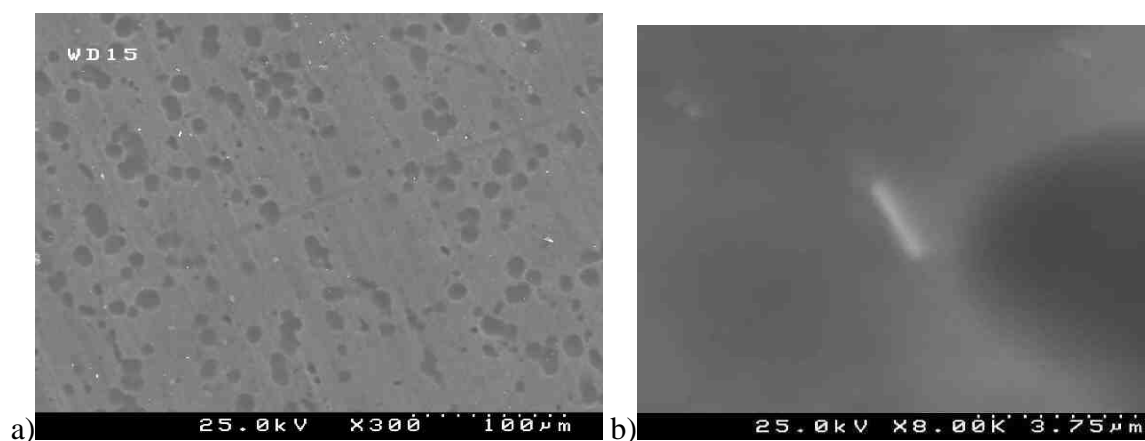
Figure 7.2.22. SEM images of AA2024 specimen coated by the sol-gel film doped with halloysites.

7.2.3.3   Corrosion protection performance

The main idea of introduction of halloysites into sol-gel coating is the reinforcement of anticorrosion protection. The EIS was used in this work for quantification of corrosion protection of different sol-gel films. Figure 7.2.23 presents impedance spectra of the AA2024 samples coated with sol-gel films containing two halloysites additives (Table 7.2.3). The spectra were taken after 21 days of accelerated immersion test in 0.5M NaCl solution. Three well-defined time-constants appear in the spectra. The high-frequency time constant at about 100 kHz is related to capacitance of the sol-gel coating. The second one at 1 Hz is ascribed to the presence of intermediate oxide layer. The third time-constant at around 0.01 Hz is related to the signs of corrosion process. Although both coatings provide effective corrosion protection and good barrier properties, the one with halloysites containing MBT demonstrates higher low frequency impedance that reflects better corrosion protection performance (Figure 7.2.23). The low-frequency time constant in the case of SgZrHSMBT sample is less distinct compared to the one of sample SgZrHS. This testifies that the coating impregnated by halloysites with inhibitor has better anticorrosion protection due to the presence of MBT inhibitor. More detailed analysis and the results of fitting of impedance data are presented below.

Figure 7.2.24 shows the evolution of the resistance (R_{coat}) and capacitance (C_{coat}) of different sol-gel films. The initial resistance of the coatings is around $6*10^4$ Ohm*cm^2. It rapidly decreases during the first days of immersion followed by a continuous decrease until around $1*10^3$ Ohm*cm^2 (Figure 7.2.24a). The capacitance rapidly increases from $1*10^{-8}$ F/cm^2 during the first day of immersion and then monotonously grows until about $1.5*10^{-8}$ F/cm^2 (Figure 7.2.24b). In both cases the evolution of the parameters of the coatings is almost identical indicating similar barrier protective properties of both coatings.

In spite of the similarities of barrier properties of the coatings the corrosion protection of alloy is different. Figure 7.2.25a shows the evolution of the intermediate oxide layer resistance (R_{ox}) calculated after fitting of the impedance spectra. The initial R_{ox} of both samples is practically the same. However, there is a difference after two days of immersion. The resistance of sample SgZrHSMBT is higher by about 2-3 times compared to sample SgZrHS indicating higher stability of metal/coating interface (Figure 7.2.25a). A similar trend can be seen for polarisation resistance (R_{polar}). The initial R_{polar} is comparable between the two samples. However, after 350h of immersion there is a noticeable difference. After about 400h of immersion of sample SgZrHSMBT there is a breakdown and decrease of impedance at low frequency. The R_{polar} has decreased to around $6*10^6$ Ohm*cm^2. However, impedance was recovered after that to about $2*10^7$ Ohm*cm^2 (Figure 7.2.25b). Similar breakdown is present on R_{ox} curve. Such behaviour can be an indication of the corrosion development and subsequent healing by the released MBT inhibitor. In contrast to that, R_{polar} of sample SgZrHS is constantly decreasing during immersion. The polarisation resistance decreases in this case because of stable corrosion activity developed on the alloy since there is no inhibitor in the sol-gel coating.

Figure 7.2.23. Bode plots for Sol-gel films doped with halloysites with or without MBT after 21 days of immersion in 0.5M NaCl solution.
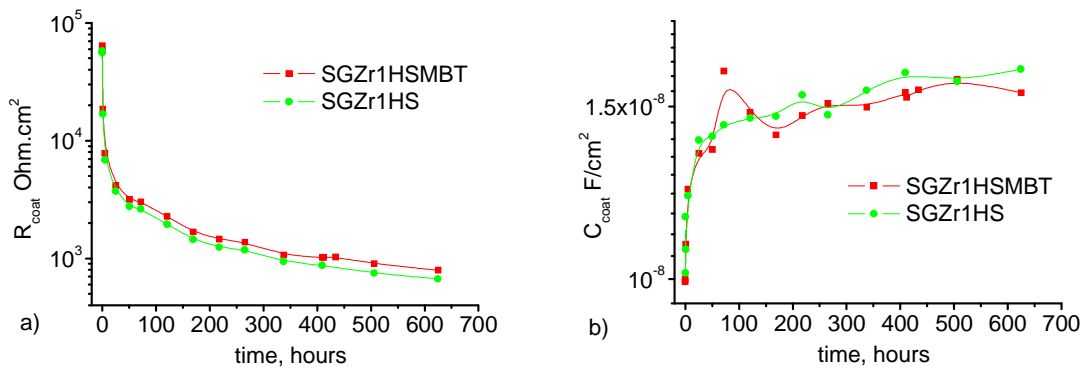
Figure 7.2.24. Evolution of sol-gel films resistance and capacitance for coatings doped with halloysites with or without MBT during immersion in 0.5M NaCl solution.

Figure 7.2.25. Evolution of intermediate oxide layer resistance a) and polarization resistance b) for coatings doped with halloysites with or without MBT during immersion in 0.5M NaCl solution.

The higher corrosion protection of sol-gel coating containing halloysites with MBT can be explained by the inhibiting action of MBT which is an effective inhibitor of corrosion of AA2024. The function of inhibitor-doped halloysites is to store and provide slow release of inhibitor, blocking initial corrosion processes and healing micro defects in the coating. The halloysite-based nanocontainers prevent interaction of the inhibitor with components of the sol-gel matrix during the synthesis and thereby deactivation of inhibitor.

Summarizing

Halloysites nanotubes can be used for development of new generation of anticorrosion coatings based on inhibitor-loaded nanocontainers. Halloysite nanotubes act as a reservoir for inhibitor molecules preventing its direct interaction with the coating matrix and undesirable leakage. Polyelectrolyte multilayers around the halloysite nanotubes provide effective storage and prolonged release of MBT inhibitor "on demand" in the damaged zones conferring an active corrosion protection and self-healing ability. Application of the cheap halloysite nanotubes will considerably reduce the costs of such coatings opening perspectives to exploit them commercially.

7.2.4 Sol-gel coatings loaded with cerium molybdate nanowires

The use of inhibiting compounds with low solubility is another possible way to provide prolonged release of inhibitor and active corrosion protection. Cerium molybdate compound is one of the potential candidates for the role of inhibitor. The proposed compound has low solubility in water and is composed of two ions namely cerium and molybdate that are known corrosion inhibitors. Corrosion protection performance of cerium molybdate has been studied in section 5.3. The results showed an improved corrosion protection of AA2024 in NaCl solution in the presence of cerium molybdate nanowires. Inhibitive ions being released from the compound effectively block the cathodic process on copper rich intermetallics of alloy and reduce the corrosion impact. In addition to corrosion protective properties the compound is synthesised in the form of nanowires with width around 50 nm and length more than some microns. However, according to light scattering measurements the mean size of nanoparticles is less than 400 nm (Figure 5.3.1b). The addition of nanoparticles to the sol-gel can prevent formation of defects in the sol-gel coatings, which can occur when incorporating large particles.

In this study a nanoparticulated inhibitive compound based on cerium molybdate was directly introduced in the sol-gel to impart active corrosion protection properties of coatings applied on AA2024. The additives were introduced in different sol-gel solutions in order to test the compatibility with the components of the sol-gel system. Sol-gel coatings with additives of inhibitor were characterised from the point of view of corrosion protection and microstructure.

7.2.4.1   Preparation of the sol-gel coatings doped with cerium molybdate compound

Zr based sol-gel formulation was prepared according to the procedure (paragraph 4.3.1). Necessary amount of ethanol stabilized slurry of cerium molybdate was introduced at different steps of the sol-gel synthesis procedure either in the alkosol 1 of TPOZ with EthAcAc or in the alkosol 3 with mixture of TPOZ and GPTMS (Table 4.3.1). Figure 7.2.26 demonstrates that the powder is finely dispersed in the sol-gel matrix with no agglomeration. The suspension is stable during some days of ageing which demonstrates high stability of the obtained sol-gel. The respective reference names and synthesis step of inhibitor addition are shown in Table 7.2.4. The concentration of inhibitor in the final sol-gel solution was 0.3 wt.% and 0.6 wt.% respectively. The reference undoped coating (SgZr1) was also prepared for comparison.

Figure 7.2.26. Optical photograph of the sol-gel formulation doped with cerium molybdate nanoparticles.

Table 7.2.4. Compositions of different sol-gel systems and respective reference name.

	TPOZ EthAcAc (1 alkosol)	GPTMS 2propanol (2 alkosol)	TPOZ GPTMS (3 alkosol)	Reference name
-	-	-	-	SgZr1
0.3 wt.% cerium molybdate	+	-	-	SgZrMo1
0.3 wt.% cerium molybdate	-	-	+	SgZrSiMo3
0.6 wt.% cerium molybdate	-	-	+	SgZrSiMo3x2

7.2.4.2   Microstructural characterisation of doped sol-gel coatings

The microstructure of the sol-gel coatings deposited on AA2024 before immersion was studied by TEM. Figure 7.2.27 shows typical cross-section view of cerium molybdate doped sol-gel coating. It can be seen that synthesized sol-gel films are uniform, defect- and crack-free. The estimated thickness of the sol-gel film is around 1-1.5 µm. The section (Figure 7.2.27a) shows the presence of round shaped features ascribed to the zirconia nanoparticles obtained in-situ during the sol-gel synthesis route. A cerium molybdate compound has irregular shape and dark color on the TEM photograph because of the presence of heavy elements compared to elemental composition of the sol-gel matrix. The compound is homogeneously distributed in the sol-gel matrix, which can be seen from TEM images (Figure 7.2.27a,b). EDS spectra made on the dark black inclusions with a diameter around 20-60nm shows the clear signals from Ce, whereas the signal from Mo is overlapped by the signal of Zr from the sol-gel matrix (Figure 7.2.27b,c). The obtained TEM images do not show large particles or agglomerates (around 300 nm) which were shown previously by light scattering measurements (Figure 5.3.1). The formation of a

suspension with smaller particles could be because of the action of ultrasonic agitation that was used during the synthesis of the sol-gel solution. Apparently the larger particles were successfully dispersed in the sol-gel solution.
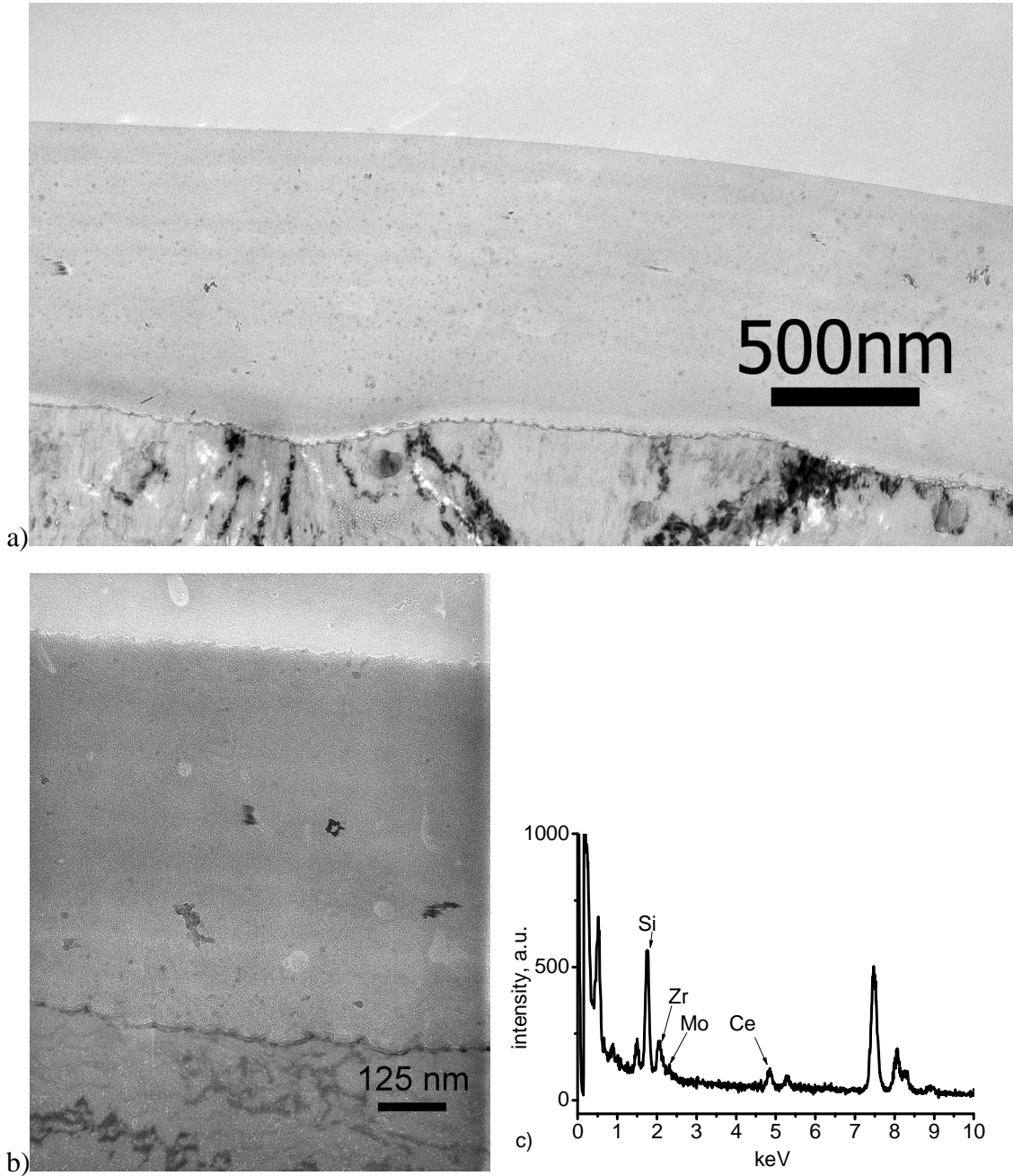
Figure 7.2.27. TEM micrograph of cross-section of sol-gel coatings doped with cerium molybdate inhibitor and EDS analysis performed on the dark black inclusions.

7.2.4.3   Corrosion protection of the sol-gel coatings: EIS study

Corrosion protection efficiency of the sol-gel coatings was evaluated during 28 days of immersion in 0.5M NaCl solution. Figure 7.2.28 shows Bode plots of the sol-gel coatings doped by cerium molybdate nanowires after 21 days of immersion in 0.5M NaCl solution. The impedance spectra show three typical time constants that are usually observed in the impedance spectra of the sol-gel coated aluminum alloy (Figure 6.1.12). The capacitive response of the sol-gel coating appears at high frequencies about 10^5 Hz. The relaxation process at middle frequencies (10^{-1}-10 Hz) is ascribed to the intermediate oxide layer. The appearance of the time constant at low frequencies $<10^{-1}$ Hz is ascribed to the corrosion activity of the substrate and can be seen only at longer immersion time.

A rough evaluation of the impedance spectra show an improvement of the corrosion protective properties of the sol-gel coatings doped with cerium molybdate. The addition of the compound to the sol-gel in mixed Alkosol 3 solution (SgZrMo0.3) during the synthesis leads to improvement of the barrier properties of the sol-gel film compared to the undoped coating (Figure 7.2.28). There is no significant degradation of the barrier properties of the coatings due to addition of inhibitor to the sol-gel.

A more detailed analysis of the corrosion protection properties of different sol-gel coatings is achieved by fitting the impedance data with appropriate equivalent circuit models. At the beginning of immersion impedance spectra are adequately fitted by the equivalent circuit that includes only two time constants representing sol-gel coating (C_{coat} and R_{coat}) and intermediate oxide layer (C_{ox}) (Figure 3.3.14a). A resistive part (R_{ox}) appears in the spectra when electrolyte penetrates through the coating and oxide layer (Figure 3.3.14b). Longer immersion time results in appearance of a time constant related to the corrosion activity (C_{dl} and R_{polar}) (Figure 3.3.14c) that was also taken into the account when making fitting of spectra.

Figure 7.2.29a presents evolution of the resistance (R_{coat}) of the undoped and inhibitor doped sol-gel coatings during immersion in 0.5M NaCl solution. The sol-gel film resistance is almost equal for all coating systems at the beginning. A fast drop of the resistance occurs after 1 day of immersion and monotonous decrease at longer immersion time. The samples SgZrSiMo3 and SgZrSiMo3x2 show higher sol-gel coating resistance during the all immersion time. The addition of nanoparticulated inhibitor can reinforce the sol-gel matrix therefore increasing its barrier properties. On the contrary, SGZrMo1 sample shows lower resistance compared to undoped sample during immersion time. The hydrolysis reaction of Zr propoxide can be affected by the addition of cerium molybdate compound that negatively influences the barrier properties of the final sol-gel films.

Initial capacitance of the sol-gel films for samples SgZrSiMo3 and SgZrSiMo3x2 is slightly lower compared to sample SgZrMo1 and bare sample SgZr1. Such behavior might be attributed to slightly thicker sol-gel coatings formed when cerium molybdate is added to the alkosol 3. The increase of the capacitance during immersion is most probably caused by the penetration of water in pores of the coating.
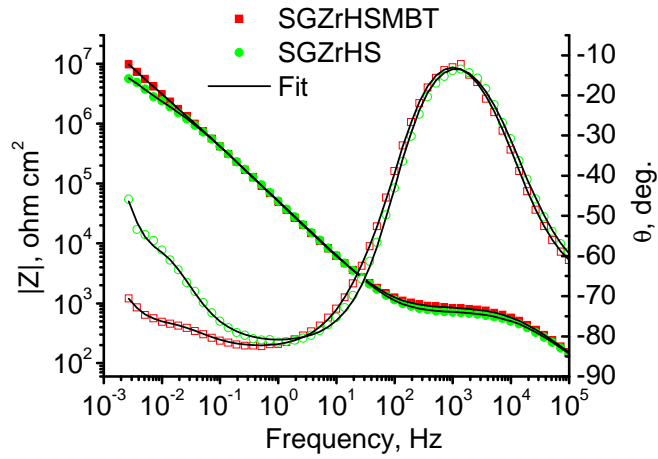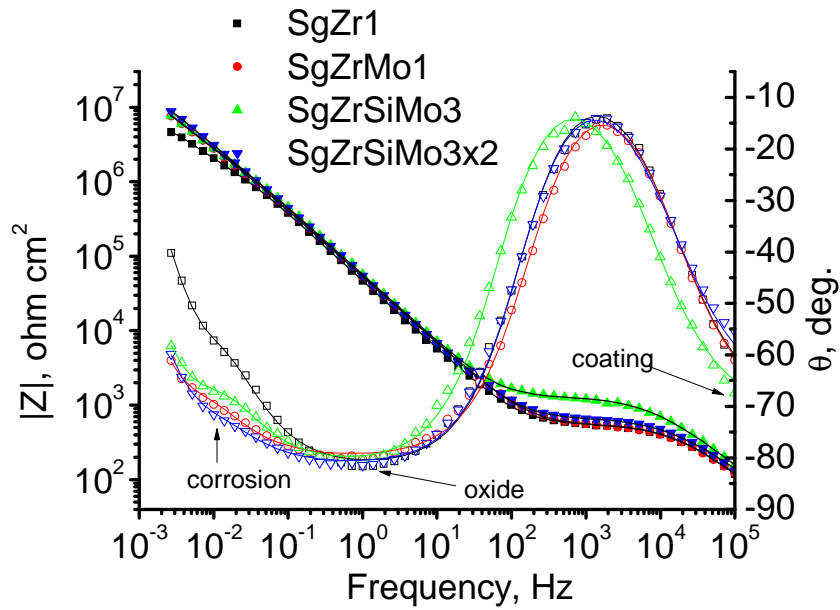
Figure 7.2.28. Bode plots for Sol-gel films undoped and doped with cerium molybdate after 21 days of immersion in 0.5M NaCl solution.
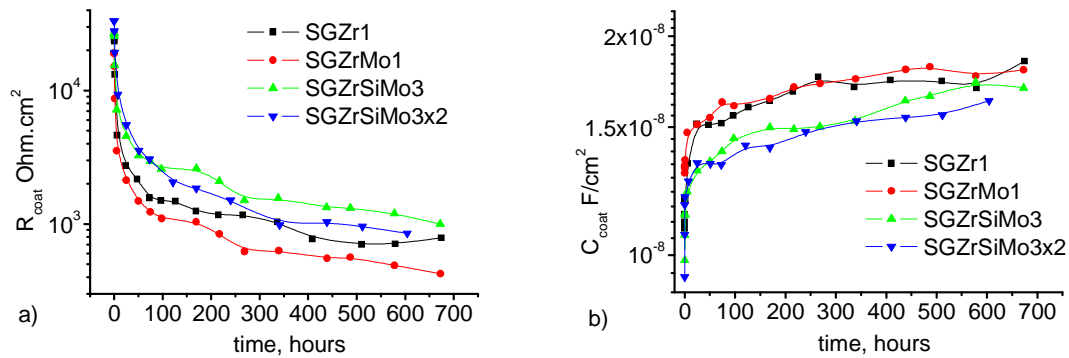
Figure 7.2.29. Evolution of sol-gel films resistance and capacitance for coatings doped with cerium molybdate during immersion in 0.5M NaCl solution.

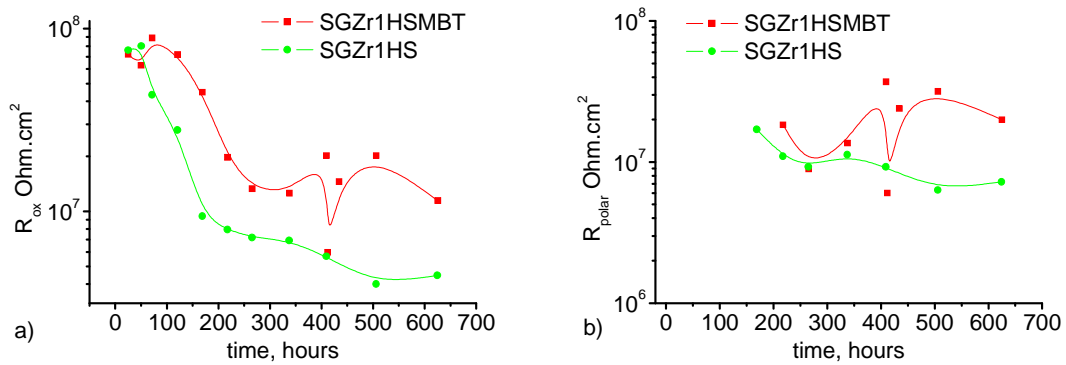Evolution of the resistance of the intermediate oxide layer R_{ox} is presented in Figure 7.2.30a for different sol-gel coatings. A good performance was demonstrated by the SgZrSiMo3 sample that shows the highest initial resistance. After one day of immersion the resistance was around $9*10^7$ Ohm*cm^2. During the first 200h of immersion there is a slow decrease of R_{ox} until $3.5*10^6$ Ohm*cm^2, followed by a second drop until $5*10^6$

Ohm*cm^2 (Figure 7.2.30a). On the contrary, samples SgZrSiMo3x2 and SgZrMo1 initially show low resistance $3.8*10^7$ and $2*10^7$ Ohm*cm^2 respectively compared to undoped coating $5*10^7$ Ohm*cm^2. However, during the first 100 – 200 h of immersion a noticeable increase of R$_{ox}$ occurs approximately until $8*10^7$ and $7*10^7$ Ohm*cm^2 for SgZrSiMo3x2 and SgZrMo1 samples respectively (Figure 7.2.30a). Longer immersion caused a drop of resistance to about $9*10^6$ Ohm*cm^2.

The evolution of the oxide resistance demonstrates that there is an enhanced corrosion protection during the first 200h of immersion in NaCl electrolyte. Such active protection is clearly conferred by the cerium molybdate additive. In the case of SgZrSiMo3x2 and SgZrMo1 sol-gel coatings there is a recovering of the resistance of intermediate oxide layer, which can be a result of self-healing of defects by the inhibitive species.

For undoped coating the corrosion process becomes distinguishable from the intermediate oxide film after several days of immersion. The polarization resistance (R$_{polar}$) for SgZr1 during immersion varies around $7*10^6$ Ohm*cm^2. For inhibitor doped sol-gel coatings polarization resistance becomes possible to resolve only after much longer time of immersion. For SgZrMo1, SgZrSiMo3 and SgZrSiMo3x2 coatings a corrosion response was revealed after 250, 320 and 150h of immersion respectively (Figure 7.2.30b). At longer immersion time the overall values of R$_{polar}$ are higher than for undoped coating indicating the higher protection (Figure 7.2.30b). The experimental results testify that the addition of cerium molybdate imparts active corrosion protective properties to the coating system reducing the corrosion impact during immersion in NaCl solution.
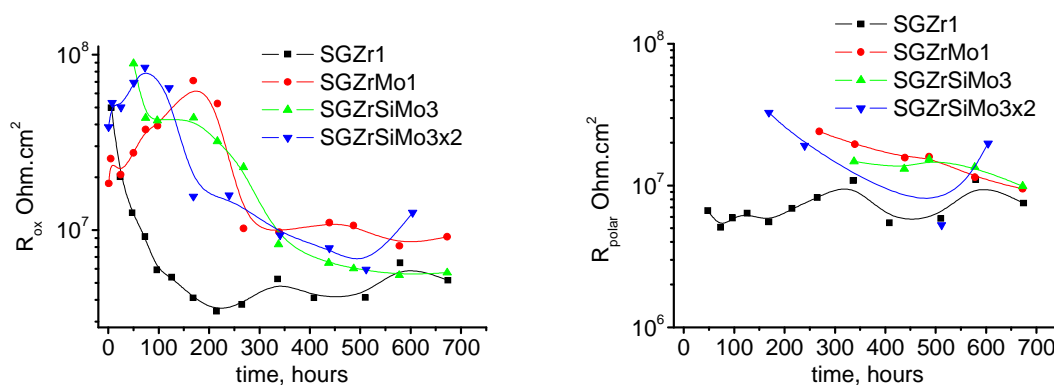
Figure 7.2.30. Evolution of intermediate oxide layer resistance R$_{ox}$ a) and polarization resistance R$_{polar}$ b) for coatings doped with cerium molybdate during immersion in 0.5M NaCl solution.

7.2.4.4 Self-healing properties of the sol-gel coatings

The results of impedance measurements show enhanced corrosion behavior of the sol-gel coatings doped with inhibitor. Values of oxide layer resistance were essentially higher than that for undoped sol-gel coatings during first 4-7 days of immersion in NaCl solution (Figure 7.2.30a). Moreover, the appearance of the time constant associated with the corrosion process was delayed in this case (Figure 7.2.30b). Such performance can be attributed to the self-healing effect provided by the addition of cerium molybdate into the sol-gel formulation. The self healing is clearly demonstrated when comparing the evolution of impedance represented as a Complex plane plots during immersion (Figure 7.2.31). During 7 days of immersion there is a significant increase of low frequency impedance part. However, at longer immersion time the inhibiting effect was suppressed followed by a continuous decrease of impedance. The development of corrosion is most probably attributed to a lack of release of inhibitive species from the coating.

Corrosion activity of alloy and signs of self-healing due to action of cerium molybdate additive were revealed using microstructural analysis. SEM micrograph obtained after corrosion testing of sample SgZrMo1 is presented in Figure 7.2.32a. The picture shows the presence of a pit formed during corrosion of alloy. The EDS analysis performed in the place of the pit shows increased signals of Ce and Mo associated with the formation of precipitates in the place of corrosion activity (Figure 7.2.32b). The EDS spectrum made on uncorroded surface does not show any significant signals of Ce or Mo (Figure 7.2.32b).
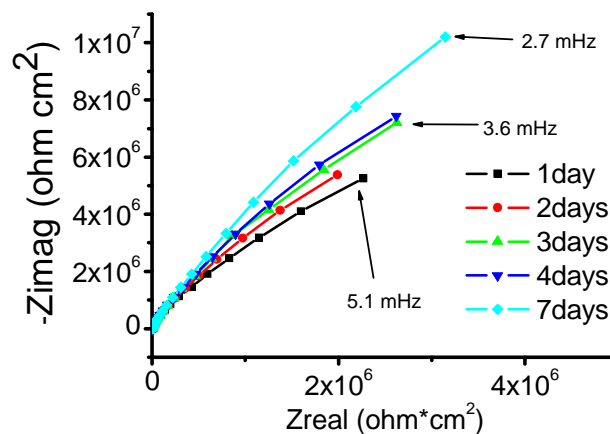
Figure 7.2.31. Increase of impedance during 7 days of immersion of sample SgZrMo1.
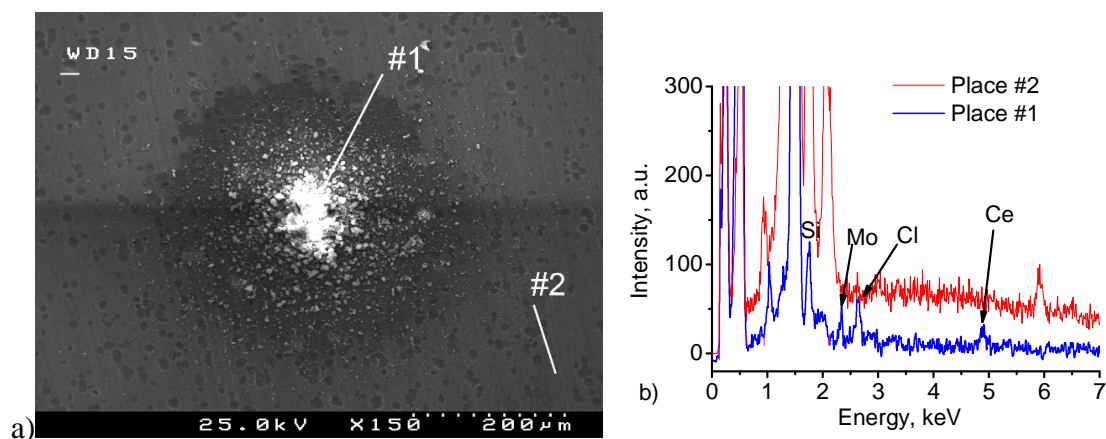
Figure 7.2.32. SEM micrograph made on sample SGZrMo1 after some days of corrosion testing in 0.5M NaCl solution a) and EDS spectrum taken at the place of the pit and at the sol-gel matrix b).

The presented results allow speculating on the mechanism of the corrosion protection by sol-gel coatings doped with cerium molybdate inhibitor. The impedance results obtained during initial immersion of the sol-gel coated samples in NaCl solution demonstrate low resistance of the R_{ox} layer for samples SgZrMo1 and SgZrSiMo3x2. This effect can be associated with the action of cerium molybdate compound on the hydrolysis and condensation reactions of the sol-gel and bonding strength to the metallic substrate. However, the R_{ox} increases during the first 100-200 days of immersion (Figure 7.2.30). Such increase is related to the action of incorporated inhibitor that releases during the immersion and blocks the corrosion process. The sample SgZrSiMo3 demonstrates an enhanced corrosion protection at the beginning of immersion compared to samples SgZrMo1 and SgZrSiMo3x2 (Figure 7.2.30). This can be related to better properties of the sol-gel coating formed case of sample SgZrSiMo3. It seems that interface between the sol-gel and metal is better stabilized in this case thus the resistance of the oxide layer is higher at the initial immersion. During immersion the inhibitor can leach out in the places of microdefects and suppress the corrosion activity of the metal. When a pit is initiated it supports the cathodic and anodic activities as was discussed in paragraph 6.4. The corrosion process is accompanied by the increase of pH at the cathodic site or decrease of pH at the anodic site of a pit. The changes of pH at the corrosion sites can increase dissolution of the incorporated inhibitor and accelerate its release from the coatings. The results obtained by SEM/EDS (Figure 7.2.32) confirm that in the place of a pit there are signals from Ce and Mo which testifies the accumulation of inhibitor at the place of defect. As the result of inhibitor release the corrosion process becomes suppressed. The impedance results showing R_{ox} increase during initial immersion prove the inhibiting effect of cerium molybdate additive (Figure 7.2.30).

294

Summarizing

The addition of cerium molybdate nanoparticles is a promising way to impart active corrosion protection properties to the sol-gel pretreatment. The prepared coatings are uniform, defect and crack free and have fine distribution of the cerium molybdate nanoparticles inside the sol-gel coating.

Nanoparticles addition in the sol-gel matrix makes no adverse effect on the barrier properties of the sol-gel coatings. The addition of inhibitor at the third step of hydrolysis (in the zirconia-silica hybrid matrix) increases barrier properties of coating. Such increase of barrier protection can be associated with the increase of the sol-gel coating thickness or reinforcement of the coating by cerium molybdate nanoparticles.

Corrosion protection efficiency of sol-gel coatings is enhanced when cerium molybdate was added. During the first 200h of accelerated immersion test there is an active corrosion protection and self-healing of the defects conferred by the release of Ce and Mo species from the cerium molybdate nanoparticles.

CONCLUSIONS

8   General conclusions and future work

8.1   General conclusions of the work

The main work performed in the frame of the PhD project was focused on the achievement of a strategic objective namely the development and deep investigation of alternative to chromates pre-treatments for corrosion protection of AA2024. To successfully achieve the goal novel pre-treatments based on hybrid sol-gel films doped with different corrosion inhibitors were developed. The created protection systems can be used as candidates for substitution of toxic chromate containing pre-treatments in industry. To achieve the main objective the following tasks have been addressed during the fulfilment of the work:

1. Deep study of corrosion mechanisms of 2024 aluminium alloy;

2. Investigation of new effective corrosion inhibitors to be used in pre-treatments;

3. Development and optimization of new hybrid sol-gel pre-treatments applied on AA2024;

4. Doping of hybrid sol-gel pre-treatments with the most efficient corrosion inhibitors analysed in task 2.

5. Development of a new approach on immobilization of the corrosion inhibitors in form of nanocontainers in the cases where direct addition of inhibitor is problematic;

6. Detailed investigation of the corrosion protection efficiency and self-healing mechanisms of the developed coatings

The particular progress beyond the state of the art reached during the presented work is summarized below.

The **corrosion mechanism** of AA2024 in chloride solutions was studied in details. This task was extremely important in order to design effective strategies for active corrosion protection of the alloy giving a basis for finding new efficient inhibitors. The corrosion activity of alloy was studied using localized techniques like AFM, SKPFM, SEM/EDS and integral electrochemical techniques as EIS and DC-polarization. The SKPFM is demonstrated to be a very valuable technique that can be effectively used for

the investigation of the localized corrosion activity and inhibition of AA2024. Results obtained with the help of SKPFM are conclusive and can be used for the analysis of the corrosion susceptibility and inhibiting performance of different chemicals. The obtained results clearly demonstrate the role of alloy microstructure on the corrosion initiation and propagation [i,ii]. The model of the localized corrosion activity of AA2024 was proposed and supported by thermodynamic analysis and experimental results. The most relevant findings related to the localized corrosion activity of the alloy are:

- Copper rich intermetallics (S-phase) play the main role in the localized corrosion activity of AA2024. Initially active elements namely Mg and Al are dissolved from S-phase leaving copper rich remnant. The dissolution can occur due to chemical reaction of Al and Mg with water or electrochemical process involving copper as cathode and Al and Mg as anode.

- Rate of the S-phase dissolution increases when pH is lower, that is in agreement with the thermodynamic analysis.

- The copper rich inclusions have more noble potential and initiate localized corrosion attack involving the surrounding aluminum matrix. The process of copper re-deposition plays an important role in further development of the local corrosion attack. The re-deposited copper increases the effective surface area of the cathodic zone and, therefore, accelerates corrosion of the alloy making it self-catalytic.

The obtained findings demonstrate the important influence of copper, magnesium and aluminium in localized corrosion initiation and activity of intermetallics. Therefore, in order to prevent localized corrosion, different compounds were selected from the point of view of their ability to form insoluble compounds with alloying elements of S-phase and their ability to block electrochemical process at the intermetallic inclusions. The appropriate **corrosion inhibitors** are essential to provide active anti-corrosion effect to the developed pre-treatments. The selected inhibitors are cerium nitrate, cerium molybdate, benzotriazole, mercaptobenzothiazole, salicylaldoxime, quinaldic acid and 8-hydroxyquinoline [iii,iv]. The mechanism of the inhibiting action was presented and discussed with respect to corrosion activity of AA2024. Nonetheless the results can also be used for the effective corrosion protection of other alloys that resemble corrosion behaviour similar to AA2024. The most relevant findings related to the inhibitor action are the following:

Corrosion inhibition by inorganic inhibitors

- Ce or La salts form insoluble precipitates at the intermetallic inclusions hindering cathodic and anodic process. The formation of hydroxides occurs due to increase of pH at locations of intermetallics that are electrochemically active and support ORR cathodic processes.

- The deposition does not occur immediately upon contact with inhibitive solution. Initial development of the corrosion process is needed in order to generate enough hydroxyl ions. The growth of hydroxide deposits studied in-situ by AFM technique exhibits linear time dependence indicating that the corrosion processes are progressing in stationary state that results from a balance between diffusion and electrochemical reaction. The chloride ions strongly influence the rate of the corrosion processes and in turn the rate of the hydroxide deposits formation. The formation of the hydroxide deposits decelerates the re-deposition of copper and the broadening of cathodic zones as shown by SKPFM.

- Cerium nitrate possess superior inhibition properties in comparison with lanthanum nitrate. Such assumption has been verified by the performed thermodynamical analysis. The efficiency of cerium nitrate is due to formation of extremely insoluble cerium (IV) hydroxide on the active intermetallics surface.

- The inhibition performance of cerium molybdate was attributed to the formation of precipitates of Mo oxide or hydroxide-species atop the S-phase. The formation of precipitates is thermodynamically possible via the reduction reaction of molybdate anion to insoluble Mo (IV) oxide.

- The EIS measurements demonstrate that the efficiency of protection by cerium molybdate is much higher compared to 0.05 or 0.001 M solutions of sodium molybdate in 0.05 M NaCl. This behaviour is explained by the synergistic action between the cerium and molybdate ions.

Corrosion inhibition by organic inhibitors

- Triazole and thiazole derivatives reduce corrosion activity of copper containing intermetallics in NaCl solution by forming a protective film on copper surface. The formation of the protective film is most probably occurs via reaction of BTA and MBT with cuprous species. In the case of MBT, topographic maps indicate the formation of precipitates on the copper-rich intermetallics.

- The presence of SAL, 8HQ and QA inhibitors in the corrosive medium leads to significant weakening of the corrosion processes. The inhibiting action is based on the formation of insoluble complexes both on alloy matrix and on intermetallic zones that prevents the dissolution of Mg, Al and Cu. The presence of layers of inhibitors on the surface is proven by XPS and EIS analysis. The results of XPS and EIS analysis show that 8HQ forms a thicker layer on the surface than SAL and QA.

As result of the study of inhibition mechanisms the compounds were selected to be added to the hybrid sol-gel pre-treatments.

The development of **hybrid sol-gel film** with adequate barrier properties and enhanced adhesion to the metal is a key for efficient pre-treatments. In this work two types of sol-gel pre-treatments have been developed and characterized [v]. The first type is based on the combination of TPOT and GPTMS and the second type is based on TPOZ and GPTMS. Investigation of ageing of the sol-gel formulation has been additionally performed for titania-containing sol-gel in order to find ways to prolong self-life of the sol-gel formulation. The obtained results show that the variation of temperature and water ratio can increase the stability of the sol-gels during ageing, which is important for industrial applications where long shelf-life is requested. In addition the coatings were characterized using industrial tests. Both sol-gel coatings demonstrate good adhesion to metal substrate and to the paint and are promising candidates for the substitution of chromate based pre-treatments. The cleaning of the alloy before sol-gel deposition is important for the sol-gel adhesion and corrosion susceptibility of the alloy. The most important findings are:

- The obtained sol-gel films are dense, uniform and crack free with a thickness around 1.5 µm. The hybrid films are nanostructured and composed by the siloxane matrix with dispersed zirconia or titania nanoparticles.

- The best corrosion protective properties show hybrid titania-silica films prepared using titanium (IV) propoxide and acetylacetone as starting compounds. For zirconia-containing films, better protective properties were found when using ethylacetoacetate as a complexing agent.

- Additional stability of the sol-gel formulation can be achieved when using low temperature during ageing. The corrosion protective properties of the final coatings made after ageing of the sol-gel show similar protection efficiency compared with the coatings prepared from the fresh sols.

- The use of lower water/(OR) ratio for the synthesis of the sol-gel improves the characteristics of the coatings obtained after 1 month of ageing. No significant influence of temperature during the ageing was found on the corrosion performance of the obtained coatings.

- Three steps cleaning process including alkaline etching removes almost all intermetallic inclusions from the alloy surface. In case of cleaning process using two steps some intermetallic inclusions stay on the surface and induce corrosion of the coated alloy during immersion in NaCl solution.

The developed coatings were studied using microstructural and electrochemical techniques. The **mechanism of the corrosion activity of the sol-gel coated alloy** was proposed based on the results of electrochemical and microstructural analysis. It describes the origins of the localized corrosion attack and the development and progress of pitting corrosion activity. SVET and the combination of micropotentiometry and microamperometry were demonstrated as valuable methods that give important information on the mechanism of corrosion in micro defects [vi]. The testing of the sol-gel

coatings demonstrates their high stability and reasonable barrier properties. However the hybrid pre-treatments are lacking the active corrosion protection.

An additional study has been performed due to the lack of experimental protocols to investigate self-healing properties of the coatings using EIS and SVET techniques. Therefore the validity of the main electrochemical techniques has been investigated with respect to the ability to monitor active corrosion protection and self-healing on AA2024 substrate [vii]. EIS was demonstrated as a valuable non-destructive method that allows monitoring the evolution of parameters of coating and metal/coating interface during immersion in corrosive electrolyte. The increase of the low frequency impedance during immersion of a corroding sample can be correlated with the active corrosion protection originating from the self-repairing of the defects. Though, the self healing can not be predicted and the impedance measurement must be made in an appropriate time. Nevertheless, EIS is a powerful technique for the analysis of the corrosion protection ability of sol-gel coatings. SVET can be used to detect the localized corrosion activity in microdefects and change of the activity with time. Information obtained by SVET can be used to follow the kinetics of the localized corrosion process and corrosion inhibition.

- Sol-gel coatings delay the corrosion of metallic substrate. However, corrosion starts when the aggressive environment reaches the metal surface. Typical corrosion features present on the sol-gel coated alloy are pits, blisters and cracks. Pits mainly show anodic activity, however the copper enriched zone inside may support cathodic activity. The cathodic process of oxygen reduction also occurs in damaged zones of the coating such as cracks and blisters.

- The results obtained using microelectrode techniques revealed dual electrochemical nature of a local anode. In spite of positive currents measured by SVET technique at local anode there is a noticeable drop in oxygen concentration that suggests a cathodic process of oxygen reduction going also in anodic place. This is not revealed by SVET and shows the limitations of SVET for investigation of the localized corrosion activity on the sol-gel coated alloy.

- The low frequency impedance during immersion can be correlated to the active corrosion protection originated from the self-repairing of the defects in the presence of the corrosion inhibitor. The SVET results obtained on micro-level are in good accordance with the EIS measurements. The decrease of the low frequency impedance after the defect formation is related to the disruption of the coating and the oxide barrier and the consequent localized corrosion activity in the defected area. The addition of the corrosion inhibitor heals the defect leading to lower corrosion currents and high impedance.

The sol-gels were doped with cerium nitrate, 8hydroxyquinoline (8HQ) and benzotriazole corrosion inhibitors to achieve additional active corrosion protection effect and **self-healing ability** [viii]. Unlike for benzotriazole, the corrosion protective properties

of the sol-gel coatings are better when cerium nitrate and 8HQ inhibitors are added. The positive effect of cerium nitrate addition on the corrosion protective effectiveness has been demonstrated before for zirconia-silica hybrid sol-gels [ix] and silane based systems [x]. The incorporated cerium nitrate and 8HQ inhibitors act mainly as cathodic inhibitors decreasing the rate of cathodic process. Although 8hydroxyquinoline provides an anodic protection of aluminum, the polarization measurements of AA2024 in solution with 8HQ show that the open circuit potential becomes shifted to the cathodic potentials and there is no any shift of the pitting potential of the alloy. However, the decrease of the anodic current on the polarization curve might be related to the partial inhibition of the localized dissolution of intermetallics. Nevertheless, cerium (III) inhibitor is ineffective and the protection efficiency of 8HQ is lower in acidic solution. The acidic conditions are usually formed in corrosion pits. Such behavior of inhibitors is related to the mechanism of inhibition of cerium nitrate and 8HQ. Therefore when corrosion pit is developed on the sol-gel coated alloy the incorporated cerium nitrate can inhibit only cathodic process whereas the incorporated 8HQ can reduce the cathodic and partially the anodic processes.

A direct introduction of inhibitor into the sol-gel coating can increase the overall corrosion protection properties. However, there are several disadvantages that limit the applicability of such approach. The first issue is the interaction between inhibitor and components of the sol-gel coating resulting in coating degradation and deactivation of inhibitor therefore playing negative role. The second one is the low effective loading of inhibitors in the coating. Since an inhibitor interacts with the sol-gel components it results in degradation of the barrier protective properties of the coatings and such degradation becomes much more significant when exciding a certain critical concentration of the inhibitor. The critical concentration can be around some weight percents or less with respect to the sol-gel and such a low concentration might not allow providing active corrosion protection. The third issue is the uncontrollable release or leachability of inhibitor from the sol-gel matrix. In some circumstances the release is very low because of strong interaction of inhibitor and matrix or too high when interactions are weak. Thus the active corrosion protection will be either impeded or very short. It is important to take into account such limitations and perform a study of a particular inhibiting compound for doping the sol-gel formulations in order to get more efficient corrosion protection. The relevant findings concerning the inhibitor loaded sol-gel coatings are presented below:

- Cerium salt and 8-hydroxyquinoline at low concentration do not influence sufficiently the barrier properties of the films when added at different stages of the sol-gel synthesis. However, the overall corrosion protection can be affected depending on the stage where inhibitor was added.

- The addition of 8HQ during hydrolysis of zirconia-precursor leads to decrease of corrosion protection properties and in particular to low values of the intermediate oxide layer resistance. This effect can be caused by the interaction of the zirconium alkoxides or partially hydrolyzed species with 8HQ and formation of complexes that in turn can negatively influence the hydrolysis and condensation

reactions during the sol-gel synthesis and film formation. The addition of cerium-based inhibitor at any hydrolyzing step improves the corrosion protective properties of the coatings.

- BTA added to the sol-gel film significantly decreases its barrier properties and results in fast corrosion activity of alloy. The inhibiting action of BTA becomes superimposed by the fast degradation of the coating thus reducing the corrosion protection by the sol-gel coatings.

- The mechanism of the corrosion protection by inhibitor doped sol-gel coatings is related to the inhibition of the corrosion process in the micro defects. After the corrosion started the leached inhibitor diffuses to the place where corrosion appeared and slows down or stops the activity in that place thus providing a protection of the alloy.

The adverse effects of corrosion inhibitors on the protective properties require the development of new strategies of incorporation of the inhibiting species in the hybrid films. Novel approaches of **inhibitor storage and delivery** in nanoporous titania networks, silica nanocontainers, nanoclays and inhibitor nanoparticles have been developed to impart active corrosion protection to the sol-gel coatings without compromising their stability and barrier properties. The pre-treatment based on combination of TiOx nanoporous layer doped with inhibitor and hybrid sol-gel coating was studied [xi]. Another method of corrosion inhibitor delivery on demand employs the incorporation of nanocontainers with benzotriazole inhibitor in the hybrid pre-treatments [xii,xiii]. The nanocontainers were formed using silica nanoparticles layer-by-layer coated with polyelectrolyte shells acting as nanoreservoirs of corrosion inhibitor. Novel sol-gel coatings with nanocontainers of inhibitor were created using natural clay nanotubes called halloysite [xiv]. Hollow structure of this material allows incorporation and storage of inhibitor. In addition halloysites were coated by polyelectrolyte layers in order to control release of inhibitor. The use of the nanoparticles of inhibitive compounds with low solubility is an alternative approach to provide active corrosion protection of the sol-gels. Cerium molybdate nanoparticulated compound was also used as a promising inhibiting additive to the sol-gel coatings in order to impart active corrosion protection. These approaches can be successfully used to augment active corrosion protection of coating systems for different metallic substrates. For example the incorporation of Ceria and Zirconia nanoparticles in silane coatings applied on the galvanized steel substrates plays a beneficial role for the corrosion protection of the metallic substrate [xv]. The main findings related to the use of active protective systems for AA2024 are the following:

- The incorporation of BTA in the TiOx nanoporous reservoir layer eliminates the negative effect of the inhibitor on the stability of the hybrid sol-gel matrix. The formation of the self-assembled nanostructured oxide net opens the possibility of high loading of such layer with corrosion inhibitors therefore extending the active

corrosion protective properties of the coating. Sol-gel coating shows enhanced long-term corrosion protection and well-defined self-healing effects confirmed by EIS and SVET measurements

- The hybrid films with nanocontainers of BTA have pronounced protective efficiency and possess self-healing ability. Intelligent corrosion protection is achieved by the inherited property of the polyelectrolyte layers that are sensitive to pH changes. When there is a change of pH in a zone of localized corrosion activity, polyelectrolyte layers open and provide release of the incorporated inhibitor which heals the started corrosion process.

- Sol-gel systems with incorporated halloysites nanotubes loaded with inhibitor can be used for development of new generation of anticorrosion coatings based on inhibitor-loaded nanocontainers. Addition of halloysites in the sol-gel coating does not deteriorate its barrier properties. Halloysite nanotubes act as a reservoir for inhibitor molecules preventing its direct interaction with the coating matrix and undesirable leakage. The obtained coatings confer active corrosion protection with signs of self-healing ability.

- The use of ultrasound during the sol-gel synthesis helps to deagglomerate nanoparticles of cerium molybdate and increase the compatibility with the sol-gel matrix. The addition of inhibitor in the sol-gel makes no adverse effect on the barrier properties of the sol-gel coatings. During the first 200h of corrosion testing inhibitor doped sol-gel coatings offer active corrosion protection and well defined self-healing ability.

In summary the study of the corrosion mechanism of AA2024 clarified additional aspects of the localized corrosion activity of alloy using SKPFM and AFM techniques. The obtained information on localized corrosion activity was used for finding novel inhibitive compounds which were added to the sol-gel systems to impart active corrosion protection. A study of the corrosion protection properties of the sol-gel coatings with and without inhibitors revealed corrosion mechanisms and drawbacks associated with the direct inhibitor incorporation. Based on this knowledge novel pre-treatments with active corrosion protection properties have been created as an alternative to the toxic chromate based pretreatments. The presented results and approaches can be used for analysis and study of the corrosion susceptibility and corrosion inhibition of other aluminum alloys and for the development of the protection systems with active corrosion protection.

Original contributions and key publications:

- Mechanism of the localized corrosion and corrosion inhibition of AA2024 in chloride containing environment with or without cerium and lanthanum salts were investigated [i,ii].

- Corrosion inhibition of AA2024 by cerium molybdate nanowires was studied.

- Mechanisms for corrosion inhibition of AA2024 by different organic inhibitors were proposed [iii,iv].

- Hybrid sol-gel systems based on zirconium and titanium (IV) propoxide and 3-glycidoxypropyltrimethoxysilane as pretreatments for corrosion protection of AA2024 were developed and characterized [v].

- Mechanism of corrosion of the sol-gel coated AA2024 in microdefects was proposed based on the microstructural, corrosion and localized analysis by SVET and microelectrode techniques [vi].

- The possibility to employ EIS and SVET techniques for the analysis of self-healing effects on the sol-gel coated AA2024 with microdefects has been demonstrated [vii].

- Influence of inhibitors addition in the sol-gel systems on the corrosion protection and microstructure of the sol-gel coated alloy was investigated [viii].

- Application of titania self-assembled nanoporous layer was proposed as nanostructured reservoirs for self-healing sol-gel pretreatments applied on AA2024 [xi].

- Silica-core layer-by-layer coated nanocontainers of corrosion inhibitor for anticorrosion sol-gel coatings were developed [xii,xiii].

- Layer-by-layer coated halloysites nanocontainers with inhibitor for active corrosion protective coatings were created [xiv].

- Use of cerium molybdate nanowires as inhibitive additive for self-healing sol-gel coatings was proposed.

List of publications

i. K.A. Yasakau, M.L. Zheludkevich, S.V. Lamaka, M.G.S. Ferreira, Mechanism of corrosion inhibition of AA2024 by rare-earth compounds, Journal of Physical Chemistry B, 111, (2006) 5515.

ii. K.A. Yasakau, M.L. Zheludkevich, M.G.S. Ferreira, Study of the Corrosion Mechanism and Corrosion Inhibition of 2024 Aluminum Alloy by SKPFM Technique, Materials Science Forum, 587-588, (2008) 405.

iii. M.L. Zheludkevich, K.A. Yasakau, S.K. Poznyak, M.G.S. Ferreira, Triazole and Thiazole Derivatives as Corrosion Inhibitors for AA2024 Aluminium Alloy, Corrosion Science, 47, (2005) 3368.

iv. S.V. Lamaka, M.L. Zheludkevich, K.A. Yasakau, M.F. Montemor and M.G.S. Ferreira, High effective organic corrosion inhibitors for 2024 aluminium alloy. Electrochimica Acta, 52, (2007) 7231.

v. S.K. Poznyak, M.L. Zheludkevich, D. Raps, F. Gammel, K.A. Yasakau, M.G.S. Ferreira, Preparation and corrosion protective properties of nanostructured titania-containing hybrid sol-gel coatings on AA2024, Progress in Organic Coatings, 62, (2008) 226.

vi. A. C. Bastos, O. V. Karavai, M. L. Zheludkevich, K. A. Yasakau, M. G. S. Ferreira, Localized Measurements of pH and Dissolved Oxygen as Complements to SVET in the Investigation of Corrosion at Defects in Coated Aluminum Alloy, Electroanalysis, 22, (2010) 2009.

vii. M.L. Zheludkevich, K.A. Yasakau, A.C. Bastos, O.V. Karavai and M.G.S. Ferreira, On the application of Electrochemical Impedance Spectroscopy to study the self-healing properties of protective coatings, Electrochemistry Communications, 9, (2007) 2622.

viii. K.A. Yasakau, M.L. Zheludkevich, O.V. Karavai, M.G.S. Ferreira, Influence of inhibitor addition on the corrosion protection performance of sol-gel coatings on AA2024, Progress in Organic Coatings, 63, (2008) 352.

ix. M.L. Zheludkevich, R. Serra, M.F. Montemor, K.A. Yasakau, I.M. Miranda Salvado, M.G.S. Ferreira, Nanostructured Sol-Gel Coatings Doped with Cerium Nitrate as Pre-Treatments for AA2024-T3: Corrosion Protection Performance, Electrochimica Acta, 51, (2005) 208–217.

x. W. Trabelsi, P. Cecílio, M.G.S. Ferreira, K. Yasakau, M.L. Zheludkevich and M.F. Montemor, Surface evaluation and electrochemical behaviour of doped silane pre-treatments on galvanised steel substrates, Progress in Organic Coatings, 59, (2007) 214.

xi. S.V. Lamaka, M.L. Zheludkevich, K.A. Yasakau, M.F.Montemor, P. Cecílio, M.G.S. Ferreira, TiOx self-assembled networks prepared by templating approach as nanostructured reservoirs for self-healing anticorrosion pre-treatments, Electrochemistry Communications, 8, (2006) 421.

xii. M.L. Zheludkevich, D.G. Shchukin, K.A. Yasakau, H. Möhwald, M.G.S. Ferreira, Anticorrosion coatings with self-healing effect based on nanocontainers loaded with corrosion inhibitor, Chemistry of Materials, 19, (2007) 402.

xiii. Dmitry G. Shchukin, Mikhail Zheludkevich, Kiryl Yasakau, Sviatlana Lamaka, Helmuth Möhwald, Mario G.S. Ferreira, Layer-by-layer assembled nanocontainers for self-healing corrosion protection, Advanced Materials, 18, (2006) 1672.

xiv. Dmitry G. Shchukin, S.V. Lamaka, K.A. Yasakau, M.L. Zheludkevich, M.G.S. Ferreira, H. Möhwald, Active Anticorrosion Coatings with Halloysite Nanocontainers, The Journal of Physical Chemistry C, 112, (2008) 958.

xv. M.F. Montemor, W. Trabelsi, S.V. Lamaka, K.A. Yasakau, M.L. Zheludkevich, A.C. Bastos, M.G.S. Ferreira. The synergistic combination of bis-silane and CeO2.ZrO2 nanoparticles on the electrochemical behavior of galvanized steel in NaCl solutions. Electrochimica Acta, Electrochimica Acta, 53, (2008) 5913.

8.2 Recommendations for future work

The obtained results demonstrate the applicability of the sol-gel coatings as pretreatments for corrosion protection of 2024 aluminum alloy. Active corrosion protective properties of the sol-gel coatings can be enhanced when adding different nanocontainers with inhibitors. Electrochemical studies clearly show the positive effect of inhibitors addition on the corrosion protection conferred by the sol-gel coatings. Nevertheless, the obtained results still on lab-scale with technology readiness level (TRL) of 3 and there are some questions that remain unanswered. The purpose of this section is to give some recommendations for future work. These recommendations can be separated in two major parts:

1. Performing an additional study of the sol-gel systems and inhibitive additives

2. Upscailing of the sol-gel coating process for industrial level (TRL6) and testing of full protection system containing active corrosion protective pretreatments coated by primer and top coating.

The following important points should be addressed in the first part. The barrier protection properties of the proposed sol-gel pretreatments can be further improved. Different crosslinking additives and silane derivatives such as epoxy oligomers, amines, amino silanes, tetraethoxysilane, tris(trimethylsilyl)phosphate, Methyltriethoxysilane, Phenyl trimethoxysilane, Vinyltrimethoxysilane, (3-Mercaptopropyl)trimethoxysilane and others may be used to manipulate the crosslinking degree, thickness and adhesion properties of the sol-gel systems. Microstructural, chemical and corrosion characterization methods can be used for analyzing the obtained coatings.

The experiments showed that the incorporation of inhibitors in the sol-gel systems increases their active corrosion protection performance, though such effect does not last for a long time. The lack of inhibitor in the sol-gel coatings can be a major reason for a short active protection. Therefore there is a need to increase the inhibitor loading degree in the sol-gel without deterioration of the barrier protection of the coatings. Compounds with anion or cation exchange properties such as Layered double hydroxides (LDH) like Hydrotalcite and Wyoming Bentonite can be used as containers of inhibitor and incorporated in the sol-gel systems. The inhibitive ions containing in LDH or bentonite can be exchanged with ionic species present in the corrosive environment thus releasing an inhibitive agent into the solution. The other perspective approach is the synthesis and use of nanoparticulated inhibitive compounds in order to avoid the presence of bulk containers in the coatings. Halloysites nanocontainers must be additionally studied as perspective containers for different inhibitors loading and controlled delivery. A study of inhibitor release properties should be also made for different doped sol-gel coatings in order to characterize the efficiency of inhibitor delivery.

The second part of the study addresses the preparation and testing of full protection systems containing pretreatments coated by primer and top coating. The sol-gel coatings are applied by a conventional dipcoating method in laboratory scale. However in industry such method can not be applied due to great expenses associated with the use of huge amount of reagents. To solve such problem another coating method namely spray coating can be used. The preliminary experiments show that the formed film is relatively thick what causes the appearance of defects and cracks. Nevertheless, the proper adjustment of the working parameters of the spray coating machine like air flow, nozzle width, spraying speed and others can actually help to overcome the disadvantages. A complete protection system based on pretreatments obtained by a spray coating method must be analyzed in details from the point of view of corrosion protection, microstructure and adhesion.

One of the important properties of full protection system is active corrosion protection. Therefore the main direction of the study can be addressed to finding corrosion protective pigments for incorporation in the complete coating system. A good candidate as a corrosion protective pigment can be LDH which in preliminary experiments showed a positive effect on the corrosion protective properties of the complete coating system. Different inorganic or organic inhibitive anions can be loaded into LDH and tested as corrosion pigments in full protection systems. New pigments based on low soluble magnesium, strontium and zinc vanadates can be also considered as perspective corrosion protection additives due to good corrosion inhibition properties of vanadate anions. The proposed pigments are less toxic compared to chromates and can be promising substitutes of chromate based pigments in industry. The preparation of micro capsules loaded with a "healing" agent has been described in different patents and articles. A healing agent inside the capsule can be different organic inhibitor or polymerizing agents. The use of such capsules with inhibitor in protective coatings is very attractive because of high inhibitor loading which will be beneficial for self-healing abilities. The capsules may be prepared with a size around some microns which is enough for incorporation in the primer coating.

A corrosion protection system containing inhibited sol-gel pretreatment and primer with top coating can be tested using accelerated corrosion tests such as salt spray test, filiform corrosion test, adhesion tests and others. Conventional corrosion testing techniques like EIS, DC polarization can be used to monitor the degradation of the coating system in time. The localized method of corrosion analysis such as SVET has advantage to study self-healing processes in defects compared to conventional corrosion techniques. The studies performed by SVET give additional information on active corrosion protective properties of the coatings. The obtained results might be of great importance for the industry to substitute the present protection systems.

Bibliographic references

1. K. A. Korinek, Chromate Conversion Coatings, in Metals Handbook, Corrosion, 13, ASM International, Metals Park, OH, (1987), p. 389.

2. H. G. Seiler, Handbook on Toxicity of Inorganic Compounds, Marcel Dekker, NY, (1988).

3. P. L. Hagans and C. M. Haas, Chromate Conversion Coatings, in ASM Handbook, Vol. 5, Surface Engineering, ASM International, Metals Park, OH, (1994), p.405.

4. S. Xianglin, N. S. Dalal, Environ. Health Perspect., 102, (1994) 231.

5. E. A. Starke, J. T. Staley, Prog. Aerospace Sci., 32, (1996) 131.

6. R. W. Revie, "Uhlig's corrosion handbook," New York, Wiley (2000).

7. J. O. Park, C. H. Paik, Y. H. Huang, and R. C. Alkire, J. Electrochem. Soc., 146, (1999) 517.

8. Q. Meng and G. S. Frankel, J. Electrochem. Soc., 151, (2004) B271.

9. N. Birbilis, M. K. Cavanaugh, R. G. Buchheit, Corros. Sci. 48, (2006) 4202.

10. N. Birbilis, and R. G. Buchheit, J. Electrochem. Soc., 152, (2005) B140.

11. W. Zhang, G. S. Frankel, Electrochim. Acta, 48, (2003) 1193.

12. J. M. C. Mol, B. R. W. Hinton, D. H. Van Der Weijde, J. H. W. de Wit, S. Van Der Zwaag, J. Mat. Sci., 35, (2000) 1629.

13. D. Battocchi, J. He, G. P. Bierwagen, D. E. Tallman, Corros. Sci., 47, (2005) 1165.

14. P. Leblanc and G. S. Frankel, J. Electrochem. Soc., 149, (2002) B239.

15. R. G. Buchheit, R. P. Grant, P. F. Hiava, B. Mckenzie, and G. Zender, J. Electrochem. Soc., 144, (1997) 2621.

16. Weilong Zhang and G. S. Frankel, J. Electrochem. Soc., 149, (2002) B510.

17. J. A. Dean, Lange's Handbook of chemistry, 12-th edition, McGraw-Hill Book Company, NY, (1978).

18. R. G. Buchheit, L. P. Montes, M. A. Martinez, J. Michael, and P. F. Hlava, J. Electrochem. Soc., 146, (1999) 4424.

19. M. Pourbaix, Atlas of electrochemical equilibrium in aqueous solutions, National Association of Corrosion Engineers, Houston, TX, (1974).

20. L. L. Shreir, G. T. Burstein, R. A. Jarman, Corrosion: Metal - Environment reactions, Butterworth-Heinemann, Oxford, BO, (1994).

21. G. S. Frankel, J. Electrochem. Soc., 145, (1998) 2186.

22. H. H. Uhlig, J. Electrochem. Soc., 97, (1950) 215C.

23. N. Sato, Electrochimica Acta, 16, (1971) 1683.

24. P. Marcus and J. M. Herbelin, Corrosion Science, 34, (1993) 1123.

25. G. Faita, F. Mazza, and G. Bianchi, Role of Water and Ionic Solvation, in Localized Corrosion Phenomena, R.W. Stahle et al. Ed., NACE, Houston, TX, (1974).

26. D. Jones, Principles and Prevention of Corrosion, sec. edition, Prentice Hall, Inc., NJ, (1996).

27. R. H. Jones, D. R. Baer, M. J. Danielson, J. S. Vetrano, Metall. Mater. Trans., A 32, (2001) 1251.

28. J. R. Galvele and S. M. de De Micheli, Corros. Sci., 10, (1970) 795.

29. K. Urushino and K. Sugimoto, Corros. Sci., 19, (1979) 225.

30. H. A. Katzman, G. M. Malouf, R. Bauer, and G. W. Stupian, Appl. Surf. Sci., 2, (1979) 416.

31. M. A. Heine and M. J. Pryor, J. Electrochem Soc., 114, (1967) 1001.

32. J. Zhao, G. S. Frankel, and R. L. McCreery, J. Electrochem. Soc., 145, (1998) 2258.

33. J. Vander Kloet, W. Schmidt, A.W. Hassel, M. Stratmann, Electrochim. Acta, 49, (2004) 1675.

34. A. Sehgal, G. S. Frankel, B. Zoofan, and S. Rokhlin, J. Electrochem. Soc., 147, (2000) 140.

35. P. Schmutz and G. S. Frankel, J. Electrochem. Soc., 146, (1999) 4461.

36. A. Kolics, A. S. Besing, and A. Wieckowski, J. Electrochem. Soc., 148, (2001) B322.

37. W. J. Clark, J. D. Ramsey, R. L. McCreery, and G. S. Frankel, J. Electrochem. Soc. 149, (2002) B179.

38. M. Kendig, S. Jeanjaquet, R. Addison, J. Waldrop, Surf. Coat. Technol., 140, (2001) 58.

39. M. Kendig, R. Addison, and S. Jeanjaquet, J. Electrochem. Soc., 146, (1999) 4419.

40. R. L. Cook, Jr. and S. R. Taylor, Corrosion, 56, (2000) 321.

41. R. L. Twite, G. P. Bierwagen, Prog. Org. Coat., 33, (1998) 91.

42. P. Roberge, Handbook of corrosion engineering, McGraw-Hill, New-York, (2000).

43. F. M. Seon, J. Less, Common Met. 148, (1989) 73.

44. A. J. Aldykewicz, Jr., H. S. Isaacs, and A. J. Davenport, J. Electrochem. Soc., 142, (1995) 3342.

45. A. J. Aldykewicz, A. J. Davenport, H. S. Isaacs, J. Electrochem. Soc., 143, (1996) 147.

46. M. Bethencourt, F. J. Botana, J. J. Calvino, M. Marcos and M. A. Rodriguez-Chacon, Corros. Sci., 40, (1998) 1803.

47. M. A. Jakab, F. Presuel-Moreno and J. R. Scully, J. Electrochem. Soc., 153, (2006) B244.

48. T. A. Markley, M. Forsyth, A. E. Hughes, Electrochim. Acta, 52, (2007) 4024.

49. M. Iannuzzi, T. Young, and G. S. Frankel, J. Electrochem. Soc., 153, (2006) B533.

50. M. Iannuzzi, G.S. Frankel, Corros. Sci., 49, (2007) 2371.

51. K. D. Ralston, S. Chrisanti, T. L. Young, and R. G. Buchheit, J. Electrochem. Soc., 155, (2008) C350.

52. C. B. Breslin, G. Treacy, W. M. Carroll, Corros. Sci., 36, (1994) 1143.

53. K. C. Emregul, A. A. Aksut, Corros. Sci., 45, (2003) 2415.

54. B. A. Shaw, G. D. Davis, T. L. Fritz, K. A. Olver, J. Electrochem. Soc., 137, (1990) 359.

55. F. J. Presuel-Moreno, M. A. Jakab, and J. R. Scully, J. Electrochem. Soc., 152, (2005) B376.

56. R. L. Twite, G. P. Bierwagen, Prog. Org. Coat., 33, (1998) 91.

57. R. C. MacQueen, R. R Miron, R. D. Granata, J. Coat. Technol., 68, (1996) 75.

58. Y.I. Kuznetsov, Organic Inhibitors of Corrosion of Metals, Plenum Press, New York, (1996).

59. F. Zucchi, G. Trabanelli and M. Fonsati, Corros. Sci., 38, (1996) 2019.

60. G.P. Cicileoa, B. M. Rosalesa, F. E. Varelab, J.R. Vilche, Corros. Sci., 41, (1999) 1359.

61. L. Garrigues, N. Pebere, F. Dabosi, Electrochim. Acta, 41, (1996) 1209.

62. M. M. Stefenel, B. M. Vuano, and C. E. Mayer, Corrosion, 57, (2001) 898.

63. O. L. Blajiev, T. Breugelmans, R. Pintelon, H. Terryn, A. Hubin, Electrochim. Acta., 53, (2008) 7451.

64. D. Trornans and R. Sun, J. Electrochem. Soc., 138, (1991) 3235.

65. G. P. Bierwagen, Prog. Org. Coat., 28, (1996) 43.

66. G. W. Critchlow and D. M. Brewis, Int. J. Adhes. Adhes., 16, (1996), 255.

67. G. W. Critchlow, K. A. Yendall, D. Bahrani, A. Quinn, F. Andrews, Int. J. Adhes. Adhes., 26, (2006) 419.

68. C. E. Moffitt, D. M. Wieliczka, H.K. Yasuda, Surf. Coat. Technol., 137, (2001) 188.

69. P. Campestrini, G. Goeminne, H. Terryn, J. Vereecken, J.H.W. de Wit, J. Electrochem. Soc., 151, (2004) B59.

70. P. Campestrini, H. Terryn, J. Vereecken, J.H.W. de Wit, J. Electrochem. Soc., 151, (2004) B359.

71. M. W. Kendig, A. J. Davenport and H. S. Isaacs, Corros. Sci., 34, 1993, 41.

72. J. Zhao, L. Xia, A. Sehgal, D. Lu, R. L. McCreery, G. S. Frankel, Surf. Coat. Technol., 140, (2001) 51.

73. D. E. Tallman, G. Spinks, A. Dominis, G.G. Wallace, J. Solid. State. Electrochem., 6, (2002) 73.

74. G. Mengoli, M. Munari, P. Bianco, M. Musiani, J. Appl. Polymer Sci., 26, (1981) 4247.

75. G. Spinks, A. Dominis, G. G. Wallace, D. E. Tallman, J. Solid. State. Electrochem., 6, (2002) 85.

76. F. Beck, R. Michaelis, F. Schloten, B. Zinger, Electrochim. Acta., 39, (1994) 229.

77. G. Spinks, A. Dominis, G. G. Wallace, D. E. Tallman, J. Solid. State. Electrochem., 6, (2002) 85.

78. P. J. Kinlen, D. C. Silverman, C. R. Jeffreys, Synthetic. Met., 85, (1997) 1327.

79. D. E. Tallman, Y. Pae, G. P. Bierwagen, Corrosion, 55, (1999) 779.

80. V. Brusic, M. Angelopoulos, T. Graham, J. Electrochem. Soc., 144, (1997) 436.

81. G. Paliwoda-Porebska, M. Stratmann, M. Rohverder, K. Potje-Kamloth, Y.Lu, A. Z. Pich, H. J. Adler, Corros. Sci., 47, (2005) 3216.

82. M. Kendig, M. Hon, L. Warren, Prog. Org. Coat., 47, (2003) 183.

83. J. C. Lacroix, J. L. Camalet, S. Aeiyach, K. I. Chane-Ching, J. Petitjean, E. Chauveau, P. C. Lacaze, J. Electroanal. Chem., 481, (2000) 76.

84. L. Cecchetto, R. Ambat, A. J. Davenport, D. Delabouglise, J. P. Petit, O. Neel, Corros. Sci., 49, (2007) 818.

85. D. E. Tallman, Y. Pae, G. P. Bierwagen, Corrosion, 56, (2000) 401.

86. A. J. Epstein, J. A. O. Smallfield, H. Guan, M. Fahlman, Synth. Met., 102, (1999) 1374.

87. R. J. Racicot, S. C. Yang, R. Brown, Mater. Res. Soc. Symp., 458, (1997) 415.

88. M. A. Arenas, L. G. Bajos, J. J. de Damborenea, P. Ocon, Prog. Org. Coat., 62, (2008) 79.

89. T. P. McAndrew, Trends. Polym. Sci., 5, (1997) 7.

90. S. P. Sitaram, J. O. Stoffer, T.J. Okeefe, J. Coat. Technol., 69, (1997) 65.

91. W-K. Lu, S. Basak, R.L. Elsenbaumer, Corrosion inhibitionbn of metals by conductive polymers, in Handbook of conducting polymers, T.A. Skotheim, R.L. Elsenbaumer, J.R. Reynolds Ed., Dekker, New York (1998).

92. J. S. Solomon and D. E. Hanlin, Appl. Surf. Sci., 4, (1980) 307.

93. I. De Graeve, H. Terryn, G.E. Thompson, Electrochim. Acta, 52, (2006) 1127.

94. R. P. Digby and D. E. Packham, Int. J. Adhes. Adhes., 15, (1995) 61.

95. F. Mansfeld, and M. W Kendig, J. Electrochem. Soc., 135, (1988) 828.

96. T. Dimogerontakis, L. Kompotiatis and I. Kaplanoglou, Corros. Sci., 40, (1998) 1939.

97. M. A. Paez, O. Bustos, G. E. Thompson, P. Skeldon, K. Shimizu and G. C. Wood, J Electrochem. Soc., 147, (2000) 1015.

98. X. Zhou, G. E. Thompson, H. Habazaki, M. A. Paez, K. Shimizu, P. Skeldon and H. Wood, J Electrochem. Soc., 147, (2000) 1747.

99. G. E. Thompson, H. Habazaki, K. Shimizu, M. Sakairi, P. Skeldon, X. Zhou and G. C. Wood, Int. J. Aircraft. Eng. Aerosp. Technol., 71, (1999) 228.

100. G. W. Critchlow and D. M. Brewis, J. Adhes., 61, (1997) 213.

101. J. F. Ying, B. J. Flinn, M. Y. Zhou, P. C. Wang, K. A. R. Mitchell and T. Foster, Prog. Surf. Sci., 50, (1995) 259.

102. D. Susac, X. Sun, R. Y. Li, K. C. Wong, P. C. Wong, K. A. R. Mitchell, R. Champaneria, Appl. Surf. Sci., 239, (2004) 45.

103. J. Bibber, Met. Finish., 96, (1998) 28.

104. J. Bibber, Met. Finish., 99, (2001) 15.

105. A. E. Hughes, J. D. Gorman, T. G. Harvey, A. Galassi, and G. McAdam, Corrosion, 62, (2006) 773.

106. S. A. Kulinich, A. S. Akhtar, P. C. Wong, K. C. Wong, K. A. R. Mitchell, Thin Solid Films, 515, (2007) 8386.

107. D. Hawke and D. L. Albright, Met. Finish., 93, (1995) 34.

108. C. S. Lin, C. Y. Lee, W. C. Li, Y. S. Chen and G. N. Fang, J. Electrochem. Soc., 153, (2006) B90.

109. T. Schram, G. Goeminne, H. Terryn, W. Vanhoolst and P. Van Espen, Trans. Inst. Met. Finish., 73, (1995) 91.

110. L. Fedrizzi, F. Deflorian, P. L. Bonora, Electrochim. Acta, 42, (1997) 969.

111. L. Fedrizzi, A. Bianchi, F. Deflorian, S. Rossi, P. L. Bonora, Electrochim. Acta, 47, (2002) 2159.

112. O. Lunder, F. Lapique, B. Johnsen, K. Nisancioglu, Int. J. Adhes. Adhes., 24 (2004) 107.

113. M. F. Montemor , A. M. Simoes, M. G. S. Ferreira, M. J. Carmezim, Appl. Surf. Sci., 254, (2008) 1806.

114. O. Lunder, C. Simensen, Y. Yu, K. Nisancioglu, Surf. Coat. Technol., 184, (2004) 278.

115. F. Andreatta, A. Turco, I. de Graeve, H. Terryn, J.H.W de Wit, L. Fedrizzi, Surf. Coat. Technol. 201, (2007) 7668.

116. F. Mansfeld, V. Wang, and H. Shih, J. Electrochem. Soc., 138, (1991) L74.

117. M. Dabala, L. Armelao, A. Buchberger, I. Calliari, Appl. Surf. Sci., 172, (2001) 312.

118. W. G. Fahrenholtz, M. J. O'Keefe, H. Zhou, J. T. Grant, Surf. Coat. Technol., 155, (2002) 208.

119. M. Dabala, E. Ramous and M. Magrini, Mater. Corros., 55, (2004) 381.

120. B. F. Rivera, B. Y. Johnson, M. J. O'Keefe, W. G. Fahrenholtz, Surf. Coat. Technol., 176, (2004) 349.

121. P. Campestrini, H. Terryn, A. Hovestad, J.H.W. de Wit, Surf. Coat. Technol., 176, (2004) 365.

122. A. Decroly, J.Petitjean, Surf. Coat. Technol., 194, (2005) 1.

123. J. D. Minford, Handbook of aluminum bonding technology and data, Marcel Dekker, New York, (1993).

124. F. Mansfeld, C. Chen, C. B. Breslin, and D. Dull, J. Electrochem. Soc., 145, (1998) 2792.

125. V. Moutarlier, M. P. Gigandet, L. Ricq, J. Pagetti, Applied Surf. Sci., 183, (2001) 1.

126. X. Yua, C. Cao, Thin Solid Films, 423, (2003) 252.

127. E. Almeida, T. C. Diamantino, M. O. Figueiredo, C. Sa, Surf. Coat. Tech., 106, (1998) 8.

128. Z. Yong, J. Zhu, C. Qiu, Y. Liu, Appl. Surf. Sci., 255, (2008) 1672.

129. A. A. O. Magalhaes, I. C. P. Margarit, O. R. Mattos, J. Electroanal. Chem., 572, (2004) 433.

130. G. M. Treacy, G. D. Wilcox, M. O. W. Richardson, J. Appl. Electrochem., 29, (1999) 647.

131. J. A. Wharton, D. H. Ross, G. M. Treacy, G. D. Wilcox, K. R. Baldwin, J. Appl. Electrochem., 33, (2003) 553.

132. H. Guan and R. G. Buchheit, Corrosion, 60, (2004) 284.

133. K. H. Yang, M. D. Ger, W. H. Hwub, Y. Sungc, Y. C. Liu, Mater. Chem. Phys., 101, (2007) 480.

134. F. Mansfeld, Y. Wang, H. Shih, Electrochim. Acta, 37, (1992) 2277.

135. F. Mansfeld, F.J. Perez, Thin Solid Films, 270, (1995) 417.

136. C. Wang, F. Jiang, F. Wang, Corrosion, 60, (2004) 237.

137. L. E. M. Palomino, I. V. Aoki, H. G. de Melo, Electrochim. Acta, 51, (2006) 5943.

138. K Aramaki, Corros. Sci., 47, (2005) 1285.

139. K Aramaki, Corros. Sci., 45, (2003) 1085.

140. A. M. Beccaria and L. Chiaruttini, Corros. Sci., 41, (1999) 885

141. A. Franquet, C. Le Pen, H. Terryn, J. Vereecken, Electrochim. Acta, 48, (2003) 1245.

142. I. De Graeve, E. Tourwe, M. Biesemans, R.Willem, H. Terryn, Prog. Org. Coat., 63, (2008) 38.

143. D. Zhu, W. J. van Ooij, Corros. Sci., 45, (2003) 2177.

144. D. Zhu, W. J. van Ooij, Corros. Sci., 45, (2003) 2163.

145. W. J. van Ooij and D. Zhu, Corrosion, 157, (2001) 413.

146. A. N. Rider, D. R. Arnott, Int. J. Adhes. Adhes., 20, (2000) 209.

147. P. R. Underhill, A. N. Rider, D. L. DuQuesnay, Int. J. Adhes. Adhes., 23, (2003) 307.

148. J. M. Hu, L. Liu, J. Q. Zhang, C. N. Cao, Prog. Org. Coat., 58, (2007) 265.

149. A. M. Cabral, R. G. Duarte, M. F. Montemor, M. G. S. Ferreira, Prog. Org. Coat., 54, (2005) 322.

150. F. Zucchi, V. Grassi, A. FrignaniT, C. Monticelli, G. Trabanelli, Surf. Coat. Technol., 200, (2006) 4136.

151. M. F. Montemor, M. G. S. Ferreira, Prog. Org. Coat., 60, (2007) 228.

152. M. F. Montemor, A. M. Cabral, M. L. Zheludkevich, M. G. S. Ferreira, Surf. Coat. Technol., 200, (2006) 2875.

153. M. F. Montemor, A. Rosqvist, H. Fagerholm, M. G. S. Ferreira, Prog. Org. Coat., 51, (2004) 188.

154. W. J. van Ooij, D. Zhu, M. Stacy, A. Seth, T. Mugada, J. Gandhi, P. Puomi, Tsingua Science and Technology, 10, (2005) 639.

155. V. M. Palanivel, M.Sc. thesis, University of Cincinnati, Cincinnati, (2003).

156. D. Zhu, Ph.D. thesis, University of Cincinnati, Department of Materials Science and Engineering, Cincinnati, (2005).

157. E. P. Plueddemann, Silane Coupling Agents, 2nd ed., Plenum Press, New York, (1991).

158. V. Subramanian, W. J. van Ooij, Corrosion, 54, (1998) 204.

159. P. Puomi, Ph.D. thesis, Department of Physical Chemistry, Abo Akademi University, Abo, (2000).

160. M. A. Pefrunin, A. P. Nazarov, and Y. N. Mikhailovski, J. Electrochem. Soc., 143, (1996) 251.

161. M. Abel, R. P. Digby, I. W. Fletcher and J. F. Watts, Surf. Int. Anal., 29, (2000) 115.

162. M. Sheffer, A. Groysman, D. Mandler, Corros. Sci., 45, (2003) 2893.

163. V. Palanivel, Y. Huang, W.J. van Ooij, Prog. Org. Coat., 53, (2005) 153.

164. A. M. Cabral, W. Trabelsi, R. Serra, M. F. Montemor, M. L. Zheludkevich, M. G. S. Ferreira, Corros. Sci., 48, (2006) 3740.

165. W. Trabelsi, P. Cecilio, M. G. S. Ferreira and M. F. Montemor, Prog. Org. Coat., 54, (2005) 276.

166. M. G. S. Ferreira, R. G. Duarte, M. F. Montemor, A. M. P. Simões, Electrochim. Acta, 49, (2004) 2927.

167. W. Trabelsi, E. Triki, L. Dhouibi, M. G. S. Ferreira, M. L. Zheludkevich, M. F. Montemor, Surf. Coat. Technol., 200, (2006) 4240.

168. K. Aramaki, Corros. Sci., 44, (2002) 1621.

169. V. Palanivel, D. Zhu, W. J. van Ooij, Prog. Org. Coat., 47, (2003) 384.

170. M. F. Montemor, M. G. S. Ferreira, Electrochim. Acta, 52, (2007) 6976.

171. A. Hardy et al., In Ultrastructure Processing of Advanced Ceramics; J.D. Mackenzie, D.R. Ulrich, Ed., Wiley, New York, (1988) p 407.

172. J. Phalippou, M. Prassas, J. J. Zarzycki, J. Non-Cryst. Solids, 48, (1982) 17.

173. T. Yazawa, H. Tanaka, H. Nakamichi, T. Yokoyama, J. Membr. Sci., 60, (1991) 307.

174. H. J. Dislich, J. Non-Cryst. Solids, 72, (1985) 599.

175. K. Kamiya, S. Sakka, Y. J. Tatemichi, Mater. Sci., 15, (1980) 1765.

176. C. J. Brinker and G. Scherrer, Sol-gel Science: the Physics and Chemistry of Sol-Gel processing, Academic press, San Diego, CA, (1990).

177. J. Livage, M. Henry, Prog. Solid State Chem., 18, (1988) 259.

178. L. L. Hench, J. K. West, Chem. Rev., 90, (1990) 33.

179. T. L. Metroke, R. L. Parkhill, E. T. Knobbe, Prog. Org. Coat., 41, (2001) 233.

180. M. L. Zheludkevich, I. M. Salvado, M. G. S. Ferreira, J. Mater. Chem., 15, (2005) 5099.

181. M. Guglielmi, J. Sol-Gel Sci. Technol., 8, (1997) 443.

182. U. Schubert, N. Huesing, A. Lorenz, Chem. Mat., 7, (1995) 2010.

183. P. Judeinstein and C. Sanchez, J. Muter. Chem., 6, (1996) 511.

184. D. Niznansky and J. L. Rehspringer, J. Sol–Gel Sci. Technol., 180, (1995) 191.

185. D. Hoebbel, M. Nacken and H. Schmidt, J. Sol–Gel Sci. Technol., 12, (1998) 169.

186. Y. Castro, B. Ferrari, R. Moreno and A. Duran, J. Sol–Gel Sci. Technol., 26, (2003) 735.

187. T. P. Chou, C. Chandrasekaran and G. Z. Cao, J. Sol–Gel Sci. Technol., 26, (2003) 321.

188. R. F. Silva and W. L. Vasconcelos, Mater. Res., 2, (1999) 197.

189. C. Sanchez, G. J. de A. A. Soler-Illia, F. Ribot, T. Lalot, C. R. Mayer, and V. Cabuil, Chem. Mat., 13, (2001) 3061.

190. B. M. Novak, Adv. Mater., 5, (1993) 422.

191. H. K. Schmidt, J. Sol–Gel Sci. Technol., 8, (1997) 557.

192. L. Fedrizzi, F. J. Rodriguez, S. Rossi, F. Deflorian and R. Di Maggio, Electrochim. Acta, 46, (2001) 3715.

193. K. Watanabe, M. Sakairi, H. Takahashi, S. Hirai and S. Yamaguchi, J. Electroanal. Chem., 473, (1999) 250.

194. A. Balamurugan, S. Kannan and S. Rajeswari, Mater. Lett., 57, (2003) 4202.

195. J. Mendez-Vivar, R. Mendoza-Serna, L. Valdez-Castro, J. of Non-Cryst. Solids, 288, (2001) 200.

196. M. Rivallin, M. Benmami, A. Gaunand, A. Kanaev, Chem. Phys. Lett., 398, (2004) 157.

197. K. S. Suslick, G. J. Price, Annu. Rev. Mater. Sci., 29, (1999) 295.

198. K. S. Suslick, Science, 247, (1990) 1439.

199. M. Atik, F.P. Luna, S. H. Messaddeq, M. A. Aegerter, J. Sol–Gel Sci. Technol., 8, (1997) 517.

200. M. Vallet-Regi, I. Izquierdo-Barba and F. J. Gil, J. Biomed. Mater. Res., 67A, (2003) 674.

201. M. Atik, P. L. Neto, L. A. Avaca and M. A. Aegerter, Ceram. Int., 21, (1995) 403.

202. J. C. Yu, J. Yu, W. Ho and L. Zhang, Chem. Commun., 19, (2001) 1942.

203. B. Neppolian, Q. Wang, H. Jung, H. Choi, Ultrason. Sonochem., 15, (2008) 649.

204. K. Izami, M. Murakami, T. Deguchi, A. Morita, N. Tohge, and T, Minami, J. Am. Ceram. Soc., 72, (1989) 1465.

205. K. Miyazawa, K. Suzuki, and M. Y. Wey, J. Am. Ceram. Soc., 78, (1995) 347.

206. M. Guglielmi, D. Festa, P. Innocenzi, P. Colombo, M. Gobbin, J. Non-Cryst. Solids, 147, (1992) 474.

207. D. C. L. Vasconcelos, J. A. N. Carvalho, M. Mantel, W. L. Vasconcelos, J. Non-Cryst. Solids, 273, (2000) 135.

208. M. Khobaib, L. B. Reynolds, M. S. Donley, Surf. Coat. Technol., 140, (2001) 16.

209. S. Hofacker, M. Mechtel, M. Mager and H. Kraus, Prog. Org. Coat., 45, (2002) 159.

210. R. L. Ballard, J. P. Williams, J. M. Njus, B. R. Kiland, M. D. Soucek, Eur. Polym. J., 37, (2001) 381.

211. L. Mascia and T. Tang, J. Mater. Chem., 8, (1998) 2417.

212. S. Ono, H. Tsuge, Y. Nishi and S. Hirano, J. Sol–Gel Sci. Technol., 29, (2004) 147.

213. K.-H. Haas, Adv. Eng. Mater., 2, (2000) 571.

214. C. R. Mayer, V. Cabuil, T. Lalot, R. Thouvenot, Adv. Mater., 12, (2000) 417.

215. J. D. Mackenzie and E. P. Bescher, J. Sol–Gel Sci. Technol., 13, (1998) 371.

216. T. L. Metroke, J. S. Gandhi, A. Apblett, Prog. Org. Coat., 50, (2004) 231.

217. A. Conde, A. Duran, J. J. de Damborenea, Prog. Org. Coat., 46, (2003) 288.

218. F. Rubio, J. Rubio and J. L. Oteo, J. Sol–Gel Sci. Technol., 18, (2000) 105.

219. L. E. Amato, D. A. Lopez, P. G. Galliano and S. M. Cere, Mater. Lett., 59, (2005) 2026.

220. S. M. Kim, K. Chakrabarti, E. O. Oh and C. M. Whang, J. Sol–Gel Sci. Technol., 27, (2003) 149.

221. N. Voevodin, C. Jeffcoate, L. Simon, M. Khobaib, M. Donley, Surf. Coat. Tech., 140, (2001) 29.

222. R. L. Parkhill, E. T. Knobbe, M. S. Donley, Prog. Org. Coat., 41, (2001) 261.

223. T. L. Metroke, O. Kachurina and E. T. Knobbe, Prog. Org. Coat., 44, (2002) 295.

224. T. L. Metroke, O. Kachurina and E. T. Knobbe, Prog. Org. Coat., 44, (2002) 185.

225. T. P. Chou, C. Chandrasekaran, S. J. Limmer, S. Seraji, Y. Wu, M. J. Forbess, C. Nguyen, G. Z. Cao, J. Non-Cryst. Solids, 290, (2001) 153.

226. B. Smarsly, G. Garnweitner, R. Assink and C. J. Brinker, Prog. Org. Coat., 47, (2003) 393.

227. M. Sheffer, A. Groysman, D. Starosvetsky, N. Savchenko, D. Mandler, Corros. Sci., 46, (2004) 2975.

228. H. Ni, W. J. SimonsickJr., A. D. Skaja, J. P. Williams, M. D. Soucek, Prog. Org. Coat., 38, (2000) 97.

229. M. Mayrand, J. F. Quinson, A. Roche, V. Roisne and H. Guyon, J. Sol–Gel Sci. Technol., 12, (1998) 49.

230. R. A. Sailer and M. D. Soucek, Prog. Org. Coat., 33, (1998) 36.

231. C. Sanchez, B. LeBeau, F. Ribot, M. In, J. Sol–Gel Sci. Technol., 19, (2000) 31.

232. M. In, C. G´erardin, J. Lambart, and C. Sanchez, J. Sol-Gel Sci. Tech., 5, (1995) 101.

233. H. Schmidt, S. Langenfeld, R. Naß, Mater. Des., 18, (1997) 309.

234. F. Mammeri, E. Le Bourhis, L. Rozes and C. Sanchez, Mater. Chem., 15, (2005) 3787.

235. J. Malzbender, G. de With, Adv. Eng. Mater., 4, (2002) 296.

236. M. F. Montemor, M. G. S. Ferreira, Prog. Org. Coat., 63 (2008) 330.

237. P. H. Suegama, H. G. de Melo, A. A. C. Recco, A. P. Tschiptschin, I. V. Aoki, Surf. Coat. Technol., 202, (2008) 2850.

238. L. Liu, J. M. Hu, J. Q. Zhang, C. N. Cao, Electrochim. Acta, 52, (2006) 538.

239. Y. Chen, L. Jin and Y. Xie, J. Sol–Gel Sci. Technol., 13, (1998) 735.

240. J. Gallardo, A. Duran, I. Garcia, J. P. Celis, M. A. Arenas and A. Conde, J. Sol–Gel Sci. Technol., 27, (2003) 175.

241. A. J. Vreugdenhil, V. N. Balbyshev, M. S. Donley, J. Coat. Technol., 73, (2001) 35.

242. M. S. Donley, R. A. Mantz, A. N. Khramov, V. N. Balbyshev, L. S. Kasten, D. J. Gaspar, Prog. Org. Coat., 47, (2003) 401.

243. L. S. Kasten, V. N. Balbyshev, M. S. Donley, Prog. Org. Coat., 47, (2003) 214.

244. T. P. Chou, C. Chandrasekaran, G. Z. Cao, S. J. Limmer, C. Nguyen, J Mat Sci Let., 21, (2002) 251.

245. A. L. K. Tan, A. M. Soutar, I. F. Annergren, Y. N. Liu, Surf. Coat. Technol., 198, (2005) 478.

246. R. Supplita, T. Kochb and U. Schubert, Corros. Sci., 49, (2007) 3015.

247. A. N. Khramov, V. N. Balbyshev, L. S. Kasten and R. A. Mantz, Thin Solid Films, 514, (2006) 174.

248. X. F. Yang, D. E. Tallman, V. J. Gelling, G. P. Bierwagen, L. S. Kasten, J. Berg, Surf. Coat. Tech., 140, (2001) 44.

249. N. N. Voevodin, N. T. Grebasch, W. S. Soto, L. S. Kasten, J. T. Grant, F. E. Arnold, M. S. Donley, Prog. Org. Coat., 41, (2001) 287.

250. N. N. Voevodin, V. N. Balbyshev, M. S. Donley, Prog. Org. Coat., 52, (2005) 28.

251. Y. J. Dua, M. Damron, G. Tang, H. Zheng, C. J. Chua, J. H. Osborne, Prog. Org. Coat., 41, (2001) 226.

252. A. N. Khramov, V. N. Balbyshev, N. N. Voevodin, M. S. Donley, Prog. Org. Coat., 47, (2003) 207.

253. M. S. Donley, V. N. Balbyshev, N. N. Voevodin, Prog. Org. Coat., 52, (2005) 34.

254. L. S. Kasten, J. T. Grant, N. Grebasch, N. Voevodin, F. E. Arnold, M. S. Donley, Surf. Coat. Technol., 140, (2001) 11.

255. N. N. Voevodin, N. T. Grebasch, W. S. Soto, F. E. Arnold, M. S. Donley, Surf. Coat. Technol., 140, (2001) 24.

256. M. Garcia-Heras, A. Jimenez-Morales, B. Casal, J. C. Galvan, S. Radzki, M. A. Villegas, J. Alloys Compd., 380, (2004) 219.

257. A. Pepe, M. Aparicio, S. Cere, A. Duran, J. Non-Cryst. Solids, 348, (2004) 162.

258. L. Mascia, L. Prezzi, G. D. Wilcox, M. Lavorgna, Prog. Org. Coat., 56, (2006) 13.

259. N. N. Voevodin, V. N. Balbyshev, M. Khobaib, M. S. Donley, Prog. Org. Coat., 47, (2003) 416.

260. M. Quinet, B. Neveu, V. Moutarlier, P. Audebert, L. Ricq, Prog. Org. Coat., 58, (2007) 46.

261. A. N. Khramov, N. N. Voevodin, V. N. Balbyshev, M. S. Donley, Thin Solid Films, 447 –448, (2004) 549.

262. A. N. Khramov, N. N. Voevodin, V. N. Balbyshev, R. A. Mantz, Thin Solid Films, 483, (2005) 191.

263. A. J. Vreugdenhil, M. E. Woods, Prog. Org. Coat., 53, (2005) 119.

264. M. Rohwerder, F. Turcu, Electrochimica. Acta, 53, (2007) 290.

265. S. Yee, R. A. Oriani, M. Stratmann, J. Electrochem. Soc., 138, (1991) 55.

266. P. Schmutz and G. S. Frankel, J. Electrochem. Soc., 145, (1998) 2285.

267. M. Piens and R. Verbist, in Corrosion Control by Organic Coatings, H. Leidheiser, Jr. Ed., NACE, Houston, (1981) p. 32.

268. H. Leidheiser, Jr., Prog. Org. Coat., 7, (1979) 79.

269. E. Barsoukov and J.R. Macdonald, Impedance Spectroscopy Theory, Experiment, and Applications, Willey, New Jersey, (2005).

270. D. Schuhmann Electrochim. Acta, 35, (1990) 1527.

271. D. C. Grahame, J. Electrochem. Soc., 99, (1952) 370C.

272. J. E. B. Randles, Disc. Faraday Soc., 1, (1947) 11.

273. B. Erschler, Disc. Faraday Soc., 1, (1947) 269.

274. I. Epelboin, M. Keddam and H. Takenouti, J. Appl. Electrochem, 2, (1971) 71.

275. H. Potente and E. Braches, J. Adhes., 11, (1979) 34.

276. J. D. Scantlebury and K. N. Ho, J. Oil Colour Chem. Assoc., 62, (1979) 89.

277. L. Beaunier, I. Epelboin, J. C. Lestrade and H. Takenouti, Surface Techn., 4, (1976) 237.

278. F. Mansfeld, M. W. Kendig, and S. Tsai, Corrosion 38, 478–485.

279. J. R. Scully, D. C. Silverman, M. W. Kending, Electrochemical impedance. Analysis and interpretation, ASTM STP 1 1 88, American Society for Testing and Materials, Philadelphia, (1993).

280. D. D. MacDonald, Transient Techniques in Electrochemistry, Plenum Press, New York, (1977).

281. J. R. MacDonald, Impedance Spectroscopy, Wiley, New York (1987).

282. C. M. A. Brett and A. M. O. Brett, Electrochemistry Principles, methods and applications, Oxford University Press, Oxford, (1993).

283. A. Amirudin, D.Thierry, Prog. Org. Coat., 26, (1995) 1.

284. D. Loveday, P. Peterson, and B. Rodgers, JCT CoatingsTech., 1, (2004) 46.

285. F. Mansfeld, Corrosion, 44, (1988) 558.

286. J. R. Macdonald and M. K. Brachman, Rev. Mod. Phys., 28, (1956) 393.

287. J. Schrama, Ph.D. thesis, University of Leiden, The Netherlands, (1957).

288. D. D. Macdonald and M. U. Macdonald, J. Electrochem. Soc., 132, (1985) 2316.

289. M.U. Macdonald, S. Real and D.D. Macdonald, J. Electrochem. Soc., 133, (1986) 2018.

290. H. Shih and F. Mansfeld, Corros. Sci., 29, (1988) 933.

291. H. Shih and F. Mansfeld. Corrosion, 45, (1989) 325.

292. M. Kendig, J. Scully, Corrosion, 46, (1990) 22.

293. J. Titz, G.H. Wagner, H. Spahn, M. Ebert, K. Juttner, W.J. Lorenz, Corrosion, 46, (1990) 221.

294. F. Mansfeld, J. Appl. Electrochem., 25, (1995) 187.

295. F. Mansfeld, M. W. Kending, S. Tsai, Corrosion, 38, (1982) 478.

296. P. L. Bonora, F. Deflorian, L. Fedrizzi, Electrochem. Acta, 41, (1996) 1073.

297. D. M. Brasher and A. H. Kingsbury, J. Appl. Chem., 4, (1954) 62.

298. F. Bellucci, L. Nicodemo, Corrosion, 49, (1993) 235.

299. F. S. A. Lindqvist, Corrosion, 41, (1985) 69.

300. A. S. Castela, A. M. Simoes, Corros. Sci., 45, (2003) 1631.

301. A. S. Castela, A. M. Simoes, Corros. Sci., 45, (2003) 1647.

302. R. G. Duarte, A. S. Castela, M. G. S. Ferreira, Prog. Org. Coat., 65 (2009) 197.

303. G. W. Walter, Corros. Sci., 32, (1991) 1041.

304. G. W. Walter, Corros. Sci., 2,6 (1986) 681.

305. R. D. Armstrong and J. D. Wright, Corros. Sci., 33, (1992) 1529.

306. M. Stern and A. Geary, J. Electrochem. Soc., 104, (1957) 56.

307. C. S. Hsu, F. Mansfeld, Corrosion, 57, (2001) 747.

308. I. Fatt, Polarographic oxygen sensors. Its theory of operation and its application in biology, medicine and technology, CRC Press, Cleveland, EUA (1976).

309. I.A. Silver, Phil. Trans. R. Soc. Lond. B, 316, (1987) 161.

310. O. Bluh, B. Scott, Rev. Inst., 10, (1950) 867.

311. L. F. Jaffe, R. Nucitelli, J. Cell Biology, 63, (1974) 269.

312. P. W. Davies, Fed. Proc., 25, (1966) 332.

313. H. S. Isaacs, G. Kissel, J. Electrochem. Soc., 119, (1972) 1628.

314. H. S. Isaacs, Y. Ishikawa, Applications of the vibrating probe to localized current measurements, in Electrochemical techniques for corrosion engineering, R. Baboian Ed., NACE, Houston, (1986).

315. H. S. Isaacs, J. Electrochem. Soc., 135, (1988) 2180.

316. H. S. Isaacs, A.J. Davenport and A. Shipley, J. Electrochem. Soc., 138, (1991) 390.

317. D. A. Worsley, H. N. McMurray and A. Belghazi, Chem. Commun., (1997) 2369.

318. K. Ogle, V. Baudu, L. Garrides, X. Philippe, J. Electrochem. Soc., 147, (2000) 3654.

319. H. S. Isaacs, Corrosion, 43, (1987) 594.

320. G. Grundmeier, K-M. Juttner, M. Shtratmann, Novel electrochemical techniques in corrosion research, in Corrosion and environmental degradation, M. Schutze Ed., WILEY-VCH, Weinheim, (2000).

321. T. Yasukawa, I. Uchida, T. Matsue, Biochim. Biophys. Acta, 1369, (1998) 152.

322. I. Fatt, Polarographic oxygen sensors. Its theory of operation and its application in biology, medicine and technology, CRC press, Cleveland, (1976).

323. S. C. Taylor, C. Peers, J. Neurochem., 73, (1999) 874.

324. D. Ammann, Ion-Selective microelectrodes, Springer-Verlag, Berlin Heidelber, (1986).

325. J. O. Park, C. H. Paik, R. C. Alkire, J. Electrochem. Soc., 143, (1996) L174.

326. K. Sugimoto, K. Asano, Analysis of localized corrosion on stainless steel by micro-complex pH-pCl electrode, in Advances in localized corrosion, H. Isaacs, U Bertocci, J. Kruger and S. Smialowska Ed., NACE, Houston, (1990).

327. P. Anker, H. B. Jenny, U. Wuthier, R. Asper, D. Ammann and W. Simon, Clin. Chem., 29, (1983) 1508.

328. F. Faridbod, M.R. Ganjali, B. Larijani, P. Norouzi, S. Riahi and F. S. Mirnaghi, Sensors, 7, (2007) 3119.

329. E. Tada, K. Sugawara, H. Kaneko, Electrochim. Acta, 49, (2004) 1019.

330. C. Sheffey, Electric fields and the vibrating probe, for the uninitiated, in Ionic currents in development, A.R. Liss Ed., A.R. Liss Inc., (1986), p. xxv.

331. C. Scheffey, Rev. Sci. Instrum., 59, (1988) 787.

332. Z. Liu, P. H. Chong, A. N. Butt, P. Skeldon, G. E. Thompson, Appl. Surf. Sci., 247, (2005) 294.

333. G. Kiourtsid, S. M. Skolianos, Mater. Sci. Eng., A 248, (1998) 165.

334. Yu. Yu Lur'e, Handbook of Analytical Chemistry (Spravochnik po analiticheskoi himii), 6-th ed., Himiya, (1989).

335. Z. Szklarska-Smialowska, Corros. Sci., 41, (1999) 1743.

336. R. G Buchheit, M. A. Martinez, L. P. Montes, J. Electrochem. Soc., 147, (2000) 119.

337. N. Dimitrov, J. A. Mann, K. Sieradzki, J. Electrochem. Soc., 146, (1999) 98.

338. A. Aballe, M. Bethencourt, F. J. Botana, M. Marcos, J. Alloys Compd., 323–324, (2001) 855.

339. V. Guillaumin, G. Mankowski, Corros. Sci., 41, (1999) 421.

340. F. Andreatta, H. Terryn, J. H. W. de Wit, Electrochim. Acta, 49, (2004) 2851.

341. S. A. Hayers, P. Yu, T. J. O´Keefe, J. O. Stoffer, J. Electrochem. Soc., 149, (2002) C623.

342. B. A. Bilal, E. Muller, Z. Naturforsch., A: Phys. Sci., 47, (1992) 974.

343. G. W. Poling, Corros. Sci., 10, (1970) 359.

344. V. Brusic, M. A. Frisch, B. N. Eldridge, F. P. Novak, F. B. Kaufman, B. M. Rush and G. S. Frankel, J. Electrochem. Soc., 138, (1991) 2253.

345. D. Tromans, J. Electrochem. Soc., 145, (1998) L42.

346. C. W. Yan , H. C. Lin, C. N. Cao, Electrochim. Acta, 45, (2000) 2815.

347. M. Ohsawa, W. Suetaka, Corros. Sci. 19, (1979) 709.

348. B. Trachli, M. Keddam, H. Takenouti and A. Srhiri, Prog. Org. Coat., 44, (2002) 17.

349. C. D. Wagner, in Practical Surface Analysis: Auger and X-ray Photoelectron Spectroscopy, Appendix 5, D. Briggs, M.P. Seah Ed., Wiley, Cichester, (1990), pp. 598– 625.

350. Y. Liu, P. Bailey, T. C. Q. Noakes, G. E. Thompson, P. Skeldon, M. R. Alexander, Surf. Interf. Anal., 36, (2004) 339.

351. V. Fournier, P. Marcus and I. Olefjord, Surf. Interf. Anal., 34, (2002) 49.

352. I. V. Tananaev, I. V. Vinogradova, Zh. Neorg. Khim., 2, (1957) 2455.

353. E. S. Tinovskaya, Zh. Anal. Khim., 5, (1950) 345.

354. R. Nasanen, E. Uusitalo, Acta Chem. Scand., 8, (1954) 835.

355. G. P. Ciccileo, B. M. Rosales, F. E. Varela, J. R. Vilche, Corros. Sci., 40, (1998) 1915.

356. J. F. Flagg, D. W. Vanas, Ind. Eng. Chem. Anal. Ed., 18, (1946) 436.

357. R. F. Pietzzak, L. Gordon, Talanta, 9, (1962) 327.

358. M. Jean, Bull. Soc. Chim., 10, (1943) 201.

359. Z. S. Muhina, Zavodskaya Laboratoriya, 12, (1946) 982.

360. M. Sarkar, Analyst, 116, (1991) 537.

361. http://www.chemexper.com

362. N. Steunou, F. Robert, K. Boubekeur, F. Ribot and C. Sanchez, Inorg. Chim. Acta, 279, (1998) 144.

363. U. Schubert, J. Mater. Chem., 15, (2005) 3701.

364. A. Leaustic, F. Babonneau and J. Livage, Chem. Mater., 1, (1989) 240.

365. A. Leaustic, F. Babonneau and J. Livage, Chem. Mater., 1, (1989) 248.

366. P. D. Moran, C. E. F. Rickard, G. A. Bowmaker, R. P. Cooney, J. R. Bartlett and J. L. Woolfrey, Inorg. Chem., 37, (1998) 1417.

367. A. Yamamoto and S. Kambara, J. Amer. Chem. Soc., 79, (1957) 4344.

368. G. D. Smith, C. N. Caughlan and J. A. Campbell, Inorg. Chem., 11, (1972) 2989.

369. P. Toledano, M. In, C. Sanchez, C. R. Acad, Sci. Paris Serie II, 311, (1990) 1161.

370. G. I. Spijksma, H. J. M. Bouwmeester, D. H. A. Blank and V. G. Kessler, Chem. Commun., (2004) 1874.

371. D. Peter, T. S. Ertel and H. Bertagnolli, J. Sol-Gel Sci. Technol., 5, (1995) 5.

372. J. Liu, T. Xu, M. Gong and Y. Fu, J. Membr. Sci., 264, (2005) 87.

373. M. J. Velasco, F. Rubio, J. Rubio and J. L. Oteo, Thermochim. Acta, 326, (1999) 917.

374. M. D. Hernandez-Alonso, I. Tejedor-Tejedor, J. M. Coronado, J. Soria, M.A. Anderson, Thin Solid Films, 502, (2006) 125.

375. G. Philipp, H. Schmidt, J. Non-Cryst. Solids, 82, (1986) 31.

376. D. Hoebbel, M. Nacken and H. Schmidt, J. Sol-Gel Sci. Technol., 21, (2001) 177.

377. J. D. Mackenzie, in Science of Ceramic Chemical Processing, L.L. Hench, D.R. Ulrich Ed., Wiley, New York, (1986) p 113.

378. M. Stratmann, A. Leng, W. Fiirbeth, H. Streckel, H. Gehmecker, K.-H. Grobe-Brinkhaus, Prog. Org. Coat., 27, (1996) 261-267.

379. A. Leng, H. Streckel, M. Stratmann, Corros. Sci., 30, (1999) 547.

380. B. J. Intorre, A. E. Martell, JACS, 83, (1961) 3618.

381. L. Garrigues, N. Pebere, F. Dabosi. Electrochim Acta., 41, (1996) 1209.

382. I. Devol and E. Bardez, J. Colloid Interface Sci., 200, (1998) 241.

383. G. J. A. A. Soler-Illia, E. Scolan, A. Louis, P. A. Albouy, C.Sanchez, New J. Chem., 25, (2001) 156.

384. M. Burgos and M. Langlet, Thin Solid Films, 349, (1999) 19.

385. G. Socrates, Infrared characteristic group frequencies, John Wiley and Sons, New York, (1994).

386. C. T. Lynch, K. S. Mazdiyasni, J. S. Smith and W. J. Crawford. Anal. Chem., 36, (1964) 2332.

387. P. C. Angelome, G. J. A. A. Soler-Illia, J. Mater. Chem., 15, (2005) 3903.

388. A. Chougnet, C. Heitz, E. Sondergard, J.-M. Berquier, P.-A. Albouy, M. Klotz, J. Mater. Chem., 15, (2005) 3340.

389. I. H. Joe, A. K. Vasudevan, G. Aruldhas, A. D. Damodaran, K. G. K.Warrier, J. Solid State Chem., 131, (1997) 181.

390. S. W. Boettcher, M. H. Bartl, J. G. Hu, G. D. Stucky, J. Am. Chem. Soc., 127, (2005) 9721.

391. A. A. Antipov, G. B. Sukhorukov, Adv. Colloid Interface Sci., 111, (2004) 49.

392. G. B. Sukhorukov, A. A. Antipov, A. Voigt, E. Donath, H. Mohwald, Macromol. Rapid Commun., 22, (2001) 44.

393. C. Dejugnat, D. Halozan, G. B. Sukhorukov, Macromol. Rapid Commun., 26, (2005) 961.

394. C. Dejugnat and G. B. Sukhorukov, Langmuir, 20, (2004) 7265.

395. G. Ibarz, L. Dähne, E. Donath, and H. Mohwald, Adv. Mater., 13, (2001) 1324.

396. S. Baral, S. Brandow, B. Gaber, J. Am. Chem. Soc., 116, (1994) 29.

397. R. Price, B. Gaber, Y. Lvov, J. Microencapsulation, 17, (2001) 713.